CONVECTION AND CONDUCTION HEAT TRANSFER

Edited by **Amimul Ahsan**

INTECHWEB.ORG

Convection and Conduction Heat Transfer
Edited by Amimul Ahsan

Published by InTech
Janeza Trdine 9, 51000 Rijeka, Croatia

Publishing Process Manager Ivana Lorkovic
Technical Editor Teodora Smiljanic
Cover Designer Jan Hyrat
Image Copyright ARENA Creative, 2011. Used under license from Shutterstock.com

First published September, 2011
Printed in Croatia

A free online edition of this book is available at www.intechopen.com
Additional hard copies can be obtained from orders@intechweb.org

Convection and Conduction Heat Transfer, Edited by Amimul Ahsan
p. cm.
ISBN 978-953-307-582-2

Contents

Preface IX

Part 1 Heat Convection 1

Chapter 1 **A Mixed Convection Study in Inclined Channels with Discrete Heat Sources 3**
Paulo M. Guimarães and Genésio J. Menon

Chapter 2 **Periodically Forced Natural Convection Through the Roof of an Attic-Shaped Building 33**
Suvash Chandra Saha

Chapter 3 **Analysis of Mixed Convection in a Lid Driven Trapezoidal Cavity 55**
M. A. H. Mamun, T. R. Tanim,
M. M. Rahman, R. Saidur and Shuichi Nagata

Chapter 4 **Convective Heat Transfer of Unsteady Pulsed Flow in Sinusoidal Constricted Tube 83**
J. Batina, S. Blancher,
C. Amrouche, M. Batchi and R. Creff

Chapter 5 **Numerical Solution of Natural Convection Problems by a Meshless Method 107**
Gregor Kosec and Božidar Šarler

Chapter 6 **Hydromagnetic Flow with Thermal Radiation 133**
Cho Young Han and Se-Myong Chang

Part 2 Heat Conduction 147

Chapter 7 **Transient Heat Conduction in Capillary Porous Bodies 149**
Nencho Deliiski

Chapter 8 **Non-Linear Radiative-Conductive Heat Transfer in a Heterogeneous Gray Plane-Parallel Participating Medium 177**
Marco T.M.B. de Vilhena, Bardo E.J. Bodmann and Cynthia F. Segatto

Chapter 9 **Optimization of the Effective Thermal Conductivity of a Composite 197**
Hubert Jopek and Tomasz Strek

Chapter 10 **Computation of Thermal Conductivity of Gas Diffusion Layers of PEM Fuel Cells 215**
Andreas Pfrang, Damien Veyret and Georgios Tsotridis

Chapter 11 **Analytical Methods for Estimating Thermal Conductivity of Multi-Component Natural Systems in Permafrost Areas 233**
Rev I. Gavriliev

Chapter 12 **Heating in Biothermal Systems 257**
Huang-Wen Huang and Chihng-Tsung Liauh

Chapter 13 **A Generalised RBF Finite Difference Approach to Solve Nonlinear Heat Conduction Problems on Unstructured Datasets 281**
D. Stevens, A. LaRocca, H. Power and V. LaRocca

Part 3 Heat Transfer Analysis 297

Chapter 14 **Heat Transfer Analysis of Reinforced Concrete Beams Reinforced with GFRP Bars 299**
Rami A. Hawileh

Chapter 15 **Modelling of Heat Transfer and Phase Transformations in the Rapid Manufacturing of Titanium Components 315**
António Crespo

Chapter 16 **Measurement of Boundary Conditions - Surface Heat Flux and Surface Temperature 341**
Wei Liu

Chapter 17 **Properties and Numerical Modeling-Simulation of Phase Changes Material 349**
Pavel Fiala, Ivo Behunek and Petr Drexler

Chapter 18 **Finite Element Methods to Optimize by Factorial Design the Solidification of Cu-5wt%Zn Alloy in a Sand Mold 377**
Moisés Meza Pariona and Viviane Teleginski

Preface

The convection and conduction heat transfer, thermal conductivity, and phase transformations are significant issues in a design of wide range of industrial processes and devices. This book includes 18 advanced and revised contributions, and it covers mainly (1) heat convection, (2) heat conduction, and (3) heat transfer analysis. The first section introduces mixed convection studies on inclined channels, double diffusive coupling, and on lid driven trapezoidal cavity, forced natural convection through a roof, convection on non-isothermal jet oscillations, unsteady pulsed flow, and hydromagnetic flow with thermal radiation. The second section covers heat conduction in capillary porous bodies and in structures made of functionally graded materials, integral transforms for heat conduction problems, non-linear radiative-conductive heat transfer, thermal conductivity of gas diffusion layers and multi-component natural systems, thermal behavior of the ink, primer and paint, heating in biothermal systems, and RBF finite difference approach in heat conduction. The third section includes heat transfer analysis of reinforced concrete beam, modeling of heat transfer and phase transformations, boundary conditions-surface heat flux and temperature, simulation of phase change materials, and finite element methods of factorial design. The advanced idea and information described here will be fruitful for the readers to find a sustainable solution in an industrialized society.

Acknowledgements

All praise be to Almighty Allah, the Creator and the Sustainer of the world, the Most Beneficent, Most Benevolent, Most Merciful, and Master of the Day of Judgment. He is Omnipresent and Omnipotent. He is the King of all kings of the world. In His hand is all good. Certainly, over all things Allah hast power.

The editor would like to express appreciation to all who have helped to prepare this book. The editor expresses his gratefulness to Ms. Ivana Lorkovic, Publishing Process Manager, InTech Open Access Publisher for its continued cooperation. In addition, the editor appreciatively remembers the assistance of all authors and reviewers of this book.

Gratitude is expressed to Mrs. Ahsan, Ibrahim Bin Ahsan, Mother, Father, Mother-in-Law, Father-in-Law, and Brothers and Sisters for their endless inspirations, mental supports and also necessary help whenever any difficulty.

Amimul Ahsan, Ph.D.
Department of Civil Engineering
Faculty of Engineering
University Putra Malaysia
Malaysia

Part 1

Heat Convection

1

A Mixed Convection Study in Inclined Channels with Discrete Heat Sources

Paulo M. Guimarães and Genésio J. Menon
Federal University of Itajubá
Brazil

1. Introduction

In the last two decades, heat transfer study on discrete heat sources has become a subject of increased interest due to advances in the electronics industry. Increased power dissipation is the most significant feature of new generation electronic devices and more significant heat flux densities are obtained as a result of miniaturization. Consequently, the assumption of cooling of electronic devices has increased interest in the analysis of fluid flow and heat transfer in discrete heating situations. Previous works have studied the natural, mixed, and forced convection in inclined channels due to their practical applications such as electronic systems, high performance heat exchangers, chemical process equipments, combustion chambers, environmental control systems and so on.

An interesting study was reported on the fluid flow and heat transfer characteristics associated with cooling an in-line array of discrete protruding heated blocks in a channel by using a single laminar slot air jet (Arquis et al., 2007). Numerical experiments were carried out for different values of jet Reynolds number, channel height, slot width, spacing between blocks, block height, and block thermal conductivity. The effects of variation of these parameters were detailed to illustrate important fundamental and practical results that are relevant to the thermal management of electronic packages. In general, the effective cooling of blocks was observed to increase with the increase of Reynolds number and the decrease of channel height. Circulation cells that may appear on the top surface of the downstream blocks were shown to decrease the value of Nusselt number for these blocks. The values of surface averaged Nusselt number attained their maximum at the block just underneath the impinging air jet, decreased for the downstream blocks, and approximately reached a constant value after the third block.

A numerical study (Madhusudhana & Narasimham, 2007) was carried out on conjugate mixed convection arising from protruding heat generating ribs attached to substrates forming a series of vertical parallel plate channels. A channel with periodic boundary conditions in the transverse direction was considered for analysis where identical disposition and heat generation of the ribs on each board were assumed. The governing equations were discretised using a control volume approach on a staggered mesh and a pressure correction method was employed for the pressure–velocity coupling. The solid regions were considered as fluid regions with infinite viscosity; and the thermal coupling between the solid and fluid regions was taken into account by the harmonic thermal

conductivity method. Parametric studies were performed by varying the heat generation based on Grashof number in the range 10^4–10^7 and the fan velocity was based on Reynolds number in the range 0–1500, with air as the working fluid. In pure natural convection, the induced mass flow rate varied at 0.44 power of Grashof number. The heat transferred to the working fluid via substrate heat conduction was found to account for 41–47% of the heat removal from the ribs.

The optimum position of a discrete heater was determined by maximizing the conductance and the heat transfer and volume flow rate with the discrete heater at its optimum position in open cavities by using the finite difference-control volume numerical method and considering air (Muftuoglu & Bilgen, 2007). The relevant governing parameters were: the Rayleigh numbers from 10^6 to 10^{12}, the cavity aspect ratio from 0.5 to 2, the wall thickness from 0.05 to 0.15, the heater size from 0.15 to 0.6, and the conductivity ratio from 1 to 50. They found that the global conductance was an increasing function of the Rayleigh number and the conductivity ratio, and a decreasing function of the wall thickness. The best thermal performance was achieved by positioning the discrete heater eccentrically and slightly closer to the bottom. The Nusselt number and the volume flow rate in and out the open cavity were an increasing function of the Rayleigh number and the wall thickness, and a decreasing function of the conductivity ratio. The Nusselt number was a decreasing function of the cavity aspect ratio and the volume flow rate was an increasing function of it.

Another work conducted a numerical investigation of conjugate convection with surface radiation from horizontal channels with protruding heat sources (Premachandran & Balaji, 2006). The air flow was assumed to be steady, laminar, incompressible, and hydrodynamically and thermally developed. The geometric parameters such as spacing between the channel walls, size of the protruding heat sources, thickness of the substrate and the spacing between the heat sources were fixed. One of the most relevant conclusions was that while carrying out a thermal analysis of a stack of circuit boards with electronic chips (discrete heat sources), the consideration of radiation heat transfer was absolutely essential to accurately predict the non-dimensional maximum temperature.

The mixed convection heat transfer in a top-and-bottom-heated rectangular channel with discrete heat sources using air was experimentally investigated (Dogan et al., 2005). The lower and upper surfaces of the channel were equipped with 8x4 flush-mounted heat sources subjected to uniform heat flux. The lateral and remaining lower and upper walls were insulated. The experimental study was carried out for an aspect ratio equal to 6, Reynolds numbers varying from 955 to 2220 and modified Grashof numbers $Gr^*=1.7x10^7$ to $6.7x10^7$. The surface temperature and Nusselt number distributions on the discrete heat sources were obtained. Results showed that the surface temperatures increased with increasing Grashof number. The row-averaged Nusselt numbers decreased with the row number and then, they showed an increase towards the exit as a result of heat transfer enhancement due to the invigoration of buoyancy forces that affected the secondary flow.

A work investigated melting from heat sources that are flush-mounted on discretely heated rectangular vertical enclosures (Binet & Lacroix, 2000). It finds its application in design and operation of thermal energy storage units and the cooling of electronic equipment. The results showed that there were benefits of discrete heating when it comes to optimizing the melting process. The aspect ratio was an important factor that may have led to controlled temperatures on the heat modules. For aspect ratios over 4, controlled temperatures and long melting time were obtained. On the other hand, for aspect ratios up to 4, the source

span influence was important, whenever it was less than 0.45, and eventually, the melting times were shorter and the temperatures on the sources remained equal and moderate throughout the melting process.

The turbulent convection heat transfer was experimentally investigated in an array of discrete heat sources inside a rectangular channel filled with air (Baskaya et al., 2005). The lower surface of the channel was equipped with 8x4 flush-mounted heat sources subjected to uniform heat flux. The sidewalls and the upper wall were insulated. The experimental parametric study was made for a constant aspect ratio, different Reynolds numbers, and modified Grashof numbers. Results showed that surface temperatures increased with increasing Grashof number and decreased with increasing Reynolds number. However, the increase in the buoyancy forces affected the secondary flow and the onset of instability, and, hence, the temperatures levelled off and even dropped as a result of heat transfer enhancement. This outcome could also be observed from the variation of the row-averaged Nusselt number showing an increase towards the exit.

A constructal theory was applied to the fundamental problem of how to arrange discrete heat sources on a wall cooled by forced convection (Silva et al., 2004). They aimed to maximize the conductance between the discrete heated wall and the fluid, that is, to minimize the temperature of the hot spot on the wall, when the heat generation rate was specified. The global objective was achieved by the generation of flow configuration, in this case, the distribution of discrete heat sources. Two different analytical approaches were used: (i) large number of small heat sources, and (ii) small number of heat sources with finite length, which were mounted on a flat wall. Both analyses showed that the heat sources should have been placed non-uniformly on the wall, with the smallest distance between them near the tip of the boundary layer. When the Reynolds number was high enough, then, the heat sources should have been mounted flushed against each other, near the entrance of the channel. The analytical results were validated by a numerical study of discrete heat sources that were non-uniformly distributed inside a channel formed by parallel plates.

In the present chapter, a heat transfer study in an inclined rectangular channel with heat sources is conducted. The heat source vertical and horizontal positions are also considered. Emphasis is given to the heat transfer distributions on the heat modules, showing their correlation with velocities due to their importance when thermal control in electronic equipments is aimed.

2. Problem description

Figure (1) depicts three heat source lay-outs that will be studied. A mixed convection study is performed in a channel with height H, length L, and inclination γ. At the inlet, a constant velocity and temperature profiles, U_o and T_o, respectively, are imposed. The open boundary conditions (OBC) are arranged in a way that they are calculated, that is, the pressure terms are retrieved in the calculation (Heinrich & Pepper, 1999). Therefore, nothing is directly applied at the open boundary. For more information on this, the reader should refer to (Heinrich & Pepper, 1999). The reference and cooling temperatures T_o and T_c, respectively, are the same and equal to zero. Initially, the internal fluid domain has velocities and temperatures equal to zero. All surfaces present the no-slip condition. The regime is non-steady, two-dimensional, and laminar. Next, all three situations are described.

One heat source: One heat source with heat flux q′ of finite length B is placed at x_1 on the lower surface. Heat transfer will be analyzed according to the variation of the Reynolds

number (Re), the Grashof number (Gr), and the inclination angle (γ). B = H, and L = 15H. *Two heat sources*: Two constant-flux heat sources, $q'_1$and q'_2 of finite length B are placed at x_1 and x_2 on the lower surface. The distance between the heaters is d. Throughout this case, the geometry has x_1 = 5H, x_2 = 7H, 8H, and 9H, and hence characterizing d = 1, 2, and 3, respectively. Heat transfer will be analyzed according to the variation of Re, Gr, and d. The inclination angle is zero, that is, the channel is in the horizontal position. B = H, and L = 15H. *Three heat sources*: It is an inclined rectangular channel with height H and length L. Three constant heat sources q'_1, q'_2, and q'_3 of length B are placed on the bottom wall at x_1, x_2, and x_3, respectively. The remaining lower wall is isolated. The upper wall in contact with the fluid is constantly cooled at a uniform temperature T_c. At the inlet, constant velocity and temperature profiles, U_o and T_o, are applied as boundary conditions. Throughout this case, the geometry has x_1 = 6.75H, x_2 = 14.50H, x_3 = 22.25H, B = H = 1, and L = 30H.

3. Problem formulation and the numerical method

The problem governing equation set is given by the continuity, Navier-Stokes, and energy equations. Variables u and v are, respectively, the velocity components in x and y directions, T is the fluid temperature, t′ is the dimensional time, q′ is the heat flux, D_T is the fluid thermal diffusivity, β_T is the thermal expansion coefficient, ν is the kinematics viscosity, g is the gravity acceleration, and ρ_0 is the fluid density and $T_o = T_c$ and $\Delta T = T_h - T_c$. Considering the Boussinesq approximation and the following dimensionless parameters:

$$X=\frac{x}{B};\ Y=\frac{y}{B};\ U=\frac{u}{U_o};\ V=\frac{v}{U_o};\ P=\frac{p}{\rho_0 {U_o}^2};\ t=\frac{t'}{(B/U_o)'};\ \theta=(T-T_o)/(q'B/D_T)$$
$$Fr=\frac{\mathrm{Re}^2}{Gr}=\frac{{U_o}^2}{\beta_T g\Delta T B};\ \mathrm{Pr}=\frac{\nu}{D_T};\ Gr=\frac{\beta_T g\Delta T B^3}{\nu^2};\ \mathrm{Re}=\frac{U_o\rho_0 B}{\mu};\quad (1)$$

where Fr, Pr, Gr, Re, U_o, and μ are, respectively, the Froude number, the Prandtl number, the Grashof number, the Reynolds number, the average velocity, and the dynamic viscosity, the dimensionless governing equations can be cast into the following form:

$$\frac{\partial U}{\partial X}+\frac{\partial V}{\partial Y}=0; \quad (2)$$

$$\frac{\partial U}{\partial t}+U\frac{\partial U}{\partial X}+V\frac{\partial U}{\partial Y}=-\frac{\partial P}{\partial X}+\frac{1}{\mathrm{Re}}\left(\frac{\partial^2 U}{\partial X^2}+\frac{\partial^2 U}{\partial Y^2}\right)+\sin(\gamma)\frac{\theta}{Fr}; \quad (3)$$

$$\frac{\partial V}{\partial t}+U\frac{\partial V}{\partial X}+V\frac{\partial V}{\partial Y}=-\frac{\partial P}{\partial Y}+\frac{1}{\mathrm{Re}}\left(\frac{\partial^2 V}{\partial X^2}+\frac{\partial^2 V}{\partial Y^2}\right)+\cos(\gamma)\frac{\theta}{Fr}; \quad (4)$$

$$\frac{\partial \theta}{\partial t}+U\frac{\partial \theta}{\partial X}+V\frac{\partial \theta}{\partial Y}=\frac{1}{\mathrm{Re}\,\mathrm{Pr}}\left(\frac{\partial^2 \theta}{\partial X^2}+\frac{\partial^2 \theta}{\partial Y^2}\right); \quad (5)$$

The dimensionless boundary conditions are:

$U = V = 0$ (all walls); $\theta = 0$ (inlet and upper walls); $U = 1$ (inlet) and $\frac{\partial \theta}{\partial Y} = -1$ (heat sources).

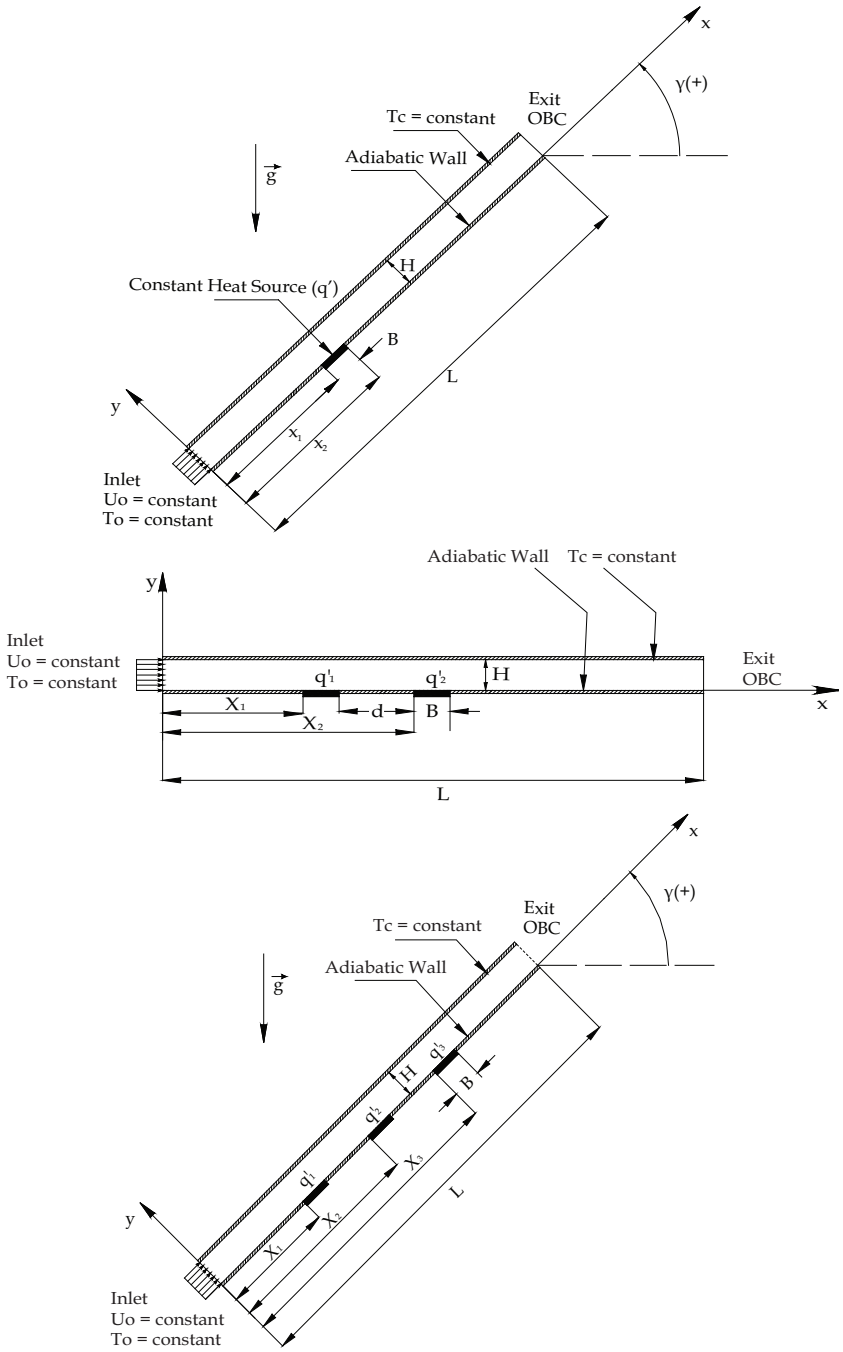

Fig. 1. Geometries and boundary conditions: cases with one, two, and three heat sources

Applying the Petrov-Galerkin formulation and the Penalty technique to Eqs. (2) to (5), the weak forms of the conservation equations may be written as follows:

$$\int_\Omega N_i\left[\frac{\partial U}{\partial t}+\frac{1}{\mathrm{Re}}\left(\frac{\partial N_i}{\partial X}\frac{\partial U}{\partial X}+\frac{\partial N_i}{\partial Y}\frac{\partial U}{\partial Y}\right)\right]d\Omega+\int_\Omega^R \lambda\frac{\partial N_i}{\partial X}\left(\frac{\partial U}{\partial X}+\frac{\partial V}{\partial Y}\right)d\Omega= \int_\Omega\left[\left(N_i+P_{i1}\right)\left(U\frac{\partial U}{\partial X}+V\frac{\partial U}{\partial Y}\right)+N_i\sin(\gamma)\frac{\theta}{Fr}\right]d\Omega-\int_{\Gamma_0}N_i\,p\,n_x\,d\Gamma \tag{6}$$

$$\int_\Omega N_i\left[\frac{\partial V}{\partial t}+\frac{1}{\mathrm{Re}}\left(\frac{\partial N_i}{\partial X}\frac{\partial V}{\partial X}+\frac{\partial N_i}{\partial Y}\frac{\partial V}{\partial Y}\right)\right]d\Omega+\int_\Omega^R \lambda\frac{\partial N_i}{\partial Y}\left(\frac{\partial U}{\partial X}+\frac{\partial V}{\partial Y}\right)d\Omega= \int_\Omega\left[\left(N_i+P_{i1}\right)\left(U\frac{\partial V}{\partial X}+V\frac{\partial V}{\partial Y}\right)+N_i\cos(\gamma)\frac{\theta}{Fr}\right]d\Omega-\int_{\Gamma_0}N_i\,p\,n_y\,d\Gamma \tag{7}$$

$$\int_\Omega\left[N_i\frac{\partial\theta}{\partial t}+\frac{1}{\mathrm{Re\,Pr}}\left(\frac{\partial N_i}{\partial X}\frac{\partial\theta}{\partial X}+\frac{\partial N_i}{\partial Y}\frac{\partial\theta}{\partial Y}\right)\right]d\Omega=\int_\Omega\left(N_i+P_{i2}\right)\left(U\frac{\partial\theta}{\partial X}+V\frac{\partial\theta}{\partial Y}\right)d\Omega+\int_{\Gamma_1}N_i\,q\,d\Gamma \tag{8}$$

where the dependent variables are approximated through the finite element method by:

$$\Phi(X,Y,t)=\sum_j N_j(X,Y)\Phi_j(t);\;\; p(X,Y,t)=\sum_k M_k(X,Y)p_k(t) \tag{9}$$

Ni and Nj are linear shape functions for the quantity Φ, that is, for U, V, and θ. M_k are the pressure piecewise element shape functions. The Petrov-Galerkin perturbations P_{ij}, which are only applied to the convective terms, are defined as:

$$P_{ij}=k_j\left(U\frac{\partial N_i}{\partial X}+V\frac{\partial N_i}{\partial Y}\right);\;\; k_j=\frac{\alpha_j\bar{h}}{|V|};\;\; \alpha_j=\coth\frac{\gamma_j}{2}-\frac{2}{\gamma_j};\;\; \gamma_j=\frac{|V|\bar{h}}{\varepsilon_j};\;\; j=1,2 \tag{10}$$

where γ is the element Péclet number, $|V|$ is the absolute value of the velocity vector that represents the fluid average velocity within the element, $\bar{h}$ is the element average size, $\varepsilon_1=1/\mathrm{Re}$, $\varepsilon_2=1/Pe$, and λ is the Penalty parameter equal to 10^9. Fig. (2) shows the general linear quadrilateral element with $|V|$ and $\bar{h}$.

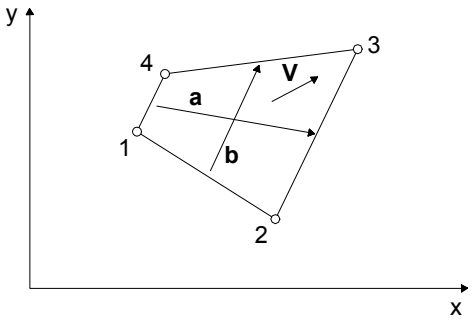

Fig. 2. General bilinear quadrilateral element with vectors a and b and element velocity V

The element average size $\bar{h}$ in the flow direction is given by :

$$\bar{h} = \frac{1}{|\mathbf{V}|}\left(|h_1| + |h_2|\right) \tag{11}$$

where h_1, h_2, a, and b are defined as:

$$h_1 = \mathbf{a}.\mathbf{V} \; ; \; h_2 = \mathbf{b}.\mathbf{V} \tag{12}$$

$$\begin{gathered} a_1 = \frac{1}{2}\left(x_2 + x_3 - x_1 - x_4\right); \; a_2 = \frac{1}{2}\left(y_2 + y_3 - y_1 - y_4\right); \\ b_1 = \frac{1}{2}\left(x_3 + x_4 - x_1 - x_2\right); \; b_2 = \frac{1}{2}\left(y_3 + y_4 - y_1 - y_2\right) \end{gathered} \tag{13}$$

Vectors **a** and **b** are the vectors that are limited by the middle points of opposite sides and h_1 and h_2 are the projections of these vectors on the flow direction. The most important characteristic of the Petrov-Galerkin method is that it does not add any transversal diffusion to the flow, that is, an orthogonal diffusion to the flow direction. α_j is the so-called artificial diffusion or the equilibrium diffusion added to the convective terms. In fact, it is the optimum diffusion found between the diffusions provided by the traditional Galerkin method and the upwind one, which are respectively, under-diffused and over-diffused methods. This helps one solve some numerical oscillations which arise from the 'battle' between elliptic and hyperbolic problems. λ is a problem-independent value, given that the governing parameters do not change drastically (Bercovier & Engelman, 1979; Carey & Krishnan, 1982). This parameter must have a high value in order to have a 'quasi-incompressible' problem. Indeed, the Penalty theory comes from the Stokes viscosity law. Recalling the pressure formula:

$$p = p_s - \left(\bar{\mu} + \frac{2}{3}\mu\right)\nabla.\mathbf{V} \tag{14}$$

where p_s is the static or thermodynamic component of pressure, p is the average pressure, $\bar{\mu}$ is the second viscosity coefficient, and μ is the first viscosity.

Stokes hypothesized that $p = p_s$, hence, $\bar{\mu} = -\frac{2}{3}\mu$. It was shown to be true for some gases; however experiments revealed that with liquids, $\lambda = \left(\bar{\mu} + \frac{2}{3}\mu\right)$ is a positive quantity that is much larger than μ. λ represents the fluid bulk viscosity. If the fluid is perfectly incompressible, λ tends to be infinite. The basic idea of the Penalty formulation is to express the pressure by

$$P = p - p_s = -\lambda\nabla.\mathbf{V} \; ; \tag{15}$$

where λ is a very large number, and P is a modified pressure, which can be seen in Eqs. (3) and (4). For linear interpolation of velocities, the pressure inside the element can be expressed by:

$$P^e = -\frac{\lambda}{A^e}\int_e^R \left(\frac{\partial U}{\partial X}+\frac{\partial V}{\partial Y}\right) de \tag{16}$$

where *e* denotes the element restriction and *Ae* the element area.
Let one neglect some terms in the momentum equations and attain to those in the stiffness matrix, just to facilitate understanding of the Penalty parameter study. Substituting Eq. (16) in (3) and (4) with some manipulation and neglection of some terms which are now not important, the final linear system of equations would present this expression.

$$\left[\mu\mathbf{K}_1+\lambda\mathbf{K}_2\right]\mathbf{d}=\mathbf{F} \tag{17}$$

where $\mathbf{F}$ is the force matrix generated by the boundary conditions, $\mathbf{d}$ is the velocity vector only. Now, let one suppose that $\mathbf{K}_2$ is not singular and λ is increased more and more in an attempt to reach incompressibility. Because μ and $\mathbf{K}_1$ are constant as λ is increased, they can be neglected and the solution to Eq. (17) would be:

$$\mathbf{d}=\frac{1}{\lambda}\mathbf{K}_2^{-1}\mathbf{F} \tag{18}$$

Being that $\mathbf{K}_2$ and $\mathbf{F}$ are also constant, it can be noted that $\mathbf{d}\to 0$ as $\lambda\to\infty$. This is called 'locking' and is strictly related to the incompatibility between the pressure and velocity spaces. Hence, the only solution to this space is the velocity vector $\mathbf{V}=0$. It must be guaranteed that the Penalty matrix $\mathbf{K}_2$ be singular. This is accomplished by using the selective reduced integration of the Penalty term and the least square quadrature with a degree of precision lower than the necessary to guarantee an optimum convergence rate of matrix $\mathbf{K}_1$. Therefore, Fig. (3) shows a pair of elements used here in order to avoid locking.

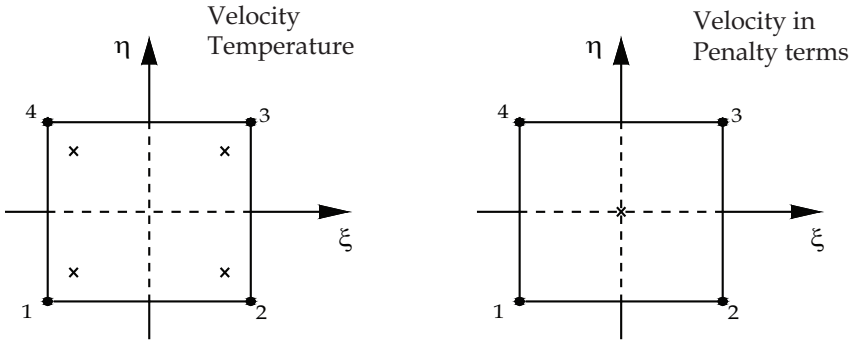

Fig. 3. Real (a) and parent (b) elements for full and reduced integration, respectively

The time integration is accomplished by the Euler backward semi-implicit method. Moreover, the convective and viscous terms are, respectively, calculated explicitly and implicitly. Finally, the average Nusselt number along a surface S of a heat source can be written as follows:

$$Nu=\frac{1}{S}\int_S\left[\frac{1}{\theta}\right]ds \tag{19}$$

4. Validation and mesh independency

The algorithm is validated by comparing the results of the present work with both the ones obtained in experimental and numerical investigations. The first comparison is accomplished not only by using experimental results (Lee & Mateescu, 1998; Armaly et al., 1983), but also by numerical ones (Lee & Mateescu, 1998; Gartling, 1990; Kim & Moin, 1985, and Sohn, 1988). The air flow of the present comparison analysis is taken as two-dimensional, laminar, incompressible, and under the unsteady regime. The domain is a horizontal upstream backward-facing step channel whose inlet has a fully developed velocity profile given by u = 24 y (0.5-y) $\overline{U}$ and v = 0 in which Re = 800. A structured mesh with 6000 quadrilateral linear elements with ΔX = 0.10 e ΔY = 0.05 and time step of Δt = 0.05 are used. By comparing the flow separation distance on the upper surface, its reattachment distance on the bottom surface and its reattachment distance on the upper wall, the deviations are in the range from 0.8% to 17.85%. Out of the 14 calculated deviations, just two are over 10%. Therefore, the results of the first comparison agree well with the ones from the literature. The second comparison is performed with the numerical results (Comini et al., 1997). The contrasting study is carried out by considering a problem involving mixed convective heat transfer with the flow being two-dimensional, laminar, and incompressible in the unsteady regime. This is a benchmark problem which involves the Rayleigh-Bérnard convection in a rectangular channel. In this case, some values are chosen such as Re = 10, Pr = 0.67, and Fr = 1/150. The grid has 4000 quadrilateral linear elements with $\Delta x = 0.1$, $\Delta y = 0.15$, $\Delta t = 0.01$ and 1000 iterations. After approximately iteration 500, the regime turns to be quasi-periodic with the average Nusselt number on the upper wall oscillating around a mean value of 2.44. This value agrees satisfactorily with 2.34 (Comini et al., 1997), resulting in a deviation of about 4%.

It is important to mention that a mesh independency is performed for the most critical situations of the cases that will be studied with the highest values of Re and Gr numbers as well as the study of mass conversation due to the use of the penalty method. Just after reaching reasonable results, the final mesh domain and the penalty parameter are used to obtain the final results. All this study can be found in the doctorate thesis of the present author (Guimarães, 2007). It is omitted here as a matter of space.

5. Results

5.1 Case with one heat source

Figure (4) shows the isotherm distributions considering the ranges for the Reynolds number, the Grashof number, and the inclination angle, respectively, as $1 \le Re \le 10$, $10^3 \le Gr \le 10^5$, and $0° \le \gamma \le 90°$. By observing the isotherms from Fig. (4), the orientation of the channel has a more significant effect on the temperature distribution for lower Re, that is, Re = 1, 5, and 10. This effect is even stronger when Gr increases. Later on this chapter, this effect on the Nusselt number will be seen again. On the other hand, for higher Reynolds, over 50 or so (not shown in Fig. (4)), the inclination angle has a weaker effect on the temperature distributions.

Figure (5) shows the effect of the source module on the velocity distributions for the horizontal cases ($\gamma = 0°$) with Re = 1, 5, and 10, considering $Gr = 10^5$. It can be noted that in the natural convection regime, the thermal plume is approximately symmetric about the centerline of the module (Fig. 4). In the thermal plume region, there are two opposite recirculating cells that are almost symmetric. Moreover, as the entrance velocity increases

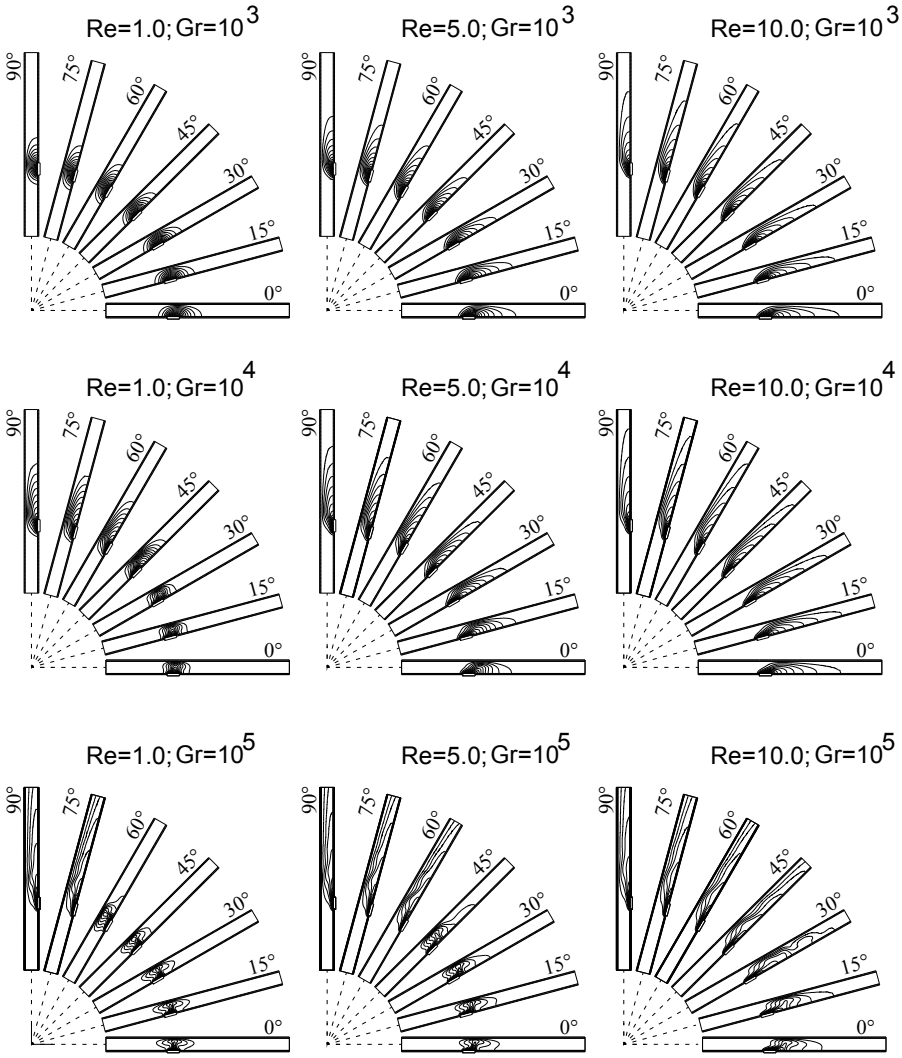

Fig. 4. Isotherms: Gr = 10^3, 10^4, 10^5; Re = 1, 5 , 10; and γ = 0°, 15°, 30°, 45°, 60°, 75°, 90°

the plume shifts and stretches towards downstream. This effect features how the natural convection starts to vanish, giving place to the mixed convection. If Re increases more, for instance, Re ≥ 100 (not shown in Fig. (5)), the forced global fluid movement dominates the flow pattern and the heat transfer process. One can note in the temperature distribution along the module in Fig. (6), for Gr = 10^5, and Re = 1, 5, 10, the transition from the natural convection to the mixed convection. As Re is higher, the maximum temperature on the module decreases. This is due to the fact that when higher velocities are present, the cell recirculation gets further from the module allowing a stronger contact of the cold fluid with the heat module.

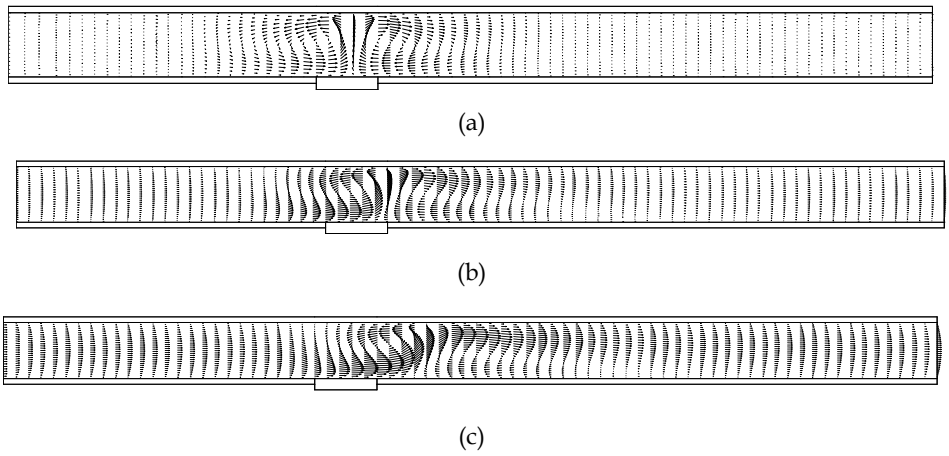

(a)

(b)

(c)

Fig. 5. Velocity distributions for Gr = 10^5, γ = 0°, and Re = (a) 1, (b) 5, and (c) 10

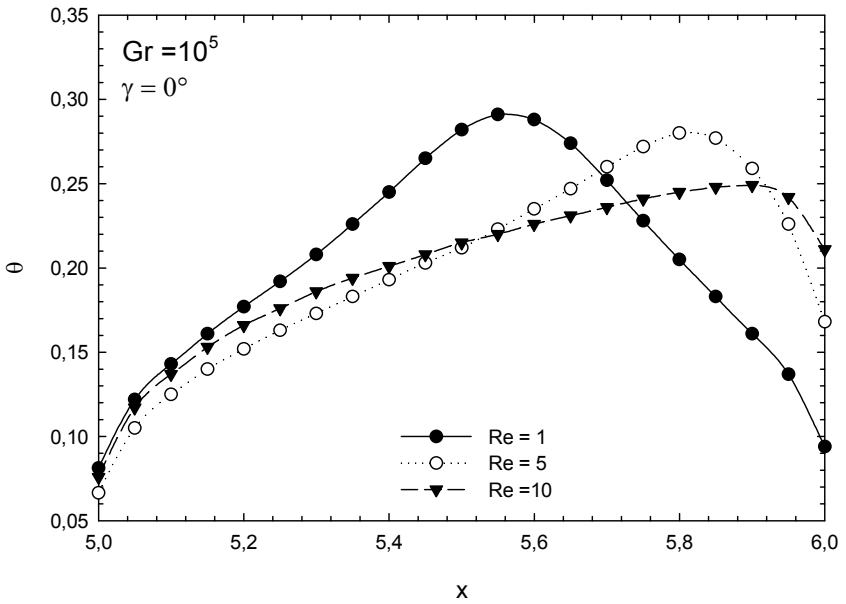

Fig. 6. Module temperature distributions for Gr = 105, γ = 0° and Re = 1, 5, and 10

Figure (7) depicts the velocities vectors for Gr = 10^5 and Re = 1, 5, and 10, for γ = 45°. As Re increases, the clockwise recirculating cell tends to vanish, whereas the anticlockwise ones tend to dominate to an extent that reversed flow exists at the exit. The presence of the reversal flow does not necessarily imply an increase of the Nusselt number on the module. It is interesting to observe the formation of secondary recirculating cells in Fig. (7c), and as a

result of this formation, the corresponding isothermal lines are distorted, as shown in Fig. (4). In Fig. (7b), the reversal flow is weak. Comparing Fig. (7) with Fig. (5), there is a small difference in the velocity vectors, hence showing the small effect of the orientation of the channel in these two cases.

(a) (b) (c)

Fig. 7. Velocity vectors for Gr = 10^5, γ = 45°, and (a) Re =1, (b) Re =5, and (c) Re =10; Here, γ = 75° is a better situation when cooling is aimed, with little difference when γ = 90°

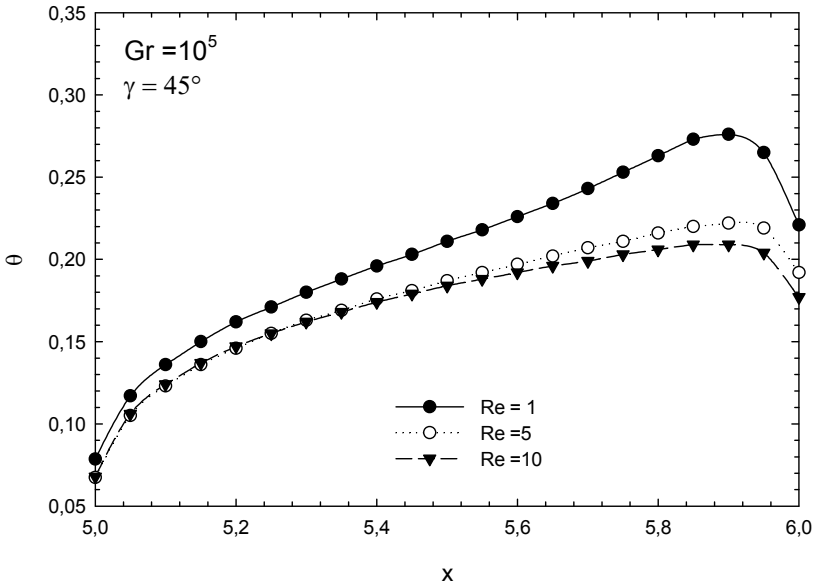

Fig. 8. Module temperature distributions or Gr = 10^5, γ = 45° and Re = 1, 5, and 10

In Figure (8), the temperature distributions along the module are shown for the cases from Fig. (7a-c). In a general way, the maximum temperature on the module decreases for the three cases. It must be remembered that the ideal work conditions in equipments with electronic circuit boards are those in which the module presents the lowest values for the

maximum temperature. Therefore, having these conditions in mind, the increase of the inclination angle provides lower values for the maximum temperature.
Figure (9) presents the velocity distributions for Gr = 10^5, Re = 1, 5, and 10, but now with the channel on the vertical position, $\gamma = 90°$. It can be noted that for all the values of Re, there is a reversal flow at the outlet that is stronger than the reversed flow for $\gamma = 45°$. For each of these three cases in Fig. (9), there is a secondary recirculating cell. There is not a significant difference in the temperature on the module for the Reynolds values Re = 1, 5, and 10; Gr = 10^5, and $\gamma = 90°$(Fig. 10)).

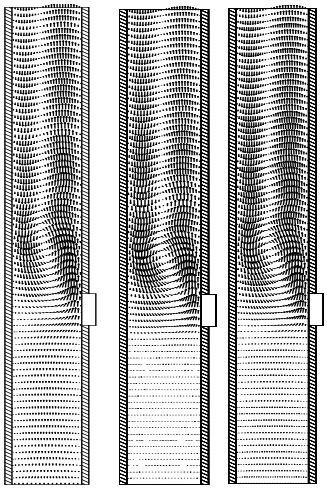

(a) (b) (c)

Fig. 9. Velocity distributions for Gr = 10^5, $\gamma = 90°$, and Re = (a) 1, (b) 5, and (c) 10

Figure (11) makes a comparison of the Nusselt numbers for $1 \leq Re \leq 500$, $0° \leq \gamma \leq 90°$ and for the three Grashof numbers Gr =10^3, 10^4, and 10^5. These results are in good agreement with those found in literature (Choi & Ortega, 1993). It was observed according to the 'five percent deviation rule' (Sparrow et al., 1959) that the natural, mixed, and forced convection can be determined. From Figs. (11a-c), the same is found here, where the mixed convection regimes are, approximately, within the ranges $1 < Re < 50$ for Gr = 10^3, $5 < Re < 100$ for Gr = 10^4, and $10 < Re < 500$ for Gr = 10^5. Practically, there is no reduction in the Nusselt number in these cases where the aiding flow is present, which also agrees with the work previously mentioned (Choi & Ortega, 1993). It can be noted that the collapse of the curves at high Re explains that the buoyancy effects and, therefore, the influence of inclination diminish as forced fluid global motion dominates.
Figure (12) shows the influence of the orientation angle in the heat transfer for all the cases studied in this work, that is, Re from 1 to 500; γ from 0° to 90°; and Gr = 10^3, 10^4, and 10^5. In a general way, Nu is strongly dependent on the orientation of the channel in the limits of the natural and forced convection. For instance, when Gr = 10^3, the natural convective cells are not sufficiently strong to influence the flow and the temperature fields (Fig. 4), that means that the heat transfer mode involved is almost conductive along the channel. As Gr increases, the variations in Nu are more significant for low Re. It is said that in the natural

and mixed convection, the most suitable situation in the cooling of an electronic module, that is, the lowest Nu, is found when the channel orientation is in the range 45°<γ<90° (considering the convention adopted in the present work), in a general way (Choi and Ortega, 1993). Analyzing Fig. (13), there is still a more favorable inclination within the range proposed by previous literature (Choi & Ortega, 1993), which is around 60° and 75°. The case for γ = 0° should be avoided. A particular case which provides a drastic increase in Nu, within the limits considered in this case, is Gr = 10^3 and Re = 1 in the range 60° ≤ γ ≤ 75°. This can also be noted in Fig. (5), in the isotherms distributions.

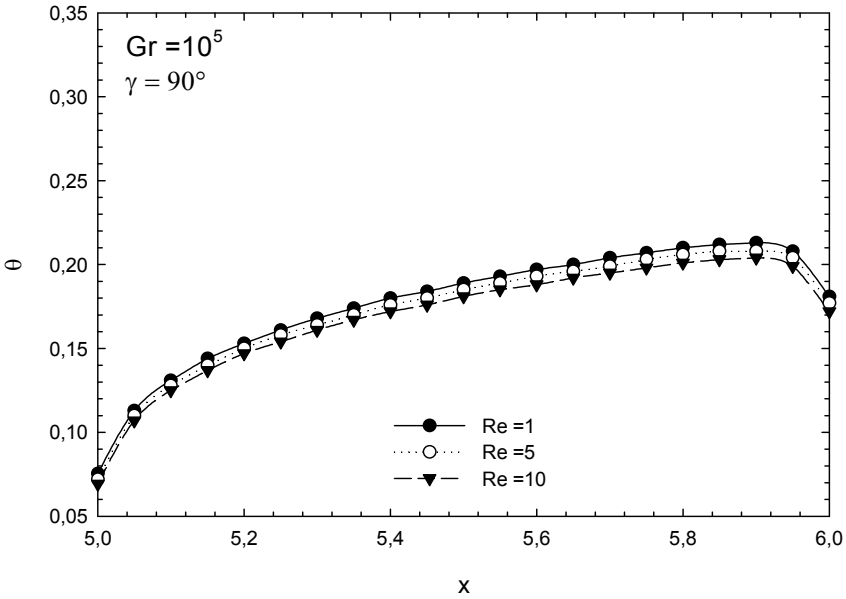

Fig. 10. Module temperature distributions for Gr = 10^5, γ = 90° and Re = 1, 5, and 10

5.2 Case with two heat sources

Figure (13) discloses the velocity vector distributions for Gr = 10^5, Re = 1, 10, and 1000 and d = 1, 2, and 3. In the case where Re = 1, almost symmetric recirculations appear and those are responsible for the thermal plumes mentioned previously. As the source modules are placed further from each other, the recirculation between the sources is powered on and, therefore, higher velocities take part in the flow. For Gr = 10^5, this does not imply a big difference in temperature on the pair of heat sources. In a general way, as Re is raised, the recirculations tend to cease, making it possible to the cold fluid be more in contact with the module surfaces, hence, invigorating the heat transfer. For high values of Re, the distance d has little influence on the velocity profiles. As mentioned before, for Re = 10, an oscillating behavior of the recirculations brought about by the buoyancy flow near the modules is observed. These oscillations reflect an attempt of the flow to be ruled by a predominant convection, that is, it is a 'fight' between buoyant and forced velocities. The first heat source develops a flow wake that hits the second one, heating it even more. The recirculation originated on the second module becomes more intense and this makes an increase in the

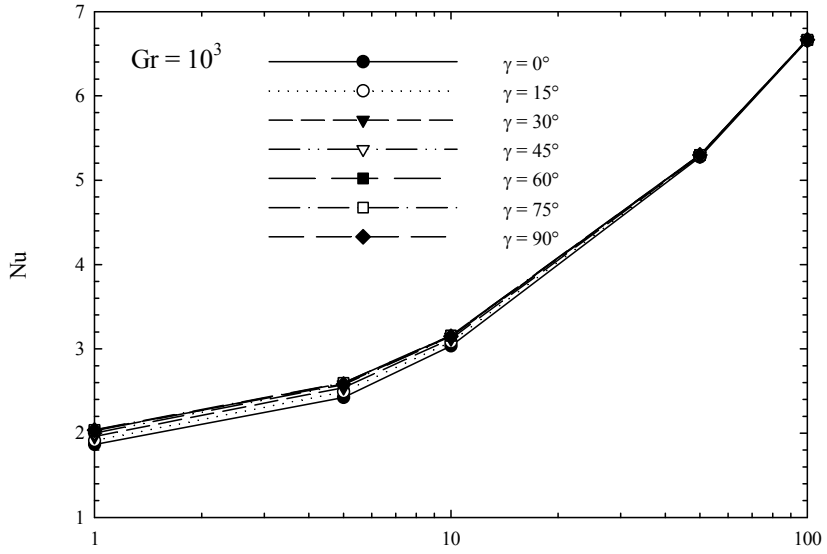
Gr = 10^3
γ = 0°
γ = 15°
γ = 30°
γ = 45°
γ = 60°
γ = 75°
γ = 90°
Nu
1
2
3
4
5
6
7
1
10
100

(a)

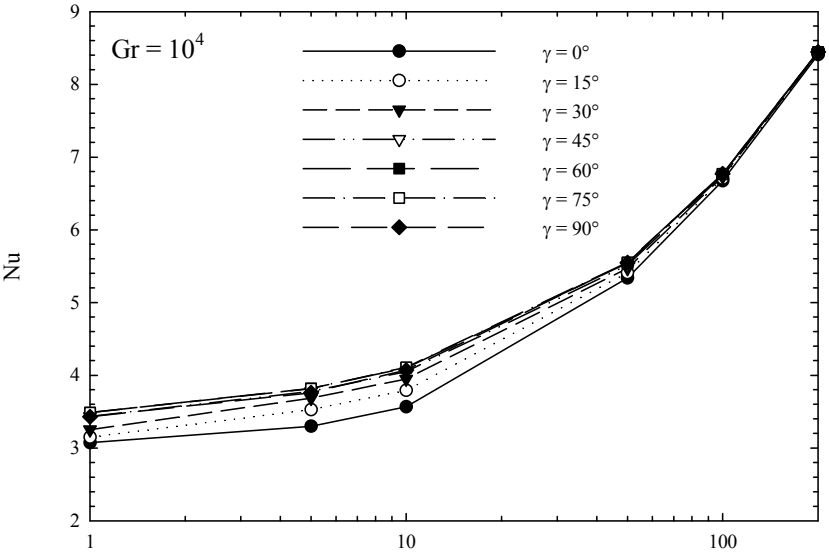
Gr = 10^4
γ = 0°
γ = 15°
γ = 30°
γ = 45°
γ = 60°
γ = 75°
γ = 90°
Nu
2
3
4
5
6
7
8
9
1
10
100

(b)

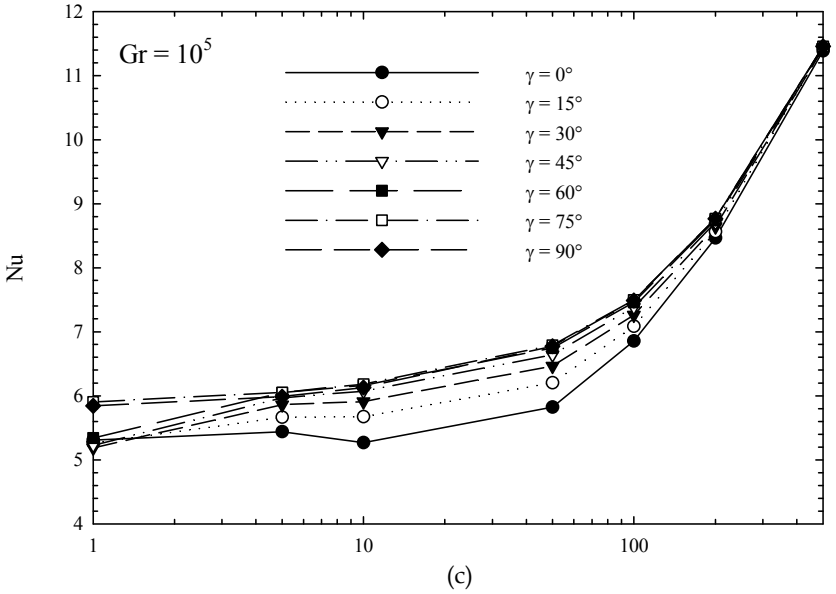

Fig. 11. Average Nusselt number vs Re: $0 \le \gamma \le 90°$, (a) Gr=10^3, (b) Gr= 0^4, and (c) Gr=10^5

fluid pressure coming from backwards. Therefore, it comes to a point that this pressure is strong enough to force that flow barrier downstream. At this moment, the main flow starts to develop and all the process repeats all over again. Consequently, time oscillations in Nu on Heater 2 will appear. This will be seen afterwards.

Figure (14) shows the isotherm distributions for Reynolds numbers Re = 1, 10, 50, 100, and 1000, distances between the heat sources d = 1, 2, and 3 and Grashof number Gr = 10^5. The isotherms are spaced by $\Delta\theta = 0.02$. It can be noted when natural convection is concerned, that is, Re = 1, the heat sources in the cases where d = 1 and 2 influence each other whereas for the case where d = 3, it does not happen. For all cases where Re = 1, there are plumes localized in the vicinity of the heaters. For Re = 1 and d = 1, the two plumes are partially glued, making it clear that this distance does make the module temperature fields impact each other. Although this is also true when d = 2, the plumes are further spaced from each other. For Re = 1 and d = 3, the plumes are almost independent. It will be seen that this behavior in Heater 1 and Re = 1 affects smoothly the Nusselt number Nu when Gr = 10^5. Moreover, for Gr = 10^3 and 10^4, the space between the modules does not interfere on heat transfer. On the other hand, when Heater 2 is taken into consideration, the heat source spacing invigorates Nu for Gr = 10^3, 10^4, and 10^5. A perfect symmetry is not present here as long as the flow has a certain forced velocity, Re = 1, in the forced stream. For all Reynolds numbers and Gr = 10^5, the solutions converge. However, for Re = 10, a periodic flow oscillation in time is brought about for all heat source distances. The temperature distributions (not shown here) where Re = 10 and d = 1, 2, and 3 are plotted in the time shots t = 15, 30, and 50, respectively. It can be perceived in these cases, higher temperature distribution on the second module. This temperature rise tends to weaken as the Reynolds number is increased. The temperature invigoration in the region around Heater 2 is due to the fact that the thermal wake from Heater 1 intensifies the buoyant flow in the localized region in the vicinity of Heater 2. It can be noted that by keeping Re constant, the distance d

plays a considerable role on the second module heating. For instance, what has just been said happens in the case where Re = 1000 and d = 1, 2, and 3.

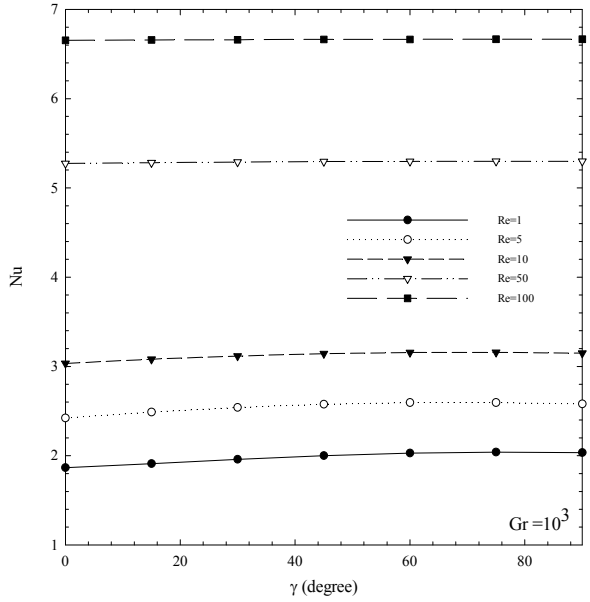

(a)

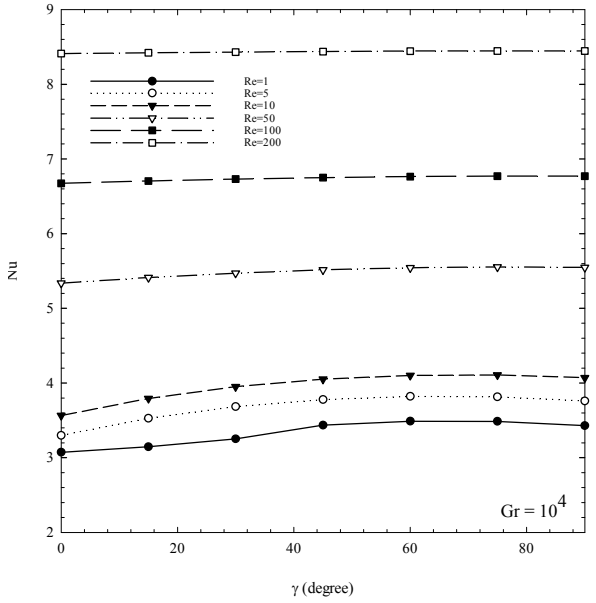

(b)

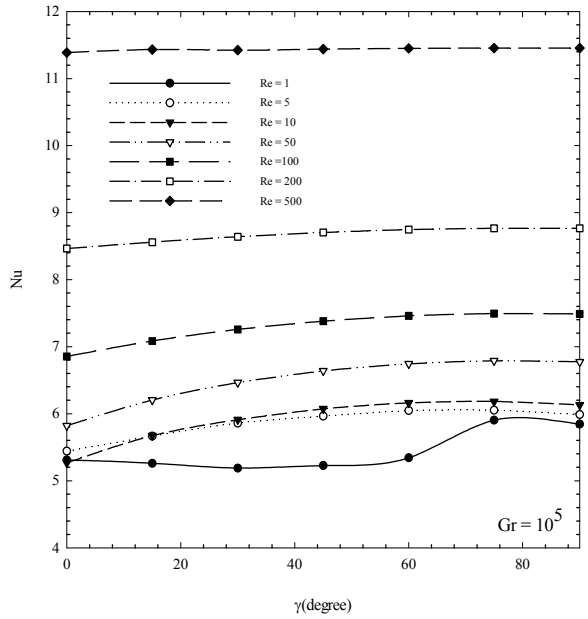

(c)

Fig. 12. Average Nusselt vs γ: 1 ≤ Re ≤ 500 and (a) Gr = 10^3, (b) Gr = 10^4, and (c) Gr = 10^5

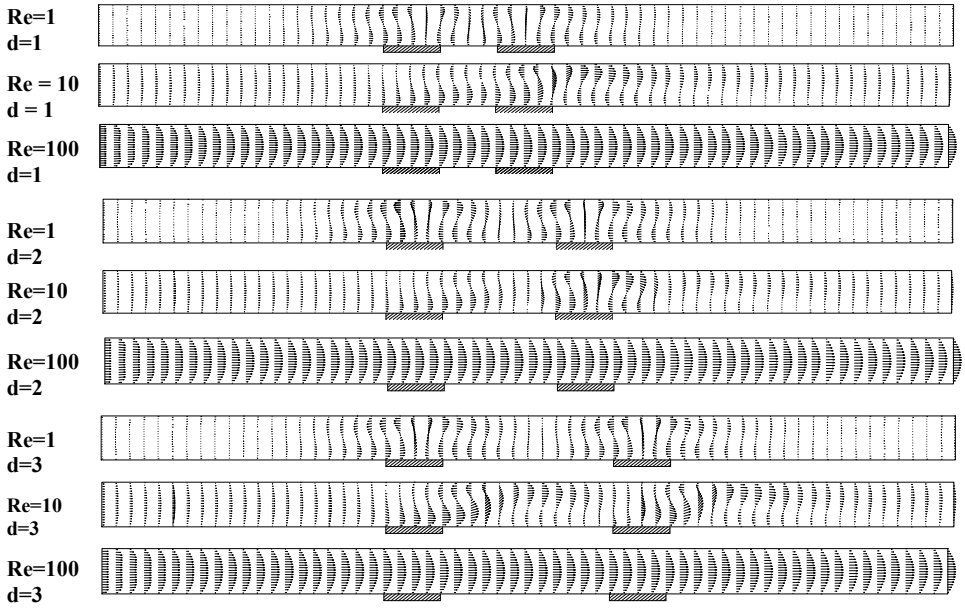

Fig. 13. Velocity vector for Gr = 10^5, Re = 1, 10, 100, and d = 1, 2, 3

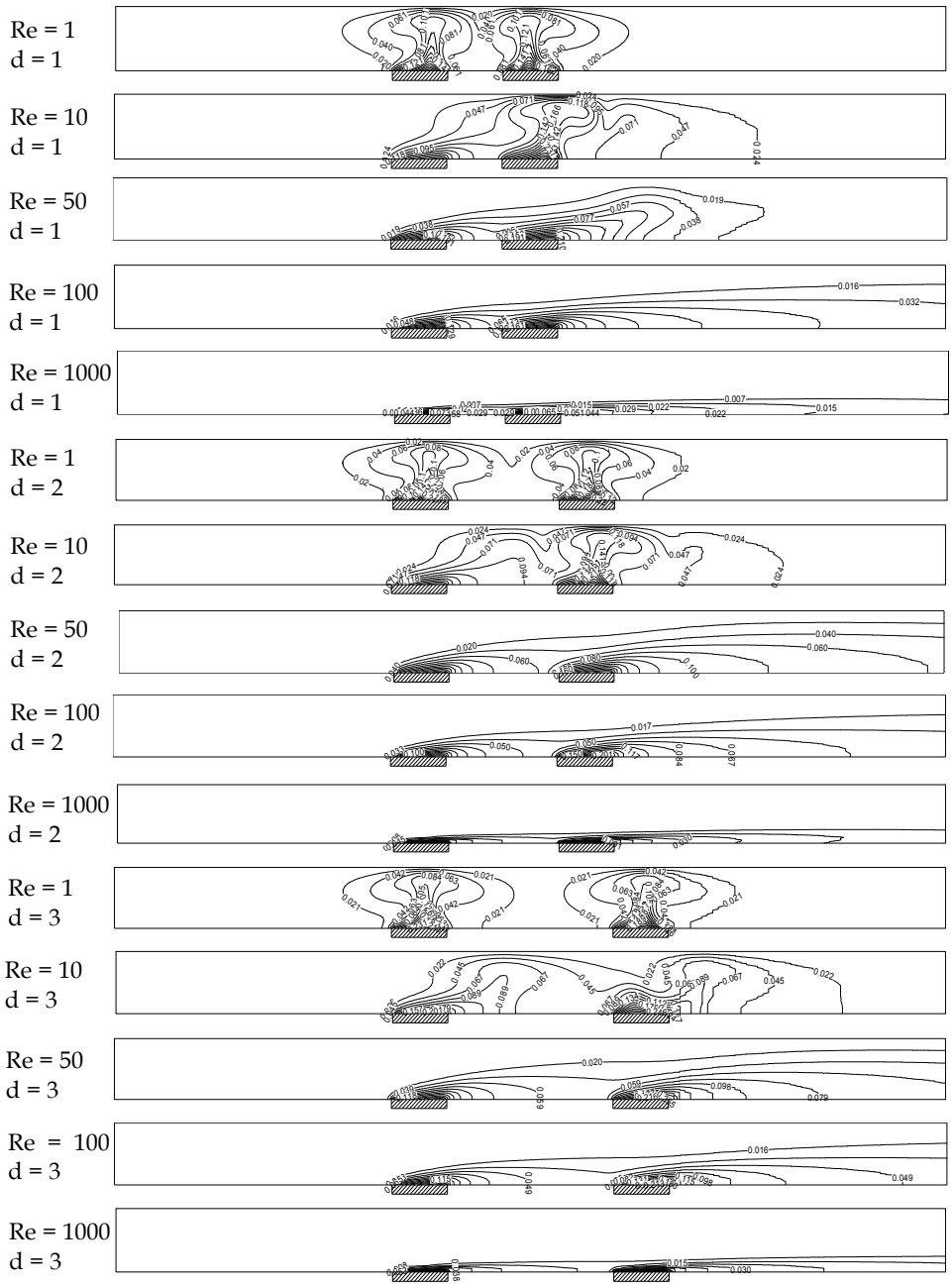

Fig. 14. Isotherms for Re = 1, 10, 100, 1000, $\gamma = 0°$, and $Gr = 10^5$, $\Delta\theta = 0.02$

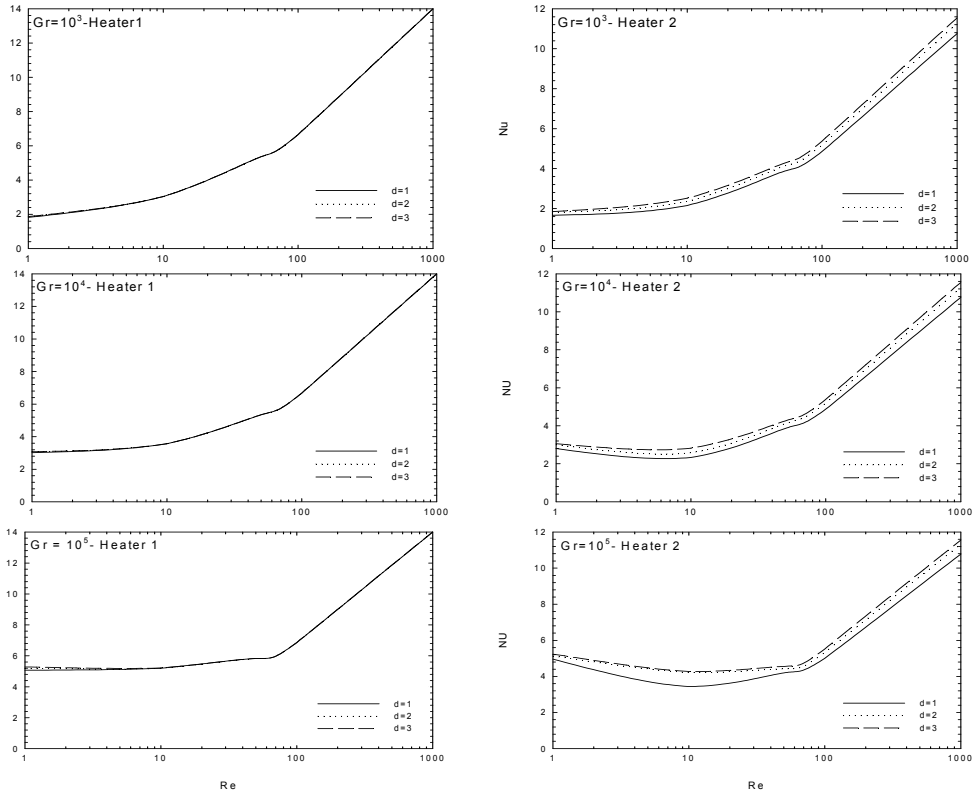

Fig. 15. Nu for Re = 1, 10, 10^2, 10^3, d = 1, 2, 3, Gr = 10^5, 10^4, and 10^5 on Heater 1 and 2

Figure (15) depicts the effect of the Reynolds number on heat transfer for Gr = 10^3, 10^4, and 10^5, Re = 1, 10, 100, and 1000, and finally, d = 1, 2, 3, in the pair of heat sources. This picture shows some points already discussed previously such as the module distance effect which is almost negligible on Heater 1 and moderate on Heater 2. It can be clearly seen the balance between forced and natural convections. In a general way, the distance d = 3 is the one which offers better work conditions since the temperatures are lower.

Figure (16) presents the temperature distributions θ on Heater 1 and 2 for Re = 100 and 1000 and d = 1, 2, and 3. The distance between the modules does not affect the temperature on Heater 1 whereas this effect can be distinctively seen on Heater 2. It is interesting noticing in Heater 2, that for Re = 100 and 1000, distances d = 2 and 3 do not present significant changes, but d = 1. Then, there is an optimum distance in which two heat sources can be placed apart to have lower temperatures and this is the case of d = 3 here, although d = 2 does not present a meaningful change in temperature either. This, in a certain way, can lead us to a better layout of the heat sources in an array. Of course, the presence of more heat sources and the geometry of the channel must be taken into account. Anyway, this behavior is food for thought for future studies.

Finally, the time distribution of the Nusselt number along Heater 1 and 2 for Gr = 10^5, Re = 10, 100, and 1000, d = 1, 2, and 3, is shown in Fig. (17). In all cases, as expected, the first

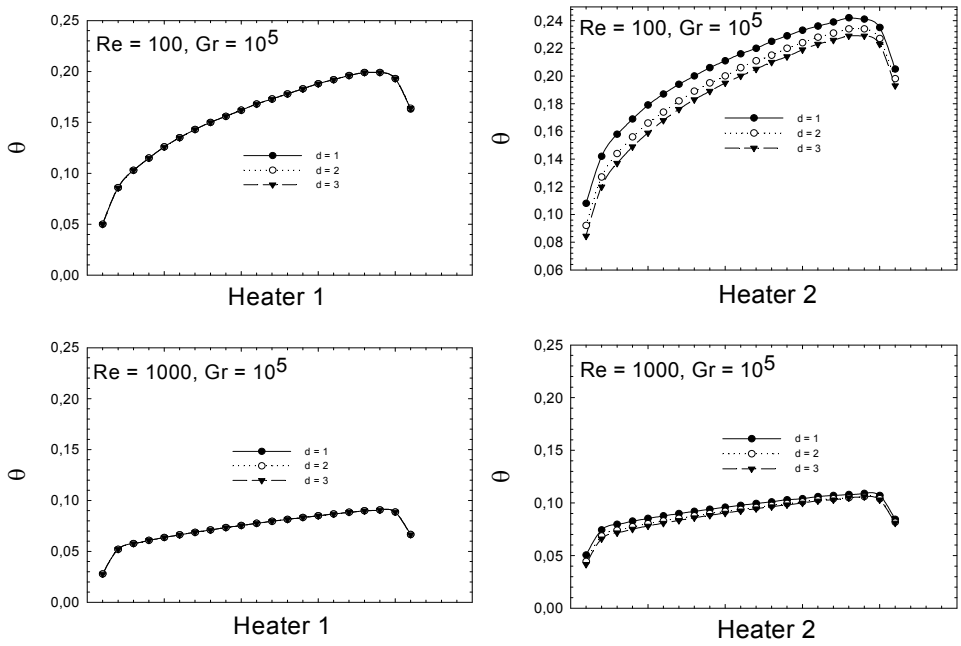

Fig. 16. Temperature on modules 1 and 2 for d = 1, 2, 3; Re = 100, 1000, and Gr = 10^5

module is submitted to higher heat transfer since it is constantly been bombarded with cold fluid from the forced convection. On the other hand, it can be seen again that a flow wake from the first source reaches the second one and this is responsible for the bifurcation of the Nusselt number curves. Here, one can note the time spent by the hot fluid coming from the first source and traveling to the second one. For example, for Re = 100 and d = 1, 2, and 3, the time shots are, respectively, around t = 1.4, 3.0, and 4.0. However, the converged values for these last cases are almost the same. As seen earlier, periodic oscillations appear for Re = 10.

5.3 Case with three heat sources

The results presented here are obtained using the finite element method (FEM) and a structured mesh with rectangular isoparametric four-node elements in which $\Delta X = 0.1$ and $\Delta Y = 0.05$. A mesh sensibility analysis was carried out (Guimaraes, 2008). The temperature distributions for Reynolds numbers Re = 1, 10, 50, and 100, Grashof number Gr = 10^5, and inclination angles $\gamma = 0°$ (horizontal), 45°, and 90° (vertical) are available in Fig. (18). For Re = 1 and $\gamma = 0°$ and 45°, there is a formation of thermal cells which are localized in regions close to the modules. When Re = 1, the flow is predominantly due to natural convection. As Re is increased, these cells are stretched and hence forced convection starts to be characterized. By keeping Re constant, the inclination angle variation plays an important role on the temperature distribution. The effect of γ on temperature is stronger when low velocities are present. For example, when Re = 10 and $\gamma = 0°$, 45° and 90°, this behavior is noted, that is, for $\gamma = 0°$ and Re = 10, a thermal cell is almost present, however, for $\gamma = 45°$and Re = 10, those cells vanish. This is more evident when Re =1 and $\gamma = 45°$ and 90°.

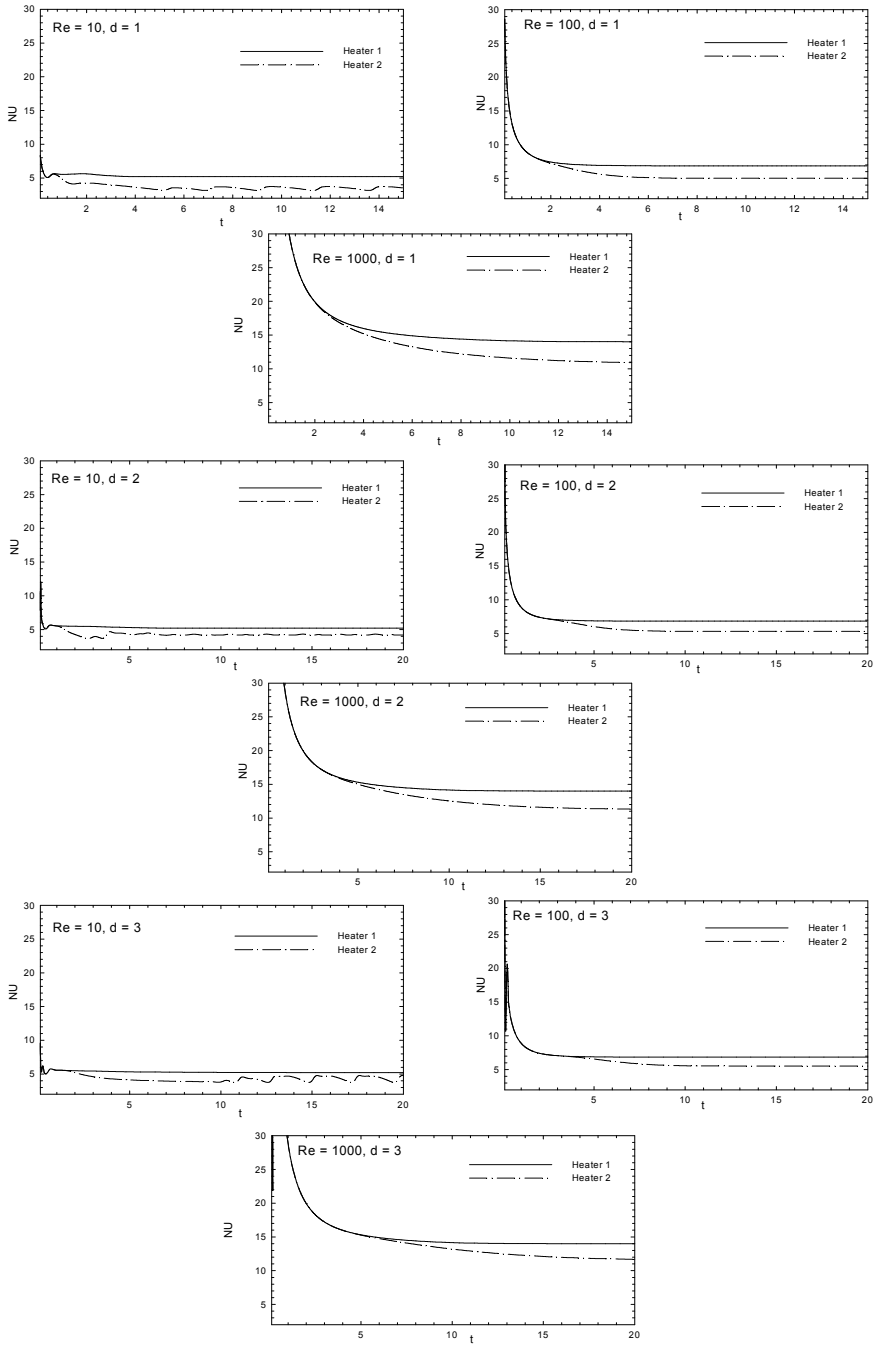

Fig. 17. Average Nusselt number vs Time: Gr = 10^5, Re = 10, 10^2, 10^3, d =1, 2 , 3, Heater 1, 2

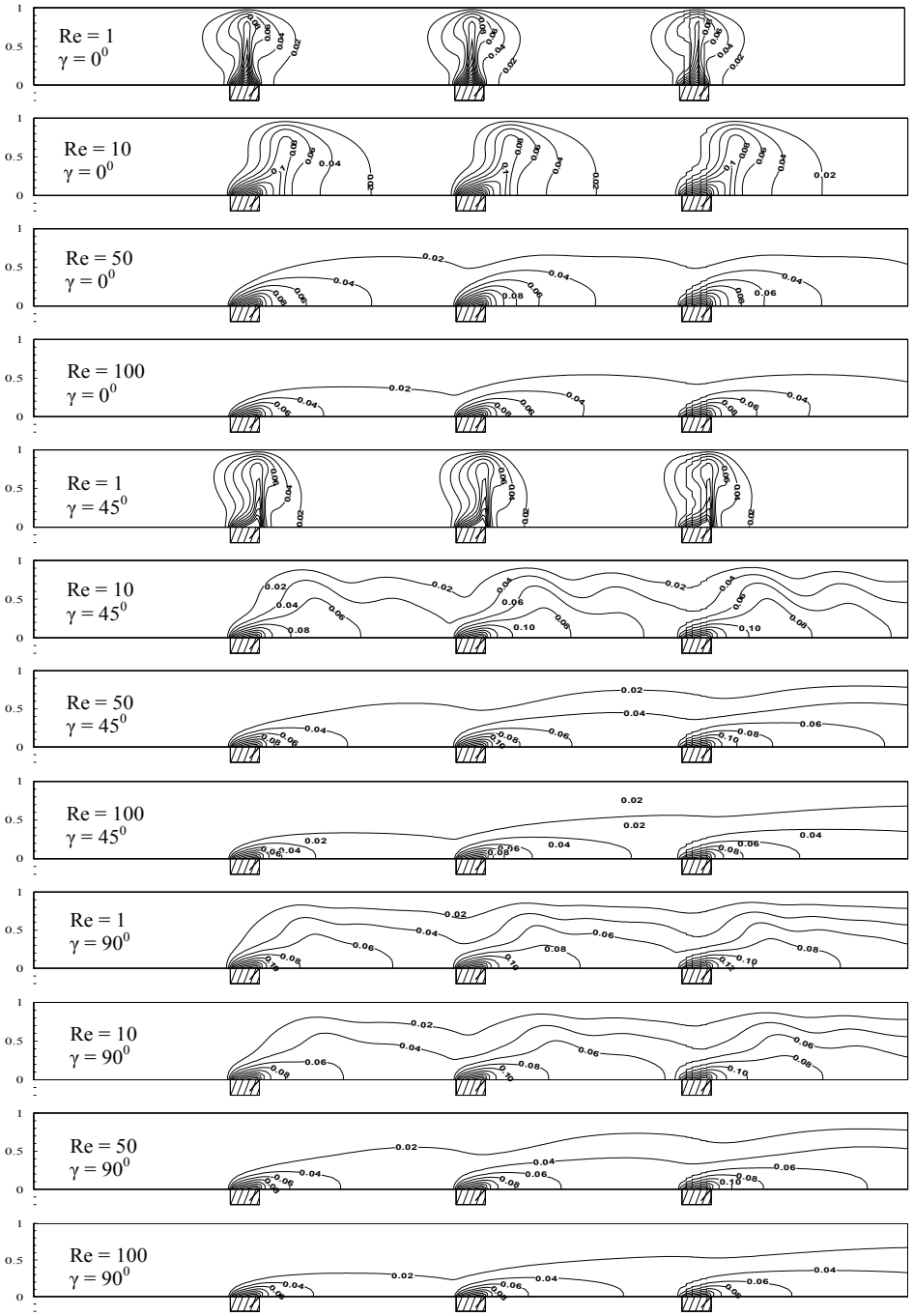

Fig. 18. Isotherms for Gr = 10^5, Re = 1, 10, 50, 100 and γ = 0°, 45°, 90°

It is worth observing that, the fluid heated in the first heater reaches the second one, and then the third one. Thus, this process of increasing temperature provides undesirable situations when cooling is aimed.

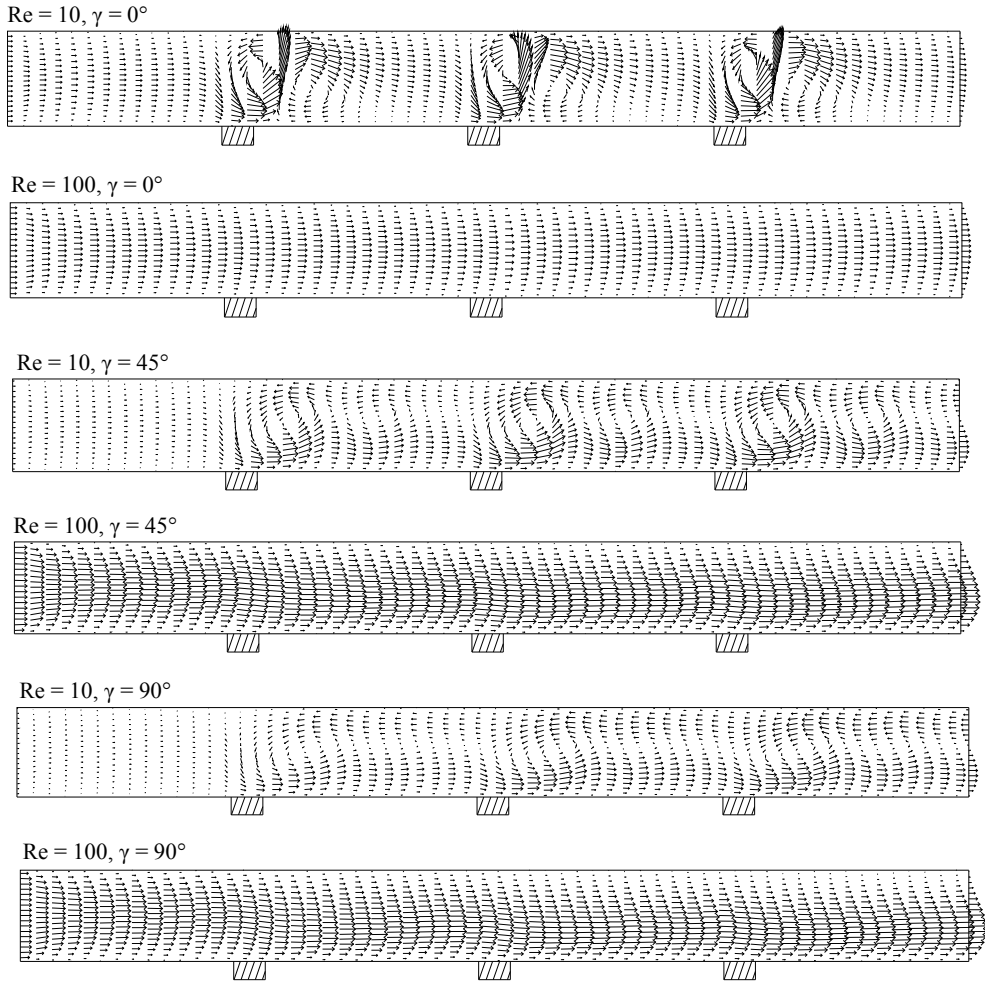

Fig. 19. Velocity vectors for Gr = 105, Re = 10 and 100, and γ = 0°, 45°and 90°

Figure (19) depicts the velocity vectors for Re = 10 and 100 and Gr = 10^5 for γ = 0°, 45°, and 90°. It can be noted that for Re = 10 and γ = 0°, 45°, and 90°, recirculations are generated by the fluid heated on the sources. For Re = 10 and γ = 0°, three independent recirculations appear. The distance among the heat sources enables the reorganization of the velocity profile until the fluid reaches the next source and then the recirculation process starts all over again. Now, concerning the cases where Re = 10 and γ = 45° and 90°, there are two kinds of recirculations, that is, a primary recirculation along all channel that encompasses

another two secondary recirculations localized just after the sources. Moreover, for these later cases, a reversal fluid flow is present at the outlet. As Re is increased by keeping γ constant, these recirculations get weaker until they disappear for high Re. Clearly, one can note the effect of the inclination on the velocity vectors when Re = 10. The strongest inclination influence takes place when it is between 0° and 45°.

Figure (20) presents the average Nusselt number distributions on the heat sources, NU_{H1}, NU_{H2}, and NU_{H3} for Reynolds numbers Re = 1, 10, 50, 100, and 1000, Grashof numbers Gr = 10^3, 10^4, and 10^5, and inclination angles γ = 0°, 45°, and 90°. In general, the average Nusselt number for each source increases as the Reynolds number is increased. By analyzing each graphic separately, it can be observed that NU_{H1} tends to become more distant from NU_{H2} and NU_{H3} as Reynolds number is increased, starting from an initial value for Re = 1 which is almost equal to NU_{H2} and NU_{H3}. This agreement at the beginning means that the heaters are not affecting one another. Here, it can be better perceived that behavior found in Fig. (13), where a heater is affected by an upstream one. That is the reason why NU_{H1} shows higher values. The only case in which the heaters show different values for Re = 1 is when Gr = 10^5 and γ = 90°. Overall, the strongest average Nusselt number variation is between 0° and 45°. Practically in all cases, NU_{H1}, NU_{H2} ,and NU_{H3} increase in this angle range, 0° and 45°, while for Gr = 10^5 and Re = 1000, NU_{H2} and NU_{H3} decrease. When electronic circuits are concerned, the ideal case is the one which has the highest Nusselt number. Thus, angles 45° and 90° are the most suitable ones with not so

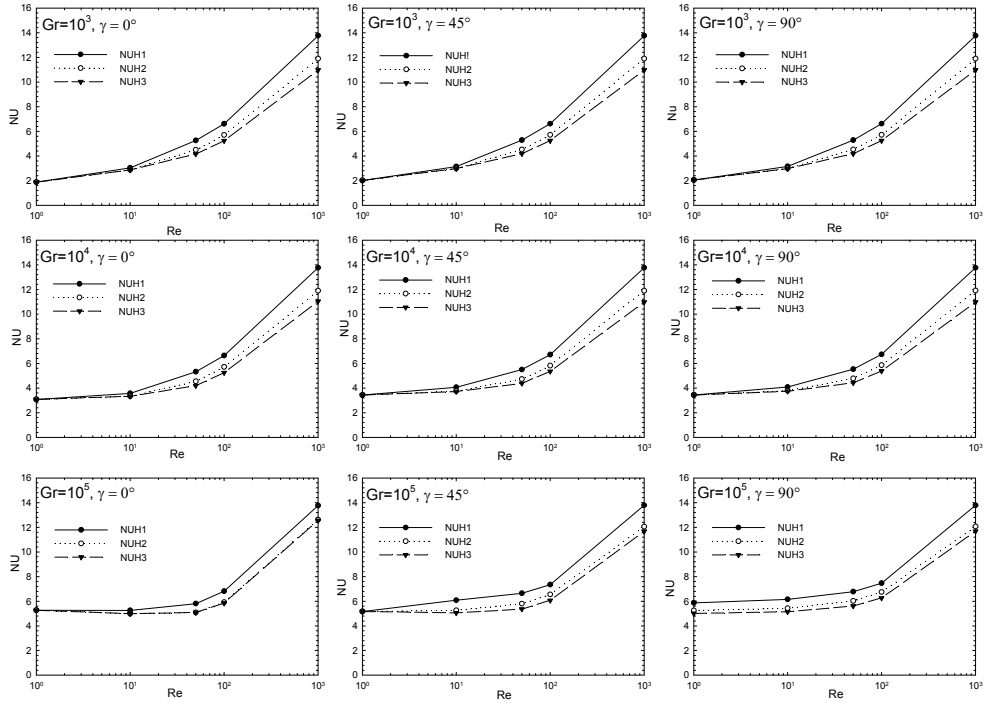

Fig. 20. Average Nusselt number vs Reynolds number for Gr = 10^3, 10^4, 10^5, γ = 0°, 45°, 90°

much difference between them. An exception would be the case where Gr = 10^5, Re = 1000, and $\gamma = 0°$.

Figure (21) presents the local dimensionless temperature distributions on the three heat sources for Re = 10, 100, 1000, Gr = 10^5, $\gamma = 0°$, 45°, and 90°. Again, the cases where Re = 10 and 100 show the lowest temperatures when $\gamma = 90°$. On the other hand, this does not happen when Re = 1000, where the horizontal position shows the lowest temperatures along the modules. All cases in which $\gamma = 0°$, the second and third sources have equal temperatures. However, the first module shows lower temperatures. As mentioned before, this characterizes the fluid being heated by a previous heat source, thus, not contributing to the cooling of an upstream one.

Figure (22) presents the average Nusselt number variation on H_1, H_2, and H_3 against the dimensionless time t considering Re = 10, 100, Gr = 10^3, 10^4, 10^5 and $\gamma = 90°$. In the beginning, all three Nusselt numbers on H_1, H_2, and H_3 have the same behavior and value. These numbers tend to converge to different values as time goes on. However, before they do so, they bifurcate at a certain point. This denotes the moment when a heated fluid wake from a previous source reaches a downstream one.

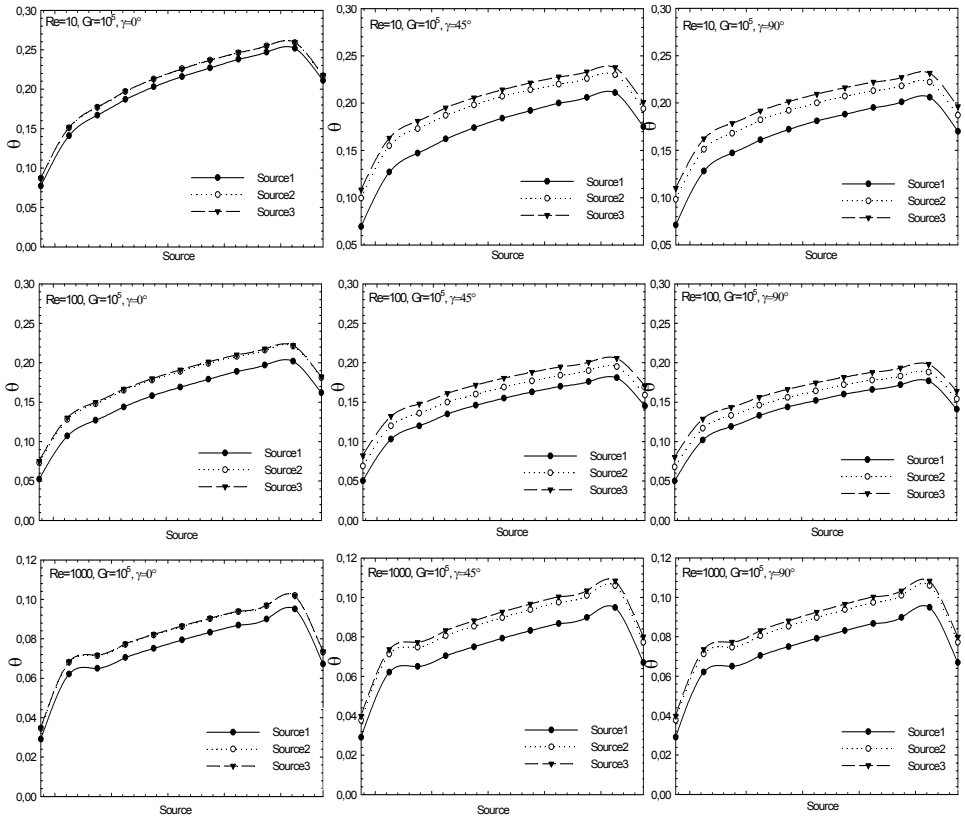

Fig. 21. Module temperatures for Re = 10, 100, 1000; Gr = 105, $\gamma = 0°$, 45°, 90°

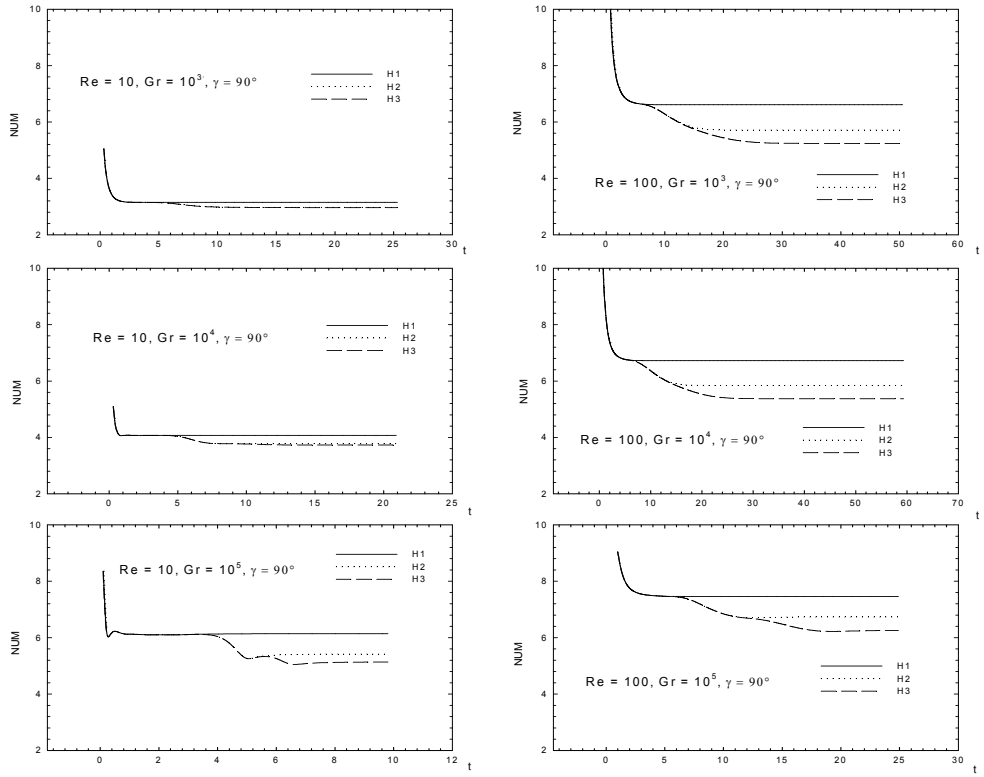

Fig. 22. Module average Nusselt number in time: Re = 10 e 100 , Gr = 10^3, 10^4, 10^5, γ = 90°

6. Conclusions

1. The mixed convection was studied in a simple channel considering the effect of the inclination angle and some physical parameters. The ranges performed were as follows: $1 \le Re \le 500$, $10^3 \le Gr \le 10^5$, and $0° \le \gamma \le 90°$. The set of governing equations were discretized and solved using the Galerkin finite element method (FEM) with the Penalty formulation in the pressure terms and the Petrov-Galerkin perturbations in the convective terms in all throughout the chapter. 5980 four-noded elements were used to discretize the spatial domain. Comparisons were performed to validate the computational code. It was observed from the results of the present problem that the effect of the inclination angle on the velocity and temperature distributions plays an important role on the heat transfer for low Re and high Gr. For high Re, the effect of the orientation was negligible. One must understand that when the words 'low' and 'high' were mentioned here, it meant low and high compared to the limits considered in this work. In general, it was also discovered that an inclination angle around 60° and 75° provided a slight most desirable work conditions when cooling is aimed. It was said that this optimal orientation would be 90° (Choi and Ortega, 1993), despite no significant changes were found after γ = 45° (according to the convection adopted here).

Some cases presented the reversed flow for low Re and high Gr. The reversal flow did not noticeably influence the heat transfer coefficient on the module, although it did change the velocity and temperature fields.

In general, the results encourage the use of inclined boards in cabinets. However, some other aspects should be addressed such as the geometrical arrangement of the boards.

2. A mixed convection study in a rectangular channel with two heat sources on the bottom wall was conducted. The upper wall was kept at a constant cold temperature and the remaining part of the lower one was adiabatic. The heat transfer was studied by ranging some physical and geometrical parameters as follows: Re = 1 to 1000; the distances between the modules d = 1, 2, and 3; and Gr = 10^3, 10^4, and 10^5. For Re = 1 and distances d = 1 and 2, the buoyant forces generated plumes that interfered in each other. For higher Reynolds numbers, the heat transfer in Heater 2 was invigorated by a hot wake brought about by Heater 1. In cases where Re = 10 and Gr = 10^5, the flow oscillations appeared and they strongly affected the flow distributions. For Re = 100 and 1000, the temperature distributions in Heater 1 were not affected by the distances between the modules whereas on Heater 2, they were distinct. An important conclusion is that there was an optimum distance in which two sources could be placed apart from each other, that is, d = 3, although d = 2 did not present a significant change in temperature either. Further investigations are encouraged taking into consideration more heaters and different arrays.
3. In this work, mixed convection heat transfer study in an inclined rectangular channel with three heat sources on the lower wall was carried out using the same. Effects on the Nusselt number along the heat sources as well as the velocity vectors in the domain were verified by varying the following parameters: γ = 0°, 45°, 90°, Re = 1, 10, 50, 100, 1000, Gr = 10^3, 10^4, 10^5. In general, the inclination angle had a stronger influence on the flow and heat transfer since lower forced velocities were present, especially when the channel was between 0° and 45°. It could be noted that in some cases some heat sources were reached by a hot wake coming from a previous module, thus, increasing their temperatures. Primary and secondary recirculations and reversal flow were present in some situations such as Re = 10, γ = 45° and 90°. In problems where heat transfer analysis on electronic circuits is aimed, cases with the lowest temperatures, and hence, the highest Nusselt numbers, are the most suitable ones. Therefore, the channel inclination angles 45° and 90° were the best ones with little difference between them. An exception was the case with Gr = 10^5 and Re = 1000, where γ = 0° was the ideal inclination.

The authors found an interesting behaviour in all three cases with one, two or three heat sources: There is a moment in all three cases studied when oscillations in time near the heat sources appear, featuring their initial strength and then reaching its maximum and, eventually, ending up going weaker until the flow does not present these time oscillations anymore. This is a very interesting physical moment that a certain dimensionless number may be created or applied in order to feature this behaviour at its maximum or its appearance length in time. However, this will be left for future works from the same authors or from new authors.

7. Acknowledgment

The authors thank the following Brazilian support entities: CAPES, CNPq, and FAPEMIG.

8. References

Arquis, E.; Rady M.A.; Nada, S.A. (2007). A numerical investigation and parametric study of cooling an array of multiple protruding heat sources by a laminar slot air jet, *International Journal of Heat and Fluid Flow*, Vol. 28, pp. 787–805.

Madhusudhana Rao, G. & Narasimham, G.S.V.L. (2007). Laminar conjugate mixed convection in a vertical channel with heat generating components, *International Journal of Heat and Mass Transfer*, Vol. 50, pp. 3561–3574.

Muftuoglu, A. & Bilgen E. (2007). Conjugate heat transfer in open cavities with a discrete heater at its optimized position, *International Journal of Heat and Mass Transfer*, doi:10.1016/j.ijheatmasstransfer.2007.04.017.

Premachandran, B. & Balaji C. (2006). Conjugate mixed convection with surface radiation from a horizontal channel with protruding heat sources, *International Journal of Heat and Mass Transfer*, Vol. 49, pp. 3568–3582.

Dogan, A.; Sivrioglu, M.; Baskaya S. (2005). Experimental investigation of mixed convection heat transfer in a rectangular channel with discrete heat sources at the top and at the bottom, *International Communications in Heat and Mass Transfer*, Vol. 32, pp. 1244–1252.

Binet, B. & Lacroix, M. (2000). Melting from heat sources flush mounted on a conducting vertical wall, *Int. J. of Numerical Methods for Heat and Fluid Flow, Vol.* 10, pp. 286–306.

Baskaya, S.; Erturhan, U.; Sivrioglu, M. (2005). An experimental study on convection heat transfer from an array of discrete heat sources, *Int. Comm. in Heat and Mass Transfer*, Vol. 32, pp. 248–257.

Da Silva, A.K.; Lorente, S.; Bejan, A. (2004). Optimal distribution of discrete heat sources on a plate with laminar forced convection, *International Journal of Heat and Mass Transfer*, Vol. 47, pp. 2139–2148.

Heinrich, J. C. & Pepper, D. W. (1999). Intermediate Finite Element Method. Ed. Taylor & Francis, USA.

Bae, J.H. & Hyun, J.M. (2003). Time-dependent buoyant convection in an enclosure with discrete heat sources, *Int. J. Thermal Sciences*.

Madhavan, P.N. & Sastri, V.M.K. (2000). Conjugate natural convection cooling of protruding heat sources mounted on a substrate placed inside an enclosure: a parametric study, *Comput. Methods Appl. Mech Engrg.*, Vol. 188, pp. 187-202.

Choi, C.Y. & Ortega, A. (1979). Mixed Convection in an Inclined Channel With a Discrete Heat Source, *International Journal of Heat and Mass Transfer*, Vol. 36, pp. 3119-3134.

Bercovier, M. & Engelman, M. (1979). A Finite Element for the Numerical Solution of Viscous Incompressible Flow, *J. Comput. Phys.*, Vol. 30, pp. 181-201.

Carey, G. F. & Krishnam (1982). Penalty Approximation of Stokes Flow, *Comput. Methods Appl. Mech. Eng.*, Vol. 35, pp. 169-206.

Lee, T. & Mateescu, D. (1988). Experimental and Numerical Investigation of 2-D Backward-Facing Step Flow, *J. Fluids and Structures*, Vol. 12, pp. 703-716.

Armaly, B. F.; Durst, F; Pereira, J.C.F. & Schonung, B. (1983). Experimental and Theoretical Investigation of Backward-Facing Step Flow, *J. Fluid Mech.*, Vol. 127, pp. 473-496.

Gartling, D.K. (1990). A Test Problem for Outflow Boundary Conditions – Flow over a Backward-Facing Step, *Int. J. Num. Meth. in Fluids*, Vol. 11, pp. 953-967.

Kim, J. & Moin, P. (1985). Application of a Fractional-Step Method to Incompressible Navier-Stokes Equations, *J. Comp. Physics*, Vol. 59, pp. 308-323.

Sohn, J. (1988). Evaluation of FIDAP on Some Classical Laminar and Turbulent Benchmarks, *Int. J. Num. Meth. in Fluids*, Vol. 8, pp. 1469-1490.

Comini, G.; Manzam, M. & Cortella, G.. Open Boundary Conditions for the Streamfunction –Vorticity Formulation of Unsteady Laminar Convection, *Num. Heat Transfer Part B,* Vol. 31, pp. 217-234.

Guimarães, P.M. (2007). Phd. Thesis: Heat transfer analysis of mixed convection using the Petrov-Galerkin technique and the penalty, Brazil.

Guimarães, P. M. (2008). Combined free and forced coonvection in an inclined channel with discrete heat sources, Int. Communications of Heat and Mass Transfer, Vol. 35, pp. 1267-1274.

2

Periodically Forced Natural Convection Through the Roof of an Attic-Shaped Building

Suvash Chandra Saha
School of Engineering and Physical Sciences, James Cook University
Australia

1. Introduction

Buoyancy-induced fluid motions in cavities have been discussed widely because of the applications in nature and engineering. A large body of literature exists on the forms of internal and external forcing, various geometry shapes and temporal conditions (steady or unsteady) of the resulting flows. Especially for the classic cases of rectangular, cylindrical or other regular geometries, many authors have investigated imposed temperature or boundary heat fluxes. Reviews of these research can be found in Ostrach (1988) and Hyun (1994). The rectangular cavity is not an adequate model for many geophysical situations where a variable (or sloping) geometry has a significant effect on the system. However, the convective flows in triangular shaped enclosures have received less attention than those in rectangular geometries, even though the topic has been of interest for more than two decades

Heat transfer through an attic space into or out of buildings is an important issue for attic shaped houses in both hot and cold climates. The heat transfer through attics is mainly governed by a natural convection process, and affected by a number of factors including the geometry, the interior structure and the insulation etc. One of the important objectives for design and construction of houses is to provide thermal comfort for occupants. In the present energy-conscious society, it is also a requirement for houses to be energy efficient, i.e. the energy consumption for heating or air-conditioning of houses must be minimized. A small number of publications are devoted to laminar natural convection in two dimensional isosceles triangular cavities in the vast literature on convection heat transfer.

The temperature and flow patterns, local wall heat fluxes and mean heat flux were measured experimentally by Flack (1980; 1979) in isosceles triangular cavities with three different aspect ratios. The cavities, filled with air, were heated/cooled from the base and cooled/heated from the sloping walls covering a wide range of Rayleigh numbers. For the case of heated bottom surface it was found that the flow remained laminar for the low Rayleigh numbers. However, as the Rayleigh number increased, the flow eventually became turbulent. The author also reported the critical Rayleigh numbers of the transition from laminar to turbulent regimes. Kent (2009a) has also investigated the natural convection in an attic space for two different boundary conditions similar to Flack (1980; 1979). The author observed that for top heating and bottom cooling case the flow is dominated by pure conduction and remains stable for higher Rayleigh numbers considered. However, the flow becomes unstable for sufficiently large Rayleigh number for the second case (top cooling and bottom heating).

A comparison study is performed by Ridouane et al. (2005) where the authors compare their numerical results produced for two different boundary conditions, (a) cold base and hot inclined walls (b) hot base and cold inclined walls with the experimental results obtained by Flack (1980; 1979). A good agreement has been obtained between the numerical predictions and the experimental measurements of Nusselt number. A numerical study of above mentioned two boundary conditions has also performed by Ridouane et al. (2006). However, the authors cut a significant portion of bottom tips and applied adiabatic boundary condition there. It is revealed from the analysis that the presence of insulated sidewalls, even of very small height, provides a huge gain of energy and helps keep the attic at the desired temperature with a minimum energy.

The attic problem under the night-time conditions was again investigated experimentally by Poulikakos & Bejan (1983a). In their study, the authors modelled the enclosure as a right-angled triangle with an adiabatic vertical wall, which corresponded to the half of the full attic domain. A fundamental study of the fluid dynamics inside an attic-shaped triangular enclosure subject to the night-time conditions was performed by Poulikakos & Bejan (1983b) with an assumption that the flow was symmetric about the centre plane. Del Campo et al. (1988) examined the entire isosceles triangular cavities for seven possible combinations of hot wall, cold wall and insulated wall using the finite element method based on a stream function or vorticity formulation. A two dimensional right triangular cavity filled with air and water with various aspect ratios and Rayleigh numbers are also examined by Salmun (1995a).

The stability of the reported single-cell steady state solution was re-examined by Salmun (1995b) who applied the same procedures developed by Farrow & Patterson (1993) for analysing the stability of a basic flow solution in a wedge-shaped geometry. Later Asan & Namli (2001) carried out an investigation to examine the details of the transition from a single cell to multi cellular structures. Haese & Teubner (2002) investigated the phenomenon for a large-scale triangular enclosure for night-time or winter day conditions with the effect of ventilation.

Holtzmann et al. (2000) modelled the buoyant airflow in isosceles triangular cavities with a heated bottom base and symmetrically cooled top sides for the aspect ratios of 0.2, 0.5, and 1.0 with various Rayleigh numbers. They conducted flow visualization studies with smoke injected into the cavity. The main objective of their research was to validate the existence of the numerical prediction of the symmetry-breaking bifurcation of the heated air currents that arise with gradual increments in Rayleigh number. Ridouane & Campo (2006) has also investigated the numerical prediction of the symmetry-breaking bifurcation. The author reported that as Ra is gradually increased, the symmetric plume breaks down and fades away. Thereafter, a subcritical pitchfork bifurcation is created giving rise to an asymmetric plume occurring at a critical Rayleigh number, $Ra = 1.42 \times 10^5$. The steady state laminar natural convection in right triangular and quarter circular enclosures is investigated by Kent et al. (2007) for the case of winter-day temperature condition. A number of aspect ratios and Rayleigh numbers have been chosen to analyse the flow field and the heat transfer.

Unlike night-time conditions, the attic space problem under day-time (heating from above) conditions has received very limited attention. This may due to the fact that the flow structure in the attics subject to the daytime condition is relatively simple. The flow visualization experiments of Flack (1979) showed that the daytime flow remained stable and laminar for all the tested Rayleigh numbers (up to about 5×10^6). Akinsete & Coleman (1982) numerically simulated the attic space with hot upper sloping wall and cooled base. Their aim was to

obtain previously unavailable heat transfer data relevant to air conditioning calculations. This study considered only half of the domain. For the purpose of air conditioning calculations, Asan & Namli (2000) and Kent (2009b) have also reported numerical results for steady, laminar two-dimensional natural convection in a pitched roof of triangular cross-section under the summer day (day-time) boundary conditions.

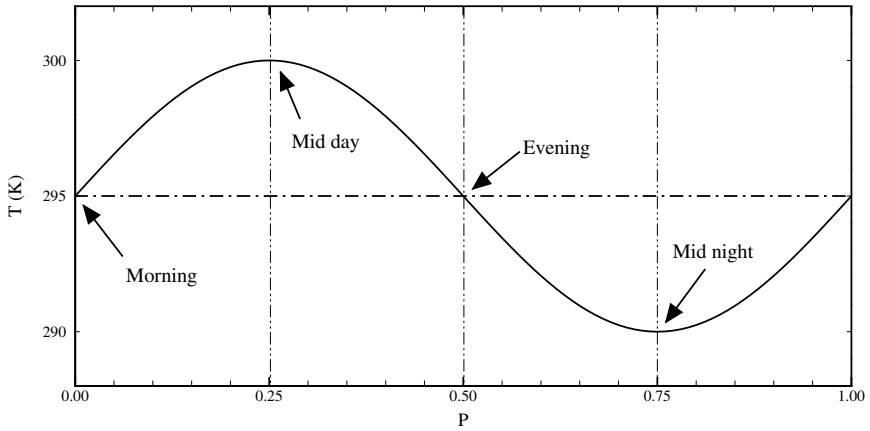

Fig. 1. Temperature boundary condition on the incline walls of the enclosure

Recently, the transient flow development inside the attic space has been analysed by using scaling analysis with numerical verification by (Saha, 2011a;b; Saha et al., 2010a;c; Saha, 2008). The authors considered different types of thermal conditions, such as, sudden heating/cooling and ramp heating/cooling. In real situations, however, the attic space of buildings is subject to alternative heating and cooling over a diurnal cycle as it can be seen in Fig. 1. A very few studies for diurnal heating and cooling effect on the attic space are reported in the literature (Saha et al., 2010b; 2007). The authors discussed a general flow structure and heat transfer due to the effect of periodic thermal forcing. A detailed explanation of choosing the period for the model attic is required as the 24-hour period for the field situation is not applicable here.

In this study, numerical simulations of natural convection in an attic space subject to diurnal temperature condition on the sloping wall have been carried out. An explanation of choosing the period of periodic thermal effect has been given with help of the scaling analysis which is available in the literature. Moreover, the effects of the aspect ratio and Rayleigh number on the fluid flow and heat transfer have been discussed in details as well as the formation of a pitchfork bifurcation of the flow at the symmetric line of the enclosure.

2. Formulation of the problem

The physical system is sketched in Fig. 2, which is an air-filled isosceles triangular cavity of variable aspect ratios. Here $2l$ is the length of the base or ceiling, T_0 is the temperature applied on the base, T_A is the amplitude of temperature fluctuation on the inclined surfaces, h is the height of the enclosure and P is the period of the thermal forcing.

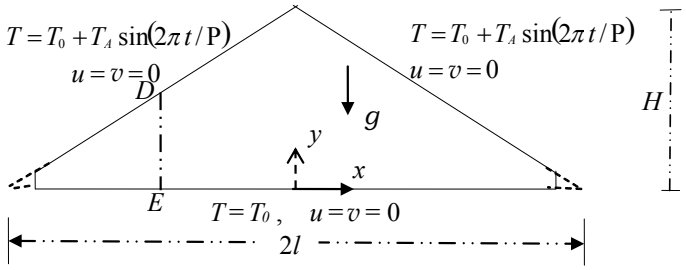

Fig. 2. A schematic of the geometry and boundary conditions of the enclosure

Under the Boussinesq approximations the governing continuity, momentum and energy equations take the following forms.

$$\frac{\partial u}{\partial x} + \frac{\partial v}{\partial y} = 0 \tag{1}$$

$$\frac{\partial u}{\partial t} + u\frac{\partial u}{\partial x} + v\frac{\partial u}{\partial y} = -\frac{1}{\rho}\frac{\partial p}{\partial x} + \nu\left(\frac{\partial^2 u}{\partial x^2} + \frac{\partial^2 u}{\partial y^2}\right) \tag{2}$$

$$\frac{\partial v}{\partial t} + u\frac{\partial v}{\partial x} + v\frac{\partial v}{\partial y} = -\frac{1}{\rho}\frac{\partial p}{\partial y} + \nu\left(\frac{\partial^2 v}{\partial x^2} + \frac{\partial^2 v}{\partial y^2}\right) + g\beta\left(T - T_0\right) \tag{3}$$

$$\frac{\partial T}{\partial t} + u\frac{\partial T}{\partial x} + v\frac{\partial T}{\partial y} = \kappa\left(\frac{\partial^2 T}{\partial x^2} + \frac{\partial^2 T}{\partial y^2}\right) \tag{4}$$

where u and v are the velocity components along $x-$ and $y-$directions, t is the time, p is the pressure, ν, ρ, β and κ are kinematic viscosity, density of the fluid, coefficient of thermal expansion and thermal diffusivity respectively, g is the acceleration due to gravity and T is the fluid temperature.

The boundary conditions for the present numerical simulations are also shown in Fig. 2. Here, the temperature of the bottom wall of the cavity is fixed at $T = T_0$. A periodic temperature boundary condition is applied to the two inclined walls. The Rayleigh number for the periodic boundary condition has been defined based on the maximum temperature difference between the inclined surface and the bottom over a cycle as

$$Ra = \frac{2g\beta T_A h^3}{\kappa\nu}$$

Three aspect ratios 0.2, 0.5 and 1.0, four Rayleigh numbers, 1.5×10^6, 7.2×10^5, 1.5×10^4, and 1.5×10^3, and a fixed Prandtl number 0.72 are considered in the present investigation. Based on the experimental observations of Flack (1979), which reported the critical Rayleigh number for the flow to become turbulent, we have chosen the maximum Rayleigh number, $Ra = 1.5 \times 10^6$ so that the flow stays in the laminar regime. It is understood that in real situations the Rayleigh number may be much higher than this and an appropriate turbulence model should be applied. This is beyond the scope of this study. In order to avoid the singularities at the tips in the numerical simulation, the tips are cut off by 5% and at the cutting points (refer to Fig. 2) rigid non-slip and adiabatic vertical walls are assumed. We anticipate that this modification of the geometry will not alter the overall flow development significantly.

3. Selection of the physical period

The period is determined in consideration of the scaling predictions of Saha et al. (2010a;b;c) which have demonstrated that the time for the adjustment of the temperature in the thermal boundary layer is by far shorter than the thermal forcing period of 24 hours in field situations. For sudden heating/cooling boundary conditions the steady state time scale for the boundary layer development from Saha et al. (2010c) is

$$t_s = \frac{(1+Pr)^{1/2}(1+A^2)^{1/2}}{ARa^{1/2}Pr^{1/2}}\left(\frac{h^2}{\kappa}\right), \tag{5}$$

and the heating-up or cooling-down time scale for the enclosure to be filled with hot or cold fluid under the same boundary conditions as in Saha et al. (2010c) is

$$t_f = \frac{(1+Pr)^{1/4}}{A^{1/2}Ra^{1/4}Pr^{1/4}(1+A^2)^{1/4}}\left(\frac{h^2}{\kappa}\right), \quad \text{for} \quad t_f > t_s \tag{6}$$

On the other hand, the quasi-steady time scale for ramp heating/cooling boundary condition of the boundary layer development for the case when the ramp time is longer than the quasi-steady time is (see Saha et al., 2010c)

$$t_{sr} = \frac{(1+Pr)^{1/3}(1+A^2)^{1/3}}{A^{2/3}Ra^{1/3}Pr^{1/3}}\left(\frac{t_p}{h^2/\kappa}\right)^{1/3}\left(\frac{h^2}{\kappa}\right), \tag{7}$$

and the heating-up or cooling-down time scale of the enclosure under the same boundary conditions from Saha et al. (2010a) is

$$t_{fr} = \frac{\left[h(1+A^2)^{1/2} - Ax_1\right]^2}{A^{1/2}\kappa Ra^{1/4}(1+A^2)^{5/4}}, \tag{8}$$

where x_1 is given by

$$x_1 \sim L\left[1-\left(1-\frac{\kappa A^{1/2}Ra^{1/4}(1+A^2)^{1/4}}{h^2}t_p\right)^{1/2}\right], \tag{9}$$

However, if the cavity is filled with cold fluid before the ramp is finished then the filling up time is given in Saha et al. (2010a) as

$$t_{fq} \sim \frac{h^{8/7}t_p^{3/7}}{\kappa^{4/7}Ra^{1/7}A^{2/7}(1+A^2)^{1/7}}, \tag{10}$$

Table 1 presents the scaling values of the steady and quasi-steady times for sudden and ramp heating/cooling boundary conditions respectively for different A and Ra. The highest Rayleigh number considered here for three different aspect ratio is $Ra = 1.5 \times 10^6$. It is noticed that the steady state times for the boundary layer for this Rayleigh number of $A = 0.2, 0.5$ and 1.0 are $8.1s$, $2.54s$ and $2.26s$ respectively. However, for the lowest Rayleigh number, $Ra = 7.2 \times 10^3$ the steady state time for $A = 0.5$ is $35.76s$. On the other hand, the quasi-steady time for the ramp temperature boundary condition depends on the length of the ramp. If we assume the ramp time to be $1000s$ then the quasi-steady times for these aspect ratios are $40.51s$, $18.62s$ and $17.23s$ respectively and for the lowest Rayleigh number, $Ra = 7.2 \times 10^3$

Aspect ratio	Steady state time (t_s) for sudden heating/cooling		Quasi-steady time (t_{sr}) for ramp heating/cooling (t_p = 1000s)	
	$Ra = 1.5\times10^6$	$Ra = 7.2\times10^3$	$Ra = 1.5\times10^6$	$Ra = 7.2\times10^3$
A=0.2	8.15s	-	40.51s	-
A=0.5	2.54s	35.76s	18.62s	108.53s
A=1.0	2.26s	-	17.23s	-

Table 1. Steady state and quasi-steady times for sudden and ramp boundary conditions respectively for different A and Ra.

the quasi-steady time for the aspect ratio $A = 0.5$ is $108.53s$ which is much shorter than the ramp time ($1000s$). If the ramp time is $200s$ the quasi-steady time of $A = 0.5$ for the lowest Rayleigh number considered here is $63.47s$. Still the quasi-steady time is about half of the ramp time. Therefore, what happened between the quasi-steady time and the ramp time is, once the quasi-steady state time t_{sr} is reached, the boundary layer stops growing according to $\kappa^{1/2}t^{1/2}$ which is only valid for conductive boundary layers. The thermal boundary layer is in a quasi-steady mode with convection balancing conduction. Further increase of the heat input simply accelerates the flow to maintain the proper thermal balance. The thickness and the velocity scales during this quasi-steady mode is (see Saha et al., 2010c)

$$\delta_T \sim \frac{h(1+A^2)^{1/4}}{Ra^{1/4}A^{1/2}}\left(\frac{t_p}{t}\right)^{1/4}. \tag{11}$$

and

$$u \sim Ra^{1/2}\frac{\kappa}{h}\left(\frac{t}{t_p}\right)^{1/2}. \tag{12}$$

respectively. When the hot fluid travels through the boundary layer and reaches the top tip of the cavity then it has no choice but to move downward along the symmetry line of the cavity. In this way the cavity is filled up with hot fluid with a horizontal stratification of the thermal field. However, during the cooling phase, the boundary layer is not stable for the Rayleigh numbers considered here. In that case initially a cold boundary layer develops adjacent to the inclined wall which is potentially unstable to the Rayleigh Bénard instability, which may manifest in a form of sinking plumes. These plumes mix up the cold fluid with the hot fluid inside the cavity until the end of the cooling phase.

Moreover, Table 2 shows the scaling values of the filling-up times for sudden and ramp heating/cooling boundary conditions for different A and Ra. It is seen that the heating-up or cooling-down times for the sudden heating/cooling boundary condition for $A = 0.5$ and $Ra = 1.5 \times 10^6$ is $42.39s$ and for $Ra = 7.2 \times 10^3$ and the same aspect ratio is $159.01s$. For aspect ratios 0.2 and 1.0 the filling-up times are $83.24s$ and $31.61s$ respectively when $Ra = 1.5 \times 10^6$. The filling-up times for ramp heating/cooling boundary conditions for $A = 0.5$ are $145.07s$ and $308.77s$ when $Ra = 1.5 \times 10^6$ and 7.2×10^3 respectively and $t_p = 1000s$. For two other aspect ratios, $A = 0.2$ and 1.0, the filling-up times are $213.32s$ and $122.67s$ respectively for $Ra = 1 \times 10^6$. However, the filling-up time for ramp boundary conditions depends on the length of the ramp time. If the ramp time is $200s$ then the filling-up time for the lowest

Aspect ratio	Filling-up time (t_f) for sudden heating/cooling		Filling-up time (t_{fr}) for ramp heating/cooling (t_p = 1000s)	
	$Ra = 1.5\times10^6$	$Ra = 7.2\times10^3$	$Ra = 1.5\times10^6$	$Ra = 7.2\times10^3$
A=0.2	83.24s	-	213.32s	-
A=0.5	42.39s	159.01s	145.07s	308.77s
A=1.0	31.61s	-	122.67s	-

Table 2. Heating-up/cooling-down times for sudden and ramp boundary conditions respectively for different A and Ra.

Rayleigh number considered here is 154.90s for $A = 0.5$. These times are very short when compared to the thermal forcing period of 24 hours in field situations. Therefore, the period of the thermal cycle may be considered as 400s or more based on the above discussions for the following numerical simulations. However, for a better understanding of the flow at in the quasi-steady mode, we have chosen a thermal forcing period of 2000s for all the simulations.

4. Numerical scheme and grid and time step dependence tests

Equations (1) - (4) are solved along with the initial and boundary conditions using the SIMPLE scheme. The finite volume method has been chosen to discretize the governing equations, with the QUICK scheme (see Leonard & Mokhtari, 1990) approximating the advection term. The diffusion terms are discretized using central-differencing with second order accurate. A second order implicit time-marching scheme has also been used for the unsteady term. An extensive mesh and time step dependence tests have been coonducted in Saha et al. (2010a;b;c)

5. Flow response to the periodic thermal forcing

The flow response to the periodic thermal forcing and the heat transfer through the sloping boundary are discussed for the case with $A = 0.5$, $Pr = 0.72$ and $Ra = 1.5 \times 10^6$ in this section.

5.1 General flow response to diurnal heating and cooling

Since the initial flow is assumed to be isothermal and motionless, there is a start-up process of the flow response. In order to minimize the start-up effect, three full thermal forcing cycles are calculated in the numerical simulation before consideration of the flow. It is found that the start-up effect for the present case is almost negligible, and the flow response in the third cycle is identical to that in the previous cycle. In the following discussion, the results of the third cycle are presented.

Fig. 3 shows snapshots of streamlines and the corresponding isotherms and vector field at different stages of the cycle. The flow and temperature structures, shown in Fig. 3 at $t = 2.00P$, represent those at the beginning of the daytime heating process in the third thermal forcing cycle. At this time, the inclined surfaces and the bottom surface of the enclosure have the same temperature, but the temperature inside the enclosure is lower than the temperature on the boundaries due to the cooling effect in the previous thermal cycle. The residual temperature structure, which is formed in the previous cooling phase, is still present at $t = 2.00P$. The

corresponding streamline contours at the same time show two circulating cells, and the temperature contours indicate stratification in the upper and lower section of the enclosure with two cold regions in the centre.

As the upper surface temperature increases further, a distinct temperature stratification is established throughout the enclosure by the time $t = 2.05P$ (see Fig. 3). The streamlines at this stage indicate that the centers of the two circulating cells have shifted closer to the inclined surfaces, indicating a strong conduction effect near those boundaries. This phenomenon has been reported previously in Akinsete & Coleman (1982) and Asan & Namli (2000) for the daytime condition with constant heating at the upper surface or constant cooling at the bottom surface.

At $t = 2.25P$, the temperature on the inclined surfaces peaks. Subsequently, the temperature drops, representing a decreasing heating effect. Since the interior flow is stably stratified prior to $t = 2.25P$, the decrease of the temperature at the inclined surface results in a cooling event, appearing first at the top corner and expanding downwards as the surface temperature drops further. At $t = 2.45P$, two additional circulating cells have formed in the upper region of the enclosure, and the newly formed cells push the existing cells downwards. The corresponding temperature contours show two distinct regions, an expanding upper region responding to the cooling effect, and a shrinking lower region with stratification responding to the decreasing heating effect. By the time $t = 2.50P$, the daytime heating ceases; the lower stratified flow region has disappeared completely and the flow in the enclosure is dominated by the cooling effect. At this time, the top and the bottom surfaces again have the same temperature, but the interior temperature is higher than that on the boundaries.

As the upper inclined surface temperature drops below the bottom surface temperature ($t = 2.70P$, Fig. 3), the cold-air layer under the inclined surfaces becomes unstable. At the same time, the hot-air layer above the bottom surface also becomes unstable. As a consequence, sinking cold-air plumes and rising hot-air plumes are visible in the isotherm contours and a cellular flow pattern is formed in the corresponding stream function contours. It is also noticeable that the flow is symmetric about the geometric symmetry plane at this time. However, as time increases the flow becomes asymmetric about the symmetric line (see isotherms at $t = 2.95P$). The large cell from the right hand side of the centreline, which is still growing, pushes the cell on the left of it towards the left tip. At the same time this large cell also changes its position and attempts to cross the centreline of the cavity and a small cell next to it moves into its position and grows.

At $t = 2.975P$, the large cell in the stream lines has crossed the centerline and the cell on the right of it grows and becomes as large as it is after a short time (for brevity figures not included). The flow is also asymmetric at this time. However, it returns to a symmetric flow at the time $t = 3.00P$ which is the same as that at $t = 2.00P$, and similar temperature and flow structures to those at the beginning of the forcing cycle are formed. The above described flow development is repeated in the next cycle.

The horizontal velocity profiles (velocity parallel to the bottom surface) and the corresponding temperature profiles evaluated along the line DE shown in Fig. 2 at different time instances of the third thermal forcing cycle are depicted in Fig. 4. At the beginning of the cycle ($t = 2.00P$) the velocity is the highest near the roof of the attic (see Fig. 4a), which is the surface driving the flow. At the same time, the body of fluid residing outside the top wall layer moves fast toward the bottom tips to fill up the gap. As time progresses the vertical velocity increases and the horizontal temperature decreases (see $t = 2.05P$). A three layer structure in the velocity field

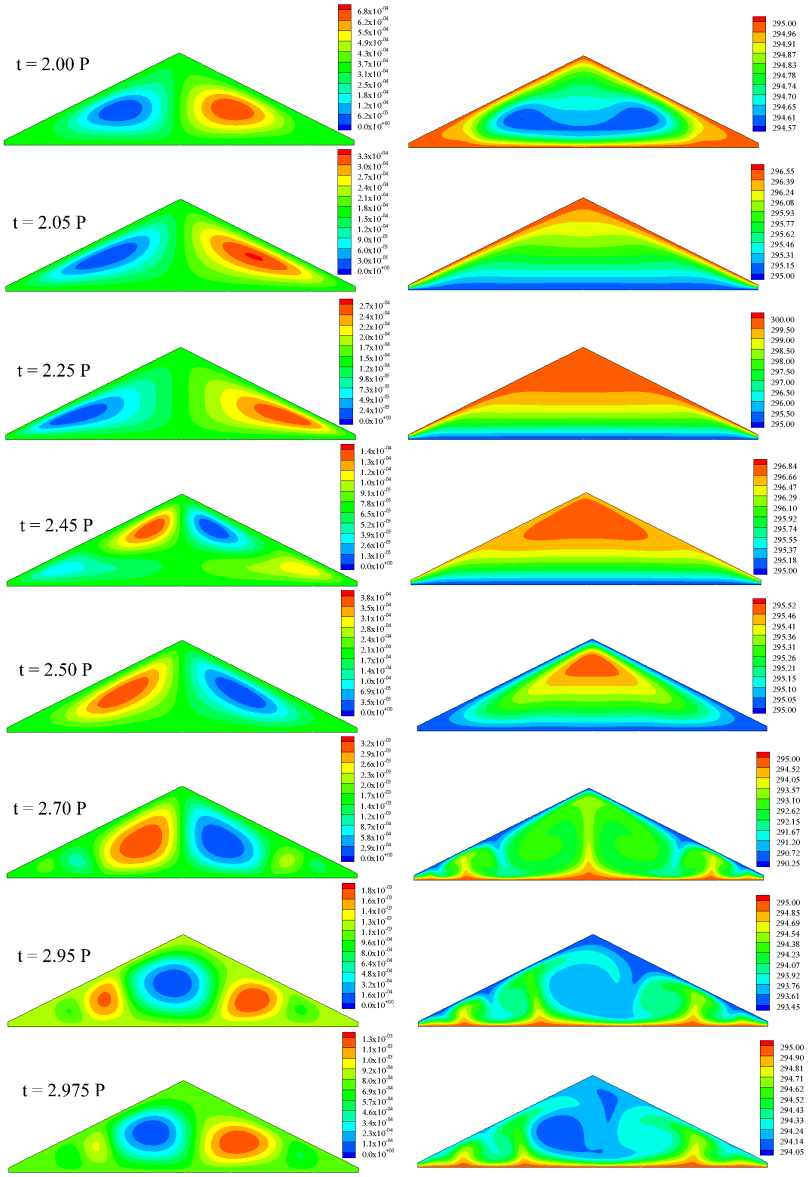

Fig. 3. A series of snapshots of stream function and temperature contours of the third cycle at different times for $A = 0.5$ and $Ra = 1.5 \times 10^6$. Left: streamlines; right: isotherms.

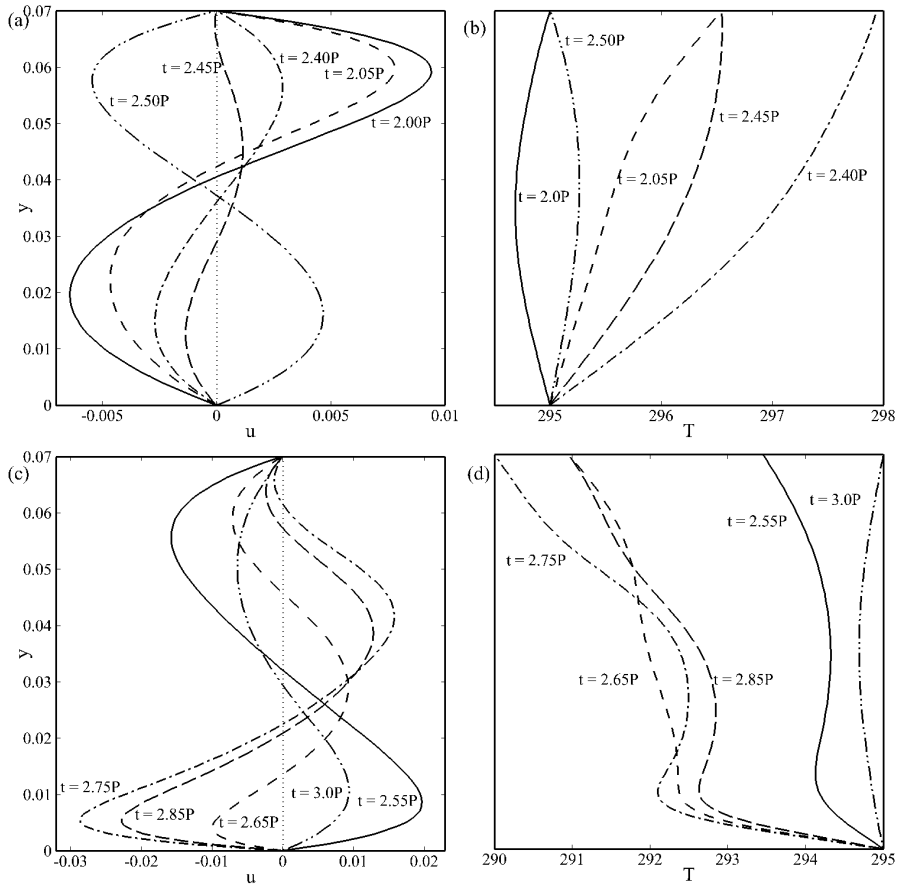

Fig. 4. Horizontal velocity profile (left) and temperature profile (right) along DE for $A = 0.5$ with $Ra = 1.5 \times 10^6$.

is found at $t = 2.45P$. At this time the top portion of the cavity is locally cooled and the bottom portion is still hot (see Fig. 3). After that time the flow completely reverses at $t = 2.50P$. It is noted that at this time the horizontal velocity is lower than that at the beginning of the cycle despite that the temperatures on the sloping boundary and the ceiling are the same at both times (see Fig. 4b). This is due to the fact that at the beginning of the cycle the flow is mainly dominated by convection as a result of the cooling effect in the second half of the previous thermal cycle. However, the flow is dominated by conduction at $t = 2.50P$ as a result of the heating effect in the first half of the current thermal cycle.

As mentioned above, at the beginning of the cycle ($t = 2.00P$) the temperatures on the horizontal and inclined surfaces are the same as shown in Fig. 4(b). However the temperature near the mid point of the profile line is lower than that at the surfaces by approximately $0.5K$, which is consistent with the previous discussion of the flow field. Subsequently the temperature of the top surface increases ($t = 2.05P$) while the bottom surface temperature

remains the same. It is noteworthy that the top surface reaches its peak temperature at $t = 2.25P$ (for brevity the profile is not included). After this time the top surface temperature starts to decrease which can be seen at time $t = 2.40P$. By comparing the temperature profiles at $t = 2.05P$ and $t = 2.45P$ shown in Fig. 4(b), it is clear that the temperatures at both the top and bottom surfaces are the same for these two time instances. However, different temperature structures are seen in the interior region. The same phenomenon has been found at the times $t = 2.50P$ and $t = 2.00P$.

In Fig. 4(c), the velocity profiles at the same location during the night-time cooling phase are displayed. In this phase the flow structure is more complicated. At $t = 2.55P$ the velocity near the bottom surface is slightly higher than that near the top. Again a three layer structure of the velocity field appeared which is seen at $t = 2.65P, 2.75P$ and $2.85P$. The maximum velocity near the ceiling occurs at $t = 2.75P$ when the cooling is at its maximum. After that it decreases and the flow reverses completely at $t = 3.0P$. The corresponding temperature profiles for the night-time condition are shown in Fig. 4(d). It is seen that the temperature lines are not as smooth as those observed for the daytime condition. At $t = 2.55P$, the temperature near the bottom surface decreases first and then increases slowly with the height and again decreases near the inclined surface. This behaviour near the bottom surface is due to the presence of a rising plume. Similar behaviour has been seen for $t = 2.75P$ and $2.85P$. However, at $t = 2.65P$ it decreases slowly after rapidly decreasing near the bottom surface. At $t = 3.00P$ again the bottom and top surface temperatures are the same with a lower temperature in the interior region.

5.2 Heat transfer across the attic

The Nusselt number, which has practical significance, is calculated as follows:

$$Nu = \frac{h_{\text{eff}} h}{k} \tag{13}$$

where the heat transfer coefficient heff is defined by

$$h_{\text{eff}} = \frac{q}{T_A} \tag{14}$$

Here q is the convective heat flux through a boundary. Since the bottom surface temperature is fixed at $295K$ and the sloping wall surface temperature cycles between 290K and 300K (refer to Figure 1), a zero temperature difference between the surfaces occurs twice in a cycle. Therefore, the amplitude of the temperature fluctuation (T_A) is chosen for calculating the heat transfer coefficient instead of a changing temperature difference, which would give an undefined value of the heat transfer coefficient at particular times.

Fig. 5 shows the calculated average Nusselt number on the inclined and bottom surfaces of the cavity. The time histories of the calculated Nusselt number on the inclined surfaces exhibit certain significant features. Firstly, it shows a periodic behaviour in response to the periodic thermal forcing. Secondly within each cycle of the flow response, there is a time period with weak heat transfer and a period with intensive heat transfer. The weak heat transfer corresponds to the daytime condition when the flow is mainly dominated by conduction and the strong heat transfer corresponds to the night-time condition. At night, the boundary layers adjacent to the inclined walls and the bottom are unstable. Therefore, sinking and rising plumes are formed in the inclined and horizontal boundary layers. These plumes dominate

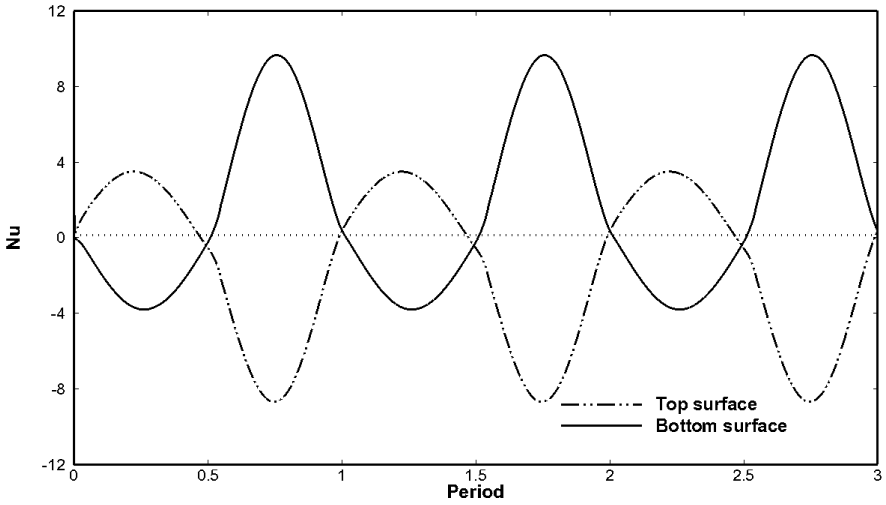

Fig. 5. Average Nusselt number on the top and bottom surfaces of the cavity for three full cycles where $Ra = 1.5 \times 10^6$ and $A = 0.5$

the heat transfer through the sloping walls of the cavity. Finally the calculated maximum Nusselt number on sloping surfaces is 8.72, occurring during the night-time period, whereas the maximum value during the day time is only 3.48, for the selected Rayleigh number and aspect ratio. The corresponding Nusselt number calculated on the bottom surface shows similar behavior as that of top surfaces. Note that the Nusselt number calculated using (13) is based on the total heat flux across the surfaces. Since the surface area of the top surface is larger ($0.595m^2$) than the bottom surface ($0.532m^2$), therefore the total surface heat flux on the top surfaces will be lower than that of the bottom surface. However, the integral of the heat transfer rate for a cycle on both surfaces has been calculated and it is found that both are the same.

5.3 Effects of the aspect ratio on the flow response

The flow responses to the periodic thermal forcing for the other two aspect ratios are shown in Figs. 6 and 7, which are compared with the flow response for $A = 0.5$ shown in Fig. 3. It is found that the aspect ratio of the enclosure has a great influence on the flow response as well as heat transfer. The residual effect of the previous cycle on the current cycle has been found similar for all aspect ratios (see at $t = 2.0P$ in Figs. 3, 6, 7) and the flow and temperature structures during the heating process is qualitatively the same for $A = 1.0$ and $A = 0.2$ as those for $A = 0.5$ for $Ra = 1.5 \times 10^6$. However, during the cooling phase there are significant changes of flow and heat transfer among these aspect ratios. For the night-time the high velocity area of these three aspect ratios exists between the two cells where the stream function gradient is higher. Therefore, the buoyancy drives the warm air upwards from the bottom of the geometry and at the same time the gravitational force acts on the cold air downwards from the top. This upward and downward movement can be seen in the temperature contours as a form of rising and sinking plumes.

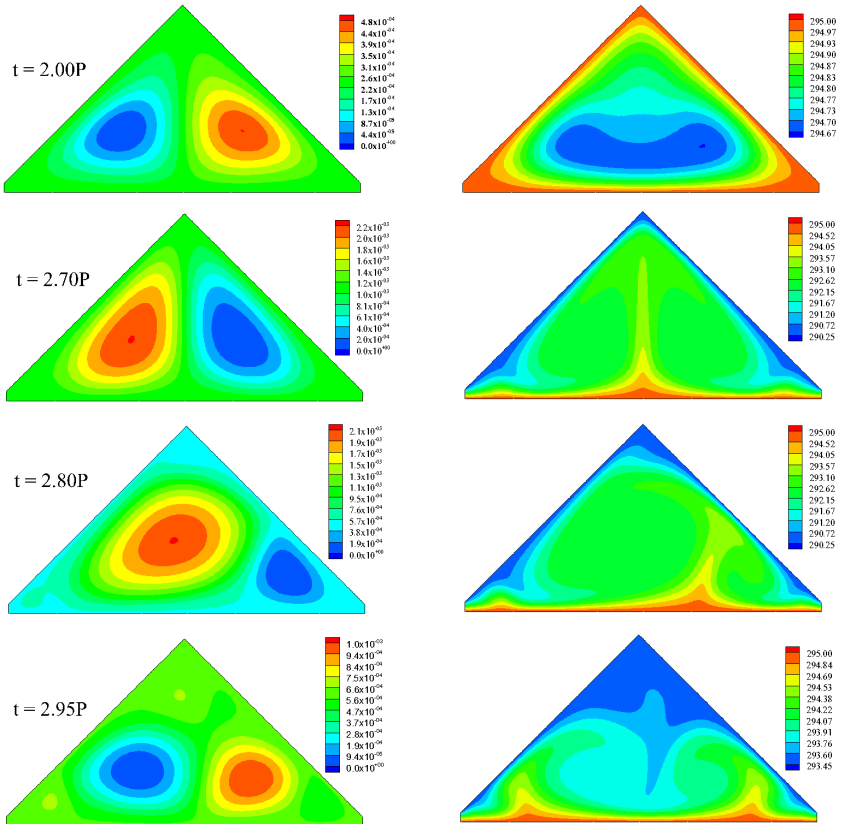

Fig. 6. A series of snapshots of stream function and temperature contours of the third cycle at different times for $A = 1.0$ and $Ra = 1.5 \times 10^6$. Left: streamlines; right: isotherms.

It has been revealed that the flow remains symmetric about the geometrical centreline throughout the cycle for aspect ratio $A = 0.2$, whereas, it is asymmetric during the cooling phase for the other two aspect ratios for $Ra = 1.5 \times 10^6$. It is also anticipated that the asymmetric solution is one of two possible mirror images of the solutions. Another noticeable variation with different aspect ratios is the formation of a circulation cell near the top of the enclosure. It is seen for $A = 1.0$ that there is an extra vortex (Fig. 6 at $t = 2.95P$) on the top of the cavity, which is completely absent for $A = 0.5$ and $A = 0.2$. The flow and temperature fields for the smallest aspect ratio $A = 0.2$ are more complex, with several circulation cells on either side of the central line and many plumes alternately rising and falling throughout the domain, as seen in Fig. 7. These cells and plumes are the result of flow instability described earlier.

Fig. 8 illustrates the horizontal velocity and temperature profiles for aspect ratio $A = 1.0$ along the line DE as shown in Fig. 2 for $Ra = 1.50 \times 10^6$. Since the flow is stable and stratified during the day (the heating phase), the structures of the velocity and temperature profiles are qualitatively the same as those for other aspect ratios.

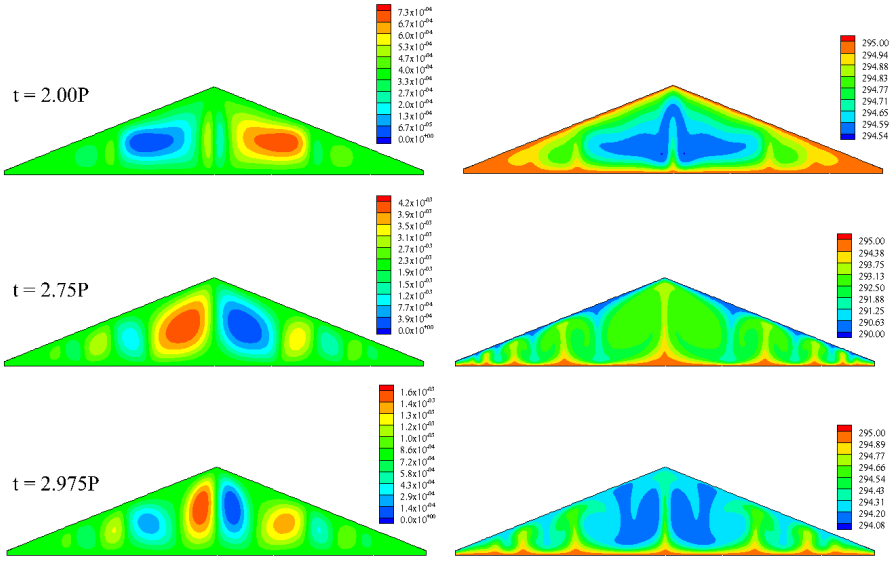

Fig. 7. A series of snapshots of stream function and temperature contours of the third cycle at different times for $A = 0.2$ and $Ra = 1.5 \times 10^6$. Left: streamlines; right: isotherms.

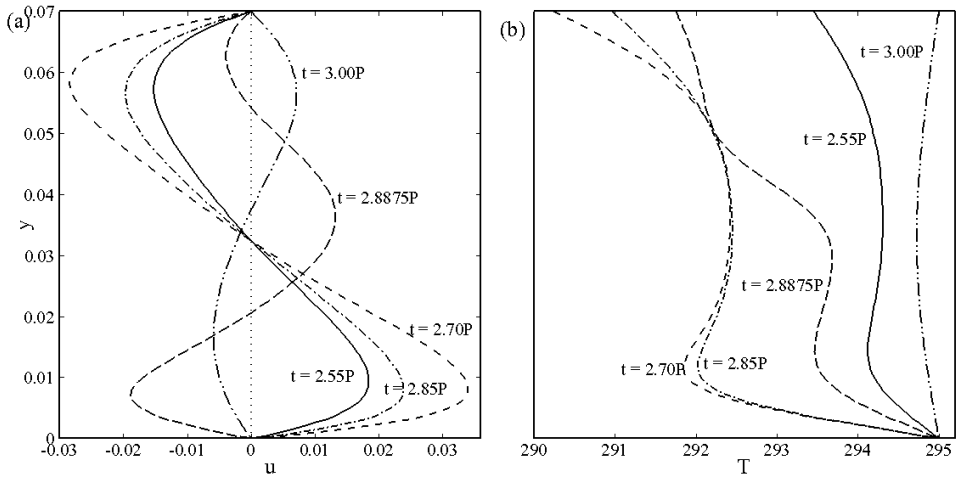

Fig. 8. Horizontal velocity profile (left) and temperature profile (right) along DE for $A = 1.0$ with $Ra = 1.50 \times 10^6$.

At the night-time the velocity and temperature profiles for $A = 1.0$ are more complicated than that for $A = 0.5$. As seen in Fig. 8, at time $t = 2.55P$ when the upper surface temperature is lower than the bottom surface, the velocity near the bottom surface is slightly higher than that near the inclined surfaces. After that the velocity increases near both the surfaces until $t = 2.75P$. Since a plume-type instability dominates the flow during the cooling phase and the flow has an asymmetric behaviour for a certain period of time, the horizontal velocity is in the same direction near both surfaces and is in an opposite direction in the middle (see $t = 2.8875P$). As the flow transits into the next thermal cycle, it becomes very weak. The corresponding temperature contours are plotted in Fig. 8(b). It is seen that the temperature profiles near the bottom surface show a wave shaped for almost the whole cooling phase due to the rising plumes (see Fig. 3). At the time $t = 2.8875P$, when three layers of the velocity structure is seen, the corresponding temperature profile also shows a wave structure.

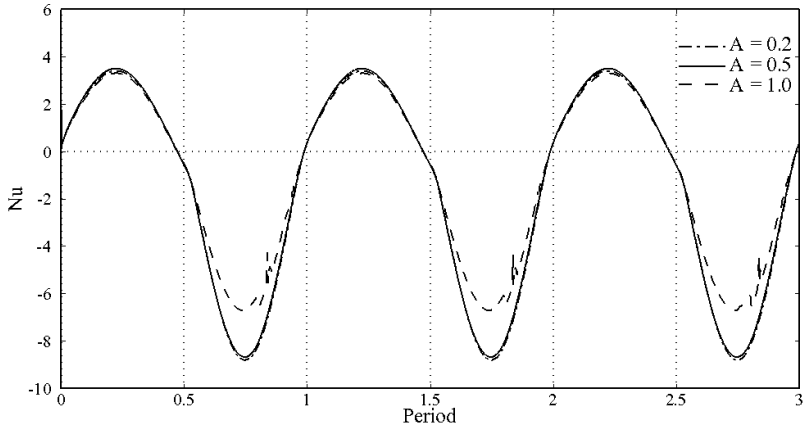

Fig. 9. Comparison of the average Nusselt number of three aspect ratios for $Ra = 1.5 \times 10^6$

Fig. 9 shows the calculated average Nusselt number on the inclined surfaces of the cavity for three different aspect ratios. The time histories of the calculated Nusselt number exhibit certain common features. Within each cycle of the flow response, there is a time period with weak heat transfer and a period with intensive heat transfer for each aspect ratio. The weak heat transfer corresponds to the day time condition when the heat transfer is dominated by conduction and the strong heat transfer corresponds to the night-time condition when convection dominates the flows and the instabilities occur in the form of rising and sinking plumes. During the day time the heat transfer rate is almost the same for all three aspect ratios. However, at the night time the heat transfer rate for $A = 1.0$ is much smaller than that for the other two aspect ratios, and there is a fluctuation of the Nusselt number for a certain period of time. This fluctuation is absent in the other two aspect ratios. This may be due to the fact that less convective cells are present in the streamlines for $A = 1.0$ than those for the other two aspect ratios. Moreover, the movement of the dominating cell for $A = 1.0$ is faster than those for other two. In addition to this, an extra cell appears on the top of the cavity for the aspect ratio $A = 1.0$. It is also noticed that there is not much difference in heat transfer for

the aspect ratios $A = 0.5$ and 0.2. The highest average Nusselt numbers for $A = 1.0, 0.5$ and 0.2 are 6.55, 8.72 and 8.76 respectively.

5.4 Effects of Rayleigh number on the flow response and heat transfer

Fig.10 shows snapshots of stream function and temperature contours for the aspect ratio 0.5 with three different Rayleigh numbers, $Ra = 1.5 \times 10^6, 7.2 \times 10^4$ and 7.2×10^3. The contours for $Ra = 7.2 \times 10^4$ are qualitatively the same as for $Ra = 1.5 \times 10^6$. It is found that in the heating phase (i.e. when the upper wall temperature is higher than the temperature of the bottom) the flow structures are qualitatively similar for all Rayleigh numbers. However, in the cooling phase the flow behaviour is strongly dependent on the Rayleigh numbers. Stream function and temperature contours are presented at two different times, $t = 2.70P$ and $2.95P$ for each Rayleigh number in Fig. 10. In the isotherms, rising and sinking plumes are visible for $Ra = 1.5 \times 10^6$ and 7.2×10^4 at both times. A cellular flow pattern is seen in the corresponding stream function contours for $Ra = 1.5 \times 10^6$. However, only two convective cells are present for $Ra = 7.2 \times 10^4$. If the Rayleigh number is decreased further ($Ra = 7.2 \times 10^3$), the flow becomes weaker. Only two cells are seen in the stream function contours and the temperature field is horizontally stratified (see the corresponding isotherms). At $t = 2.95P$, the flow seems to be asymmetric along the centre line for $Ra = 1.5 \times 10^6$. However, for the lower Rayleigh numbers the asymmetric behaviour is not visible.

Fig.11 shows the comparison of the Nusselt number among four Rayleigh numbers for a fixed aspect ratio 0.5. It is seen clearly that during the heating phase the heat transfer rate is weaker, whereas it is much stronger in the cooling phase. With the increase of the Rayleigh number, the Nusselt number increases throughout the thermal cycle, but the rate of increase is much higher in the cooling phase compared to that in the heating phase. The maximum Nusselt number in the cooling phase for $Ra = 1.5 \times 10^6$ is about 2.5 times of the maximum Nusselt number during the heating phase. It is noticeable that for the lowest Rayleigh number $Ra = 1.5 \times 10^3$, the heat transfer rate during the heating and cooling phases are almost the same. The maximum Nusselt number for the four different Rayleigh numbers, $Ra = 1.5 \times 10^6, 7.2 \times 10^5, 7.2 \times 10^4$ and 7.2×10^3 for the aspect ratio 0.5 are 8.65, 7.34, 4.26 and 3.11 respectively.

5.5 Transition between symmetric and asymmetric flows

The highest Rayleigh number considered in this study for the three aspect ratios is 1.5×10^6. Except for $A = 0.2$, the flow in the cavity for the other two aspect ratios is observed to undergo a supercritical pitchfork bifurcation for this Rayleigh number, in which case one of two possible mirror image asymmetric solutions is obtained. This asymmetric behaviour was first reported numerically and experimentally by Holtzmann et al. (2000) in their study of the case of a sudden cooling boundary condition. If the flow is asymmetric, the horizontal velocity along the midplane of the isosceles triangle would be nonzero. Based on this hypothesis, Fig.12 illustrates the absolute value of maximum horizontal velocity along the geometric center line for $A = 1.0$ and 0.5. It is seen in this figure that, for both aspect ratios, the maximum horizontal velocity is zero up to approximately $t = 0.70P$ in each cycle, suggesting that the flow is symmetric during this time. However, after this time the maximum horizontal velocity starts to increase, indicating that the flow becomes asymmetric. The asymmetry remains until shortly before the end of each cycle when the flow returns to symmetric again. The same asymmetric behaviour of the flow is seen for the Rayleigh number 7.2×10^5 for the aspect ratios 0.5 and 1.0.

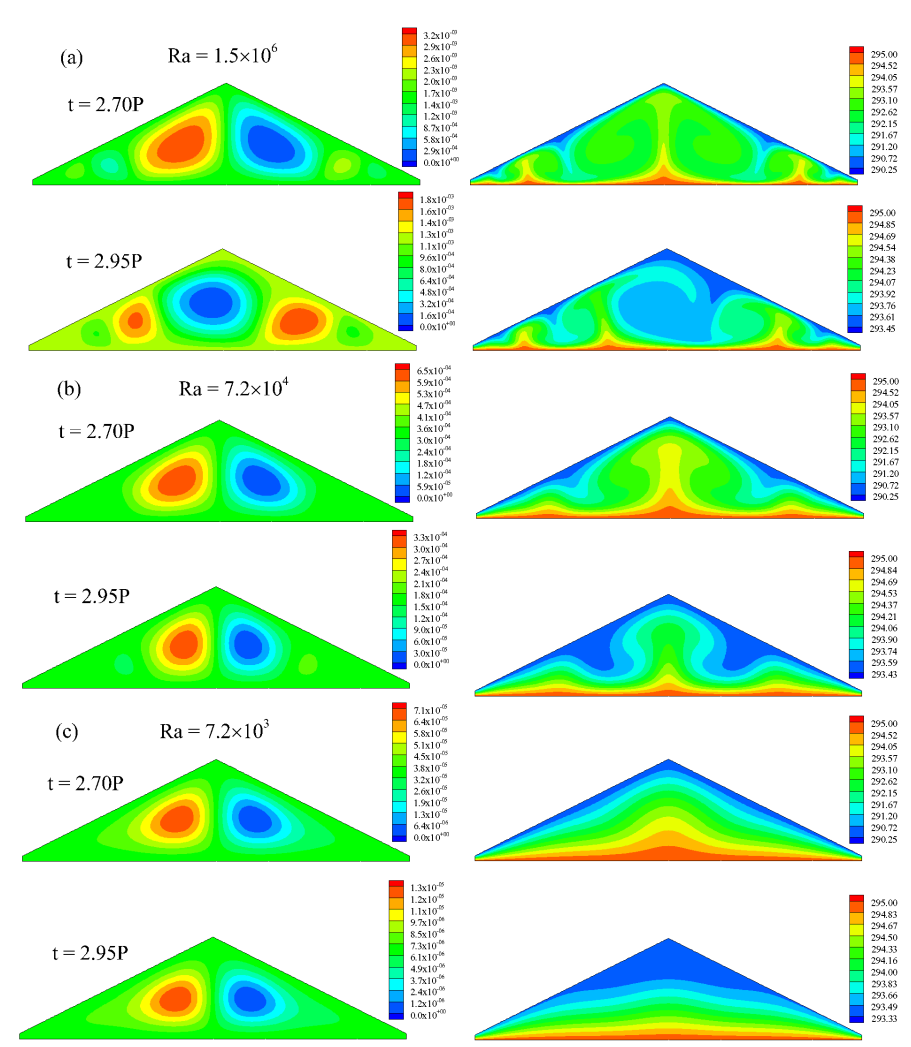

Fig. 10. Snapshots of stream function contours (left) and isotherms (right) of the third cycle at different times and different Rayleigh numbers with fixed $A = 0.5$.

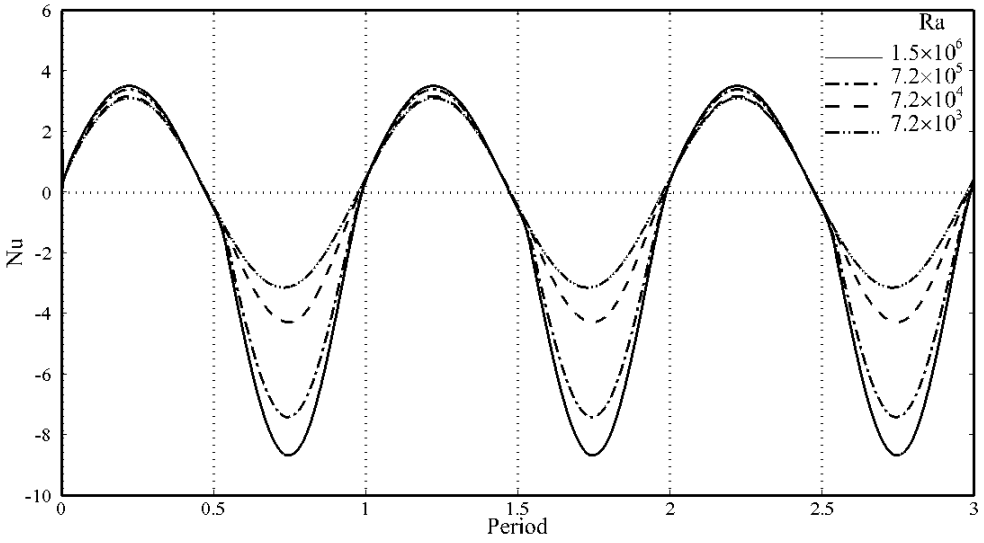

Fig. 11. Comparison of the average Nusselt number of four Rayleigh numbers for $A = 0.5$

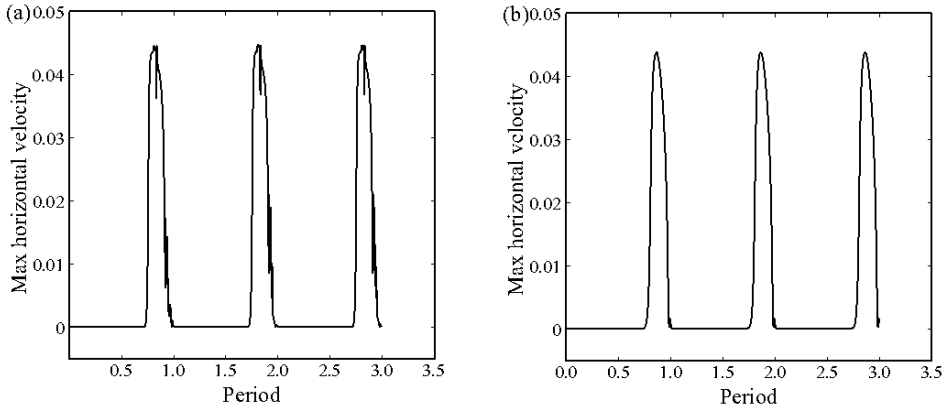

Fig. 12. The maximum horizontal velocity along the symmetry line for (a) $A = 1.0$ and (b) $A = 0.5$ with $Ra = 1.5 \times 10^6$.

The same results have been found when the average Nusselt numbers obtained for both inclined surfaces are compared for the aspect ratios 1.0 and 0.5, which are shown in Fig.13 (a) and (b) respectively. It is seen that at about $t = 0.70P$, the calculated Nusselt numbers at the left and right inclined surfaces start to diverge, but later they meet again before the end of each cycle.

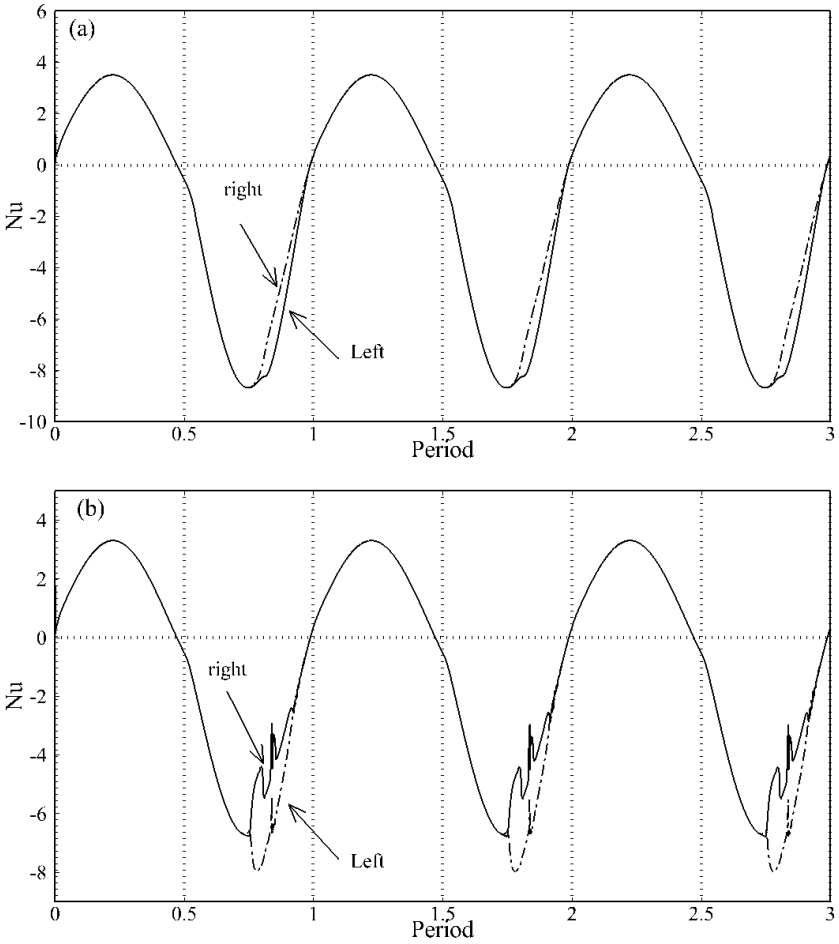

Fig. 13. Comparison of the average Nusselt number on two inclined surfaces of the enclosure for (a) $A = 1.0$ and (b) $A = 0.5$ with $Ra = 1.5 \times 10^6$

6. Conclusions

Natural convection in an attic-shaped building with the effect of periodic thermal forcing has been carried out in this study based on numerical simulations. An attempt has also been taken to predict the period of the model attic using scaling analysis. Three aspect ratios of $A = 1.0, 0.5$ and 0.2 with four Rayleigh numbers of $Ra = 1.5 \times 10^6, 7.2 \times 10^5, 7.2 \times 10^4$ and 7.2×10^3 for each aspect ratio have been considered here. Many important features are revealed from the present numerical simulations. It is found that the flow response to the temperature variation on the external surface is fast, and thus the start-up effect is almost negligible. The occurrence of sinking cold-air plumes and rising hot-air plumes in the isotherm contours and the formation of cellular flow patterns in the stream function contours confirm the presence of the Rayleigh-Bénard type instability. It is also observed that the flow undergoes a transition

between symmetry and asymmetry about the geometric symmetry plane over a diurnal cycle for the aspect ratios of $A = 1.0$ and 0.5 with the Rayleigh numbers 1.5×10^6 and 7.2×10^5. For all other cases the flow remains symmetric. A three-layer velocity structure has been found along the line at DE as shown in Fig. 2 in both the daytime heating phase (due to local cooling effect in the upper sections of the inclined walls) and night-time cooling phase when the flow becomes asymmetric. Furthermore, the flow response in the daytime heating phase is weak, whereas the flow response in the night-time cooling phase, which is dominated by convection, is intensive. At lower Rayleigh numbers the flow becomes weaker for all aspect ratios, and no asymmetric flow behaviour has been noticed.

7. Nomenclature

A	slope of the attic
g	acceleration due to gravity
h	height of the attic
h_{eff}	heat transfer coefficient
K	Kelvin
k	thermal conductivity
l	half horizontal length of the attic
Nu	Nusselt number
p	pressure
P	period of the cycle
Pr	Prandtl number
q	convective heat flux
Ra	Rayleigh number
t	time
T	temperature of the fluid
T_0	temperature of the ambient fluid
T_A	the amplitude
u, v	velocity components along the x- and y- axes respectively
x, y	cartesian coordinates

Greek letters

β	Volumetric coefficient of thermal expansion
ν	Kinematic viscosity
ρ	Density of the fluid
κ	thermal diffusivity
ΔT	temperature difference between the surface and the ambient

8. References

Akinsete, V. A. & Coleman, T. A. (2000). Heat transfer by steady laminar free convection in triangular enclosures. *Int. J. Heat Mass Transfer*, Vol. 25, 991–998.

Asan, H. & Namli, L. (2002). Numerical simulation of buoyant flow in a roof of triangular cross-section under winter day boundary conditions. *Energy Buildings*, Vol. 33, 753–757.

Asan, H. & Namli, L. (2000). Laminar natural convection in a pitched roof of triangular cross-section: Summer day boundary conditions. *Energy Buildings*, Vol. 33, 69–73.

Del Campo, E. M., Sen, M. & Ramos, E. (1988) Analysis of laminar natural convection in a triangular enclosure. *Numer. Heat Transfer.*, Vol. 13, 353–372.

Farrow, D. E. & Patterson, J. C. (1993). On the response of a reservoir sidearm to diurnal heating and cooling. *J. Fluid Mech.*, Vol. 246, 143–161.

Flack, R. D. (1980) The experimental measurement of natural convection heat transfer in triangular enclosures heated or cooled from below, *Trans. ASME: J. Heat Transfer*, Vol. 102, 770–772.

Flack, R. D. (1979) Velocity measurements in two natural convection air flows using a laser velocimeter. *Trans. ASME: J. Heat Transfer*, Vol. 101, 256–260.

Haese, P. M. & Teubner, M. D. (2002). Heat exchange in an attic space. *Int. J. Heat Mass Transfer*, Vol. 45, 4925–4936.

Holtzmann, G. A., Hill, R. W. & Ball, K. S. (2006). Laminar natural convection in isosceles triangular enclosures heated from below and symmetrically cooled from above. *Trans. ASME: J. Heat Transfer*, Vol. 122, 485–491.

Hyun, J. M. (1994). Unsteady buoyant convection in an enclosure. *Adv. Heat Transfe*, Vol. 24, 277–320.

Kent, E. F. (2009a) Numerical analysis of laminar natural convection in isosceles triangular enclosures. *Proceedings of the Institution of Mechanical Engineers Part C - Journal of Mechanical Engineering Science*, Vol. 223, 1157–1169.

Kent, E. F. (2009b). Numerical analysis of laminar natural convection in isosceles triangular enclosures for cold base and hot inclined walls. *Mechanics Research Communications*, Vol. 36, 497–508.

Kent, E. F., Asmaz, E. & Ozerbay, S. (2007). Unsteady natural convection in a water-filled isosceles triangular enclosure heated from below. *Int. J. Heat Mass Transfer*, Vol. 44, 187–200.

Leonard, B. P. & Mokhtari, S. (1990). ULTRA-SHARP Nonoscillatory Convection Schemes for High-Speed Steady Multidimensional Flow. *NASA Lewis Research Centre*, NASA TM 1-2568 (ICOMP-90-12).

Ostrach, S. (1988). Natural convection in enclosures. *Trans. ASME: J. Heat Transfer*, Vol. 110, 1175–1190.

Poulikakos, D. & Bejan, A. (1983a) Natural convection experiments in a triangular enclosure. *Trans. ASME: J. Heat Transfer*, Vol. 105, 652–655.

Poulikakos, D. & Bejan, A. (1983b) The fluid dynamics of an attic space. *J. Fluid Mech.*, Vol. 131, 251–269.

Ridouane, E. H., Campo, A. & Hasnaoui, M. (2006) Benefits derivable from connecting the bottom and top walls of attic enclosures with insulated vertical side walls. *Numer. Heat Trans. Part A-Applications*, Vol. 49, 175–193.

Ridouane, E. H. & Campo, A. (2006). Formation of a pitchfork bifurcation in thermal convection flow inside an isosceles triangular cavity. *Physics of Fluids*, Vol. 18, 074102.

Ridouane, E. H., Campo, A. & McGarry, M. (2005) Numerical computation of buoyant airflows confined to attic spaces under opposing hot and cold wall conditions. *Int. J. Therm. Sci.*, Vol. 44, 944–952.

Saha, S. C. (2011a). Unsteady natural convection in a triangular enclosure under isothermal heating. *Energy Buildings*, Vol. 43, 701–709.

Saha, S. C. (2011b). Scaling of free convection heat transfer in a triangular cavity for Pr > 1. *Energy Buildings*, under review.

Saha, S. C., Patterson, J. C. & Lei, C. (2010a). Natural convection in attics subject to instantaneous and ramp cooling boundary conditions. *Energy Buildings*, Vol. 42, 1192–1204.

Saha, S. C., Patterson, J. C. & Lei, C. (2010b).Natural convection and heat transfer in attics subject to periodic thermal forcing. *Int. J. Therm. Sci.*, Vol. 49, 1899–1910.

Saha, S. C., Patterson, J. C. & Lei, C. (2010c). Natural convection in attic-shaped spaces subject to sudden and ramp heating boundary conditions. *Heat Mass Transfer*, Vol. 46, 621–638.

Saha, S. C. (2008). Natural convection in attics subject to instantaneous and ramp cooling boundary conditions. *PhD Thesis*, School of Engineering and Physical Sciences, James Cook University.

Saha, S. C., Lei, C. & Patterson, J. C. (2007). Effect of aspect ratio on natural convection in attics subject to periodic thermal forcing. *ANZIAM J.*, Vol. 48, C677–C691.

Salmun H. (1995a). Convection patterns in a triangular domain. *Intl. J. Heat Mass Transfer.*, Vol. 18, 351–362.

Salmun H. (1995b). The stability of a single-cell steady-state solution in a triangular enclosure. *Intl. J. Heat Mass Transfer.*, Vol. 18, 363–369.

3

Analysis of Mixed Convection in a Lid Driven Trapezoidal Cavity

M. A. H. Mamun[1], T. R. Tanim[2],
M. M. Rahman[3], R. Saidur[3] and Shuichi Nagata[1]
[1]*Institute of Ocean Energy, Saga University 1 Honjo-machi, Saga 840-8502*
[2]*Mechanical Engineering Department, Ohio University, Athens, OH-45701*
[3]*Department of Mechanical Engineering,*
University of Malaya, 50603 Kuala Lumpur,
[1]*Japan*
[2]*USA*
[3]*Malaysia*

1. Introduction

Convection is the heat transfer mechanism affected by the flow of fluids. The amount of energy and matter are conveyed by the fluid can be predicted through the convective heat transfer. The convective heat transfer splits into two branches; the natural convection and the forced convection. Forced convection regards the heat transport by induced fluid motion which is forced to happen. This induced flow needs consistent mechanical power. But natural convection differs from the forced convection through the fluid flow driving force which happens naturally. The flows are driven by the buoyancy effect due to the presence of density gradient and gravitational field. As the temperature distribution in the natural convection depends on the intensity of the fluid currents which is dependent on the temperature potential itself, the qualitative and quantitative analysis of natural convection heat transfer is very difficult. Numerical investigation instead of theoretical analysis is more needed in this field.

Two types of natural convection heat transfer phenomena can be observed in the nature. One is that external free convection that is caused by the heat transfer interaction between a single wall and a very large fluid reservoir adjacent to the wall. Another is that internal free convection which befalls within an enclosure. Mathematically, the tendency of a particular system towards natural convection relies on the Grashof number, ($Gr = \frac{g\beta\nabla TL^3}{\nu^2}$), which is a ratio of buoyancy force and viscous force. The parameter β is the rate of change of density with respect to the change in temperature (T), and ν is viscosity. Thus, the Grashof number can be thought of as the ratio of the upwards buoyancy of the heated fluid to the internal friction slowing it down. In very sticky, viscous fluids, the fluid movement is restricted, along with natural convection. In the extreme case of infinite viscosity, the fluid could not move and all heat transfer would be through conductive heat transfer.

Forced convection is often encountered by engineers designing or analyzing heat exchangers, pipe flow, and flow over flat plate at a different temperature than the stream (the case of a shuttle wing during re-entry, for example). However, in any forced convection situation, some amount of natural convection is always present. When the natural convection is not negligible, such flows are typically referred to as mixed convection.
When analyzing potentially mixed convection, a parameter called the Richardson number ($Ri = Gr/Re^2$) parametizes the relative strength of free and forced convection. The Richardson number is the ratio of Grashof number and the square of the Reynolds number, which represents the ratio of buoyancy force and inertia force, and which stands in for the contribution of natural convection. When $Ri>>1$, natural convection dominates and when $Ri<<1$, forced convection dominates and when $Ri=1$, mixed convection dominates.
The thermo-fluid fields developed inside the cavity depend on the orientation and the geometry of the cavity. Reviewing the nature and the practical applications, the enclosure phenomena can loosely be organized into two classes. One of these is enclosure heated from the side which is found in solar collectors, double wall insulations, laptop cooling system and air circulation inside the room and the another one is enclosure heated from below which is happened in geophysical system like natural circulation in the atmosphere, the hydrosphere and the molten core of the earth.

Nomenclature

h convective heat transfer coefficient ($W/m^2 K$)
q" Heat Flux (W/m^2)
C_P specific heat at constant pressure ($J/kg K$)
g gravitational acceleration (m/s^2)
k thermal conductivity of the fluid ($W/m K$)
Nu Nusselt number, hW/k
Pr Prandtl number, v/α
Gr Grashof number, $g\beta\Delta TW^3/v^2$
Re Reynolds number, U_0W/v
Ri Richardson number, Gr/Re^2
A Aspect Ratio, H/W
R length of the inclined sidewalls (m)
T temperature of the fluid, (°C)
u velocity component at x-direction (m/s)
U dimensionless velocity component at X-direction
v velocity component at y-direction (m/s)
V dimensionless velocity component at Y-direction
W length of the cavity, (m)
x distance along the x-coordinate
X distance along the non-dimensional x-coordinate
Y distance along the non-dimensional y-coordinate

Greak symbols

α thermal diffusivity of the fluid (m^2/s)
β volumetric coefficient of thermal expansion (K^{-1})
γ inclination angle of the sidewalls of the cavity

θ dimensionless temperature ,$(T_H-T_C)/\Delta T$
μ dynamic viscosity of the fluid (Pa s)
ν kinematic viscosity of the fluid (m^2/s)
ρ density of the fluid (kg/m^3)
Φ rotational angle of the cavity

Subscript

a average value
v value of cold temperature
c_H value of hot temperature

1.1 Flow within enclosure

The flow within an enclosure consisting of two horizontal walls, at different temperatures, is an important circumstance encountered quite frequently in practice. In all the applications having this kind of situation, heat transfer occurs due to the temperature difference across the fluid layer, one horizontal solid surface being at a temperature higher than the other. If the upper plate is the hot surface, then the lower surface has heavier fluid and by virtue of buoyancy the fluid would not come to the lower plate. Because in this case the heat transfer mode is restricted to only conduction. But if the fluid is enclosed between two horizontal surfaces of which the upper surface is at lower temperature, there will be the existence of cellular natural convective currents which are called as Benard cells. For fluids whose density decreases with increasing temperature, this leads to an unstable situation. Benard [1] mentioned this instability as a "top heavy" situation. In that case fluid is completely stationary and heat is transferred across the layer by the conduction mechanism only. Rayleigh [2] recognized that this unstable situation must break down at a certain value of Rayleigh number above which convective motion must be generated. Jeffreys [3] calculated this limiting value of *Ra* to be 1708, when air layer is bounded on both sides by solid walls.

1.1.1 Tilted enclosure

The tilted enclosure geometry has received considerable attention in the heat transfer literature because of mostly growing interest of solar collector technology. The angle of tilt has a dramatic impact on the flow housed by the enclosure. Consider an enclosure heated from below is rotated about a reference axis. When the tilted angle becomes 90^o, the flow and thermal fields inside the enclosure experience the heating from side condition. Thereby convective currents may pronounce over the diffusive currents. When the enclosure rotates to 180^o, the heat transfer mechanism switches to the diffusion because the top wall is heated.

1.1.2 LID driven enclosure

Flow and heat transfer analysis in lid-driven cavities is one of the most widely studied problems in thermo-fluids area. Numerous investigations have been conducted in the past on lid-driven cavity flow and heat transfer considering various combinations of the imposed temperature gradients and cavity configurations. This is because the driven cavity configuration is encountered in many practical engineering and industrial applications. Such configurations can be idealized by the simple rectangular geometry with regular boundary conditions yielding a well-posed problem. Combined forced-free convection flow in lid-driven cavities or enclosures occurs as a result of two competing mechanisms. The

first is due to shear flow caused by the movement of one of the walls of the cavity while the second is due to buoyancy flow produced by thermal non homogeneity of the cavity boundaries. Understanding these mechanisms is of great significance from technical and engineering standpoints.

1.2 Application

Air-cooling is one of the preferred methods for the cooling of computer systems and other electronic equipments, due to its simplicity and low cost. It is very important that such cooling systems should be designed in the most efficient way and the power requirement for the cooling should be minimized. The electronic components are treated as heat sources embedded on flat surfaces. A small fan blows air at low speeds over the heat sources. This gives rise to a situation where the forced convection due to shear driven flow and the natural convection due to buoyancy driven flow are of comparable magnitude and the resulting heat transfer process is categorized as mixed convection. Mixed convection flow and heat transfer also occur frequently in other engineering and natural situations. One important configuration is a lid-driven (or shear- driven) flow in a differentially heated/cooled cavity, which has applications in crystal growth, flow and heat transfer in solar ponds [5], dynamics of lakes [6], thermal-hydraulics of nuclear reactors [7], industrial processes such as food processing, and float glass production [8]. The interaction of the shear driven flow due to the lid motion and natural convective flow due to the buoyancy effect is quite complex and warrants comprehensive analysis to understand the physics of the resulting flow and heat transfer process.

1.3 Motivation behind the selection of problem

Two dimensional steady, mixed convection heat transfers in a two-dimensional trapezoidal cavity with constant heat flux from heated bottom wall while the isothermal moving top wall has been studied numerically. The present study is based on the configuration of Aydin and Yang [27] where the isothermal heat source at the bottom wall is replaced by a constant flux heat source, which is physically more realistic. The main attribute for choosing the trapezoidal shape cavity is to enhance the heat transfer rate as it could be said intuitionally due to its extended cold top surface. The inclination angle of the sidewalls of the trapezoid has been changed (30°, 45° and 60°) to get the maximum heat transfer in terms of maximum Nusselt number. Then the trapezoid has been rotated (30°, 45° and 60°) and the results have been studied. The tilted position of the enclosure shows a significant influence on the heat transfer. Results are obtained for both the aiding and opposing flow conditions by changing the direction of the lid motion. This study includes additional computations for cavities at various aspect ratios, A, ranging from 0.5 to 2 and their effects on the heat transfer process is analyzed in terms of average Nusselt number. Contextually the present study will focus on the computational analysis of the influence of inclination angle of the sidewalls of the cavity, rotational angle of the cavity, Aspect ratio, direction of the lid motion and Richardson number.

1.4 Main objectives of the work

The investigation is carried out in a two dimensional lid driven trapezoidal enclosure filled with air. The inclined side walls are kept adiabatic and the bottom wall of the cavity is kept at uniform heat flux. The cooled top wall having constant temperature will move with a constant velocity. The specific objectives of the present research work are as follows:

a. To study the variation of average heat transfer in terms of Nusselt number with the variation of Richardson number at different aspect ratios of the rectangular enclosure and compare it with the established literature.
b. To find out the optimum configuration by changing the inclination angle of the side walls of the trapezoidal cavity by analyzing the maximum heat transfer.
c. To study the variation of average heat transfer in terms of Nusselt number with the variation of Richardson number of the optimum trapezoidal cavity.
d. To study the variation of average heat transfer in terms of Nusselt number at different aspect ratios of the optimum trapezoidal cavity.
e. To study the variation of average heat transfer in terms of Nusselt number with the variation of Richardson number at different aspect ratios of the optimum trapezoidal enclosure by changing the rotation angle for both aiding and opposing flow conditions..
f. To analyze the flow pattern inside the trapezoidal enclosures in terms of Streamlines and isotherms.

2. Literature review

There have been many investigations in the past on mixed convective flow in lid-driven cavities. Many different configurations and combinations of thermal boundary conditions have been considered and analyzed by various investigators. Torrance et al. [9] investigated mixed convection in driven cavities as early as in 1972. Papaniclaou and Jaluria [10-13] carried out a series of numerical studies to investigate the combined forced and natural convective cooling of heat dissipating electronic components, located in rectangular enclosures, and cooled by an external through flow of air. The results indicate that flow patterns generally consists of high of low velocity re-circulating cells because of buoyancy forces induced by the heat source. Koseff and Street [14] studied experimentally as well as numerically the recirculation flow patterns for a wide range of Reynolds (*Re*) and Grashof (*Gr*) numbers. Their results showed that the three dimensional features, such as corner eddies near the end walls, and Taylor- Gortler like longitudinal vortices, have significant effects on the flow patterns for low Reynolds numbers. Khanafer and Chamakha [15] examined numerically mixed convection flow in a lid-driven enclosure filled with a fluid-saturated porous medium and reported on the effects of the Darcy and Richardson numbers on the flow and heat transfer characteristics.

G. A. Holtzman et. al [16] have studied laminar natural convection in isosceles triangular enclosures heated from below and symmetrically cooled from above. This problem is examined over aspect ratios ranging from 0.2 to 1.0 and Grashoff numbers from 10^3 to 10^5. Its is found that a pitchfork bifurcation occurs at a critical Grashoff number for each of the aspect ratios considered, above which the symmetric solutions are unstable to finite perturbations and asymmetric solutions are instead obtained. Results are presented detailing the occurance of the pitchfork bifurcation in each of the aspect ratios considered, and the resulting flow patterns are described. A flow visualization study is used to validate the numerical observations. Difference in local values of the Nusselt number between asymmetric and symmetric solutions are found to be more than 500 percent due to the shifting of the buoyancy- driven cells. The phenomenon of natural convection in trapezoidal enclosures where upper and lower walls are not parallel, in particular a triangular geometry, is examined by H. Asan, L. Namli [17] over a parameter domain in which the aspect ratio of the enclosure ranges from 0.1 to 1.0, the Rayleigh number varies between 10^2

to 10^5 and Prandtl number correspond to air and water. It is found that the numerical experiments verify the flow features that are known from theoretical asymptotic analysis of this problem (valid for shallow spaces) only over a certain range of the parametric domain.

Moallemi and Jang [18] numerically studied mixed convective flow in a bottom heated square driven cavity and investigated the effect of Prandtl number on the flow and heat transfer process. They found that the effects of buoyancy are more pronounced for higher values of Prandtl number. They also derived a correlation for the average Nusselt number in terms of the Prandtl number, Reynolds number, and Richardson number. Mohammad and Viskanta [19] performed numerical investigation and flow visualization study on two and three-dimensional laminar mixed convection flow in a bottom heated shallow driven cavity filled with water having a Prandtl number of 5.84. They concluded that the lid motion destroys all types of convective cells due to heating from below for finite size cavities. They also implicated that the two-dimensional heat transfer results compare favorably with those based on a three-dimensional model for $Gr/Re < 1$. Later, Mohammad and Viskanta [20] experimentally and numerically studied mixed convection in shallow rectangular bottom heated cavities filled with liquid Gallium having a low Prandtl number of 0.022. They found that the heat transfer rate is rather insensitive to the lid velocity and an extremely thin shear layer exists along the major portion of the moving lid. The flow structure consists of an elongated secondary circulation that occupies a third of the cavity.

Mansour and Viskanta [21] studied mixed convective flow in a tall vertical cavity where one of the vertical sidewalls, maintained at a colder temperature than the other, was moving up or downward thus assisting or opposing the buoyancy. They observed that when shear assisted the buoyancy a shear cell developed adjacent to the moving wall while the buoyancy cell filled the rest of the cavity. When shear opposed buoyancy, the heat transfer rate reduced below that for purely natural convection. Iwatsu et al. [22] and Iwatsu and Hyun [23] conducted two-dimensional and three-dimensional numerical simulation of mixed convection in square cavities heated from the top moving wall. Mohammad and Viskanta [24] conducted three-dimensional numerical simulation of mixed convection in a shallow driven cavity filled with a stably stratified fluid heated from the top moving wall and cooled from below for a range of Rayleigh number and Richardson number.

Prasad and Koseff [25] reported experimental results for mixed convection in deep lid-driven cavities heated from below. In a series of experiments which were performed on a cavity filled with water, the heat flux was measured at different locations over the hot cavity floor for a range of Re and Gr. Their results indicated that the overall (i.e. area-averaged) heat transfer rate was a very weak function of Gr for the range of Re examined ($2200 < Re < 12000$). The data were correlated by Nusselt number vs Reynolds number, as well as Stanton number vs Reynolds number relations.

They observed that the heat transfer is rather insensitive to the Richardson number. Hsu and Wang [26] investigated the mixed convective heat transfer where the heat source was embedded on a board mounted vertically on the bottom wall at the middle in an enclosure. The cooling air flow enters and exits the enclosure through the openings near the top of the vertical sidewalls. The results show that both the thermal field and the average Nusselt number depend strongly on the governing parameters, position of the heat source, as well as the property of the heat-source-embedded board.

Aydin and Yang [27] numerically studied mixed convection heat transfer in a two-dimensional square cavity having an aspect ratio of 1. In their configuration the isothermal sidewalls of the cavity were moving downwards with uniform velocity while the top wall

was adiabatic. A symmetrical isothermal heat source was placed at the otherwise adiabatic bottom wall. They investigated the effects of Richardson number and the length of the heat source on the fluid flow and heat transfer. Shankar et al. [28] presented analytical solution for mixed convection in cavities with very slow lid motion. The convection process has been shown to be governed by an inhomogeneous biharmonic equation for the stream function. Oztop and Dagtekin [29] performed numerical analysis of mixed convection in a square cavity with moving and differentially heated sidewalls. Sharif [30] investigates heat transfer in two-dimensional shallow rectangular driven cavity of aspect ratio 10 and Prandtl number 6.0 with hot moving lid on top and cooled from bottom. They investigated the effect of Richardson number and inclination angle. G. Guo and M. A. R. Sharif [31] studied mixed convection in rectangular cavities at various aspect ratios with moving isothermal sidewalls and constant heat source on the bottom wall. They plotted the streamlines and isotherms for different values of Richardson number and also studied the variation of the average Nu and maximum surface temperature at the heat source with Richardson number with different heat source length. They simulated streamlines and isotherms for asymmetric placements of the heat source and also the effects of asymmetry of the heating elements on the average Nu and the maximum source length temperature.

3. Physical model

The physical model considered here is shown in figure 1 and 2, along with the important geometric parameters. It consists of a trapezoidal cavity filled with air, whose bottom wall and top wall are subjected to hot T_H and cold T_C temperatures respectively while the side walls are kept adiabatic. Two cases of thermal boundary conditions for the top moving wall have been considered here. The first case is (figure 1) when the moving cold wall is moving in the positive x direction (opposing flow condition). In that case the shear flow caused by moving top wall opposes the buoyancy driven flow caused by the thermal non-homogeneity of the cavity boundaries. The second case is (figure 2) when the moving cold wall is moving in the negative x direction (aiding flow condition). In that case the shear flow assists the buoyancy flow. The cavity height is H, width of the bottom hot wall is W, is inclined at angle Φ with the horizontal reference axis. γ is the inclination angle of the sidewalls of the cavity. The flow and heat transfer phenomena in the cavity are investigated for a series of Richardson numbers (*Ri*), aspect ratio (A=H/W), rotation angle of the cavity Φ.

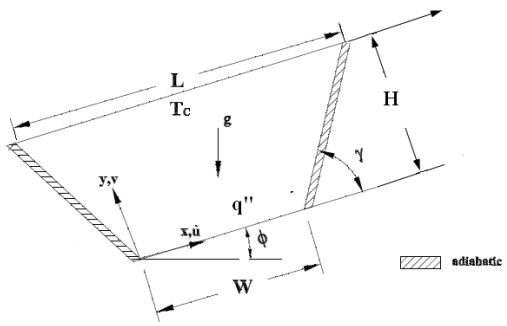

Fig. 1. Schematic diagram of the physical system considering opposing flow condition

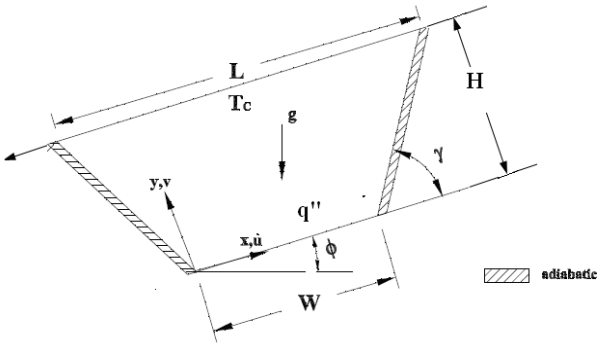

Fig. 2. Schematic diagram of the physical system considering aiding flow condition

3.1 Mathematical model

Using the Boussinesq approximation and neglecting the viscous dissipation effect and compressibility effect the dimensionless governing equations for two dimensional laminar incompressible flows can be written as follows:

$$\frac{\partial U}{\partial X}+\frac{\partial V}{\partial Y}=0 \tag{1}$$

$$U\frac{\partial U}{\partial X}+V\frac{\partial U}{\partial Y}=-\frac{\partial P}{\partial X}+\frac{1}{\mathrm{Re}}\left(\frac{\partial^2 U}{\partial X^2}+\frac{\partial^2 U}{\partial Y^2}\right) \tag{2}$$

$$U\frac{\partial V}{\partial X}+V\frac{\partial V}{\partial Y}=-\frac{\partial P}{\partial Y}+\frac{1}{\mathrm{Re}}\left(\frac{\partial^2 V}{\partial X^2}+\frac{\partial^2 V}{\partial Y^2}\right)+\frac{Gr}{\mathrm{Re}^2}\theta \tag{3}$$

$$U\frac{\partial \theta}{\partial X}+V\frac{\partial \theta}{\partial Y}=\frac{1}{\mathrm{Re}\,\mathrm{Pr}}\left(\frac{\partial^2 \theta}{\partial X^2}+\frac{\partial^2 \theta}{\partial Y^2}\right) \tag{4}$$

The dimensionless variables are as follows:

$$X=x/W,\ Y=y/W,\ \theta=(T_H-T_C)/\Delta T,\ \Delta T=q''W/k,\ U=u/U_0,\ V=v/U_0,\ P=p/\rho U_o^2$$

The dimensionless parameters, appearing in Eqs. (1)-(4) are Reynolds number $Re= U_0W/\nu$, the Prandtl number $Pr=\nu/a$, the Grashof number $Gr=\frac{g\beta\nabla TL^3}{\nu^2}$. The ratio of Gr/Re^2 is the mixed convection parameter and is called Richardson number Ri and is a measure of the relative strength of the natural convection and forced convection for a particular problem. If $Ri<<1$ the forced convection is dominant while if $Ri>>1$, then natural convection is dominant. For problems with $Ri\sim1$ then the natural convection effects are comparable to the forced convection effects.

The boundary conditions for the present problem are specified as follows:

Top wall: $U=U_0$, $V=0$, $\theta=0$

Bottom wall: U=V=0, θ=1
Right and Left wall: U=V=0,

$$\partial\theta/\partial X = 0$$

Non-dimensional heat transfer parameter Nusselt number is stated as:

3.2 Numerical method

Firstly the problem is defined as a two dimensional enclosure. Control Volume based finite volume method (FVM) is to be used to discretize the governing differential equations. The pressure- velocity coupling in the governing equations is achieved using the well known SIMPLE method for numerical computations. The set of governing equations are to be solved sequentially. A second order upwind differencing scheme is to be used for the formulation of the coefficients in the finite-volume equations. As the sides of the trapezoidal cavity are not parallel, the present numerical techniques will descretize the computational domain into unstructured triangular elements.
In order to obtain the grid independence solution, a grid refinement study is performed for the trapezoidal cavity (A=1) under constant heat flux condition keeping, Re=400, Pr=0.71, Ri= 1.0.n It is found in figure 3 that 5496 regular nodes are sufficient to provide accurate results. This grid resolution is therefore used for all subsequent computations for A≤1. For taller cavities with A>1, a proportionately large number of grids in the vertical direction is used.

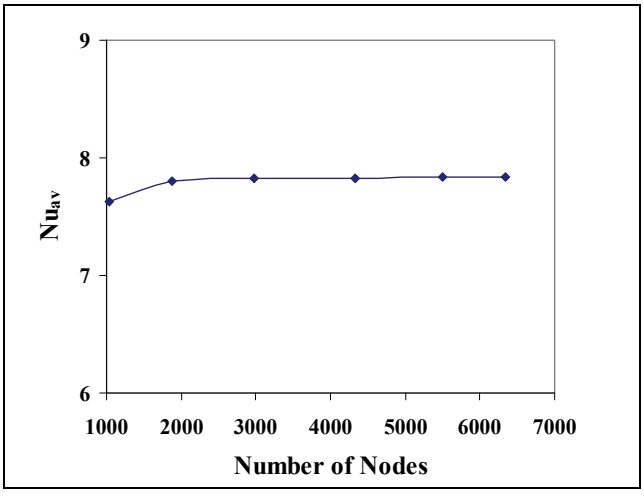

Fig. 3. Grid sensitivity test for trapezoidal cavity at Ri=1.0, Re=400 and A=1

The convergence criterion was defined by the required scaled residuals to decrease 10^{-5} for all equations except the energy equations, for which the criterion is 10^{-8}.
The computational procedure is validated against the numerical results of Iwatsu et el.[22] for a top heated moving lid and bottom cooled square cavity filled with air (*Pr*=0.71). A 60×60 mesh is used and computations are done for six different *Re* and *Gr* combinations. Comparisons of the average Nusselt number at the hot lid are shown in Table 1. The general

agreement between the present computation and that of Iwatsu et al. [22] is seen to be very well with a maximum discrepancy of about 3.9%.

Re	*Gr*= 10^2			*Gr*= 10^4			*Gr*= 10^6		
	Present	Iwatsu et al.	Diff. %	Present	Iwatsu et al.	Diff. %	Present	Iwatsu et al.	Diff. %
400	3.97	3.84	3.3	3.75	3.62	3.5	1.18	1.22	3.2
1000	6.25	6.33	1.2	6.32	6.29	0.47	1.70	1.77	3.9

Table 1. Comparison of the computed average Nusselt number at the hot plate

The computational procedure has also been validated against the numerical results of Guo and Sharif [31] shown in the figure 4.

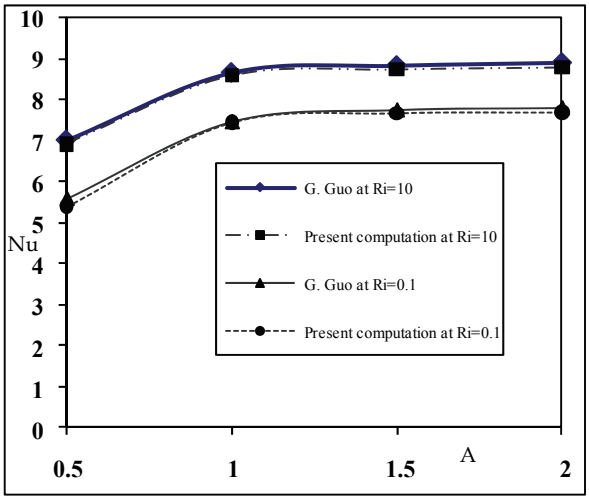

Fig. 4. Variation of the average Nusselt number with different aspect ratio at Ri=10, Re=100 and ε =0.6

Figure 4, reveals that the Average Nusselt numbers in the present study have excellent agreement with those obtained by Guo and Sharif [31] having a maximum discrepancy of about 2.3% Therefore, it can be concluded that the numerical code used in this analysis can solve the present problem with reasonable agreement.

4. Results and disscussion

Numerical results are presented in order to determine the effects of the inclination angle of the side walls, Richardson number *Ri*, Reynolds number *Re*, Aspect ratio *A*, the rotational angle of the cavity *Φ* on mixed convection flow in trapezoidal enclosure. The inclination angle of the sidewalls of the trapezoidal enclosure has been changed from 30^o to 60^o with an interval of 15^o. The values of Richardson number varies from 0.1 to 10, Aspect ratio, *A* changes from 0.5 to 2.0 taking Rotational angle 30^o, 45 ^{o}, 60^o for two different Reynolds numbers 400 and 600.

4.1 Effect of inclination angle

In this study the effect of inclination angle of the adiabatic sidewalls has been observed first. The inclination angle of the side walls has been changed to 30^o, 45^o and 60^o. The Richardson number has been changed from 0.1 to 10. The optimum inclination angle has been selected based on the average Nusselt number which is a non dimensional parameter that indicates the rate of heat transfer between the hot and cold walls. The results are obtained both for Re=400 and Re=600.

Figure 5-7 reveals the impact of varying inclination angles of the sidewalls of the trapezoidal cavity. These figures show the contours of streamlines and isotherms at different Richardson numbers. For small values of Ri number, it can be seen that the shear effect due to the movement of the top wall is dominant. The fluid flow is characterized by a primary re-circulating eddy of the size of the cavity generated by the movement of the top lid. The isothermal contour maps are clustered near the bottom and top walls resulting in steep temperature gradient there. In each case as the Richardson number increases the convection current becomes more dominant resulting in stronger flow field. Again at $\gamma=45^o$ (figure 6), the flow field is stronger than the $\gamma=30^o$ and $\gamma=60^o$ (figure 5 and figure 7), which is an indication of better heat transfer. The isothermal plots also complies with the flow field, showing minimum value of the maximum isotherms at $\gamma=45^o$.

From figure 8-9 the average value of the Nusselt number with respect to the Richardson number has been plotted. Here it can be seen that Nusselt number at $\gamma=45^o$ dominates the other two cases i.e. $\gamma=30^o$ and $\gamma=60^o$, showing better heat transfer. So it is clearly visible that trapezoid having the inclination angle $\gamma=45^o$ gives better heat transfer and consequently it can be taken as the optimum inclination angle.

4.2 Effect of rotational angle, Φ

Next the effect of rotational angle, Φ has been studied. When studying the effect of rotational angel, two distinct cases have been taken into consideration. They are aiding and opposing flow condition. The first one is when the shear driven flow opposes the convective flow and in that case the top moving lid is moving in the positive direction at a specified rotational angle [figure 1]. The second condition is the aiding flow condition where the shear driven flow aids the natural convective flow and the moving top lid moves in the opposite direction unlike the first case [figure 2]. Both these cases have been studied for a rotational angle for $\Phi=30^o$, 45^o and 60^o and their heat transfer characteristics has been studied in terms of streamlines and isothermal plots.

Unlike $\Phi=0^o$, when the buoyancy is acting only in the y direction, as the rotational angle Φ changes, the flow field changes significantly. In opposing flow condition the shear driven flow opposes the natural convective flow, At low Richardson number (Ri<1)the forced convection is dominating, creating a single circulation at the right corner of the top moving lid [figure 10-12].

As the Richardson number increases (Ri>1), natural convection becomes dominating creating a large circulation at the bottom of the cavity. This large circulation causing by natural convection goes bigger and stronger as Ri number increases as well as squeezes the upper circulation, resulting an opposing effect. If we observe the isothermal plots, it changes accordingly with streamlines. As Ri number increases, the isothermal lines changes significantly indicating that the convection is the dominating heat transfer for the specified case. The shear driven circulation at the upper right side becomes smaller and smaller as the Ri number increases because of dominating natural convection.

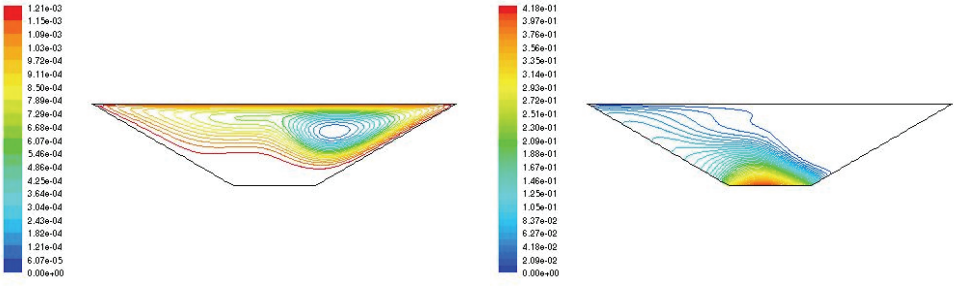

R_i = 0.1

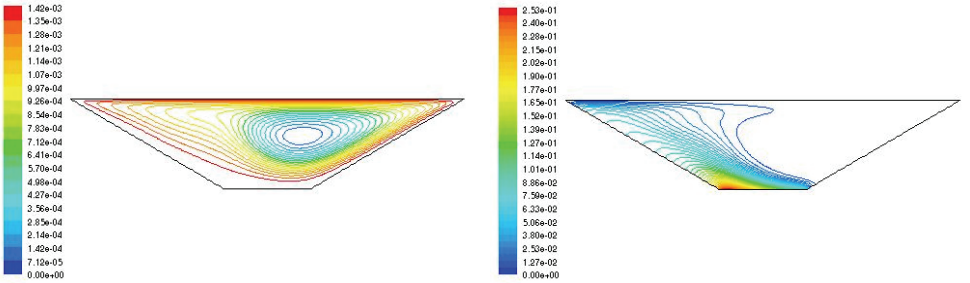

R_i = 1

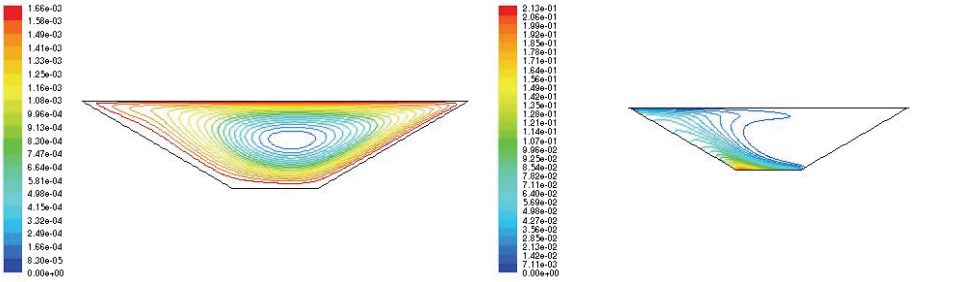

R_i = 5

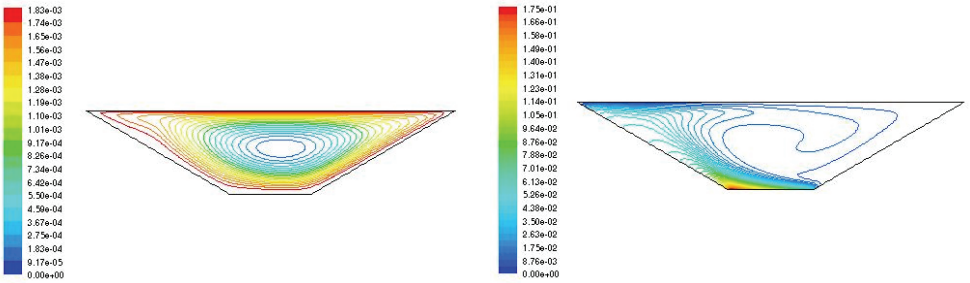

R_i = 10

Fig. 5. Contours of streamlines and isotherms at Re=400, A=1.0 and γ=30°

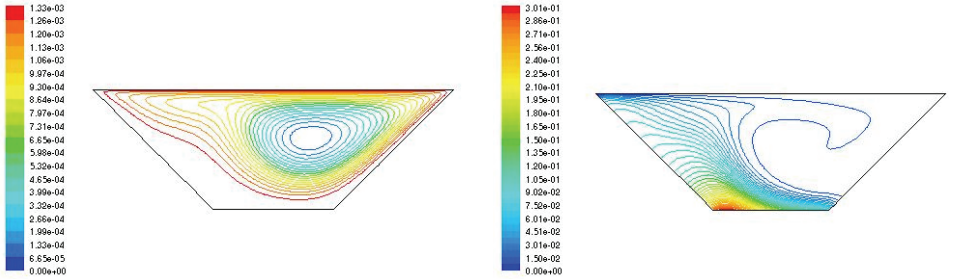

R_i = 0.1

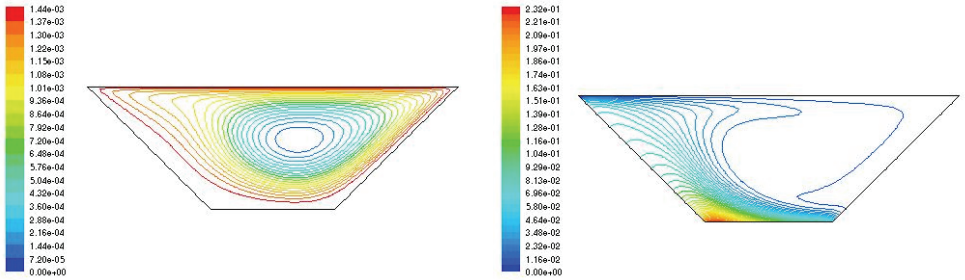

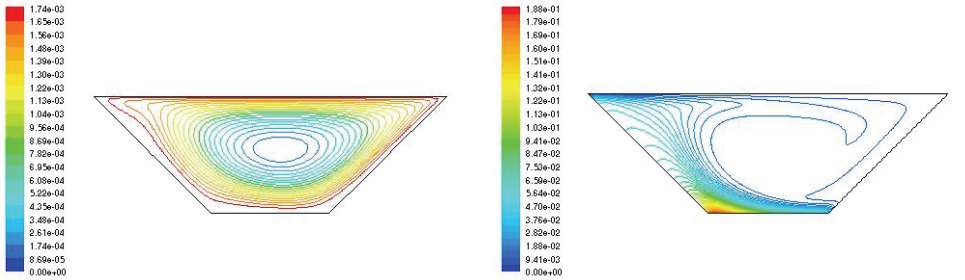

R_i = 5

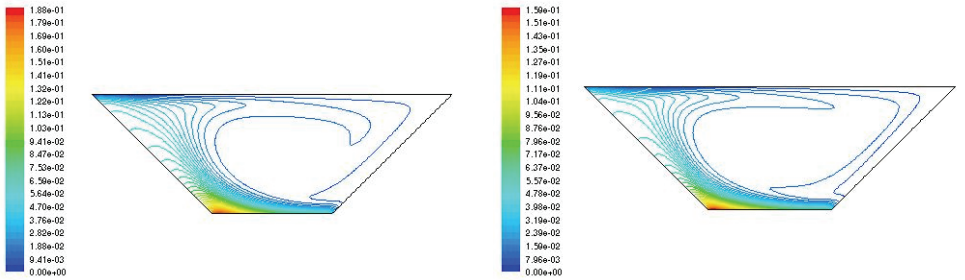

R_i = 10

Fig. 6. Contours of streamlines and isotherms at Re=400, A=1.0 and γ=45°

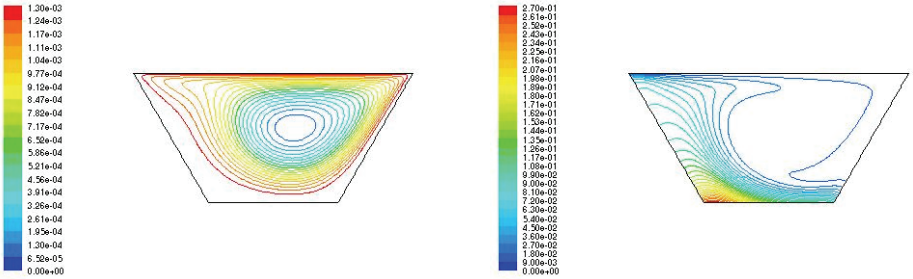

R_i = 0.1

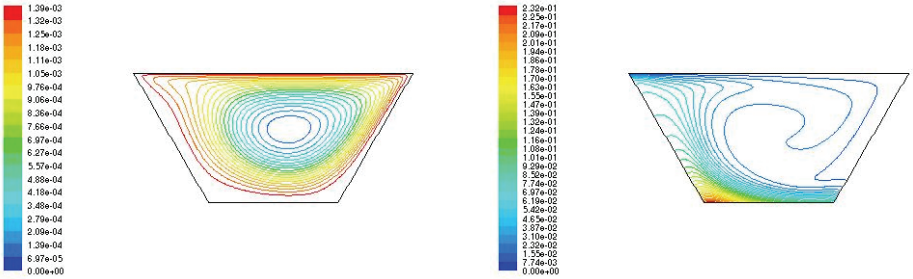

R_i = 1

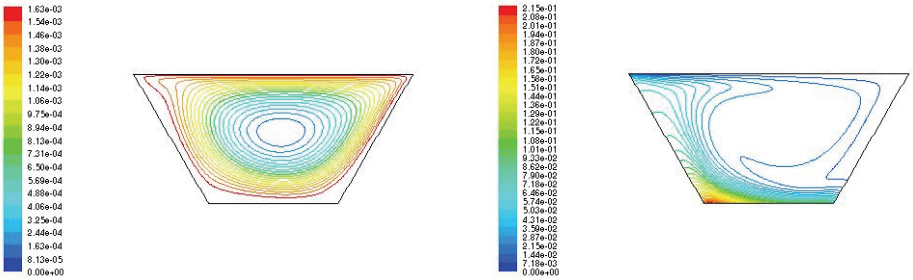

R_i = 5

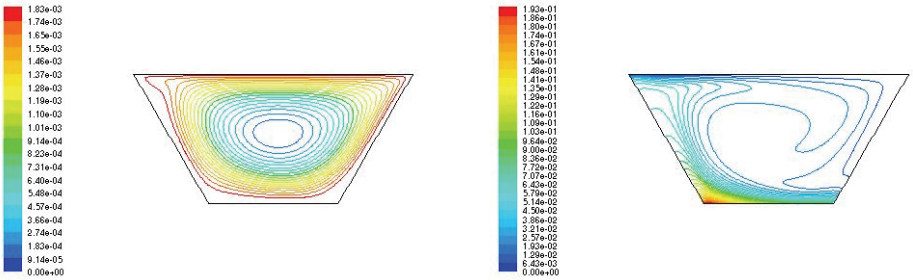

R_i = 10

Fig. 7. Contours of streamlines and isotherms at Re=400, A=1.0 and γ=60°

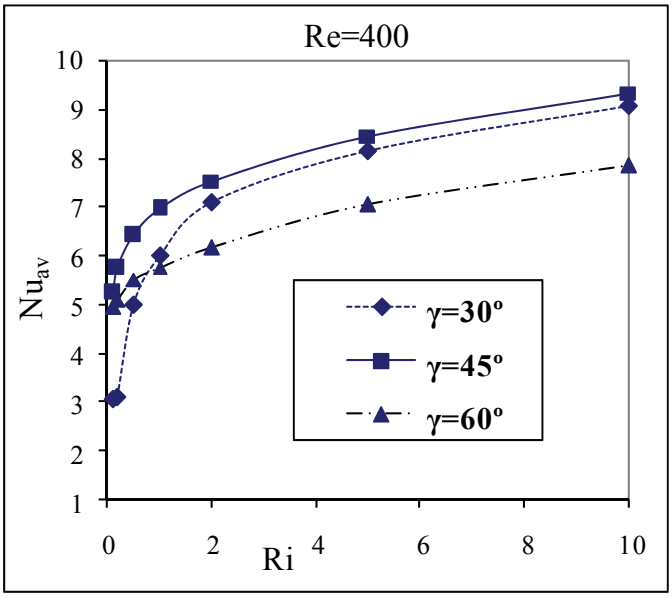

Fig. 8. Average Nusselt number, Nu_{av} vs Richardson number at Re=400, A=1

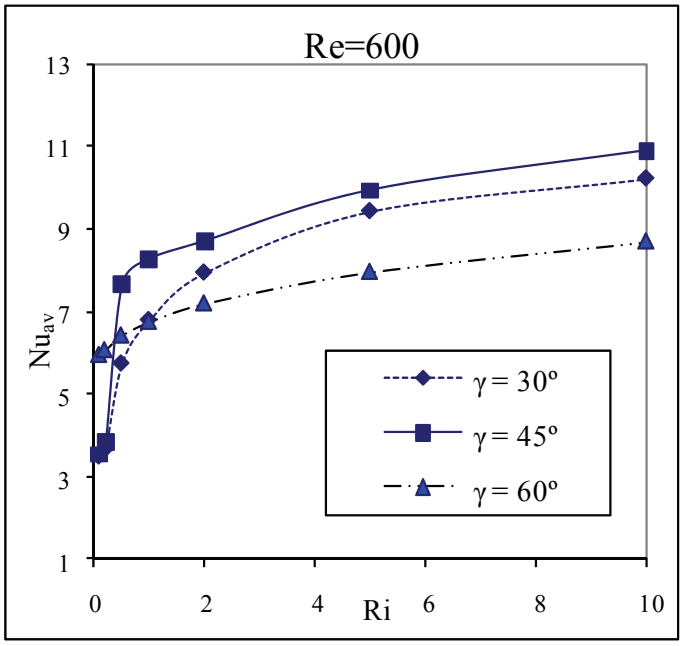

Fig. 9. Average Nusselt number, Nu_{av} vs Richardson number at Re=600, A=1

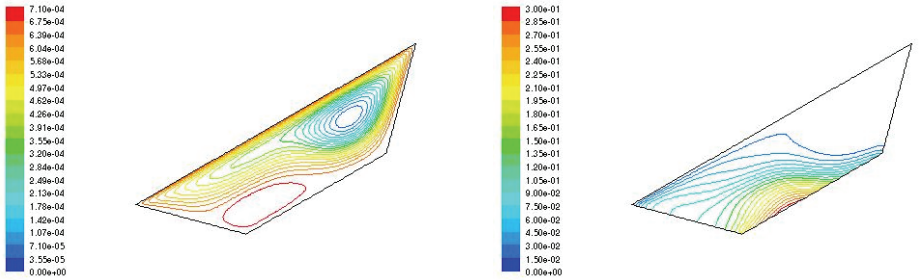

R_i = 0.1

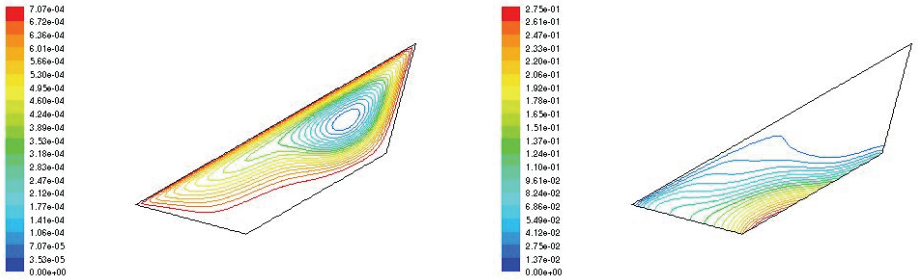

R_i = 1

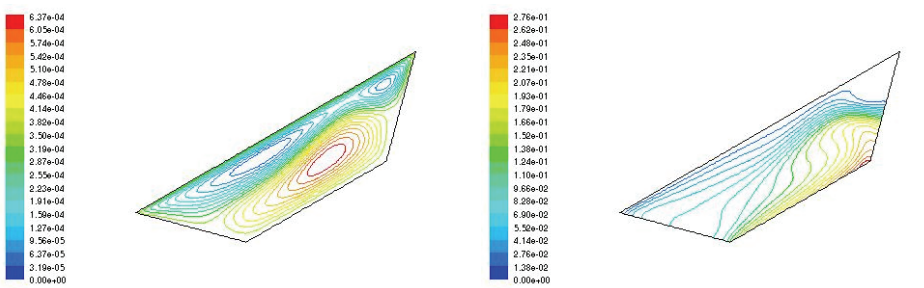

R_i = 5

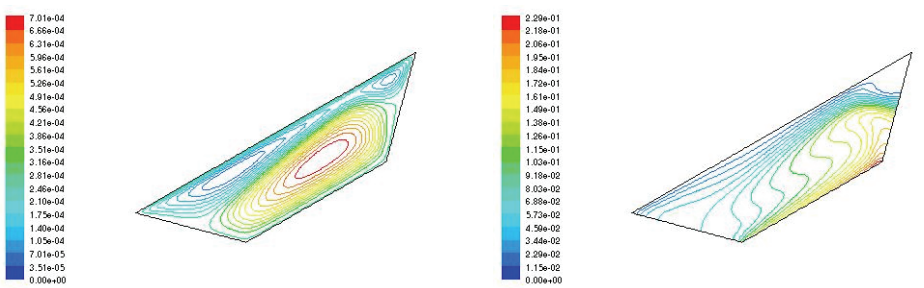

R_i = 10

Fig. 10. Contours of streamlines and isotherms at Re=400, A=0.5 and Φ=30°, opposing flow

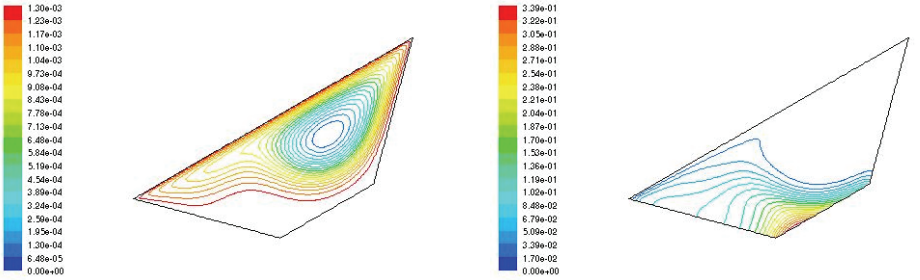

R_i = 0.1

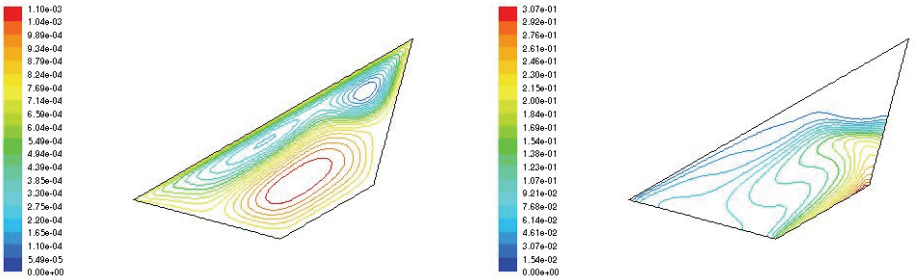

R_i = 1

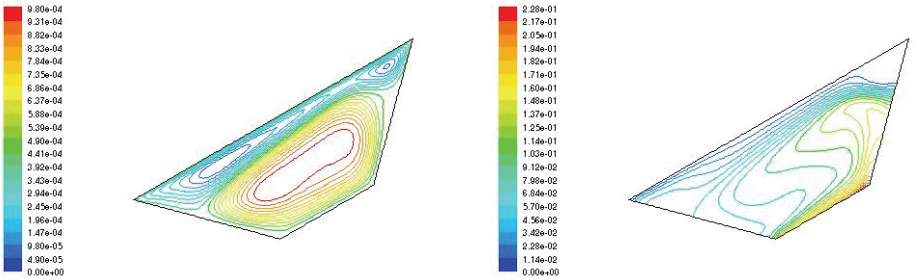

R_i = 5

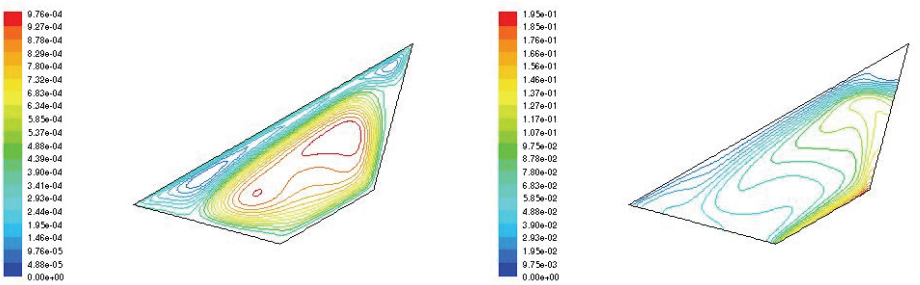

R_i = 10

Fig. 11. Contours of streamlines and isotherms at Re=400, A=1 and Φ=30°, opposing flow

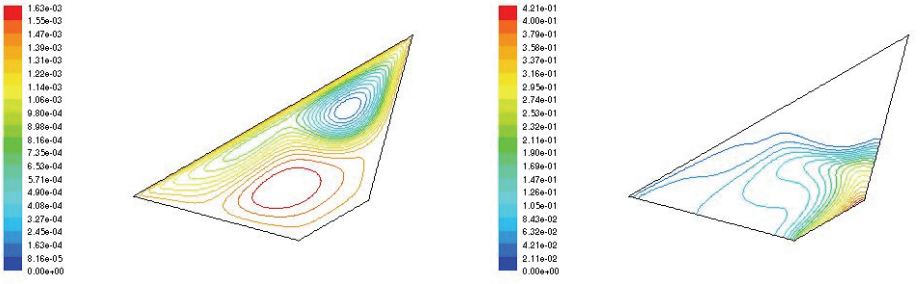

$R_i = 1$

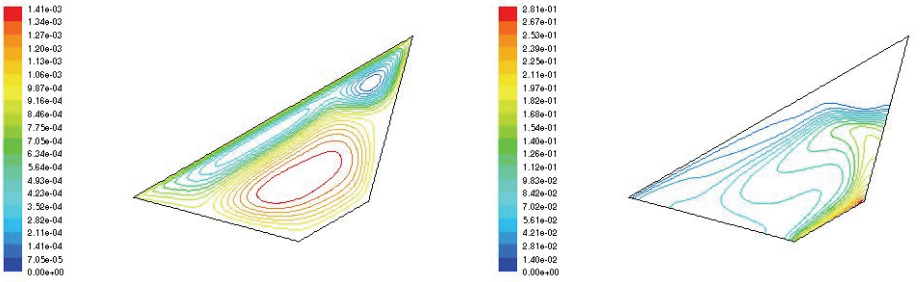

$R_i = 1$

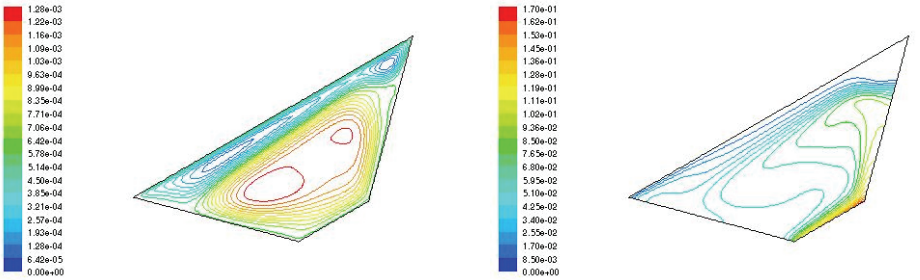

$R_i = 1$

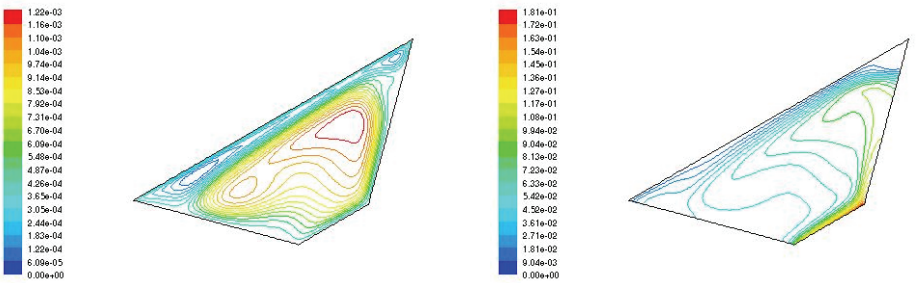

$R_i = 1$

Fig. 12. Contours of streamlines and isotherms at Re=400, A=1.5 and Φ=30°, opposing flow

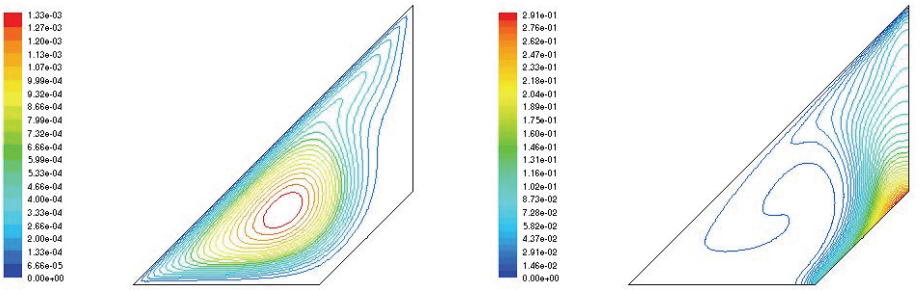

R_i = 0.1

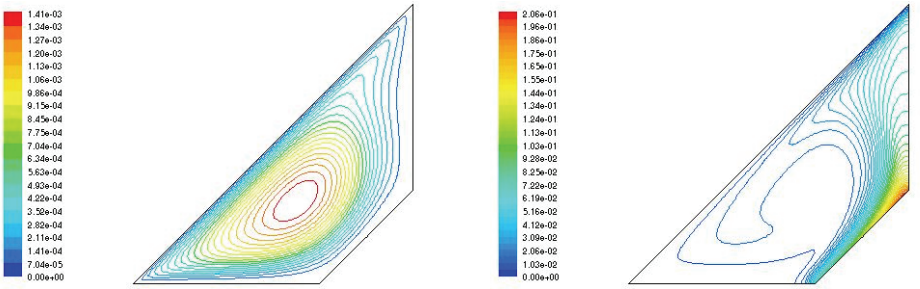

R_i = 1

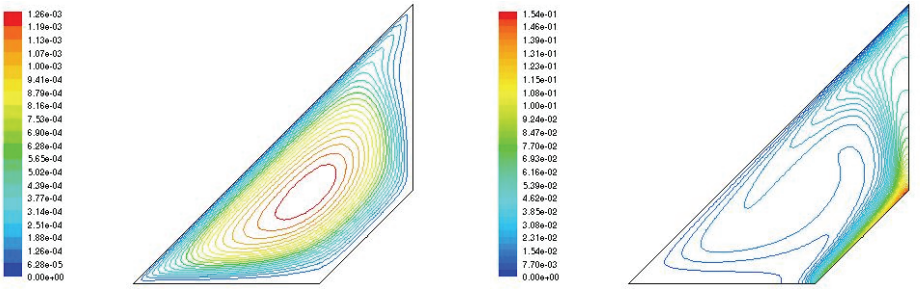

R_i = 5

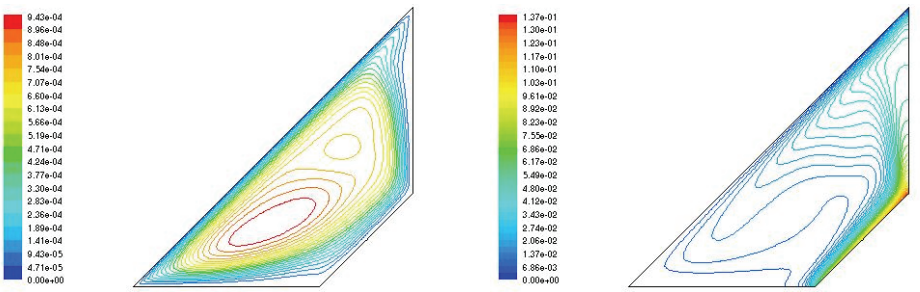

R_i = 10

Fig. 13. Contours of streamlines and isotherms at Re=400, A=1 and Φ=45°, aiding flow

In the case of aiding flow, condition when the forced convection aids the natural convection a different scenario has been observed [e.g. figure 13]. In all the cases, a single circulation of the size of the cavity has been observed. Unlike the opposing flow condition, in that case the natural convection aids the shear driven flow from the smaller value of *Ri* number, resulting a much stronger convective current. As the *Ri* number increases, the convection flow fields become more and more stronger resulting better and better heat transfer. The isotherms changes significantly as the Richardson number increases and gives the minimum value at higher *Ri* number.

As the aspect ratio, *A* increases the convective flow fields become more and more stronger. As cavity volume increases with aspect ratio and more volume of cooling air is involved in cooling the heat source leading to better cooling effect. The effect of aspect ratio at different rotational angle has also been studied. In all the cases, it can be observed that Nu_{av} increases with increasing aspect ratio for all rotational angles, leading to better heat transfer.

Fig. 14-18 shows a comparative analysis of aiding and opposing flow conditions. There it can be seen that, the aiding flow condition always dominates the opposing flow condition in terms of Nu_{av} , which indicates better heat transfer at all rotational angle. The aiding flow condition provides stronger convective currents, which has been visible in the study, as the natural convection aids the shear driven flow. As a result the maximum value of the isotherms is lower in case of aiding flow condition, indicating lower temperature. But in opposing condition the natural convection opposes the shear driven flow, providing weak convective currents.

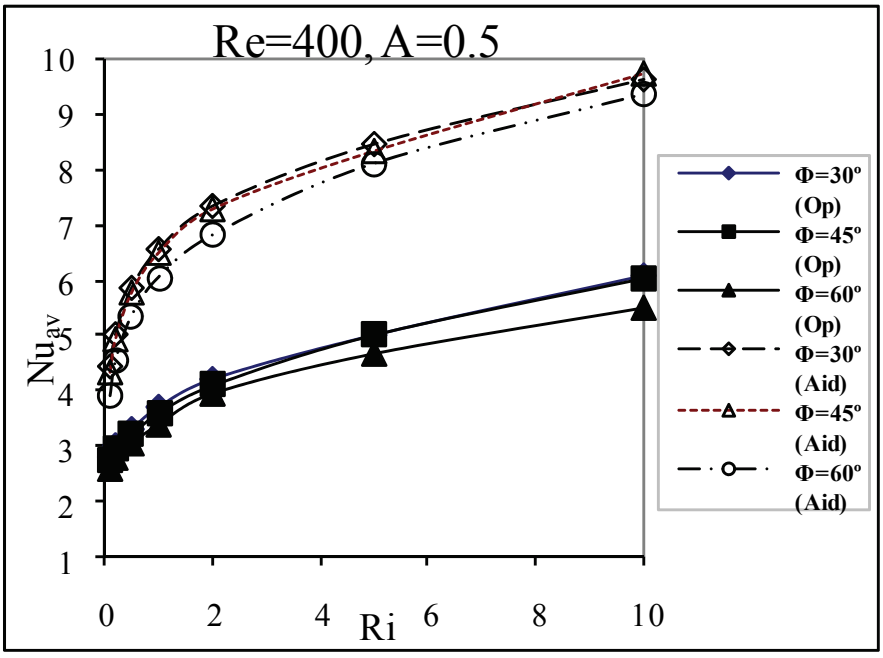

Fig. 14. Variation of Nu_{av} with Ri at A=0.5, Re=400

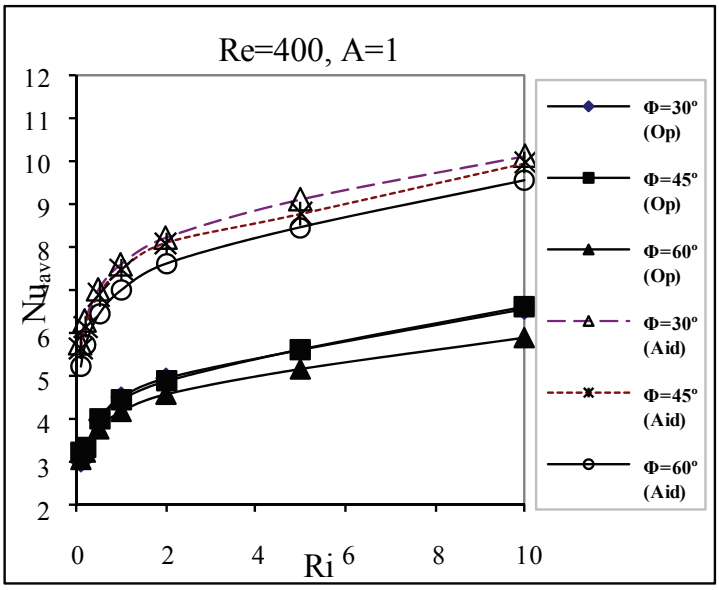

Fig. 15. Variation of Nu_{av} with Ri at A=1, Re=400

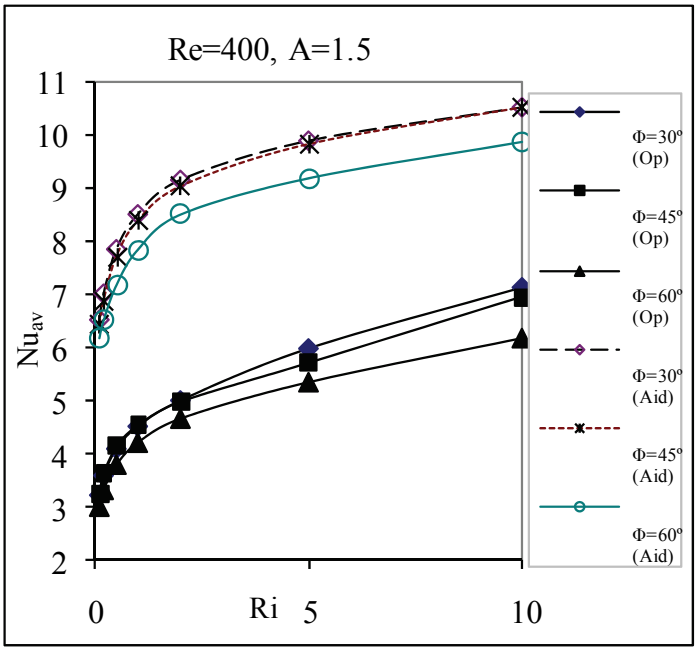

Fig. 16. Variation of Nu_{av} with Ri at A=1.5, Re=400

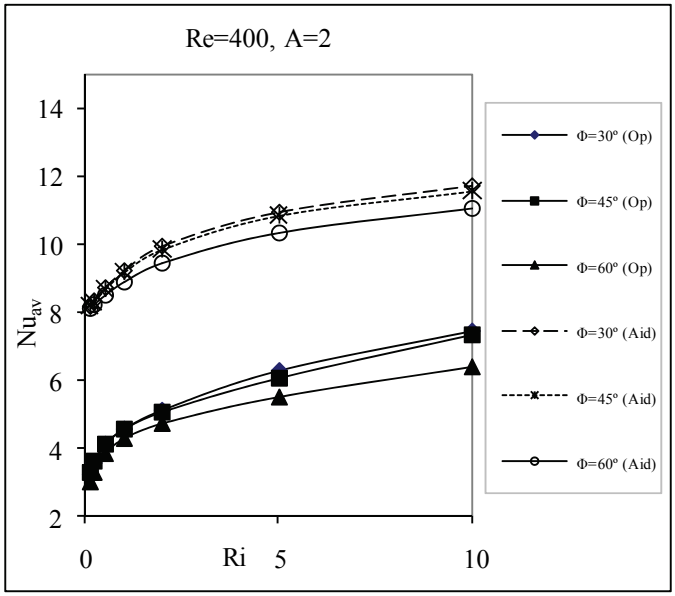

Fig. 17. Variation of Nu_{av} with Ri at A=2, Re=400

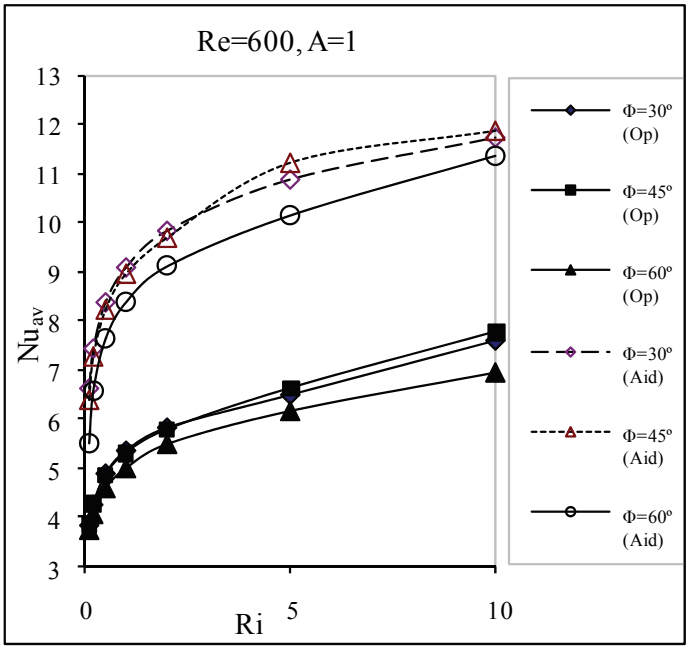

Fig. 18. Variation of Nu_{av} with Ri at A=1, Re=600

The Nu_{av} is also sensitive to rotational angle, figure 14-18. At Re=400 it can be seen that, Nusselt number decreases as the rotational angle, Φ increases. Nu_{av} increases marginally at $\Phi=30^o$ from $\Phi=45^o$ but at $\Phi=60^o$, Nu_{av} drops significantly for all the aspect ratios, figure 14-17.The flow fields also changes accordingly. At Re=600, the maximum heat transfer has been obtained at $\Phi=45^o$, in terms of average Nusselt number, figure 18. Nu_{av} increases marginally at $\Phi=45^o$ from $\Phi=30^o$ but drops significantly at $\Phi=60^o$, indicating poor heat transfer at $\Phi=60^o$.

4.3 Effect of Richardson number, *Ri*

The value of the Richardson number, $Ri=Gr/Re^2$ provides a measure of the importance of buoyancy driven natural convection relative to the lid driven forced convection. When the Buoyancy effects are relatively small, $Ri<1$, the gross flow features are similar to those of a conventional non-stratified fluid at comparable values of Re. The main circulation fills the entire cavity of the size of the cavity generated by the movement of the top wall. Minor cells may be visible near the bottom corners. The streamlines and isotherms indicated that the hydrodynamic and thermal boundary layers are not developed fully at low Richardson number. The isothermal lines are mostly undistorted and horizontal lines except the large recirculation area inside the cavity at low Richardson number. In the large recirculation zone temperature gradients are very weak. This implies that, due to the vigorous actions of the mechanically driven circulations, fluids are well mixed; consequently, temperature differences in much of this interior region are very small.

When $Ri>1$, natural convection begins to dominate the forced convection. The Buoyancy assists the core flow and thus the convection current becomes more and more strong with increasing Richardson number. As Richardson number increases, the main circulation occupies the whole cavity and it become more symmetrical inside the cavity. If we see the isothermal plots, we can see that as the Richardson number increases the isothermal lines becomes more and more denser at the upper cold lid. The crowded streamlines and isothermal lines indicate that the hydrodynamic and thermal boundary layers have been developed along the hot wall and cold wall, respectively, reflecting rigorous heat transfer rate occurred. Consequently the maximum temperature reduces due to this large heat transfer rate.

The average Nusselt number as a function of Richardson number has been plotted in figure 19-20 for different Reynolds number. It can be observed that as the Richardson number increases the average Nusselt number increases accordingly for all the aspect ratios. When $Ri<1$, Nu_{av} grows only slightly with increasing Ri. After Ri is more than 1, Nu_{av} is found to increase more rapidly. Since Re is kept constant the forced convection effect remains invariant as Ri increases for a particular case. When $Ri>1$, the natural convection aids more and more in the heat transfer process in addition to the forced convection which results in more rapid increase of $Nu_{av.}$

4.4 Effect of aspect ratio, *A*

Changing the aspect ratio, A (A=H/W) causes a change in heat transfer characteristics. In order to investigate the convection heat transfer at different aspect ratios, computations has been done for cavities at aspect ratios of 0.5, 1, 1.5 and 2.0. Keeping Reynolds number fixed at 400 and 600 the Richardson number has been changed from 0.1 to 10. If we compare the flow fields at different aspect ratios from 0.5 to 2.0, it can be revealed that in the convection region adjacent to the heat source, the isotherms become thinner and denser producing higher temperature gradients with increasing aspect ratio. The streamlines becomes stronger as the aspect ratio increases. This is due to the fact that the cavity volume increases with

aspect ratio and more volume of cooling air is involved in cooling the heat source leading to better cooling effect.

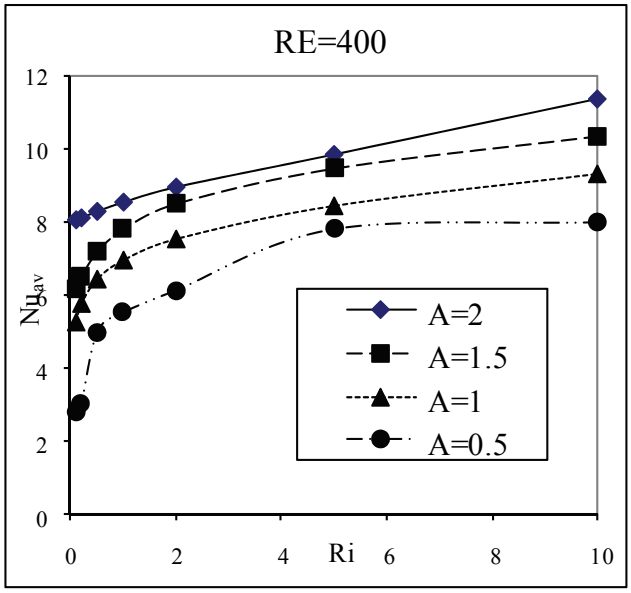

Fig. 19. Variation of Nu_{av} with Ri at Re=400 and Φ=0°

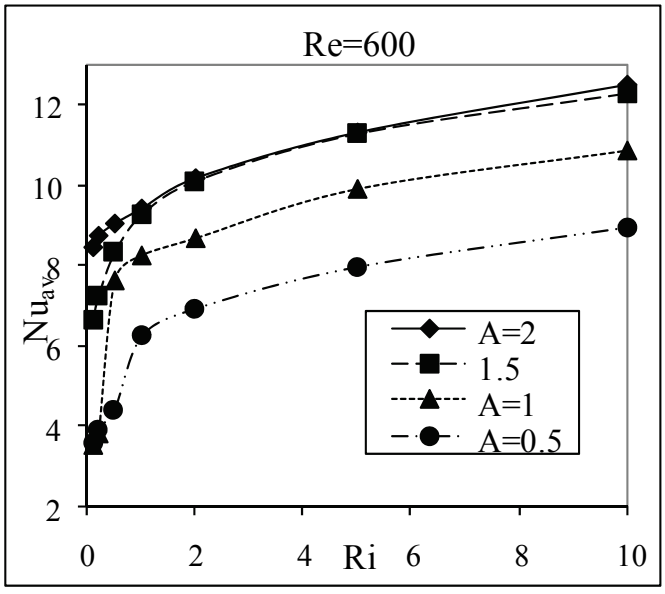

Fig. 20. Variation of Nu_{av} with Ri at Re=600 and Φ=0°

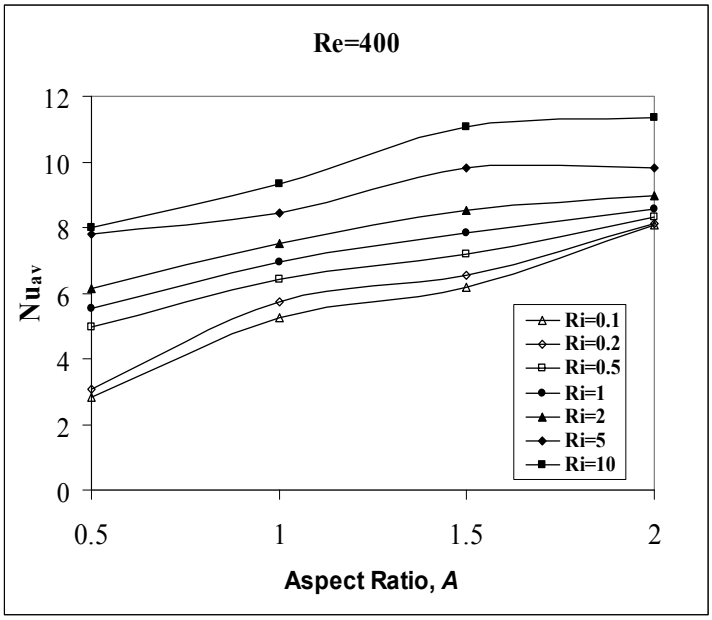

Fig. 21. Variation of Nu_{av} with A at Re=400 and $\Phi=0^o$

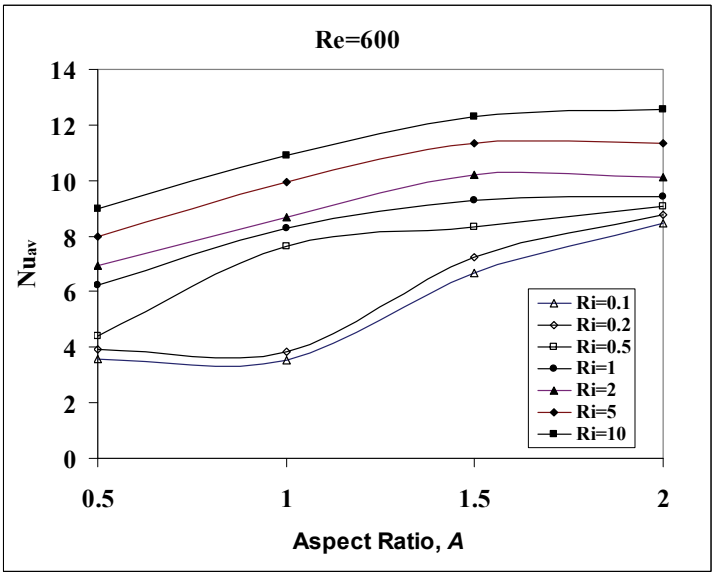

Fig. 22. Variation of Nu_{av} with A at Re=600 and $\Phi=0^o$

The average Nusselt number at the heat source surface has been plotted in figure 21-22 for a range of *Ri* and aspect ratios. For a particular aspect ratio, the Nu_{av} increases with increasing

Ri. As a result, the maximum temperature decreases monotonously which can be recognized from the isothermal plots. As the aspect ratio increases from 0.5 to 1 the Nu_{av} increases for a particular *Ri*.
At higher Reynolds number i.e. Re=600, with increasing aspect ratio some secondary eddy at the bottom surface of the cavity has been observed. This is of frictional losses and stagnation pressure. As the *Ri* increases, natural convection dominates more and the bottom secondary eddies blends into the main primary flow. For A>1.5 the variation is almost flat indicating that the aspect ratio does not play a dominant role on the heat transfer process at that range.

4.5 Effect of Reynolds number, *Re*

This study has been done at two different Reynolds numbers. They are Re=400 and Re=600. With a particular case keeping *Ri* and *A* constant, as the Reynolds number increases the convective current becomes more and more stronger and the maximum value of the isotherms reduces. As we know $Ri=Gr/Re^2$. *Gr* is square proportional of *Re* for a fixed *Ri*. So slight change of Re and Ri causes huge change of Gr. Gr increases the buoyancy force. As buoyancy force is increased then heat transfer rate is tremendously high. So changes are very visible to the change of *Re*. From figure 19-20, it can be observed that as the *Re* increases the average Nusselt number also increases for all the aspect ratios.

5. Conclusion

Two dimensional steady, mixed convection heat transfer in a two-dimensional trapezoidal cavity with constant heat flux from heated bottom wall while the isothermal moving top wall in the horizontal direction has been studied numerically for a range of Richardson number, Aspect ratio, the inclination angle of the side walls and the rotational angle of the cavity. A number of conclusions can be drawn form the investigations:

- The optimum configuration of the trapezoidal enclosure has been obtained at $\gamma=45^o$, as at this configuration the Nu_{av} was maximum at all Richardson number.
- As the Richardson number increases the Nu_{av} increases accordingly at all Aspect ratios, because at higher Richardson number natural convection dominates the forced convection.
- As Aspect Ratio increases from 0.5 to 2.0, the heat transfer rate increases. This is due to the fact that the cavity volume increases with aspect ratio and more volume of cooling air is involved in cooling the heat source leading to better cooling effect.
- The direction of the motion of the lid also affects the heat transfer phenomena. Aiding flow condition always gives better heat transfer rate than opposing flow condition. Because at aiding flow condition, the shear driven flow aids the natural convective flow, resulting a much stronger convective current that leads to better heat transfer.
- The Nu_{av} is also sensitive to rotational angle Φ. At Re=400 it can be seen that, Nusselt number decreases as the rotational angle, Φ increases. Nu_{av} increases marginally at $\Phi=30$ from $\Phi=45^o$ but at $\Phi=60^o$, Nu_{av} drops significantly for all the aspect ratios.

6. Further recommandations

The following recommendation can be put forward for the further work on this present research.

1. Numerical investigation can be carried out by incorporating different physics like radiation effects, internal heat generation/ absorption, capillary effects.
2. Double diffusive natural convection can be analyzed through including the governing equation of concentration conservation.
3. Investigation can be performed by using magnetic fluid or electrically conducting fluid within the trapezoidal cavity and changing the boundary conditions of the cavity's wall.
4. Investigation can be performed by moving the other lids of the enclosure and see the heat transfer effect.
5. Investigation can be carried out by changing the Prandtl number of the fluid inside the trapezoidal enclosure.
6. Investigation can be carried out by using a porous media inside the trapezoidal cavity instead of air.

7. References

[1] H. Benard, "Fouration de centers de gyration a L'arriere d'cen obstacle en movement", Compt. Rend, vol. 147, pp. 416-418, 1900.

[2] L. Rayleigh, "On convection currents in a horizontal layer of fluid when the higher temperature is on the underside", Philos. Mag., vol. 6, no. 32, pp. 529-546, 1916.

[3] H. Jeffreys, "Some cases of instabilities in fluid motion", Proc. R. Soc. Ser.A, vol. 118, pp. 195-208, 1928.

[4] F.P. Incropera, Convection heat transfer in electronic equipment cooling, J.Heat Transfer 110 (1988) 1097–1111.

[5] C. K. Cha and Y. Jaluria, Recirculating mixed convection flow for energy extraction, Int. j. Heat Mass Transfer 27.1801-1810 11984).

[6] J. Imberger'and P. F. Hamblin, Dynamics of lakes, reservoirs, and cooling ponds, A. Rev. FIuid Mech. 14, 153-187 (1982).

[7] F. J. K. Ideriah, Prediction of turbulent cavity flow driven by buoyancy and shear, J. Mech. Engng Sci. 22, 287-295 (1980).

[8] L. A. B. Pilkington, Review lecture: The float glass process, Proc. R. Sot. Lond., IA 314, 1-25 (1969).

[9] K. Torrance, R. Davis, K. Eike, P. Gill, D. Gutman, A. Hsui, S. Lyons, H. Zien, Cavity flows driven by buoyancy and shear, J. Fluid Mech. 51 (1972) 221–231.

[10] E. Papanicolaou, Y. Jaluria, Mixed convection from and isolated heat source in a rectangular enclosure, Numer. Heat Transfer, Part A 18 (1990) 427-461

[11] E. Papanicolaou, Y. Jaluria, Transition to a periodic regime in mixed convection in a square cavity, J. Fluid Mech. 239 (1992) 489-509

[12] E. Papanicolaou, Y. Jaluria, Mixed convection from a localized heat source in a cavity with conducting walls: A numerical study, Numer. Heat Transfer, Part A 23 (1993) 463-484

[13] E. Papanicolaou, Y. Jaluria, Mixed convection from simulated electronic components at varying relative positions in a cavity J. Heat Transfer, 116 (1994) 960-970

[14] J. R. Kosef and R. L. Street, The Lid-Driven Cavity Flow: A Synthesis of Quantitative and Qualitative Observations, ASME J. Fluids Eng., 106(1984) 390-398.

[15] K. Khanafer and A. J. Chamkha, Mixed convection flow in a lid-driven enclosure filled with a fluid saturated porous medium, Int. J. Heat Mass Transfer, 36 (1993) 1601-1608.

[16] G. A. Holtzman, R. W. Hill, K. S. Ball, Laminar natural convection in isosceles triangular enclosures heated from below and symmetrically cooled from above, J. Heat Transfer 122 (2000) 485-491.
[17] H. Asan, L. Namli, The laminar natural convection in a pitched roof of triangular cross-section for summer day boundary conditions, Energy and Buildings 33 (2001) 753-757.
[18] M.K. Moallemi, K.S. Jang, Prandtl number effects on laminar mixed convection heat transfer in a lid-driven cavity, Int. J. Heat Mass Transfer 35 (1992) 1881–1892.
[19] A.A. Mohammad, R. Viskanta, Laminar flow and heat transfer in Rayleigh–Benard convection with shear, Phys. Fluids A 4 (1992) 2131–2140.
[20] A.A.Mohammad, R.Viskanta,Flow structures and heat transfer in a lid-driven cavity filled with liquid gallium and heated from below, Exp. Thermal Fluid Sci. 9 (1994) 309–319.
[21] R.B. Mansour, R. Viskanta, Shear-opposed mixed-convection flow heat transfer in a narrow, vertical cavity, Int. J. Heat Fluid Flow 15 (1994) 462–469.
[22] R. Iwatsu, J.M. Hyun, K. Kuwahara, Mixed convection in a driven cavity with a stable vertical temperature gradient, Int. J. Heat Mass Transfer 36 (1993) 1601–1608.
[23] R. Iwatsu, J.M. Hyun, Three-dimensional driven cavity flows with a vertical temperature gradient, Int. J. Heat Mass Transfer 38 (1995) 3319–3328.
[24] A. A. Mohammad, R. Viskanta, Flow and heat transfer in a lid-driven cavity filled with a stably stratified fluid, Appl. Math. Model. 19 (1995) 465–472.
[25] A.K. Prasad, J.R. Koseff, Combined forced and natural convection heat transfer in a deep lid-driven cavity flow, Int. J. Heat Fluid Flow 17 (1996) 460–467.
[26] T.H. Hsu, S.G. Wang, Mixed convection in a rectangular enclosure with discrete heat sources, Numer. Heat Transfer, Part A 38 (2000) 627–652.
[27] O. Aydin, W.J. Yang, Mixed convection in cavities with a locally heated lower wall and moving sidewalls, Numer. Heat Transfer, Part A 37 (2000) 695–710.
[28] P.N. Shankar, V.V. Meleshko, E.I. Nikiforovich, Slow mixed convection in rectangular containers, J. Fluid Mech. 471 (2002) 203–217.
[29] H.F. Oztop, I. Dagtekin, Mixed convection in two-sided lid-driven differentially heated square cavity, Int. J. Heat Mass Transfer 47 (2004) 1761–1769.
[30] M. A. R. Sharif, Laminar mixed convection in shallow inclined driven cavities with hot moving lid on top and cooled from bottom, Applied Thermal Engineering 27 (2007) 1036–1042.
[31] G. Guo, M. A. R. Sharif, Mixed convection in rectangular cavities at various aspect ratios with moving isothermal sidewalls and constant flux heat source on the bottom wall, Int. J. Thermal Sciences 43 (2004) 465–475.

4

Convective Heat Transfer of Unsteady Pulsed Flow in Sinusoidal Constricted Tube

J. Batina[1], S. Blancher[1], C. Amrouche[2], M. Batchi[2] and R. Creff[1]
[1]*Laboratoire des Sciences de l'Ingénieur Appliquées à la Mécanique et l'Electricité*
Université de Pau et des Pays de l'Adour, Avenue de l'Université – 64000 Pau;
[2]*Laboratoire de Mathématiques Appliquées- CNRS UMR 5142*
Université de Pau et des Pays de l'Adour, Avenue de l'Université – 64000 Pau;
France

1. Introduction

In many industrial engineering and other technological processes, it is crucial to characterise heat and mass transfer, for example to avoid thermo mechanical damages.
Particularly, in the inlet region of internal pulsed flows, unsteady dynamic and thermal effects can present large amplitudes. These effects are mainly located in the wall region. This suggests the existence of intense unsteady stresses at the wall (shear, friction or thermal stresses). Our studies (André et al., 1987; Batina, 1995; Creff et al., 1985) show that there could exist an 'adequacy' of different parameters such as Reynolds or Prandtl numbers, leading to large amplitudes for the unsteady velocity and temperature in the entry zone if compared to those encountered downstream in the fully developed region. Consequently, in order to obtain convective heat transfer enhancement, most of the studies are linked to:

- Firstly, the search for optimal geometries (undulated or grooved channels, tube with periodic sections, etc.) : among those geometrical studies, one can quote the investigations of Blancher, 1991; Ghaddar et al., 1986, for the wavy or grooved plane geometries, in order to highlight the influence of the forced or natural disturbances on heat transfer.
- Secondly, the search for particular flow conditions (transient regime, pulsed flow, etc.): for example those linked to the periodicity of the pressure gradient (Batina, 1995; Batina et al. 2009; Chakravarty & Sannigrahi, 1999; Hemida et al., 2002), or those which impose a periodic velocity condition (Lee et al., 1999; Young Kim et al., 1998) or those which carry on time periodic deformable walls.

The main objective of this study is to analyse the special case of convective heat transfer of an unsteady pulsed, laminar, incompressible flow in axisymmetric tubes with periodic sections. The flow is supposed to be developing dynamically and thermally from the duct inlet. The wall is heated at constant and uniform temperature.
One of the originality of this study is the choice of Chebyshev polynomials basis in both axial and radial directions for spectral methods, the use of spectral collocation method and the introduction of a shift operator to satisfy non homogeneous boundary conditions for spectral Galerkin formulation. A comparison of results obtained by the two spectral methods is given. A Crank - Nicolson scheme permits the resolution in time.

1.1 Nomenclature

a	thermal diffusity $\left[m^2/s\right]$	λ	dimensionless total wavelength
e	reduced amplitude	θ	dimensionless temperature:
h	wall function	$\theta=(T-T_\infty)/(T_W-T_\infty)$	
H	periodic sinusoidal radius $[m]$	μ	dynamic viscosity $\left[Ns/m^2\right]$
L	geometric half-length tube $[m]$	$\nu=\mu/\rho$	kinematic viscosity: $\left[m^2/s\right]$
R	tube radius at the constriction $[m]$	ρ	fluid density $\left[Kg/m^3\right]$
r	radial co-ordinate $[m]$	τ	modulation flow rate
T	fluid temperature $[K]$	ω	vorticity function $[1/s]$
T_∞	duct inlet temperature $[K]$	ψ	stream function $\left[m^3/s\right]$
t	time $[s]$	Ω	pulsation $[rad/s]$
u	axial velocity $[m/s]$	*Dimensionless numbers*	
$\bar{u}_0$	mean bulk velocity $[m/s]$	Re	Reynolds number: $Re=R\bar{u}_0/\nu$
v	radial velocity $[m/s]$	Pr	Prandtl number: $Pr=\nu/a$
z	axial co-ordinate $[m]$	Nu	Nusselt number
Greek symbols		$\theta_{0\mathrm{m}}(x)$	averaged bulk temperature
Φ_W wall heat flux $\left[W/m^2\right]$		*Subscripts:*	*0* steady flow; W*:* wall

1.2 Suggested keywords

Convective heat transfer – sinusoidal constricted tube – axisymmetric geometry – pulsed laminar, incompressible flow – spectral collocation method – Chebyshev-Gauss-Lobatto mesh – spectral Galerkin formulation – shift operator method – Crank - Nicolson resolution in time.

2. General hypothesis and governing equations

2.1 General hypothesis

We consider a Newtonian incompressible fluid flow developing inside an axisymmetric cylindrical duct with periodic sinusoidal radius. The unsteadiness imposed to the flow corresponds to a source of periodic pulsations generating plane waves. This flow is described in terms of an unsteady pulsed flow superimposed on a steady one, without reverse flow at the entry and the exit sections. With regard to the thermal problem, the wall is heated at constant and uniform temperature, and the fluid inlet temperature is equal to

the upstream ambient temperature. Physical constants are supposed to be independent of the temperature, which involves that the motion and energy equations are uncoupled.

2.2 Governing equations

With the 2D hypothesis, we use the vorticity-stream function formulation (ω,ψ) for the Navier-Stokes equations in which the incompressibility condition is automatically satisfied. In fact, the essential advantage of this formulation compared to the primitive variables (velocity-pressure formulation) is the reduction of the number of unknown functions and the non-used of the pressure. On the other hand, Navier-Stokes equations become a fourth order Partial Differential Equations whose expressions in cylindrical coordinates are:

$$\frac{\partial\hat{\omega}}{\partial t}-\frac{1}{r}\frac{\partial\psi}{\partial z}\frac{\partial\hat{\omega}}{\partial r}+\frac{1}{r}\frac{\partial\psi}{\partial r}\frac{\partial\hat{\omega}}{\partial z}+\frac{2}{r^2}\frac{\partial\psi}{\partial z}\hat{\omega}=\nu\left(\frac{\partial^2\hat{\omega}}{\partial r^2}+\frac{\partial^2\hat{\omega}}{\partial z^2}-\frac{1}{r}\frac{\partial\hat{\omega}}{\partial r}\right)=\nu\Delta\hat{\omega} \tag{1}$$

It is important to note that we have only one unknown function, i.e.: ψ. The vorticity function ω is linked to ψ by the relation:

$$\hat{\omega}=r\omega=-\left(\frac{\partial^2\psi}{\partial r^2}+\frac{\partial^2\psi}{\partial z^2}-\frac{1}{r}\frac{\partial\psi}{\partial r}\right)=-\Delta\psi \tag{2}$$

Velocity components are given by:

$$u=\frac{1}{r}\frac{\partial\psi}{\partial r}\ \text{ and }\ v=-\frac{1}{r}\frac{\partial\psi}{\partial z} \tag{3}$$

The energy equation is:

$$\left(\frac{\partial T}{\partial t}+u\frac{\partial T}{\partial z}+v\frac{\partial T}{\partial r}\right)=a\left(\frac{\partial^2 T}{\partial r^2}+\frac{\partial^2 T}{\partial z^2}+\frac{1}{r}\frac{\partial T}{\partial r}\right) \tag{4}$$

3. Boundary conditions

The present problem is unsteady. This unsteadiness is generated at the initial instant *t=0*, and is sustained during all the time by a source of upstream pulsations. For both steady and unsteady flow, the following boundary conditions are available for any time $t\geq 0$:

- *Entry*: for the thermal problem, the inlet fluid temperature is equal to the upstream ambient temperature: $T=T_\infty$.
- *Exit*: the flow velocity is normal to the exit section and verifies the classical condition:

$$v=0\ \text{ and }\ \frac{\partial T}{\partial z}=\frac{\partial u}{\partial z}=0\,. \tag{5}$$

- *Axis*: the flow preserves at each time an axial symmetry:

$$\frac{\partial u}{\partial r}=v=\frac{\partial T}{\partial r}=0\,. \tag{6}$$

- *Wall*: no slip condition is imposed and the wall is heated at constant temperature:

$$u = v = 0 \quad ; \; T = T_W \, . \tag{7}$$

For dynamic conditions at the entry section, we impose:
- *Steady flow (t=0 time step)*

- *Entry*: for the dynamic problem, Poiseuille profile boundary condition is chosen

$$u(z=0,r) = 2\overline{u}_0 \left(1 - \left(\frac{r}{R} \right)^2 \right) \tag{8}$$

- *Unsteady flow (t>0)*

- *Entry*: the source of imposes a periodic pressure gradient modulation. Then the velocity axial component and the stream function ψ have a Fourier series expansion in time:

$$f(z=0,r,t) = f_0(z=0,r) \left(1 + \sum_{n=1}^{N_F} \tau^n . sin(n\Omega t) \right) \tag{9}$$

where *f* represents u or ψ. At this section, to avoid reverse flow, we impose: $\tau < 1$.

4. New formulation and resolution of the dynamic and thermal problem

4.1 New formulation of the dynamic problem

4.1.1 Dimensionless quantities and variables transformations

One chooses for dimensionless variables:

$$\tilde{r} = \frac{r}{R} \; ; \; \tilde{z} = \frac{z}{R} \; ; \; \tilde{t} = \frac{t}{\overline{t}_0} \; ; \; \tilde{\omega} = \frac{\hat{\omega}}{\overline{\omega}_0} \; ; \; \tilde{\psi} = \frac{\psi}{\overline{\psi}_0} \; ; \; \tilde{u} = \frac{u}{\overline{u}_0} \; ; \; \tilde{v} = \frac{v}{u_o} \tag{10}$$

with

$$\overline{t}_0 = \frac{L}{\overline{u}_0} \; ; \; \overline{\omega}_0 = \frac{\overline{u}_0}{R} \; ; \; \overline{\psi}_0 = \overline{u}_0 R^2 \tag{11}$$

The Reynolds number *Re* is based on the radius at the duct constriction:

$$\mathrm{Re} = R\overline{u}_0 / \nu \tag{12}$$

In order to obtain a computational square domain permitting the use of two dimensional Chebyshev polynomials, we proceed to a space variables transformation. This one is inspired by Sobey, 1980, and modified by Blancher, 1991. It has been adapted to the axisymmetric geometry used in this study. Afterwards, we note by $H(z)$ the duct periodic radius. Then we define:

$$\rho = \frac{\tilde{r}}{h(x)} \quad ; \quad x = \frac{\tilde{z}}{\lambda} - 1 \tag{13}$$

with

$$\lambda = \frac{L}{R} ; \; h(x) = \frac{1}{R} H\left[(x+1).L \right] \tag{14}$$

and (see equation 73)

$$H(z)=R\left\{1+\frac{e}{2}\left[1-\cos\left(\pi.n_O\frac{z}{L}\right)\right]\right\}\Leftrightarrow h(x)=1+\frac{e}{2}\left[1-\cos\left(\pi.n_O(x+1)\right)\right] \tag{15}$$

Finally, the study domain is transformed into a rectangle $-1\le x\le 1$ and $0\le\rho\le 1$ representing the half - space of the square: $[-1,1]\times[-1,1]$.

4.1.2 New system of unsteady dynamic governing equations

Considering the transformation of variables defined before, the new stream – vorticity formulation of this problem is:

$$\begin{cases}\breve{\omega}=-\Delta_f\tilde{\psi}\\ h^2\dfrac{\partial\breve{\omega}}{\partial\tilde{t}}+\dfrac{1}{\rho}\left(\dfrac{\partial\tilde{\psi}}{\partial\rho}\dfrac{\partial\breve{\omega}}{\partial x}-\dfrac{\partial\tilde{\psi}}{\partial x}\dfrac{\partial\breve{\omega}}{\partial\rho}\right)+\dfrac{2}{\rho^2}\left(\dfrac{\partial\tilde{\psi}}{\partial x}-2\rho\dfrac{h'}{h}\dfrac{\partial\tilde{\psi}}{\partial\rho}\right)\breve{\omega}=\dfrac{1}{\hat{\mathrm{Re}}}\Delta_g\breve{\omega}\end{cases} \tag{16}$$

where:

$$\Delta_f\tilde{\psi}=\left\{h^2\frac{\partial^2\tilde{\psi}}{\partial x^2}-2\rho h'h\frac{\partial^2\tilde{\psi}}{\partial x\partial\rho}+\left[\lambda^2+\rho^2h'^2\right]\frac{\partial^2\tilde{\psi}}{\partial\rho^2}+\left[\rho\left(2h'^2-hh''\right)-\frac{\lambda^2}{\rho}\right]\frac{\partial\tilde{\psi}}{\partial\rho}\right\} \tag{17}$$

and

$$\begin{cases}\breve{\omega}=\lambda^2h^2\tilde{\omega}\\ \Delta_g\breve{\omega}=-\left[\begin{array}{l}A_g(x,\rho)\dfrac{\partial^2\breve{\omega}}{\partial x^2}+B_g(x,\rho)\dfrac{\partial^2\breve{\omega}}{\partial\rho^2}+C_g(x,\rho)\dfrac{\partial\breve{\omega}}{\partial\rho}\\ +D_g(x,\rho)\dfrac{\partial^2\breve{\omega}}{\partial x\partial\rho}+E_g(x,\rho)\dfrac{\partial^2\breve{\omega}}{\partial x}+F_g(x,\rho)\breve{\omega}\end{array}\right]\end{cases} \tag{18}$$

with:

$$\begin{cases}A_g(x,\rho)=h^2\ \ ;\ \ B_g(x,\rho)=\lambda^2+\rho^2h'^2\ \ ;\ \ C_g(x,\rho)=\rho\left(6h'^2-hh''\right)-\dfrac{\lambda^2}{\rho}\ \ ;\\ D_g(x,\rho)=-2\rho hh'\quad ;\quad E_g(x,\rho)=-4hh'\quad ;\quad F_g(x,\rho)=2\left(3h'^2-hh''\right)\end{cases} \tag{19}$$

$$\hat{\mathrm{Re}}=\tilde{\mathrm{Re}}\,\lambda^2=\mathrm{Re}\,\lambda \tag{20}$$

$$\Delta_f\tilde{\psi}=\left\{h^2\frac{\partial^2\tilde{\psi}}{\partial x^2}-2\rho h'h\frac{\partial^2\tilde{\psi}}{\partial x\partial\rho}+\left[\lambda^2+\rho^2h'^2\right]\frac{\partial^2\tilde{\psi}}{\partial\rho^2}+\left[\rho\left(2h'^2-hh''\right)-\frac{\lambda^2}{\rho}\right]\frac{\partial\tilde{\psi}}{\partial\rho}\right\} \tag{21}$$

4.1.3 The dynamic steady problem formulation

The dynamic steady problem corresponding to problem (16) is written as follows:

$$\begin{cases} \breve{\omega} = -\Delta_f \tilde{\psi} \\ \dfrac{1}{\rho}\left(\dfrac{\partial\tilde{\psi}}{\partial\rho}\dfrac{\partial\breve{\omega}}{\partial x} - \dfrac{\partial\tilde{\psi}}{\partial x}\dfrac{\partial\breve{\omega}}{\partial\rho}\right) + \dfrac{2}{\rho^2}\left(\dfrac{\partial\tilde{\psi}}{\partial x} - 2\rho\dfrac{h'}{h}\dfrac{\partial\tilde{\psi}}{\partial r}\right)\breve{\omega} = \dfrac{1}{\widehat{\mathrm{Re}}}\Delta_g\breve{\omega} \end{cases} \tag{22}$$

Important: for reason of convenience, the radius ρ will be noted r.

4.2 New formulation of the thermal problem

For the thermal problem, the temperature $\tilde{\theta}$ is made dimensionless in a classic way:

$$\tilde{\theta} = \frac{T - T_\infty}{T_W - T_\infty} \tag{23}$$

4.2.1 The thermal unsteady problem formulation

Using (1) and (10)-(15), the dimensionless energy equation can be written as follows:

$$h^2\frac{\partial\tilde{\theta}}{\partial\tilde{t}} + h^2\tilde{u}\frac{\partial\tilde{\theta}}{\partial x} + h\left(\tilde{\mathrm{v}}\lambda - \tilde{u}rh'\right)\frac{\partial\tilde{\theta}}{\partial r} = \frac{1}{\widehat{\mathrm{Re}}\,\mathrm{Pr}}\Delta_f\tilde{\theta} \tag{24}$$

with:

$$\Delta_f\tilde{\theta} = h^2\frac{\partial^2\tilde{\theta}}{\partial x^2} - 2rh'h\frac{\partial^2\tilde{\theta}}{\partial x\partial r} + \left[\lambda^2 + r^2h'^2\right]\frac{\partial^2\tilde{\theta}}{\partial r^2} + \left[r\left(2h'^2 - hh''\right) + \frac{\lambda^2}{r}\right]\frac{\partial\tilde{\theta}}{\partial r} \tag{25}$$

4.2.2 The thermal steady problem formulation

The dimensionless steady state energy problem related to the equation (24) is:

$$h^2\tilde{u}\frac{\partial\tilde{\theta}}{\partial x} + h\left(\tilde{\mathrm{v}}\lambda - \tilde{u}rh'\right)\frac{\partial\tilde{\theta}}{\partial r} = \frac{1}{\widehat{\mathrm{Re}}\,\mathrm{Pr}}\Delta_f\tilde{\theta} \tag{26}$$

5. Numerical resolution using spectral methods

5.1 Trial functions and development orders

The spectral methods consist in projecting any unknown function $f(x,r,t)$ on trial functions as follows:

$$f(x,r,t) = \sum_{k=0}^{N_x}\sum_{l=0}^{N_r} f_{kl}(t)P_l(r)Q_k(x) \tag{27}$$

where N_x and N_r are the development orders according to the axis x and r respectively. The basis functions $P_l(r)$ and $Q_k(x)$ are generally trigonometric or polynomial functions (Chebyshev, Legendre, etc.) according to different boundary conditions situations. The time dependant coefficients $f_{kl}(t)$ are the unknowns of the problem. For our problem, the function f represents $\bar{\omega}$, $\tilde{\psi}$ or $\tilde{\theta}$. For a steady problem, the coefficients $f_{kl}(t)$ are time independent.

It is necessary to study the influence of the physical parameters such as the Reynolds number to remain in 2D hypothesis. From a numerical point of view we will show the influence of the polynomials degrees particularly for the thermal problem.

5.2 The choice of basis functions

Because no symmetry condition is imposed at the boundaries of our half-domain of study, we choose basis functions constructed from Chebyshev polynomials (Bernardi & Maday, 1992; Canuto et al., 1988) instead of trigonometric trial functions. Then, $P_l(r)$ and $Q_k(x)$ are written as linear combination of Chebyshev polynomials. Their expressions depend on the boundary conditions and the spectral method used (Galerkin or collocation method).
Generally, with Galerkin method, Dirichlet or Neuman boundary conditions imposed to trial functions must be homogeneous, but it is not necessary for collocation method (see Galerkin and collocation methods below).
The basis $P_l(r)$ and $Q_k(x)$ are written as a linear combination of Chebyshev polynomials such as (Gelfgat, 2004; Shen, 1994, 1995, 1997):

$$P_l(r) = T_l(r) + \sum_{i=1}^{n} \alpha_l T_{l+i}(r) \text{ and } Q_k(x) = T_k(x) + \sum_{i=1}^{m} \beta_k T_{k+i}(x) \tag{28}$$

where n (respectively m) is the number of boundary conditions according to the radial direction r (respectively the axial direction x), and $T_k(x)$ is the Chebyshev polynomial of degree k.

5.2.1 Advantages and limitations of spectral methods

Spectral methods are used successfully in many problems of physics, mainly those involving periodic physical phenomena in space and / or in time. Its main advantage is its high degree of accuracy, compared with some methods such as finite differences, finite elements or finite volumes (Bernardi & Maday, 1992; Canuto et al., 1988; Gelfgat, 2004; Shen, 1994, 1995, 1997). Spectral methods are particularly suitable to study instabilities phenomena, self-maintained or forced, occuring in Computational Fluid Dynamics. However, spectral methods are limited to simple geometries. For complicated study domains, an alternative way may be using spectral finite elements. The second disadvantage of these methods is their cost of implementing and their high CPU calculations. The matrices obtained are usually full and strategies for solving linear or nonlinear systems remain limited.

6. Numerical resolution of the dynamic and thermal problem using spectral galerkin formulation

6.1 Numerical resolution of the dynamic steady problem

The steady dynamic problem is given by the equation (22). Generally, this problem is written with classical homogeneous boundary conditions. One of the originalities of this study is the use of a relevment function allowing the introduction of non homogeneous boundary conditions. For this reason, the unknown stream function $\tilde{\psi}(x,r)$ is written by mean of the Poiseuille stream function $\varphi_0(r)$ corresponding to the Poiseuille velocity imposed at the duct entry as:

$$\tilde{\psi}(x,r) = \psi_0(x,r) + \varphi_0(r) \tag{29}$$

where the stream function $\psi_0(x,r)$ verifies homogeneous boundary conditions in both directions x and r.
The equation (22) becomes:

$$\frac{1}{r^2}\frac{\partial\psi_0}{\partial x}\left(\alpha(\omega)+\alpha_\Phi\right)+\frac{1}{r}\frac{\partial\psi_0}{\partial r}\left(\beta(\omega)+\beta_\Phi\right)+\frac{1}{r}\frac{\partial\varphi_0}{\partial r}\beta(\omega)-\frac{1}{\widehat{\mathrm{Re}}}\gamma(\omega)=\frac{1}{\widehat{\mathrm{Re}}}\gamma_\Phi-\frac{1}{r}\frac{\partial\varphi_0}{\partial r}\beta_\Phi \quad (30)$$

with:

$$\begin{aligned}&\alpha(\omega)=2\omega-r\frac{\partial\omega}{\partial r};\alpha_\Phi=2\Phi-r\frac{\partial\Phi}{\partial r};\beta(\omega)=\frac{\partial\omega}{\partial x}-4\frac{h'}{h}\omega;\beta_\Phi=\frac{\partial\Phi}{\partial x}-4\frac{h'}{h}\Phi;\\&\gamma(\omega)=\Delta_g\omega;\gamma_\Phi=\Delta_g\Phi;\end{aligned} \quad (31)$$

$$\Phi(x,r)=-\Delta_f\varphi_0(r). \quad (32)$$

The corresponding Galerkin method consists in projecting the discretized equations on a Chebyshev polynomials basis, taking into account the whole boundary conditions (Canuto et al., 1988). Then, according to the general formulation of spectral methods, the stream-function ψ_0 is projected on trial functions as follows:

$$\psi_0(x,r)=\sum_{k=0}^{N_x}\sum_{1=0}^{N_r}\psi_{kl}P_{2l}(r)Q_k(x) \quad (33)$$

Because of the symmetry property on the whole axisymmetric domain of the problem, $P_{2l}(r)$ will be an even function. To construct the basis $P_{2l}(r)$, we choose a linear combination of Chebyshev polynomials such as (Gelfgat, 2004; Shen, 1994, 1995, 1997):

$$P_{2l}(r)=T_{2l}(r)+\sum_{i=1}^{n}\alpha_{li}T_{2(l+i)}(r) \quad (34)$$

where n is the number of boundary conditions according to radial direction r ($n=3$ here, see bellow).
The coefficients α_{li} are determined so that $P_{2l}(r)$ satisfies the corresponding homogeneous boundary conditions:

$$\frac{\partial P_{2l}}{\partial r}=0 \text{ at } r=\pm1 \quad (\text{because}\frac{\partial\tilde{\psi}}{\partial r}=0 \text{ at } r=\pm1) \quad (35)$$

$$P_{2l}(r)=0 \quad \text{at } r=\pm1 \quad (\text{flow-rate condition at } r=\pm1) \quad (36)$$

$$P_{2l}(r)=0 \quad \text{at } r=0 \quad (\text{axial symmetry}) \quad (37)$$

So, one can determine all coefficients α_{li}. Finally we have:

$$P_{2l}(r)=T_{2l}(r)-\frac{l+1}{l+2}T_{2(l+1)}(r)-T_{2(l+2)}(r)+\frac{l+1}{l+2}T_{2(l+3)}(r) \quad (38)$$

A similar analysis is available for the choice of $Q_k(x)$ basis functions:

$$Q_k(x) = T_k(x) + \sum_{i=1}^{m} \beta_{ki} T_{(k+i)}(x) \tag{39}$$

where $m = 3$ here (see bellow). The velocity boundary conditions imply that the stream function must satisfy the corresponding homogeneous boundary conditions as:

$$Q_k'(-1) = 0 \text{ at } x = -1 \ (\tilde{v} = 0 \text{ at } x = -1) \tag{40}$$

$$Q_k(-1) = 0 \text{ at } x = -1 \text{ (Poiseuille profile } x = -1) \tag{41}$$

$$Q_k'(1) = 0 \text{ at } x = 1 \ (\tilde{v} = 0 \text{ at } x = 1) \tag{42}$$

Finally we obtain:

$$Q_k(x) = T_k(x) - \frac{(k+3)^2(k+1)}{(k+2)^2(k+2)} T_{k+1}(x) - \frac{k^2}{(k+2)^2} T_{k+2}(x) + \frac{(k+3)^2(k+1)}{(k+2)^2(k+2)} T_{k+3}(x) \tag{43}$$

Let us define the Chebyshev scalar product as:

$$(\psi, \phi) = \iint_{\Delta} \psi(x,r)\phi(x,r)\left(\frac{1}{\sqrt{1-x^2}} \cdot \frac{1}{\sqrt{1-r^2}}\right) dx dr \tag{44}$$

where Δ is the square: $\Delta = [-1,1] \times [-1,1]$.
Taking as test function:

$$\phi(x,r) = Q_k(x) P_{2l}(r), \text{ for } 0 \le \mathrm{k} \le \mathrm{N_x}, \ 0 \le \mathrm{l} \le \mathrm{N_r} \tag{45}$$

the Galerkin spectral method consist to make scalar products between the non linear equation (30) and each test function $Q_i(x) P_{2j}(r)$, by writing:

$$\begin{aligned} &\left(\frac{1}{r^2} \frac{\partial \psi_0}{\partial x} \left(\alpha(\omega) + \alpha_\Phi\right) + \frac{1}{r} \frac{\partial \psi_0}{\partial r} \left(\beta(\omega) + \beta_\Phi\right) + \frac{1}{r} \frac{\partial \varphi_0}{\partial r} \beta(\omega) - \frac{1}{\widehat{\mathrm{Re}}} \gamma(\omega), Q_i(x) P_{2j}(r) \right) = \\ &= \left(\frac{1}{\widehat{\mathrm{Re}}} \gamma_\Phi - \frac{1}{r} \frac{\partial \varphi_0}{\partial r} \beta_\Phi, Q_i(x) P_{2j}(r) \right) \end{aligned} \tag{46}$$

Finally, we obtain a system of $N_{xr} = (N_x + 1)(N_r + 1)$ non linear equations with N_{xr} unknowns, solved by Newton algorithm.

6.2 Numerical resolution of the dynamic unsteady problem

From equation (16), introducing the unknown ψ function such as:

$$\tilde{\psi}(x,r,t) = \psi(x,r,t) + \varphi(r) A(t) \tag{47}$$

and using the equations (46), we define the operator in which the unknown coefficients depend now on time:

$$L_\psi(x,r,t) = -\left(\frac{1}{r^2} \frac{\partial \psi}{\partial x} \left(\alpha(\omega) + \alpha_\Phi\right) + \frac{1}{r} \frac{\partial \psi}{\partial r} \left(\beta(\omega) + \beta_\Phi\right) + \frac{1}{r} \frac{\partial \varphi}{\partial r} \beta(\omega) - \frac{1}{\widehat{\mathrm{Re}}} \gamma(\omega) \right) + \frac{1}{\widehat{\mathrm{Re}}} \gamma_\Phi - \frac{1}{r} \frac{\partial \varphi}{\partial r} \beta_\Phi \tag{48}$$

Then the previous problem (16) can take the following form:

$$h^2 \frac{\partial \breve{\omega}}{\partial t} = L_\psi(x,r,t) \text{ where } \breve{\omega} = \omega + \omega_\Phi \tag{49}$$

The operator $L_\psi(x,r,t)$ is nonlinear. Notice that ω_Φ is the contribution coming from Poiseuille extension. The temporal discretization of (49) is made by using the ε –method, reduced here to Crank - Nicolson method. The advantage of this method is to be unconditionally stable. It leads to the equation below with $\varepsilon = 1/2$, which corresponds to a two order scheme:

$$\begin{cases} h^2 \dfrac{\omega^{n+1} - \omega^n}{\Delta t} + h^2 \dfrac{\partial \omega_\Phi(x,r,t)}{\partial t} = \varepsilon L_{\psi^{n+1}}(x,r,t) + (1-\varepsilon) L_{\psi^n}(x,r,t) \\ \omega^n = -\Delta_f \psi^n, \forall n \end{cases} \tag{50}$$

where the initial condition is given by the solution of the steady problem.
The unknowns $\psi_{kl}(t)$ are obtained by solving with Newton algorithm, at each time step, the non linear system obtained with scalar products between relation (50) and test functions $Q_i(x)P_{2j}(r)$, as in equation (46).

6.3 Numerical resolution of the thermal unsteady problem

6.3.1 Choices of the basis functions

The dimensionless energy equation is given by (25) and (25). The choice of the temperature basis functions is made in the same way as in the dynamic problem. In order to apply the Galerkin method, we consider the boundary conditions (heading 3) for the temperature θ. Let us set:

$$\tilde{\theta}(x,r,t) = \theta(x,r,t) + \theta_R(r) \tag{51}$$

where θ is the solution satisfying the homogeneous boundary conditions and $\theta_R(r)$ is a smoothed gap temperature imposed at the entry. The homogeneous temperature θ, truncated at development orders M_x according to the axis x and M_r according to the radius r, is projected on the trial functions as follows:

$$\theta(x,r,t) = \sum_{k=0}^{M_x} \sum_{l=0}^{M_r} \theta_{kl}(t) q_k(x) p_{2l}(r) \tag{52}$$

where $p_{2l}(r)$ and $q_k(x)$ are built from Chebyshev polynomials as in heading 5. According to temperature boundary conditions (heading 3), we obtain, at last:

$$q_k(x) = T_k(x) + \frac{4(k+1)}{(k+1)^2 + (k+2)^2} T_{k+1}(x) - \frac{(k+1)^2 + k^2}{(k+1)^2 + (k+2)^2} T_{k+2}(x), \quad \text{if } 0 \le k \le M_x \tag{53}$$

The polynomial $p_{2l}(r)$ is given by:

$$p_{2l}(r) = T_{2l}(r) - T_{2(l+1)}(r), \qquad \text{if } 0 \le l \le M_r \tag{54}$$

6.3.2 Resolution of the steady energy equation

With (24) and $\tilde{\theta}(x,r)=\theta(x,r)+\theta_R(r)$, the steady thermal problem is written as follows:

$$\frac{1}{r}\frac{\partial\psi}{\partial r}.\frac{\partial\theta}{\partial x}-\frac{1}{r}\frac{\partial\psi}{\partial x}.\frac{\partial\theta}{\partial r}+2(1-r^2)\frac{\partial\theta}{\partial x}-\frac{1}{\widehat{\mathrm{Re}}\,\mathrm{Pr}}\Delta_f\theta=\frac{1}{r}\frac{\partial\psi}{\partial x}.\frac{\partial\theta_R}{\partial r}+\frac{1}{\widehat{\mathrm{Re}}\,\mathrm{Pr}}\Delta_f\theta_R \tag{55}$$

This problem is discretized by Galerkin spectral method explained above. The linear system obtained is solved by a Gauss type classical method.

6.3.3 Resolution of the unsteady energy equation

The unsteady problem is written as follows:

$$\begin{aligned}&\frac{\partial\theta}{\partial t}=-\frac{1}{h^2}\left(\frac{1}{r}\frac{\partial\psi}{\partial r}.\frac{\partial\theta}{\partial x}-\frac{1}{r}\frac{\partial\psi}{\partial x}.\frac{\partial\theta}{\partial r}+\frac{1}{r}\frac{\partial\varphi}{\partial r}\frac{\partial\theta}{\partial x}-\frac{1}{\widehat{\mathrm{Re}}\,\mathrm{Pr}}\Delta_f\theta\right)+\frac{1}{h^2}\left(\frac{1}{r}\frac{\partial\psi}{\partial x}.\frac{\partial\theta_R}{\partial r}+\frac{1}{\widehat{\mathrm{Re}}\,\mathrm{Pr}}\Delta_f\theta_R\right)\\&\theta(x,r,0)=\theta_0(x,r)\end{aligned} \tag{56}$$

where $\theta_0(x,r)$ is the steady thermal problem solution. The equation (56) is numerically integrated in time by using the second order Crank-Nicolson scheme ($\varepsilon=\frac{1}{2}$) which is formulated as follows:

$$\frac{\theta^{n+1}-\theta^n}{\Delta t}=\varepsilon L_{\theta^{n+1}}(x,r,t)+(1-\varepsilon)L_{\theta^n}(x,r,t) \tag{57}$$

where

$$\begin{aligned}L_\theta(x,r,t)=&-\frac{1}{h^2}\left(\frac{1}{r}\frac{\partial\psi}{\partial r}.\frac{\partial\theta}{\partial x}-\frac{1}{r}\frac{\partial\psi}{\partial x}.\frac{\partial\theta}{\partial r}+\frac{1}{r}\frac{\partial\varphi}{\partial r}A(t)\frac{\partial\theta}{\partial x}-\frac{1}{\widehat{\mathrm{Re}}\,\mathrm{Pr}}\Delta_f\theta\right)\\&+\frac{1}{h^2}\left(\frac{1}{r}\frac{\partial\psi}{\partial x}.\frac{\partial\theta_R}{\partial r}+\frac{1}{\widehat{\mathrm{Re}}\,\mathrm{Pr}}\Delta_f\theta_R\right)\end{aligned} \tag{58}$$

By projecting (57) in the Galerkin basis $\left(q_i(x)p_{2j}(r)\right)_{ij}$, one obtains at each time step a system of linear equations solved by the classical Gauss method.

One can notice that the use of Chebyshev polynomials in both axial and radial directions is not obvious, and contribute to emphasize this numerical method.

7. Numerical resolution of the dynamic and energy problem using spectral collocation method

7.1 Numerical resolution of the dynamic problem

For reasons of simplicity, we describe explicitly only the resolution of the steady dynamic problem. For the unsteady problem, we use Crank-Nicolson method for time integration as in (50); the unsteady problem resolution in space is identical to the steady case.

The main interest of collocation method compared with Galerkin formulation is its simplicity: it is not necessary to build a relevment function to take into account non homogeneous boundary conditions. We introduce these conditions directly in the matrix of the system and/or in the basis trial functions. For this reason, it is easy to compute collocation procedure. Let us explain this method for the steady dynamic problem.

According to the general formulation of spectral methods (27), the stream-function $\tilde{\psi}$ is projected on trial functions in the same manner as equation (33):

$$\tilde{\psi}(x,r)=\sum_{k=0}^{N_x}\sum_{l=0}^{N_r}\psi_{kl}P_{2l}(r)Q_k(x) \tag{59}$$

We can apply the same approach used in Galerkin method to determine trial functions $P_{2l}(r)$ and $Q_k(x)$. All conditions given by (35-42) are available, except the second condition (36) for $P_{2l}(r)$ and the second condition (41) for $Q_k(x)$. Then, with the method given by (34), we obtain:

$$P_{2l}(r)=T_{2l}(r)+\frac{(l+2)^2-l^2}{(l+2)^2+(l+1)^2}T_{2(l+1)}(r)-\frac{(l+1)^2+l^2}{(l+2)^2+(l+1)^2}T_{2(l+2)}(r) \tag{60}$$

and

$$Q_k(x)=T_k(x)-\frac{k^2}{(k+2)^2}T_{k+2}(x) \tag{61}$$

The vorticity function can be written as follows:

$$\tilde{\omega}=\sum_{k=0}^{N_x}\sum_{l=0}^{N_r}A_{kl}(x,r)\psi_{kl} \tag{62}$$

where:

$$\begin{cases} A_{kl}(x,r)=A_f P_l(r)Q_k''(x)+B_f P_l''(r)Q_k(x)+C_f P_l'(r)Q_k(x)+D_f P_l'(r)Q_k'(x) \\ A_f=h^2 \quad ; \quad B_f=r^2+r^2h'^2 \quad ; \quad C_f=\rho\left(2h'^2-hh''\right)-\dfrac{\lambda^2}{r} \quad ; \quad D_f=-2rhh' \end{cases} \tag{63}$$

Then, substituting $\tilde{\psi}$ and $\tilde{\omega}$ by their expressions (59), (62) in the steady dynamic equation (22), we obtain the following discretized dynamic equation:

$$\begin{aligned} &\frac{1}{r}\left[\left(\sum_{k=0}^{N_x}\sum_{l=0}^{N_r}P_l'(r)Q_k(x)\psi_{kl}\right)\cdot\left(\sum_{k=0}^{N_x}\sum_{l=0}^{N_r}A_{kl}^{x}(x,r)\psi_{kl}\right)\right. \\ &\qquad\left.-\left(\sum_{k=0}^{N_x}\sum_{l=0}^{N_r}P_l(r)Q_k'(x)\psi_{kl}\right)\cdot\left(\sum_{k=0}^{N_x}\sum_{l=0}^{N_r}A_{kl}^{r}(x,r)\psi_{kl}\right)\right] \\ &+\frac{2}{r^2}\left[\left(\sum_{k=0}^{N_x}\sum_{l=0}^{N_r}P_l(r)Q_k'(x)\psi_{kl}\right)-r\frac{h'}{h}\left(\sum_{k=0}^{N_x}\sum_{l=0}^{N_r}P_l'(r)Q_k(x)\psi_{kl}\right)\right]\left(\sum_{k=0}^{N_x}\sum_{l=0}^{N_r}A_{kl}(x,r)\psi_{kl}\right) \\ &=\frac{1}{\mathrm{Re}}\sum_{k=0}^{N_x}\sum_{l=0}^{N_r}\left[\begin{array}{l} A_g(x,r)A_{kl}^{xx}(x,r)+B_g(x,r)A_{kl}^{rr}(x,r)+C_g(x,r)A_{kl}^{r}(x,r) \\ +D_g(x,r)A_{kl}^{xr}(x,r)+E_g(x,r)A_{kl}^{rr}(x,r)+F_g(x,r)A_{kl}(x,r) \end{array}\right]\psi_{kl} \end{aligned} \tag{64}$$

with:

$$A_{kl}^{\alpha}(x,r)=\frac{\partial A_{kl}(x,r)}{\partial \alpha} \text{ and } A_{kl}^{\alpha\beta}(x,r)=\frac{\partial^2 A_{kl}(x,r)}{\partial \alpha \partial \beta} \tag{65}$$

where α or β represents the space variable x or r. The relation (65) is a function of local point $(x,r)\in\Delta$, where Δ is the square $[-1,1]\times[-1,1]$.
The collocation method consists to write the above equation on specific points $\left(x=x_i, r=r_j\right)_{\substack{0\le j\le N_r \\ 0\le j\le N_x}}$ of Δ, called collocation points. We chose the collocation points of Chebyshev-Gauss-Lobatto [5], defined by:

$$x_i=-\cos(i\pi/N_x) \text{ and } r_j=-\cos(j\pi/N_r) \tag{66}$$

with $0\le i\le N_x$ and $0\le j\le N_r$.
We recall that homogeneous boundary conditions are imposed on trial functions $P_{2l}(r)$ and $Q_k(x)$. The non homogeneous boundary conditions, like Poiseuille profile at the duct entry or flow-rate condition at the wall, are directly imposed in the matrix system .
The nonlinear system obtained is solved by the Newton algorithm.

7.2 Numerical resolution of the thermal problem

Steady and unsteady energy equations are solved in the same manner as the dynamic problem, using spectral collocation method and Crank-Nicolson time-solver method described above.
Concerning trial functions for steady and unsteady thermal problems, we use directly Chebyshev polynomials:

$$p_l(r)=T_l(r) \text{ and } q_k(x)=T_k(x) \tag{67}$$

All boundary conditions are imposed in the matrix system.

8. Convective heat transfer

The local convective heat transfer coefficient h_T is written as follows:

$$h_T(x,t)=\frac{\Phi_W}{\Delta T_{ref}} \tag{68}$$

where ΔT_{ref} is a typical difference temperature reference. That one depends on the wall boundary conditions hypotheses. The main difficulty with convective unsteady heat transfer lies in the temperature reference choice. After several tests, we have chosen:

$$\Delta T_{ref}(x,t)=T_W-T_m(x,t) \tag{69}$$

where $T_m(x,t)$ is the mean bulk temperature given by:

$$T_m(x,t)=\frac{\int_0^1 u(x,r,t).T(x,r,t).rdr}{\int_0^1 u(x,r,t).rdr} \tag{70}$$

The instantaneous convective heat transfer in unsteady flows can formally be defined by the local Nusselt number $Nu(x,t)$, given by the relation:

$$Nu(x,t) = \frac{Rh_T(x,t)}{k} \tag{71}$$

With the variables transform (heading 4), the Nusselt number can be written as follows:

$$Nu(x,t) = \frac{1}{h\lambda}\sqrt{\lambda^2 + h'^2}\,\frac{\left(\dfrac{\partial\theta(x,t)}{\partial r}\right)_W}{1-\theta_m(x,t)} \tag{72}$$

where h' is the derivative oh the function h.

9. Numerical results

9.1 Definition of geometrical, physical and numerical parameters

All results have been computed with Galerkin spectral method, except those used to make the comparison between Galerkin and collocation method (headings 6 and 7). The source of pulsations is located at the inlet section.The studied fluid is air, under normal conditions of temperature and pressure. The fluid flow is submitted to a pure sinusoidal pulsation. The previous studies [1, 2] showed that the numerical results are in the more stable mode if the ratio R/L is small, compared to the unit. Consequently, the basic geometry parameters are:

$$R = 0{,}02\ m\ ;\ L = 0{,}08\ m\ \ ;\ e = E/R = 2\ ,\ R_V = 3R = 0{,}06\ m\ .$$

The sinusoidal surface of the wall is represented by the function *h*:

$$h(x) = 1 + \frac{e}{2}\left[1 - \cos\left(\pi.n_O(x+1)\right)\right] \tag{73}$$

where n_O indicates the number of geometrical periods chosen here equals to 3.

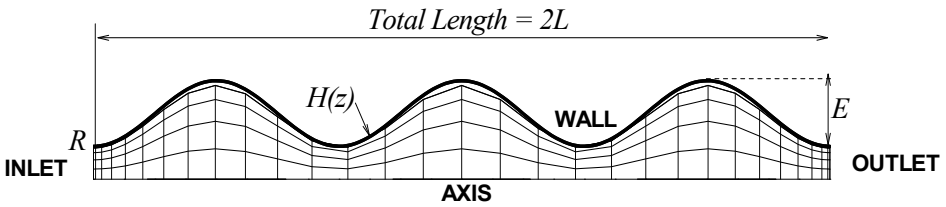

Fig. 1. Geometry of the study domain showing the projection of the Chebyshev -Gauss-Lobatto mesh grid on the physical geometry (Nx=30 , Nr=5)

9.1.1 Choice for the orders of truncature

To ensure the accuracy of our results from the numerical point of view, we try several orders of truncature in the Chebyshev basis developments (Batchi, 2005) for details. When the orders of truncature increase, let $e_{\alpha\beta}$ be the error calculated between two consecutive

truncature orders α and β of the stream function coefficients ψ_{kl} (respectively the temperature coefficients θ_{kl}) relative to the steady flow. The expression of $e_{\alpha\beta}$ is:

$$e_{\alpha\beta} = \max_{k,l} \left| f_{kl}^{\alpha} - f_{kl}^{\beta} \right| \tag{74}$$

where f^{α} represents ψ or θ, for the truncature order α.

For the dynamic point of view, we note first that the truncature errors $e_{\alpha\beta}$ depend mainly on the parameter *Nx*. This means that the increase in the number of polynomials in the radial direction does not improve the convergence of the results. Secondly, figure 2.a shows that, globally, the amplitudes of $e_{\alpha\beta}$ decrease when the values of *Nx* increase. With *Nr* fixed to 5 and $Nx \geq 30$, the truncature errors $e_{\alpha\beta}$ are negligible, about 2.10^{-4}.

For a given value of *Mr*, we observe in figure 2.b a good convergence of the temperature coefficients when *Mx* increases. But, unlike dynamic field, for the range of *Mr* values between 5 and 9, the analysis of the thermal field leads to slightly different conclusions. Indeed, probably due to the temperature conditions imposed on the entry section, the thermal field is more sensitive to the parameter *Mr* than dynamic field. For a fixed value of *Mx*, the temperature truncature errors increase with *Mr*. Then, optimal convergence is obtained for *Mr* = 5. For this value, the truncature error is less than 10^{-8} when $Mx > 56$.

In conclusion, we have selected for the dynamic problem: *Nx* = 30 and *Nr* = 5, and for the thermal problem, we have chosen: *Mx* =120 and *Mr* = 5.

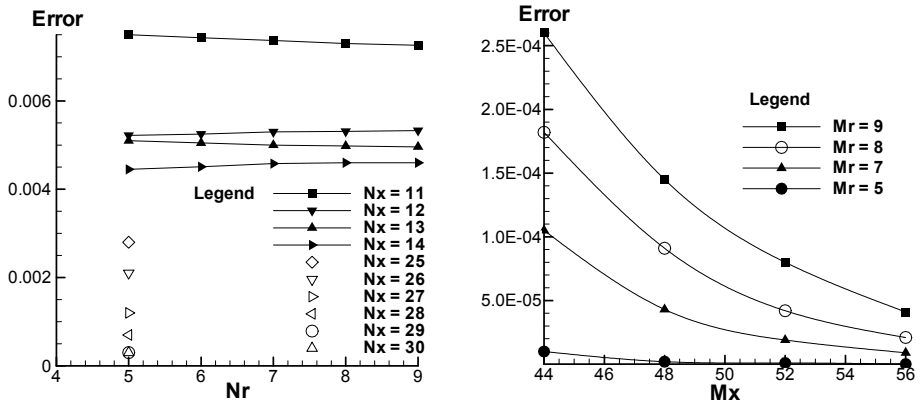

(a) (b)

Fig. 2. a) Maximum truncature error in the Chebyshev basis development of the stream function ψ (steady flow, Re = 30). b) Maximum truncature error in the Chebyshev basis development of the temperature function θ (steady flow, Re=30, Pr = 0.73)

9.2 The steady flow

9.2.1 Study of the dynamic field

In order to study the dynamic behaviour of the flow according to the flow-rate, we varied the Reynolds number from 1 to 50. Figure 3 shows that the flow remains "with parallel lines", i.e. of crawling type, until $\mathrm{Re} = 10$. From this value, a vortex initially appears in the

first geometrical period, with a center shifted upstream and close to the wall. Then, when Re increases, a less bulky vortex appears in the two other geometrical periods. The center of each vortex moves towards the downstream while moving away from the wall more and more gradually. These results perfectly agree with those previously shown by Blancher, 1991; Batina et al., 2004, 2009.

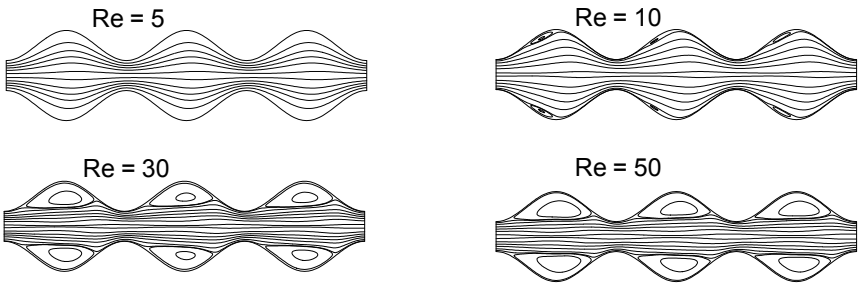

Fig. 3. Streamlines parametric study versus Reynolds number (steady flow)

9.2.2 Thermal study

Figure 4 shows a comparative study of the convective heat transfer by means of the Nusselt number, in stationary regime. One can clearly see that the vortex has a negative influence on the heat transfer on almost the totality of the duct, except for the entry. Locally, we observe a light heat transfer enhancement at the constriction which increases with the amplitude of geometry.

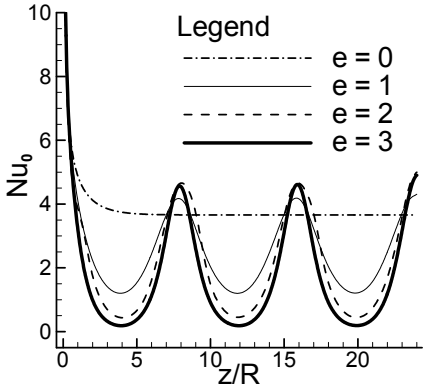

Fig. 4. Heat transfer comparison (steady case): parametric study according to the reduced amplitude e of the geometry

9.3 The unsteady flow

In order to maintain the bidimensional hypothesis, the flow is submitted to low frequencies ($0 \le f \le 5Hz$) and the amplitude of pulsation τ do not exceed 0.7. The number of time steps

by period is equal to 24. The Reynolds number is fixed to 30 corresponding to a total filling of the furrows. The corresponding steady regime is taken as initial condition for the unsteady mode (instant *t=0*).

To understand better the fluid dynamic behaviour in pulsed regime, figure 5 shows the detail of the streamlines for one period *T*. We note that the vortices quickly disappear during the first instants, from *t=0* to *t=2T/8*. This interval of time corresponds to the phase of the flow acceleration, with a maximum reached for *t=2T/8*. After that, a phase of deceleration appears, with a passage to zero for *t=T/2*. The size of the vortex is maximal for *t=6T/8*. This stage corresponds to the maximum of the flow deceleration ($\Omega t = 3\pi / 2$). In the central zone, the flow moves in positive direction, and close to the wall, the flow moves in opposite direction. After this, the fluid moves more closer to the wall. For the acceleration phase which follows, the flow tends to take its initial aspect again. However, with *t=T*, we approximately find the form of the flow for *t=0*.

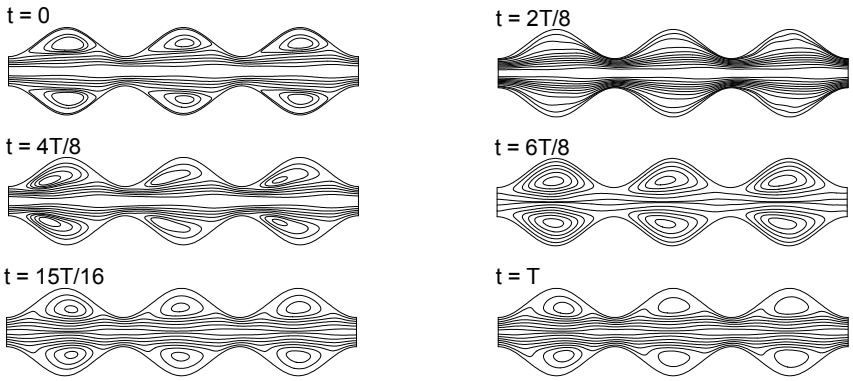

Fig. 5. Time history streamlines during one period, Ω=0.3, Re=30, Pr=0.73, $\tau = 0.7$

9.3.1 Temporal evolution of the unsteady temperature field

Let us locate first particular control points in the duct (figure 6). Each point is chosen because we expect significant results on dynamical and thermal phenomena close to this region.

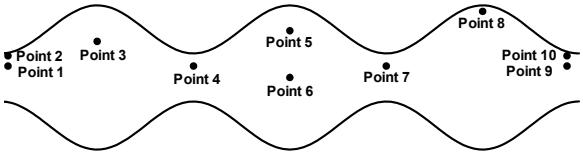

Fig. 6. Localization of control points for the description of the time-history phenomena

In order to have a global vision of the dynamic and thermal unsteady phenomena, we carried out a spectral analysis with the FFT method, for the velocity and temperature fields, on three temporal periods (t >10). The figures 7.a and 7.b show that the most significant

dynamic fluctuations are located at each constriction of the tube for axial velocities and downstream the constriction for radial velocities.

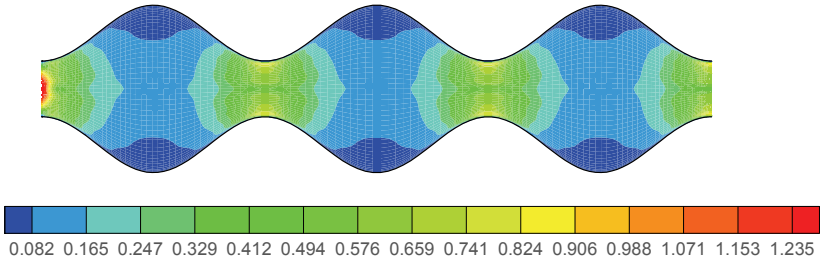

(a)

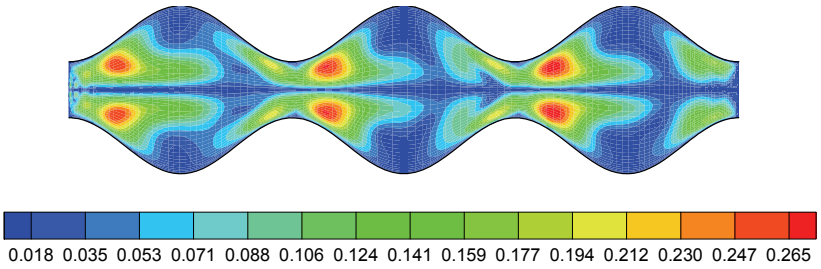

(b)

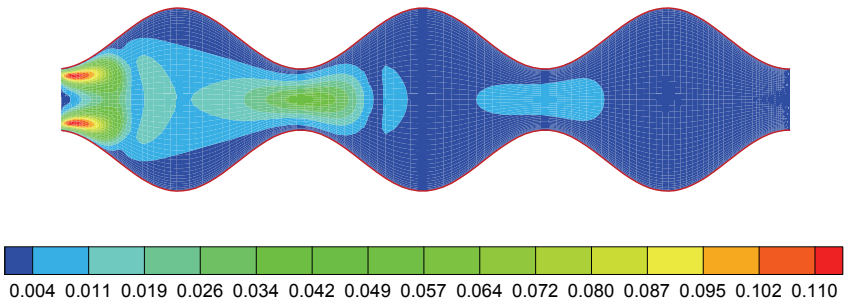

(c)

Fig. 7. Amplitudes fluctuations of the axial velocity (a), the radial velocity (b) and the temperature (c). Re=30, Pr=0.73, $\tau = 0.7$

One can thus expect a substantial modification of the thermal convective heat transfer in these privileged areas, due to the thermal boundary modifications corresponding to the entry section duct, and in the minimum sections as shown in figure 7.c.

9.4 Unsteady convective heat transfer

On figure 8, we study, on the control point 4, the Nusselt number evolution versus the pulsation frequency Ω. This amplitude analysis is obtained by the FFT method realised on the instantaneous Nusselt number defined by equation (71). We observe the decrease of the Nusselt number amplitudes when Ω increases.

The instantaneous heat transfer does not correspond to a measurable physical reality. Thus it is necessary to consider the time averaged Nusselt number. So, we define:

$$\overline{Nu}(x) = \langle Nu(x,t) \rangle = \frac{\omega}{2\pi} \int_0^{\frac{2\pi}{\omega}} Nu(x,t)\, dt \tag{75}$$

To evaluate the contribution of the pulsation on the heat transfer, we compare $\overline{Nu}(x)$ with the Nusselt number $Nu_0(x)$ obtained in steady flow. We confirm in figure 9, a very significant increase of the heat transfer located at the constriction, and conversely a high reduction at maximum radius areas (zones of dead fluid).

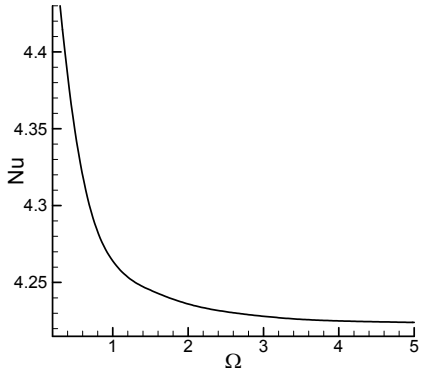

Fig. 8. Evolution of Nusselt number (FFT method) versus the pulsation frequency on the control point 4 (Re=30; Pr=0.73; τ=0.7)

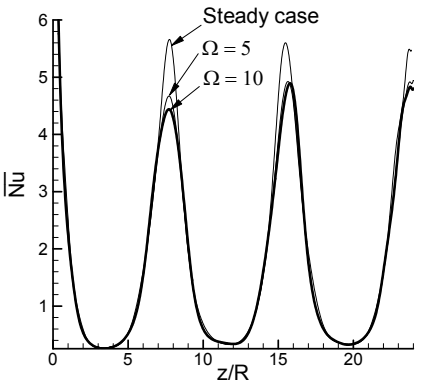

Fig. 9. Heat transfer comparison in steady and unsteady flow(Ω=10, Ω=5, $\tau = 0.7$)

9.5 Comparison between Galerkin and collocation spectral methods

9.5.1 Dynamic and thermal results comparison

In order to make comparison between Galerkin and collocation spectral methods, classical parameters are chosen: Re=30, Nx = 30 and Nr = 5 for both methods.

When the flow is pulsed, we chose to study the dynamic and thermal fields at points 1, 7, 8 and 9 of figure 6. Apart the periodicity previously highlighted, these curves show once again that there is nearly no difference between the two methods as shown in figures 10.

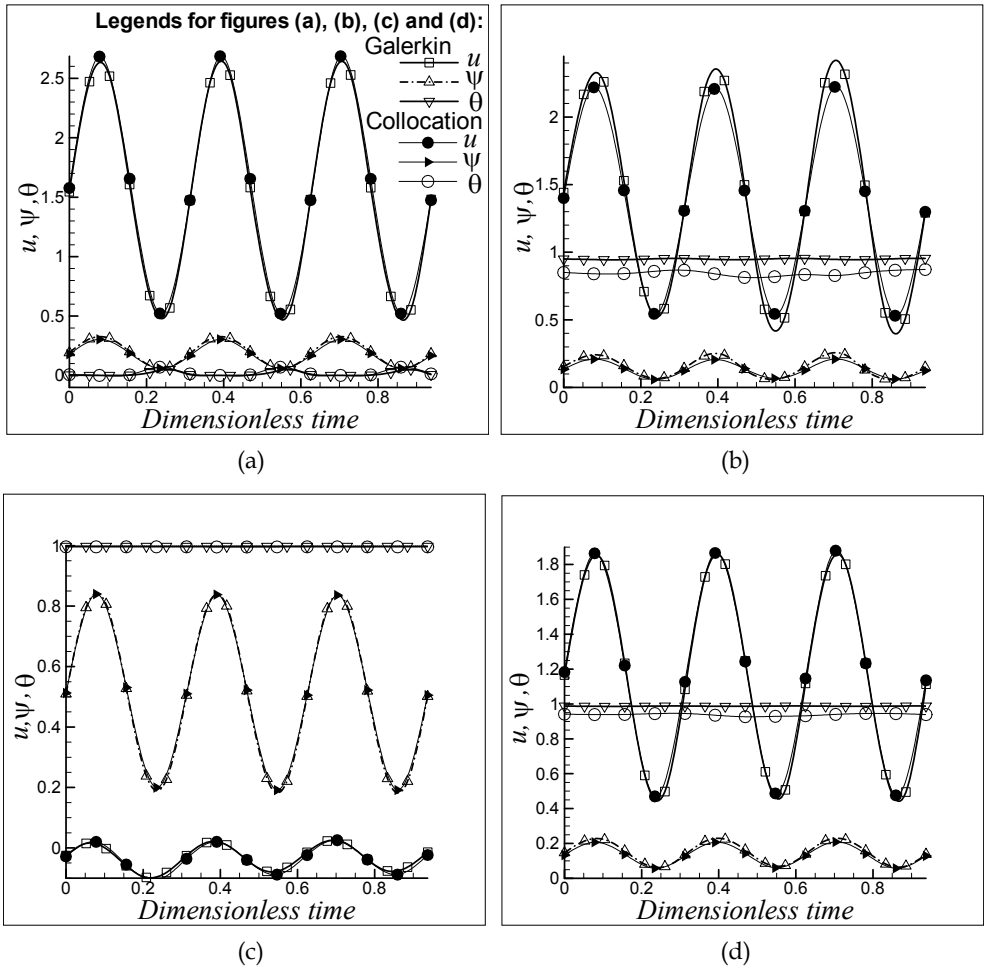

Fig. 10. Comparison between Galerkin and collocation methods during 3 periods, for control points: (a): point 1; (b): point 7; (c): point 8; (d): point 9. (Ω=0.3, Re=30, Pr=0.73, $\tau = 0.7$)

In steady flow, the longitudinal evolution of heat transfer characterized by the Nusselt number shows a slight difference between the two models, located particularly in the vicinity of geometry furrows and constrictions (figure 11.a.). However, this difference does

not exceed two or three percent. In terms of unsteady heat transfer, comparison between the two methods shows that the average Nusselt number $\overline{Nu}(x)$ given by equation (75) presents slight differences similar to those observed in steady state regime (figure 11.b.).

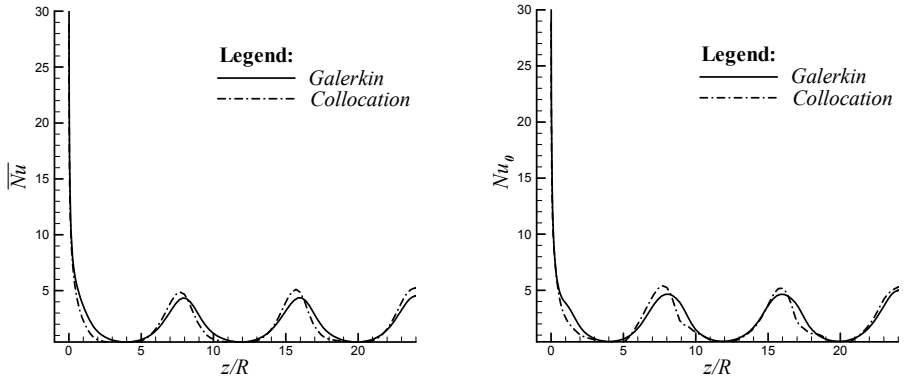

Fig. 11. Heat transfer comparison between Galerkin and collocation methods. (a): steady case; (b): unsteady case (Ω=0.3, Re=30, Pr=0.73, $\tau = 0.7$)

9.5.2 Comparison of performances and speed computations

We have shown that Galerkin and collocation spectral methods, developed to the same truncature orders, give results with similar accuracy. The essential difference between these methods lies in their performances, rapidity and simplicity of computational implementation. The table below summarizes their performances. Let us define before:

- On the one hand: CPU_{0G} and CPU_{0C} the CPU time to obtain the steady regime with Galerkin and collocation method respectively; CPU_{1G} and CPU_{1C} the CPU time to compute one period of the unsteady regime with Galerkin and collocation method respectively;
- On the other hand: $Newton_{0G}$ and $Newton_{0C}$ the number of Newton iterations to compute the steady regime with Galerkin and collocation method respectively; $Newton_{1G}$ and $Newton_{1C}$ the number of Newton iterations to compute one time step with Galerkin and collocation method respectively.

At last, we define the ratios:

$$CPU_0 = \frac{CPU_{0G}}{CPU_{0C}} \; ; \; CPU_1 = \frac{CPU_{1G}}{CPU_{1C}} \; ; \; Newton_0 = \frac{Newton_{0G}}{Newton_{0C}} \; ; \; Newton_1 = \frac{Newton_{1G}}{Newton_{1C}} \qquad (76)$$

Then, we obtain the following results:, performed on the same computer:

CPU_0	CPU_1	$Newton_0$	$Newton_1$
2.4	5.2	3.2	3.2

Table 1. Comparison of performances between Galerkin and collocation spectral methods

10. Conclusions

In this paper, numerical studies have been carried out on pulsating flows through axisymmetric sinusoidal ducts. Thus, the study emphasizes on the heat transfer modifications in this particular flows with rates modulation close to the unit. The results obtained have shown that the flow is influenced by many parameters including Reynolds numbers, rate modulation and amplitude of geometry. We observe that the results are encouraging and offer good perspectives in pulsed internal flows cases. From numerical point of view, the results obtained confirm the previous general conclusions in axisymmetric geometries (André et al., 1987, 1981; Batina et al., 1989, 1991, 2009), i.e.:

- For the steady regime: all classical results are obtained with high precision.
- For the unsteady regime, dynamic and thermal fields show an important heat transfer enhancement in the entry zone. A dynamic and thermal shock occur nearly this area. Mechanical tube behaviour can be modified in this region and the shear stress occurring during the pulsation can induce some damage if the tube is connected to a big tank. This phenomenon is of great interest in industrial structures. Nevertheless, convective heat transfer decrease when the fluid moves forward in the tube.

The numerical solution was performed using Galerkin and collocation spectral methods whose main features were recalled. The numerical results obtained show that:

- Steady and unsteady regimes do not depend on the spectral method used;
- The unsteady dynamic and thermal phenomena are periodic in time, with a frequency equal to the frequency of pulsations.

However, the collocation method is simpler to use and its computer calculations are faster.

Out of these general conclusions, this study focusing on sinusoidal geometries induce especially zones of dead fluid that locally have a negative influence on heat transfer, particularly for the steady flow. The spatial periodicity of the steady flow in this type of geometry is acquired only at the end of the second, even third geometrical period. The transient phenomena are therefore relatively short in time. Thus, the dynamic and thermal flow behaviours become periodic.

Compared to models based on classical methods such as asymptotic developments, finite differences, finite volumes, finite elements, etc, our numerical method leads to the following remarks:

- The accuracy of the present model is high.
- The present computational code is easier to build compared to finite elements one, for example.
- If we consider the CPU time, the present model needs few minutes to compute the numerical equations. This result traduces the efficiency of our model which is easier and more adapted to solve this particular problem. Nevertheless, compared to some industrial codes, our model have some disadvantages, such as:
  - the non linear coupled unsteady terms in Navier Stokes and Energy equations are not taken into account in the present model
  - this problem require smoother geometries
  - the order of polynomials developments increases strongly the computing time
  - when the modulation flow-rate approaches or exceeds the unity, we must choose carefully some data to assume the algorithms convergence. For example, when $\tau > 100\%$, convergence conditions impose small time steps, and the CPU time on classical computers can make our code prohibitive.

Actually, our model is extended to non linear coupled problems of unsteady Navier Stokes and Energy equations, and the results are very encouraging. Moreover, our model treats successfully the problem of heat and mass transfer in natural convection.
In a final analysis, our numerical method based on a suitable spectral method is of a good accuracy. One of its originality is the choice of Chebyshev polynomials basis in both axial and radial directions, and the use of a shift operator technique allow the introduction of non homogeneous boundary conditions in Galerkin formulation. The automatic construction of these polynomials basis is of a great interest. These particular mathematical and numerical tools have permitted the resolution of this non obvious problem which consists on pulsated unsteady flows associated to simultaneous developments dynamic and thermal fields.

11. References

André, P.; Creff, R. & Batina, J. (1981). Etude des conditions particulières de fréquence favorisant les transferts thermiques en écoulements pulsés en canalisation cylindrique, *International Journal of Heat and Mass Transfer*, Vol. 24, pp. 1211-1219.

André, P.; Creff, R. & Batina, J. (1987). Study of thermal fluid for pulsed flow with compressible fluids, *Numerical Methods in Thermal Problems*., Fifth international conference., Montreal, Canada, Pineridge Press, pp. 149-154, 1987.

Batchi, M. (2005). Etude Mathématique et Numérique des Phénomènes de Transferts Thermiques liés aux Ecoulements Instationnaires en Géométrie Axisymétrique, *Thèse de Doctorat Mathématiques Appliquées*, Université de Pau.

Batina, J.; Creff, R.; André, P. & Blancher, S. (1989). Numerical model for dynamic and thermal developments of a turbulent pulsed ducted flow, *Proceedings Eurotherm*, n°9, pp. 50-57, Bochum, Germany.

Batina, J.; André, P.; Creff, R. & Blancher, S. (1991). Dynamic and thermal developments of a pulsed laminar compressible ducted flow, *Proceedigs Eurotherm*, n°25, pp. 227-234, Pau, France.

Batina, J. (1995). Etude numérique des écoulements instationnaires pulsés en canalisation cylindrique, *Thèse de Doctorat Physique*, Université de Pau.

Batina, J.; Creff, R. & Batchi, M. (2004). Etude thermique convective d'un écoulement interne en géométrie axisymétrique sinusoïdale, *Actes du congrès SFT 04*, pp. 987-992.

Batina, J.; Batchi, M.; Blancher, S.; Creff, R. & Amrouche, C. (2009). Convective heat transfer augmentation through vortex shedding in sinusoidal constricted tube., *International Journal of Numerical Methods for Heat and Fluid Flow*, Vol.19, N°.3/4, pp. 374-395.

Bernardi, C. & Maday, Y. (1992). *Approximations spectrales de problèmes aux limites elliptiques*, Springer-Verlag.

Blancher, S. (1991). Transfert convectif stationnaire et stabilité hydrodynamique en géométrie périodique, *Thèse de Doctorat Physique*, Université de Pau.

Canuto, C.; Hussaini, M.Y.; Quarteroni, A. & Zang, T.A. (1988). *Spectral methods in fluids dynamics,* Springer-Verlag.

Chakravarty, S. & Sannigrahi A.K. (1999). A nonlinear mathematical model of blood flow in a constricted artery experiencing body acceleration, *Mathematical and Computer Modeling*, vol. 29, pp. 9-25.

Creff, R.; André, P. & Batina, J. (1985). Dynamic and Convective Results for a Developping Laminar Unsteady Flow, *International Journal of Numerical Methods in Fluids*, Vol. 5, pp. 745-760.

Ghaddar, N.K.; Magen, M.; Mikic, B.B. & Patera, A. (1986). Numerical investigation of incompressible flow in grooved channels, Resonance and oscillatory heat transfer enhancement, *Journal of Fluid Mechanics*, vol.168, pp. 541-567.

Gelfgat, A.Y. (2004). Stability and slightly supercritical oscillatory regimes of natural convection in a 8:1 cavity: solution of the benchmark problem by a global Galerkin method, *International Journal of Numerical Methods in Fluids*, vol. 44, pp. 135-146.

Hemida, H.N.; Sabry, M.N.; Abdel-Rahim, A. & Mansour, H. (2002). Theoretical analysis of heat transfer in laminar pulsating flow, *International Journal of Heat and Mass Transfer*, vol. 45, pp. 1767-178.

Lee, B.S.; Kang, L.S. & Lim, H.C. (1999). Chaotic mixing and mass transfer enhancement by pulsatile laminar flow in an axisymmetric wavy channel, *International Journal of Heat and Mass Transfer*, Vol. 42, pp. 2571-2581.

Moschandreau, T. & Zamir, M. (1997). Heat transfer in a tube with pulsating flow and constant heat flux, *International Journal of Heat and Mass Transfer*, vol.. 40, n°10, pp. 2461-2466.

Shen, J. (1994). Efficient spectral-Galerkin method I: direct solvers for the second and fourth order equations using Legendre polynomials, *SIAM J. Sci. Comput*, vol.15, n°6, pp. 1489-1505.

Shen, J. (1995). Efficient spectral-Galerkin methods II: direct solvers of second and fourth order equations by using Chebyshev polynomials, *SIAM J. Sci. Comput*, vol.16, n°8, pp. 74-87.

Shen, J. (1997). Efficient spectral-Galerkin methods III: polar and cylindrical geometries, *SIAM J. Sci. Comput*, vol.18, n°6, 1583-1604.

Sobey, I.J. (1980). On flow through channels. Part 1: Calculated flow patterns, *Journal of Fluid Mechanics*, vol. 96, pp. 1-26.

Young Kim, S.; Ha Kang, B. & Min Hyun, J. (1998). Forced convection heat transfer from two heated blocks in pulsating channel flow, *International Journal of Heat and Mass Transfer*, vol. 41, n°3, pp. 625-634.

5

Numerical Solution of Natural Convection Problems by a Meshless Method

Gregor Kosec and Božidar Šarler
University of Nova Gorica
Slovenia

1. Introduction

Natural convection is a phenomenon where fluid motion is generated by density changes due to the temperature or concentration variations in a gravity field. The computational modelling of systems with natural convection (Bejan, 2004) has become a highly popular research subject due to its pronounced influence in better understanding of nature as well as in the development of the advanced technologies. Melting of the polar ice caps, the global oceans dynamics, various weather systems, water transport, soil erosion and denudation, magma transport and manufacturing of nano-materials, improving casting processes, energetic studies, exploitation of natural resources, welding, casting and advanced solidifications are two typical contemporary example groups where natural convection plays an important role. This chapter deals with the numerical approach towards solution of this type of problems by a meshless technique.

The main part of the solution procedure is focused on the general transport equation treatment and the pressure velocity coupling strategy. The transport phenomena are solved by a local meshless method and explicit time stepping. The local variant of Radial Basis Function Collocation Method (LRBFCM) has been previously developed for diffusion problems (Šarler and Vertnik, 2006), convection-diffusion solid-liquid phase change problems (Vertnik and Šarler, 2006) and subsequently successfully applied in industrial process of direct chill casting (Vertnik, *et al.*, 2006).

The fluid flow, which is generally a global problem, is treated by the proposed local iterative method. Instead of solving the pressure Poisson equation or/and pressure correction Poisson equation (Divo and Kassab, 2007) a more simplified local pressure-velocity coupling (LPVC) (Kosec and Šarler, 2008a) algorithm is proposed where the pressure-correction is predicted from the local mass continuity violation similar to the SOLA algorithm (Hong, 2004).

The presented solution procedure represents a variant of already developed global approach (Šarler, *et al.*, 2004a, Šarler, 2005). In this chapter, such a local solution procedure is tested with the standard free fluid flow benchmark test (de Vahl Davis natural convection test (de Vahl Davis, 1983)). The test is especially convenient for benchmarking purposes as there are several numerical solutions published in the literature (Divo and Kassab, 2007, Hortmann, *et al.*, 1990, Manzari, 1999, Prax, *et al.*, 1996, Sadat and Couturier, 2000, Šarler, 2005, Wan, *et al.*, 2001).

In addition to the basic test, the proposed local solution procedure is tested on the tall cavity, natural convection in the porous media and melting of a pure material (Gobin - Le Quéré test) driven by a natural convection tests. Numerous analyses and comparisons with the published data are performed in order to assess the characteristics of the proposed numerical approach in details. The comprehensive verification procedure shows excellent agreements with the previously published data, based on different numerical methods.

2. Governing equations

2.1 De Vahl Davis test

The de Vahl Davis natural convection benchmark problem is described by three coupled partial differential equations (PDEs). The PDEs are mass, momentum and energy conservation equations where all material properties are considered to be constant. The Boussinesq approximation is used for density hypothesis and the phenomena is thus described by the following system of equations

$$\nabla \cdot \mathbf{v} = 0\,, \tag{1}$$

$$\rho \frac{\partial \mathbf{v}}{\partial t} + \rho \nabla \cdot (\mathbf{v}\mathbf{v}) = -\nabla P + \nabla \cdot \left(\mu \nabla \mathbf{v}\right) + \mathbf{b}\,, \tag{2}$$

$$c_p \rho \frac{\partial T}{\partial t} + c_p \rho \nabla \cdot (T\mathbf{v}) = \nabla \cdot \left(\lambda \nabla T\right), \tag{3}$$

$$\mathbf{b} = \rho\left[1 - \beta_T (T - T_{\text{ref}})\right]\mathbf{g}\,, \tag{4}$$

where t, $\mathbf{v}\left(v_x, v_y\right)$, ρ, P, μ, $\mathbf{b}$, λ, β_T, T_{ref} and $\mathbf{g}$ stand for time, velocity, density, pressure, viscosity, body force, thermal conductivity, thermal expansion coefficient, reference temperature and gravitational acceleration, respectively. The south and the north sides of the domain are thermally insulated while the east and the west sides are set to different temperatures. Due to the consideration of the viscous fluid within enclosure, the no-slip and impermeable velocity boundary conditions are used (Figure 1). The boundary conditions are formulated as follows

$$\tilde{\mathbf{v}}\left(\tilde{\mathbf{p}}_\Gamma, \tilde{t}\right) = 0\,, \tag{5}$$

$$\tilde{T}\left(\tilde{p}_x = 0, \tilde{t}\right) = 1\,, \tag{6}$$

$$\tilde{T}\left(\tilde{p}_x = 1, \tilde{t}\right) = 0\,, \tag{7}$$

$$\frac{\partial}{\partial \tilde{p}_y}\tilde{T}\left(\tilde{p}_y = 0, \tilde{t}\right) = \frac{\partial}{\partial \tilde{p}_y}\tilde{T}\left(\tilde{p}_y = 1, \tilde{t}\right) = 0\,, \tag{8}$$

and the initial conditions as follows

$$\tilde{\mathbf{v}}\left(\tilde{\mathbf{p}}_\Omega, \tilde{t} = 0\right) = 0\,, \tag{9}$$

$$\tilde{T}\left(\tilde{\mathbf{p}}_{\Omega}, \tilde{t}=0\right)=0.5\,, \tag{10}$$

where Ω and Γ stand for interior and boundary nodes indexes, respectively.

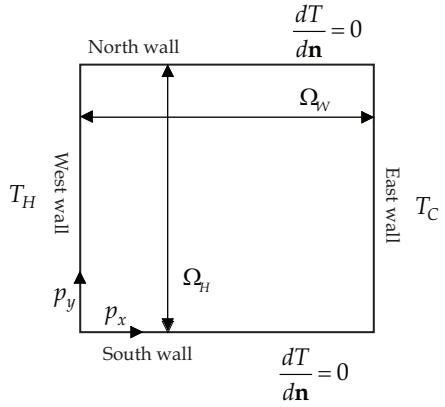

Fig. 1. The natural convection benchmark test schematics

The introduced dimensionless quantities (embellishment ~) are defined as

$$\tilde{p}_x=\frac{p_x}{\Omega_W} \qquad \tilde{p}_y=\frac{p_y}{\Omega_H}\,, \tag{11}$$

$$\tilde{v}_x=\frac{v_x\Omega_W\rho c_p}{\lambda} \qquad \tilde{v}_y=\frac{v_y\Omega_H\rho c_p}{\lambda}\,, \tag{12}$$

$$\tilde{T}=\frac{T-T_C}{T_H-T_C}\,, \tag{13}$$

$$\tilde{t}=\frac{\lambda}{\rho c_p\Omega_H^2}t\,, \tag{14}$$

where Ω_W and Ω_H stand for domain width and height, respectively. The problem is characterized by three dimensionless numbers; the thermal Rayleigh number $\left(\mathrm{Ra}_T\right)$, the Prandtl number $\left(\mathrm{Pr}\right)$ and the domain aspect ratio $\left(\mathrm{A}_R\right)$ defined as

$$\mathrm{Ra}_T=\frac{|\mathbf{g}|\beta_T\left(T_H-T_C\right)\Omega_H{}^3\rho^2c_p}{\lambda\mu}\,, \tag{15}$$

$$\mathrm{Pr}=\frac{\mu c_p}{\lambda}\,, \tag{16}$$

$$\mathrm{A_R}=\frac{\Omega_W}{\Omega_H}\,, \tag{17}$$

where the ratio between the Prandtl and the Rayleigh number is known as the Grashof number

$$\mathrm{Gr}=\frac{\mathrm{Ra}_T}{\mathrm{Pr}}\,. \tag{18}$$

The de Vahl Davis benchmark is limited to the natural convection of the air in a rectangular cavity with aspect ratio $\mathrm{A_R}=1$ and $\mathrm{Pr}=0.71$. In this work additional tests are done for lower Prandtl number and higher aspect ratio in order to test the method in regimes similar to those in the early stages of phase change simulations of metal like materials where the oscillatory "steady-state" develops.

2.2 Porous media natural convection

A variant of the test, where instead of the free fluid, the domain is filled with porous media, is considered in the next test. Similar to the de Vahl Davis benchmark test, the porous natural convection case is also well known in the literature (Chan, *et al.*, 1994, Jecl, *et al.*, 2001, Ni and Beckermann, 1991, Prasad and Kulacky, 1984, Prax, *et al.*, 1996, Raghavan and Ozkan, 1994, Šarler, *et al.*, 2000, Šarler, *et al.*, 2004a, Šarler, *et al.*, 2004b) and therefore a good quantitative comparison is possible.

The only difference from de Vahl Davis case is in the momentum equation, and the consecutive velocity boundary conditions. Instead of the Navier-Stokes the Darcy momentum equation is used to describe the fluid flow in the porous media

$$\rho\frac{\partial \mathbf{v}}{\partial t}+\rho\nabla\cdot(\mathbf{vv})=-\nabla P-\frac{\mu}{K}\mathbf{v}+\mathbf{b}\,, \tag{19}$$

where K stands for permeability. The main difference in the momentum equation is in its order. The Navier-Stokes equation is of the second order while the Darcy equation is of the first order and therefore different boundary conditions for the velocity apply. Instead of the no-slip boundary condition for velocity, the slip and impermeable velocity boundary conditions are used. This is formulated as

$$\mathbf{v}\left(\mathbf{p}_\Gamma,t\right)\cdot\mathbf{n}=0\,. \tag{20}$$

Instead of the thermal Rayleigh and Prandtl numbers, the filtration Rayleigh number defines $\left(\mathrm{Ra}_T\right)$ the problem

$$\mathrm{Ra}_F=\frac{|\mathbf{g}|K\beta_T\left(T_H-T_C\right)\Omega_H\,\rho^2 c_p}{\lambda\mu}\,. \tag{21}$$

2.3 Phase change driven by natural convection

The benchmark test is similar to the previous cases with an additional phase change phenomenon added. The solid and the liquid thermo-physical properties are assumed to be equal. In this case the energy transport is modelled through enthalpy (h) formulation. The concept is adopted in order to formulate a one domain approach. The phase change phenomenon is incorporated within the enthalpy formulation with introduction of liquid fraction (f_L). The problem is thus defined with equations (1), (2), (4) and

$$\rho\frac{\partial h}{\partial t}+\rho\nabla\cdot(h\mathbf{v})=\nabla\cdot\left(\lambda\nabla T\right), \tag{22}$$

$$h(T)=c_pT+f_L L, \tag{23}$$

with

$$f_L(T)=\begin{cases} T\geq T_F+\delta T_L; & 1 \\ T_F+\delta T_L>T>T_F; & \dfrac{T-T_F}{\delta T_L} \\ T\leq T_F; & 0 \end{cases}. \tag{24}$$

The phase change of the pure material occurs exactly at the melting temperature which produces discontinues in the enthalpy field due to the latent heat release. The constitutive relation (24) incorporates a smoothing interval near the phase change in order to avoid numerical instabilities.

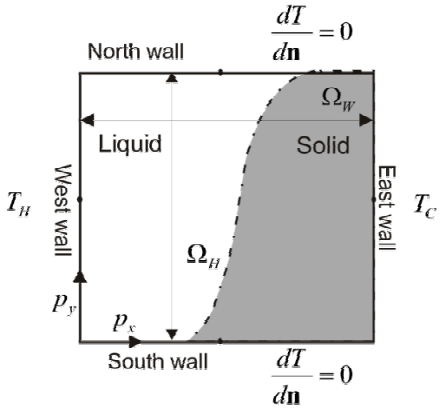

Fig. 2. The pure phase change test schematics

The boundary conditions are set to

$$\tilde{\mathbf{v}}\left(\tilde{\mathbf{p}}_\Gamma,\tilde{t}\right)=0, \tag{25}$$

$$\tilde{T}\left(\tilde{p}_x=0,\tilde{t}\right)=1, \tag{26}$$

$$\tilde{T}\left(\tilde{p}_x=1,\tilde{t}\right)=\tilde{T}_F=0, \tag{27}$$

$$\frac{\partial}{\partial\tilde{p}_y}\tilde{T}\left(\tilde{p}_y=0,\tilde{t}\right)=\frac{\partial}{\partial\tilde{p}_y}\tilde{T}\left(\tilde{p}_y=1,\tilde{t}\right)=0, \tag{28}$$

and initial state to

$$\tilde{\mathbf{v}}\left(\tilde{\mathbf{p}}_\Omega,\tilde{t}=0\right)=0, \tag{29}$$

$$\tilde{T}\left(\tilde{\mathbf{p}}_{\Omega}, \tilde{t}=0\right)=0\,. \tag{30}$$

Velocity in the solid state is forced to zero by multiplying it with the liquid fraction. This approach introduces additional smoothing in the artificial "mushy" zone. This smoothing produces an error of the same magnitude as smoothing of the enthalpy jump at the phase change temperature. The problem is schematically presented in Figure 2.
Additional dimensionless number to characterize the ratio between the sensible and latent heat, the Stefan number, is introduced

$$\mathrm{Ste}=\frac{c_p\left(T_H-T_C\right)}{L}\,. \tag{31}$$

3. Solution procedure

There exist several meshless methods such as the Element free Galerkin method, the Meshless Petrov-Galerkin method, the point interpolation method, the point assembly method, the finite point method, the smoothed particle hydrodynamics method, the reproducing kernel particle method, the Kansa method (Atluri and Shen, 2002a, Atluri and Shen, 2002b, Atluri, 2004, Chen, 2002, Gu, 2005, Kansa, 1990a, Kansa, 1990b, Liu, 2003), etc. However, this chapter is focused on one of the simplest classes of meshless methods in development today, the Radial Basis Function (Buhmann, 2000) Collocation Methods (RBFCM) (Šarler, 2007). The meshless RBFCM was used for the solution of flow in Darcy porous media for the first time in (Šarler, *et al*., 2004a). A substantial breakthrough in the development of the RBFCM was its local formulation, LRBFCM. Lee at al. (Lee, 2003) demonstrated that the local formulation does not substantially degrade the accuracy with respect to the global one. On the other hand, it is much less sensitive to the choice of the RBF shape and node distribution. The local RBFCM has been previously developed for diffusion problems (Šarler and Vertnik, 2006), convection-diffusion solid-liquid phase change problems (Vertnik and Šarler, 2006) and subsequently successfully applied in industrial process of direct chill casting (Vertnik, *et al*., 2006).
In this chapter a completely local numerical approach is used. The LRBFCM spatial discretization, combined with local pressure-correction and explicit time discretization, enables the consideration of each node separately from other parts of computational domain. Such an approach has already been successfully applied to several thermo-fluid problems (Kosec and Šarler, 2008a, Kosec and Šarler, 2008b, Kosec and Šarler, 2008c, Kosec and Šarler, 2008d, Kosec and Šarler, 2009) and it shows several advantages like ease of implementation, straightforward parallelization, simple consideration of complex physical models and CPU effectiveness.
An Euler explicit time stepping scheme is used for time discretization and the spatial discretization is performed by the local meshfree method. The general idea behind the local meshless numerical approach is the use of a local influence domain for the approximation of an arbitrary field in order to evaluate the differential operators needed to solve the partial differential equations. The principle is represented in Figure 3.
Each node uses its own support domain for spatial differential operations; the domain is therefore discretized with overlapping support domains. The approximation function is introduced as

$$\theta(\mathbf{p}) = \sum_{n=1}^{N_{Basis}} \alpha_n \Psi_n(\mathbf{p}) , \tag{32}$$

where θ, N_{Basis}, α_n and Ψ_n stand for the interpolation function, the number of basis functions, the approximation coefficients and the basis functions, respectively. The basis could be selected arbitrarily, however in this chapter only Hardy's Multiquadrics (MQs)

$$\Psi_n(\mathbf{p}) = \sqrt{\left(\mathbf{p}-\mathbf{p}^n\right)\cdot\left(\mathbf{p}-\mathbf{p}^n\right)/\sigma_C^2 + 1} , \tag{33}$$

with σ_C standing for the free shape parameter of the basis function, are used. By taking into account all support domain nodes and equation (32), the approximation system is obtained. In this chapter the simplest possible case is considered, where the number of support domain nodes is exactly the same as the number of basis functions. In such a case the approximation simplifies to collocation. With the constructed collocation function an arbitrary spatial differential operator (L) can be computed

$$L\theta(\mathbf{p}) = \sum_{n=1}^{N_{Basis}} \alpha_n L\Psi_n(\mathbf{p}) \cdot \tag{34}$$

In this work only five node support domains are used and therefore a basis of five MQs is used as well.

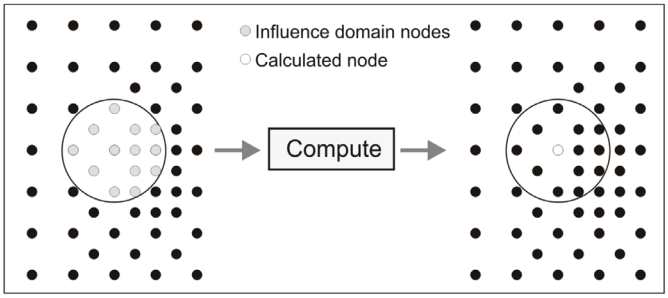

Fig. 3. The local meshless principle

The implementation of the Dirichlet boundary condition is straightforward. In order to implement Neumann and Robin boundary conditions, however, a special case of interpolation is needed. In these boundary nodes the function directional derivative instead of the function value is known and therefore the equation in the interpolation system changes to

$$\Theta_{BC} = \sum_{n=1}^{N_{Basis}} \alpha_n \frac{\partial}{\partial \mathbf{n}} \Psi_n(\mathbf{p}) , \tag{35}$$

in the Neumann boundary nodes and to

$$\Theta_{BC} = \sum_{n=1}^{N_{Basis}} \alpha_n \left(a \frac{\partial}{\partial \mathbf{n}} \Psi_n(\mathbf{p}) + b\Psi_n(\mathbf{p}) \right) , \tag{36}$$

in the Robin boundary nodes.

With the defined time and spatial discretization schemes, the general transport equation under the model assumptions can be written as

$$\frac{\theta_1 - \theta_0}{\Delta t} = D\nabla^2 \theta_0 - \nabla \theta_0 \cdot \left(\rho \mathbf{v}_0 \right) + S_0 \,, \tag{37}$$

where $\theta_{0,1}$, D, Δt and S_0 stand for the field value at current and next time step, general diffusion coefficient, time step and for source term, respectively.
To couple the mass and momentum conservation equations a special treatment is required. The intermediate velocity ($\hat{\mathbf{v}}$) is computed by

$$\hat{\mathbf{v}} = \mathbf{v}_0 + \frac{\Delta t}{\rho}\left(-\nabla P_0 + \nabla \cdot \left(\mu \nabla \mathbf{v}_0 \right) + \mathbf{b}_0 - \nabla \cdot \left(\rho \mathbf{v}_0 \mathbf{v}_0 \right) \right). \tag{38}$$

The equation (38) did not take in account the mass continuity. The pressure and the velocity corrections are added

$$\hat{\mathbf{v}}^{m+1} = \hat{\mathbf{v}}^m + \hat{\mathbf{v}} \quad \hat{P}^{m+1} = \hat{P}^m + \hat{P} \,, \tag{39}$$

where m, $\hat{v}$ and $\hat{P}$ stand for pressure velocity iteration index, velocity correction and pressure correction, respectively. By combining the momentum and mass continuity equations the pressure correction Poisson equation emerges

$$\nabla \cdot \hat{\mathbf{v}}^m = \frac{\Delta t}{\rho} \nabla^2 \hat{P} \,. \tag{40}$$

Instead of solving the global Poisson equation problem, the pressure correction is directly related to the divergence of the intermediate velocity

$$\hat{P} = \ell^2 \frac{\rho}{\Delta t} \nabla \cdot \hat{\mathbf{v}}^m \,, \tag{41}$$

where ℓ stands for characteristic length. The proposed assumption enables direct solving of the pressure velocity coupling iteration and thus is very fast, since there is only one step needed in each node to evaluate the new iteration pressure and the velocity correction. With the computed pressure correction the pressure and the velocity can be corrected as

$$\hat{\mathbf{v}}^{m+1} = \hat{\mathbf{v}}^m - \zeta \frac{\Delta t}{\rho} \nabla \hat{P} \;\text{ and }\; \hat{P}^{m+1} = \hat{P}^m + \zeta \hat{P} \,, \tag{42}$$

where ζ stands for relaxation parameter. The iteration is performed until the criterion $\nabla \cdot \hat{\mathbf{v}} < \varepsilon_V$ is met in all computational nodes.

4. Results

The results of the benchmark tests are assessed in terms of streamfunction $\left(\tilde{\Psi} \right)$, cavity Nusselt number $\left(\mathrm{Nu} \right)$ and mid-plane velocity components.

$$\tilde{\psi}(\tilde{\mathbf{p}}) = \int_0^1 \tilde{v}_x \left(\tilde{\mathbf{p}} \right) d\tilde{p}_y \,, \tag{43}$$

$$\mathrm{Nu}(\tilde{\mathbf{p}}) = -\frac{\partial \tilde{T}(\tilde{\mathbf{p}})}{\partial \tilde{p}_x} + \tilde{v}_x(\tilde{\mathbf{p}})\tilde{T}(\tilde{\mathbf{p}}) \,. \tag{44}$$

The Nusselt number is computed locally on five nodded influence domains, while the streamfunction is computed on one dimensional influence domains each representing an x row, where all the nodes in the row are used as an influence domain. The streamfunction is set to zero in south west corner of the domain $\tilde{\psi}(0,0) = 0$.
The de Vahl Davis test represents the first benchmark test in the series and therefore some additional assessments regarding the numerical performance as well as the computational effectiveness are done. One of the tests is focused on the global mass continuity conservation, which indicates the pressure-velocity coupling algorithm effectiveness. The global mass leakage is analysed by implementing

$$\begin{gathered} \rho^{\mathrm{avg}}(t+\Delta t) = \rho^{\mathrm{avg}}(t) + \Delta t \rho \frac{1}{N_D} \sum_{n=1}^{N_D} \nabla \cdot \mathbf{v}_n \;\; ; \rho^{\mathrm{avg}}(t=0) = \rho \\ \Delta\rho = \left| \rho - \rho^{\mathrm{avg}}(N_t \Delta t) \right| \end{gathered} \,, \tag{45}$$

where ρ^{avg}, N_D and $\Delta\rho$ stand for average density, number domain nodes and density change.
The pressure-velocity coupling relaxation parameter ζ is set to the same value as the dimensionless time-step in all cases. The reference values in the Boussinesq approximation are set to the initial values.

4.1 De Vahl Davis test

The classical de Vahl Davis benchmark test is defined for the natural convection of air ($\mathrm{Pr} = 0.71$) in the square closed cavity ($\mathrm{A_R} = 1$). The only physical free parameter of the test remains the thermal Rayleigh number. In the original paper (de Vahl Davis, 1983) de Vahl Davis tested the problem up to the Rayleigh number 10^6, however in the latter publications, the results of more intense simulations were presented with the Rayleigh number up to 10^8. Lage and Bejan (Lage and Bejan, 1991) showed that the laminar domain of the closed cavity natural convection problem is roughly below $\mathrm{Gr}<10^9$. It was reported (Janssen and Henkes, 1993, Nobile, 1996) that the natural convection becomes unsteady for $\mathrm{Ra} = 2 \cdot 10^8$. This section deals with the steady state solution and therefore regarding to the published analysis, a maximum $\mathrm{Ra}_T = 10^8$ case is tested.
A comparison of the present numerical results with the published data is stated in Table 1 where the $\tilde{\psi}^{\mathrm{mid}} = \tilde{\psi}(0.5,0.5)$, $\mathrm{Nu}^{\mathrm{avg}}$, $\tilde{v}_x^{\max}(0.5,\tilde{p}_y)$ and $\tilde{v}_x^{\max}(\tilde{p}_y,0.5)$ stand for mid-point streamfunction, average Nusselt number and maximum mid-plane velocities, respectively. The results of the present work are compared to the (de Vahl Davis, 1983) (a), (Sadat and Couturier, 2000) (b), (Wan, *et al.*, 2001) (c) and (Šarler, 2005) (d). The specifications of the simulations are stated in Table 2.
The temperature contours (yellow-red continuous plot) and the streamlines are plotted in Figure 4 with the streamline contour plot step 0.05 for $\mathrm{Ra}=10^3$, 0.2 for $\mathrm{Ra}=10^4$, 0.5 for $\mathrm{Ra}=10^5$, 1 for $\mathrm{Ra}=10^6$, 1.5 for $\mathrm{Ra}=10^7$ and 2.5 for $\mathrm{Ra}=10^8$. The Nusselt number time development is plotted in Figure 5 in order to characterize the system dynamics.
Due to the completely symmetric problem formulation ($\tilde{T}(\tilde{\mathbf{p}}_\Omega, \tilde{t}=0) = 0.5$) the cold side and the hot side average Nusselt numbers should be the same at all times and therefore the

difference between the two can be understood as a numerical error of the solution procedure. A simple relative error measure is introduced as

$$\mathrm{E}=\left|\frac{\mathrm{Nu}^{\mathrm{avg}}\left(\tilde{p}_x=1,\tilde{p}_y\right)-\mathrm{Nu}^{\mathrm{avg}}\left(\tilde{p}_x=0,\tilde{p}_y\right)}{\mathrm{Nu}^{\mathrm{max}}\left(\tilde{\mathbf{p}}\right)}\right|, \tag{46}$$

where $\mathrm{Nu}^{\mathrm{avg}}$ and $\mathrm{Nu}^{\mathrm{max}}$ stand for average and maximum Nusselt number. The Nusselt number as a function of time is presented in Figure 5. The hot-cold side errors (E) are plotted in Figure 6 and the mid-plane velocities are presented in Figure 7.

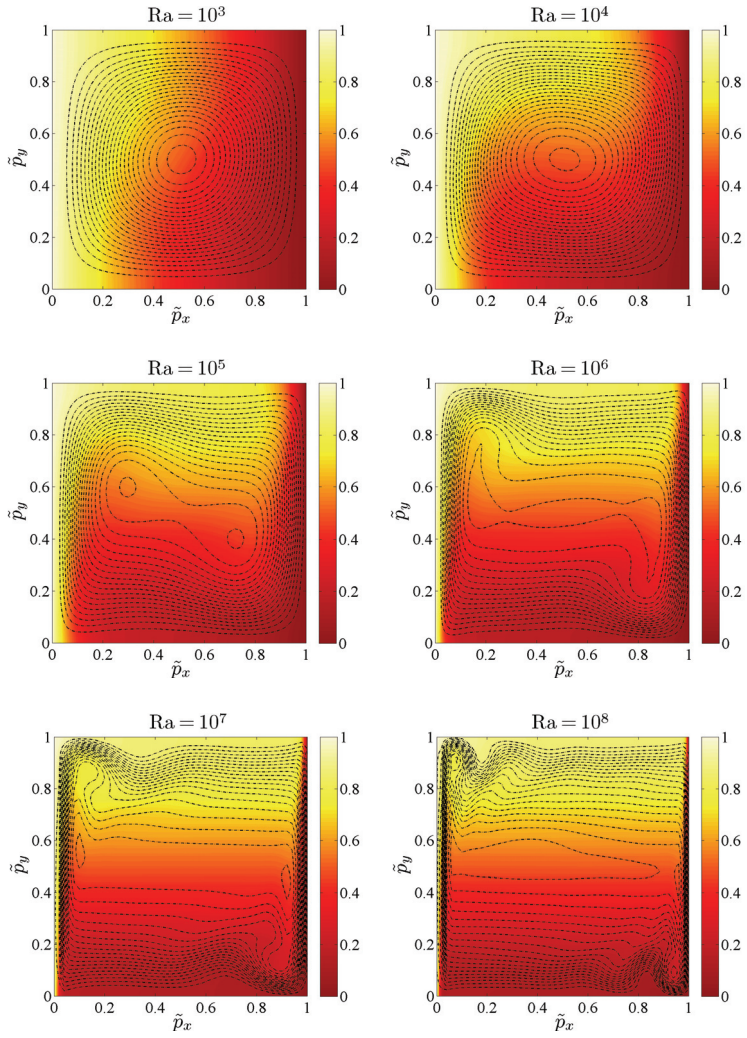

Fig. 4. Temperature and streamline contour plots for de Vahl Davis benchmark test

Ra	$\tilde{v}_x^{\max}$	$\tilde{p}_y$	$\tilde{v}_y^{\max}$	$\tilde{p}_x$	$\mathrm{Nu}^{\mathrm{avg}}$	$\tilde{\psi}^{\mathrm{mid}}$	reference / N_D
	3.679	0.179	3.634	0.813	1.116	1.174	(a)
	3.686	0.188	3.489	0.813	1.117		(c)
10^3	3.566		3.544			1.165	(d)
	3.991	0.170	3.931	0.825	1.101	1.298	1677
	3.699	0.177	3.653	0.812	1.098	1.194	6557
	3.695	0.179	3.645	0.820	1.089	1.196	10197
10^4	19.51	0.120	16.24	0.823	2.234	5.098	(a)
	19.79	0.120	16,17	0.823	2.243		(c)
	19.04		15.80			4.971	(d)
	19.81	0.120	16.24	0.825	2.075	5.155	1677
	19.83	0.120	16.27	0.825	2.120	5.167	6557
	20.03	0.120	16.45	0.830	2.258	5.240	10197
10^5	68.22	0.066	34.81	0.855	4.510	9.142	(a)
	68.52	0.064	34.63	0.852	4.534	9.092	(b)
	70.63	0.072	33.39	0.835	4.520		(c)
	67.59		32.51			8.907	(d)
	67.65	0.070	33.67	0.850	4.624	8.896	1677
	68.98	0.062	34.60	0.850	4.813	9.135	6557
	69.69	0.069	35.03	0.860	4.511	9.278	10197
10^6	216.75	0.038	65.33	0.851	8.798	16.53	(a)
	219.41	0.038	64.43	0.852	8.832	16.29	(b)
	227.11	0.04	65.4	0.86	8.8		(c)
	211.67		61.55			15.91	(d)
	195.98	0.045	63.73	0.850	6.1	15.15	1677
	219.48	0.038	64.87	0.851	7.67	16.13	6557
	221.37	0.039	65.91	0.860	8.97	16.51	10197
10^7	687.43	0.023	145.68	0.888	16.59	28.23	(b)
	714.48	0.022	143.56	0.922	16.65		(c)
	632.60	0.020	127.70	0.925	10.43	24.93	1677
	654.803	0.035	143.55	0.902	14.70	27.51	6557
	687.20	0.021	149.61	0.900	16.92	28.61	10197
10^8	2180.1	0.011	319.19	0.943	30.94	50.81	(b)
	2259.08	0.012	296.71	0.93	31.48		(c)
	2060.86	0.010	264.96	0.939	29.33	44.85	6557
	2095.23	0.009	278.49	0.930	32.12	47.12	10197

Table 1. A comparison of the results

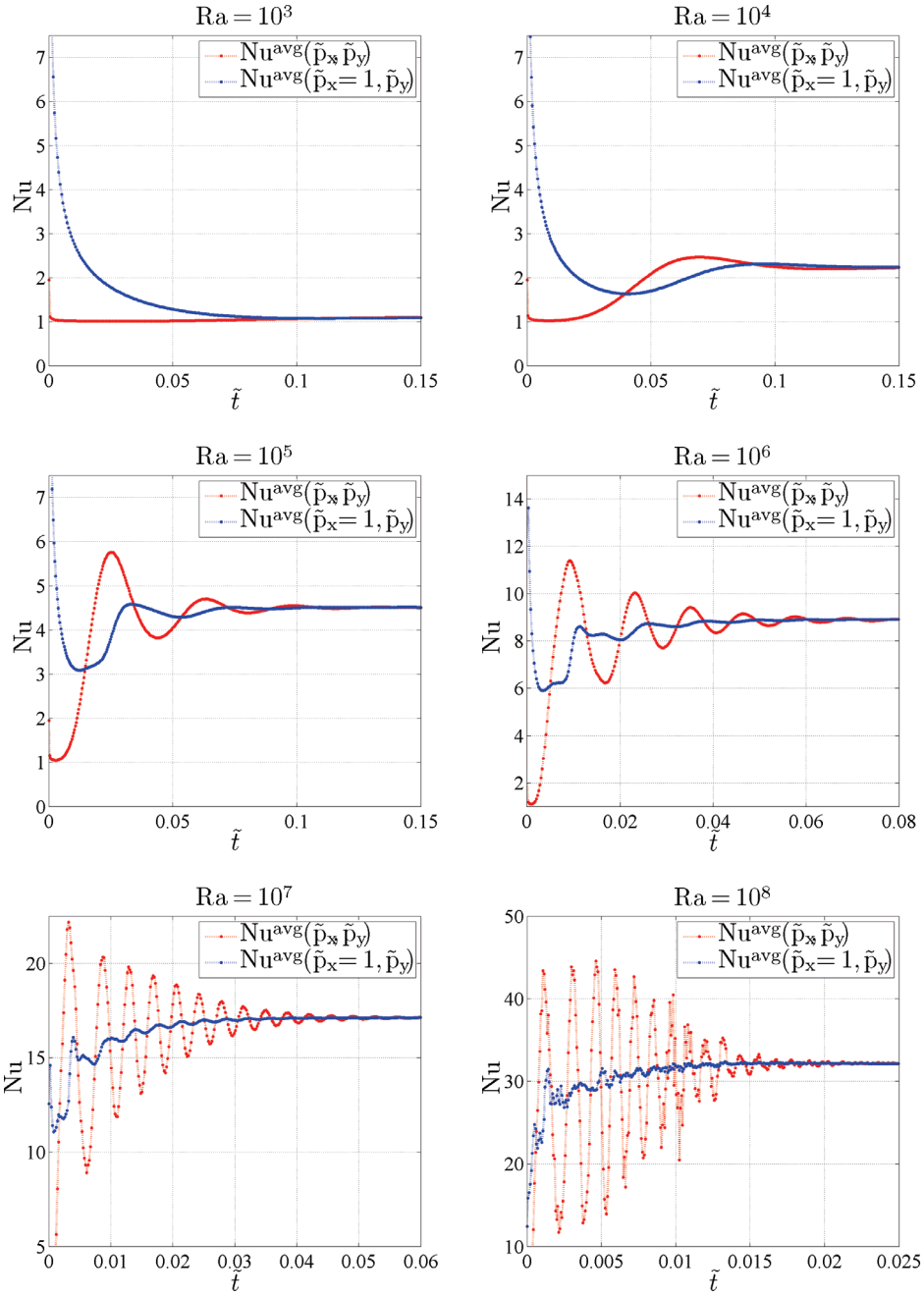

Fig. 5. The Nusselt number as a function of time. The red plot stands for the domain average and the blue for the cold side average Nusselt number

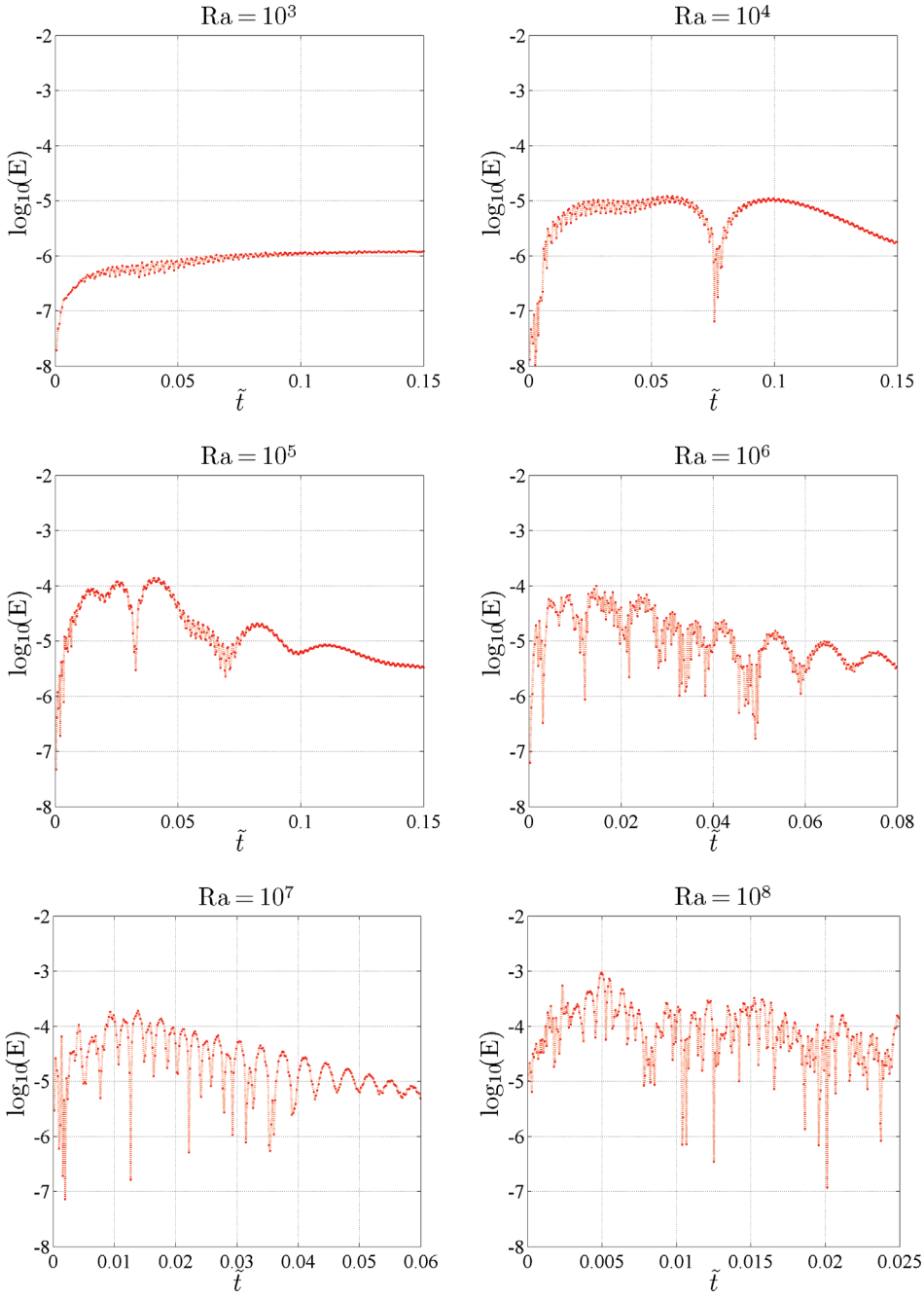

Fig. 6. The Nusselt number hot-cold side error as a function of time

Ra	ε_v	1677 nodes			6557 nodes			10197 nodes			$\Delta\rho / \rho$
		$\Delta\tilde{t}$	t_c[s]	N_{Pv}	$\Delta\tilde{t}$	t_c[s]	N_{Pv}	$\Delta\tilde{t}$	t_c[s]	N_{Pv}	
10^3	10e-4	1e-04	6	3208	1e-4	26	26837	5e-05	65	3662	3.37e-7
10^4	10e-3	1e-04	5	3154	1e-4	15	3259	5e-05	51	3706	8.44e-6
10^5	10e-2	1e-te04	5	1590	1e-4	14	1244	5e-05	43	4090	1.06e-5
10^6	1	1e-04	4	5527	1e-4	14	5608	1e-05	283	144089	1.38e-4
10^7	5	1e-05	6	18250	1e-5	85	71340	5e-06	270	184697	3.01e-4
10^8	25				5e-6	192	193708	5e-06	387	219885	5.90e-4

Table 2. Numerical specifications with time and density loss analysis

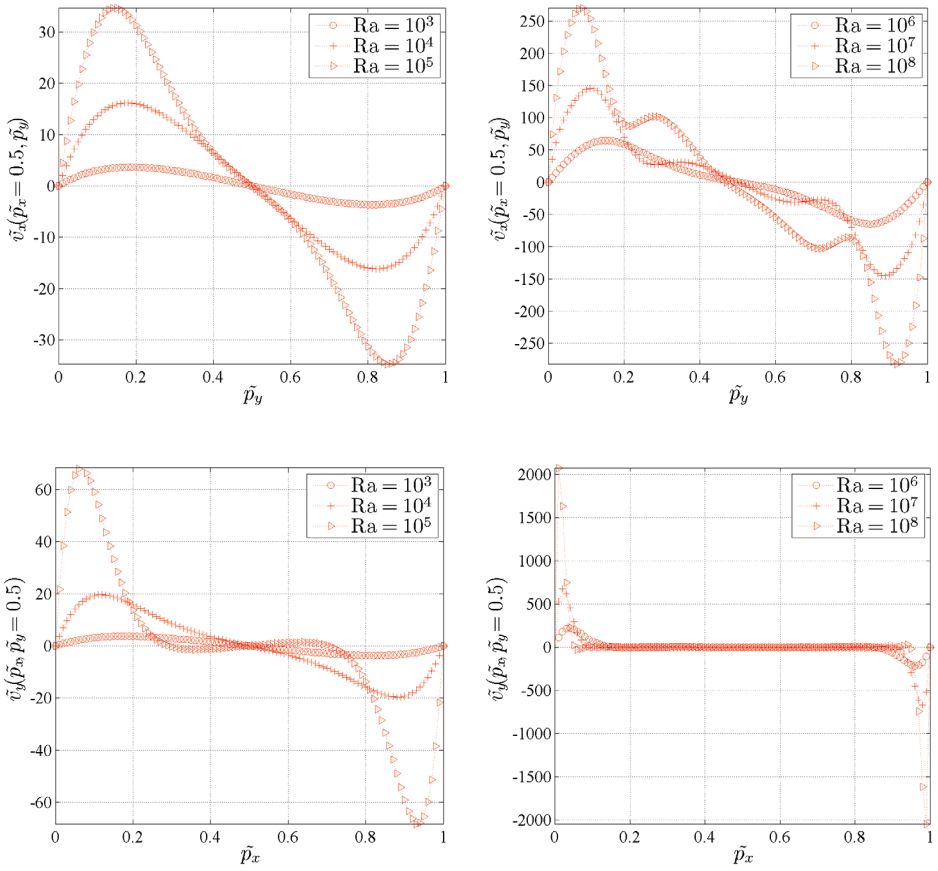

Fig. 7. Velocity mid-plane profiles

4.2 Low Prandtl number - tall cavity test

The next test is merely a generalization of de Vahl Davis with the same governing equations, initial state and boundary conditions, where the cold side of the domain is set to the initial temperature. The tall cavity with aspect ratio $A_R = 1/4$ is filled with metal like (Al-4.5%Cu) low Prandtl fluid $Pr = 0.0137$ at the Rayleigh number $Ra = 2.81 \cdot 10^5$ is considered. The case is especially interesting due to its oscillating »steady-state« which is a result of a balance between the buoyancy and the shear forces. This case is also relevant for fluid flow behaviour at initial stages of melting of low Prandtl materials (metals), since it has a similar geometrical arrangement. The test case has been already computed by two different numerical methods (Založnik, *et al.*, 2005) (spectral FEM and FVM) with good mutual agreement. Respectively, these solutions have been used for assessment of the present method as well.

The temperature contours and the streamlines are plotted as continuous red to yellow fill and dotted lines with a contour step 0.2, respectively, in Figure 8.

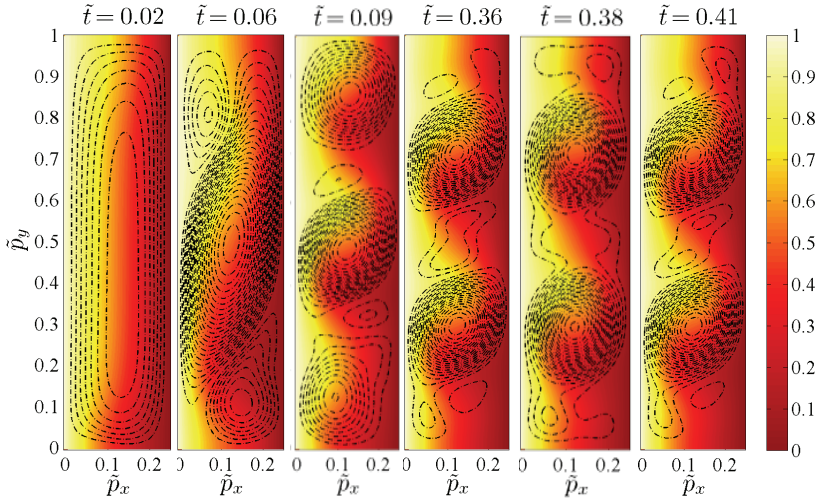

Fig. 8. The early stage time development and "steady-state" oscillations of a tall cavity natural convection - streamline and temperature contour plots

A comparison with the already published data is done on the analysis of the hot side Nusselt number time development $\mathrm{Nu}^{\mathrm{avg}}\left(\tilde{p}_x = 0, \tilde{p}_y\right)$. To confirm the agreement of the results, the hot side Nusselt number frequency domains are compared, where the early stages of signal development are omitted. From Figure 9 one can see that the agreement with reference results is excellent. In Figure 9 the frequency domains for different node distributions are compared, as well. The Nu_{freq} stands for Nusselt number transformation to the frequency domain and $\tilde{f}$ stands for dimensionless frequency.

The presented case is highly sensitive; even the smallest changes in the case setup affect the results dramatically, for example, changing the aspect ratio for less than 1 % results in completely different flow structure. Instead of two there are three major oscillating vortices. On the other hand, the presented results are computed with the completely different numerical approach in comparison with the reference solutions (meshless spatial

discretization against FVM and Spectral method, explicit against implicit time discretization scheme and LPVC against SIMPLE pressure-velocity coupling) and still the comparison shows a high level of agreement. The presented comparison infers on a high level of confidence in the present novel meshless method and the local solution approach.

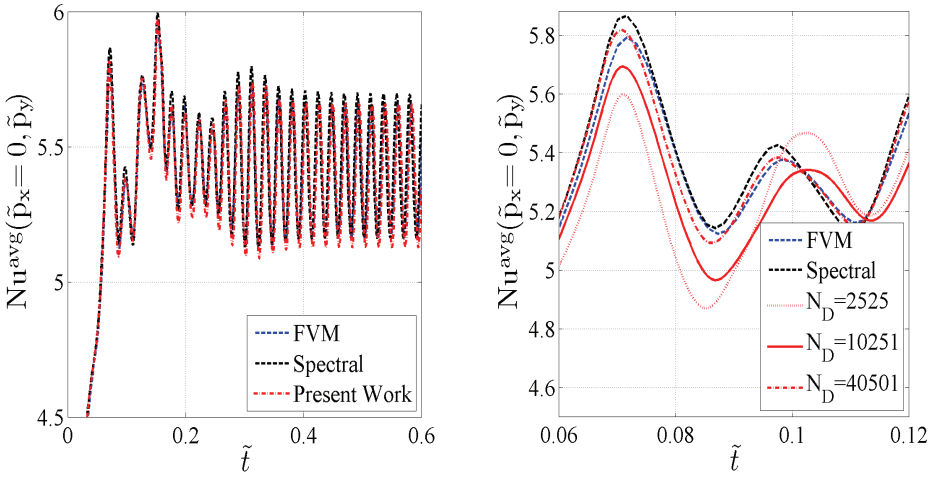

Fig. 9. The hot side average Nusselt number time development comparison

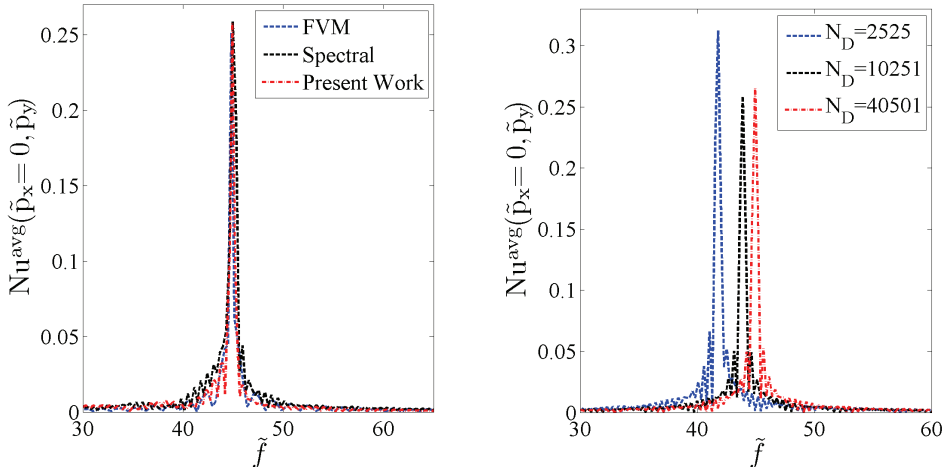

Fig. 10. The hot side average Nusselt number in the frequency domain

4.3 Porous media test

The next test is focused on the assessments of the solution procedure behaviour when working with fluid flow in the Darcy porous media. Again, a symmetrical differentially heated rectangular cavity is considered with impermeable velocity boundary condition.

Ra_F	A_R	$\tilde{v}_x^{max}$	$\tilde{v}_y^{max}$	Nu^{avg}	$\tilde{\psi}^{mid}$	reference / N_D	ε_v	$\Delta\tilde{t}$
50	1			1.979	2.863	(a)		
		11.174	18.112	1.941	2.860	10197	0.01	1e-04
		11.214	17.928	1.962	2.853	40397	0.01	1e-05
		11.236	17.845	1.975	2.848	160797	0.01	1e-05
10^2	1	17.380	35.889	3.101	4.375	(a)		
				3.103		(b)		
				3.010		(c)		
		17.500	37.454	3.040	4.510	10197	0.1	1e-04
		17.562	37.055	3.071	4.607	40397	0.1	1e-05
		17.603	36.873	3.086	4.655	160797	0.1	1e-05
10^3	1			13.42		(b)		
		72.560	441.771	13.044	17.062	10197	1	1e-04
		74.741	435.107	13.455	18.791	40397	1	1e-05
		75.577	432.335	13.529	19.658	160797	1	1e-05
10^4	1	257.394	4946.968	36.720	35.436	10197	1	5e-05
		287.375	4880.108	44.295	49.235	40397	5	5e-06
		287.375	4880.197	44.295	49.310	160797	5	1e-06
50	0.5			2.135	2.148	(a)		
		16.562	23.402	2.130	2.090	20297	0.1	1e-04
10^2	0.5	27.109	52.136	3.720	3.509	20297	1	1e-05
10^3	0.5	120.724	732.806	22.452	15.928	20297	1	1e-05
50	2			1.386	2.639	(a)		
		7.039	11.710	1.367	2.608	20297	0.1	1e-05
10^2	2	10.779	23.283	11.944	4.630	20297	1	1e-05
10^3	2	45.111	241.218	7.250	19.576	20297	1	1e-05

Table 3. A comparison of the results and numerical parameters

Three different aspect ratios are tested A_R = [0.5,1,2] for filtration Rayleigh numbers up to 10^4. The results are compared against (a) (Šarler, *et al.*, 2000), (b) (Ni and Beckermann, 1991), and (c) (Prax, *et al.*, 1996) with good agreement achieved (Table 3). In addition to the previously treated cases in quoted works, results for $Ra_F = 10^3$ and $Ra_F = 10^4$ are newly represented in this work. The pressure-velocity coupling algorithm was tested for up to 160797 uniformly distributed nodes and it behaves convergent. The temperature and the

streamfunction contours are presented in Figure 11 for tall cavity, Figure 12 for low cavity and Figure 13 for square cavity with streamline steps 2, 5, 15 and 40 for $Ra_F = 50$, $Ra_F = 10^2$, $Ra_F = 10^3$ and $Ra_F = 10^4$, respectively. Additional comparison of the results with reference Finite Volume Method (FVM) solution, previously used in (Šarler, *et al.*, 2000) for mid-plane velocities, hot side Nusselt number, mid-plane and top temperature profiles is done for case with $A_R = 1$ and filtration Rayleigh number $Ra_F = 100$ (Figure 14). The comparison shows good agreement with the generally accepted solution.

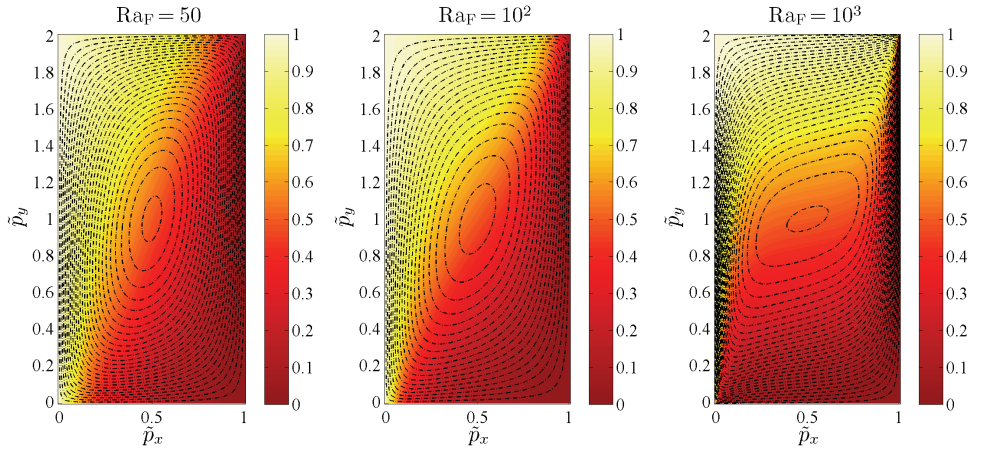

Fig. 11. Temperature and streamline contour plots for the test with $A_R = 1/2$

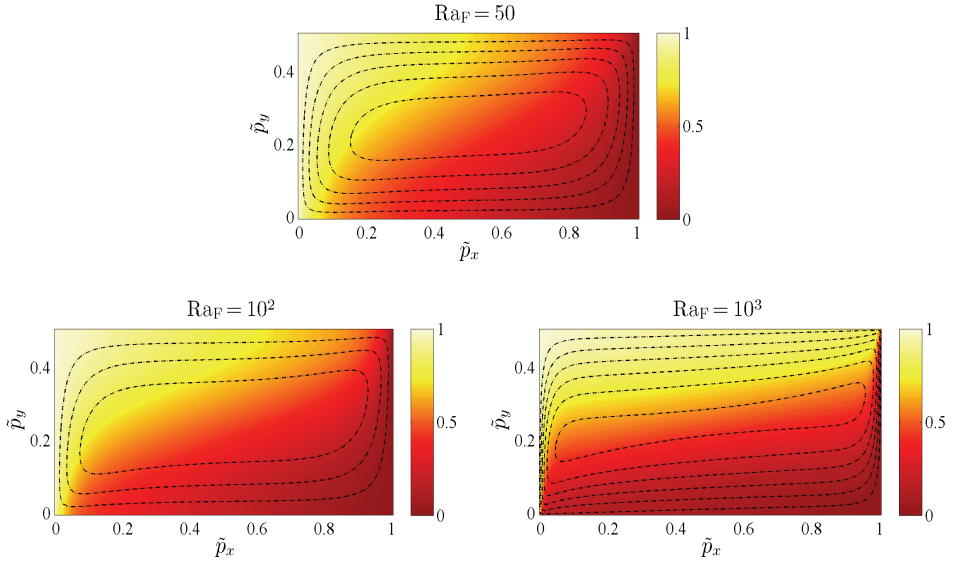

Fig. 12. Temperature and streamline contour plots for the test with, $A_R = 2$

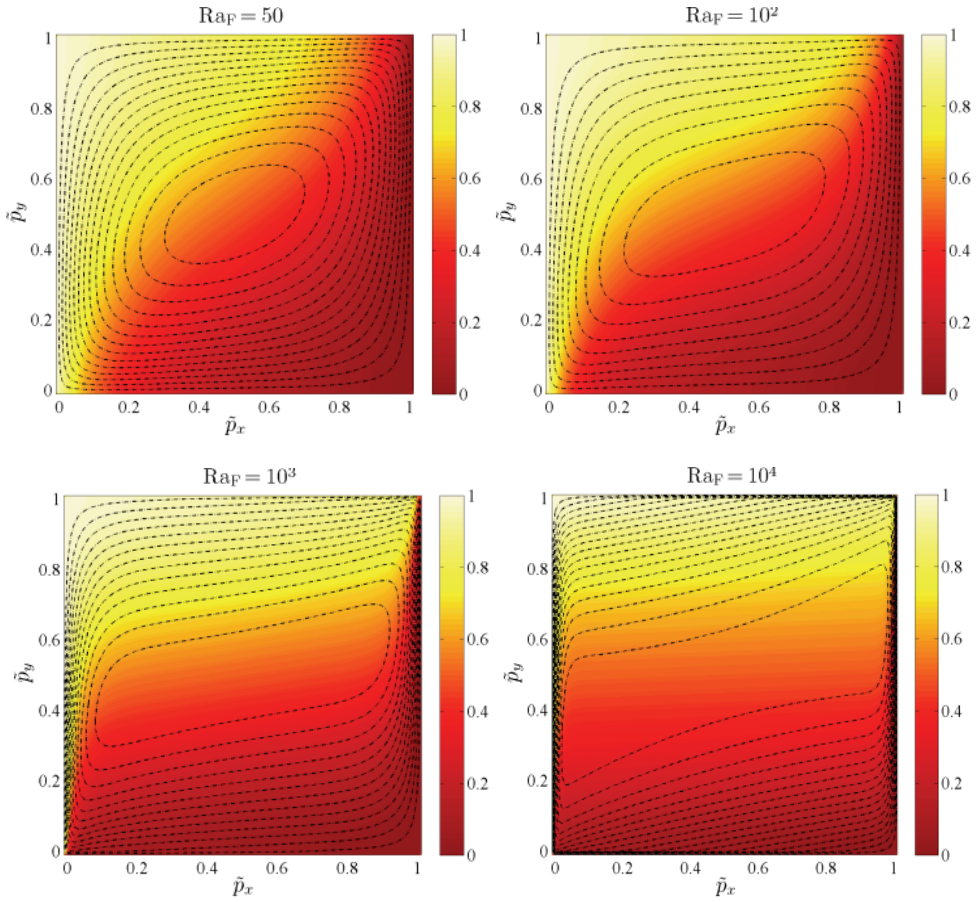

Fig. 13. Temperature and streamline contour plots for the test with $A_R = 1$

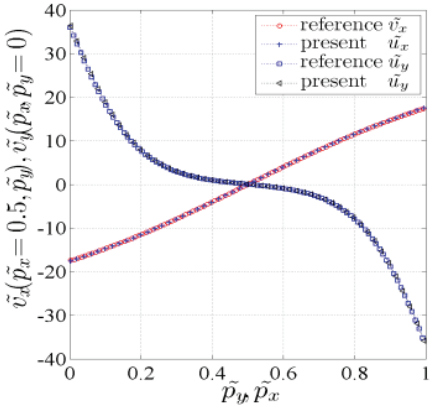

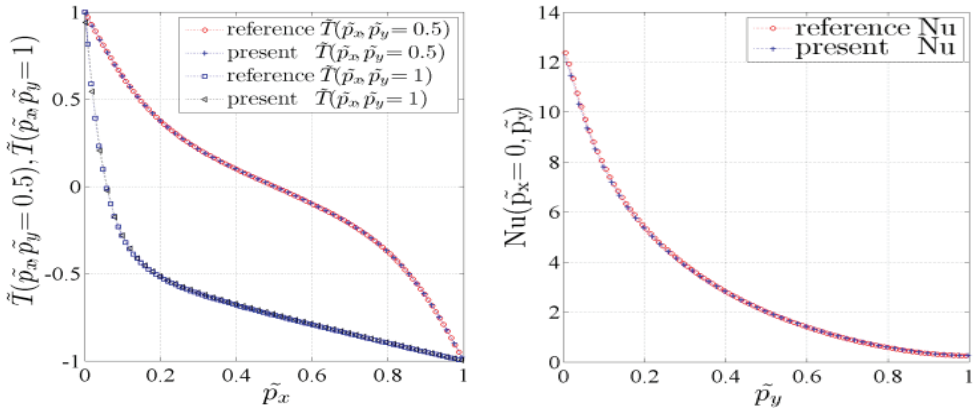

Fig. 14. A comparison of cross-sections quantities. The mid-plane velocities, the mid-plane and top temperatures and hot side Nusselt number, respectively

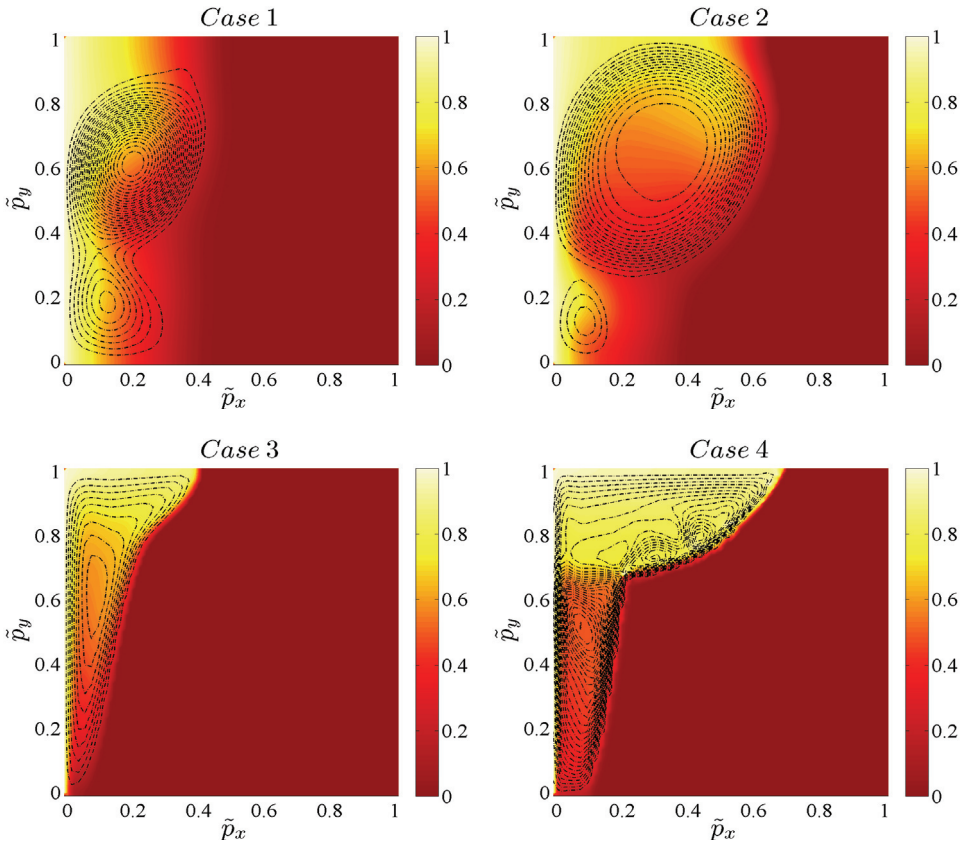

Fig. 15. Temperature and streamline contour plots for pure melting benchmark test

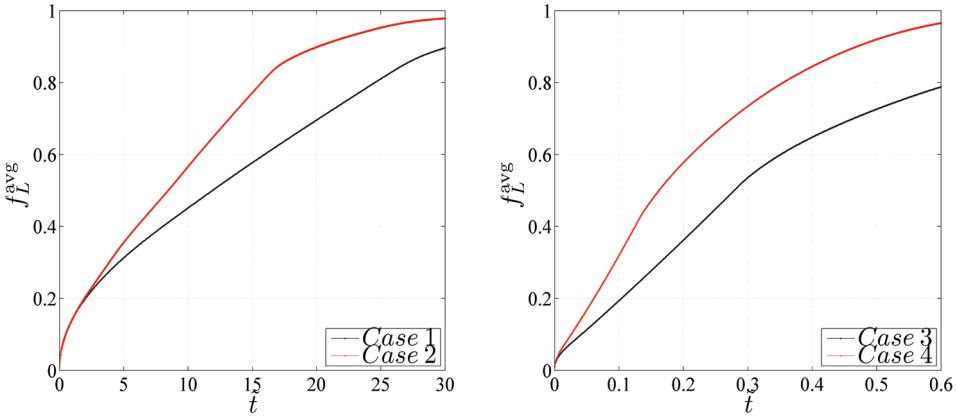

Fig. 16. The average liquid fraction as a function of time

4.4 Melting

All computations are performed on the 10197 uniformly distributed nodes with the pressure-velocity relaxation parameter set to the same numerical value as the time-step. The organic-like (high Prandtl Number) and metal-like (low Prandtl number) materials are subjected to the melting simulation in order to assess the method. The benchmark cases definitions together with the global mass continuity check and time-steps are presented in Table 4. The reference values in the Boussinesq approximation are set to the initial values. A comparison of the results or demonstration for all four cases is done at specific dimensionless time $\tilde{t}_C$, stated in Table 4, unless stated otherwise. The streamfunction and temperature contour plots are shown in Figure 15 with streamline steps: 0.1, 0.5 and 4.0 for *Cases* 1,2 and 3,4, respectively. The phase change front comparison is demonstrated in Figure 17.

The average liquid fraction (f_L^{avg}) time development for all four cases are presented in Figure 16 and the hot side average Nusselt number $\left(\mathrm{Nu}^{avg}(\tilde{p}_x = 0, \tilde{p}_y)\right)$ in Figure 18.

Additional node distribution convergence analysis is done for the *Case* 1 at time $\tilde{t} = 10$. The results are presented for phase change front and mid-plane temperature profile in Figure 19. For mid-plane velocity profiles the results are shown in Figure 20. In Figure 21 the average cavity temperature $\left(\tilde{T}^{avg}\right)$ and liquid fractions $\left(f_L^{avg}\right)$ as a function of the number of computational nodes shown. The results confirm convergent behaviour in all analyses.

	Pr	Ste	Ra	$\Delta\tilde{t}$	$\Delta\rho / \rho\|_{\tilde{t}_C}$	$\tilde{t}_C$
Case 1	0.02	0.01	2.5e4	1.0e-5	1.74e-6	10
Case 2	0.02	0.01	2.5e5	5.0e-6	8.02e-6	10
Case 3	50	0.1	1.0e7	1.0e-4	2.58e-5	0.1
Case 4	50	0.1	1.0e8	1.0e-5	1.31e-8	0.1

Table 4. The benchmark test definition

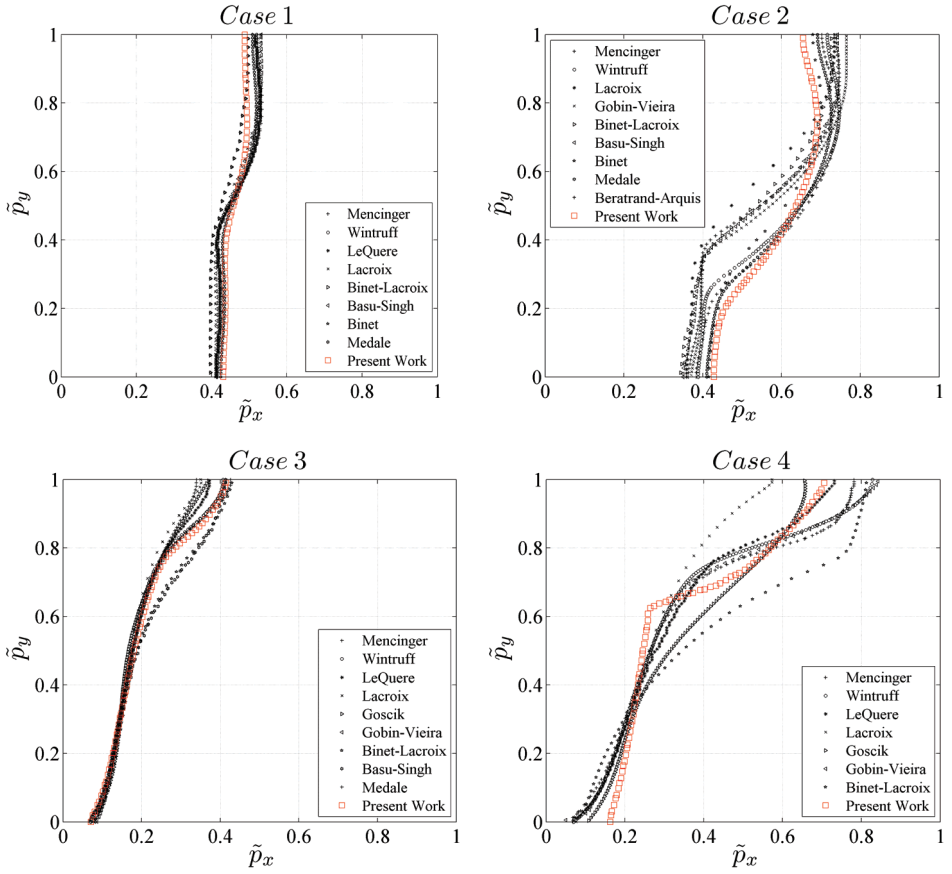

Fig. 17. The phase change front position comparison

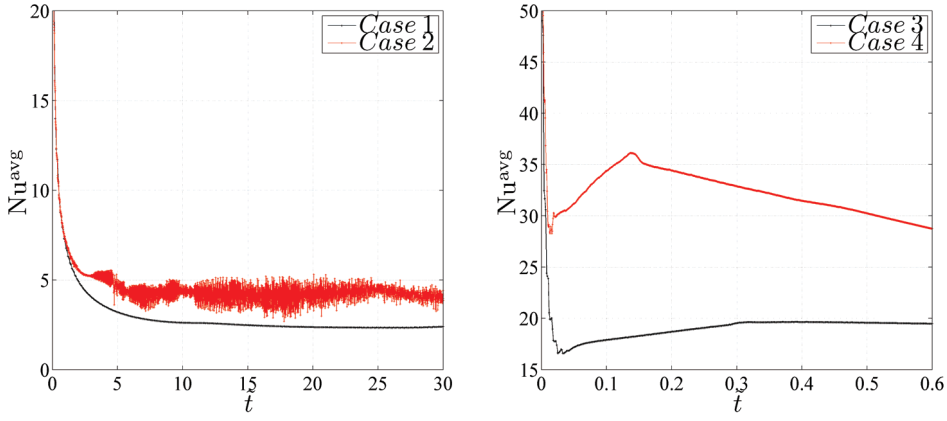

Fig. 18. The hot side average Nusselt number as a function of time

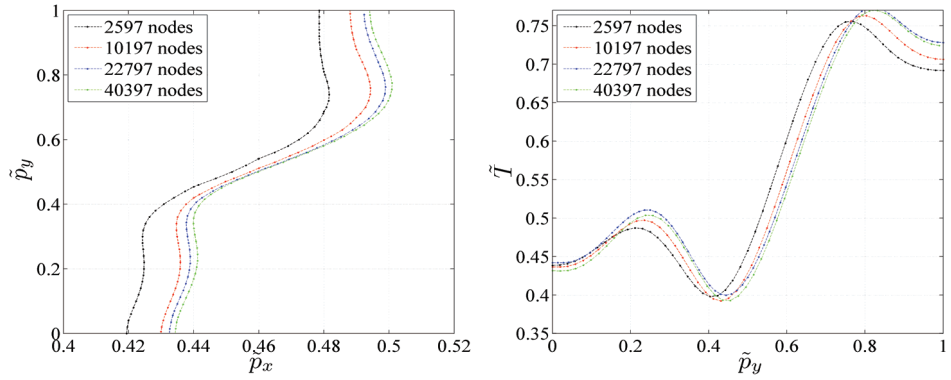

Fig. 19. The phase change front position (left) and mid-plane temperature (right) profile for *Case* 1 as a function of different discretizations at $\tilde{t} = 10$

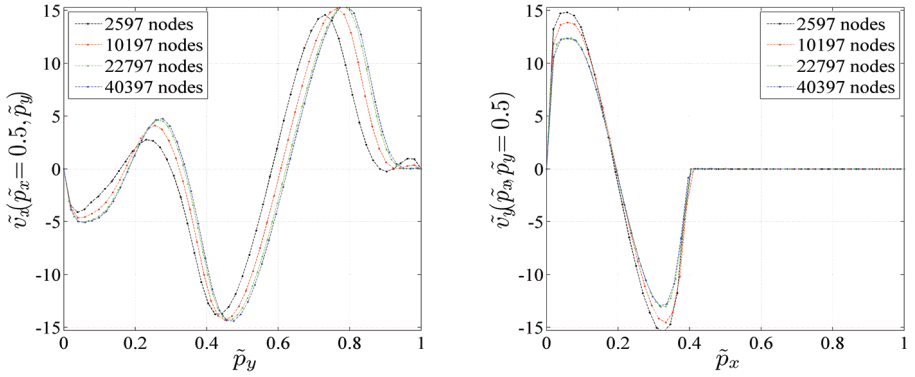

Fig. 20. The mid-plane velocities profiles for *Case* 1 as a function of different discretizations at $\tilde{t} = 10$

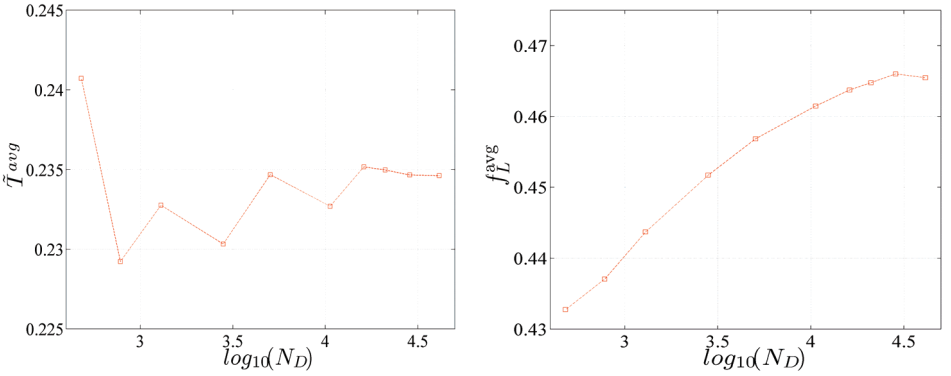

Fig. 21. The cavity average temperature (left) and cavity average liquid fraction (right) as a function of domain nodes count

5. Conclusions

In this chapter it is shown that the proposed numerical method as well as the proposed solution procedure performs well for the natural convection problems at different flow constitutive relations and regimes.
A detailed analysis of the de Vahl Davis test has been performed in order to assess the method in details. The mass leakage test and the cold-hot side Nusselt number comparison both confirmed that the method is accurate when such type of problems are considered. Furthermore, a comparison with already published data shows good agreement as well. The test involving a tall cavity, where the method is compared to the two completely different approaches, gives excellent agreement in case of the oscillatory flow regimes. The time average hot side Nusselt number development shows good quantitative comparison with the benchmark data. To complete the tests, the natural convection in a Darcy momentum regime is performed. Again, good agreement with the published data is achieved.
The final test is the phase change driven by a natural convection. The present results show good agreement with other approaches in terms of interphase boundary dynamics and complicated flow structures despite the simplest LRBFCM implementation. The Nusselt number oscillations in the *Case* 2 were already reported by Mencinger (Mencinger, 2003). The oscillations are a result of an unstable flow regime in the low Prandtl fluid, similar as in the tall cavity natural convection case, where the periodic solutions occur. The potential instabilities can occur in the natural convection in liquid metals, due to their low Prandtl number (Založnik, *et al*., 2005, Založnik and Šarler, 2006). Complex flow patterns and fast transients can occur already in laminar regimes at relatively low Rayleigh numbers. With another words; lowering the Prandtl number increases the nonlinearity of the natural convection. Generally, the main sources of instabilities for all presented cases stems from nonlinearities due to the complex liquid flow pattern and enthalpy behaviour at the phase change interphase. The enthalpy jump problem is partly resolved by introducing numerical smoothing of the phase change, at least enough to get stable results, but at the price of physical model accuracy. A detailed discussion on the parameter range with appearance of the flow physics based oscillations can be found in the work (Hannoun, et al., 2003). However, the results are in good agreement with the already known solutions (Gobin and Le Quéré, 2000). There is a bit higher deviance in the *Case* 4, still the deviations of other authors for that case is very high and it is difficult to conclude which solution is more credible.

6. Acknowledgment

The authors would like to express their gratitude to Slovenian Research Agency for support in the framework of the projects Young Researcher Programme 1000-06-310232 (G. K.) and project P2-0379 (B. Š.).

7. References

Atluri, S. N. & Shen, S. (2002a), *The Meshless Method*, Tech Science Press, Encino.

Atluri, S. N. & Shen, S. (2002b), The meshless local Petrov-Galerkin (MLPG) method: a simple & less-costly alternative to the finite element and boundary element methods, *CMES: Computer Modeling in Engineering & Sciences*, Vol. 3, pp. 11-52.

Atluri, S. N. (2004), *The Meshless Method (MLPG) for Domain and BIE Discretization*, Tech Science Press, Forsyth.

Bejan, A. (2004), *Convection Heat Transfer* John Wiley & Sons, New Jersey.

Buhmann, M. D. (2000), *Radial Basis Functions*, Cambridge University Press, Cambridge.
Chan, B. K. C.; Ivey, C. M. & Barry, J. M. (1994), Natural convection in enclosed porous media with rectangular boundaries, *Wärme und Stoffübertragung*, Vol. 7, pp. 22-30.
Chen, W. (2002), New RBF collocation schemes and kernel RBFs with applications, *Lecture Notes in Computational Science and Engineering*, Vol. 26, pp. 75-86.
de Vahl Davis, G. (1983), Natural convection of air in a square cavity: a bench mark numerical solution, *International Journal of Numerical Methods in Fluids*, Vol. 3, pp. 249-264.
Divo, E. & Kassab, A. J. (2007), Localized meshless modeling of natural-convective viscous flows, *Numerical Heat Transfer*, Vol. B129, pp. 486-509.
Gobin, D. & Le Quéré, P. (2000), Melting from an isothermal vertical wall, synthesis of a numerical comparison excercise, *Computer Assisted Mechanics and Engineering Sciences* Vol. 198, pp. 289-306.
Gu, G.R. Liu; Y.T. (2005), *An Introduction to Meshfree Methods and Their Programming*, Springer, Dordrecht.
Hannoun, N.; Alexiades, V. & Zee Mai, T. (2003), Resolving the controversy over tin and gallium melting in a rectangular cavity heated from the side, *Numerical Heat Transfer* Vol. B44, pp. 253-276.
Hong, C. P. (2004), *Computer Modelling of Heat and Fluid Flow Materials Processing*, Institute of Physics Publishing Bristol.
Hortmann, M.; Perić, M. & Scheuerer, G. (1990), Finite volume multigrid prediction of laminar natural convection - bench-mark solutions, *International Journal for Numerical Methods in Fluids*, Vol. 11, pp. 189-207.
Janssen, R. J. A. & Henkes, R. A. W. M. (1993), Accuracy of finite-volume disretizations for the bifurcating natural-convection flow in a square cavity, *Numerical Heat Transfer*, Vol. B24, pp. 191-207.
Jecl, R.; Škerget, L. & Petrešin, E. (2001), Boundary domain integral method for transport phenomena in porous media, *International Journal for Numerical Methods in Fluids*, Vol. 35, pp. 35-59.
Kansa, E. J. (1990a), Multiquadrics - a scattered data approximation scheme with application to computational fluid dynamics, part I, *Computers and Mathematics with Applications*, Vol. 19, pp. 127-145.
Kansa, E. J. (1990b), Multiquadrics - a scattered data approximation scheme with application to computational fluid dynamics, part II, *Computers and Mathematics with Applications*, Vol. 19, pp. 147-161.
Kosec, G. & Šarler, B. (2008a), Solution of thermo-fluid problems by collocation with local pressure correction, *International Journal of Numerical Methods for Heat and Fluid Flow*, Vol. 18, pp. 868-882.
Kosec, G. & Šarler, B. (2008b), Convection driven melting of anisotropic metals, *International Journal of Cast Metals Research*, Vol. 22, pp. 279-282.
Kosec, G. & Šarler, B. (2008c), Local RBF collocation method for Darcy flow, *CMES: Computer Modeling in Engineering & Sciences*, Vol. 25, pp. 197-208.
Kosec, G. & Šarler, B. (2008d), Meshless aproach to solving freezing driven by a natural convection, *Materials Science Forum*, Vol. 649, pp. 205-210.
Kosec, G. & Šarler, B. (2009), Solution of phase change problems by collocation with local pressure correction, *CMES: Computer Modeling in Engineering & Sciences*, Vol. 47, pp. 191-216.
Lage, J. L. & Bejan, A. (1991), The Ra-Pr domain of laminar natural convection in an enclosure heated from the side, *Numerical Heat Transfer*, Vol. A19, pp. 21-41.
Lee, C.K.; Liu, X.; Fan, S.C. (2003), Local muliquadric approximation for solving boundary value problems, *Computational Mechanics*, Vol. 30, pp. 395-409.

Liu, G.R. (2003), *Mesh Free Methods*, CRC Press, Boca Raton.
Manzari, M. T. (1999), An explicit finite element algorithm for convection heat transfer problems, *International Journal of Numerical Methods for Heat and Fluid Flow*, Vol. 9, pp. 860-877.
Mencinger, J. (2003), Numerical simulation of melting in two-dimensional cavity using adaptive grid, *Journal of Computational Physics*, Vol. 198, pp. 243-264.
Ni, J. & Beckermann, C. (1991), Natural convection in a vertical enclosure filled with anisotropic porous media, *ASME Journal of Heat Transfer*, Vol. 113, pp. 1033-1037.
Nobile, E. (1996), Simulation of time-dependent flow in cavities with the additive-correction multigrid method, part II: Apllications, *Numerical Heat Transfer, Part B*, Vol. 30, pp.
Prasad, V. & Kulacky, F. A. (1984), Convective heat transfer in a rectangular porous cavity. Effect of aspect ratio on flow structure and heat transfer, *ASME Journal of Heat Transfer*, Vol. 106, pp. 158-65.
Prax, C.; Sadat, H. & Salagnac, P. (1996), Diffuse approximation method for solving natural convection in porous Media, *Transport in Porous Media*, Vol. 22, pp. 215-223.
Raghavan, R. & Ozkan, E. A. (1994), *Method for computing unsteady flows in porous media*, John Wiley and Sond inc., Essex.
Sadat, H. & Couturier, S. (2000), Performance and accuracy of a meshless method for laminar natural convection, *Numerical Heat Transfer*, Vol. B37, pp. 455-467.
Šarler, B.; Gobin, D.; Goyeau, B.; Perko, J. & Power, H. (2000), Natural convection in porous media - dual reciprocity boundary element method solution of the Darcy model, *International Journal of Numerical Methods in Fluids*, Vol. 33, pp. 279-312.
Šarler, B.; Perko, J. & Chen, C. S. (2004a), Radial basis function collocation method solution of natural convection in porous Media, *International Journal of Numerical Methods for Heat & Fluid Flow*, Vol. 14, pp. 187-212.
Šarler, B.; Perko, J.; Gobin, D.; Goyeau, B. & Power, H. (2004b), Dual reciprocity boundary element method solution of natural convection in Darcy-Brinkman porous media, *Engineering Analysis with Boundary Elements*, Vol. 28, pp. 23-41.
Šarler, B. (2005), A radial basis function collocation approach in computational fluid dynamics, *CMES: Computer Modeling in Engineering & Sciences*, Vol. 7, pp. 185-193.
Šarler, B. & Vertnik, R. (2006), Meshfree explicit local radial basis function collocation method for diffusion problems, *Computers and Mathematics with Applications*, Vol. 51, pp. 1269-1282.
Šarler, B. (2007), *From global to local radial basis function collocation method for transport phenomena*, Springer, Berlin, pp. 257-282.
Vertnik, R. & Šarler, B. (2006), Meshless local radial basis function collocation method for convective-diffusive solid-liquid phase change problems, *International Journal of Numerical Methods for Heat and Fluid Flow*, Vol. 16, pp. 617-640.
Vertnik, R.; Založnik, M. & Šarler, B. (2006), Solution of transient direct-chill aluminium billet casting problem with simultaneous material and interphase moving boundaries by a meshless method, *Engineering Analysis with Boundary Elements*, Vol. 30, pp. 847-855.
Wan, D. C.; Patnaik, B. S. V. & Wei, G. W. (2001), A new benchmark quality solution for the buoyancy-driven cavity by discrete singular convolution, *Numerical Heat Transfer*, Vol. B40, pp. 199-228.
Založnik, M.; Xin, S. & Šarler, B. (2005), Verification of a numerical model of macrosegregation in direct chill casting, *International Journal of Numerical Methods for Heat & Fluid Flow*, Vol. 18, pp. 308-324.
Založnik, M. & Šarler, B. (2006), "Thermosolutal flow in metals and implications for DC casting", *Modeling of Casting, Welding and Advanced Solidification Processes XI.*

6

Hydromagnetic Flow with Thermal Radiation

Cho Young Han[1] and Se-Myong Chang[2]
[1]*Korea Aerospace Research Institute,*
[2]*Kunsan National University,*
Republic of Korea

1. Introduction

Magnetohydrodynamic (MHD) flows, which is the simplest plasma model, has been the subject of a great number of empirical and theoretical investigations in many industrial fields. Especially the MHD flows associating with heat transfer have received considerable attention so far, as their applications reside in many industrial fields such as electric propulsion for space exploration, crystal growth in liquids, cooling of nuclear reactors, electronic packages, micro electronic devices, etc.

The most common type of body force, which acts on fluid, is attributed to gravity so that the body force vector can be deduced from the gravitational acceleration. On the other hand, when an electrically conducting fluid is subjected to a magnetic field, the fluid motion induces an electric current such that the fluid velocity is reduced on account of interaction between the electric current and the fluid motion. Therefore, in case of free convection of an electrically conducting fluid in the presence of a magnetic field, there should be two body forces, i.e., a buoyancy force and a Lorentz force. They interact with each other, and in turn influence the transport phenomena of heat and mass.

Among various studies for MHD free flows, rather small amount of studies have been accomplished for the confined enclosures. Seki et al. (1979) studied the laminar natural convection of mercury subjected to a magnetic field parallel to gravity in a rectangular enclosure. Numerical results were obtained and compared to their experiment in the consideration of a partially heated vertical wall by a uniform heat generator. Rudraiah et al. (1995) performed a numerical simulation about natural convection in a two-dimensional cavity filled with an electrically conducting fluid in the presence of a magnetic field aligned to gravity. They selected the Grashof and Hartmann numbers as controlling parameters to examine the effect of a magnetic field on free convection and associated heat transfer. The three-dimensional free convective flow in a cubical enclosure in the presence of a transverse magnetic field was analysed by Kolsi et al. (2007) numerically.

For the free convection in an inclined enclosure under a magnetic field, the following representative works have been conducted. Bian et al. (1996) have studied the effect of a transverse magnetic field on buoyancy-driven convection in an inclined rectangular porous cavity, saturated with an electrically conducting fluid. Recently Wang et al. (2007) investigated numerically the natural convection in an inclined enclosure filled with porous media when a strong magnetic field was applied. They modelled the cubic enclosure, such that the direction of an applied magnetic field is varied in accordance with the inclination

angle. Differentially heated two side walls were kept to be vertical regardless of an inclination angle in their analysis.
Investigations considering the variation in the orientation of an external magnetic field applied were carried out too. The effect of direction of an external magnetic field on a low Prandtl number fluid in a cubical enclosure was numerically examined by Ozoe & Okada (1989). Hua & Walker (1995) examined the three-dimensional liquid metal MHD flow in rectangular ducts with thin conducting walls and an inclined transverse magnetic field against the principal axes. On the other hand, Bessaih et al. (1999) studied the buoyancy-induced flow of gallium in cavities simulating the apparatus for crystal growth. The combined effect on the flow structure of wall electrical conductivity and magnetic field orientation were numerically investigated in their work. Sivasankaran & Ho (2008) conducted the numerical analysis for natural convection of water near its density maximum in the presence of a magnetic field in a cavity with temperature dependent properties. They observed the effect of the direction of an external magnetic field on the flow field and accompanying heat transfer when varying it from 0 to $\pi/2$ radians.
Moreover many researchers have taken an interest in the effect of thermal radiation on the hydromagnetic flow and heat transfer problems, by reason of its great importance in diverse industrial fields. Radiation effect can be quite significant at high operating temperature. Many processes in engineering areas occur at high temperatures and the knowledge of radiation heat transfer becomes very important for the design of pertinent equipments. The effects of thermal radiation on hydromagnetic boundary layer flows were studied by Chamkha (2000), Seddeek (2002), Ghaly (2002) and Raptis et al. (2004). However they converted the complex radiation problem to the simpler conduction one accounting for the radiation conductivity by introducing the similarity transformation as a sort of the one-dimensional analysis. This analytical approach is not suitable for the assessment of the radiant heat exchange between surfaces of an enclosure operating under the high temperature environment, as the multi-dimensional analysis should be required in this case. Mahmud & Fraser (2002) examined analytically radiation effects on mixed convection through a vertical channel in the presence of a transverse magnetic field, but the underlying drawbacks are similar to those for studies aforementioned.
The aim of present chapter is to investigate in detail the effect of a magnetic field as well as thermal radiation on free convection associating with heat transfer in an enclosure filled with an electrically conducting fluid. Basically the full two-dimensional analysis is performed rather than the boundary layer type of analysis, even when considering the thermal radiation. It is motivated by a desire to find any effects of the controlling parameters on the thermally driven hydromagnetic flows found in many engineering applications. In this context this chapter can be classified into three subjects. In the first place the changes in the buoyant flow patterns and temperature distributions due to the tilting of the enclosure are examined, neglecting thermal radiation. Secondly the flow and thermal field variation is investigated in terms of the orientation of an external magnetic field. Finally the effect of combined radiation and a magnetic field on the convective flow and heat transfer characteristics of an electrically conducting fluid is analysed and discussed in detail.

2. Analysis model

For many electrically conducting fluids used in laboratories, the electrical conductivity is usually small. Subsequently the magnetic Reynolds number should be very small. Therefore it is reasonable to assume that the induced magnetic field by the motion of the electrically

conducting fluid is negligible compared to the external magnetic field applied. Based on this assumption the electromagnetic retarding force and the buoyancy force terms are appeared in the relevant momentum equations, respectively, such that the governing equations are not amenable to the boundary layer type of analysis. In this simulation the SIMPLER algorithm (Patankar, 1980) is involved to estimate the flow field, which is numerically stable and being widely used. The resultant solution of the governing equations is to be proposed in association with the finite-volume method (Chai et al., 1994), which is compatible with assessing the radiant heat exchange between enclosure walls. The effect of controlling parameters pertaining to fluid flow, heat transfer characteristics and radiation involvement is evaluated numerically.

2.1 Governing equations

A schematic of the two-dimensional rectangular enclosure with width L and height H is shown in Fig. 1. It is filled with the electrically conducting fluid that is viscous and incompressible. The left- and right-hand-side walls are kept at T_C and T_H, respectively. The ceiling and floor are assumed to be insulated for both conduction and radiation.

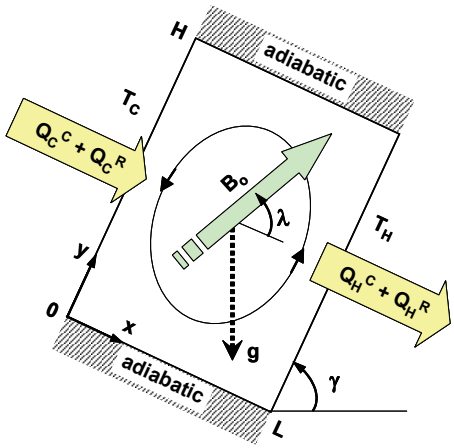

Fig. 1. Schematic diagram of the enclosure

The medium within the enclosure does not participate in radiation. Such nonparticipating medium example is intrinsically important in the analysis of nongray gas effects because there are wavelength regions where the medium is essentially transparent. All four walls of the enclosure are radiatively active surfaces, which are black and diffuse, so that the radiative interaction between walls is taken into account.

The fluid is permeated by the uniform magnetic field B_o. The enclosure is tilted at an angle of γ with respect to the horizontal plane, and the orientation of an external magnetic field could vary from 0 to 2π radians corresponding to an angle of λ. In addition the induced electric current does not distort considerably the magnetic field applied. The fluid properties including the electrical conductivity are assumed to be constant except for the density, so that the Boussinesq approximation is used. Neglecting viscous and ohmic dissipations, the governing equations for mass, momentum and energy of the steady laminar flow are as follows.

Continuity

$$\frac{\partial u}{\partial x}+\frac{\partial v}{\partial y}=0 \tag{1}$$

X-momentum

$$\frac{\partial}{\partial x}(u^2)+\frac{\partial}{\partial y}(u v)=-\frac{1}{\rho}\frac{\partial p}{\partial x}+\nu\nabla^2 u-g\beta(T-T_o)\cos\gamma+\frac{\sigma B_o^2}{\rho}(-u\sin^2\lambda+v\cos\lambda\sin\lambda) \tag{2}$$

Y-momentum

$$\frac{\partial}{\partial x}(u v)+\frac{\partial}{\partial y}(v^2)=-\frac{1}{\rho}\frac{\partial p}{\partial y}+\nu\nabla^2 v+g\beta(T-T_o)\sin\gamma+\frac{\sigma B_o^2}{\rho}(u\cos\lambda\sin\lambda-v\cos^2\lambda) \tag{3}$$

Energy

$$\frac{\partial}{\partial x}(u T)+\frac{\partial}{\partial y}(v T)=\alpha\nabla^2 T \tag{4}$$

In the above equations, u and v are the velocity component in the x and y directions. The density, pressure and temperature are denoted by ρ, p and T, respectively. The relevant fluid properties are kinematic viscosity ν, thermal diffusivity α, electrical conductivity σ and volumetric expansion coefficient β. The governing equations are nondimensionalised using the following variables:

$$x^*=x/L,\ y^*=y/L,\ u^*=u/u_o,\ v^*=v/u_o \tag{5}$$

$$p^*=\frac{p}{\rho_o u_o^2},\ T^*=\frac{T-T_o}{T_H-T_C} \tag{6}$$

$$Pr=\nu/\alpha,\ Ra=\frac{g\beta\Delta T L^3}{\nu\alpha},\ Gr=Ra/Pr,\ Ha=B_o L\sqrt{\frac{\sigma}{\mu}} \tag{7}$$

$$\delta=\frac{T_H-T_C}{T_o},\ Pl=\frac{k/L}{4\bar{\sigma}T_o^3},\ q^{R}{}^*=\frac{q^R}{\bar{\sigma}T_o^4} \tag{8}$$

The reference velocity is defined as $u_o = \alpha / L$. The overheat ratio is expressed by δ, while the reference temperature is defined as the arithmetic mean of the two isothermal wall temperatures, i.e., $T_o = (T_H + T_C) / 2$. The Prandtl, Rayleigh, Grashof, Hartmann and Planck numbers are represented by Pr, Ra, Gr, Ha and Pl, respectively, where μ and k are dynamic viscosity and thermal conductivity. Radiative heat flux q^R is nondimensionalised by the reference emissive power, i.e., $\bar{\sigma}T_o^4$, in which $\bar{\sigma}$ is Stefan-Boltzmann constant. Based on the presumptions above, the dimensionless governing equations can be shown as follows.

Continuity

$$\frac{\partial u^*}{\partial x^*}+\frac{\partial v^*}{\partial y^*}=0 \tag{9}$$

X-momentum

$$\frac{\partial}{\partial x^*}(u^{*2})+\frac{\partial}{\partial y^*}(u^* v^*)=-\frac{\partial p^*}{\partial x^*}+Pr\nabla^{*2} u^*-Gr\,Pr^2 T^*\cos\gamma+Pr\,Ha^2(-u^*\sin^2\lambda+v^*\cos\lambda\sin\lambda) \quad (10)$$

Y-momentum

$$\frac{\partial}{\partial x^*}(u^* v^*)+\frac{\partial}{\partial y^*}(v^{*2})=-\frac{\partial p^*}{\partial y^*}+Pr\nabla^{*2} v^*+Gr\,Pr^2 T^*\sin\gamma+Pr\,Ha^2(u^*\cos\lambda\sin\lambda-v^*\cos^2\lambda) \quad (11)$$

Energy

$$\frac{\partial}{\partial x^*}(u^* T^*)+\frac{\partial}{\partial y^*}(v^* T^*)=\nabla^{*2} T^* \quad (12)$$

2.2 Dimensionless boundary conditions

The boundary conditions for two isothermal walls are as follows:

$$u^* = v^* = 0,\ T^* = -0.5 \text{ at } x^* = 0 \quad (13)$$

$$u^* = v^* = 0,\ T^* = 0.5 \text{ at } x^* = 1 \quad (14)$$

Non-slip conditions of the velocities are assigned on the ceiling and floor. The thermal boundary condition at adiabatic ceiling and floor is found from the following energy balancing equation, in which the net radiation into the wall surface is balanced by conductive heat loss from the wall:

$$-\frac{\partial T^*}{\partial y^*}\bigg|_w+\frac{q_w^{R*}}{4Pl\delta}=0 \quad (15)$$

2.3 Heat transfer rates

To estimate the heat transfer rates at two isothermal walls, various types of average Nusselt numbers are defined as follows:

$$\overline{Nu}_w^C=\frac{1}{A}\int_0^A\left[-\frac{\partial T^*}{\partial x^*}\right]_w dy^* \quad (16)$$

$$\overline{Nu}_w^R=\frac{1}{4Pl\delta}\frac{1}{A}\int_0^A \text{sign}(\hat{n}_w)\cdot q_w^{R^*} dy^* \quad (17)$$

$$\overline{Nu}_w^T=\overline{Nu}_w^C+\overline{Nu}_w^R \quad (18)$$

From the above equations, A means the aspect ratio, i.e., A = H/L. The conductive and radiative average Nusselt numbers at the walls are represented by $\overline{Nu}_w^C$ and $\overline{Nu}_w^R$, respectively. Their sum, $\overline{Nu}_w^T$ is the total average Nusselt number, which denotes the total amount of heat transfer at the wall. Since the steady state is assumed in this study, the total average Nusselt numbers at both hot and cold walls are same.

3. Numerical analysis

A numerical analysis of thermo-fluid dynamics characteristics is conducted by adopting the SIMPLER algorithm developed by Patankar (1980). While the convection term is discretised using the QUICK finite-difference scheme (Thakur & Shyy, 1993), the central difference method is chosen for the diffusion term. In order to compute the radiative heat fluxes on enclosure walls, the finite-volume method (FVM) for radiation heat transfer is implemented here as proposed by Chai et al. (1994). After some preliminary calculations for checking convergence and accuracy, the spatial domain is discretised into 51 × 51 non-uniform control volumes in the x and y directions. In the case of radiation, 48 control angles are employed to estimate the radiative wall heat fluxes accordingly.

Computations are proceeded by the following procedures. To begin with, the radiative wall heat fluxes are determined by FVM. The velocity field is estimated from the momentum equation. After the updated temperature is estimated from the energy equation based on the interior point temperature at the previous iteration, the wall conductive heat fluxes are estimated. Then, these values of the wall conductive heat flux and the radiative wall heat flux are used to update the non-prescribed wall surface temperatures by solving the energy balance equation (15). In computation, to reduce the error in the wall conductive heat flux, the grid system should be clustered near the walls. Since the calculation of radiative heat fluxes is not necessarily required at every iteration to produce a reliable steady-state result, the radiative heat flux is updated at every tenth iteration. However, the wall surface temperature is recalculated and changed at each iteration with an estimated wall conductive heat flux.

Finally, the convergence criteria for main variables are checked if the steady state is reached. Computations are terminated when the difference in total average Nusselt numbers for the hot and cold walls is within less than 10^{-3} tolerance to meet the overall energy balance in the enclosure.

$$\left| \overline{\mathrm{Nu}}_{\mathrm{H}}^{\mathrm{T}} - \overline{\mathrm{Nu}}_{\mathrm{C}}^{\mathrm{T}} \right| \le 10^{-3} \tag{19}$$

4. Results and discussion

A numerical investigation is presented for free convection in a two-dimensional enclosure filled with an electrically conducting fluid in the presence of an external magnetic field. The enclosure is such that the two opposing side walls are differentially heated with a temperature difference specified, while the top and bottom walls are insulated. Those four walls are radiatively active surfaces, and the enclosure is tilted as well as the orientation of an external magnetic field can be arbitrary. As a whole computations are carried out for the Grashof numbers ranging from 1×10^4 to 2×10^6, and Hartmann numbers from 0 to 100. The assumption of two-dimensional laminar flow is valid for above values of the Grashof numbers (Larson & Viskanta, 1976).

It is difficult to study the influence of all parameters involved in the present problem on the flow and thermal field. Therefore a selected set of parameters is accounted for this numerical investigation. The aspect ratio, A = H/L, of the enclosure is set to be of 1, and the Prandtl number of 0.733 is utilised. The overheat ratio is taken to be $\delta = 2/3$, i.e., $T_H = 2\ T_C$. The constant fluid property and Boussinesq approximations are reasonable for above values (Fusegi & Farouk, 1989). The Planck number is assigned to be 0.02.

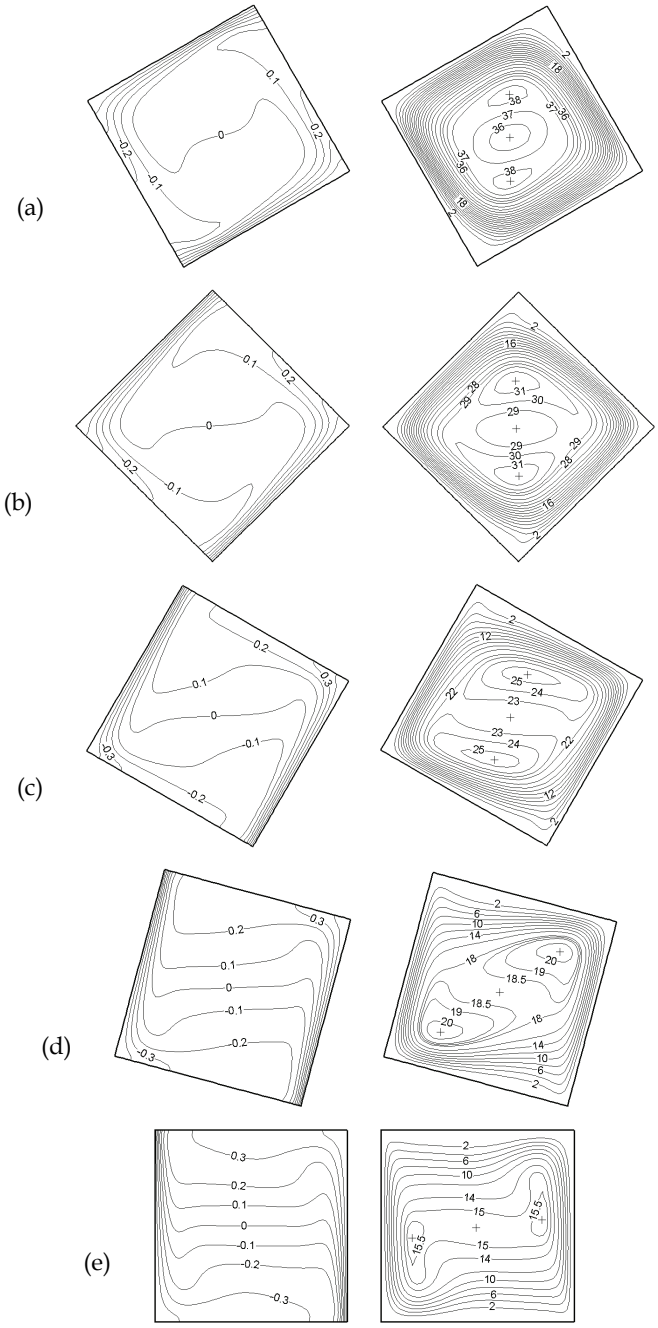

Fig. 2. Isotherm and streamline contours for Gr = 10^6 and Ha = 0: (a) $\gamma = \pi/6$, (b) $\gamma = \pi/4$, (c) $\gamma = \pi/3$, (d) $\gamma = 5\pi/12$ and (e) $\gamma = \pi/2$ radians

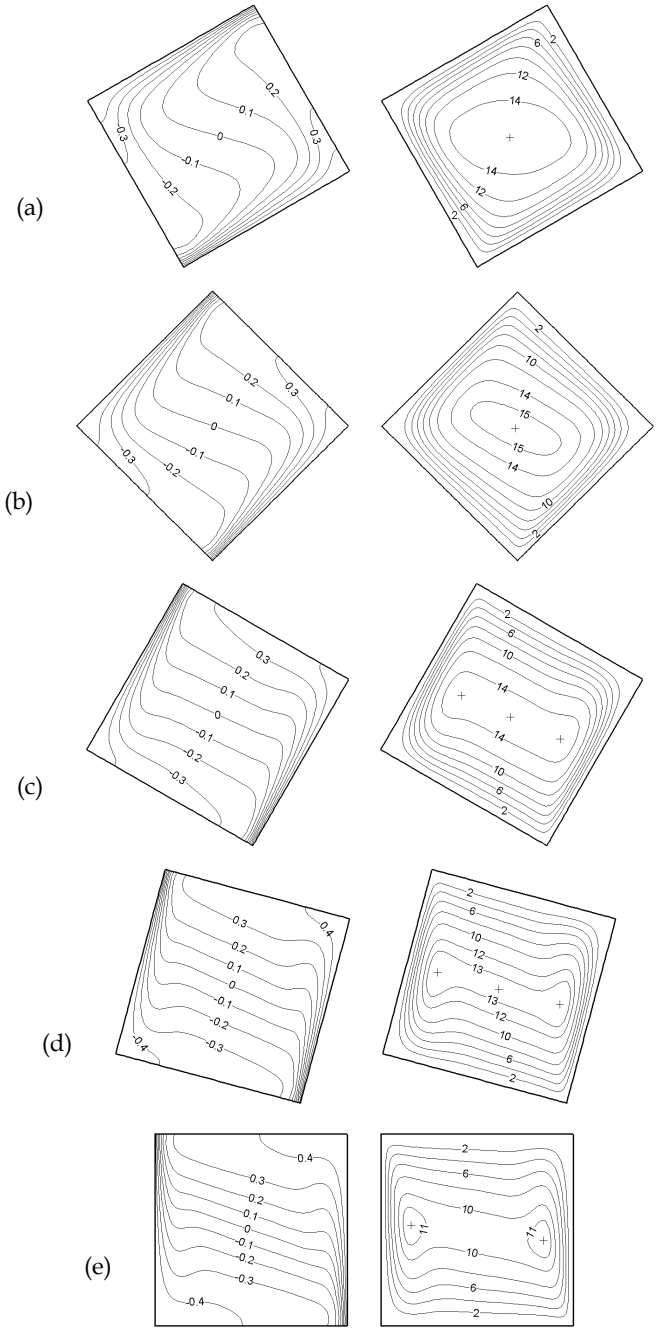

Fig. 3. Isotherm and streamline contours for Gr = 10^6 and Ha = 50: (a) $\gamma = \pi/6$, (b) $\gamma = \pi/4$, (c) $\gamma = \pi/3$, (d) $\gamma = 5\pi/12$ and (e) $\gamma = \pi/2$ radians

Isotherm and streamline plots will be reported for different values of controlling parameters. The contour lines of isotherm plots correspond to equally-spaced values of the dimensionless temperature T*, i.e., $\Delta T^* = 0.1$, in the range between -0.5 and +0.5. On the other hand the dimensionless stream function is obtained from the velocity field solution by integrating the integral $\Psi^* = \int_0^1 u^* dy^*$ along constant x* lines, setting $\Psi^* = 0$ at $x^* = y^* = 0$.

The contour lines of the streamline plots are correspondent to equally-spaced values of the dimensionless stream function, unless otherwise specified.

4.1 Influence of the tilting of an enclosure without radiation

A numerical investigation is presented for natural convection of an electrically conducting fluid in a tilted square cavity in the presence of a vertical magnetic field aligned to the gravity, i.e., $\lambda = -\gamma$.

In the present study, the Grashof number is fixed as $Gr = 10^6$. Computations are carried out for tilted angles ranging from 0 to $\pi/2$ radians, and the thermal radiation is neglected.

Figure 2 shows the isotherm and streamline contours for natural convection in inclined cavities in the absence of a magnetic field. The multi-cellular inner core consists of a central roll (designated by "+" in the figures) sandwiched between two rolls. As the tilting angle decreases, the fluid motion becomes progressively intensive. The temperature is stratified at the core region in case of $\gamma = \pi/2$ rad. When the tilting angle decreases, this trend is maintained until $\gamma = \pi/4$ rad. The stratification of the temperature field in the interior begins to diminish as the inclination angle reaches $\pi/6$ rad due to the increasing buoyant action.

The results depicted in Fig. 3 demonstrate the influence of the magnetic field on the fluid flow and the temperature distributions along with the tilting angle. For relatively strong Hartmann number (Ha =50), the temperature stratification in the core tends to diminish, and the thermal boundary layers at the two side walls disappear, together with the decrease in inclination angle. Also, the streamlines are elongated, and the core region becomes broadly stagnated. Furthermore, the axes of the streamlines are changed, which is due to the retarding effect of the Lorentz force. In addition, the flow strength displays maximum at $\gamma = \pi/4$ rad in this case, then, it decreases when γ reaches $\pi/6$ rad. This phenomenon is different from the previous result for pure free convection; hence, a considerable interaction between the buoyant and the magnetic forces is evidently caused by the tilting, as the magnitude of the Lorentz force in the x and y directions is subjected to the inclination angle.

4.2 Effect of the orientation of a magnetic field without radiation

Hydromagnetic flow in a horizontal enclosure ($\gamma = \pi/2$ rad) under a uniform magnetic field is studied. The changes in the flow and thermal field based on the orientation of an external magnetic field, which varies from 0 to 2π radians, are investigated in the absence of the thermal radiation. Assuming constant buoyant action, Gr is fixed as 10^6.

The source terms caused by the Lorentz force in Eqs. (10) & (11) are such that they are function of $\sin^2\lambda$ and $\cos\lambda\sin\lambda$ as well as $\cos^2\lambda$, which have the common period of π radians. Thus the numerical simulation is conducted with directional variation of a magnetic field applied from $\lambda = 0$ to π rad on account of the phase difference of π radians.

In Fig. 4, thermo-fluidic behaviour in an enclosure is displayed as to the slanted angle of a magnetic field when Ha = 50. The flow intensity varies in accordance with the change of λ and it becomes strongest as $\lambda = 3\pi/4$ rad. This phenomenon can be explained from the flow

retardation induced by direct interaction between the magnetic field and the velocity component perpendicular to the direction of the magnetic field. As for streamlines, the orientation of a magnetic field affects the elongation of streamlines. A uni-cellular inner core is formed along with a transverse magnetic field. Following the change in λ, the inner core gets a multi-cellular structure accompanying the elongation of streamlines at the central region. In terms of the thermal field, the tilting of isotherms is most severe with a vertical magnetic field.

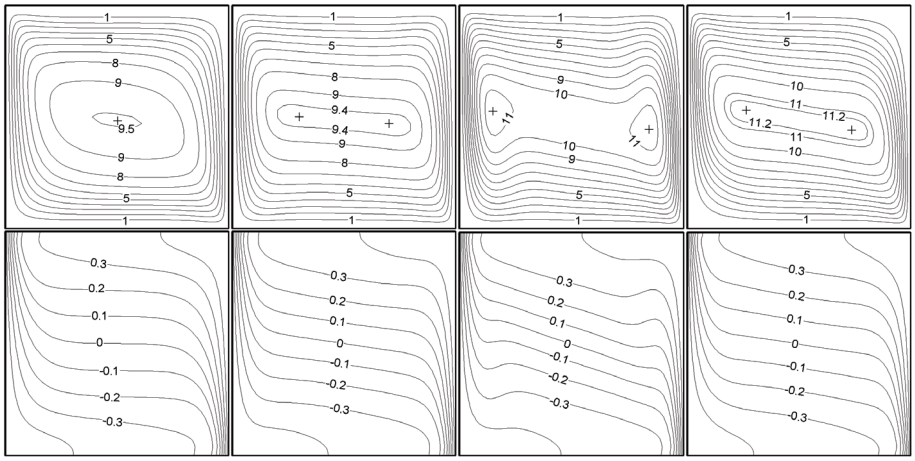

Fig. 4. Streamlines and isotherms for Gr = 10^6 and Ha = 50: (a) λ = 0, π and 2π; (b) λ = π/4 and 5π/4; (c) λ = π/2 and 3π/2; (d) λ = 3π/4 and 7π/4 radians

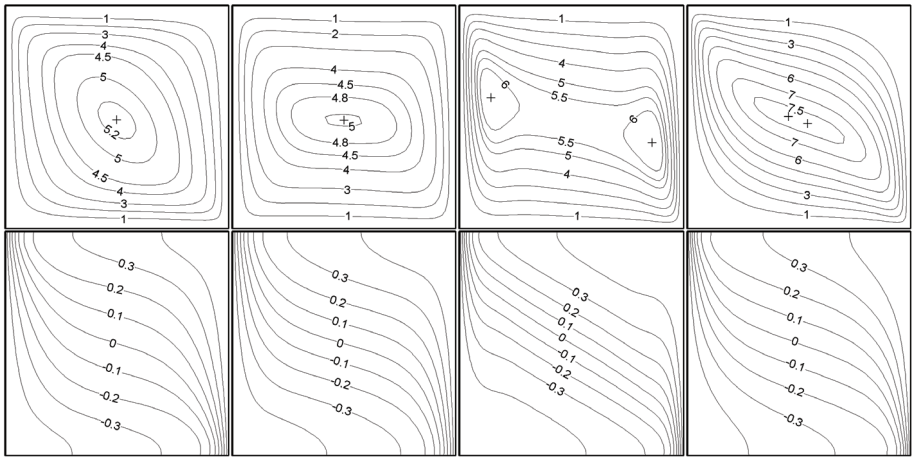

Fig. 5. Streamlines and isotherms for Gr = 10^6 and Ha = 100: (a) λ = 0, π and 2π; (b) λ = π/4 and 5π/4; (c) λ = π/2 and 3π/2; (d) λ = 3π/4 and 7π/4 radians

The changes in flow and thermal fields together with λ are illustrated in Fig. 5, in the case of a strong magnetic field, i.e., Ha = 100. The tendency in the variation of flow and thermal fields influenced by λ, seems to be similar to that for the prior case. A multi-cellular core structure, however, start to appear at the later stage comparing with the case of Ha = 50; in contrast a uni-cellular core structure is recovered at the earlier stage. It is inferred that stronger magnetic field plays a role to suppress the transition of the inner core structure as λ varies 0 to $\pi/2$ radians. Inclination of isotherms is obvious than Fig. 4. With a vertically permeated magnetic field, the inclination of isotherms is most conspicuous.

4.3 Effect of combined radiation and a magnetic field

Computation is carried out for free convection of an electrically conducting fluid in a square enclosure encompassed with radiatively active walls in the presence of a vertically assigned magnetic field parallel to the gravity. In that case, γ is fixed as $\pi/2$ rad so that λ is - $\pi/2$ rad. Radiation-affected temperature and buoyant flow fields in a square enclosure are demonstrated with Gr = 2×10^6, in the absence of an external magnetic field, i.e., Ha = 0, as presented in Fig. 6 (a). The radiative interaction between the hot and cold walls is significant so that the colder region is extended further into the mid-region. The temperature gradients at the adiabatic walls are steeper owing to the increased interaction by means of the surface radiation. The flow field displays a multi-cellular structure, and the inner core consists of two convective rolls in upper and lower halves, respectively.

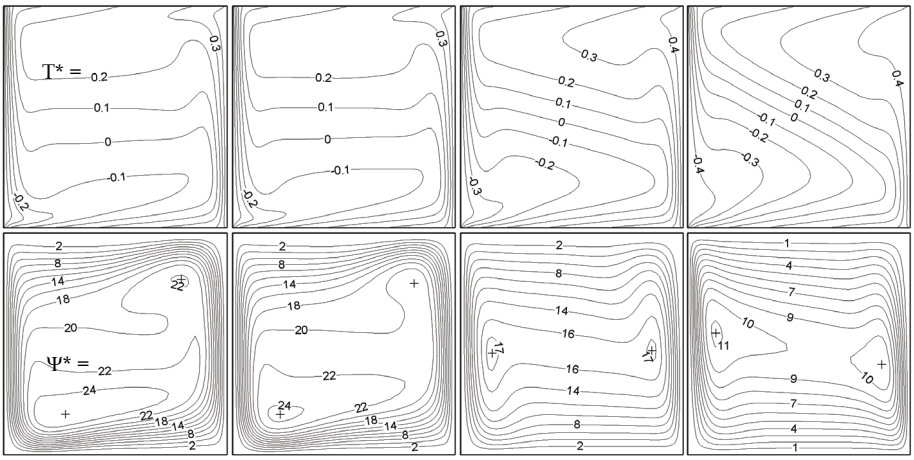

(a) (b) (c) (d)

Fig. 6. Isotherm and streamline contours with Gr = 2×10^6: (a) Ha = 0, (b) Ha = 10, (c) Ha = 50 and (d) Ha = 100

It is seen that for a weak magnetic field (Ha = 10), as shown in Fig. 6 (b), the isotherms and streamlines are almost similar to those in the absence of an external magnetic field, i.e., Ha = 0. The flow field becomes less intensive a little bit than that corresponding to the streamline plot in Fig. 6 (a). As a relatively strong magnetic field is applied, i.e., Ha = 50, the thermal and flow fields are considerably changed as depicted in Fig. 6 (c). The streamlines are elongated laterally and the axis of the streamline is slanted. The former convective roll at

the lower left part of the enclosure moves upward. On the contrary the convective roll which was at the upper right region moves downward as to increase in the strength of a magnetic field applied. In the case of the thermal field, severe temperature gradients caused by the surface radiation are maintained at adiabatic top and bottom walls. In mid-region the tilting of isotherms coincides with steeper temperature gradient observed by in-between distance of isotherms getting narrower. These tendencies are preserved until Ha reaches 100, as illustrated in Fig. 6 (d). Besides such typical influence of a magnetic field as the tilting of isotherms and streamlines, appears to be emphasised with the suppression of convection in an enclosure.

Gr	Radiation	Ha	Left cold wall		Right hot wall		$\overline{Nu}^{T}$
			$\overline{Nu}^{C}$	$\overline{Nu}^{R}$	$\overline{Nu}^{C}$	$\overline{Nu}^{R}$	
2×10^4	Without	0	2.523	0.000	2.523	0.000	2.523
		10	2.220	0.000	2.220	0.000	2.220
		50	1.118	0.000	1.118	0.000	1.118
		100	1.116	0.000	1.116	0.000	1.116
	With	0	4.049	36.733	2.105	38.678	40.783
		10	3.754	36.759	1.874	38.641	40.513
		50	3.021	36.841	1.368	38.494	39.862
		100	2.997	36.846	1.357	38.487	39.843
2×10^5	Without	0	5.090	0.000	5.090	0.000	5.090
		10	4.983	0.000	4.983	0.000	4.983
		50	2.997	0.000	2.997	0.000	2.997
		100	1.454	0.000	1.454	0.000	1.454
	With	0	6.138	36.486	3.639	38.987	42.624
		10	5.986	36.513	3.530	38.970	42.499
		50	4.083	36.704	2.068	38.721	40.787
		100	3.174	36.808	1.446	38.537	39.982
2×10^6	Without	0	9.904	0.000	9.904	0.000	9.904
		10	9.863	0.000	9.863	0.000	9.863
		50	8.891	0.000	8.891	0.000	8.891
		100	6.640	0.000	6.640	0.000	6.640
	With	0	10.413	36.047	6.946	39.514	46.460
		10	10.339	36.073	6.914	39.499	46.412
		50	9.025	36.313	6.050	39.289	45.338
		100	6.699	36.531	4.178	39.054	43.230

Table 1. Nusselt numbers estimated

The rate of heat transfer across the enclosure is attained by evaluating the conductive, radiative, and total average Nusselt numbers, i.e., $\overline{Nu}^{C}$, $\overline{Nu}^{R}$, and $\overline{Nu}^{T}$, respectively, at the hot and cold walls, and tabulated in Table 1 for various combinations of parameters. From this table it can be demonstrated that the introduction of a magnetic field suppresses the convection in the enclosure. With the thermal radiation getting involved in, the radiative contribution to the combined heat transfer is predominant at both hot and cold walls. In addition the convective contribution to the combined heat transfer at the cold wall is always larger than that at the hot wall disregarding the Grashof number and the radiation effect.

5. Conclusions

Free convection in a two-dimensional enclosure filled with an electrically conducting fluid in the presence of an external magnetic field was investigated numerically. The effects of the controlling parameters on the thermally driven hydromagnetic flows have been scrutinised.
In the first place the changes in the buoyant flow patterns and temperature distributions due to the tilting of the enclosure were examined neglecting thermal radiation. In general terms, the effect of the tilting angle on the flow patterns and associated heat transfer was found to be considerable. The variation of flow strength was affected by the orientation of the cavity with imposition of the magnetic field because the effective electromagnetic retarding force in each flow direction was subjected closely to the inclination angle. The flow structure and the temperature field were enormously affected by the strength of the magnetic field, regardless of the tilting angle.
Secondly the flow and thermal field variation was investigated in terms of the orientation of an external magnetic field. The flow intensity and structure varied in accordance with the change of the direction of an external magnetic field. The flow retardation appeared by direct interaction between the magnetic field and the velocity component perpendicular to the direction of the magnetic field. In terms of the thermal field, the tilting of isotherms was observed.
Finally the effects of combined radiation and a magnetic field on the convective flow and heat transfer characteristics of an electrically conducting fluid were investigated. It was concluded that the radiation was the dominant mode of heat transfer and surpassed convective heat transfer so that it played an important role in developing the hydromagnetic free convective flow in a differentially heated enclosure.
As a consequence, all the numerical analyses so far have been subjected to the rectangular enclosure. Hence the future studies are supposed to be related to the general geometries containing an electrically conducting fluid with the permeation of an external magnetic field as well as the participation in radiation.

6. Acknowledgment

This work is partly supported by KETEP (Korea Institute of Energy Technology Evaluation and Planning) under the Ministry of Knowledge Economy, Korea (2008-E-AP-HM-P-19-0000).

7. References

Bessaih, R.; Kadja, M. & Marty, Ph. (1999). Effect of wall electrical conductivity and magnetic field orientation on liquid metal flow in a geometry similar to the horizontal Bridgman configuration for crystal growth. *Int. J. Heat Mass Transfer*, Vol.42, pp. 4345-4362

Bian, W.; Vasseur, P., Bilgen, E. & Meng, F. (1996). Effect of an electromagnetic field on natural convection in an inclined porous layer. *Int. J. Heat and Fluid Flow*, Vol.17, pp. 36-44

Chai, J. C.; Lee, H. S. & Patankar, S. V. (1994). Finite-volume method for radiation heat transfer. *J. Thermophysics and Heat Transfer*, Vol.8, pp. 419-425

Chamkha, A. J. (2000). Thermal radiation and buoyancy effects on hydromagnetic flow over an accelerating permeable surface with heat source or sink. *Int. J. Engng Sci.*, Vol.38, pp. 1699-1712

Fusegi, T. & Farouk, B. (1989). Laminar and turbulent natural convection-radiation interactions in a square enclosure filled with a nongray gas. *Numer. Heat Transfer A*, Vol.15, pp. 303-322

Ghaly, A. Y. (2002). Radiation effects on a certain MHD free-convection flow. *Chaos, Solitons and Fractals*, Vol.13, pp. 1843-1850

Hua, T. Q. & Walker, J. S. (1995). MHD flow in rectangular ducts with inclined non-uniform transverse magnetic field. *Fusion Engineering and Design*, Vol.27, pp. 703-710

Kolsi, L.; Abidi, A., Borjini, M. N., Daous, N. & Aissia, H. B. (2007). Effect of an external magnetic field on the 3-D unsteady natural convection in a cubical enclosure. *Numer. Heat Transfer A*, Vol.51, pp. 1003-1021

Larson, D. W. & Viskanta, R. (1976). Transient combined laminar free convection and radiation in a rectangular enclosure. *J. Fluid Mech.*, Vol.78, pp. 65-85

Mahmud, S. & Fraser, R. A. (2002). Analysis of mixed convection-radiation interaction in a vertical channel: entropy generation. *Exergy, an Internal Journal*, Vol.2, pp. 330-339

Ozoe, H. & Okada, K. (1989). The effect of the direction of the external magnetic field on the three-dimensional natural convection in a cubical enclosure. *Int. J. Heat Mass Transfer*, Vol.32, pp. 1939-1954

Patankar, S. V. (1980). *Numerical Heat Transfer and Fluid Flow*, Hemisphere, McGraw-Hill, Washington, DC

Raptis, A.; Perdikis, C. & Takhar, H. S. (2004). Effect of thermal radiation on MHD flow. *Applied Mathematics and Computation*, Vol.153, pp. 645-649

Rudraiah, N.; Barron, R. M., Venkatachalappa, M. & Subbaraya, C. K. (1995). Effect of a magnetic field on free convection in a rectangular enclosure. *Int. J. Engng Sci.*, Vol.33, pp. 1075-1084

Seddeek, M. A. (2002). Effects of radiation and variable viscosity on a MHD free convection flow past a semi-infinite flat plate with an aligned magnetic field in the case of unsteady flow. *Int. J. Heat Mass Transfer*, Vol.45, pp. 931-935

Seki, M.; Kawamura, H. & Sanokawa, K. (1979). Natural convection of mercury in a magnetic field parallel to the gravity. *J. Heat Transfer*, Vol.101, pp. 227-232

Sivasankaran, S. & Ho, C. J. (2008). Effect of temperature dependent properties on MHD convection of water near its density maximum in a square cavity. *Int. J. Therm. Sci.*, Vol.47, pp. 1184-1194

Thakur, S. & Shyy, W. (1993). Some implementational issues of convection schemes for finite-volume formulations. *Numer. Heat Transfer B*, Vol.24, pp. 31-55

Wang, Q. W.; Zeng, M., Huang, Z. P., Wang, G. & Ozoe, H. (2007). Numerical investigation of natural convection in an inclined enclosure filled with porous medium under magnetic field. *Int. J. Heat Mass Transfer*, Vol.50, pp. 3684-3689

Part 2

Heat Conduction

7

Transient Heat Conduction in Capillary Porous Bodies

Nencho Deliiski
University of Forestry
Bulgaria

1. Introduction

Capillarity is a well known phenomenon in physics and engineering. Porous materials such as soil, sand, rocks, mineral building elements (cement stone or concrete, gypsum stone or plasterboards, bricks, mortar, etc.), biological products (wood, grains, fruit, etc.) have microscopic capillaries and pores which cause a mixture of transfer mechanisms to occur simultaneously when subjected to heating or cooling.
In the most general case each capillary porous material is a peculiar system characterized by the extremely close contact of three intermixed phases: gas (air), liquid (water) and solid. Water may appear in them as physically bounded water and capillary water (Chudinov, 1968, Twardowski, Richinski & Traple, 2006). Both the bounded water and the capillary water can be found in liquid or hard aggregate condition.
Physically bounded water co-operates with the surface of a solid phase of the materials and has different properties than the free water. The maximum amount of bounded water in porous materials corresponds to the maximal hygroscopicity, i.e. moisture absorbed by the material at the 100% relative vapour pressure. The maximum hygroscopicity of the biological capillary porous bodies is known as fibre saturation point. Capillary water fills the capillary tube vessels, small pores or sharp, narrow indentions of bigger pores. It is not bound physically and is called free water. Free water is not in the same thermodynamic state as liquid water: energy is required to overcome the capillary forces, which arise between the free water and the solid phase of the materials.
For the optimization of the heating and/or cooling processes in the capillary porous bodies, it is required that the distribution of the temperature and moisture fields in the bodies and the consumed energy for their heating at every moment of the process are known. The intensity of heating or cooling and the consumption of energy depend on the dimensions and the initial temperature and moisture content of the bodies, on the texture and micro-structural features of the porous materials, on their anisotropy and on the content and aggregate condition of the water in them, on the law of change and the values of the temperature and humidity of the heating or cooling medium, etc. (Deliiski, 2004, 2009).
The correct and effective control of the heating and cooling processes is possible only when its physics and the weight of the influence of each of the mentioned above as well as of many other specific factors for the concrete capillary porous body are well understood. The summary of the influence of a few dozen factors on the heating or cooling processes of the

capillary porous bodies is a difficult task and its solution is possible only with the assistance of adequate for these processes mathematical models.

There are many publications dedicated to the modelling and computation of distribution of the temperature and moisture content in the subjected to drying capillary porous bodies at different initial and boundary conditions. Drying is fundamentally a problem of simultaneous heat and mass transfer under transient conditions. Luikov (1968) and later Whitaker (1977) defined a coupled system of non-linear partial differential equations for heat and mass transfer in porous bodies. Practically all drying models of capillary porous bodies are based on these equations and include a description of the specific initial and boundary conditions, as well as of thermo- and mass physical characteristics of the subjected to drying bodies (Ben Nasrallah & Perre, 1988, Doe, Oliver & Booker, 1994, Ferguson & Lewis, 1991, Kulasiri & Woodhead 2005, Murugesan et al., 2001, Zhang, Yang & Liu 1999, etc.).

As a rule the non-defective drying is a very long continuous process, which depending on the dimensions of the bodies and their initial moisture content can last many hours, days or even months. However there are a lot of cases in the practice where the capillary porous bodies are subjected to a relatively short heating and/or cooling, as a result of which a significant change in their temperature and a relatively small change in their moisture content occurs. A typical example for this is the change in temperature in building elements under the influence of the changing surrounding temperature during the day and night or during fire.

Widely used during the production of veneer, plywood or furniture parts technological processes of thermal treatment of wood materials (logs, lumber, etc.) with the aim of plasticizing or ennoblement of the wood are characterized by a controlled change in the temperature in the volume of the processed bodies, without it being accompanied by significant changes in their moisture content. In these as well as in other analogous cases of heating and/or cooling of capillary porous bodies the calculation of the non-stationary change in the temperature field in the bodies can be carried out with the assistance of models, which do not take into account the change in moisture content in the bodies. The number of such published models is very limited, especially in comparison to the existing large variety of drying models.

Axenenko (1995) presents and uses a 1D model for the computation of the temperature change in the exposed to fire gypsum plasterboards. According to the author, after obtaining the temperature fields inside the plasterboard, changes in the material properties and temperature deformations can be calculated and used as initial data for the study of the structural behaviour of the entire plasterboard assembly.

Considerate contribution to the calculation of the non-stationary distribution of the temperature in frozen and non-frozen logs and to the duration of their heating has been made by H. P. Steinhagen. For this purpose, he, alone, (Steinhagen, 1986, 1991) or with co-authoring (Steinhagen, Lee & Loehnertz, 1987), (Steinhagen & Lee, 1988) has created and solved a 1-dimensional, and later a 2-dimensional (Khattabi & Steinhagen, 1992, 1993) mathematical model, whose application is limited only for $u \geq 0{,}3$ kg.kg^{-1}. The development of these models is dominated by the usage of the method of enthalpy, which is rather more complicated than its competing temperature method.

The models contain two systems of equations, one of which is used for the calculation of the change in temperature at the axis of the log, and the other – for the calculation of the temperature distribution in the remaining points of its volume. The heat energy, which is

needed for the melting of the ice, which has been formed from the freezing of the hygroscopically bounded water in the wood, although the specific heat capacity of that ice is comparable by value to the capacity of the frozen wood itself (Chudinov, 1966), has not been taken into account. These models assume that the fibre saturation point is identical for all wood species and that the melting of the ice, formed by the free water in the wood, occurs at 0^{o}C. However, it is known that there are significant differences between the fibre saturation point of the separate wood species and that the dependent on this point quantity of ice, formed from the free water in the wood, thaws at a temperature in the range between -2°C and -1°C (Chudinov, 1968).

This paper presents the creation and numerical solutions of the 3D, 2D, and 1D mathematical models for the transient non-linear heat conduction in anisotropic frozen and non-frozen prismatic and cylindrical capillary porous bodies, where the physics of the processes of heating and cooling of bodies is taken into account to a maximum degree and the indicated complications and incompleteness in existing analogous models have been overcome. The solutions include the non-stationary temperature distribution in the volume of the bodies for each $u \geq 0$ kg.kg^{-1} at every moment of their heating and cooling at prescribed surface temperature, equal to the temperature of the processing medium or during the time of convective thermal processing.

2. Nomenclature

a = temperature conductivity (m^2.s^{-1})
b = width (m)
c = specific heat capacity (W.kg^{-1}.K^{-1})
d = thickness (m)
D = diameter (m)
L = length (m)
q = internal source of heat, W.m^{-3}.s^{-1}
R = radius (m)
r = radial coordinate: $0 \leq r \leq R$ (m)
T = temperature (K)
t = temperature (°C): $t = T - 271{,}15$
u = moisture content (kg.kg^{-1} = %/100)
x = coordinate on the thickness: $0 \leq x \leq d/2$ (m)
y = coordinate on the width: $0 \leq y \leq b/2$ (m)
z = longitudinal coordinate: $0 \leq z \leq L/2$ (m)
α = heat transfer coefficient between the body and the processing medium (W.m^{-2}.K^{-1})
β = coefficients in the equations for determining of λ
γ = coefficients in the equations for determining of λ
λ = thermal conductivity (W.m^{-1}.K^{-1})
ρ = density (kg.m^{-3})
τ = time (s)
φ = angular coordinate (rad)
Δr = distance between mesh points in space coordinates for the cylinders (m)
Δx = distance between mesh points in space coordinates for the prisms (m)
$\Delta\tau$ = interval between time levels (s)

Subscripts:

a = anatomical direction
b = basic (for density, based on dry mass divided to green volume)
bw = bound water
c = center (of the body)
cr = cross sectional to the fibers
d = dimension
e = effective (for specific heat capacity)
fsp = fiber saturation point
fw = free water
i = nodal point in radial direction for the cylinders: 1, 2, 3, …, (R/Δr)+1
or in the direction along the thickness for the prisms: 1, 2, 3, …, [d/(2Δx)]+1
j = nodal point in the direction along the prisms' width: 1, 2, 3, …, [b/(2Δx)]+1
k = nodal point in longitudinal direction: 1, 2, 3, …, [L/(2Δr)]+1 for the cylinders
or 1, 2, 3, …, [L/(2Δx)]+1 for the prisms
m = medium
nfw = non-frozen water
0 = initial (at 0°C for λ)
p = parallel to the fibers
p/cr = parallel to the cross sectional
p/r = parallel to the radial
r = radial direction (radial to the fibers)
t = tangential direction (tangential to the fibers)
w = wood
x = direction along the thickness
y = direction along the width
z = longitudinal direction

Superscripts:

n = time level 0, 1, 2, …
20 = 20°C

3. Mechanism of heat distribution in capillary porous bodies

During the heating or cooling of the capillary porous materials along with the purely thermal processes, a mass-exchange occurs between the processing medium and the materials. The values of the mass diffusion in these materials are usually hundreds of times smaller than the values of their temperature conductivity. These facts determine a not so big change in defunding mass in the materials, which lags significantly from the distribution of heat in them during the heating or cooling. This allows to disregarding the exchange of mass between the materials and the processing medium and the change in temperature in them to be viewed as a result of a purely thermo-exchange process, where the heat in them is distributed only through thermo-conductivity.
Because of this the mechanism of heat distribution in capillary porous bodies can be described by the equation of heat conduction (also known as the equation of Fourier-Kirchhoff). Its most compact form is as follows:

$$c\rho\frac{\partial T}{\partial \tau} = -\mathrm{div}(\lambda \mathrm{grad} T) \pm q \,. \tag{1}$$

This form holds for each coordinate system and for each processing medium – both for immobile and mobile.
In the most general case c, ρ and λ of the capillary porous bodies depend on T and u, i.e. in equation (1) the functional dependencies participate $c(T,u)$, $\rho(T,u)$ and $\lambda(T,u)$.
As it was described in the introduction, the water contained in these bodies can be found in liquid or hard aggregate condition. It is known that the specific heat capacity of the liquid (non-frozen) water at 0°C is equal to 4237 $J.kg^{-1}.K^{-1}$, and the specific heat capacity of ice is 2261 $J.kg^{-1}.K^{-1}$, i.e. almost two times smaller (Chudinov, 1966, 1984). Because of this, the frozen water in capillary porous bodies causes smaller values of c in comparison to the case, when the water in them is completely liquid.
The ice in capillary porous bodies can be formed from the freezing of higroscopically bounded water or of the free water in them. It is widely accepted that the phase transition of water into ice and vice versa to be expressed with the help of the so-called "latent heat" in the ice of the frozen body. When solving problems, connected to transient heat conduction in frozen bodies, it makes sense to include the latent heat in the so-called effective specific heat capacity c_e (Chudinov, 1966), which is equal to the sum of the own specific heat capacity of the body c and the specific heat capacity of the ice, formed in them from the freezing of the hygroscopically bounded water and of the free water, i.e.

$$c_e = c + c_{bw} + c_{fw} \,. \tag{2}$$

When solving the problems, it must be taken into consideration that the formation and thawing of both types of ice in these bodies takes place at different temperature ranges. Because of this for each of the diapasons in equation (2) the sum of c with c_{bw} and/or c_{fw} (shown below as an example) participates. When modeling processes of transient heat conduction in anisotropic capillary porous bodies it is also necessary to take into consideration that the thermal conductivity of these bodies λ apart from T and u depends additionally on the direction of the influencing heat flux towards the anatomic directions of the body – radial, tangential and longitudinal to the fibers.

4. Mathematical models for transient heat conduction in prismatic bodies

If it is assumed, that the anatomical directions of a prismatic capillary porous body coincide with the coordinate axes, in the absence of an internal source of heat q in equation (1), the following form of this equation in the Cartesian coordinate system is obtained:

$$\begin{aligned} c_e(T,u)\rho(T,u)\frac{\partial T(x,y,z,\tau)}{\partial \tau} = \frac{\partial}{\partial x}\left[\lambda_x(T,u)\frac{\partial T(x,y,z,\tau)}{\partial x}\right] + \\ + \frac{\partial}{\partial y}\left[\lambda_y(T,u)\frac{\partial T(x,y,z,\tau)}{\partial y}\right] + \frac{\partial}{\partial z}\left[\lambda_z(T,u)\frac{\partial T(x,y,z,\tau)}{\partial z}\right] \end{aligned} \,. \tag{3}$$

After the differentiation of the right side of equation (3) on the spatial coordinates x, y, and z, excluding the arguments in the brackets for shortening of the record, the following mathematical model of the process of non-stationary heating or cooling (further calling thermal processing) of the capillary porous bodies with prismatic form is obtained:

$$c_e\rho\frac{\partial T}{\partial \tau}=\lambda_r\frac{\partial^2 T}{\partial x^2}+\frac{\partial \lambda_r}{\partial T}\left(\frac{\partial T}{\partial x}\right)^2+ \\ +\lambda_t\frac{\partial^2 T}{\partial y^2}+\frac{\partial \lambda_t}{\partial T}\left(\frac{\partial T}{\partial y}\right)^2+\lambda_p\frac{\partial^2 T}{\partial z^2}+\frac{\partial \lambda_p}{\partial T}\left(\frac{\partial T}{\partial z}\right)^2 \tag{4}$$

with an initial condition

$$T(x,y,z,0)=T_0 \tag{5}$$

and boundary conditions:

- during the time of thermal processing of the prisms at their prescribed surface temperature, equal to the temperature of the processing medium:

$$T(0,y,z,\tau)=T(x,0,z,\tau)=T(x,y,0,\tau)=T_m(\tau), \tag{6}$$

- during the time of convective thermal processing of the prisms:

$$\frac{\partial T(0,y,z,\tau)}{\partial x}=-\frac{\alpha_r(0,y,z,\tau)}{\lambda_r(0,y,z,\tau)}\left[T(0,y,z,\tau)-T_m(\tau)\right], \tag{7}$$

$$\frac{\partial T(x,0,z,\tau)}{\partial y}=-\frac{\alpha_t(x,0,z,\tau)}{\lambda_t(x,0,z,\tau)}\left[T(x,0,z,\tau)-T_m(\tau)\right], \tag{8}$$

$$\frac{\partial T(x,y,0,\tau)}{\partial z}=-\frac{\alpha_p(x,y,0,\tau)}{\lambda_p(x,y,0,\tau)}\left[T(x,y,0,\tau)-T_m(\tau)\right]. \tag{9}$$

The system of equations (4) ÷ (9) presents a 3D mathematical model, which describes the change in temperature in the volume of capillary porous bodies with prismatic form during the time of their thermal processing at corresponding initial and boundary conditions.
When the length of the subjected to thermal processing body exceeds its thickness by at least $(2\div 2,5)\frac{2\lambda_p}{\lambda_r+\lambda_t}$ times, then the heat transfer through the frontal sides of the body can be neglected, because it does not influence the change in temperature in the cross-section, which is equally distant from the frontal sides. In these cases for the calculation of the change in T in this section (i.e. only along the coordinates x and y) the following 2D model can be used:

$$c_e\rho\frac{\partial T}{\partial \tau}=\lambda_r\frac{\partial^2 T}{\partial x^2}+\frac{\partial \lambda_r}{\partial T}\left(\frac{\partial T}{\partial x}\right)^2+\lambda_t\frac{\partial^2 T}{\partial y^2}+\frac{\partial \lambda_t}{\partial T}\left(\frac{\partial T}{\partial y}\right)^2 \tag{10}$$

with an initial condition

$$T(x,y,0)=T_0 \tag{11}$$

and boundary conditions:

- for thermal processing of the prisms at their prescribed surface temperature:

$$T(0,y,\tau)=T(x,0,\tau)=T_{\mathrm{m}}(\tau), \tag{12}$$

- for convective thermal processing of the prisms:

$$\frac{\partial T(0,y,\tau)}{\partial x}=-\frac{\alpha_{\mathrm{r}}(0,y,\tau)}{\lambda_{\mathrm{r}}(0,y,\tau)}\left[T(0,y,\tau)-T_{\mathrm{m}}(\tau)\right], \tag{13}$$

$$\frac{\partial T(x,0,\tau)}{\partial y}=-\frac{\alpha_{\mathrm{t}}(x,0,\tau)}{\lambda_{\mathrm{t}}(x,0,\tau)}\left[T(x,0,\tau)-T_{\mathrm{m}}(\tau)\right]. \tag{14}$$

When the thickness of the body is smaller than its width by at least $2\div 3$ times, and than its length by at least $(2\div 2,5)\frac{\lambda_{\mathrm{p}}}{\lambda_{\mathrm{r}}}$ times, then the non-stationary change in T, for example along the radial direction x of the body, coinciding with its thickness in the section, equally distant from the frontal sides, can be calculated using the following 1D model:

$$c_{\mathrm{e}}\rho\frac{\partial T}{\partial\tau}=\lambda_{\mathrm{r}}\frac{\partial^2 T}{\partial x^2}+\frac{\partial\lambda_{\mathrm{r}}}{\partial T}\left(\frac{\partial T}{\partial x}\right)^2 \tag{15}$$

with an initial condition

$$T(x,0)=T_0 \tag{16}$$

and boundary conditions:

- for thermal processing of the prisms at their prescribed surface temperature:

$$T(0,\tau)=T_{\mathrm{m}}(\tau), \tag{17}$$

- for convective thermal processing of the prisms:

$$\frac{\partial T(0,\tau)}{\partial x}=-\frac{\alpha_{\mathrm{r}}(0,\tau)}{\lambda_{\mathrm{r}}(0,\tau)}\left[T(0,\tau)-T_{\mathrm{m}}(\tau)\right]. \tag{18}$$

5. Mathematical models for transient heat conduction in cylindrical bodies

The mechanism of the heat distribution in the volume of cylindrical capillary porous bodies during their thermal processing can be described by the following non-linear differential equation with partial derivatives, which is obtained from the equation (3) after passing in it from rectangular to cylindrical coordinates (Deliiski, 1979)

$$\begin{aligned}c_{\mathrm{e}}(T,u)\rho(T,u)\frac{\partial T(r,z,\tau)}{\partial\tau}&=\lambda_{\mathrm{r}}(T,u)\left[\frac{\partial^2 T(r,z,\tau)}{\partial r^2}+\frac{1}{r^2}\frac{\partial^2 T(r,z,\tau)}{\partial\phi^2}+\frac{1}{r}\frac{\partial T(r,z,\tau)}{\partial r}\right]+\\&+\frac{\partial\lambda_{\mathrm{r}}(T,u)}{\partial T}\left\{\left[\frac{\partial T(r,z,\tau)}{\partial r}\right]^2+\frac{1}{r^2}\left[\frac{\partial T(r,z,\tau)}{\partial\phi}\right]^2\right\}+\lambda_{\mathrm{p}}(T,u)\frac{\partial^2 T(r,z,\tau)}{\partial z^2}+\frac{\partial\lambda_{\mathrm{p}}(T,u)}{\partial T}\left[\frac{\partial T(r,z,\tau)}{\partial z}\right]^2\end{aligned}. \tag{19}$$

If heating or cooling cylindrical bodies of material, which is homogenous in their cross section, the distribution of T in their volume does not depend on φ, but only depends on r and z. Consequently, when excluding the participants in the equation (19), containing φ and when also omitting the arguments in the brackets for the shortening of the record, the following 2D mathematical model is obtained, which describes the change of temperature in the volume of capillary porous bodies with cylindrical form:

$$c_{\mathrm{e}}\rho\frac{\partial T}{\partial \tau}=\lambda_{\mathrm{r}}\left(\frac{\partial^2 T}{\partial r^2}+\frac{1}{r}\frac{\partial T}{\partial r}\right)+\frac{\partial \lambda_{\mathrm{r}}}{\partial T}\left(\frac{\partial T}{\partial r}\right)^2+ \\ +\lambda_{\mathrm{p}}\frac{\partial^2 T}{\partial z^2}+\frac{\partial \lambda_{\mathrm{p}}}{\partial T}\left(\frac{\partial T}{\partial z}\right)^2 \tag{20}$$

with an initial condition

$$T(r,z,0)=T_0 \tag{21}$$

and boundary conditions:

- for thermal processing of the bodies at their prescribed surface temperature:

$$T(0,z,\tau)=T(r,0,\tau)=T_{\mathrm{m}}(\tau), \tag{22}$$

- for convective thermal processing of the bodies:

$$\frac{\partial T(0,z,\tau)}{\partial r}=-\frac{\alpha_{\mathrm{r}}(0,z,\tau)}{\lambda_{\mathrm{r}}(0,z,\tau)}\left[T(0,z,\tau)-T_{\mathrm{m}}(\tau)\right], \tag{23}$$

$$\frac{\partial T(r,0,\tau)}{\partial z}=-\frac{\alpha_{\mathrm{p}}(r,0,\tau)}{\lambda_{\mathrm{p}}(r,0,\tau)}\left[T(r,0,\tau)-T_{\mathrm{m}}(\tau)\right]. \tag{24}$$

When the length of the body exceeds its diameter by at least $(2\div 2,5)\frac{\lambda_{\mathrm{p}}}{\lambda_{\mathrm{r}}}$ times, then the heat transfer through the frontal sides of the body can be neglected, because it does not influence the change in temperature of its cross section, which is equally distant from the frontal sides. In such cases, for the calculation of the change in T only along the coordinate r of this section, the following 1D model can be used:

$$c_{\mathrm{e}}\rho\frac{\partial T}{\partial \tau}=\lambda_{\mathrm{r}}\left(\frac{\partial^2 T}{\partial r^2}+\frac{1}{r}\frac{\partial T}{\partial r}\right)+\frac{\partial \lambda_{\mathrm{r}}}{\partial T}\left(\frac{\partial T}{\partial r}\right)^2 \tag{25}$$

with an initial condition

$$T(r,0)=T_0 \tag{26}$$

and with boundary conditions, which are identical to the ones in equations (17) and (18), but with derivative of T along r instead of along x in (18).

6. Transformation of the models for transient heat conduction in suitable form for programming

Analytical solution of mathematical models, which contain non-linear differential equations with partial derivatives in the form of (4) and (20), is practically impossible without significant simplifications of these equations and of their boundary conditions.

For the numerical solution of models with such equations the methods of finite differences or of the finite elements can be used. When the bodies have a correct shape – prismatic or cylindrical, the method of finite differences is preferred, because its implementation requires less computational resources from the computers.

For the numerical solution of the above presented models for transient heat conduction it makes sense to use the explicit form of the finite-difference method, which allows for the exclusion of any simplifications. The large calculation resources of the contemporary computers eliminate the inconvenience, which creates the limitation for the value of the step along the time coordinate $\Delta\tau$ by using the explicit form (refer to equation (47)).

According to the main idea of the finite-difference method, the temperature, which is a uninterrupted function of space and time, is presented using a grid vector, and the derivatives $\frac{\partial T}{\partial x}$, $\frac{\partial T}{\partial y}$, $\frac{\partial T}{\partial z}$ and $\frac{\partial T}{\partial \tau}$ are approximated using the built computational mesh along the spatial and time coordinates through their finite-difference (discrete) analogues.

For this purpose the subjected to thermal processing body, or 1/8 of it in the presence of mirror symmetry towards the other 7/8, is "pierced" by a system of mutually perpendicular lines, which are parallel to the three spatial coordinate axes. The distances between the lines, also called as the step of differentiation, is constant for each coordinate direction (Fig. 1). The knots from 0 to 6 with temperatures accordingly from T_0 to T_6 are centers for the presented and neighboring it volume elements. The length of the sides of the volume element Δx, Δy and Δz are steps of differentiation, the size of which determines the distance between the separate knots of the mesh. The entire time of thermal processing of the body is also separated into definite number n intervals (steps) with equal duration $\Delta\tau$. A volume element of a subjected to thermal processing body used for the solution of equation (4) is shown on Fig. 1, together with its belonging part from the rectangular calculation mesh.

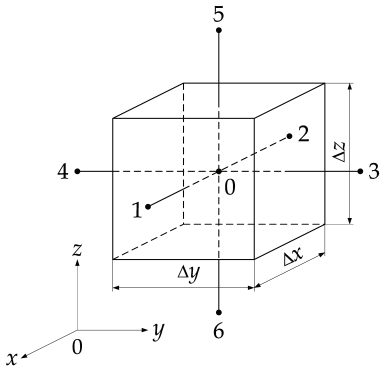

Fig. 1. A volume element of the body with a built on it calculation mesh for the solution of equation (4) using the explicit form of the finite-difference method

As a result of the described procedures, the process for the solution of the non-linear differential equation with partial derivatives (4) is transformed to the solution of the equivalent to it system of linear finite-difference equations, requiring the carrying out of numerous one-type, but not complicated algebraic operations. In the built in the body 3D rectangular mesh, the heat transfer is taken into consideration only along its gradient lines. For each cross point of three mesh lines, called a knot, a finite-difference equation is derived, using which the temperature of this knot is calculated.

Finite-difference equations are obtained by substituting derivatives in the differential equation (4), with their approximate expressions, which are differences between the values of the function in selected knots of the calculation mesh. The temperature in knot 0 with coordinates (x_i, y_j, z_k, τ_n) on Fig. 1 is designated as $T_0 = T^n_{i,j,k}$, and the temperature in neighboring knots accordingly as $T_1 = T^n_{i+1,j,k}$ (knot 1), $T_2 = T^n_{i-1,j,k}$ (knot 2), $T_3 = T^n_{i,j+1,k}$ (knot 3), $T_4 = T^n_{i,j-1,k}$ (knot 4), $T_5 = T^n_{i,j,k+1}$ (knot 5), and $T_6 = T^n_{i,j,k-1}$ (knot 6). For the calculation of temperature T_0 in each following moment of time $(n+1)\Delta\tau$ the values of the temperatures from T_1 to T_6 in the preceding moment $n\Delta\tau$ need to be known.

6.1 Discrete analogues of models for transient heat conduction in prismatic bodies

The transformation of the non-linear differential equation with partial derivatives (4) in its discrete analogue with the help of the explicit form of the finite-difference method is carried out using the shown on Fig. 2 coordinate system for the positioning of the knots of the calculation mesh, in which the distribution of the temperature in a subjected to thermal processing capillary porous body with prismatic form is computed.

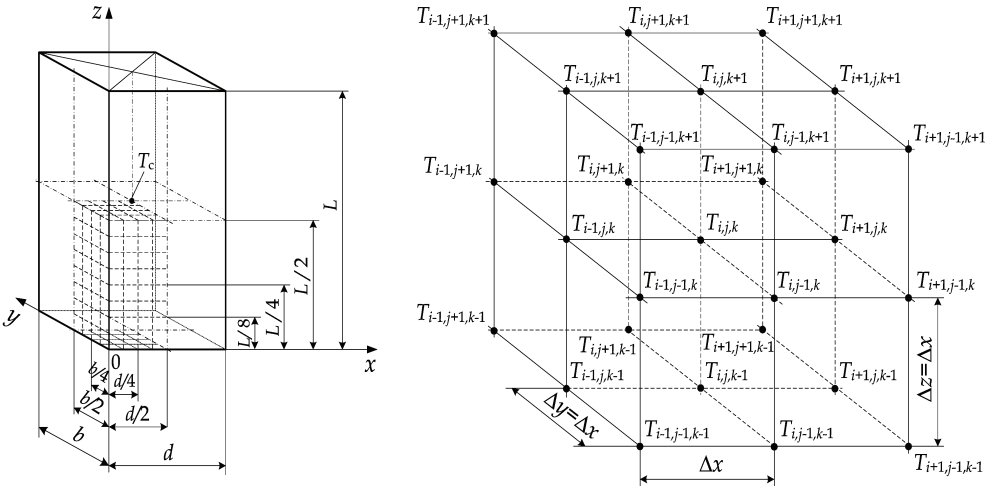

Fig. 2. Positioning of the knots in the calculation mesh on 1/8 of the volume of a subjected to thermal processing prismatic capillary porous body

For the carrying out of the differentiation of λ along T in equation (4), it is necessary to have the function $\lambda(T)$ in the separate anatomical directions of the capillary porous body. For the purpose of determination of subsequent transformations of the models, we accept that

the functions $\lambda_r(T)$, $\lambda_t(T)$ and $\lambda_p(T)$ are linear both for containing ice, as well as for not containing ice bodies and are described with an equation of the kind:

$$\lambda = \lambda_0\gamma\left[1+\beta(T-273,15)\right]. \tag{27}$$

Then after carrying out the differentiation of λ along T in equation (4) and substituting in it with finite differences of the first derivative along the time and the first and second derivatives along the spatial coordinates, the following system of equations is obtained:

$$\begin{aligned} c_e\rho\frac{T_{i,j,k}^{n+1}-T_{i,j,k}^{n}}{\Delta\tau} = {} & \lambda_{0r}\gamma\left\{\left[1+\beta\left(T_{i,j,k}^{n}-273,15\right)\right]\frac{T_{i+1,j,k}^{n}+T_{i-1,j,k}^{n}-2T_{i,j,k}^{n}}{\Delta x^2}+\beta\frac{(T_{i,j,k}^{n}-T_{i-1,j,k}^{n})^2}{\Delta x^2}\right\}+ \\ & +\lambda_{0t}\gamma\left\{\left[1+\beta(T_{i,j,k}^{n}-273,15)\right]\frac{T_{i,j+1,k}^{n}+T_{i,j-1,k}^{n}-2T_{i,j,k}^{n}}{\Delta y^2}+\beta\frac{(T_{i,j,k}^{n}-T_{i,j-1.k}^{n})^2}{\Delta y^2}\right\}+ \\ & +\lambda_{0p}\gamma\left\{\left[1+\beta(T_{i,j,k}^{n}-273,15)\right]\frac{T_{i,j,k+1}^{n}+T_{i,j,k-1}^{n}-2T_{i,j,k}^{n}}{\Delta z^2}+\beta\frac{(T_{i,j,k}^{n}-T_{i,j,k-1}^{n})^2}{\Delta z^2}\right\} \end{aligned} \tag{28}$$

After transformation of the equation (28) it is obtained, that the value of the temperature in whichever knot of the built in the volume of a subjected to thermal processing body 3D mesh at the moment $(n+1)\Delta\tau$ is determined depending on the already computed values for the temperature in the preceding moment $n\Delta\tau$ using the following system of finite differences equations:

$$\begin{aligned} T_{i,j,k}^{n+1} = {} & T_{i,j,k}^{n}+ \\ & +\frac{\gamma\Delta\tau}{c_e\rho}\left\{\begin{aligned} & \frac{\lambda_{0r}}{\Delta x^2}\left[\left[1+\beta\left(T_{i,j,k}^{n}-273,15\right)\right]\left(T_{i+1,j,k}^{n}+T_{i-1,j,k}^{n}-2T_{i,j,k}^{n}\right)+\beta\left(T_{i,j,k}^{n}-T_{i-1,j,k}^{n}\right)^2\right]+ \\ & +\frac{\lambda_{0t}}{\Delta y^2}\left[\left[1+\beta\left(T_{i,j,k}^{n}-273,15\right)\right]\left(T_{i,j+1,k}^{n}+T_{i,j-1,k}^{n}-2T_{i,j,k}^{n}\right)+\beta\left(T_{i,j,k}^{n}-T_{i,j-1,k}^{n}\right)^2\right]+ \\ & +\frac{\lambda_{0p}}{\Delta z^2}\left[\left[1+\beta\left(T_{i,j,k}^{n}-273,15\right)\right]\left(T_{i,j,k+1}^{n}+T_{i,j,k-1}^{n}-2T_{i,j,k}^{n}\right)+\beta\left(T_{i,j,k}^{n}-T_{i,j,k-1}^{n}\right)^2\right] \end{aligned}\right\}. \end{aligned} \tag{29}$$

The initial condition (5) in the 3D mathematical model is presented using the following finite differences equation:

$$T_{i,j,k}^{0} = T_0. \tag{30}$$

The boundary conditions (6) ÷ (9) get the following easy for programming form:

- for thermal processing of the prisms at their prescribed surface temperature:

$$T_{1,j,k}^{n+1} = T_{i,1,k}^{n+1} = T_{i,j,1}^{n+1} = T_m^{n+1}, \tag{31}$$

- for convective thermal processing of the prisms:

$$T_{1,j,k}^{n+1} = \frac{T_{2,j,k}^{n}+G_{1,j,k}T_m^{n+1}}{1+G_{1,j,k}} \quad \text{where} \quad G_{1,j,k} = \frac{\alpha_r\Delta x}{\lambda_{0r}\gamma[1+\beta\left(T_{1,j,k}^{n}-273,15\right)]}, \tag{32}$$

$$T_{i,1,k}^{n+1} = \frac{T_{i,2,k}^{n} + G_{i,1,k} T_{\mathrm{m}}^{n+1}}{1 + G_{i,1,k}} \quad \text{where} \quad G_{i,1,k} = \frac{\alpha_{\mathrm{t}} \Delta x}{\lambda_{0\mathrm{t}} \gamma [1 + \beta (T_{i,1,k}^{n} - 273{,}15)]}, \tag{33}$$

$$T_{i,j,1}^{n+1} = \frac{T_{i,j,2}^{n} + G_{i,j,1} T_{\mathrm{m}}^{n+1}}{1 + G_{i,j,1}} \quad \text{where} \quad G_{i,j,1} = \frac{\alpha_{\mathrm{p}} \Delta x}{\lambda_{0\mathrm{p}} \gamma [1 + \beta (T_{i,j,1}^{n} - 273{,}15)]}. \tag{34}$$

In the boundary conditions (31) ÷ (34) is reflected the requirement for the used for the solution of the models computation environment of FORTRAN, that the knots of the mesh, which are positioned on the corresponding surface of the subjected to thermal processing prism, to be designated with number 1, i.e. $1 \le i \le \mathrm{M}$; $1 \le j \le \mathrm{N}$; $1 \le k \le \mathrm{KD}$ (Dorn & McCracken 1972). Using the system of equations (29) ÷ (34) the distribution of the temperature in subjected to thermal processing prismatic materials can be calculated, whose radial, tangential and parallel to the fibers direction coincide with its coordinate axes x, y and z.
Since the subjected to thermal processing in the practice prismatic materials usually do not have a clear radial or clear tangential sides, but are with partially radial or partially tangential, then in equation (29) instead of the coefficients λ_0 in the observed two anatomical directions their average arithmetic value can be substituted, which determines the thermal conductivity at 0°C cross sectional to the body's fibers $\lambda_{0\mathrm{cr}}$:

$$\lambda_{0\mathrm{cr}} = \frac{\lambda_{0\mathrm{r}} + \lambda_{0\mathrm{t}}}{2}. \tag{35}$$

Also the thermal conductivity at 0°C in the direction parallel to the fibers $\lambda_{0\mathrm{p}}$ can be expressed through $\lambda_{0\mathrm{cr}}$ using the equation

$$\lambda_{0\mathrm{p}} = K_{\mathrm{p/cr}} \lambda_{0\mathrm{cr}}, \tag{36}$$

where the coefficient $K_{\mathrm{p/cr}} = \dfrac{\lambda_{0\mathrm{p}}}{\lambda_{0\mathrm{cr}}}$ depends on the type of the capillary porous material.
For the unification of the calculations it makes sense to use one such step of the calculation mesh along the spatial coordinates $\Delta x = \Delta y = \Delta z$ (refer to Fig. 2). Taking into consideration this condition, and also of equations (35) and (36), the system of equations (29) becomes

$$T_{i,j,k}^{n+1} = T_{i,j,k}^{n} + \frac{\lambda_{0\mathrm{cr}} \gamma \Delta \tau}{c_{\mathrm{e}} \rho \Delta x^2} \left\{ \begin{array}{l} \left[1 + \beta (T_{i,j,k}^{n} - 273{,}15)\right] \\ \left[T_{i+1,j,k}^{n} + T_{i-1,j,k}^{n} + T_{i,j+1,k}^{n} + T_{i,j-1,k}^{n} + K_{\mathrm{p/cr}} (T_{i,j,k+1}^{n} + T_{i,j,k-1}^{n}) - (4 + 2K_{\mathrm{p/cr}}) T_{i,j,k}^{n}\right] + \\ + \beta \left[(T_{i,j,k}^{n} - T_{i-1,j,k}^{n})^2 + (T_{i,j,k}^{n} - T_{i,j-1,k}^{n})^2 + K_{\mathrm{p/cr}} (T_{i,j,k}^{n} - T_{i,j,k-1}^{n})^2 \right] \end{array} \right\}. \tag{37}$$

In this case in equations (32) and (33) instead of α_{r} and α_{t}, α_{cr} must be used, and instead of $\lambda_{0\mathrm{r}}$ and $\lambda_{0\mathrm{t}}$, $\lambda_{0\mathrm{cr}}$ must be used.
The discrete analogue of the 2D model, in which equations (10) ÷ (14) participate, becomes

$$T_{i,j}^{n+1} = T_{i,j}^{n} + \frac{\lambda_{0\mathrm{cr}} \gamma \Delta \tau}{c_{\mathrm{e}} \rho \Delta x^2} \left\{ \begin{array}{l} \left[1 + \beta \left(T_{i,j}^{n} - 273{,}15\right)\right] \left(T_{i+1,j}^{n} + T_{i-1,j}^{n} + T_{i,j+1}^{n} + T_{i,j-1}^{n} - 4T_{i,j}^{n}\right) + \\ + \beta \left[\left(T_{i,j}^{n} - T_{i-1,j}^{n}\right)^2 + \left(T_{i,j}^{n} - T_{i,j-1}^{n}\right)^2 \right] \end{array} \right\} \tag{38}$$

with an initial condition

$$T_{i,j}^{0} = T_0 \tag{39}$$

and boundary conditions:

- for thermal processing of the prisms at their prescribed surface temperature:

$$T_{1,j}^{n+1} = T_{i,1}^{n+1} = T_{\mathrm{m}}^{n+1}, \tag{40}$$

- for convective thermal processing of the prisms:

$$T_{1,j}^{n+1} = \frac{T_{2,j}^{n} + G_{1,j} T_{\mathrm{m}}^{n+1}}{1 + G_{1,j}} \quad \text{where} \quad G_{1,j} = \frac{\alpha_{\mathrm{cr}} \Delta x}{\lambda_{0\mathrm{cr}} \gamma [1 + \beta (T_{1,j}^{n} - 273{,}15)]}, \tag{41}$$

$$T_{i,1}^{n+1} = \frac{T_{i,2}^{n} + G_{i,1} T_{\mathrm{m}}^{n+1}}{1 + G_{i,1}} \quad \text{where} \quad G_{i,1} = \frac{\alpha_{\mathrm{cr}} \Delta x}{\lambda_{0\mathrm{cr}} \gamma [1 + \beta (T_{i,1}^{n} - 273{,}15)]}. \tag{42}$$

The discrete analogue of the 1D model, in which equations (15) ÷ (18) participate, becomes

$$T_i^{n+1} = T_i^n + \frac{\lambda_{0\mathrm{cr}} \gamma \Delta \tau}{c_{\mathrm{e}} \rho \Delta x^2} \left\{ \left[1 + \beta \left(T_i^n - 273{,}15 \right) \right] \left(T_{i+1}^n + T_{i-1}^n - 2T_i^n \right) + \beta \left(T_i^n - T_{i-1}^n \right)^2 \right\} \tag{43}$$

with an initial condition

$$T_i^0 = T_0 \tag{44}$$

and boundary conditions:

- for thermal processing of the prisms at their prescribed surface temperature:

$$T_1^{n+1} = T_{\mathrm{m}}^{n+1}, \tag{45}$$

- for convective thermal processing of the prisms:

$$T_1^{n+1} = \frac{T_2^n + G_1 T_{\mathrm{m}}^{n+1}}{1 + G_1} \quad \text{where} \quad G_1 = \frac{\alpha_{\mathrm{cr}} \Delta x}{\lambda_{0\mathrm{cr}} \gamma [1 + \beta (T_1^n - 273{,}15)]}. \tag{46}$$

Using the system of equations (37) and (30) ÷ (36) of the 3D case, (38) ÷ (42) of the 2D case and (43) ÷ (46) of the 1D case, the integration of the differential equation (4) and of its reduced along the spatial coordinates analogues, is transformed to a consequent determination of the values of T in the knots of the calculation mesh, built in the subjected to thermal processing prismatic material, where during the computations the distribution of T is used in the preceding moment, distanced from the current by $\Delta\tau$.

The value of the step $\Delta\tau$ is determined by the requirement for stability of the solution of the corresponding system of equations. It must not exceed the smaller of the two values obtained from the equations

$$\Delta\tau = \frac{c_{\mathrm{e}}(T_{\min}, u) \rho(T_{\min}, u) \Delta x^2}{K_{\mathrm{d}} \lambda(T_{\min}, u)} \quad \text{and} \quad \Delta\tau = \frac{c_{\mathrm{e}}(T_{\max}, u) \rho(T_{\max}, u) \Delta x^2}{K_{\mathrm{d}} \lambda(T_{\max}, u)}, \tag{47}$$

in which $T_{\min}$ and $T_{\max}$ are correspondingly the smallest and biggest of all values of the temperatures, encountered in the initial and boundary conditions of the heat transfer when solving the mathematical model, and K_{d} is a coefficient, reflecting the dimensioning of the heat flux when calculating the step $\Delta\tau$: for a 3D heat flux $K_{\mathrm{d}} = 6K_{\mathrm{p/cr}}$; for a 2D heat flux $K_{\mathrm{d}} = 4$ and for a 1D heat flux $K_{\mathrm{d}} = 2$.

6.2 Discrete analogues of models for transient heat conduction in cylindrical bodies

For the obtaining of a discrete analogues of equations (20) ÷ (24) the explicit form of the finite-difference method has been used in a way comparable to the reviewed above case of 2D thermal processing of prismatic bodies. The transformation of the non-linear differential equation with partial derivatives (20) in its discrete analogue is carried out using the shown on Fig. 3 coordinate system for the positioning of the knots from the calculation mesh, in which the distribution of temperature in the longitudinal section of subjected to thermal processing cylindrical body is calculated. The calculation mesh for the solution of the 2D model with the help of the finite-differences method is built on ¼ of the longitudinal section of the cylindrical body due to the circumstance that this ¼ is mirror symmetrical towards the remaining ¾ of the same section.

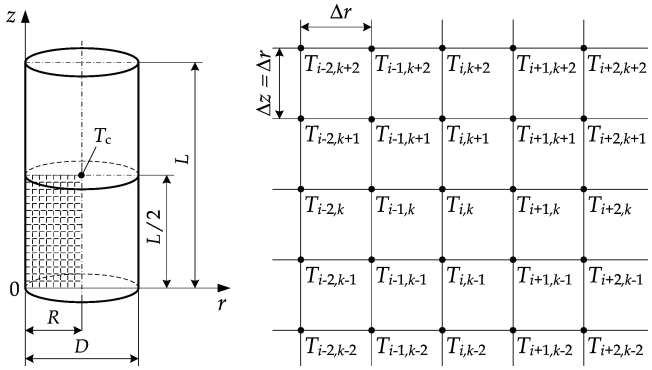

Fig. 3. Positioning of the knots of the calculation mesh on ¼ of the longitudinal section of a subjected to thermal processing cylindrical body

Taking into consideration equations (2) and (27) and using the coefficient $K_{\mathrm{p/r}} = \dfrac{\lambda_{0\mathrm{p}}}{\lambda_{0\mathrm{r}}}$, after applying the explicit form of the finite-differences method to equations (20) ÷ (24), they are transformed into the following system of equations:

$$T_{i,k}^{n+1} = T_{i,k}^{n} + \frac{\lambda_{0\mathrm{r}}\gamma\Delta\tau}{c_{\mathrm{e}}\rho\Delta r^2}\left\{\begin{array}{l}\left[1+\beta\left(T_{i,k}^{n}-273{,}15\right)\right] \\ \left[\begin{array}{l}T_{i-1,k}^{n}+T_{i+1,k}^{n}+K_{\mathrm{p/r}}\left(T_{i,k-1}^{n}+T_{i,k+1}^{n}\right)- \\ \left(2+2K_{\mathrm{p/r}}\right)T_{i,k}^{n}+\dfrac{1}{i-1}\left(T_{i-1,k}^{n}-T_{i,k}^{n}\right)\end{array}\right]+ \\ \beta\left[\left(T_{i-1,k}^{n}-T_{i,k}^{n}\right)^2+K_{\mathrm{p/r}}\left(T_{i,k-1}^{n}-T_{i,k}^{n}\right)^2\right]\end{array}\right\} \tag{48}$$

with an initial condition

$$T_{i,k}^{0} = T_0 \tag{49}$$

and boundary conditions:

- for heating or cooling of the bodies at their prescribed surface temperature:

$$T_{1,k}^{n+1} = T_{i,1}^{n+1} = T_{\mathrm{m}}^{n+1}\,, \tag{50}$$

- for convective heating or cooling of the bodies in the processing medium:

$$T_{1,k}^{n+1} = \frac{T_{2,k}^{n} + G_{1,k} T_{\mathrm{m}}^{n+1}}{1 + G_{1,k}} \quad \text{where} \quad G_{1,k} = \frac{\alpha_{\mathrm{r}} \Delta x}{\lambda_{0\mathrm{r}} \gamma [1 + \beta (T_{1,k}^{n} - 273{,}15)]}\,, \tag{51}$$

$$T_{i,1}^{n+1} = \frac{T_{i,2}^{n} + G_{i,1} T_{\mathrm{m}}^{n+1}}{1 + G_{i,1}} \quad \text{where} \quad G_{i,1} = \frac{\alpha_{\mathrm{p}} \Delta x}{\lambda_{0\mathrm{p}} \gamma [1 + \beta (T_{i,1}^{n} - 273{,}15)]}\,. \tag{52}$$

The discrete analogue of the 1D model, in which equations (25), (26), (17) and (18) participate, takes the form

$$T_i^{n+1} = T_i^{n} + \frac{\lambda_{0\mathrm{r}} \gamma \Delta \tau}{c_{\mathrm{e}} \rho \Delta r^2} \left\{ \begin{bmatrix} 1 + \beta (T_i^{n} - 273{,}15) \end{bmatrix} \begin{bmatrix} T_{i-1}^{n} + T_{i+1}^{n} - 2T_i^{n} + \dfrac{1}{i-1} (T_{i-1}^{n} - T_i^{n}) \end{bmatrix} + \beta (T_{i-1}^{n} - T_i^{n})^2 \right\} \tag{53}$$

with an initial condition presented through equation (44) and boundary conditions, presented through equations (45) and (46), where in (46) instead of α_{cr} and $\lambda_{0\mathrm{cr}}$, α_{r} and $\lambda_{0\mathrm{r}}$ are used. The value of the $\Delta\tau$, which guarantees the obtaining of robust solutions for the presented models, is determined by the condition for stability, described by equation (47). When solving the 2D model $K_{\mathrm{d}} = 4K_{\mathrm{p/r}}$, and when solving the 1D model $K_{\mathrm{d}} = 2$ in (47).

7. Mathematical description of the thermo-physical characteristics of the capillary porous bodies

The mathematical description of the thermo-physical characteristics of the capillary porous bodies consists of the deduction of summarized dependencies as a function of the factors which have an influence on them, which with maximum precision correspond to the their experimentally determined values in the interesting for the practice sufficiently wide ranges for the change in the factors. It is necessary to have such a description when solving the above presented mathematical models of the transient heat conduction in capillary porous bodies.

The following thermo-physical characteristics are present in these models: specific heat capacity, thermal conductivity and density of the capillary porous bodies.

The mathematical description of the above mentioned characteristics of the wood, which is a typical representative of the studied bodies, is shown as an example below.

7.1 Mathematical description of the specific heat capacity of the wood

The mathematical description of c_e is done according to equation (2) and is based on an analysis of the physics of the wood frosting and defrosting process. The description reveals the facts determined by Chudinov (1966, 1984), which state that the thawing of the ice from the situated in the wood free water occurs in the temperature range between 271,15 and 272,15 K, and the thawing of the ice from the situated in the wood hygroscopically bounded water depends on the temperature, which is $T < 271{,}15$ K.

Besides this, at $T < 271{,}15$, a certain portion, u_{nfw}, from the hygroscopically bounded water is found in a non-frozen state, where the value of u_{nfw} is calculated by equation (58).

The own specific heat capacity of the wood c is described mathematically using the shown on Fig. 4 experimentally determined in the dissertations of Kanter (1955) and Chudinov (1966) data for its change as a function of t and u. In the description apart from t and u, the independent parameter u_{fsp} has been input, which is different for the separate wood species and reflects the influence of the anatomic characteristics of the wood on c.

From the analysis on Fig. 4 it can be seen that at t = -2°C and all values for the content of water $u > 0{,}3$ kg.kg^{-1} during the thawing of wood a jump in the values of c is observed. This jump is explained by the phase transition of the frozen free water in the wood at the given values for t and u, when the influence on c of a significant difference in the specific heat capacity of the water in a liquid and hard aggregate condition is observed.

On Fig. 4 the jump of c for $u = 0{,}2$ kg.kg^{-1} occurs at a temperature around –17°C. It is characterized by the phase transition of the frozen part of the hygroscopically bounded water in the wood at these values for t and u. Both at $u = 0$, and at $u = 0{,}1$ kg.kg^{-1} there is a lack of a jump in the values for c, because even at –40°C there is no ice in the wood.

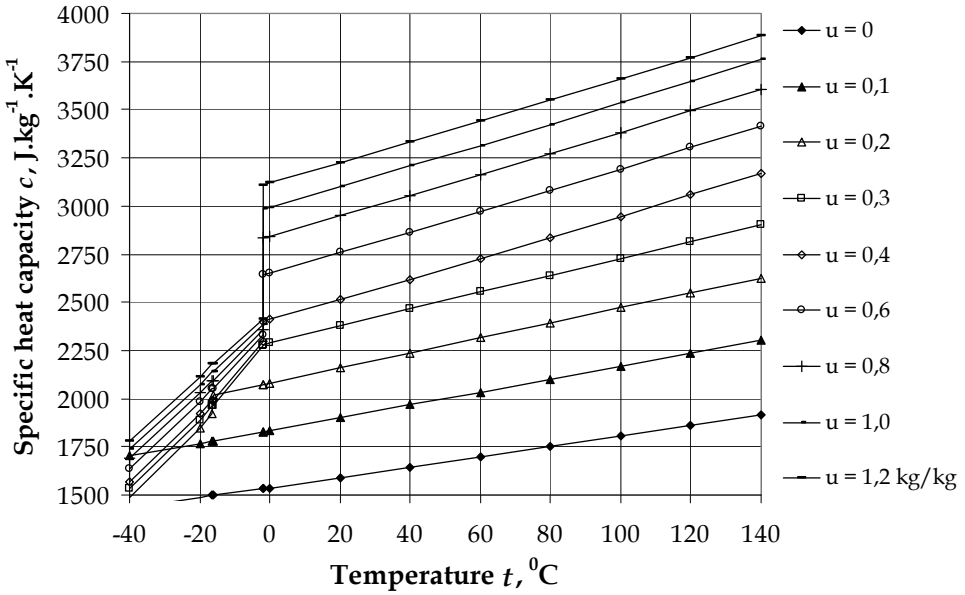

Fig. 4. Change in the specific heat capacity of the wood c depending on t and u

The following equations for $c(T,u,u_{\text{fsp}})$ have been derived, which are valid for all wood species for the intervals $0 \le u \le 1{,}2$ kg.kg^{-1} and $223 \le T \le 373$ K (Deliiski 1990, 2003b, 2004):

- When T > 271,15 K, or when $T \le 271{,}15$ K and simultaneously with this $u \le u_{\text{nfw}}$:

$$c = \frac{2097u + 826}{1+u} + \frac{9{,}92u + 2{,}55}{1+u}T + \frac{0{,}0002}{1+u}T^2 \,, \quad @ \quad u < u_{\text{fsp}} \tag{54}$$

$$c = \frac{2862u + 555}{1+u} + \frac{5{,}49u + 2{,}95}{1+u}T + \frac{0{,}0036}{1+u}T^2 \,, \quad @ \quad u \ge u_{\text{fsp}} \tag{55}$$

- When $T \le 271{,}15$ K and simultaneously with this $u > u_{\text{nfw}}$:

$$c = K_c \frac{526 + 2{,}95T + 0{,}0022T^2 + 2261u + 1976u_{\text{nfw}}}{1+u} \,, \tag{56}$$

$$K_{\text{c}} = 1{,}06 + 0{,}04u + \frac{0{,}00075\left(T - 271{,}15\right)}{u_{\text{nfw}}} \,, \tag{57}$$

where the content of non-frozen water in the wood u_{nfw} is equals to

$$u_{\text{nfw}} = 0{,}12 + \left(u_{\text{fsp}} - 0{,}12\right)\exp\left[0{,}0567\left(T - 271{,}15\right)\right]. \tag{58}$$

The calculated according to equation (58) change in u_{nfw} depending on t at $u_{\text{fsp}} = 0{,}2$ kg. kg^{-1}, $u_{\text{fsp}} = 0{,}3$ kg. kg^{-1} and $u_{\text{fsp}} = 0{,}4$ kg. kg^{-1} is shown on Fig. 5.

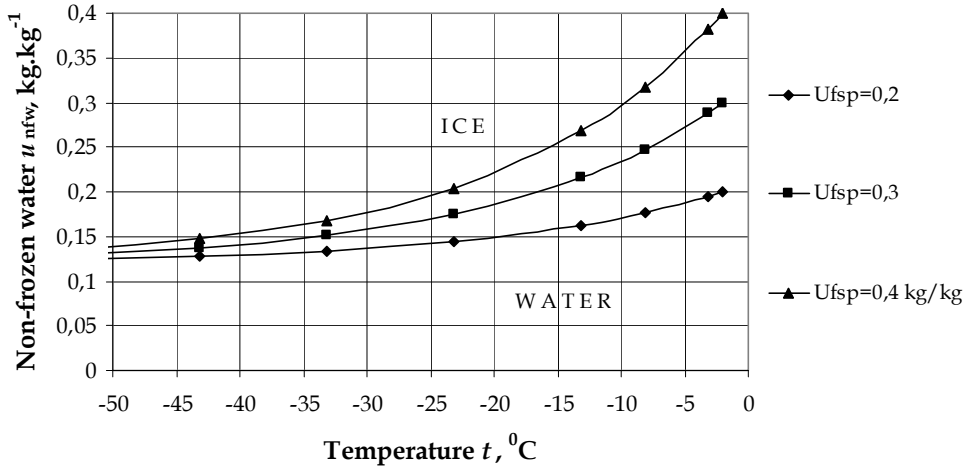

Fig. 5. Change in the content of non-frozen water in the wood u_{nfw} depending on t and u_{fsp}

Taking into consideration the latent heat in the phase transition (crystallization) of the water, equal to $3{,}34.10^5$ J.kg^{-1} (Chudinov, 1966) the following equation has been obtained for the calculation of c_{fw} (Deliiski, 2003b, 2004, 2009, Dzurenda & Deliiski, 2010):

$$c_{\text{fw}} = 3{,}34.10^5 \frac{u - u_{\text{fsp}}}{1+u} \quad @ \quad 271{,}15 < T \le 272{,}15 \;\; \& \;\; u > u_{\text{fsp}} \,. \tag{59}$$

The change in the calculated according to equation (59) values for c_{fw} depending on u and u_{fsp} of the wood is shown on Fig. 6. It can be seen that the decrease in u_{fsp} at a given u causes a proportional increase of the capacity c_{fw} due to the increase in the numerator in equation (59). The increase of u causes an increase of c_{fw}, which is caused by the increase of the quantity of ice in the more humid wood, which was formed from the free water.

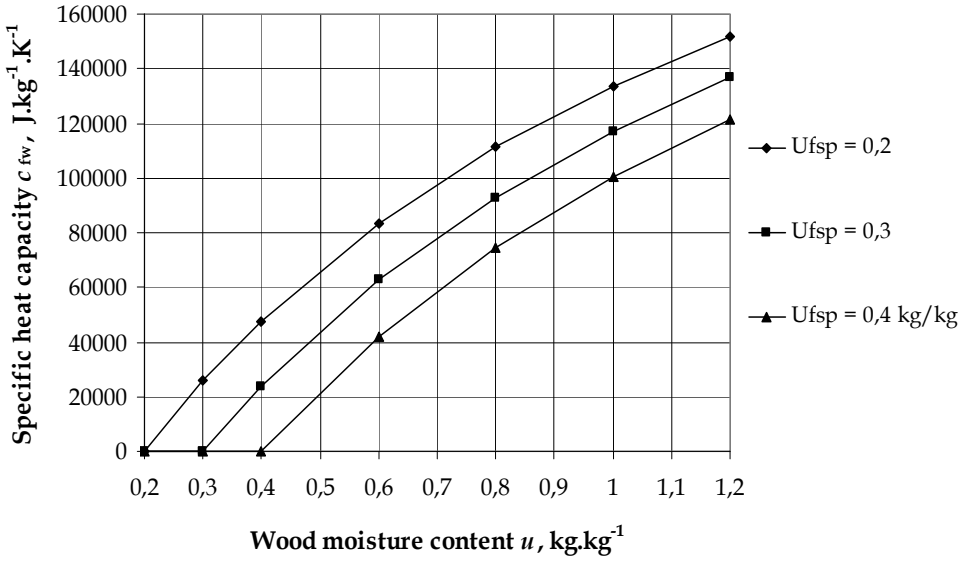

Fig. 6. Change in the specific heat capacity c_{fw} depending on u and u_{fsp}

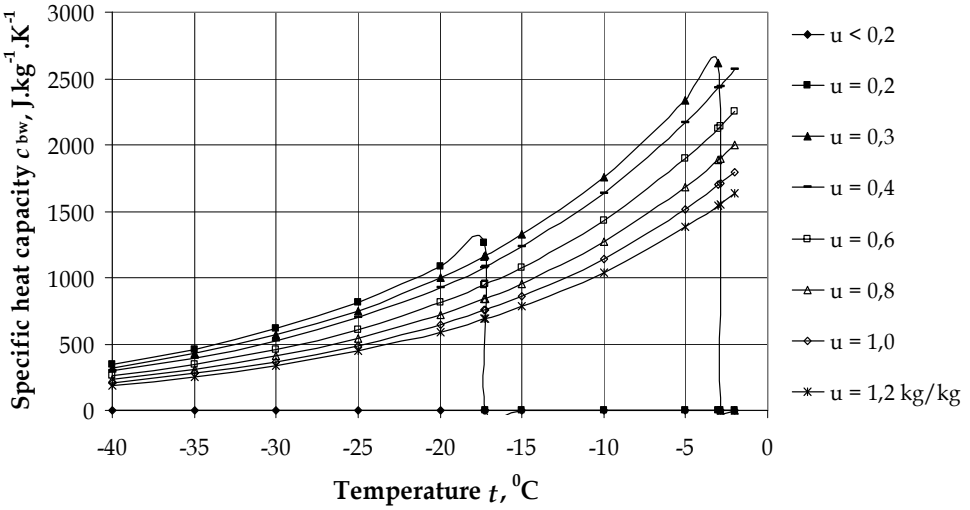

Fig. 7. Change in c_{bw} of beech wood depending on T and u at $u_{fsp} = 0,31$ kg.kg^{-1}

For the calculation of c_{bw} the following equation (Deliiski 2003b, 2009) has been obtained:

$$c_{bw} = 1,8938.10^4\left(u_{fsp} - 0,12\right)\frac{\exp\left[0,0567\left(T - 271,15\right)\right]}{1+u} \quad @ \quad u > u_{nfw}\,. \tag{60}$$

The change in the calculated according to equation (60) values for c_{bw} depending on T and u is shown on Fig. 7 for the comparatively more often subjected to thermal processing beech wood with $u_{fsp} = 0,31$ kg.kg^{-1}.
When T and u are outside of the indicated in equations (59) and (60) ranges, the values of c_{fw} and c_{bw} have been assumed to be equal to zero during the solution of the models.

7.2 Mathematical description of the thermal conductivity of the wood

A mathematical description of the thermal conductivity of the wood λ has been done using the shown on Fig. 8 experimentally determined in the dissertation by Kanter (1955) and Chudinov (1966) data for its change as a function of t and u. The graphs of this figure relate to the change in the thermal conductivity cross sectional to the fibers λ_{cr} of birch wood, having ρ_b = 515 kg.m^{-3} and $u_{fsp} = 0,3$ kg.kg^{-1}.
The data for $\lambda_{cr}(t,u)$ shown on Fig. 8, as well as the data for $c(t,u)$ on Fig. 4 find a wide use in both the European (Shubin, 1990, Trebula, 1996, Videlov, 2003, etc.) and the American specialized literature (Steinhagen, 1986, 1991, etc.) when calculating various processes of thermal processing of wood. From the analysis on Fig. 8 it can be seen that at $u > u_{fsp}$ the temperature t = -2°C for the defrosting of the wood is critical, because at this temperature a jump in the values of λ_{cr} is observed. This jump increases with the increase in u. It is explained by a significant difference in the thermal conductivity of the water in liquid and in hard aggregate condition.

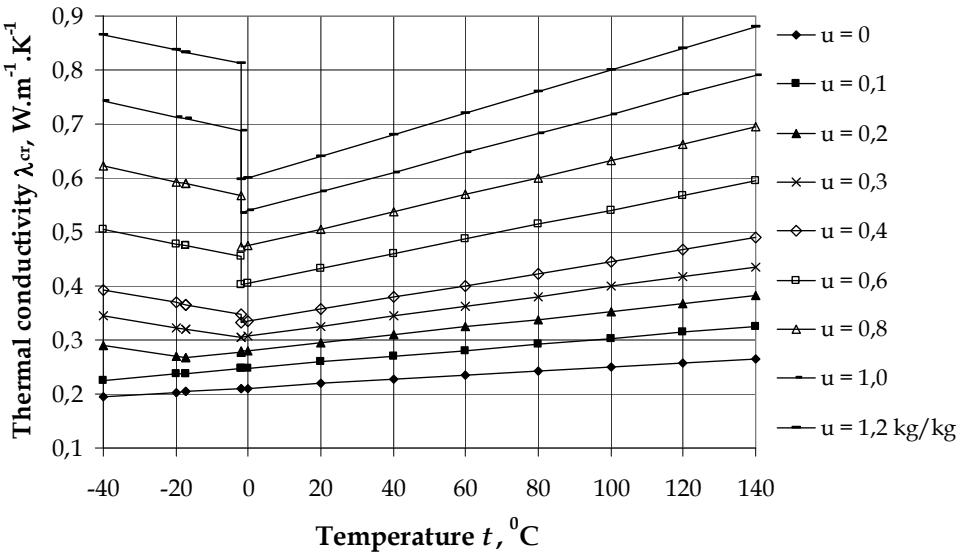

Fig. 8. Change in the thermal conductivity cross sectional to the fibers λ_{cr} of birch wood with $\rho_b = 515$ kg.m^{-3} and $u_{fsp} = 0,30$ kg.kg^{-1} depending on t and u

In the description of λ_{cr}, as well as in that of c_e, u_{fsp} has been introduced as an independent variable for different wood species, instead of the ordinarily used averaged value of $u_{fsp} = 0,30$ kg.kg^{-1} for all wood species. The following equations for the calculation of the coefficients of λ in equation (27) for the ranges $0 \le u \le 1,2$ kg.kg^{-1} and $223 \le T \le 373$ K have been derived (Deliiski, 1994, 2003b, Dzurenda & Deliiski, 2010):

$$\lambda_0 = K_a \nu \left[0,165 + \left(1,39 + 3,8u\right)\left(3,3.10^{-7}\rho_b^2 + 1,015.10^{-3}\rho_b\right)\right], \tag{61}$$

$$\nu = 0,15 - 0,07u \quad @ \quad u \le u_{fsp} + 0,1 \text{ kg.kg}^{-1}, \tag{62}$$

$$\nu = 0,1284 - 0,013u \quad @ \quad u > u_{fsp} + 0,1 \text{ kg.kg}^{-1}. \tag{63}$$

The equations, which have been suggested by Chudinov (1966, 1968) and shown in (Deliiski, 1977) can be used for the determining of the values of the coefficient K_a in equation (61), which takes into account the influence on λ_0 of the heat flux towards the separate anatomic directions of the wood, i.e. for the determining of λ_r, λ_t and λ_p. The coefficients γ and β in equation (27) are calculated by the following equations:

- When T > 271,15 K or when $T \le 271,15$ K and simultaneously with this $u < u_{nfw}$:

$$\gamma = 1,0, \tag{64}$$

$$\beta = \left(2,05 + 4u\right)\left(\frac{579}{\rho_y} - 0,124\right).10^{-3} \quad @ \quad u \le u_{fsp} + 0,1 \text{ kg.kg}^{-1}, \tag{65}$$

$$\beta = 3,65\left(\frac{579}{\rho_y} - 0,124\right).10^{-3} \quad @ \quad u > u_{fsp} + 0,1 \text{ kg.kg}^{-1}. \tag{66}$$

- When $T \le 271,15$ K and simultaneously with this $u \ge u_{fsp}$ or when $T \le T_{nfw}$ and simultaneously with this $0,125 \le u < u_{fsp}$:

$$\gamma = 1 + 0,34[1,15\left(u - u_{fsp}\right)], \tag{67}$$

$$\beta = 0,002(u - u_{fsp}) - 0,0038\left(\frac{579}{\rho_b} - 0,124\right), \tag{68}$$

$$T_{nfw} = 271,15 + \frac{\ln\dfrac{u_{nfw} - 0,12}{u_{fsp} - 0,12}}{0,0567}. \tag{69}$$

For the calculation of λ in the cases, when $T \le T_{nfw}$ and simultaneously with this $0,125 \le u < u_{fsp}$, the value of λ_{nfw} is initially determined by substituting $T = T_{nfw}$ in equation (27) as well as the values of γ from equation (64) and of β from equation (65). After this, with the usage of the coefficient β from equation (68), the values of λ are calculated with the following equation:

$$\lambda = \lambda_{nfw}[1 + \beta\left(T - T_{nfw}\right)] \quad @ \quad T \le T_{nfw} \;\&\; 0,125 \le u \le u_{fsp}. \tag{70}$$

Equation (70), together with equation (27), make the calculation of λ applicable for all temperatures larger than –50°C (i.e. $T = 223,15$ K), because only at $T = 223,15$ K and the minimum possible for the wood species $u_{fsp} = 0,2$ kg.kg^{-1}, the value of u_{nfw} is $u_{nfw} = 0,125$ kg.kg^{-1} (Fig. 5).

7.3 Mathematical description of the wood density

The mathematical description of the wood density ρ depending on the moisture content u and basic wood density ρ_b which influence it has been carried out using the shown on Fig. 9 experimental values set by (Sergovski, 1975) and shown in (Deliiski, 1977, 2003b). The following equations, which are applicable to all wood species, have been derived:

$$\rho = \rho_b \frac{1+u}{1-9,3.10^{-4}\rho_b\left(u_{fsp}-u\right)} \quad @ \quad u \le u_{fsp}\,, \tag{71}$$

$$\rho = \rho_b(1+u) \quad @ \quad u > u_{fsp}\,, \tag{72}$$

where according to (Siau 1984)

$$u_{fsp} = u_{fsp}^{20} - 0,001(T - 293,15)\,. \tag{73}$$

The values for u_{fsp}^{20} are given in the specialized literature (Siau, 1984, Videlov, 2003, etc.).

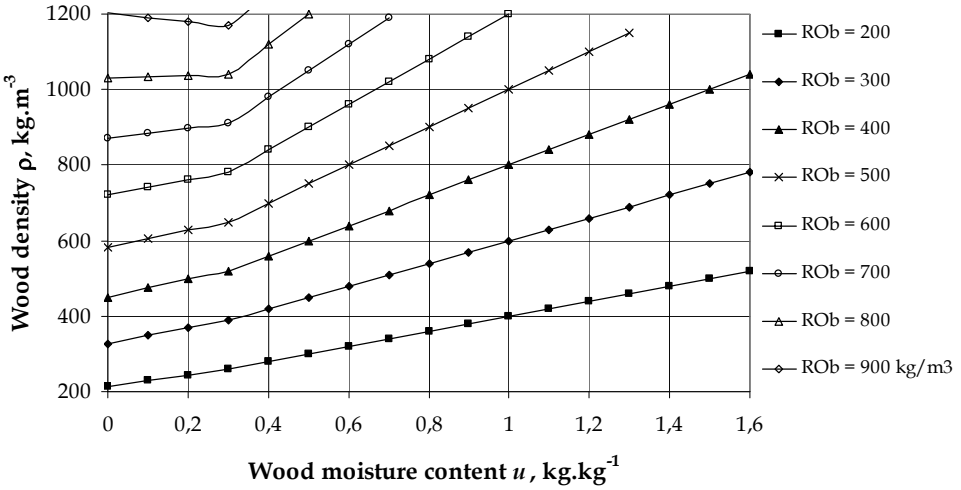

Fig. 9. Change in ρ of all wood species depending on u and ρ_b

8. Computer solution of the models for transient heat conduction in the bodies

For the numerical solution of the above presented models for transient heat conduction in prismatic and cylindrical capillary porous bodies a software package has been prepared in

FORTRAN (Dorn & McCracken, 1972), which has been input in the developed by Microsoft calculation environment of VISUAL FORTRAN PROFESSIONAL (Deliiski 2003b).
The software package can be used for the calculation and colour visualization (either as animation of the whole process or as 3D, 2D, 1D graphs of each desired moment of the process) of the non-stationary distribution of the temperature fields in the materials containing or not containing ice during their thermal processing. The computation of the change in the temperature field in the volume of materials containing ice in the beginning of their thermal processing is interconnected for the periods of the melting of the ice and after that, taking into account the flexible spatial boundary of the melting ice.
The computation of the temperature fields is done interconnectedly and for the processes of heating and consequent cooling of the materials, i.e. the calculation of the non-stationary change in temperatures in the volume of the materials during the time of their cooling begins from the already reached during the time of calculations distribution of temperature in the end of the heating. Based on the calculations it can be determined when the moment of reaching in the entire volume of the heated wood has occurred for the necessary optimal temperatures needed for bending of the parts or for cutting the veneer, as well as the stage of the ennoblement of the wood desired by the clients.

8.1 Non-stationary thermal processing of prismatic wood materials

With the help of the 3D model the change in t in the volume of non-frozen beech prisms with $t_0 = 0^0C$ and frozen beech prisms with $t_0 = -10^0C$ with d = 0,4 m, b = 0,4 m, L = 0,8 m, $\rho_b = 560$ kg.kg^{-1}, u = 0,6 kg.kg^{-1} and $u_{fsp}^{20} = 0,31$ kg.kg^{-1} has been calculated during the time of thermal processing during 20 hours at a prescribed surface temperature $t_m = 80^0$C.
The change in t_m and t is shown on Fig. 10 in 6 characteristic points of the volume of the prisms with coordinates, which are given in the legend of the graphs. The increase in t_m from $t_{m0} = 0^0$C to $t_m = 80^0$C is done exponentially with a time constant equal to 1800 s.

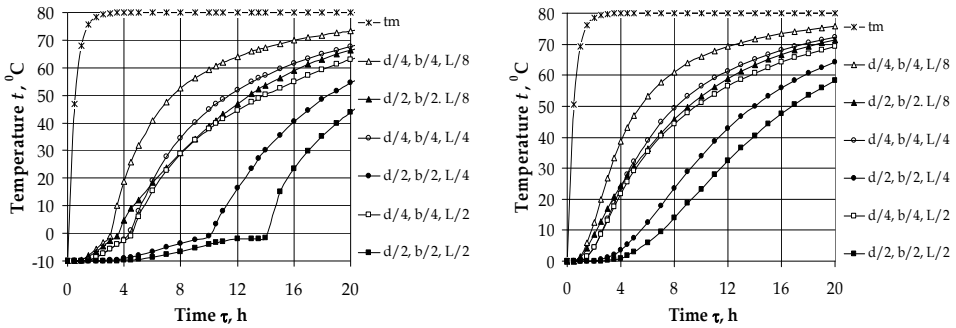

Fig. 10. 3D heating at $t_m = 80^0$C of frozen (left) and non-frozen (right) beech prisms with dimensions 0,4 x 0,4 x 0,8 m, $\rho_b = 560$ kg.kg^{-1}, u = 0,6 kg.kg^{-1} and $u_{fsp}^{20} = 0,31$ kg.kg^{-1}

With the help of the 2D model the change in temperature in 5 characteristic points of cross section of non-frozen oak prisms with $t_0 = 0^0$C and frozen oak prisms with $t_0 = -10^0$C has been calculated during the time of their thermal processing with prescribed surface temperature $t_m = 60^0$C and during the time of the consequent cooling with surface convection at $t_m = 20^0$C.

The prisms have the following characteristics: d = 0,25 m, b = 0,40 m, L > 1,0 m, ρ_b = 670 kg.kg^{-1}, u = 0,6 kg.kg^{-1} and $u_{fsp}^{20} = 0,29$ kg.kg^{-1}. The heating of the prisms continues until the reaching of the minimally required for cutting of veneer temperature in their centre, equal to $t_c = 50^0$C .

During the time of cooling of the heated prisms a redistribution and equalization of t in their cross section takes place, which is especially appropriate for the obtaining of quality veneer. The change in t_m and t is shown on Fig. 11 in 5 characteristic points from the cross section of the prisms with coordinates, which are given in the legend of the graphs.

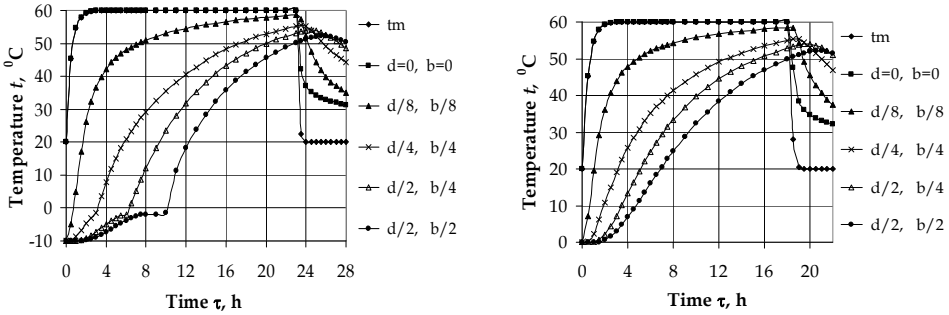

Fig. 11. 2D heating at $t_m = 60^0$C and consequent cooling at $t_m = 20^0$C of frozen (left) and non-frozen (right) oak prisms with cross section 0,25 x 0,40 m, ρ_b = 670 kg.kg^{-1} and u = 0,6 kg.kg^{-1}

8.2 Non-stationary thermal processing of cylindrical wood materials

With the help of the 2D model the change in the t in the longitudinal section of non-frozen beech prisms with $t_0 = 0^0$C and frozen beech prisms with $t_0 = -2^0$C with D = 0,4 m, L = 0,8 m, $\rho_b = 560$ kg.kg^{-1}, u = 0,6 kg.kg^{-1} and $u_{fsp}^{20} = 0,31$ kg.kg^{-1} has been calculated during the time of thermal processing during 20 hours at a prescribed surface temperature $t_m = 80^0$C . The change in t_m and t is shown on Fig. 12 in 4 characteristic points of the longitudinal section of the logs with coordinates, which are given in the legend of the graphs.

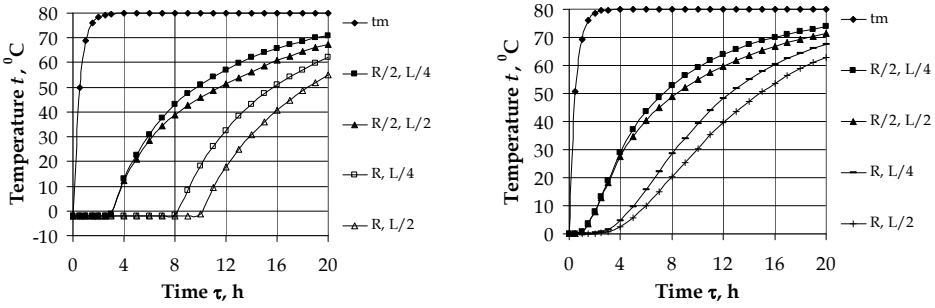

Fig. 12. 2D heating at $t_m = 80^0$C of frozen (left) and non-frozen (right) beech logs with R=0,2 m, L=0,8 m, ρ_b = 560 kg.kg^{-1}, u = 0,6 kg.kg^{-1} and u_{fsp}^{20} = 0,31 kg.kg^{-1}

The change in t in the longitudinal section of non-frozen beech logs with $t_0 = 0^0\text{C}$ and in frozen beech logs with $t_0 = -10^0\text{C}$ has been also calculated with the given above parameters during the time of a 3-stage high temperature thermal processing in autoclave and during the time of the consequent cooling with surface convection at $t_m = 20^0\text{C}$ (Fig. 13).

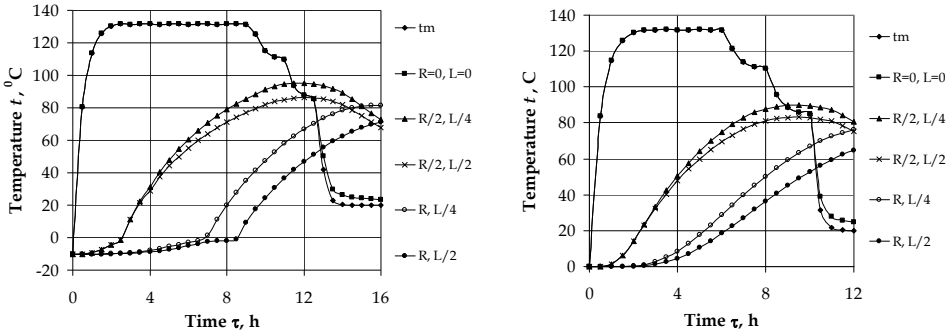

Fig. 13. 2D high temperature heating in autoclave and consequent cooling of frozen (left) and non-frozen (right) beech logs with R=0,2 m, L=0,8 m, ρ_b = 560 kg.kg^{-1} and u = 0,6 kg.kg^{-1}

Using 3D graphs and 2D diagrams a part of the results is shown on Fig. 14 from the simulation studies on the heat transfer in the radial and longitudinal direction of the frozen beech logs with t_0 = -2°C, whose temperature field is shown on the left side on Fig. 12. The non-stationary temperature distribution during specific time intervals of the thermal processing is clearly observed from the 3D graphs (left columns on Fig. 14). The 2D diagrams which show in more detail the results from the simulations can be used rather for qualitative than quantitative analysis of the thermal processing of the materials (right columns on Fig. 14).

On the left parts of Fig. 10, Fig. 11, Fig. 12 and Fig. 13 the characteristic non-linear parts can be seen well, which show a slowing down in the change in t in the range from -2°C to -1°C, in which the melting of the ice takes place, which was formed in the wood from the freezing of the free water in it. This signifies the good quality and quantity adequacy of the mathematical models towards the real process of heating of ice-containing wood materials. The calculated with the help of the models results correspond with high accuracy to wide experimental data for the non-stationary change in t in the volume of the containing and not containing ice wood logs, which have been derived in the publications by (Schteinhagen, 1986, 1991) and (Khattabi & Steinhagen, 1992, 1993).

The results presented on the figures show that the procedures for calculation of non-stationary change in t in prepared software package, realizing the solution of the mathematical models according to the finite-differences method, functions well for the cases of heating and cooling both for frozen and non-frozen materials at various initial and boundary conditions of the heat transfer during the thermal processing of the materials.

The good adequacy and precision of the models towards the results from numerous own and foreign experimental studies allows for the carrying out of various calculations with the models, which are connected to the non-stationary distribution of t in prismatic and cylindrical materials from various wood species and also to the heat energy consumption by the wood at random encountered in the practice conditions for thermal processing.

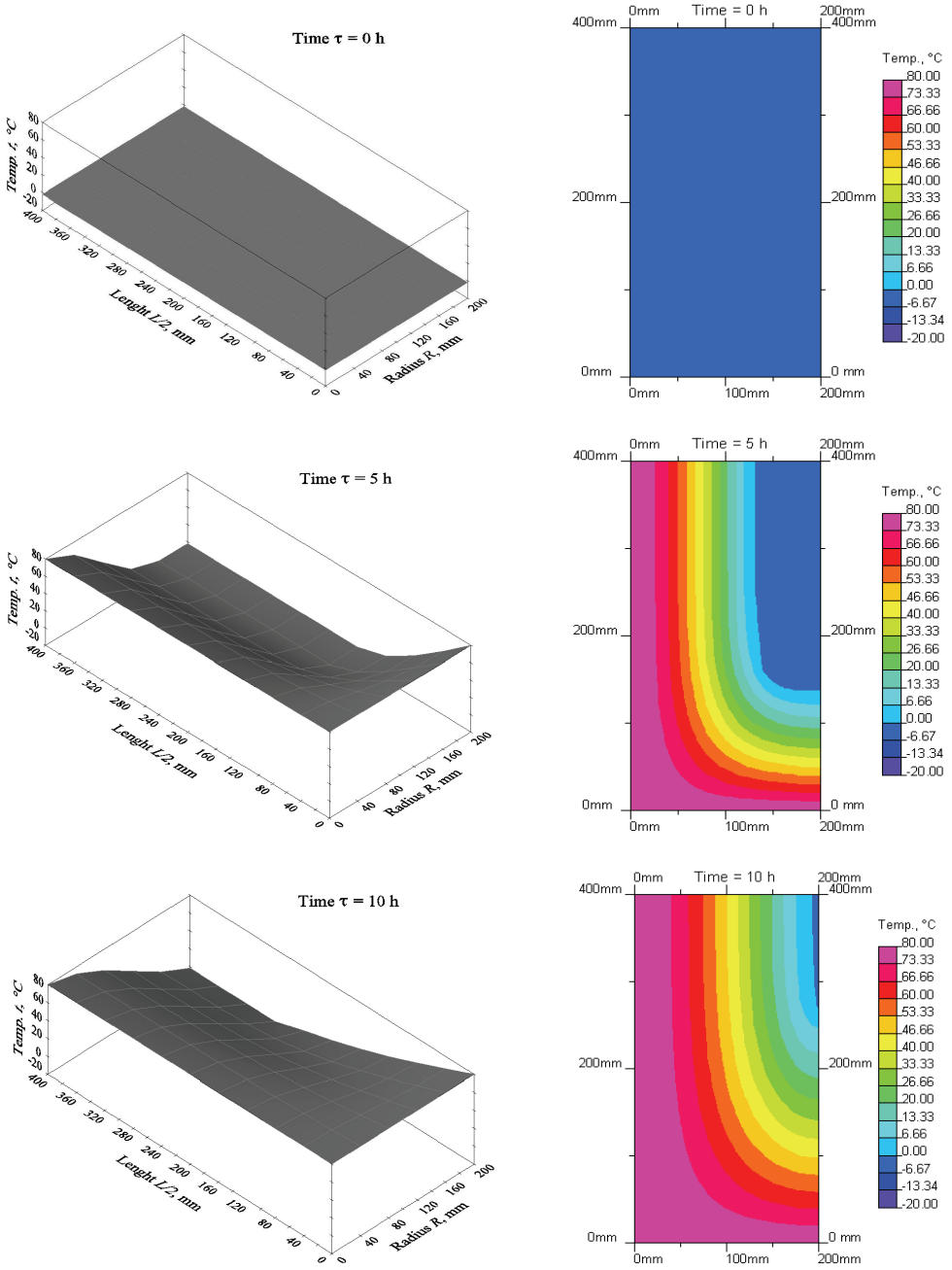

Fig. 14. 3D graphs and 2D contour plots for the temperature distribution with time in ¼ of longitudinal section of beech log with R = 0,2 m, L = 0,8 m, u = 0,6 kg·kg^{-1} and t_0 = -2°C

9. Conclusion

This paper describes the creation and solution of non-linear mathematical models for the transient heat conduction in anisotropic frozen and non-frozen capillary porous bodies with prismatic and cylindrical shape and at any $u \geq 0$ kg.kg^{-1}. The mechanism of the heat distribution in the entire volume of the bodies is described only by one partial differential equation of heat conduction. For the first time the own specific heat capacity of the bodies and the specific heat capacity of the ice, formed in them from the freezing of the hygroscopically bounded water and of the free water are taken into account in the models.
The models take into account the physics of the described processes and allow the 3D, 2D and 1D calculation of the temperature distribution in the volume of subjected to heating and/or cooling anisotropic or isotropic bodies in the cases, when the change in their moisture content during the thermal processing is relatively small. For the solution of the models an explicit form of the finite-difference method is used, which allows for the exclusion of any simplifications in the models.
For the usage of the models it is required to have the knowledge and mathematical description of several properties of the subjected to thermal processing frozen and non-frozen capillary porous materials. In this paper the approaches for mathematical description of thermo-physical characteristics of materials from different wood species, which are typical representatives of anisotropic capillary porous bodies, widely subjected to thermal treatment in the practice are shown as examples.
For the numerical solution of the models a software package has been prepared in FORTRAN, which has been input in the developed by Microsoft calculation environment of Visual Fortran Professional. The software allows for the computations to be done for heating and cooling of the bodies at prescribed surface temperature, equal to the temperature of the processing medium or during the time of convective thermal processing. The computation of the change in the temperature field in the volume of materials containing ice in the beginning of their thermal processing is interconnected for the periods of the melting of the ice and after that, taking into account the flexible boundary of the melting ice. The computation of the temperature fields is done interconnectedly and for the processes of heating and consequent cooling of the materials, i.e. the calculation of the change in temperatures in the volume of the materials during the time of their cooling begins from the already reached during the time of calculations distribution of temperature in the end of the heating. It is shown how based on the calculations it can be determined when the moment of reaching in the entire volume of the heated and after that cooling body has occurred for the necessary optimal temperatures needed, for example, for bending of wood parts or for cutting the veneer from plasticised wooden prisms or logs.
The models can be used for the calculation and colour visualization (either as animation of the whole process or as 3D, 2D, 1D graphs of each desired moment of the process) of the distribution of the temperature fields in the bodies during their thermal processing. The development of the models and algorithms and software for their solution is consistent with the possibility for their usage in automatic systems with a model based (Deliiski 2003a, 2003b, 2009) or model predicting control of different processes for thermal treatment.

10. Acknowledgement

This work was supported by the Scientific Research Sector of the University of Forestry, Sofia, Bulgaria.

11. References

Axenenko, O. (1995). Structural Failure of Plasterboard Assembles in Fires. In: *Australian Mathematical Society Gazette*, Available from: http://www.austms.org.au/Gazette/1995/Jun95/struct.html

Ben Nasrallah, S., Perre, P. (1988). Detailed Study of a Model of Heat and Mass Transfer During Convective Drying of Porous Media, *International Journal of Heat and Mass Transfer*, Volume 31, № 5, pp. 297-310

Chudinov, B. S. (1966). *Theoretical Research of Thermo-physical Properties and Thermal Treatment of Wood,* Dissertation for Dr.Sc., SibLTI, Krasnoyarsk, USSR (in Russian)

Chudinov, B. S. (1968). *Theory of Thermal Treatment of Wood*, Publishing Company "Nauka", Moscow, USSR (in Russian)

Chudinov, B. S. (1984). *Water in Wood,* Publishing Company "Nauka", Moscow, USSR (in Russian)

Deliiski, N. (1977). Berechnung der instationären Temperaturverteilung im Holz bei der Erwärmung durch Wärmeleitung. Teil I.: Mathematisches Modell für die Erwärmung des Holzes durch Wärmeleitung. *Holz Roh- Werkstoff*, Volume 35, № 4, pp. 141−145

Deliiski, N. (1979). Mathematical Modeling of the Process of Heating of Cylindrical Wood Materials by Thermal Conductivity. Scientific Works of the Higher Forest-technical Institute in Sofia, Volume XXV- MTD, 1979, pp. 21-26 (in Bulgarian)

Deliiski, N. (1990). Mathematische Beschreibung der spezifischen Wärmekapazität des aufgetauten und gefrorenen Holzes, *Proceedings of the VIIIth International Symposium on Fundamental Research of Wood*. Warsaw, Poland, pp. 229-233

Deliiski, N. (1994). Mathematical Description of the Thermal Conductivity Coefficient of Non-frozen and Frozen Wood. *Proceedings of the 2nd International Symposium on Wood Structure and Properties '94*, Zvolen, Slovakia, pp. 127-134

Deliiski, N. (2003a). Microprocessor System for Automatic Control of Logs' Steaming Process. *Drvna Industria,* Volume 53, № 4, pp. 191-198.

Deliiski, N. (2003b). *Modelling and Technologies for Steaming Wood Materials in Autoclaves.* Dissertation for Dr.Sc., University of Forestry, Sofia (in Bulgarian)

Deliiski, N. (2004). Modelling and Automatic Control of Heat Energy Consumption Required for Thermal Treatment of Logs. *Drvna Industria*, Volume 55, № 4, pp. 181-199

Deliiski, N. (2009). Computation of the 2-dimensional Transient Temperature Distribution and Heat Energy Consumption of Frozen and Non-frozen Logs. *Wood Research*, Volume 54, № 3, pp. 67−78

Doe, P. D., Oliver, A. R., Booker, J. D. (1994). A Non-linear Strain and Moisture Content Model of Variable Hardwood Drying Schedules. *Proceedings of the 4th IUFRO International Wood Drying Conference,* Rotorua, New Zealand, pp. 203-210

Dorn, W. S., McCracken, D. D. (1972). *Numerical Methods with FORTRAN IV: Case Studies*, John Willej & Sons, Inc., New York

Dzurenda, L., Deliiski, N. (2010). *Thermal Processes in the Technologies for Wood Processing*, TU in Zvolen, ISBN 978-80-228-2169-8, Zvolen, Slovakia (in Slovakian)

Ferguson, W. J., Lewis, R. W. (1991). A Comparison of a Fully Non-linear and a Partially Non-linear Heat and Mass Transfer of a Timber Drying Problem, *Proceedings of the 7th Conference on Numerical methods in Thermal Problems*, Vol. VII, Part 2, pp. 973-984

Kanter, K. R. (1955). *Investigation of the Thermal Properties of Wood.* Dissertation, MLTI, Moscow, USSR (in Russian)

Khattabi, A., Steinhagen, H. P. (1992). Numerical Solution to Two-dimensional Heating of Logs. *Holz Roh-Werkstoff*, Volume 50, № 7-8, pp. 308-312

Khattabi, A., Steinhagen, H. P. (1993). Analysis of Transient Non-linear Heat Conduction in Wood Using Finite-difference Solutions. *Holz Roh- Werkstoff*, Volume 51, № 4, pp. 272-278

Kulasiri, D., Woodhead, I. (2005). On Modelling the Drying of Porous Materials: Analytical Solutions to Coupled Partial Differential Equations Governing Heat and Moisture Transfer. In: *Mathematical Problems in Engineering*, Volume 3, 2005, pp. 275–291, Available from: http://emis.impa.br/EMIS/journals/HOA/MPE/Volume2005_3/291.pdf

Luikov, A. V. (1966). *Heat and Mass Transfer in Capillary Porous Bodies*, Pergamon Press

Murugesan, K., Suresh, H. N., Seetharamu, K. N., Narayana, P. A. A. & Sundararajan, T. (2001). A Theoretical Model of Brick Drying as a Conjugate Problem. *International Journal of Heat and Mass Transfer*, Volume 44, № 21, pp. 4075–4086

Sergovski, P. S. (1975). *Hydro-thermal Treatment and Conserving of Wood.* Publishing Company "Lesnaya Promyshlennost", Moskow, URSS (in Russian)

Siau, J. F. (1984). *Transport Processes in Wood,* Springer-Verlag, NewYork

Shubin, G. S. (1990). *Drying and Thermal Treatment of Wood,* ISBN 5-7120-0210-8, Publishing Company "Lesnaya Promyshlennost", Moskow, URSS (in Russian)

Steinhagen, H. P. (1986). Computerized Finite-difference Method to Calculate Transient Heat Conduction with Thawing. *Wood Fiber Science,* Volume 18, № 3, pp. 460-467

Steinhagen, H. P. (1991). Heat Transfer Computation for a Long, Frozen Log Heated in Agitated Water or Steam - A Practical Recipe. *Holz Roh- Werkstoff*, Volume 49, № 7-8, pp. 287-290

Steinhagen, H. P., Lee, H. W. (1988). Enthalpy Method to Compute Radial Heating and Thawing of Logs. *Wood Fiber Science,* Volume 20, № 4, pp. 415-421

Steinhagen, H. P., Lee, H. W., Loehnertz, S. P. (1987). LOGHEAT: A Computer Program of Determining Log Heating Times for Frozen and Non-Frozen Logs. *Forest Products Journal,* Volume 37, № 11-12, pp. 60-64

Trebula, P. (1996). *Drying and Hydro-thermal Treatment of Wood*, TU in Zvolen, IZBN 80-228-0574-2, Zvolen, Slovakia (in Slovakian)

Twardowski, K., Rychinski, S., Traple, J. (2006). A Role of Water in the Porosity of Ground-rock Media. *Acta Montanistica Slovaca* 11 (1), Faculty of Drilling, Oil and Gas AGH-UST, Krakow, pp. 208-212

Videlov, C. (2003). *Drying and Thermal Treatment of Wood*, University of Forestry in Sofia, ISBN 954-8783-63-0, Sofia (in Bulgarian)

Whitaker, S. (1977). Simultaneous Heat, Mass and Momentum Transfer in Porous Media: A Theory of Drying. *Advances in Heat Transfer*, Volume 13, pp. 119–203

Zhang, Z., Yang, S., Liu, D. (1999). Mechanism and Mathematical Model of Heat and Mass Transfer During Convective Drying of Porous Materials. *Heat Transfer – Asian Research,* Volume 28 № 5, pp. 337-351

8

Non-Linear Radiative-Conductive Heat Transfer in a Heterogeneous Gray Plane-Parallel Participating Medium

Marco T.M.B. de Vilhena, Bardo E.J. Bodmann and Cynthia F. Segatto
Universidade Federal do Rio Grande do Sul
Brazil

1. Introduction

Radiative transfer considers problems that involve the physical phenomenon of energy transfer by radiation in media. These phenomena occur in a variety of realms (Ahmad & Deering, 1992; Tsai & Ozişik, 1989; Wilson & Sen, 1986; Yi et al., 1996) including optics (Liu et al., 2006), astrophysics (Pinte et al., 2009), atmospheric science (Thomas & Stamnes, 2002), remote sensing (Shabanov et al., 2007) and engineering applications like heat transport by radiation (Brewster, 1992) for instance or radiative transfer laser applications (Kim & Guo, 2004). Furthermore, applications to other media such as biological tissue, powders, paints among others may be found in the literature (see ref. (Yang & Kruse, 2004) and references therein). Although radiation in its basic form is understood as a photon flux that requires a stochastic approach taking into account local microscopic interactions of a photon ensemble with some target particles like atoms, molecules, or effective micro-particles such as impurities, this scenario may be conveniently modelled by a radiation field, i.e. a radiation intensity, in a continuous medium where a microscopic structure is hidden in effective model parameters, to be specified later. The propagation of radiation through a homogeneous or heterogeneous medium suffers changes by several isotropic or non-isotropic processes like absorption, emission and scattering, respectively, that enter the mathematical approach in form of a non-linear radiative transfer equation. The non-linearity of the equation originates from a local thermal description using the Stefan-Boltzmann law that is related to heat transport by radiation which in turn is related to the radiation intensity and renders the radiative transfer problem a radiative-conductive one (Ozisik, 1973; Pomraning, 2005). Here, local thermal description means, that the domain where a temperature is attributed to, is sufficiently large in order to allow for the definition of a temperature, i.e. a local radiative equilibrium.

The principal quantity of interest is the intensity I, that describes the radiation energy flow through an infinitesimal oriented area $d\hat{\Sigma} = \hat{n}d\Sigma$ with outward normal vector $\hat{n}$ into the solid angle $d\hat{\Omega} = \hat{\Omega}d\Omega$, where $\hat{\Omega}$ represents the direction of the flow considered, with angle θ of the normal vector and the flow direction $\hat{n} \cdot \hat{\Omega} = \cos\theta = \mu$. In the present case we focus on the non-linearity of the radiative-conductive transfer problem and therefore introduce the simplification of an integrated spectral intensity over all wavelengths or equivalently all frequencies that contribute to the radiation flow and further ignore possible effects due to polarization. Also possible effects that need in the formalism properties such as coherence

and diffraction are not taken into account. In general the Radiative-Conductive Transfer Equation is difficult to solve without introducing some approximations, like linearisation or a reduction to a diffusion like equation, that facilitate the construction of a solution but at the cost of predictive power in comparison to experimental findings, or more sophisticated approaches. The present approach is not different in the sense that approximations shall be introduced, nevertheless the non-linearity that represents the crucial ingredient in the problem is solved without resorting to linearisation or perturbation like procedures and to the best of our knowledge is the first approach of its kind. The solution of the modified or approximate problem can be given in closed analytical form, that permits to calculate numerical results in principle to any desired precision. Moreover, the influence of the non-linearity can be analysed in an analytical fashion directly from the formal solution. Solutions found in the literature are typically linearised and of numerical nature (see for instance (Asllanaj et al., 2001; 2002; Attia, 2000; Krishnapraka et al., 2001; Menguc & Viskanta, 1983; Muresan et al., 2004; Siewert & Thomas, 1991; Spuckler & Siegel, 1996) and references therein). To the best of our knowledge no analytical approach for heterogeneous media and considering the non-linearity exists so far, that are certainly closer to realistic scenarios in natural or technological sciences. A possible reason for considering a simplified problem (homogeneous and linearised) is that such a procedure turns the determination of a solution viable. It is worth mentioning that a general solution from an analytical approach for this type of problems exists only in the discrete ordinate approximation and for homogeneous media as reported in reference (Segatto et al., 2010).

Various of the initially mentioned applications allow to segment the medium in plane parallel sheets, where the radiation field is invariant under translation in directions parallel to that sheet. In other words the only spatial coordinate of interest is the one perpendicular to the sheet that indicates the penetration depth of the radiation in the medium. Frequently, it is justified to assume the medium to have an isotropic structure which reduces the angular degrees of freedom of the radiation intensity to the azimuthal angle θ or equivalently to its cosine μ. Further simplifications may be applied which are coherent with measurement procedures. One the one hand measurements are conducted in finite time intervals where the problem may be considered (quasi-)stationary, which implies that explicit time dependence may be neglected in the transfer equation. On the other hand, detectors have a finite dimension (extension) with a specific acceptance angle for measuring radiation and thus set some angular resolution for experimental data. Such an uncertainty justifies to segment the continuous angle into a set of discrete angles (or their cosines), which renders the original equation with angular degrees of freedom a set of equations known as the S_N approximation to be introduced in detail in section 3.

Our chapter is organised as follows: in the next section we motivate the radiative-conductive transfer problem. Sections 3 and 4 are dedicated to the hierarchical construction procedure of analytical solutions for the heterogeneous radiative-conductive transfer problem from its reduction to the homogeneous case, using two distinct philosophies. In section 4.3 we apply the method to specific cases and present results. Last, we close the chapter with some remarks and conclusions.

2. The radiative conductive transfer problem

In problems of radiative transfer in plane parallel media it is convenient to measure linear distances normal to the plane of stratification using the concept of optical thickness τ which is measured from the boundary inward and is related through the density ρ, an attenuation

coefficient κ and the geometrical projection on the direction perpendicular to that plane, say along the z-axis, so that $d\tau = -\kappa\rho dz$. Further the temperature is measured in multiples of a reference temperature $T(\tau) = \Theta(\tau)T_r$, typically taken at $\tau = 0$.
Based on the photon number balance and in the spirit of a Boltzmann type equation one arrives at the radiative transfer equation in a volume that shall be chosen in a way so that no boundaries that separate media with different physical properties cross the control volume. To this end, five photon number changing contributions shall be taken into account which may be condensed into the four terms that follow. The first term describes the net rate of streaming of photons through the bounding surface of an infinitesimal control volume, the second term combines absorption and out-scattering from μ to all possible directions μ' in the control volume. The third term contemplates in-scattering from all directions μ' into the direction μ, and last not least a black-body like emission term according to the temperature dependence of Stefan-Boltzmann's law for the control volume.

$$\frac{dI(\tau,\mu)}{d\tau} + \frac{1}{\mu} I(\tau,\mu) = \frac{\omega(\tau)}{2\mu} \int_{-1}^{1} \mathcal{P}(\mu') I(\tau,\mu')\, d\mu' + \frac{1-\omega(\tau)}{\mu} \Theta^4(\tau) \tag{1}$$

Here, ω is the single scattering albedo and $\mathcal{P}(\mu)$ signifies the differential scattering coefficient or also called the phase function, that accounts for the rate at which photons are scattered into an angle $d\mu'$ and with inclination μ with respect to the normal vector of the sheet. Note, that the phase function is normalized $\frac{1}{2}\int \mathcal{P}(\mu)\, d\mu = 1$.
Upon simplifying the phase function in plane geometry one may expand the angular dependence in Legendre Polynomials $P_n(\mu)$,

$$\mathcal{P}(\mu,\mu') = \sum_{\ell=0}^{\infty} \beta_n P_n(\mu'-\mu)\ ,$$

with β_n the expansion coefficients that follow from orthogonality. Further one may employ the addition formula for Legendre polynomials using azimuthal symmetry (hence the zero integral)

$$P_\ell(\mu'-\mu) = P_\ell(\mu)P_\ell(\mu') + 2\sum_{m=1}^{n} \frac{(n-m)!}{(n+m)!} P_n^m(\mu) P_n^m(\mu') \underbrace{\int_0^{2\pi} \cos(m(\phi-\phi'))\, d\phi'}_{=0}\ ,$$

and write the integral on the right hand side of side of equation (1) as

$$\int_{-1}^{1} \mathcal{P}(\mu,\mu') I(\tau,\mu')\, d\mu' = \sum_{\ell=0}^{\infty} \beta_\ell \int_{-1}^{1} P_\ell(\mu) P_\ell(\mu') I(\tau,\mu')\, d\mu'\ ,$$

where the summation index refers to the degree of anisotropy. For practical applications only a limited number of terms indexed with ℓ have to be taken into account in order to characterise qualitatively and quantitatively the anisotropic contributions to the problem. Also higher ℓ terms oscillate more significantly and thus suppress the integral's significance in the solution. The degree of anisotropy may be indicated truncating the sum by an upper limit L. The integro-differential equation (1) together with the afore mentioned manipulations may be cast into an approximation known as the S_N equation upon reducing the continuous angle cosine to a discrete set of N angles. This procedure opens a pathway to apply standard vector algebra techniques to obtain a solution from the equation system, discussed in detail in section 3.

In order to define boundary conditions we have to specify in more details the scenario in consideration. In the further we analyse non-linear radiative-conductive transfer in a grey plane-parallel participating medium with opaque walls, where specular (mirror like) as well as diffuse reflections occur besides thermal photon emission according to the Stefan-Boltzmann law (see (Elghazaly, 2009) and references therein). If one thinks the medium being subdivided into sheets of thickness $\Delta\tau$ with sufficiently small depth so that for each sheet a homogeneous medium applies, than for each face or interface the condition for the top boundary (at $\tau = \tau_i$) is

$$I(\tau,\mu) = \epsilon(\tau)\Theta^4(\tau) + \rho^s(\tau)I(\tau,-\mu) + 2\rho^d(\tau)\int_0^1 I(\tau,-\mu')\mu'\,d\mu'\,, \tag{2}$$

with ρ^s and ρ^d the specular and diffuse reflections at the boundary, which are related to the emissivity ϵ by $\epsilon + \rho^s + \rho^d = 1$. For the limiting bottom boundary ($\tau = \tau_i + \Delta\tau$) μ and μ' change their sign in the argument of $I(\tau,\mu^{(\prime)})$ in equation (2). Suppose we have N_S sheets and $N_S + 1$ boundaries, one might think that for a first order differential equation (1) in τ the supply of $N_S + 1$ boundary conditions results in an ill-posed problem with no solutions at all. However, we still have to set up an equation that uniquely defines the non-linearity in terms of the radiation intensity.
The relation may be established in two steps, first recognizing that the dimensionless radiative flux is expressed in terms of the intensity by

$$q_r^* = 2\pi\int_{-1}^1 I(\tau,\mu)\mu\,d\mu\,, \tag{3}$$

and the energy equation for the temperature that connects the radiative flux to a temperature gradient is

$$\frac{d^2}{d\tau^2}\Theta(\tau) = \frac{1}{4\pi N_c}\frac{d}{d\tau}q_r^*(\tau) = \frac{1}{4\pi N_c}\frac{d}{d\tau}\left(2\pi\int_{-1}^1 I(\tau,\mu)\mu\,d\mu\right)\,. \tag{4}$$

HereN_c is the conduction-radiation parameter, defined as

$$N_c = \frac{k\beta_{ext}}{4\sigma\mathfrak{n}^2T_r^3}\,, \tag{5}$$

with k the thermal conductivity, β_{ext} the extinction coefficient, σ the Stefan-Boltzmann constant and $\mathfrak{n}$ the refractive index. Note that the radiative flux results from the integration of the intensity over angular variables, so that the thermal conductivity is considered here isotropic. Equation (4) is subject to prescribed temperatures at the top- and bottommost boundary

$$\Theta(0) = \Theta_T \qquad \text{and} \qquad \Theta(\tau_0) = \Theta_B\,. \tag{6}$$

3. The S_N approximation for the heterogeneous problem

The set of equations (1) and (4), that are continuous in the angle cosine, may be simplified using an enumerable set of discrete angles following the collocation method, that defines the

radiative convective transfer problem in the S_N approximation

$$\frac{dI_n(\tau)}{d\tau} + \frac{1}{\mu_n} I_n(\tau) = \frac{\omega(\tau)}{2\mu_n} \sum_{\ell=0}^{L} \beta_\ell P_\ell(\mu_n) \sum_{k=1}^{N} w_k P_\ell(\mu_k) I_k(\tau) + \frac{1-\omega(\tau)}{\mu_n} \Theta^4(\tau) \,, \tag{7}$$

$$\frac{d\Theta(\tau)}{d\tau} - \frac{d\Theta(\tau)}{d\tau}\bigg|_{\tau=0} = \frac{1}{2N_c} \sum_{k=1}^{N} w_k \left(I_k(\tau) - I_k(0) \right) \mu_k \,, \tag{8}$$

for $n = 1, \ldots, N$ and are subject to the following boundary conditions.

$$I_n(0) = \epsilon(0)\Theta^4(0) + \rho^s(0) I_{N-n+1}(0) + 2\rho^d(0) \sum_{k=1}^{\frac{N}{2}} w_k I_{N-k+1}(0)\mu_k$$

$$I_{N-n+1}(\tau_0) = \epsilon(\tau_0)\Theta^4(\tau_0) + \rho^s(\tau_0) I_n(\tau_0) + 2\rho^d(\tau_0) \sum_{k=1}^{\frac{N}{2}} w_k I_k(\tau_0)\mu_k \tag{9}$$

Note, that the integrals over the angular variables are replaced by a Gaussian quadrature scheme with weight factors w_k, where k refers to one of the discrete directions μ_k.

3.1 The S_N approach in matrix representation

For convenience we introduce a shorthand notation in matrix operator form, where the column vector

$$\mathbf{\Phi}(\tau) = (\mathbf{I}, \Theta(\tau))^T = (I_1(\tau), \cdots, I_N(\tau), \Theta(\tau))^T$$

combines the anisotropic intensities and the isotropic temperature function, the non-linear terms and boundary terms from integration (i.e. the temperature gradient and the conduction radiation intensity at $\tau = 0$) are absorbed in an inhomogeneity

$$\mathbf{\Psi} = \left(\frac{1-\omega(\tau)}{\mu_1}\Theta^4(\tau), \cdots, \frac{1-\omega(\tau)}{\mu_n}\Theta^4(\tau), \frac{d\Theta}{d\tau}(0) - \frac{1}{2N_c} \sum_{k=1}^{N} w_k I_k(0)\mu_k \right)^T$$

which allows to cast the equation system (7) and (8) in compact form

$$\frac{d}{d\tau}\mathbf{\Phi} - \mathcal{L}_M \mathbf{\Phi} = \mathbf{\Psi} \tag{10}$$

where $\mathcal{L}_M$ has the following elements.

$$(\mathcal{L}_M)_{nk} = \delta_{nk}(1 - \delta_{n,N+1})\frac{1}{\mu_n} + f_{nk} \qquad \text{for} \quad n,k = 1, \ldots, N+1 \tag{11}$$

Here, δ_{ij} is the Kronecker delta, θ_H the Heaviside functional

$$\delta_{ij} = \begin{cases} 1 \text{ for } i = j \\ 0 \text{ else} \end{cases} \,, \qquad \theta_H(x) = \begin{cases} 1 \text{ for } x > 0 \\ 0 \text{ else} \end{cases}$$

and the factors f_{nk} are

$$f_{nk} = \theta_H(N - n + 1/2)\theta_H(N - k + 1/2)\frac{\omega(\tau)}{2\mu_n} \sum_{\ell=0}^{L} \beta_\ell P_\ell(\mu_n) w_k P_\ell(\mu_k)$$
$$+ (1 - \delta_{k,N+1})\delta_{n,N+1}\frac{\mu_k}{2N_c} \,. \tag{12}$$

Note, that the increment $1/2$ in the Heaviside functional was introduced merely to make the argument positive definite in the range of interest which otherwise could lead to conflicts with possible definitions for $\theta_H(x)$ at $x = 0$.
The boundary conditions are combined accordingly, except for the limiting temperatures (equation (6)) that are kept separately for simplicity because they would add only an additional diagonal block leading to a reducible representation and thus this does not bring any advantage.

$$\mathcal{B}_D\mathbf{I} - \mathcal{B}_M\mathbf{I} = \mathbf{\Gamma} \tag{13}$$

Equation (13) has a block form where one block represents forward angle contributions $\mu > 0$ and the other one backward terms $\mu < 0$ originating from the top and bottom boundary, respectively. Here, $\mathcal{B}_D$ is the $N \times N$ unit matrix, and

$$\mathcal{B}_M = \begin{pmatrix} 0 & \rho^s\mathcal{C}_{N/2} + 2\rho^d\mathcal{G}^-_{N/2} \\ \rho^s\mathcal{C}_{N/2} + 2\rho^d\mathcal{G}^+_{N/2} & 0 \end{pmatrix} \tag{14}$$

with $\mathcal{C}_{N/2}$ an $N/2 \times N/2$ matrix which results from column reversion in the unit matrix, i.e. after mapping column position k to position $N/2 - k + 1$. The remaining matrices that control the diffuse forward and backward reflection ($\mathcal{G}^{\pm}_{N/2}$), respectively have the elements

$$\begin{aligned} \left(\mathcal{G}^+_{N/2}\right)_{nk} &= \theta_H(N/2 - n + 1/2)\theta_H(k - N/2 - 1/2)\mu_{N-k+1}w_{N-k+1} \\ \left(\mathcal{G}^-_{N/2}\right)_{nk} &= \theta_H(n - N/2 - n - 1/2)\theta_H(N/2 - k + 1/2)\mu_k w_k \,. \end{aligned} \tag{15}$$

In these expressions the Heaviside functions restrict the non-zero elements to the off-diagonal blocks with row indices $n \in \{1, \ldots, N/2\}$ and column indices $k \in \{N/2 + 1, \ldots, N\}$ and with row indices $n \in \{N/2 + 1, \ldots, N\}$ and column indices $k \in \{1, \ldots, N/2\}$, respectively. The vector representation for the intensity is

$$\mathbf{I} = (\mathbf{I}_+, \mathbf{I}_-)^T \quad \text{with} \quad \mathbf{I}_+ = (I_1(\tau), \ldots, I_{N/2}(\tau)) \quad \text{and} \quad \mathbf{I}_- = (I_{N/2+1}(\tau), \ldots, I_N(\tau)) \,.$$

The inhomogeneity $\mathbf{\Gamma}$ has the same emission term in each component.

$$\Gamma_n = \epsilon(\tau)\Theta^4(\tau) \qquad \forall n$$

3.2 Constructing the solution by the decomposition method

The principal difficulty in constructing a solution for the radiative conductive transfer problem in the S_N approximation (10) subject to the boundary conditions (13) and (6) is due to the fact that the single scattering albedo $\omega(\tau)$, the emissivity $\epsilon(\tau)$ and the specular and diffuse reflection ($\rho^s(\tau)$ and $\rho^d(\tau)$) have an explicit dependence on the optical depth τ, that is the heterogeneity of the medium in consideration. It is worth mentioning that the proposed methodology is quite general in the sense that it can be applied to other approximations of equation (1) that make use of spectral methods, as for instance the spherical harmonic P_N-, the Chebychev Ch_N- and the Walsi W_N-approximation (Vilhena & Segatto, 1999; Vilhena et al., 1999), among others.
In the sequel we report on two approaches to solve the heterogeneous problem (equations. (10), (13), (6)). The principal idea of this techniques relies on the reduction of the Radiative Conductive transfer problem in heterogeneous media to a set of problems in domains of homogeneous media. In the first approach we consider the standard approximation of the

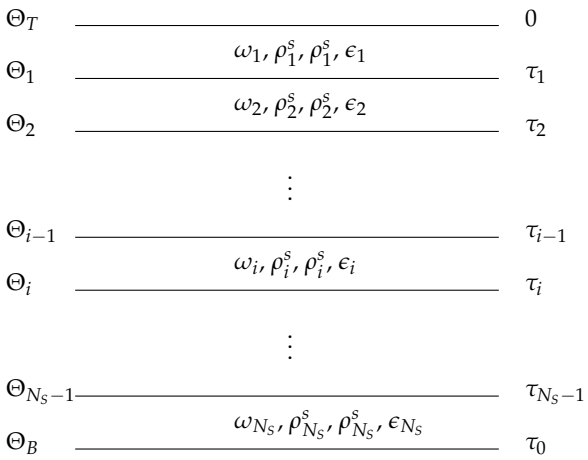

Fig. 1. Schematic illustration of a heterogeneous medium in form of a multi-layer slab.

heterogeneous medium in form of a multi-layer slab (see figure 1). For each of the layers the problem reduces to a homogeneous problem but with the same number of boundary conditions as the original problem. The procedure that determines the solution for each slab is presented in detail in section 4. In order to solve the unknown boundary values of the intensities and the temperatures at the interfaces between the slabs, matching these quantities using the bottom boundary values of the upper slab and the top boundary values of the lower slab eliminates these incognitos.

In the second approach we introduce a new procedure to work the heterogeneity. To begin with, we take the averaged value for the albedo coefficient $\omega(\tau)$,

$$\bar{\omega} = \frac{1}{\tau_0} \int_0^{\tau_0} \omega(\tau)\, d\tau \tag{16}$$

and rewrite the problem as a homogeneous problem plus an inhomogeneous correction. Note that $\mathcal{L}_M$ as well as Ψ depend on the local albedo coefficient $\omega(\tau)$. Since the terms containing the coefficient are linear in ω permits to separate an average factor $\bar{\omega}$ and the difference $\omega(\tau) - \bar{\omega}$.

$$\frac{d}{d\tau}\mathbf{\Phi} - \mathcal{L}_M(\bar{\omega})\mathbf{\Phi} = \mathbf{\Psi}(\bar{\omega}) + \mathcal{L}_M(\omega(\tau) - \bar{\omega})\mathbf{\Phi} + \mathbf{\Psi}(\omega(\tau) - \bar{\omega}) \tag{17}$$

Now, following the idea of the Decomposition method proposed originally by Adomian (Adomian, 1988), to solve non-linear problems without linearisation, we handle equation (17), constructing the following recursive system of equations. Here, $\mathbf{\Psi} = \sum_{m=0}^{\infty} \mathbf{\Psi}_m$ is a formal decomposition and the non-linearity is written in terms of the so-called Adomian polynomials $\Theta^4(\tau) = \sum_{m=0}^{\infty} \hat{A}_m(\tau)$. The first equation of the recursive system is the same as in a homogeneous slab, and the influence of the heterogeneity is governed by the source term. The homogeneous problem is explicitly solved in section 4 so that we concentrate here

on the inhomogeneity.

$$\frac{d}{d\tau}\mathbf{\Phi}_0 - \mathcal{L}_M(\bar{\omega})\mathbf{\Phi}_0 = \mathbf{\Psi}_0(\bar{\omega})$$
$$\frac{d}{d\tau}\mathbf{\Phi}_i - \mathcal{L}_M(\bar{\omega})\mathbf{\Phi}_i = \mathbf{\Psi}_i(\bar{\omega}) + \mathcal{L}_M(\omega(\tau)-\bar{\omega})\mathbf{\Phi}_{i-1} + \mathbf{\Psi}_{i-1}(\omega(\tau)-\bar{\omega}) \quad \text{for} \quad i \leq 1$$
$$\text{with} \qquad \mathbf{\Psi}_{i-1}(\omega(\tau)-\bar{\omega}) = (\bar{\omega}-\omega(\tau))A_m(\tau)(\mu_1^{-1},\ldots,\mu_1^{-N},0)^T \tag{18}$$

Note, that the $N+1$-th component of $\mathbf{\Psi}_0(\bar{\omega})$ contains the inhomogeneous term of the temperature equation.

$$(\mathbf{\Psi}_0(\bar{\omega}))_{N+1} = \mathbf{\Psi}_{N+1} = \frac{d\Theta}{d\tau}(0) - \frac{1}{2N_c}\sum_{k=1}^{N} w_k I_k(0)\mu_k \tag{19}$$

The determination of the Adomian polynomials $A_m(\tau)$ in equation (18) in terms of the temperature is shown in section 4.
To complete our analysis considering the boundary conditions, the first equation of the recursive system satisfies the boundary condition, whereas the remaining equations satisfy homogeneous boundary conditions. By this procedure we guarantee that the solution $\mathbf{\Phi}$ determined from the recursive scheme and truncated at a convenient limit $\mathcal{M}$ satisfies the boundary conditions of the problem (13) and (6). Therefore we are now in a position to construct a solution with a prescribed accuracy by controlling the number of terms in the series solution given by equation (18). From the previous discussion it becomes apparent that it is possible by the proposed procedure to obtain a solution of the heterogeneous problem by a reduction to a set of homogeneous problems. To complete the construction of a solution for the heterogeneous problem in the next section we present the derivation of the solution of the S_N radiative-conductive transfer problem in a homogeneous slab.

4. The solution for the homogeneous radiative conductive heat transfer problem

In this section we consider the non-linear radiative-conductive transfer problem in a grey plane-parallel participating medium with combined specular and diffuse reflection (Siewert & Thomas, 1991) and its solution in an analytical form using a composite method by Laplace transform and the decomposition method (Adomian, 1988). Before the advent of the decomposition method analytical solutions were restricted to a few special problems like the Bernoulli and Ricatti equations, to mention only two. The basic idea of the decomposition technique understands the following steps: The non-linear problem is interpreted as an operator equation (as already introduced in section 3) and split into a sum of linear and non-linear terms. Next, one expands the solution (in the present discussion the intensity I) and the non-linear term (here the quartic dimensionless temperature term Θ^4), respectively, as a series $I(\tau) = \sum_{m=1}^{\infty} \mathbf{U}_m$ and $\Theta^4 = \sum_{m=1}^{\infty} \hat{A}_m$, where $\hat{A}_m$ are to be determined self consistently according to Adomian's procedure (Adomian, 1988). Upon insertion of these expansions in the split equation, one may construct a set of linear recursive problems that can be solved by classical methods for linear problems.
Although the method is designed for general non-linear problems, it is not straight forward to apply it to any given problem and to any desired precision. One specific equation system which we solve in the sequel considers the S_N problem equation (10) for non-linear radiative-conductive heat transfer in plane parallel geometry as introduced in ref. (Ozisik,

1973), the index N signifies here the number of the discrete directions of the angular space. More specifically, we circumvent limitations that arose in the discussion of the same problem in ref. (Vargas & Vilhena, 1999). Furthermore, differently than some iterative schemes found in the literature (Abulwafa, 1999; Ozisik, 1973; Siewert & Thomas, 1991), we construct an analytical solution sequence which in the limit of the truncation parameter $\mathcal{M} \to \infty$ converges to the exact solution of the equation that characterises the S_N problem.
For any arbitrary truncation and using Laplace transform (LT) the original S_N problem may be cast into LTS_N form, which allows for matrix orthogonalisation and thus opens the advantage of handling S_N problems with N as large as for instance $\sim$ 1500; for further details see references. (Segatto et al., 1999) and (Goncalves et al., 2000). Once the $\hat{A}_m$ polynomials are known up to $\mathcal{M}$ the LTS_N provides the sum up to $\mathcal{M}$ of the expanded solution.
The hybrid LTS_N Adomian approach is not new, see references. (Vargas & Vilhena, 1999) and (Brancher et al., 1999), but in the present discussion we present a procedure based on the same reasoning but in a novel and optimised form. This progress is partially due to the more effective handling of the boundary conditions. In a previous attempt (Vargas et al., 2003) the boundary conditions entered in every step of recursion which posed limitations on the solutions so that it was only possible to resolve angles with $N = 30$ and truncate the expansion after the first term. As the following discussion will show, the present approach henceforth denoted the $D_{\mathcal{M}}LTS_N$ approach circumvents these shortcomings (here $D_{\mathcal{M}}LTS_N$ stands for Decomposition Laplace Transform S_N approach).

4.1 The LTS_N formalism

The dimensionless non-linear S_N radiative transfer equation in a grey plane-parallel homogeneous medium results from equation (7) upon substitution of the albedo coefficient by its average value.

$$\frac{d}{d\tau} I_n(\tau) + \frac{1}{\mu_n} I_n(\tau) = \frac{\bar{\omega}}{2\mu_n} \sum_{\ell=0}^{L} \beta_\ell P_\ell(\mu_n) \sum_{k=1}^{N} P_\ell(\mu_k) I_k(\tau) + \frac{1-\bar{\omega}}{\mu_n} \Theta^4(\tau) \tag{20}$$

for $n = 1, \ldots, N$ and subject to the boundary conditions with constant emissivity and reflectivity.

$$I_n(0) = \epsilon_1 \Theta_1^4 + \rho_1^s I_{N-n+1}(0) + 2\rho_1^d \sum_{k=1}^{N/2} w_k \mu_k I_{N-k+1}(0) \,, \tag{21}$$

$$I_{N-n+1}(\tau_0) = \epsilon_2 \Theta_2^4 + \rho_2^s I_n(\tau_0) + 2\rho_2^d \sum_{k=1}^{N/2} w_k \mu_k I_k(\tau_0) \,. \tag{22}$$

Note, that β_ℓ are the expansion coefficients explicitly given in case study 4.3.1.
The equation for the temperature (8) may be solved by integrating twice from the boundary $\tau = 0$ to any $\tau \in [0, \tau_0]$.

$$\Theta(\tau) = \Theta_1 + (\Theta_2 - \Theta_1)\frac{\tau}{\tau_0} - \frac{1}{4\pi N_c}\frac{\tau}{\tau_0}\int_0^{\tau_0} q_r^*(\tau')d\tau' + \frac{1}{4\pi N_c}\int_0^{\tau} q_r^*(\tau')d\tau' \tag{23}$$

Recalling, that equation (8) relates the intensity to the temperature, equation (23) shows the connection between the temperature and the radiative flux that permits to cast the problem into a form that depends only on the directional intensity $\mathbf{I}$.

In order to apply the decomposition method to the problem (20) and (23), we expand the non-linear source term into a series of Adomian polynomials Adomian (1988), which are determined in the next section.

$$\Theta^4(\tau) = \sum_{m=0}^{\infty} \hat{A}_m(\tau) \tag{24}$$

Upon inserting this *ansatz* in equation (20) yields a first order matrix differential equation:

$$\frac{d}{d\tau}\mathbf{I}(\tau) - \mathbf{A}\mathbf{I}(\tau) = \sum_{m=0}^{\infty} \hat{A}_m(\tau)\mathbf{M}. \tag{25}$$

Here $\mathbf{I}(\tau) = (\mathbf{I}_+(\tau), \mathbf{I}_-(\tau))^T$ is the intensity radiation vector, where the sub-vectors $\mathbf{I}_+(\tau)$ and $\mathbf{I}_-(\tau)$ are the intensity radiation for the positive ($0 < \mu < 1$) and negative ($-1 < \mu < 0$) directions, respectively, and of order $N/2$ each. Further, $\mathbf{M}$ is a vector of order N with entries:

$$\mathbf{M} = (1-\omega)\left(\frac{1}{\mu_1}, \ldots, \frac{1}{\mu_N}\right)^T \tag{26}$$

Finally, the components of matrix $\mathbf{A}$ have the form:

$$A_{ij} = -\frac{1}{\mu_i}\delta_{ij} + \frac{\omega}{2\mu_i}\sum_{\ell=0}^{L} \beta_\ell P_\ell(\mu_i) P_\ell(\mu_j)\ , \tag{27}$$

where δ_{ij} is the Kronecker symbol. The radiation intensity can formally be written as a series:

$$\mathbf{I}(\tau) = \sum_{m=0}^{\infty} \mathbf{U}_m(\tau) \tag{28}$$

which upon substitution in equation (25) results in:

$$\sum_{m=0}^{\infty}\left(\frac{d}{d\tau}\mathbf{U}_m(\tau) - \mathbf{A}\mathbf{U}_m(\tau)\right) = \sum_{m=0}^{\infty} \hat{A}_m(\tau)\mathbf{M} \tag{29}$$

One possibility of solving the equation system (29) starts with the initialisation

$$\frac{d}{d\tau}\mathbf{U}_0(\tau) - \mathbf{A}\mathbf{U}_0(\tau) = 0 \tag{30}$$

$$\frac{d}{d\tau}\mathbf{U}_m(\tau) - \mathbf{A}\mathbf{U}_m(\tau) = \hat{A}_{m-1}(\tau)\mathbf{M}\ , \qquad m = 1, 2, ..., \infty \tag{31}$$

which is then solved by the Laplace transform procedure (i.e. the LTS_N method) for any arbitrary but finite $m \leq \mathcal{M}$. Here, $\mathcal{M}$ is a truncation of the series which has to be chosen such that the remaining dropped terms are only a small correction to the approximate solution. Details of the method may be found in references. (Segatto et al., 1999) and (Goncalves et al., 2000). In the further we make use of the results of the Laplace transformed equations (30) and (31) and write $\mathbf{U}_m$ in form of a Laplace inversion. The Adomian polynomials are given explicitly in equation (36).

So far the LTS_N solution to the first problem of the recursive system has the form:

$$\mathbf{U}_0(\tau) = \mathbf{X}\mathbf{E}(\mathbf{D}\tau)\mathbf{V}^{(0)} \tag{32}$$

where **D** and **X** are respectively the matrices of eigenvalues and eigenfunctions resulting from the spectral decomposition of the matrix **A**. The components of the diagonal matrix $\mathbf{E}(\mathbf{D}\tau)$ are:

$$\mathbf{E}(\mathbf{D}\tau) = \begin{cases} e^{d_{ii}\tau} & \text{if} \quad d_{ii} < 0 \\ e^{d_{ii}(\tau-\tau_0)} & \text{if} \quad d_{ii} > 0 \end{cases} \tag{33}$$

Note, that the matrix expression **D**, **E** and eigenvectors **X** are from the solution of the Laplace transformed problem equations (30) and (31). In equation (33) d_{ii} are entries of the eigenvalue matrix **D**. Further the general solution for the remaining problems are given by

$$\mathbf{U}_m(\tau) = \mathbf{X}\mathbf{E}(\mathbf{D}\tau)\mathbf{V}^{(m)} + \mathbf{X}\mathbf{e}^{\mathbf{D}\tau}\mathbf{X}^{-1} * \hat{A}_{m-1}(\tau)\mathbf{M} \tag{34}$$

for $m = 1, \ldots, \mathcal{M}$ and $(*)$ denotes the convolution operator. The constant vectors $\mathbf{V}^{(m)}$ are determined from the application of the inhomogeneous boundary conditions

$$\begin{aligned} \mathbf{U}_0(0) &= \mathbf{I}(0) \\ \mathbf{U}_0(\tau_0) &= \mathbf{I}(\tau_0) \end{aligned} \qquad \text{for} \qquad m = 0$$

and the homogeneous boundary conditions

$$\begin{aligned} \mathbf{U}_m(0) &= 0 \\ \mathbf{U}_m(\tau_0) &= 0 \end{aligned} \qquad \text{for} \qquad m = 1, \ldots, \mathcal{M}$$

on the left hand side of equation (34). The effectiveness of this recursive scheme is due to the fact that the boundary condition for the problem (20) is already absorbed in the first recursion instruction whereas the remaining problems satisfy homogeneous boundary conditions only. To complete the construction of the analytical solution of problem (20) by the decomposition method, we present in the next section, a convergent scheme to generate the Adomian polynomials $\hat{A}_m$ for $m \in \{1, \ldots, \mathcal{M}\}$, for any generic $\mathcal{M}$.

4.2 The determination of the $\hat{A}_m$ polynomials

The role of the Adomian polynomials is to constitute the non-linear term in equation (20), i.e. the dimensionless non-linear temperature term Θ^4. Using a finite functional expansion in $T_m(\tau)$ for the dimensionless temperature $\Theta(\tau) = \sum_{m=0}^{\mathcal{M}} T_m(\tau)$ implies

$$\begin{aligned} \Theta^4 = \sum_{m=0}^{\mathcal{M}} \hat{A}_m = T_0^4 + 4T_0^3 \sum_{i=1}^{\mathcal{M}} T_i + \frac{12T_0^2}{2!}\left(\sum_{i=1}^{\mathcal{M}} T_i\right)^2 \\ + \frac{24T_0}{3!}\left(\sum_{i=1}^{\mathcal{M}} T_i\right)^3 + \frac{24}{4!}\left(\sum_{i=1}^{\mathcal{M}} T_i\right)^4, \end{aligned} \tag{35}$$

where one of the possible identifications of the $\hat{A}_m$ is to group together terms with T_i in the right hand side of the equation (35) in a way, such that the index i of T_i ranges from 0 to m. This can be seen explicitly in equation (36) where $\hat{A}_0$ depends on T_0 only, $\hat{A}_1$ on T_0, T_1, or generically, $\hat{A}_m = \hat{A}_m(T_0, \ldots, T_m)$. Note, that the significance of the T_m becomes clear further down in equation (39) and is used here merely as a term of a functional expansion. The

resulting scheme for the Adomain polynomials reads then, which for later use we indicate in factorized form:

$$\begin{aligned}
\hat{A}_0 &= T_0^4 = T_0 T_0 T_0^2 \\
\hat{A}_1 &= 4T_0^3 T_1 + 6T_0^2 T_1^2 + 4T_0 T_1^3 + T_1^4 = T_1(2T_0 + T_1)(2T_0^2 + 2T_0 T_1 + T_1^2) \\
\hat{A}_2 &= 4T_0^3 T_2 + 12T_0^2 T_1 T_2 + 12T_0 T_1^2 T_2 + 4T_1^3 T_2 + 6T_0^2 T_2^2 + 12T_0 T_1 T_2^2 \\
&\qquad + 6T_1^2 T_2^2 + 4T_0 T_2^3 + 4T_1 T_2^3 + T_2^4 \\
&= T_2(2T_0 + 2T_1 + T_2)(2T_0^2 + 4T_0 T_1 + 2T_1^2 + 2T_0 T_2 + 2T_1 T_2 + T_2^2) \\
&\vdots
\end{aligned} \tag{36}$$

In shorthand notation the recursive scheme for the Adomian polynomials may be written as

$$\hat{A}_m = T_m S_m R_m \tag{37}$$

where S_m and R_m are determined by the formulas for $m = 1, \ldots, \mathcal{M}$.

$$S_m = S_{m-1} + T_m + T_{m-1} \qquad \text{and} \qquad R_m = R_{m-1} + S_{m-1} T_{m-1} + S_m T_m \tag{38}$$

The recursive procedure according to equation (36) starts with $S_0 = T_0$ and $R_0 = T_0^2$. From equation (23), we construct then the recursive formulation for the temperature.

$$\begin{aligned}
T_0(\tau) &= \Theta_1 + (\Theta_2 - \Theta_1)\frac{\tau}{\tau_0} \\
T_{m+1}(\tau) &= -\frac{1}{2N_c}\frac{\tau}{\tau_0}\left\langle \mathbf{W}, \int_0^{\tau_0} \mathbf{U}_m(\tau')d\tau' \right\rangle + \frac{1}{2N_c}\left\langle \mathbf{W}, \int_0^{\tau} \mathbf{U}_m(\tau')d\tau' \right\rangle
\end{aligned} \tag{39}$$

Here $m = 0, \ldots, \mathcal{M}$ and the column vector $\mathbf{W} = (w_1\mu_1, ..., w_N\mu_N)^T$ contains as components the discrete directions μ_i and the Gaussian quadrature weights w_i. The bracket signifies the vector inner product. Note, that equation (39) establishes the Adomian polynomials in terms of the temperature at the boundaries and the expansion terms of the intensity, which in principle could be determined until infinity.

4.3 Numerical results

In this section we present three cases that show the robustness and quantitative coincidence of the $D_{\mathcal{M}}LTS_N$ approach with solutions of the S_N radiative-conductive problem in a slab in the literature. As results we evaluate the normalised temperature, conductive, radiative and total heat fluxes.

$$Q_r(\tau) = \frac{1}{4\pi N_c} q_r^*(\tau) \quad Q_c(\tau) = -\frac{d}{d\tau}\Theta(\tau) \quad \text{and} \quad Q(\tau) = Q_r(\tau) + Q_c(\tau)$$

4.3.1 Case 1

In this case we determine the numerical values for $\mathcal{M}$ and N in order to get results with a considerable accuracy. The numerical values of the parameters used in cases 1 to 2 are given in table 1. The coefficient β_ℓ is defined considering a binomial scattering law which also permits a comparison with the results of (Siewert & Thomas, 1991).

$$\beta_\ell = \left(\frac{2\ell+1}{2\ell-1}\right)\left(\frac{L+1-\ell}{L+1+\ell}\right)\beta_{\ell-1} \qquad 0 \le \ell \le L \qquad \text{and} \qquad \beta_0 = 1$$

ϵ_1	ϵ_2	ρ_1^s	ρ_2^s	ρ_1^d	ρ_2^d	Θ_1	Θ_2	ω	τ_0	N_c	L
0.6	0.4	0.1	0.2	0.3	0.4	1.0	0.5	0.95	1.0	0.05	299

Table 1. Parameters of case 1.

$\mathcal{M}$	$\Theta(\tau)$	$Q_c(\tau)$	$Q_r(\tau)$	$Q(\tau)$
0	0.8177177955027018	0.5016457699309158	1.5158278540320405	2.0174736239629563
1	0.7698084721160902	0.4588373285860757	1.5859093685802235	2.0447466971662993
5	0.7775834780564881	0.4652872714487863	1.5788014097534921	2.0440886812022785
10	0.7775905224102305	0.4652925878442414	1.5787962534790447	2.0440888413232861
20	0.7775905213060152	0.4652925870115464	1.5787962542859926	2.0440888412975391
50	0.7775905213060152	0.4652925870115464	1.5787962542859926	2.0440888412975391
100	0.7775905213060152	0.4652925870115464	1.5787962542859926	2.0440888412975391
200	0.7775905213060152	0.4652925870115464	1.5787962542859926	2.0440888412975391

Table 2. The $D_{\mathcal{M}}LTS_{300}$ results for $\mathcal{M}$ ranging from 0 to 200, assuming $\tau/\tau_0 = 0.5$.

The numerical results for Θ, $Q_r(\tau)$, $Q_c(\tau)$ and $Q(\tau)$ are shown in table 2,3 and 4. The stability and convergence of the method was tested for $\tau/\tau_0 = 0.5$, varying $\mathcal{M}$ from 0 to 200, and using for N the values 300, 350 and 400, respectively. The displayed precision with 16 digits was adopted to show the smooth convergence with increasing $\mathcal{M}$ in the three cases for N.

$\mathcal{M}$	$\Theta(\tau)$	$Q_c(\tau)$	$Q_r(\tau)$	$Q(\tau)$
0	0.8177176602853717	0.5016457476711904	1.5158274669152312	2.0174732145864214
1	0.7698083890454525	0.4588373328783077	1.5859091448625833	2.0447464777408908
5	0.7775833829280683	0.4652872682514292	1.5788011774222819	2.0440884456737112
10	0.7775904272568637	0.4652925846297308	1.5787960211505467	2.0440886057802774
20	0.7775904261526551	0.4652925837970406	1.5787960219574921	2.0440886057545327
50	0.7775904261526551	0.4652925837970406	1.5787960219574921	2.0440886057545327
100	0.7775904261526551	0.4652925837970406	1.5787960219574921	2.0440886057545327
150	0.7775904261526551	0.4652925837970406	1.5787960219574921	2.0440886057545327
200	0.7775904261526551	0.4652925837970406	1.5787960219574921	2.0440886057545327

Table 3. The $D_{\mathcal{M}}LTS_{350}$ results for $\mathcal{M}$ ranging from 0 to 200, assuming $\tau/\tau_0 = 0.5$.

$\mathcal{M}$	$\Theta(\tau)$	$Q_c(\tau)$	$Q_r(\tau)$	$Q(\tau)$
0	0.8177175726732399	0.5016457333417628	1.5158272165190925	2.0174729498608555
1	0.7698083350919457	0.4588373357092782	1.5859090000727045	2.0447463357819826
5	0.7775833211907642	0.4652872662455577	1.5788010270489736	2.0440882932945312
10	0.7775903655034493	0.4652925826127813	1.5787958707789687	2.0440884533917498
20	0.7775903643992450	0.4652925817800941	1.5787958715859125	2.0440884533660064
50	0.7775903643992450	0.4652925817800941	1.5787958715859125	2.0440884533660064
150	0.7775903643992450	0.4652925817800941	1.5787958715859125	2.0440884533660064
200	0.7775903643992450	0.4652925817800941	1.5787958715859125	2.0440884533660064

Table 4. The $D_{\mathcal{M}}LTS_{400}$ results for $\mathcal{M}$ ranging from 0 to 200, assuming $\tau/\tau_0 = 0.5$.

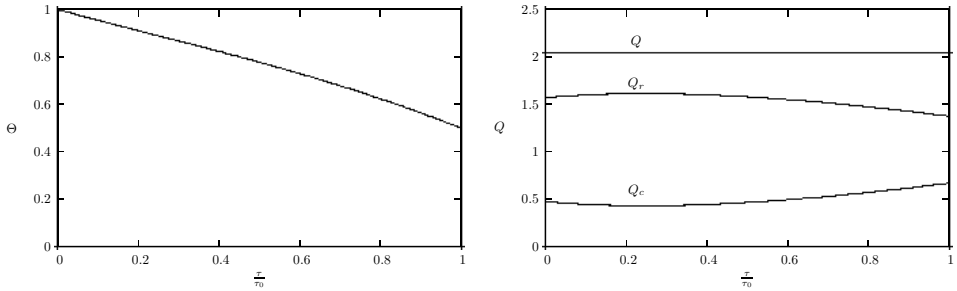

Fig. 2. Numerical results for $D_{10}LTS_{350}$ that exactly reproduce the results of reference (Siewert & Thomas, 1991) within the adopted precision. The temperature profile Θ (left), the conductive Q_c, radiative Q_r and total heat flux Q (right) against the relative optical depth $\frac{\tau}{\tau_0}$.

Comparing the corresponding lines in tables 2 to 4 for different N one observes that an analytical expression with $\mathcal{M} = 10$ and $N = 300$ is already close to the solution with $\mathcal{M}$ as large as 200 or ideally in the limit $\mathcal{M} \to \infty$. However, in the subsequent problems we set $\mathcal{M} = 10$ and $N = 350$ in order to reproduce within the adopted precision the numerical results of ref. (Siewert & Thomas, 1991) where the P_N method was applied to the same problem.

4.3.2 Case 2

The numerical evaluation in case 1 may now be refined varying the optical depth which was maintained fixed previously. To this end we determine $\Theta(\tau)$, $Q_c(\tau)$, $Q_r(\tau)$ and $Q(\tau)$ for τ/τ_0 ranging from 0 to 1. The numerical results are shown in figure 2 which coincide with the findings in reference (Siewert & Thomas, 1991) beyond a six digit precision. In their work Siewert and Thomas left open the question of convergence of their applied method, which by virtue of numerical coincidence with the present approach may be positively answered. Although not presented here with mathematical rigour, convergence of the decomposition method is formally guaranteed (see references (Adomian, 1988; Cherruault, 1989; Pazos & Vilhena, 1999a;b)) by the manifest exact solution in the limit $\mathcal{M} \to \infty$.

4.3.3 Case 3

A third comparison is elaborated making contact to a work by (Abulwafa, 1999), considering a conductive radiative problem in a slab assuming isotropy ($L = 0$) and with thickness τ_0, which also serves as a unit length. The parameter set is with either $\omega = 0.9$ or $\omega = 0.5$, with $\epsilon_1 = \epsilon_2 = \Theta_1 = 1$ and $\rho_1^d = \rho_2^d = \rho_1^s = \rho_2^s = 0$. In this article the author uses a variational technique to solve the radiative problem, while an iterative method is implemented to include the non-linearity effect of the temperature distribution of the medium from the conductive energy equation. Figure 3 shows the numerical findings of $D_{10}LTS_{350}$ in comparison to results from (Abulwafa, 1999) for two conduction-radiation parameters $N_c = 0.5$ and $N_c = 0.1$, respectively.

The comparison of the $D_{\mathcal{M}}LTS_N$ results with the ones of reference (Abulwafa, 1999) shows a fairly good agreement between the methods. It seems that a decrease in N_c opens slightly the difference between the two solutions, whereas increase in ω closes the difference between the solutions. Moreover, the larger N_c the closer one gets to a linear temperature profile. The difference is probably due to the fact that the approach in reference (Abulwafa, 1999) makes

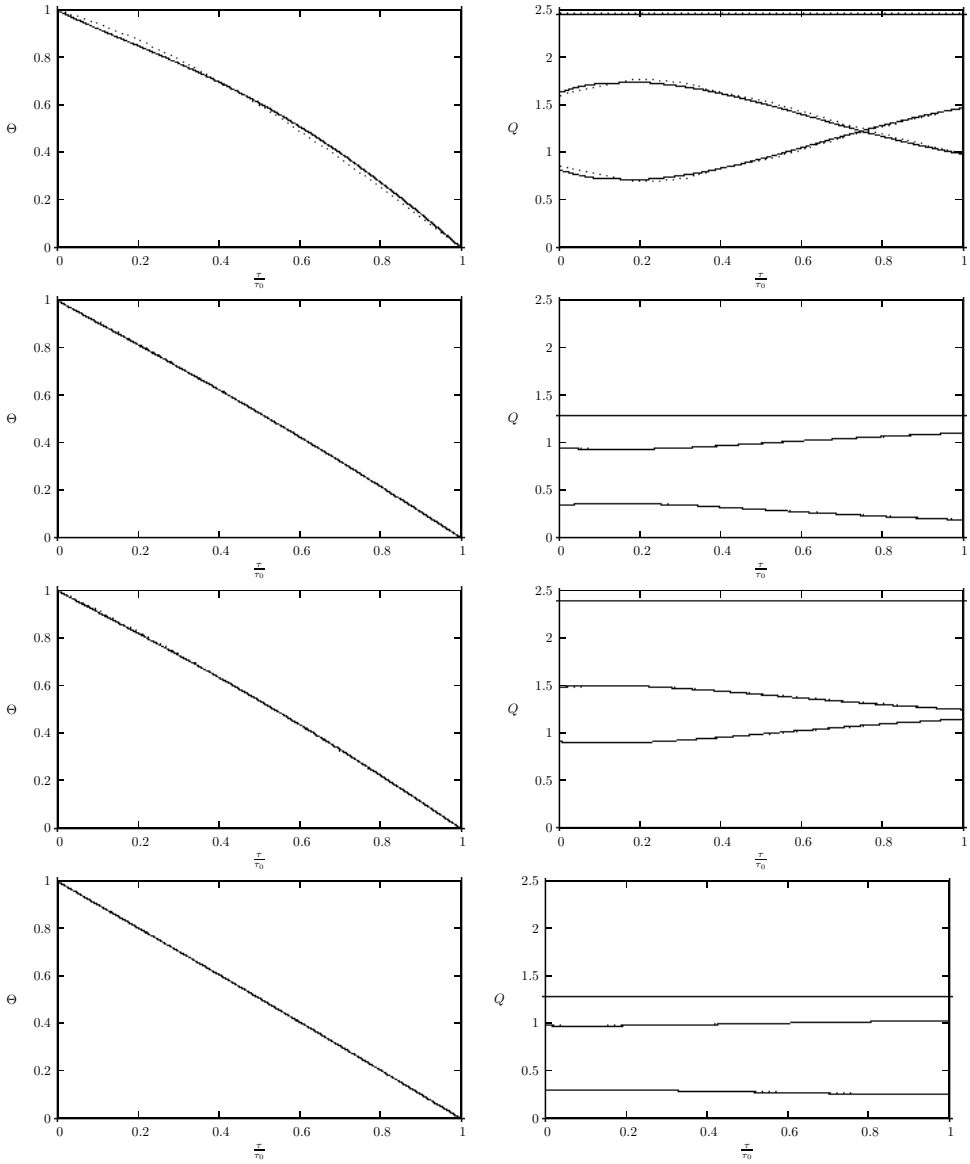

Fig. 3. Numerical comparisons of the $D_{\mathcal{M}}LTS_N$ (solid line) and Abulwafa's results (dotted line) for the parameter combinations $(\omega, N_c) = \{(0.5, 0.1), (0.5, 0.5), (0.9, 0.1), (0.9, 0.5)\}$ from top to bottom. The temperature profile Θ (left) and the conductive Q_c, radiative Q_r and total heat flux Q (right) against the relative optical depth $\frac{\tau}{\tau_0}$. The total heat fluxes are the constant curves, the conductive (radiative) heat fluxes show predominantly convex (concave) behaviour in the considered range (see also figure 2).

use of a trial function. In general in such type of approaches convergence depends crucially on how close the trial function is to the true solution. The comparison of cases 2 and 3 and the quantitative agreement with two different approaches shows the quality of the present method, especially because of the fact that it reproduces the exact analytical solution in the limit $\mathcal{M} \to \infty$ and thus allows to implement computationally a genuine convergence criterion. Some further information concerning the computational issue, the three cases were calculated on a Notebook computer with 64-bit Athlon 3200+ processor (1Ghz, 512kb Cache) and 1GB RAM. All calculations terminated with less than a minute execution time (some examples returned the result within seconds) and used typically between 10 and 20 iterations.

5. Conclusion

In the present work we discussed and compared an analytical approach to the non-linear S_N radiative-conductive transfer problem in plane-parallel geometry and a heterogeneous medium using a composite method by the Laplace transform and the Adomian decomposition (Adomian, 1988). We showed by two options how the heterogeneous problem may be cast into a set of homogeneous problems, so that the general solution may be obtained by a hierarchical algorithm. The Laplace technique opens pathways to resort to classical methods for linear problems, whereas the decomposition procedure allows to disentangle the non-linear contribution of the problem, that permits to solve the equations by a recursion scheme. It is worth mentioning two limiting cases, i.e. with single scattering albedo either $\omega = 0$ or $\omega = 1$. The latter case turns Adomian obsolete, because the non-linear term vanishes, whereas $\omega = 0$ diagonalizes the equation system and thus turns Laplace obsolete, since the solution may be obtained directly by integration.

The decomposition method as originally introduced is designed for general non-linear problems, but several ways are possible to construct a solution (Cardona et al., 2009; Segatto et al., 2008). The present study may be considered a guideline on how to distribute the influence of the boundary conditions and the non-linearity in order to solve the given problem. The boundary condition is absorbed in the part of the solution that belongs to the inversion of the differential operator without the non-linear contribution and the non-linear part simplifies to a problem for homogeneous boundary conditions only. Since existence and uniqueness of the solution for radiative-conductive transfer problems was discussed in references (Kelley, 1996; Thompson et al., 2004; 2008) the only critical issue of the recursive scheme is convergence. According to (Adomian, 1988; Cherruault, 1989; Pazos & Vilhena, 1999a;b) the resulting scheme is manifest exact and converges in the limit $\mathcal{M} \to \infty$ to the exact analytical solution. A genuine control of errors opens thus the possibility of model validation in comparison to experimental findings. In numerical approaches it is not straight forward to distinguish between model and numerical uncertainties, especially when non-linearities are present in the problem. Moreover, in general error analysis in numerical procedures is based on a heuristic basis, whereas the present approach permits a mathematical proof of convergence. This may not be that crucial for homogeneous problems, or those that permit linear approximations, but in the case of a heterogeneous problem in form of a multi-slab medium the question of convergence certainly plays a major role, especially because of the matching of solutions at the slab interfaces.

We are completely aware of the fact that the present procedure is limited by the convergence relation between the optical depth and the convergence radius of the Adomian approximation.

Nevertheless, we consider our work as an essential step for implementation of problems considering heterogeneous media. Furthermore, for thick media were the total optical depth lies outside the convergence radius a multi-slab treatment shall be used. In section 3 we showed explicitly how dependencies of the Albedo, the emissivity and the reflectivity on the optical depth are handled reducing partially the problem to a homogeneous one and including corrections in form of source terms. As an additional task due to this particular procedure matching of the partial solutions at the interfaces of the slabs has to be performed in addition, as a consequence of the local character of the physical parameter in each slab. So far, our findings show that for the S_N problem the series truncated with $\mathcal{M} = 10$ yields already a fairly good solution in form of an analytical expression. One advantage in comparison to numerical approaches lies in the fact that the dependence of the solution on the physical parameter may be analytically explored from the resulting expressions.
In section 4.3 we solved a selection of cases that may constitute a partial problem in a more complex medium and showed systematically, how a reliable solution may be obtained following the construction steps of 4.1 and 4.2. The application given in case 1 indicates the limits for $\mathcal{M}$ and N, and showed in case 2 that for a sequence of optical depths the same numerical results appear as given in ref. (Siewert & Thomas, 1991). Since convergence in the present approach is guaranteed one may elaborate a genuine convergence criterion depending on a desired precision. As a third test we compared our results for an isotropic problem to ref. (Abulwafa, 1999), where also agreement between the findings was verified. Since the proposed method reproduces the exact analytical solution in the limit $\mathcal{M} \to \infty$, approximate analytical expressions with finite $\mathcal{M}$ gain the character of benchmark results, which are of special interest in applications considering heterogeneous media.

6. References

Abulwafa, E.M. (1999). Conductive-radiative heat transfer in an inhomogeneous slab with directional reflecting boundaries. *Journal of Physics D*, Vol. 32, No. 14, (July 1999), 1626-1632.

Adomian, G., 1988. A review of the Decomposition method in applied-mathematics. *Journal of Mathematical Analysis and Applications*, Vol. 135, No. 2, (November 1988), 501-544.

Ahmad, S. & Deering, D. (1992). A Simple Analytical Function for Bidirectional Reflectance. *Journal of Geophysical Research D*, Vol. 97, No. 17 (April 1992), 18867–18886, 18867-18886.

Asllanaj, F., Jeandel, G., Roche, J.R. (2001). Numerical Solution of Radiative Transfer Equation Coupled with Non-linear Heat Conduction Equation. *International Journal of Numerical Methods for Heat and Fluid Flow*, Vol. 11, No. 5 (July 2001), 449-473.

Asllanaj, F., Milandri, A., Jeandel, G., Roche, J.R. (2002). A Finite Difference Solution of Non-linear Systems of RadiativeâĂŞConductive Heat Transfer Equations. *International Journal for Numerical Methods in Engineering*, Vol. 54, No. 11, (August 2002), 1649-1668.

Attia, M.T. (2000). On the Exact Solution of a Generalized Equation of Radiative Transfer in a Two-region Inhomogeneous Slab. *Journal of Quantitative Spectroscopy & Radiative Transfer*, Vol. 66, No. 6, (September 2000), 529-538.

Brancher, J.D., Vilhena, M.T., Segatto, C.F. (1999). The One-dimensional LTS_N Formulation For High Degree Of Anisotropy. *Journal of Quantitative Spectroscopy & Radiative Transfer*, Vol. 61, No. 1, (January 1999), 39-43.

Brewster, M.Q. (1992). *Thermal Radiative Transfer and Properties*, John Wiley & Sons Inc., ISBN: 978-0-471-53982-7, New York.

Cardona, A.V., Vilhena, M.T., Bodmann, B.E.J., Segatto, C.F. (2009). An Improvement of the Double Discrete Ordinate Approximation Solution by Laplace Technique for Radiative-Transfer Problems Without Azimuthal Symmetry and High Degree of Anisotropy. *Journal of Engineering Mathematics*, Vol. 67, No. 3,(July 2009), 193-204.

Cherruault, Y. (1989). Convergence of Adomian's Method. *Kybernetes*, Vol. 18, No. 2, (April 1989), 31-38.

Elghazaly, A. (2009). Conductive-Radiative Heat Transfer in a Scattering Medium with Angle-Dependent Reflective Boundaries. *Journal of Nuclear and Radiation Physics*, Vol. 4, No. 1, (May 2009), 31-41.

Gonçalves, G.A., Segatto, C.F., Vilhena, M.T. (2000). The LTS_N Particular Solution in a Slab for an Arbitrary Source and Large Quadrature. *Journal of Quantitative Spectroscopy & Radiative Transfer*, Vol. 66, No. 3 (August 2000), 271-276.

Kelley, C.T. (1996). Existence and Uniqueness of Solutions of Nonlinear Systems of Conductive-Radiative Heat Transfer Equations. *Transport Theory and Statistical Physics*, Vol. 25, No. 2, (March 1996), 249-260.

Kyunghan Kim, K. & Guo, Z. (2004). Ultrafast Radiation Heat Transfer in Laser Tissue Welding and Soldering. *Numerical Heat Transfer, Part A*, Vol. 46, No. 1 (January 2004) 23-40.

Krishnapraka, C.K., Narayana, K.B., Dutta, P. (2001). Combined Conduction and Radiation Heat Transfer in a Gray Anisotropically Scattering Medium with Diffuse-Specular Boundaries. *International Communications in Heat and Mass Transfer*, Vol. 28, No. 1, (January 2001), 77-86.

Liu, X., Smith, W.L., Zhou, D.K, Larar, A. (2006) Principal component-based radiative transfer model for hyperspectral sensors: theoretical concept. *Applied Optics*, Vol. 45, No. 1, (January 2006) 201-209.

Mengüç, M.P. & Viskanta, R. (1983). Comparison of Radiative Transfer Approximations for a Highly Forward Scattering Planar Medium. *Journal of Quantitative Spectroscopy & Radiative Transfer*, Vol. 29, No. 5, (May 1983), 381-394.

Muresan, C., Vaillon, R., Menezo, Ch., Morlot, R. (2004). Discrete Ordinates Solution of Coupled Conductive Radiative Heat Transfer in a Two-layer Slab with Fresnel Interfaces Subject to Diffuse and Obliquely Collimated Irradiation. *Journal of Quantitative Spectroscopy & Radiative Transfer*, Vol. 84, No. 4, (April 2004), 551-562.

Ozisik, M.N. (1973). *Radiative Transfer and Interaction with Conduction and Convection*, John Wiley & Sons Inc., ISBN: 0-471-65722-0, New York.

Pazos, R.P., Vilhena, M.T. (1999). Convergence of the *LT* Method: Approach of C_0 Semi groups. *Progress in Nuclear Energy*, Vol. 34, No. 1, (January 1999), 77-86.

Pazos, R.P., Vilhena, M.T. (1999). Convergence in Transport Theory. *Applied Numerical Mathematics*, Vol. 30, No. 1, (May 1999), 79-92.

Pinte, C., Harries, T.J., Min, M., Watson, A.M., Dullemond, C.P., Woitke, P., Ménard, F., Durán-Rojas, M.C. (2009). Benchmark Problems for Continuum Radiative Transfer. High Optical Depths, Anisotropic Scattering, and Polarisation. *Astronomy and Astrophysics*, Vol. 498, No. 3, (May 2009), 967-980.

Pomraning, G.C. (2005). *The Equations of Radiation Hydrodynamics*, Dover Publ. Inc., ISBN: 0-486-44599-2, Mineola, New York.

Segatto, C.F., Vilhena, M.T., Gomes, M.G. (1999). The One-Dimensional *LT* Solution In a Slab With High Degree of Quadrature. *Annals of Nuclear Energy*, Vol. 26, No. 10, (July 1999), 925-934.

Segatto, C.F., Vilhena, M.T., Gonçalez, T.T. (2008). An Analytical Integral Formulation for Time-Dependent S_N Transport Equation in a Slab by Double Laplace Transform Technique. *Kerntechnik* Vol. 73, (April 2008), 176-178.

Segatto, C.F. ; Vargas, R.F. ; Vilhena, M.T. ; Bodmann, B.E.J. (2010). A Solution for the Non-linear SN Radiative Conductive Problem in a Grey Plane-parallel Participating Medium. *International Journal of Thermal Sciences*, Vol. 49, No. 9 (September 2010), 1493-1499.

Shabanov, N.V., Huang, D., Knjazikhina, Y., Dickinson, R.E., Mynenia, R.B. (2007). Stochastic Radiative Transfer Model for Mixture of Discontinuous Vegetation Canopies. *Journal of Quantitative Spectroscopy & Radiative Transfer*, Vol. 107, No. 2, (September 2007) 236-262.

Siewert, C.E. & Thomas, J.R. (1991). A Computational Method for Solving a Class of Coupled ConductiveâĂŞradiative Heat Transfer Problems. *Journal of Quantitative Spectroscopy & Radiative Transfer*, Vol. 45, No. 5, (May 1991) 273-281.

Spuckler, C.M. & Siegel, R. (1996). Two-flux and Diffusion Methods for Radiative Transfer in Composite Layers. *Journal of Heat Transfer*, Vol. 118, No. 1, (February 1996), 218-222.

Thomas, G.E., Stamnes, K. (2002). *Radiative Transfer in the Atmosphere and Ocean*, Cambridge University Press, ISBN: 0-521-89061-6, Cambridge.

Thompson, M. Segatto, C.F., de Vilhena, M.T. (2004). Existence Theory for the Solution of a Stationary Nonlinear Conductive-Radiative Heat-Transfer Problem in Three Space Dimensions. *Transport Theory and Statistical Physics*, Vol. 33, No. 5-7, (August 2004), 563-576.

Thompson, M., de Vilhena, M.T., Bodmann, B.E.J. (2004). Existence Theory for Radiative Flows. *Transport Theory and Statistical Physics*, Vol. 37, No. 2 (March 2008), 307-326.

Tsai, J.R. & Ozişik, M.N. (1989). Radiation in Spherical Symmetry with Anisotropic Scattering and Variable Properties. *Journal of Quantitative Spectroscopy & Radiative Transfer*, Vol. 42, No. 3, (September 1989), 187-199.

Vargas, R.M.F. & Vilhena, M.T. (1999). A Closed-Form Solution for One-Dimensional Radiative Conductive Problem by the Decomposition and *LT* Methods. *Journal of Quantitative Spectroscopy and Radiative Transfer*, Vol. 61, No. 3, (Februaury 1998), 303-308.

Vargas, R.M.F., Cardona, A.V., Vilhena, M.T., Barros, R.C. (2003). On the Decomposition Method Applied to Linear and Non-linear Discrete Ordinates Problems in Slab Geometry. *Progress in Nuclear Energy*, Vol. 42, No. 4, (April 2003), 439-456.

Vilhena, M.T. & Segatto, C.F. (1999). The State of Art of the LTSn Method. In: *Mathematica and Computational, Reactor Physics and Environmental Analysis in Nuclear Applications*, Aregones M., Ahnert C., Cabellos D., (Ed.), 1618-1631, Proceedings of MC'99, ISBN: 699-0944-4, September, 1999, Madrid.

Vilhena, M.T., Barichelo, L.B., Zabadal, J.R., Segatto, C.F., Cardona, A.V., Pazos, R.P. (1999). Solution to the Multidimensional Linear Transport Equation by the Spectral Method. *Progress in Nuclear Energy*, Vol. 35, No. 3,4, (1999), 275-291.

Wilson, S.J. & Sen, K.K. (1986). Generalized Eddington Approximation Method for Radiative Transfer Problems in Slab Medium. *Journal of Quantitative Spectroscopy & Radiative Transfer*, Vol. 35, No. 6, (June 1986), 467-472.

Yang, L. & Kruse, B. (2004). Revised KubelkaâĂŞMunk theory. I. Theory and application. *Journal of the Optical Society of America A*, Vol. 21, No. 10 (October 2004) 1933-1941.

Yi, W., Yingkui, M., Peizhu, M. (1996). A Linear Spline Approximation for Radiative Transfer Problems in Slab Medium. *Journal of Quantitative Spectroscopy & Radiative Transfer*, Vol. 55, No. 1 (January 1996), 1-5.

9

Optimization of the Effective Thermal Conductivity of a Composite

Hubert Jopek and Tomasz Strek
Poznan University of Technology, Institute Of Applied Mechanics
Poland

1. Introduction

Composite materials by definition are a combination of two or more materials. Although the idea of combining two or more components to produce materials with controlled properties has been known and used from time immemorial, modern composites were developed only several decades ago and have found by now intensive application in different fields of engineering (Vasiliev&Morozov, 2001).
These materials are used in various design to improve the characteristic of various construction and reduce their weight. The properties of these materials and the problems of obtaining structural elements based upon them have been studied by researchers and engineers all over the world. The fields of composite applications are diversified (Freger et al., 2004). They include structural elements of flying vehicles, their casinos, wings, fuselages, tails and nose cones, jet engine stators, panels form various purposes, main rotors of helicopters, heat – proofing components, construction elements such as panels, racks, shields, banking elements, etc.
Any property of a composite which is made of two (or more) materials has the value which is the resultant of a few factors. Obviously, the most important are the values of a certain property of each constituent material. However, one of the factor that also influences the resultant value of a property of a composite as a whole is its geometrical structure. Such resultant properties are commonly called effective properties of a composite. Temperature is the most important of all environmental factors affecting the behaviour of composite materials, mainly because composites are rather sensitive to temperature and have relatively low effective thermal conductivity. For instance, advanced composites for engineering applications are characterized with low density providing high specific strength and stiffness, low thermal conductivity resulting in high heat insulation, and negative thermal expansion coefficient allowing us to construct hybrid composite elements that do not change their dimensions under heating (Vasiliev & Morozov, 2001).
Because experimental evaluation of effective properties (e.g. thermal conductivity) of composites is expensive and time consuming, computational methods have been found to provide efficient alternatives for predicting the best parameters of composites, especially those having complex geometries. To achieve a reliable prediction, one needs to work on two aspects: a good description of the structural details of fibrous materials, and an efficient numerical method for the solution of energy equations through the fibrous structures (Wang et al. 2009). The need to determine the thermal conductivity of fibres for design purposes has been the motivation of work (Al-Sulaiman et al., 2006). Authors developed four

empirical formulas to predict the thermal conductivities of fibre reinforced composite laminates and their constituents. In the paper (Boguszewski et al., 2008) the analysis of structure and features of phases composite was considered in order to study heat transfer phenomena. Models of three phases composite matrix, filler and interface with discontinuities were analyzed. Distance between particles was also considered. The paper (Kidalov & Shakhov, 2009) presents results in studying the possibility of developing composites in diamond-containing systems with a view of obtaining materials with a high thermal conductivity. The main objectives of project (Weber, 2001) were to develop a model to predict thermal conductivity of the carbon filled polymer composites and to determine if synergism between the fillers exists. Thermally conductive polymer composites can replace metals in many applications. The article (Zhou&Li, 2008) presents a numerical procedure to design two-phase periodic microstructural composites with tailored thermal conductivities, which is generalized as a topology optimization problem. The objective function is formulated in a least-square of the difference between the target and effective conductivities. Various microstructures both in 2- and 3-dimensions are presented to demonstrate such a systematic procedure of conductive material design. The effective thermal conductivity enhancement of carbon fibre composites was investigated in contribution (Wang et al., 2009) using a three-dimensional numerical method. The authors of the paper (Wang&Pan, 2008) have developed a random generation-growth method to reproduce the microstructures of open-cell foam materials via computer modelling, and then solve the energy transport equations through the complex structure by using a high-efficiency lattice Boltzmann method. The effective thermal conductivities of open-cell foam materials are thus numerically calculated and the predictions are compared with the existing experimental data. In the paper (Karkri, 2010) thermal properties of composites are investigated numerically and experimentally. In the numerical study, finite elements method is used for modelling heat transfer and to calculate the effective thermal conductivity of the composite for three elementary cells, such as simple cubic, body centered cubic and face centered cubic. The effect of the filler concentrations, the ratio of thermal conductivities of filler to matrix material and the Kapitza resistance of the contact inclusion/matrix on the effective conductivity was investigated. In the paper (Brucker&Majdalani, 2005), several analytical expressions are derived for an effective thermal conductivity. These explicit solutions embody many possible heat pathways and base plate geometries that arise in microelectronic packages. From a physical stand point, the effective thermal conductivity represents a figure-of-merit that assumes an intermediate value greater than that of the coolant, and smaller than that of the metal.

The objective of this contribution is to investigate the effective hybrid numerical method to predict effective thermal conductivity of composite material with fibres distributed in matrix phase. This method is combination of finite element method and genetic algorithm (FEM-GA). FEM-GA was used to find distribution of fibre in composite domain giving maximum, minimum or required value of effective thermal conductivity. The Algorithm is implemented in Comsol Multiphysics environment using Comsol Script language (Comsol, 2007). Comsol solver uses finite element method which today has been widely employed in solving field problems arising in modern industrial practices (Zienkiewicz & Taylor, 2000).

It is assumed that both the matrix and fibres of the considered composite are homogenous, isotropic and their thermal conductivities are constant. The fibres are cylindrical, arranged parallel, continuous with circular cross-section. The fibre diameter is relatively small in comparison to their length, thus fibres can be treated as infinitely long. Fibres can be different in size and thermal properties (thermal conductivity).

2. Fibrous composite material

In the present paper, a composite material consisting of two materials is analysed. It is a fibrous material with unidirectional fibres. The material of the matrix is homogenous and its thermal conductivity is constant. Fibres are also homogenous, however, they may differ from each other when it comes to radius or thermal conductivity.

2.1 Effective thermal conductivity

Composite materials typically consist of stiff and strong material phase, often as fibres, held together by a binder of matrix material, often an organic polymer. Matrix is soft and weak, and its direct load bearing is negligible. In order to achieve particular properties in preferred directions, continuous fibres are usually employed in structures having essentially two dimensional characteristics.

Applying the fundamental definition of thermal conductivity to a unit cell of unidirectional fibre reinforced composite with air voids, one can deduce simple empirical formula to predict the thermal conductivity of the composite material with estimated air void volume percent (Al-Sulaiman et al., 2006). The ability to accurately predict the thermal conductivity of composite has several practical applications. The most basic thermal-conductivity models (McCullough, 1985) start with the standard mixture rule

$$\lambda_{eff} = \sum_{i=1}^{n} \lambda_i V_i \tag{1}$$

and inverse mixture rule

$$\lambda_{eff} = \left(\sum_{i=1}^{n} \frac{V_i}{\lambda_i} \right)^{-1}, \tag{2}$$

where λ_{eff} is the effective thermal conductivity, λ_i, V_i - thermal conductivity and volume fraction of *i-th* composite constituents (e.g. resin, fibre, void).

The composite thermal conductivity in the filler direction is estimated by the rule of mixtures. The rule of mixtures is the weighted average of filler and matrix thermal conductivities. This model is typically used to predict the thermal conductivity of a unidirectional composite with continuous fibres. In the direction perpendicular to the fillers (through plane direction), the series model (inverse mixing rule) is used to estimate composite thermal conductivity of a unidirectional continuous fibre composite.

Another model similar to the two standard-mixing rule models is the geometric model (Ott, 1981)

$$\lambda_{eff} = \sum_{i=1}^{n} \lambda_i^{V_i} \tag{3}$$

Numerous existing relationships are obtained as special cases of above equations. Filler shapes ranging from platelet, particulate, and short-fibre, to continuous fibre are consolidated within the relationship given by McCullough (McCullough, 1985).

The effective thermal conductivity for a composite solid depends, however, on the geometry assumed for the problem. In general, to calculate the effective thermal conductivity of fibrous materials, we have to solve the energy transport equations for the temperature and heat flux fields. For a steady pure thermal conduction with no phase change, no convection and no contact thermal resistance, the equations to be solved are a series of Poisson equations subject to temperature and heat flux continuity constraints at the phase interfaces.

After the temperature field is solved, the effective thermal conductivity, λ_{eff}, can be determined

$$\lambda_{eff} = \frac{L \int q dA}{\Delta T \int dA}, \tag{4}$$

where q is the steady heat flux through the cross-section area dA between the temperature difference ΔT on a distance L. Heat flow through the unit area of the surface with normal n is linked with the temperature gradient in the n-direction by Fourier's law as

$$q = -\lambda \frac{\partial T}{\partial n} \tag{5}$$

2.2 Composite structure

The elementary cell of the considered composite is a cross-sectional square and it is perpendicular to fibres direction. Perfect contact between the matrix and the cell is assumed, heat transfer does not depend on time, and only conductive transfer is considered. Also, none of materials' properties depends on temperature, so the problem is linear and can be described by Laplace equation in each domain.

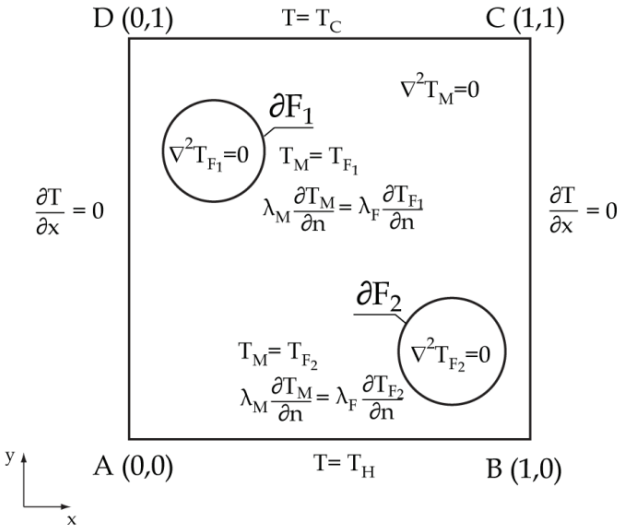

Fig. 1. Composite elementary cell structure

Governing equation of the problem both in the matrix domain and in each fibre domain takes the following form:

$$\nabla^2 \mathrm{T} = 0. \tag{6}$$

Boundary condition applied to the cell are defined as follows:

$$\frac{\partial \mathrm{T_M}}{\partial \mathrm{x}} = 0 \quad for\ \mathrm{x} = 0\ and\ \mathrm{x} = 1, \tag{7}$$

$$T_C = 290K \quad for \quad y = 0, \tag{8}$$

$$T_H = 300K \quad for \quad y = 1, \tag{9}$$

$$T_M = T_F \quad for \quad \partial F, \tag{10}$$

$$\lambda_M \frac{\partial T_M}{\partial n} = \lambda_F \frac{\partial T_F}{\partial n} \quad for \quad \partial F. \tag{11}$$

Symbols used at the Fig 1. denote as follows: T_C- cooling temperature at the top of the cell, T_H- heating temperature at the bottom of the cell, λ – thermal conductivity, indices M and F refer to the matrix and fibres.
Hence, one can see that the composite is heated from the bottom and cooled from the above. Symmetry condition is applied on the sides of the cell, which means that the heat flux on these boundaries equals zero. Thermal continuity and heat flux continuity conditions are applied on the boundary of each fibre.

2.3 Relation between geometry and conductivity

As we have already mentioned, the geometrical structure of the composite material may have a great impact on the resultant effective conductivity of the composite. Commonly, researchers assume that fibres are arranged in various geometrical arrays (triangular, rectangular, hexagonal etc.) or they are distributed randomly in the cross-section. In both cases the composite can be assumed as isotropic in the cross-sectional plane. However, anisotropic materials are also very common. What is more, one may intentionally create composite because of desired resultant properties of such materials. The influence of topological configuration of fibres in unidirectional composite is shown at Figs 2A-2C. The plot (Fig 2C) shows the relation between the effective thermal conductivity and the angle β by which fibres are rotated from horizontal to vertical alignment
The minimal value of effective thermal conductivity is shown at Fig 2B, maximal value at Fig 2B[1].

3. Numerical procedures

Numerical calculations were performed by hybrid method which consisted of two procedures: finite element method used for solving differential equation and genetic algorithm for optimization. Both procedures were implemented in COMSOL Script.

3.1 Finite element method (FEM)

A case in which heat transfer can be considered to be adequately described by a two-dimensional formulation is shown in Fig 3. Two dimensional steady heat transfer in considered domain is governed by following heat transfer equation:

$$\frac{\partial}{\partial x}\left(\lambda \frac{\partial T}{\partial x}\right) + \frac{\partial}{\partial y}\left(\lambda \frac{\partial T}{\partial y}\right) + \dot{Q} = 0, \tag{12}$$

in the domain Ω.

[1] All figures in this paper presenting the elementary composite cell use the same sizes and the same temperature scale as figures Fig 2A and Fig 2B, so the scales are omitted on the next figures. Isolines are presented in reversed grayscale.

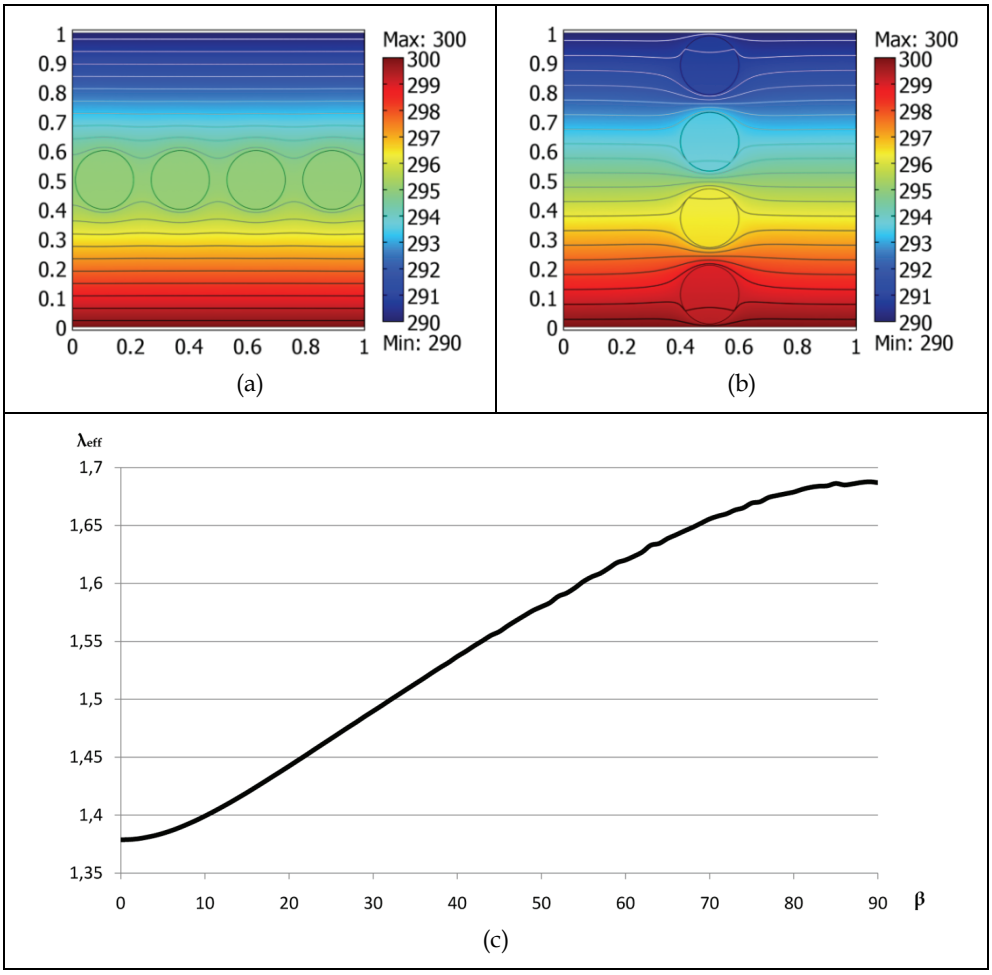

Fig. 2. (a) Horizontal alignment, λ_{eff}=1,37 (b)Vertical alignment λ_{eff}=1,68 (c) Relation between effective thermal conductivity λ_{eff} and the angle β of rotation of four fibres aligned. The conductivity of matrix λ_M=2, fibres conductivity λ_F=0.1. Fibres radius R=0.1

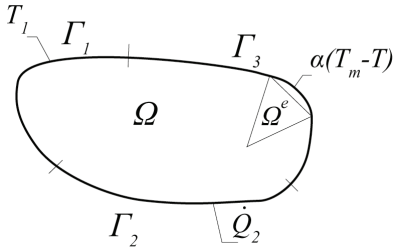

Fig. 3. Geometry of domain with boundary conditions

In the considered problem one can take under consideration three types of heat transfer boundary conditions:

$$T(x,y) = T_1 \tag{13}$$

on boundary Γ_1,

$$\left(\lambda\frac{\partial T}{\partial x}n_x\right) + \left(\lambda\frac{\partial T}{\partial y}n_y\right) = \dot{Q}_2 \tag{14}$$

on boundary Γ_2 and

$$\left(\lambda\frac{\partial T}{\partial x}n_x\right) + \left(\lambda\frac{\partial T}{\partial y}n_y\right) = \alpha(T_m - T) \tag{15}$$

on boundary Γ_3. In above equations T_m denotes external temperature, $\dot{Q}_2$ is a heat source, α – heat transfer coefficient, λ – thermal conductivity coefficient, n_x and n_y – components of normal vector to boundary.

In developing a finite element approach to two-dimensional conduction we assume a two-dimensional element having M nodes such that the temperature distribution in the element is described by

$$T^e(x,y) = \sum_{j=1}^{M} T_j^e \cdot N_j^e(x,y) = [N]\{T\} \tag{16}$$

where $N_j^e(x,y)$ is the interpolation function associated with nodal temperature T_j^e , $[N]$ is the row matrix of interpolation functions, and $\{T\}$ is the column matrix (vector) of nodal temperatures.

Applying Galerkin's finite element method (Zienkiewicz&Taylor, 2000), the residual equations corresponding to steady heat transfer equation are

$$\int_{\Omega^e}\left(\frac{\partial}{\partial x}\left(\lambda\frac{\partial T^e}{\partial x}\right) + \frac{\partial}{\partial y}\left(\lambda\frac{\partial T^e}{\partial y}\right) + \dot{Q}\right)N_i^e(x,y)dxdy = 0. \tag{17}$$

Using Green's theorem in the plane we obtain

$$\int_{\Omega^e}\left(\frac{\partial}{\partial x}\left(\lambda\frac{\partial T^e}{\partial x}N_i^e\right) + \frac{\partial}{\partial y}\left(\lambda\frac{\partial T^e}{\partial y}N_i^e\right)\right)dxdy = \int_{\Gamma^e}\left(\lambda\frac{\partial T^e}{\partial x}dy - \lambda\frac{\partial T^e}{\partial y}dx\right)N_i^e \tag{18}$$

and by transforming left-hand side we obtain:

$$\begin{aligned}&\int_{\Omega^e}\left(\frac{\partial}{\partial x}\left(\lambda\frac{\partial T^e}{\partial x}\right) + \frac{\partial}{\partial y}\left(\lambda\frac{\partial T^e}{\partial y}\right)\right)N_i^e dxdy = \\ &= -\int_{\Omega^e}\left(\lambda\frac{\partial T^e}{\partial x}\frac{\partial N_i^e}{\partial x} + \lambda\frac{\partial T^e}{\partial y}\frac{\partial N_i^e}{\partial y}\right)dxdy + \int_{\Gamma^e}\left(\lambda\frac{\partial T^e}{\partial x}dy - \lambda\frac{\partial T^e}{\partial y}dx\right)N_i^e.\end{aligned} \tag{19}$$

Using

$$\dot{Q} = \left(\lambda\frac{\partial T}{\partial x}n_x\right) + \left(\lambda\frac{\partial T}{\partial y}n_y\right) \tag{20}$$

in the Galerkin residual equation we obtain

$$\int_{\Omega^e}\left(\left(\lambda\frac{\partial T^e}{\partial x}\frac{\partial N_i^e}{\partial x}\right)+\left(\lambda\frac{\partial T^e}{\partial y}\frac{\partial N_i^e}{\partial y}\right)\right)dxdy=\int_{\Omega^e}\dot{Q}N_i^e dxdy+\int_{\Gamma^e}\left(\lambda\frac{\partial T^e}{\partial x}dy-\lambda\frac{\partial T^e}{\partial y}dx\right)N_i^e. \quad (21)$$

Taking under consideration boundary condition

$$\int\limits_{\Omega^e}\left(\left(\lambda\frac{\partial T^e}{\partial x}\frac{\partial N_i^e}{\partial x}\right)+\left(\lambda\frac{\partial T^e}{\partial y}\frac{\partial N_i^e}{\partial y}\right)\right)dxdy= \quad (22)$$

$$=\int_{\Omega^e}\dot{Q}N_i^e dxdy+\int_{\Gamma_2^e}\dot{Q}_2N_i^e ds+\int_{\Gamma_3^e}\alpha(T_m-T_1)\,N_i^e ds,$$

Where

$$\dot{Q}ds=\left(\lambda\frac{\partial T}{\partial x}n_x ds\right)+\left(\lambda\frac{\partial T}{\partial y}n_y ds\right) \quad (23)$$

Using (16) in equation (22) we obtain

$$\int\limits_{\Omega^e}\left(\left(\lambda\frac{\partial N_i^e}{\partial x}\sum_{j=1}^{M}\left(T_j^e\frac{\partial N_j^e}{\partial x}\right)\right)+\left(\lambda\frac{\partial N_i^e}{\partial y}\sum_{j=1}^{M}\left(T_j^e\frac{\partial N_j^e}{\partial y}\right)\right)\right)dxdy= \quad (24)$$

$$=\int\limits_{\Omega^e}\dot{Q}N_i^e dxdy+\int\limits_{\Gamma_2^e}\dot{Q}_2N_i^e ds-\int\limits_{\Gamma_3^e}\alpha\sum_{j=1}^{M}\left(T_j^eN_j^e\right)\,N_i^e ds+\int\limits_{\Gamma_3^e}\alpha T_m\,N_i^e ds.$$

The equation (24) we can rewrite for the whole considered domain which gives us the following matrix equation

$$\boldsymbol{K}\boldsymbol{a}=\boldsymbol{f} \quad (25)$$

where $\boldsymbol{K}$ is the conductance matrix, $\boldsymbol{a}$ is the solution for nodes of elements, and $\boldsymbol{f}$ is the forcing functions described in column vector.
The conductance matrix

$$\boldsymbol{K}=\boldsymbol{K}_c^e+\boldsymbol{K}_{\Gamma_3}^e \quad (26)$$

and the forcing functions

$$\boldsymbol{f}=\boldsymbol{f}_q^e+\boldsymbol{f}_{\Gamma_2}^e+\boldsymbol{f}_{\Gamma_3}^e \quad (27)$$

are described by following integrals

$$K_{c,ij}^e=\int_{\Omega^e}\left(\left(\lambda\frac{\partial N_i^e}{\partial x}\frac{\partial N_j^e}{\partial x}\right)+\left(\lambda\frac{\partial N_i^e}{\partial y}\frac{\partial N_j^e}{\partial y}\right)\right)dxdy, \quad (28)$$

$$K_{\Gamma_3,ij}^e=\int_{\Gamma_3^e}\alpha N_i^eN_j^e ds, \quad (29)$$

$$f_{q,i}^e=\int_{\Omega^e}\dot{Q}N_i^e dxdy, \quad (30)$$

$$f^e_{\Gamma_2,i} = \int_{\Gamma^e_2} \dot{Q}_2 N^e_i ds, \tag{31}$$

$$f^e_{\Gamma_3,i} = \int_{\Gamma^e_3} \alpha T_m \, N^e_i ds \tag{32}$$

Equations 25-32 represent the general formulation of a finite element for two-dimensional heat conduction problem. In particular these equations are valid for an arbitrary element having *M* nodes and, therefore, any order of interpolation functions. Moreover, this formulation is valid for each composite constituent.

3.2 Genetic algorithm (GA)

Genetic algorithm is one of the most popular optimization techniques (Koza, 1992). It is based on an analogy to biological mechanism of evolution and for that reason the terminology is a mixture of terms used in optimization and biology. Optimization in a simple case would be a process of finding maximum (or minimum) value of an objective function:

In GA each potential solution is called an individual whereas the space of all the feasible values of solutions is a search space. Each individual is represented in its encoded form, called a chromosome. The objective function which is the measure of quality of each chromosome in a population is called a fitness function. The optimization problem can be expressed in the following form:

$$\mathrm{f}(\hat{\mathrm{x}}) \geq \mathrm{f}(\mathrm{x}), \mathrm{x} \in \mathrm{D}, \tag{33}$$

where: $\hat{\mathrm{x}}$ denotes the best solution, f is an objective function, x represents any feasible solution and D is a search space. Chromosomes ranked with higher fitness value are more likely to survive and create offspring and the one with the highest value is taken as the best solution to the problem when the algorithm finishes its last step. The concept of GA is presented at fig 4.

Algorithm starts with initial population that is chosen randomly or prescribed by a user. As GA is an iterative procedure, subsequent steps are repeated until termination condition is satisfied. The iterative process in which new generations of chromosomes are created involves such procedures as selection, mutation and cross-over. Selection is the procedure used in order to choose the best chromosomes from each population to create the new generation. Mutation and cross-over are used to modify the chromosomes, and so to find new solutions. GA is usually used in complex problems i.e. high dimensional, multi-objective with multi connected search space etc. Hence, it is common practice that users search for one or several alternative suboptimal solutions that satisfy their requirements, rather than exact solution to the problem. In this paper GA optimizes geometrical arrangement of fibres in a composite materials as it influences effective thermal conductance of this composite. It has been developed many improvements to the original concept of GA introduced by Holland (Holland, 1975) such as floating point chromosomes, multiple point crossover and mutation, etc. However, binary encoding is still the most common method of encoding chromosomes and thus this method is used in our calculations.

3.2.1 Encoding

We consider an elementary cell of a composite that is 2-D domain and there are *N* fibres inside the cell, the position of each fibre is defined by its coordinates, which means we need

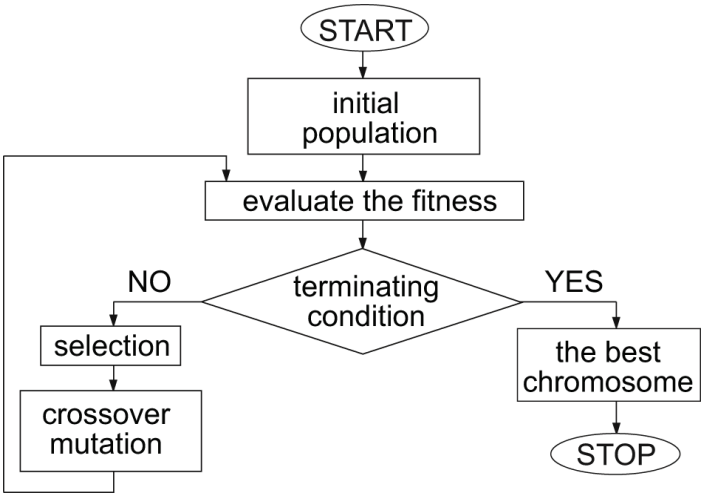

Fig. 4. Genetic algorithm scheme

to optimize $2N$ variables x_i. Furthermore, it is assumed that each coordinate is determined with finite precision p_i and limited to a certain range $D_i = [a_i, b_i]$ - a, b denoting the lower and upper limit of the range respectively. It means that each domain D_i needs to be divided into $(b_i - a_i)10^{p_i}$ sub-domains. Hence we can calculate h_i – number of bits required to encode variables:

$$(\mathrm{b_i} - \mathrm{a_i})10^{\mathrm{p_i}} \leq 2^{\mathrm{h_i}} - 1. \tag{34}$$

Consequently, we can calculate the number of bits H required to encode a chromosome:

$$\mathrm{H} = \sum_{\mathrm{i}=1}^{2\mathrm{N}} \mathrm{h_i} \tag{35}$$

In our calculation we assume three significant digits precision which means we need 2^{10} bits to encode each variable.

3.2.2 Fitness and selection

Selection is a procedure in which parents for the new generation are chosen using the fitness function. There are many procedures possible to select chromosomes which will create another population. The most common are: roulette wheel selection, tournament selection, rank selection, elitists selection.

In our case, modified fitness proportionate selection also called roulette wheel selection is used. Based on values assigned to each solution by fitness function $f(x_i)$, the probability $P(x_i)$ of being selected is calculated for every individual chromosome. Consequently, the candidate solution whose fitness is low will be less likely selected as a parent whereas it is more probable for candidates with higher fitness to become a parent. The probability of selection is determined as follows:

$$\mathrm{P}(\mathrm{x_i}) = \frac{\mathrm{f}(\mathrm{x_i})}{\sum_{\mathrm{k}=1}^{\mathrm{S}} \mathrm{f}(\mathrm{x_k})} \tag{36}$$

where S is the number of chromosomes in population.

Modification of the roulette wheel selection that we introduced is caused by the fact that we needed to perform constrained optimization. The constrains are the result of the fact that fibres cannot overlap with each other. There are some possible options to handle this problem, one of which would to use penalty function. During calculations, however, it turned out that this approach is less effective than the other one based on elitist selection. We decided that in case of chromosome representing arrangement of overlapping fibres such chromosome should be replaced with the best one.

3.2.3 Genetic operators

Cross-over operation requires two chromosomes (parents) which are cut in one, randomly chosen point (locus) and since this point the binary code is swapped between the chromosomes creating two, new chromosomes, as it is shown at Fig. 5.
Mutation procedure in case of binary representation of solution is an operation of bit inversion at randomly chosen position Fig6. The following purpose of this procedure is to introduce some diversity into population and so to avoid premature convergence to local maximum.

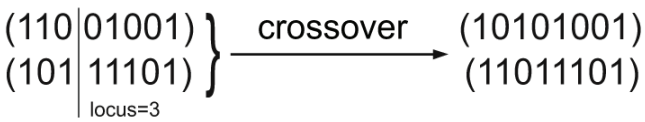

Fig. 5. Crossover procedure scheme

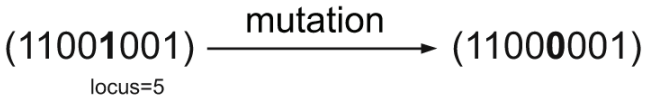

Fig. 6. Mutation procedure scheme

4. Numerical results

All optimization problems considered in this chapter are governed by Eq. 6 for each constituent of the composite with appropriate boundary conditions (7-11). In our calculations we assumed the same sizes of the unit cell i.e. 1x1cm (Fig1.). Temperatures on the lower and upper boundaries were: T_C=290K (upper), T_H=300K (lower) respectively. We analysed several cases in which the number of fibres N_f and fibres radii R were changed, also thermal conductivity of the matrix λ_M and fibres λ_F were also changed. Finite element calculation were made using second order triangular Lagrange elements. The stationary problem of heat transfer was solved using direct UMFPACK linear system solver. The mesh structure depends on the number and positions of fibres and so the number of mesh elements was not larger than 5000.
We performed three types of optimization in terms of effective thermal conductivity: minimization, maximization and determination of arrangement which gives desired value of effective thermal conductivity. In the latter case we defined the objective function as the minimization of the deviation from the expected value. The results of optimization are presented at Figs 7-9.

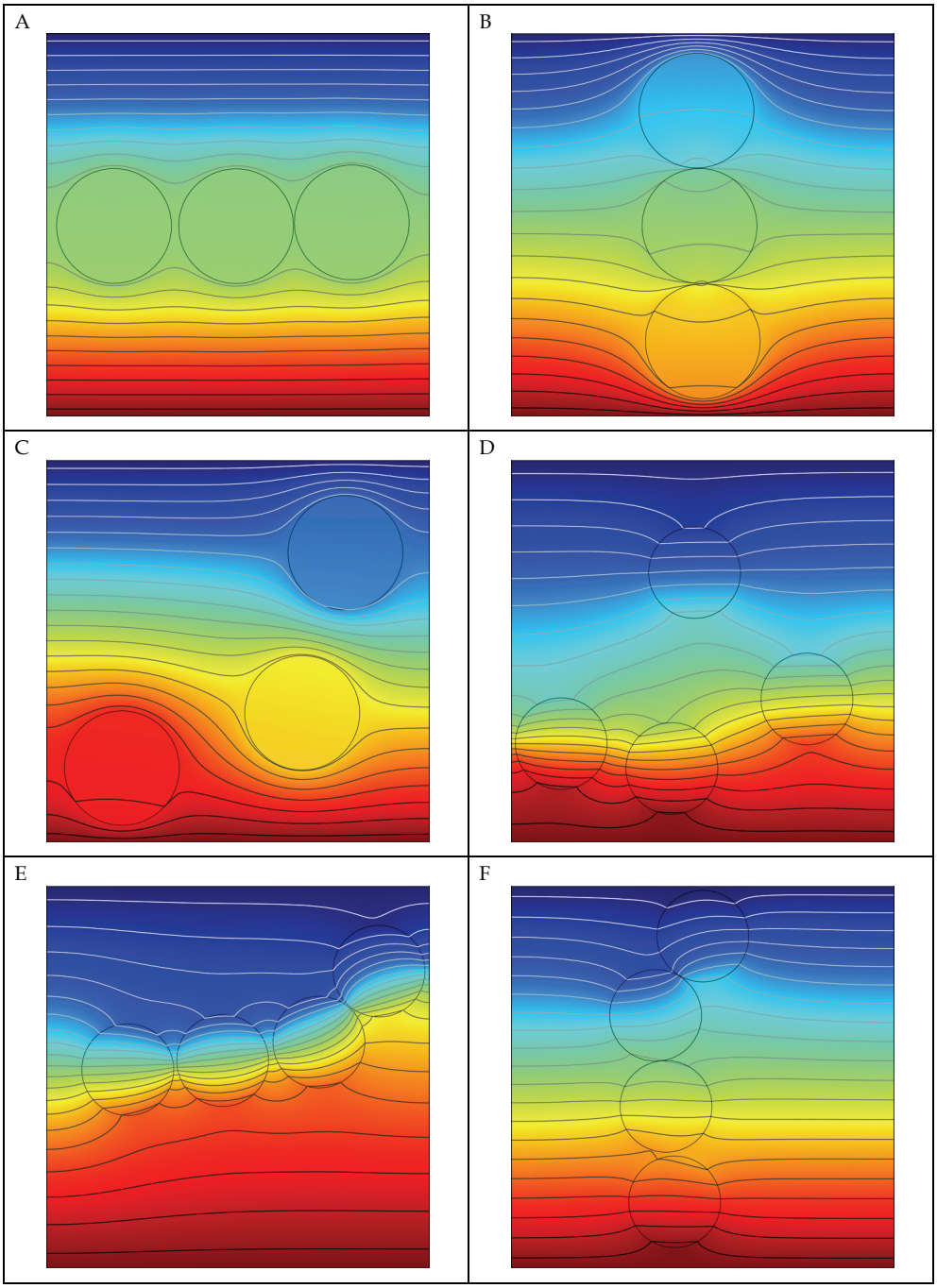

Fig. 7. Resultant arrangement for three and four fibres

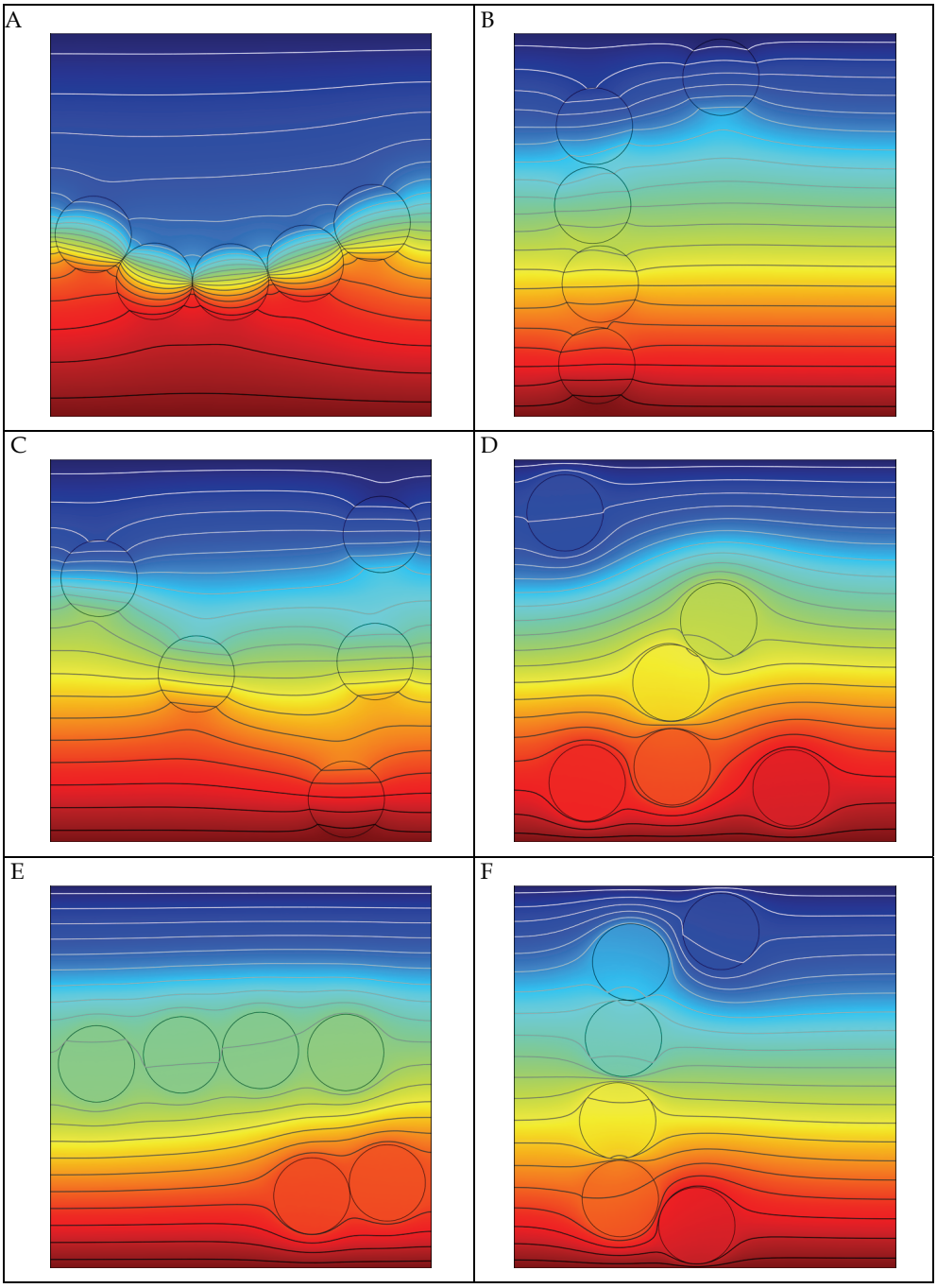

Fig. 8. Resultant arrangement for five and six fibres

4.1 Optimization of three and four fibres arrangement

In the beginning we assumed the same sizes of the fibres, as well as the same value of thermal conductivity for each fibre. Numerical values of parameters used in calculations, and the resultant effective thermal conductivity was shown in Table 1. The 'Opt.' column refers to optimization criteria i.e. minimum, maximum or expected value of λ_{eff} The column entitled $\boldsymbol{\lambda_{eff}}$ contains obtained results. Not surprisingly did minimization and maximization results agree with results presented in section 2.3. Figures 7A and 7E present the arrangement obtained during minimization. All fibres are aligned horizontally perpendicularly to heat flux direction, next to each other. In case of maximization (Figs 7B, 7F) fibres are aligned vertically – along with heat flux direction.

However, there are many possible ways of arrangement of intermediate values of effective thermal conductivity – fibres do not have to be aligned anymore as it was assumed at Fig 2C. We also presented one of possible arrangements that result in a composite with effective thermal conductivity equal to the one expected for each number of fibres: (Figs 7C, 7D). If one would like to achieve certain value of effective thermal conductivity with respect to some geometrical assumptions (for instance minimum/maximum distance between fibres) it is also possible to perform such optimization, however penalty function should be implemented or objective function modified to include such conditions.

Figure's number	N_F	R	λ_F	λ_M	Opt.	$\boldsymbol{\lambda_{eff}}$
Fig 7A	3	0.15	2.0	0.1	Min	**0.13**
Fig 7B	3	0.15	2.0	0.1	Max	**0.23**
Fig 7C	3	0.15	2.0	0.1	0.15	**0.15**
Fig 7D	4	0.12	0.1	2.0	1.35	**1.35**
Fig 7E	4	0.12	0.1	2.0	Min	**1.1**
Fig 7F	4	0.12	0.1	2.0	Max	**1.56**

Table 1. The values assigned for calculations and the resultant λ_{eff} for three and four fibres

4.2 Optimization of five and six fibres arrangement

Calculation performed for five and six fibres were similar to those presented above for three and four fibres. However, the more fibres the more complex problem. As it was mentioned in section 3.2.1 each fibre is described by two variables changing within the range [0,1] with the 10^{-3} precision which means 2^{10} bits. Consequently, by adding one fibre we enlarge the search space by 2^{20} elements. So, the search space dimension for three fibres arrangement optimization equals 2^{60}, while for six fibres it equals 2^{120}. The size of search space has a direct impact on calculation time and so it takes far more time to find optimal solution.

The terminating condition of GA was set to 2000 iterations for three and four fibres. It resulted in almost perfect arrangement in case of three fibres whereas the arrangement for four fibres was not equally well. While increasing the number of fibres to five and six fibres, we also increased the number of iteration to 10000.

Another important aspect of the considered problem was that in case of five and six fibres of assumed radii (Table 2) it was not possible to align them in one row so the relation presented in section 2.3 could not be applied anymore.

The minimization results for five and six fibres were presented at Figs 8A and 8E, the maximization results at Figs 8B and 8F and the arrangement for expected value of effective

thermal conductivity at Figs. 8C, 8D. One can notice that the arrangement of fibres is also close to horizontal in case of minimization and close to vertical in case of maximization, although fibres are not localised next to each other and initialization of the second row in case of six fibres can be observed. In general, however, we may not assume that fibres are always aligned in rows in case of minimum and maximum values of effective thermal conductivity. The situation changes when the thermal conductivity of fibres is not the same in each fibre. The result for such situation was presented in the next section.

	N_F	R	λ_F	λ_M	Opt.	λ_{eff}
Fig 8A	5	0.1	0.1	2.0	Min	**1,0**
Fig 8B	5	0.1	0.1	2.0	Max	**1,61**
Fig 8C	5	0.1	0.1	2.0	1.5	**1.5**
Fig 8D	6	0.1	2.0	0.1	0.15	**0.15**
Fig 8E	6	0.1	2.0	0.1	Min	**0.13**
Fig 8F	6	0.1	2.0	0.1	Max	**0.19**

Table 2. The values assigned for calculations and the resultant λ_{eff} for five and six fibres

4.3 Optimization of four and five fibres arrangement with different radii and thermal conductivity of fibres

Apart from the simplest case in which the composite consisted of identical fibres we also analysed the case in which fibres differ from each other. We used two sizes of fibres with different values of thermal conductivities. All parameters used in calculations were presented in Table 3. The symbol N_R denotes the number of fibres having the same dimension and properties.

	N_F	N_R	R	λ_F	λ_M	Opt.	λ_{eff}
Fig 9A	4	2	0.12	0.1	2.0	Min	**1.68**
		2	0.15	10			
Fig 9B	4	2	0.12	0.1	2.0	Max	**2.39**
		2	0.15	10			
Fig 9C	4	2	0.12	0.1	2.0	2.0	**2,0**
		2	0.15	10			
Fig 9D	5	4	0.075	0.1	0.1	1.85	**1.85**
		1	0.15	10			
Fig 9E	5	4	0.075	0.1	0.1	Min	**1.65**
		1	0.15	10			
Fig 9F	5	4	0.075	20.1	0.1	Max	**2.08**
		1	0.15	10			

Table 3. The values assigned for calculations and the resultant λ_{eff} for four and five fibres of different radii and thermal conductivities

We performed the optimization of the arrangement of four and five fibres in a composite cell. The minimization results were presented at Figs 9A, 9E while maximization at Figs 9B, 9F. The arrangements obtained for the assumed values of effective thermal conductivity for four and five fibres were presented at Figs 9C,9D respectively. It is remarkable, that in these

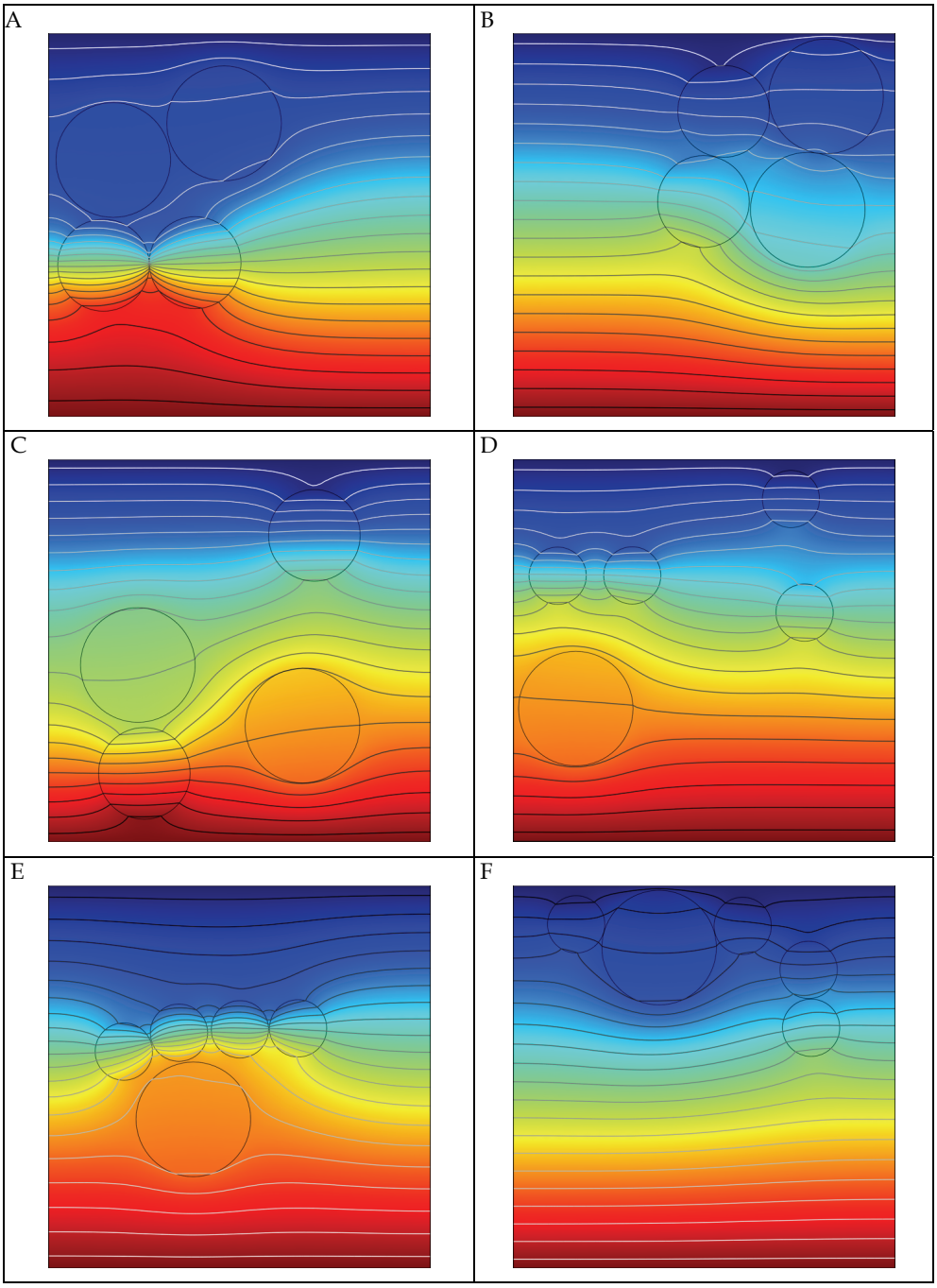

Fig. 9. Resultant arrangements for fibres of different sizes and thermal conductivities

cases the optimal arrangement of fibres is no longer that predictable. Fibres are not aligned in a row, although there was enough space. However, fibres still tend to be close to each other but spatial configuration is changed.

5. Conclusion

This study has examined the effect of multi fibres filler in composite on thermal conductivity. Three types of optimization were performed in terms of effective thermal conductivity: minimization, maximization and determination of arrangement which gives expected value of effective thermal conductivity. Hybrid method combining optimization with genetic algorithm and differential equation solver by finite element method were used to find optimal arrangement of fibres position in composite matrix was used in this work. Proposed algorithm was implemented in Comsol Multiphysics environment.

It was proved that the geometrical structure of the composite (matrix and filler arrangement) may have a great impact on the resultant effective conductivity of the composite. In many research works it is assumed that fibres are arranged in various geometrical arrays or they are distributed randomly in the cross-section.

Through this study, some areas were found that need to be investigated further. Composite constituents can be anisotropic, and with temperature dependent thermal conductivity of constituents (e.g. resin, fibre, void).

6. References

Al-Sulaiman FA, Mokheimer EM, Al-Nassar YN (2006). Prediction of the thermal conductivity of the constituents of fiber reinforced composite laminates, *Heat Mass Transfer*, 42, 5, 370–377.

Al-Sulaiman FA, Al-Nassar YN and Mokheimer EM (2006). Composite Laminates: Voids Effect Prediction of the Thermal Conductivity of the Constituents of Fiber-Reinforced, *Journal of Composite Materials*, 40; pp.797-814.

Boguszewski T., Ciupiński Ł., Kurzydłowski K.J. (2008). Numerical Calculation of The Thermal Conductivity Coefficient in Diamond-Copper Composite, *Kompozyty/Composites*, Vol. 8, Nr 3, pp.232-235.

Brucker Kyle A., Majdalani Joseph (2005). Effective thermal conductivity of common geometric shapes, *International Journal of Heat and Mass Transfer*, 48, pp.4779–4796.

Comsol Multiphysics User's Guide (2007). *Modeling Guide and Model Library*, Documentation Set, Comsol AB.

Duc N.D., Boi L.V., Dac N.T. (2008). Determining thermal expansion coefficients of three-phase fiber composite material reinforced by spherical particles, VNU Journal of Science, *Mathematics – Physics*, 24, pp.57-65.

Freger G.E., Kestelman V.N., Freger D.G. (2004). *Spirally Anisotropic Composites*, Springer-Verlag Berlin Heidelberg.

Holland J. H. (1975). *Adaptation in natural and artificial systems*, The University Michigan Press Ann Arbor.

Kidalov Sergey V., Shakhov Fedor M. (2009). Thermal Conductivity of Diamond Composites, *Materials*, 2, pp.2467-2495.

Koza J. R. (1992). *Genetic programming. On the Programming of Computers by Means of Natural Selection*, MIT Press, Cambridge.

Karkri M. (2010). Effective thermal conductivity of composite: Numerical and experimental study, *Proceedings of the COMSOL Conference 2010*, Paris.

McCullough R. (1985), Generalized Combining Rules for Predicting Transport Properties of Composite Materials, *Composites Science and Technology*, Vol. 22, pp.3-21.

Ott H.J. (1981), Thermal Conductivity of Composite Materials, *Plastic and Rubber Processing and Applications*, Vol. 1, 1981, pp. 9-24.

Vasiliev Valery V. Morozov Evgeny V. (2001). *Mechanics and Analysis of Composite Materials*, Elsevier.

Wang M., Pan N. (2008). Modeling and prediction of the effective thermal conductivity of random open-cell porous foams, *International Journal of Heat and Mass Transfer*, 51, pp. 1325–1331.

Wang M., Kang Q., Pan N. (2009). Thermal conductivity enhancement of carbon fiber composites, *Applied Thermal Engineering*, 29, pp.418–421.

Weber E.H. (2001). *Development and Modeling of Thermally Conductive Polymer/Carbon Composites*, Doctoral Thesis, Michigan Technological University.

Zhou S., Qing Li (2008). Computational Design of Microstructural Composites with Tailored Thermal Conductivity, *Numerical Heat Transfer*, Part A, 54, pp.686–708.

Zienkiewicz O.C., Taylor R.L. (2000). *The Finite Element Method*, Vol. 1-3: The Basis, Solid Mechanics, Fluid Dynamics (5th ed.), Butterworth-Heinemann, Oxford.

10

Computation of Thermal Conductivity of Gas Diffusion Layers of PEM Fuel Cells

Andreas Pfrang, Damien Veyret and Georgios Tsotridis
European Commission, Joint Research Centre, Institute for Energy
P.O. Box 2, NL-1755 ZG Petten,
The Netherlands

1. Introduction

While fuel cells in general are expected to play a major role in the future energy supply, proton exchange membrane (PEM) fuel cells are considered especially interesting for automotive applications due to their relatively low operating temperature which allows for fast start-up and flexibility in power output. Other promising applications of PEM fuel cells are back-up power units, small portable power supplies, micro combined heat and power installations, but also large scale stationary PEM fuel cell plants.

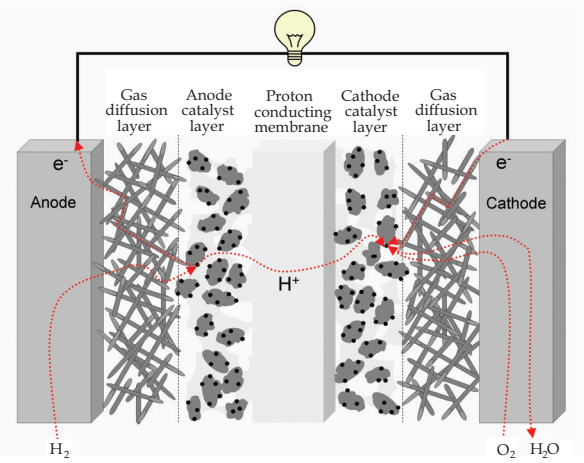

Fig. 1. Sketch of a PEM fuel cell (not to scale). A PEM fuel cell contains two gas diffusion layers, one on the anode and one on the cathode side

Fig. 1 illustrates the principle of a PEM fuel cell. At the anode (left hand side) protons are produced from hydrogen and have to move through the proton-conducting (but not electron-conducting) membrane to the cathode side (right hand side). Electrons will be transported via the electrical load outside the fuel cell to the cathode side where water is produced as 'waste'.

The two gas diffusion layers (GDL) have multiple functions in a PEM fuel cell: provide gas access to the catalyst layers, allow removal of product water on the cathode side while also keeping the membrane and electrode layers humidified when gas conditions are sub-saturated, mechanically stabilize the membrane-electrode assembly while compensating for thickness variations of the membrane, and providing electrical and thermal conductivity.
A GDL has typically a thickness of 200 to 400 μm and consists of carbon fiber papers or carbon fiber felts which are impregnated with polytetrafluoroethylene (PTFE) to achieve a partial hydrophobization of the surfaces (Mathias et al., 2003). Carbon binder can be added for a mechanical joining of neighbouring fibers. Furthermore, a microporous layer (MPL, typical pore sizes around 100 nm) consisting of a mixture of carbon black and PTFE is often applied with a thickness of a few 10 μm on the side facing the catalyst layer for a further optimization of the water management (Paganin et al., 1996; Giorgi et al., 1998; Mathias et al., 2003).
An operating PEM fuel cell is not isothermal, mainly because heat is generated within the membrane electrode assembly and at the same time this assembly can be considered 'insulated' by the gas diffusion layers (Burheim et al., 2011) leading to temperature gradients within the fuel cell. A detailed knowledge of the temperature distribution and therefore of thermal conductivity of the GDLs is essential for a proper understanding and the optimization of not only heat transfer in the PEM fuel cell, but also for water management and optimization of cell performance and durability. A direct measurement of thermal conductivity is possible and has been performed mainly for the through–plane direction (see Table 2). Nevertheless, the direct measurement is for several reasons non-trivial: due to the anisotropy of the GDLs, the thermal conductivity is expected to be anisotropic as well. Furthermore, the through-plane thermal conductivity as well as the contact resistance change with a compression of the GDL (Burheim et al., 2010; Sadeghi et al., 2011a). Recently, the measurement of in-plane thermal conductivities has been reported (Sadeghi et al., 2011b; Teertstra et al., 2011).
Alternatively, the anisotropic thermal conductivity of gas diffusion layers can be calculated based on the 3D microstructure of the GDL and the knowledge of thermal conductivity of the different materials which are present in the GDL. This approach is presented in the following using X-ray computed tomography structure data of gas diffusion layers as well as randomly computer-generated 3D structures based on structural models of gas diffusion layers.

2. Materials and methods

2.1 3D structure of gas diffusion layers

The computation of anisotropic thermal conductivity requires the knowledge of the 3D structure of the gas diffusion layer, i.e. also the 3D distribution of the different materials that are present in the gas diffusion layer. This is especially important as the thermal conductivities of these different materials differ considerably: air 0.026 W m^{-1} K^{-1} (Taine & Petit, 1989) , PTFE 0.25 W m^{-1} K^{-1} (Marotta & Fletcher, 1996) and a typical value for PAN-based carbon fibers with relatively high strength and at the same time relatively high modulus is 120 W m^{-1} K^{-1} (Toray Industries, 2005a).

2.1.1 Characterization of 3D structures by X-ray computed tomography

The first approach presented here is the application of X-ray computed tomography (CT) where a 3D image of an object is determined by digital processing of a large series of two-

dimensional X-ray images taken around a single axis of rotation (see Fig. 2). The 3D image of the object consists of voxels with a certain gray value. Each voxel is then assigned to one material that is present in the object e.g. by considering its gray value. This assignment is denoted as 'segmentation'.

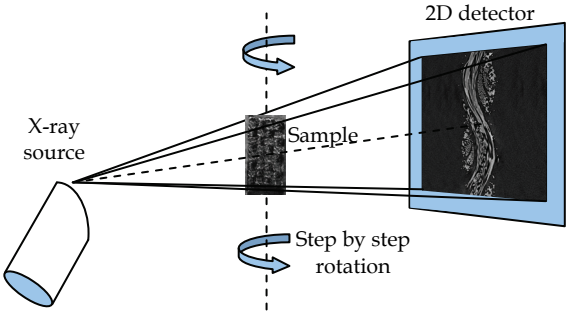

Fig. 2. Principle of X-ray computed tomography (CT). A carbon cloth is shown as sample

X-ray computed tomography (Ostadi et al., 2008; Pfrang et al., 2010) as well as synchrotron based tomography (Becker et al., 2008; Becker et al., 2009) have been used for imaging of gas diffusion layers at resolutions below 1 µm.
Also membranes and membrane electrode assemblies (Garzon et al., 2007; Pfrang et al., 2011) have been imaged by X-ray computed tomography and even functioning fuel cells have been imaged by synchrotron-based methods and soft X-ray radiography e.g. for imaging of liquid water in the GDL (Sinha et al., 2006; Bazylak, 2009; Sasabe et al., 2010; Tsushima & Hirai, 2011).

Gas diffusion layer	PTFE / wt%	Thickness / mm	Porosity
E-Tek, EC-CC1-060T	30	0.33	0.75
E-Tek, EC-TP1-060T	30	0.19	0.72
SGL Carbon, Sigracet 35 BC (with microporous layer)	5	0.325	0.80

Table 1. Properties of gas diffusion layers investigated by X-ray computed tomography (Toray Industries, 2005b; SGL Group, 2009; Pfrang et al., 2010)

Here, CT data from three different commercially available gas diffusion layers will be discussed which were imaged by a nanotom X-ray computed tomography system (GE Sensing and Inspection Technologies, phoenix X-ray, Wunstorf, Germany) at a resolution below 1 µm. Table 1 shows PTFE content, thickness and porosity of the investigated gas diffusion layers. Segmentation into solid material (i.e. carbon and PTFE) and air was carried out based on a gray level threshold. Further details can be found in (Pfrang et al., 2010).

2.1.2 Random generation of 3D structures

The second approach is the random generation of three-dimensional fiber structures using the FiberGeo module of the Geodict software package (Fraunhofer ITWM, 2011). Geometric

parameters such as fiber diameter and length, fiber volume fraction were specified as well as the size of the grid as specified by the number of voxels in x, y and z-direction, n_x, n_y and n_z.

The degree of orientation anisotropy was characterized by the anisotropy parameter β. Using spherical coordinates, β characterizes the directional distribution of fibers. The density of the directional distribution is given by Equation (1), (Schladitz et al., 2006):

$$P(\theta,\phi) = \frac{1}{4\pi} \frac{\beta \sin\theta}{\left(1 + \left(\beta^2 - 1\right)\cos^2\theta\right)} \tag{1}$$

with the inclination $\theta \in [0, \pi)$ and the azimuth $\varphi \in [0, 2\pi)$. The density is thus independent of φ, i.e. the density exhibits rotational symmetry with respect to the z-axis. The case β = 1 describes the isotropic system. For $\beta \to \infty$, the cylinders tend to be more and more parallel to the xy-plane. For $\beta \to 0$ the cylinders tend to be more and more parallel to the z-axis.

For the randomly generated structures presented here, the selected structure size was 200 x 200 x 271 voxels with a voxel length of 0.7 µm. The fiber volume fraction was 21 % and an anisotropy factor ß of 1000 was chosen. The fibers had a diameter of 10 voxels and were assumed to have infinite length. For further details of the random generation of 3D structures, see also (Veyret & Tsotridis, 2010).

Additionally, model structures consisting of layers of equidistant parallel fibers were generated for the examination of the influence of PTFE distribution on thermal conductivity. For each model structure (see e.g. Fig. 6, before and after the addition of PTFE), the distance between adjacent fiber layers was fixed, but model structures were generated for 6 different layer distances. As the filling factor of the carbon fibers was kept constant at 22 %, the lateral distance between parallel fibers within a layer was adjusted accordingly.

The addition of PTFE to the fiber structures – the randomly generated structures as well as the model structures – was implemented by using the 'add binder'-function in GeoDict, where pores are filled starting from the smallest pores and then continuing to bigger pores until the desired binder volume fraction is reached. The algorithm used here to determine the size of a pore does not distinguish between through pores, closed pores and blind pores and is in this sense purely geometrical. A pore radius is determined by fitting spheres into the pore volume, i.e a point belongs to a pore of radius larger than r, if it is inside any sphere of radius r, which can be fitted into the pore space (Fraunhofer ITWM, 2011).

2.2 Numerical method for the computation of effective thermal conductivity

For the computation of the effective thermal conductivity of fibrous materials, the steady, purely diffusive, three-dimensional heat transfer equation has to be solved. In the case of large three-dimensional geometries (e.g. large data sets from CT imaging, see section 2.1.1 or generated randomly, see section 2.1.2), partial differential equation solvers are not efficient. (Wiegmann & Zemitis, 2006) use a different approach where the energy equation is solved by harmonic averaging. Fast Fourier transform and bi-conjugate gradient stabilized (BiCGStab) methods are then used to solve the Schur-complement formulation. This method – where convection and radiation transport, as well as thermal contact resistance and phase changes are not taken into account – is implemented in the GeoDict software which was also used for the random generation of 3D structures. Further details can be found in (Veyret & Tsotridis, 2010).

Whereas in the randomly generated 3D structures the distribution of PTFE and carbon is well known, these two materials could not be distinguished in the CT data. As a rough approximation, all solid voxels in the CT datasets were assumed to have a thermal conductivity that was calculated as the weighted average of the thermal conductivities of the carbon fibers and the thermal conductivity of PTFE, even though these two materials do not intermix. The remaining, non-solid voxels were assumed to be filled with air.

3. Results and discussion

3.1 Estimation of thermal conductivity of heterogeneous materials

Several analytical models for the estimation of thermal conductivity of heterogeneous materials exist (Progelhof et al., 1976; Carson et al., 2005; Wang et al., 2006) and can be applied to gas diffusion layers. In the following, the most fundamental models – parallel model, series model, Maxwell Eucken model, effective medium theory model and co-continous model – are presented. Furthermore it is possible to use combinations of two or more of these fundamental models for the estimation of thermal conductivity (Krischer, 1963; Wang et al., 2006).

If conduction is the only or the dominating heat transfer mechanism, it may be assumed that thermal conductivity of a porous material will lie between the parallel and series model values. Equation (2) describes the result using the parallel model which considers the thermal resistances to be in parallel, i.e. heat can flow through both materials in parallel. The parallel model gives the upper bound of effective thermal conductivity of the heterogeneous material.

$$k_{h,p} = f k_s + (1-f) k_{air} \tag{2}$$

k_h is the thermal conductivity of the heterogeneous material; the second subscript denotes the model used for its estimation (e.g. p for parallel). f is the filling factor i.e. the volume fraction of the solid phase, k_s is the thermal conductivity of the solid phase and k_{air} the thermal conductivity of air. The volume fraction of air is 1-f.

In the series model (see equation (3)), the thermal resistances are considered to be in series with respect to the heat flux and $k_{h,s}$ gives the lower bound of effective thermal conductivity.

$$k_{h,s} = \frac{1}{f / k_s + (1-f) / k_{air}} \tag{3}$$

The effective medium theory (EMT) model (see equation (4)) assumes a random, mutual dispersion of two components (Carson et al., 2005).

$$k_{h,EMT} = \frac{1}{4}\left((3f-1)k_s + (2-3f)k_{air} + \sqrt{\left[(3f-1)k_s + (2-3f)k_{air}\right]^2 + 8k_{air}k_s} \right) \tag{4}$$

Equation (5) shows the result of the co-continuous model (Wang et al., 2008) where both phases are assumed to be continuous.

$$k_{h,C\text{-}C} = \frac{k_{h,s}}{2}\left(\sqrt{1 + 8k_{h,p} / k_{h.s}} - 1 \right) \tag{5}$$

Even though this model is independent of parallel and series model, the result $k_{h,\,C\text{-}C}$ can be expressed as function of $k_{h.\,p}$ and $k_{h,\,s}$, which are the thermal conductivities calculated for the parallel and series model (see equations (2) and (3)).
Whereas all four models mentioned so far are symmetric with respect to exchange of the two phases, the Maxwell-Euken model (Eucken, 1940) is not, as one phase is assumed to be dispersed in a second, continuous phase. The heterogeneous conductivity calculated following the Maxwell-Euken model $k_{h,\,M\text{-}E}$ is given in (6) where the index 'cont' refers to the continuous phase and the index 'dis' to the dispersed phase.

$$k_{h,\,M\text{-}E} = \frac{k_{cont} f_{cont} + k_{dis} f_{dis} \dfrac{3k_{cont}}{2k_{cont} + k_{dis}}}{f_{cont} + f_{dis} \dfrac{3k_{cont}}{2k_{cont} + k_{dis}}} \tag{6}$$

Obviously, each of the models assumes a certain geometry which does not reflect exactly the microstructure of a GDL. Gas diffusion layers typically exhibit anisotropy of the microstructure as carbon fibers are preferentially oriented in–plane. Furthermore, carbon fibers are expected to exhibit an anisotropic thermal conductivity as e.g. pyrolytic graphite (Wen & Huang, 2008) – the degree of anisotropy depending on the type of fiber – due to their anisotropic, partly graphite-like structure. Both, the anisotropy in microstructure and the anisotropy of thermal conductivity in carbon fibers is not into account in any of the presented models.

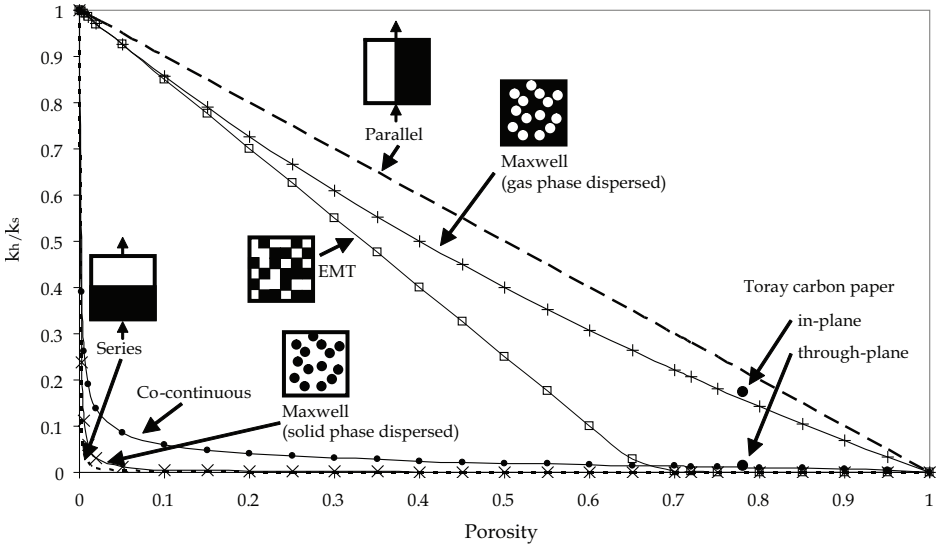

Fig. 3. Estimated thermal conductivity of the heterogeneous material k_h normalized with respect to the thermal conductivity of the solid phase k_s dependent on porosity. Different models were used for the estimation using a ratio of k_s/k_{air} of 120 $Wm^{-1}K^{-1}$ / 0.026 $Wm^{-1}K^{-1}$. For some models, the assumed structure is shown as insert; the small arrows indicate the direction of heat flux where appropriate. Additionally, the thermal conductivity of Toray carbon paper as given by the manufacturer (Toray Industries, 2005b) is shown

Nevertheless, the models can be applied to gas diffusion layers and Fig. 3 shows normalized thermal conductivity estimated using the models mentioned above assuming a ratio of thermal conductivities k_s/k_{air} of 120 $Wm^{-1}K^{-1}$ / 0.026 $Wm^{-1}K^{-1}$ which is an estimate for gas diffusion layers consisting of carbon fibers in air. As an example of a GDL, the in-plane and through-plane thermal conductivities of Toray carbon paper without the addition of PTFE as given by the manufacturer (Toray Industries, 2005b) are included assuming a k_s of 120 $Wm^{-1}K^{-1}$.
Overall, the presented models allow estimating the order of magnitude of the thermal conductivity of gas diffusion layers, but – also due to the anisotropic microstructure of a typical GDL – a more precise a-priori estimation seems impossible.

3.2 Computation of thermal conductivity of gas diffusion layers

As more accurate thermal conductivity data is required, one further approach is the computation based on 3D structure data (Becker et al., 2008; Pfrang et al., 2010; Veyret & Tsotridis, 2010; Zamel et al., 2010). Fig. 4 illustrates the two approaches applied here: the characterization of GDL 3D structure by X-ray computed tomography (section 2.1.1), left and the random generation of 3D models of the GDL structure (section 2.1.2), right. Both approaches have certain advantages and drawbacks: While the randomly generated structures allow an accurate definition of the distribution of each material, in CT it was not possible to discriminate carbon from PTFE due to similar X-ray adsorption. CT, on the other hand, provides the realistic 3D structure; whereas there are deviations from the real structure after random structure generation (e.g. straight fibers are assumed). In both approaches there are limitations with respect to spatial resolution; resolution of X-ray CT is limited while essentially computer hardware and computing time limit the number of voxels of randomly generated structures.
Even though PTFE cannot be discriminated from carbon fibers by the contrast in the CT datasets, the carbon fibers are clearly visible in the 3D structure (see top left of Fig. 4) and the micro porous layer (MPL) is clearly visible in the cross-section (see bottom left of Fig. 4).
For one of the samples investigated by CT – EC-TP1-060T – a corresponding randomly generated structural model was generated. This sample was selected as it contains relatively straight fibers (as compared to the carbon cloth) and does not contain a micro porous layer. The parameters for the structure generation were chosen according to the manufacturer's datasheet (Toray Industries, 2005b): 22 % filling factor of carbon; these 22 % were distributed into 21 % carbon fiber and 1 % carbon binder. After fiber generation and addition of the carbon binder, 30 wt. % of PTFE were added.
The results are given in Table 2 with gray background together with a selection of thermal conductivity data published in the literature. For in-plane thermal conductivity, two values are given if the thermal conductivity was determined independently for two orthogonal in-plane directions, and one value is given when the average in-plane conductivity was determined.
In an earlier study (Ihonen et al., 2004), thermal conductivity for several types of GDLs was estimated to 0.2-0.4 W/m K, which was considered unrealistically low in the study. Nevertheless, this estimated range is in agreement with more recent measurements. Finally, a study on the computation of thermal conductivity based on model structures with different geometries was published by (Zamel et al., 2010) where the calculated values are given relative to the thermal conductivity of the solid phase and therefore the values are not given in Table 2. It is reasonable to give this ratio, because the thermal conductivity of carbon fibers is often not known as it depends on the type of carbon fiber and can vary by

orders of magnitude (Blanco et al., 2002) depending e.g. on the heat treatment of the fibers. This may explain the apparent discrepancy between the results for structural models of carbon paper by (Becker et al., 2008) and (Veyret & Tsotridis, 2010) where thermal conductivity values of 17 W/ m K and 130 W/ m K were used, respectively.

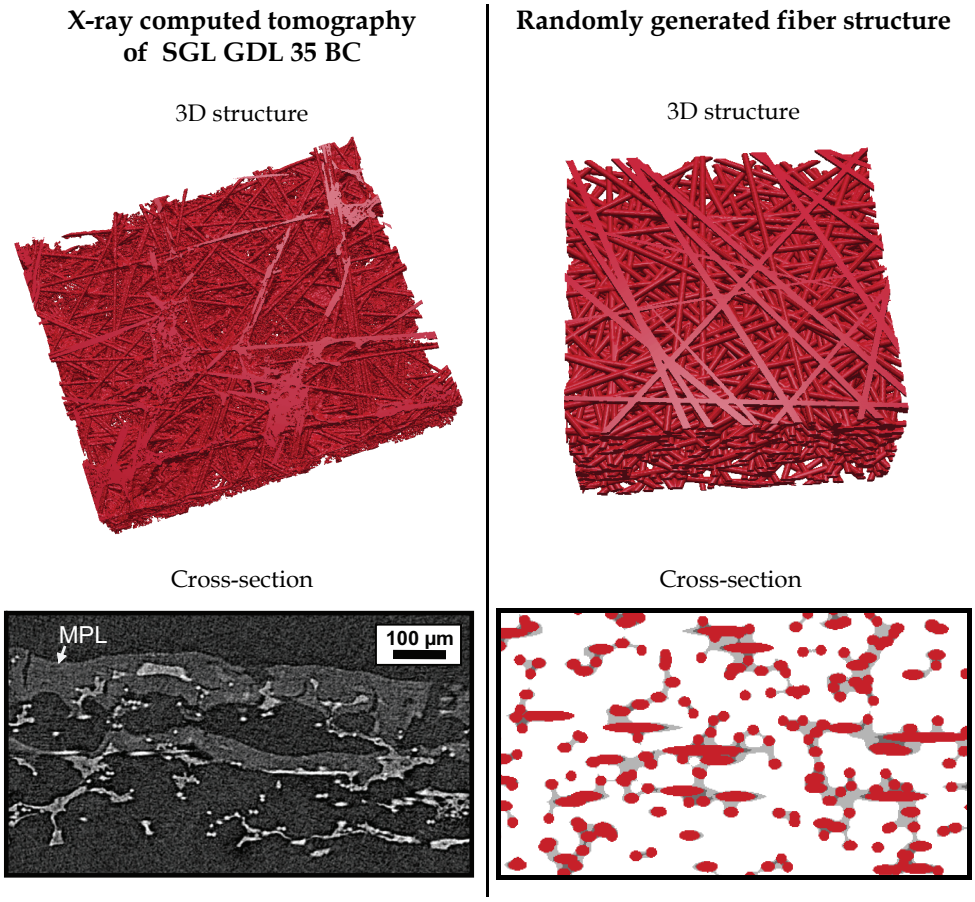

Fig. 4. 3D structure and cross-section of a GDL as determined by X-ray computed tomography (left) and randomly generated (right). The micro porous layer (MPL) is clearly visible in the CT cross section. In the 3D structure of the randomly generated structure only the carbon fibers are shown (not carbon binder and PTFE), while in the cross section, the fibers (red) can be clearly discriminated from carbon binder (dark gray) and PTFE (light gray)

The focus of earlier work was on through-plane thermal conductivity of the GDL, as the heat flows predominantly through-plane in a PEM fuel cell. Nevertheless, for a detailed understanding of the heat flux, also in-plane thermal conductivity is relevant, e.g. because thermal contact between bipolar plate and GDL is not homogeneous due to the gas flow channels in the bipolar plate. Only recently measurements of in-plane thermal conductivity were published (Sadeghi et al., 2011b; Teertstra et al., 2011).

When considering all data from Table 2, the range of thermal conductivity values for the through-plane direction is 0.13-2.8 W / m K, as compared to a range of 1.75-21 W / m K for the in-plane direction. As carbon fibers have a higher thermal conductivity than PTFE or air, this can be explained by the preferred orientation of the carbon fibers in-plane, i.e. heat can be transported mainly along the fibers in-plane, whereas for through-plane heat transfer from fiber to fiber is required to a larger extent.
In a PEM fuel cell, the GDL is subject to compression and consequently in most experimental setups used for the determination of thermal conductivity the GDL is investigated under compression. As a general trend, an increase of thermal conductivity and a reduction of thermal resistance were found with increasing compression. More recently, also the effect of load cycling – i.e. cycles of increasing compression up to a maximum value and releasing compression to 0 – was investigated and steady-state (in the investigated case reached after 5 cycles) properties were determined (Sadeghi et al., 2010).
Further, it was found that residual water in the GDL leads to a significant increase of through-plane thermal conductivity (Burheim et al., 2010; Burheim et al., 2011). The influence of PTFE distribution on thermal conductivity is discussed in section 3.3.
In the following paragraphs, our data on thermal conductivity will be compared with literature data. For the computation for E-Tek EC-CC1-060T, only one measurement on a similar sample – but without PTFE – is available and gives a clearly lower thermal conductivity. One explanation could be that the addition of PTFE leads to an increase of thermal conductivity, but this is not in accordance with the trend of a decrease of thermal conductivity observed for other samples. Because PTFE cannot be discriminated from carbon fibers in the CT dataset, it seems reasonable to assume that the thermal contact between fibers is overestimated in our computation (as an arithmetic average of thermal conductivity between carbon and PTFE was used in the computation for all solid voxels) which results in an overestimation of thermal conductivity.
For Sigracet 35 BC, the MPL was not considered in the computation of thermal conductivity, i.e. it was replaced by air. This obviously leads to an overall underestimation of thermal conductivity as observed.
One way forward would be the clear identification of MPL material (maybe applying advanced segmentation techniques or using improved CT imaging techniques) and its inclusion into the computation.
When comparing our results computed from the CT data of EC-TP1-060T and the randomly generated model (based on EC-TP1-060T), through-plane thermal conductivities agree well - 1.7 vs. 1.65 W / m K – whereas in-plane thermal conductivities are significantly larger for the randomly generated model. The in-plane heat flux is expected to flow mainly along the fibers. Therefore the different thermal conductivities assumed for solid voxels – 120 W / m K for the carbon fibers in the randomly generated model vs. 93 W / m K as weighted average between carbon and PTFE for the CT dataset – could explain this difference. Nevertheless, the computed thermal conductivities lie well within the range of values available in the literature for Toray carbon paper based materials for through-plane as well as in-plane direction.

3.3 Influence of PTFE distribution

Experimental results have shown that an increase of PTFE loading leads to a reduction of through-plane thermal conductivity (Khandelwal & Mench, 2006; Burheim et al., 2011) in several, but not all types of gas diffusion layers (see Table 2).

Table 2. (continues) Published values of thermal conductivity of gas diffusion layers

Gas diffusion layer	PTFE / %	Thermal conductivity / W m^{-1} K^{-1}		Remarks	Type of data	Technique	Reference
		through-plane	in-plane				
E-Tek EC-CC1-060	0	0.28 -0.32		4.6 -13.9 bar compression dry GDL	ex situ	unidirectional heat flux and measuring temperature difference	(Burheim et al., 2011)
E-Tek EC-CC1-060T	30	1.4	5.6, 6.2	based on x-ray CT data	computation	EJ-Heat solver (Wiegmann & Zemitis, 2006)	(Pfrang et al., 2010)
E-Tek ELAT carbon cloth LT1200-W, thickness 275 um	0	0.22			ex situ	unidirectional heat flux and measuring temperature difference	(Khandelwal & Mench, 2006)
E-Tek ELAT carbon cloth, thickness 180 µm	0	0.2		combined value for catalyst surface + GDL	in situ	calculated from temperature profiles in running fuel cell	(Vie & Kjelstrup, 2004)
E-Tek ELAT carbon cloth, thickness 410 µm	not av.	0.13 -0.19			in situ	estimated from temperature differences in running fuel cell	(Burford & Mench, 2004)
Freudenberg FCCT H2315	0	0.14 -0.15		4.6 -13.9 bar compression dry GDL	ex situ	unidirectional heat flux and measuring temperature difference	(Burheim et al., 2011)
Freudenberg FCCT H2315 T10A	10	0.15 -0.16					
SGL Sigracet 10 AA	0	0.30 -0.42		4.6 -13.9 bar compression dry GDL	ex situ	unidirectional heat flux and measuring temperature difference	(Burheim et al., 2011)
		0.7 -0.87		4.6 -13.9 bar compression residual water			
SGL Sigracet 10 BA	5	0.26 -0.33		4.6 -13.9 bar compression dry GDL	ex situ	unidirectional heat flux and measuring temperature difference	(Burheim et al., 2011)
	5	1.18		conductivity almost independent of compression up to 5.5 MPa	ex situ	unidirectional heat flux and measuring temperature difference	(Nitta et al., 2008)
SGL Sigracet 24 AA	0	0.48			ex situ	unidirectional heat flux and measuring temperature difference	(Khandelwal & Mench, 2006)
SGL Si gracet 24 BA	5	0.31					
SGL Sigracet 24 DA	20	0.22					
SGL Sigracet 25BC and 35BC	5	0.6 -0.9		0.04 -1.3 MPa compression	ex situ	guarded hot plate, two similar samples with different thicknesses used	(Radhakrishnan, 2009)
SGL Sigracet 35 BC	5	0.16	1.9, 2.0	based on x-ray CT data (without MPL)	computation	EJ-Heat solver (Wiegmann & Zemitis, 2006)	(Pfrang et al., 2010)
SGL Carbon, thickness 420 µm	yes	0.26 -0.34		estimate based on experiment	ex situ	unidirectional heat flux and measuring temperature difference	(Ramousse et al., 2008)
SolviCore carbon paper	30	0.25 -0.52		0.7 - 13.8 bar compression	ex situ	ASTM Standard D-5470 -06 with modifications; unidirectional heat flux	(Karimi et al., 2010)
	30		3.2 -3.87	in vacuum	ex situ	thermal resistance measurements using the parallel thermal conductance (PTC) technique	(Teertstra et al., 2011)
	not av.	0.27 -0.40		4.6 -13.9 bar compression dry GDL	ex situ	unidirectional heat flux and measuring temperature difference	(Burheim et al., 2010)
		0.45 -0.57		4.6 -13.9 bar compression residual water			
SpectraCarb carbon paper	0	0.26 -0.7		0.7 - 13.8 bar compression	ex situ	ASTM Standard D-5470 -06 with modifications; unidirectional heat flux	(Karimi et al., 2010)
	12, 19, 29	0.28 -0.6					
	0		12.8, 13.8	in vacuum	ex situ	thermal resistance measurements using the parallel thermal conductance (PTC) technique	(Teertstra et al., 2011)
	6, 11, 19		9.78 -14.2				

Table 2. (continued) (results by the authors marked by gray background)

Gas diffusion layer	PTFE / %	Thermal conductivity / W m^{-1} K^{-1}		Remarks	Type of data	Technique	Reference
		through-plane	in-plane				
Toray carbon paper TGP-H-060	0	2.8		compression 1.9 MPa	in situ	estimated from temperature differences in running fuel cell	(Kawase et al., 2009)
	0	1.8 -1.2		temperature 26 - 73 °C	ex situ	unidirectional heat flux and measuring temperature difference	(Khandelwal & Mench, 2006)
	5	0.41 -0.66		4.6 -13.9 bar compression dry GDL	ex situ	unidirectional heat flux and measuring temperature difference	(Burheim et al., 2011)
		1.6		4.6 -13.9 bar compression residual water			
E-Tek EC-TP1-060T based on Toray TGP -H-060	30	1.7	8.9, 8.0	based on x-ray CT data	computation	EJ -Heat solver (Wiegmann & Zemitis, 2006)	(Pfrang et al., 2010)
Carbon paper EC-TP1-060T (structural model)	30	1.65	13.8	based on structural model	computation	EJ -Heat solver (Wiegmann & Zemitis, 2006)	This work
Toray carbon paper, Quintech, thickness 190 µm	0	0.36 -1.36		estimate based on experiment	ex situ	unidirectional heat flux and measuring temperature difference	(Ramousse et al., 2008)
Toray carbon paper, Quintech, thickness 230 µm	yes	0.20 -0.30					
Toray carbon paper TGP-H-060 / -090 and -120	0	1.7	21		datasheet	not available	(Toray Industries, 2005b)
Toray carbon paper TGP-H-060 and -120	0	1.6 -1.9		0.04 -1.3 MPa compression	ex situ	guarded hot plate, two similar samples with different thicknesses used	(Radhakrishnan, 2009)
	5	1.4 -2.1		0.2 -1.5 MPa compression	ex situ	unidirectional heat flux and measuring temperature difference	(Sadeghi et al., 2011a)
Toray carbon paper TGP-H-090	5	1.4 -1.5		4.6 -13.9 bar compression residual water	ex situ	unidirectional heat flux and measuring temperature difference	(Burheim et al., 2011)
		0.5 -0.73		4.6 -13.9 bar compression dry GDL			
	10	0.48 -0.69					
	60	0.28 -0.32					
Toray carbon paper, Quintech, thickness 280 µm	0	0.33 -0.59		estimate based on experiment	ex situ	unidirectional heat flux and measuring temperature difference	(Ramousse et al., 2008)
Toray carbon paper TGP-H-120	5	0.62 -0.89		4.6 -13.9 bar compression dry GDL	ex situ	unidirectional heat flux and measuring temperature difference	(Burheim et al., 2011)
		1.4		4.6 -13.9 bar compression residual water			
	5	1.55 -2.1		at quasi steady state, load cycling 0.25 -1.5 MPa, in vacuum	ex situ	unidirectional heat flux and measuring temperature difference	(Sadeghi et al., 2010)
	5-30		17.3 -17.8	in vacuum	ex situ	thermal resistance measurements using GDL samples of different lengths	(Sadeghi et al., 2011b)
	30		15.1	in vacuum	ex situ	thermal resistance measure ments using the parallel thermal conductance (PTC) technique	(Teertstra et al., 2011)
Carbon paper (structural model)	≤ 20	0.296	1.75, 2.05	based on synchrotron 3D structure data	computation	EJ -Heat solver (Wiegmann & Zemitis, 2006)	(Becker et al., 2008)
		0.388	2.55	compressed by 20%, based on synchrotron 3D structure data			
Carbon paper (structural model)	0	1.86	9.79, 9.82	based on structural model	computation	EJ -Heat solver (Wiegmann & Zemitis, 2006)	(Veyret & Tsotridis, 2010)
	0-25	1.86 -1.2					

Assuming that the structure of the GDL remains unchanged, one would expect that the addition of material that has a higher thermal conductivity than air – like PTFE – should increase the overall thermal conductivity.

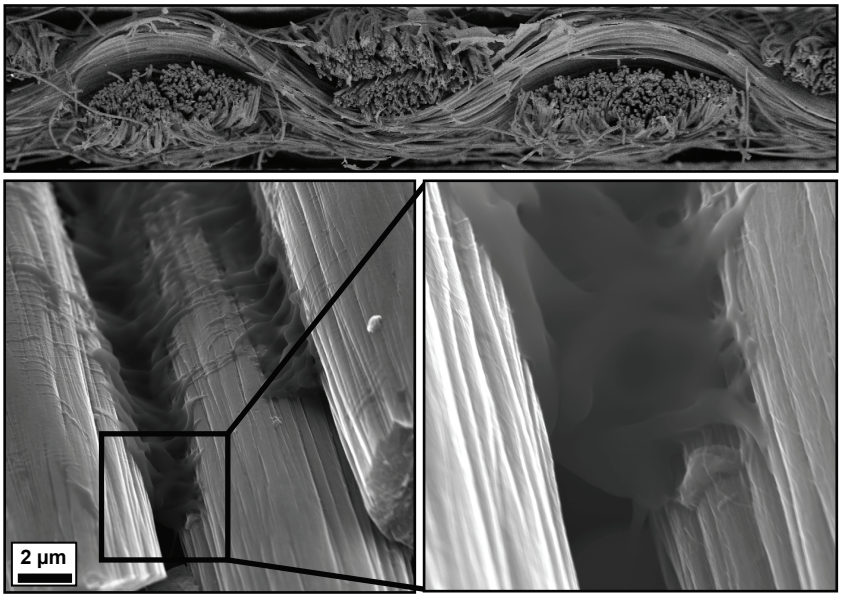

Fig. 5. Scanning electron micrographs of the cross section of carbon cloth EC-CC1-060T: the top image gives an overview of the whole thickness of the cross section, the bottom two images show carbon fibers with PTFE in between

However, since the thermal conductivity of PTFE is orders of magnitude smaller than that of carbon, PTFE potentially can insulate carbon fibers from each other, i.e. the contact region between carbon fibers can have a big impact on the thermal conductivity of the GDL. This is especially relevant for carbon papers where the carbon fibers are oriented preferably in-plane, which means that through-plane heat transfer requires heat transfer from fiber to fiber. Fig. 5 shows scanning electron micrographs of the cross section of carbon cloth EC-CC1-060T. In the selected region, PTFE separates two neighbouring carbon fibers. For a further illustration of this possible insulation effect, thermal conductivity of model structures of layers of parallel fibers with a filling factor of 22 % were randomly generated using GeoDict (see Fig. 6). Model structures with different distances between the fiber layers were investigated and thermal conductivity of each of these structures was evaluated without PTFE and after the addition of 30 wt. % of PTFE. These model structures are surely not a realistic description of any GDL, but they will be used to examine different possible geometries of the contact region between fibers. As these fibers are oriented exactly in-plane, the model structures represent an extreme case with respect to through-plane conductivity in the sense that heat transfer along the fibers cannot contribute significantly.
The computed thermal conductivities of these model structures are summarized in Fig. 7. For the case of touching fibers (distance 0 µm), there is only a small increase in thermal conductivity due to the addition of PTFE around the contact region between fibers.

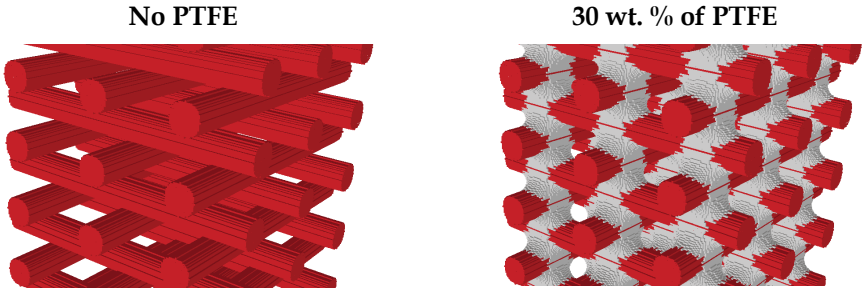

Fig. 6. Detail of model structures of layers of equidistant parallel fibers. The filling factor of the carbon fibers is 22 %. Without PTFE (left) and with 30 wt. % of PTFE shown in gray (right)

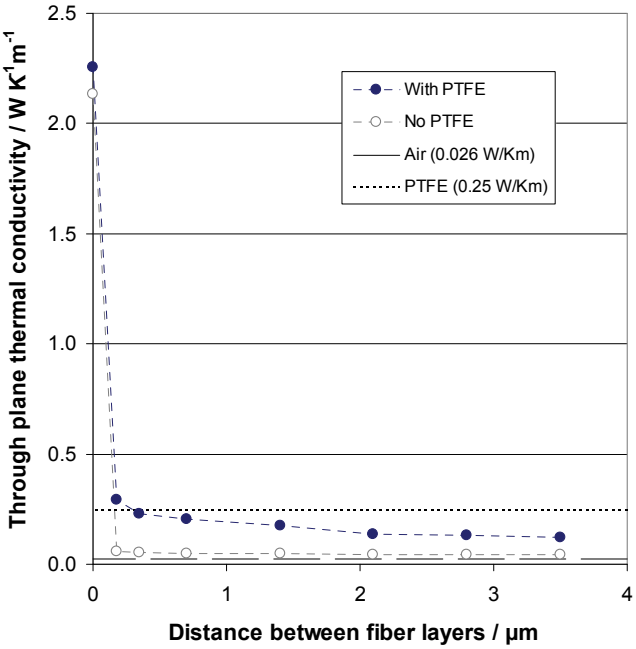

Fig. 7. Computed through-plane thermal conductivity dependent on the distance between fiber layers (based on model structures as illustrated in Fig. 6). For comparison, the thermal conductivities of pure air and pure PTFE are included into the graph

In both cases, with and without PTFE, the conductivity drops sharply from distance 0, i.e. contact between the fibers layers, to a distance of 0.175 µm, the smallest considered distance. For the model structures without PTFE, the conductivity drops to values close to the thermal conductivity of air. These cases are of course not realistic for a GDL as fibers will always be in contact due to the compression of the GDL, but it is illustrated that heat transfer between non-touching fibers is strongly inhibited.

For the model structures with PTFE, the conductivity drops to values below the thermal conductivity of PTFE, which is in the same order of magnitude as thermal conductivities measured for realistic gas diffusion layers (compare Table 2).
It has to be mentioned that in the model structures the contact area between touching fibers (distance 0 μm) was defined by the voxel size of the model structures. It is clear that this contact area will have a huge impact on heat flux through the contact. In this context, the presence of carbon binder – which is used for the mechanical stabilization of the GDL – can play an important role.
Overall, it is obvious from the results presented in Fig. 7 that the contact region between fibers is important for the thermal conductivity of a GDL. When looking back to the models estimating thermal conductivity of heterogeneous materials (section 2.1) and considering the contact area between fibers consisting of PTFE and carbon, both extreme cases – parallel heat flux through carbon and PTFE and heat flux in series through the two components – seem to be potentially realistic for the description of a specific single contact between two fibers in a gas diffusion layer. The macroscopic thermal conductivity of a GDL will depend strongly on the statistical distribution of the different contact geometries.
Considering the drop of thermal conductivity with the increase of PTFE loading observed experimentally, it might be speculated that PTFE can be introduced between fibers thereby reducing the direct contact area between fibers which would explain the observed drop in thermal conductivity. Of course compression as well as mechanical cycling potentially can lead to a modification of contacts between fibers, i.e. the statistical distribution of contact geometries and thereby thermal conductivity could change. Reversible as well as irreversible modifications of contact geometries – and consequently thermal conductivity could occur under mechanical loading.
Also the observation that the presence of residual liquid water leads to an increase of through-plane thermal conductivity (Burheim et al., 2011) can possibly be explained; the water – with a thermal conductivity of 0.6 W/ m K (Taine & Petit, 1989) – could either improve heat flux at already existing contacts between fibers or even provide new heat flux paths that were 'insulated' by air before the addition of water.

4. Conclusion

Three commercially available gas diffusion layers of PEM fuel cells were investigated by 3D X-ray computed tomography (CT). The 3D structure of carbon fiber based gas diffusion layers was clearly resolved, but carbon fibers and PTFE could not be discriminated. Further, 3D fiber structures were randomly generated using GeoDict and model structures of layers of equidistant parallel fibers were generated. Binder material – this could be PTFE only or carbon and PTFE – was added to these fiber structures.
The application of analytical models for the estimation of thermal conductivity of heterogeneous materials was discussed. Based on the measured and generated 3D structures, the macroscopic, anisotropic effective thermal conductivities of the gas diffusion layers were computed. The average in-plane thermal conductivity for all structures is by about a factor 4 to 12 larger than the average through-plane thermal conductivity. These results were compared with the available literature data on thermal conductivity of gas diffusion layers and a good agreement was found.
Finally, it was shown that – due to the big difference between the thermal conductivities of PTFE and carbon – the impact of the contact area between carbon fibers and the spatial

distribution of PTFE in the contact region between carbon fibers on the macroscopic thermal conductivity is considerable. Therefore an improved characterisation of the contact region between carbon fibers could be a worthwhile objective for future similar studies. This includes also the discrimination of PTFE and carbon in CT datasets.
Overall, it was shown that the computation of thermal conductivity of gas diffusion layers based on 3D structure can lead to an improved understanding of the thermal properties of a GDL. Both approaches presented here have advantages: CT measurements guarantee a realistic 3D structure, while the random generation of 3D structures allows the precise definition of the distribution of all components which can be especially relevant for virtual GDL design.

5. Acknowledgment

This work has been carried out within the multiannual programme of the European Commission's Joint Research Centre, as part of the FCPOINT activities. The authors thank Marc Steen (Institute for Energy, European Commission) for critical reading of the manuscript, Gaby Janssen (Energy Research Centre of the Netherlands, ECN) for the provision of gas diffusion layers and GE sensing and inspection technologies/phoenix X-ray (Wunstorf, Germany) for X-ray computed tomography data.

6. References

Bazylak, A. (2009). Liquid water visualization in PEM fuel cells: A review. *International Journal of Hydrogen Energy* Vol. 34, No. 9, pp. 3845-3857, ISSN 03603199

Becker, J., Flückiger, R., Reum, M., Büchi, F. N., Marone, F. & Stampanoni, M. (2009). Determination of material properties of gas diffusion layers: Experiments and simulations using phase contrast tomographic microscopy. *Journal of the Electrochemical Society* Vol. 156, No. 10, pp. B1175-B1181, ISSN 00134651

Becker, J., Schulz, V. & Wiegmann, A. (2008). Numerical determination of two-phase material parameters of a gas diffusion layer using tomography images. *Journal of Fuel Cell Science and Technology* Vol. 5, No. 2, pp. art. no. 021006, ISSN 1550624X

Blanco, C., Appleyard, S. P. & Rand, B. (2002). Study of carbon fibres and carbon-carbon composites by scanning thermal microscopy. *Journal of Microscopy* Vol. 205, No. 1, pp. 21-32, ISSN 00222720

Burford, D. J. & Mench, M. M. (2004). *Heat transport and temperature distribution in PEFCS*. American Society of Mechanical Engineers, Heat Transfer Division, Anaheim, CA.

Burheim, O. S., Pharoah, J. G., Lampert, H., Vie, P. J. S. & Kjelstrup, S. (2011). Through-plane thermal conductivity of PEMFC porous transport layers. *Journal of Fuel Cell Science and Technology* Vol. 8, No. 2, ISSN 1550624X

Burheim, O. S., Vie, P. J. S., Pharoah, J. G. & Kjelstrup, S. (2010). Ex situ measurements of through-plane thermal conductivities in a polymer electrolyte fuel cell. *Journal of Power Sources* Vol. 195, No. 1, pp. 249-256, ISSN 03787753

Carson, J. K., Lovatt, S. J., Tanner, D. J. & Cleland, A. C. (2005). Thermal conductivity bounds for isotropic, porous materials. *International Journal of Heat and Mass Transfer* Vol. 48, No. 11, pp. 2150-2158, ISSN 00179310

Eucken, A. (1940). Allgemeine Gesetzmässigkeiten für das Wärmeleitvermögen verschiedener Stoffarten und Aggregatzustände. *Forschung auf dem Gebiete des Ingenieurwesens* Vol. 11, No. 1, pp. 6-20, ISSN 00157899

Fraunhofer ITWM (2011). GeoDict, In: *Homepage of the GeoDict software*, 16 February 2011, Available from: www.geodict.com

Garzon, F. H., Lau, S. H., Davey, J. R. & Borup, R. L. (2007). *Micro and nano X-ray tomography of PEM fuel cell membranes after transient operation*. ECS Transactions, Washington, DC.

Giorgi, L., Antolini, E., Pozio, A. & Passalacqua, E. (1998). Influence of the PTFE content in the diffusion layer of low-Pt loading electrodes for polymer electrolyte fuel cells. *Electrochimica Acta* Vol. 43, No. 24, pp. 3675-3680, ISSN 00134686

Ihonen, J., Mikkola, M. & Lindbergh, G. (2004). Flooding of gas diffusion backing in PEFCs: Physical and electrochemical characterization. *Journal of the Electrochemical Society* Vol. 151, No. 8, pp. A1152-A1161, ISSN 00134651

Karimi, G., Li, X. & Teertstra, P. (2010). Measurement of through-plane effective thermal conductivity and contact resistance in PEM fuel cell diffusion media. *Electrochimica Acta* Vol. 55, No. 5, pp. 1619-1625, ISSN 00134686

Kawase, M., Inagaki, T., Kawashima, S. & Miura, K. (2009). *Effective thermal conductivity of gas diffusion layer in through-plane direction*. ECS Transactions, Vienna.

Khandelwal, M. & Mench, M. M. (2006). Direct measurement of through-plane thermal conductivity and contact resistance in fuel cell materials. *Journal of Power Sources* Vol. 161, No. 2, pp. 1106-1115, ISSN 03787753

Krischer, O. (1963). *Die wissenschaftlichen Grundlagen der Trocknungstechnik*, Springer, ISBN 3-540-03018-2, Berlin

Marotta, E. E. & Fletcher, L. S. (1996). Thermal contact conductance of selected polymeric materials. *Journal of Thermophysics and Heat Transfer* Vol. 10, No. 2, pp. 334-342, ISSN 08878722

Mathias, M. F., Roth, J., Fleming, J. & Lehnert, W. (2003). Diffusion media materials and characterisation, In: *Handbook of Fuel Cells - Fundamentals, Technology and Applications, Volume 3*, Vielstich, W., Gasteiger, H. A. & Lamm, A., pp. 517-537, John Wiley, ISBN 0-471-49926-9, Chichester

Nitta, I., Himanen, O. & Mikkola, M. (2008). Thermal conductivity and contact resistance of compressed gas diffusion layer of PEM fuel cell. *Fuel Cells* Vol. 8, No. 2, pp. 111-119, ISSN 16156846

Ostadi, H., Jiang, K. & Prewett, P. D. (2008). Micro/nano X-ray tomography reconstruction fine-tuning using scanning electron microscope images. *Micro and Nano Letters* Vol. 3, No. 4, pp. 106-109, ISSN 17500443

Paganin, V. A., Ticianelli, E. A. & Gonzalez, E. R. (1996). Development and electrochemical studies of gas diffusion electrodes for polymer electrolyte fuel cells. *Journal of Applied Electrochemistry* Vol. 26, No. 3, pp. 297-304, ISSN 0021891X

Pfrang, A., Veyret, D., Janssen, G. J. M. & Tsotridis, G. (2011). Imaging of membrane electrode assemblies of proton exchange membrane fuel cells by X-ray computed tomography. *Journal of Power Sources* Vol. 196, No. 12, pp. 5272-5276, ISSN 03787753

Pfrang, A., Veyret, D., Sieker, F. & Tsotridis, G. (2010). X-ray computed tomography of gas diffusion layers of PEM fuel cells: Calculation of thermal conductivity. *International Journal of Hydrogen Energy* Vol. 35, No. 8, pp. 3751-3757, ISSN 03603199

Progelhof, R. C., Throne, J. L. & Ruetsch, R. R. (1976). Methods for predicting the thermal conductivity of composite systems: a review. *Polymer Engineering and Science* Vol. 16, No. 9, pp. 615-625, ISSN 00323888

Radhakrishnan, A. (2009). *Thermal conductivity measurement of gas diffusion layer used in PEMFC*. Rochester Institute of Technology, Rochester.

Ramousse, J., Didierjean, S., Lottin, O. & Maillet, D. (2008). Estimation of the effective thermal conductivity of carbon felts used as PEMFC gas diffusion layers. *International Journal of Thermal Sciences* Vol. 47, No. 1, pp. 1-6, ISSN 12900729

Sadeghi, E., Djilali, N. & Bahrami, M. (2010). Effective thermal conductivity and thermal contact resistance of gas diffusion layers in proton exchange membrane fuel cells. Part 2: Hysteresis effect under cyclic compressive load. *Journal of Power Sources* Vol. 195, No. 24, pp. 8104-8109, ISSN 03787753

Sadeghi, E., Djilali, N. & Bahrami, M. (2011a). Effective thermal conductivity and thermal contact resistance of gas diffusion layers in proton exchange membrane fuel cells. Part 1: Effect of compressive load. *Journal of Power Sources* Vol. 196, No. 1, pp. 246-254, ISSN 03787753

Sadeghi, E., Djilali, N. & Bahrami, M. (2011b). A novel approach to determine the in-plane thermal conductivity of gas diffusion layers in proton exchange membrane fuel cells. *Journal of Power Sources* Vol. 196, No. 7, pp. 3565-3571, ISSN 03787753

Sasabe, T., Tsushima, S. & Hirai, S. (2010). In-situ visualization of liquid water in an operating PEMFC by soft X-ray radiography. *International Journal of Hydrogen Energy* Vol. 35, No. 20, pp. 11119-11128, ISSN 03603199

Schladitz, K., Peters, S., Reinel-Bitzer, D., Wiegmann, A. & Ohser, J. (2006). Design of acoustic trim based on geometric modeling and flow simulation for non-woven. *Computational Materials Science* Vol. 38, No. 1, pp. 56-66, ISSN 09270256

SGL Group (2009). Sigracet GDL 34 & 35 series gas diffusion layer, In: *Sigracet Fuel Cell Components*, 16 February 2011, Available from: http://www.sglgroup.com/export/sites/sglcarbon/_common/downloads/product/product-groups/su/fuel-cell-components/GDL_34_35_Series_Gas_Diffusion_Layer.pdf

Sinha, P. K., Halleck, P. & Wang, C. Y. (2006). Quantification of liquid water saturation in a PEM fuel cell diffusion medium using X-ray microtomography. *Electrochemical and Solid-State Letters* Vol. 9, No. 7, pp. A344-A348, ISSN 10990062

Taine, J. & Petit, J. P. (1989). *Transferts thermiques, mécanique des fluides anisothermes*, Dunod, ISBN 2-04-018760-X, Paris

Teertstra, P., Karimi, G. & Li, X. (2011). Measurement of in-plane effective thermal conductivity in PEM fuel cell diffusion media. *Electrochimica Acta* Vol. 56, No. 3, pp. 1670-1675, ISSN 00134686

Toray Industries (2005a). Functional and composite properties, In: *Torayca product lineup*, 11 March 2011, Available from: http://www.torayca.com/techref/en/images/fcp02.html

Toray Industries (2005b). Toray carbon paper, In: *Torayca product lineup*, 16 February 2011, Available from: http://www.torayca.com/properties/en/images/report_eng09_2.html

Tsushima, S. & Hirai, S. (2011). In situ diagnostics for water transport in proton exchange membrane fuel cells. *Progress in Energy and Combustion Science* Vol. 37, No. 2, pp. 204-220, ISSN 0360-1285

Veyret, D. & Tsotridis, G. (2010). Numerical determination of the effective thermal conductivity of fibrous materials. Application to proton exchange membrane fuel cell gas diffusion layers. *Journal of Power Sources* Vol. 195, No. 5, pp. 1302-1307, ISSN 03787753

Vie, P. J. S. & Kjelstrup, S. (2004). Thermal conductivities from temperature profiles in the polymer electrolyte fuel cell. *Electrochimica Acta* Vol. 49, No. 7, pp. 1069-1077, ISSN 00134686

Wang, J., Carson, J. K., North, M. F. & Cleland, D. J. (2006). A new approach to modelling the effective thermal conductivity of heterogeneous materials. *International Journal of Heat and Mass Transfer* Vol. 49, No. 17-18, pp. 3075-3083, ISSN 00179310

Wang, J., Carson, J. K., North, M. F. & Cleland, D. J. (2008). A new structural model of effective thermal conductivity for heterogeneous materials with co-continuous phases. *International Journal of Heat and Mass Transfer* Vol. 51, No. 9-10, pp. 2389-2397, ISSN 00179310

Wen, C. Y. & Huang, G. W. (2008). Application of a thermally conductive pyrolytic graphite sheet to thermal management of a PEM fuel cell. *Journal of Power Sources* Vol. 178, No. 1, pp. 132-140, ISSN 03787753

Wiegmann, A. & Zemitis, A. (2006). EJ-HEAT: A fast explicit jump harmonic averaging solver for the effective heat conductivity of composite materials. *Fraunhofer ITWM* Vol. 94

Zamel, N., Li, X., Shen, J., Becker, J. & Wiegmann, A. (2010). Estimating effective thermal conductivity in carbon paper diffusion media. *Chemical Engineering Science* Vol. 65, No. 13, pp. 3994-4006, ISSN 00092509

11

Analytical Methods for Estimating Thermal Conductivity of Multi-Component Natural Systems in Permafrost Areas

Rev I. Gavriliev
Melnikov Permafrost Institute SB RAS
Russia

1. Introduction

Frozen soils consist of soil solids, ice, unfrozen water, and gas (vapour). The solid particles vary in size and composition and may be composed of one or more minerals or of organic material. Based on particle size, soils are classified into soil types which vary between the many classification systems in use throughout the world. The classification which is most generally used in Russia is that of V.V. Okhotin (Sergeev, 1971), with the basic soil types being sand, sand-silt, silt-clay, and clay which are further subdivided into a large number of subtypes. Soils that have been subject to repeated cycles of freezing and thawing generally have higher silt contents.

The bound water is structurally and energetically heterogeneous. Water bonding to the mineral particles is provided predominantly by the active centres on the surface and the exchange cations. The most important active centres for water adsorption in the crystalline lattice of clay minerals are hydroxyl groups and coordinately unsaturated atoms of oxygen, silicon, aluminium and other elements.

In quantitative terms, it is an undeniable fact that the pore water freezes over a range of negative temperatures rather than at a single temperature, depending on soil moisture content and solute concentration. This is due to distortion of the bound water structure by the active centres on the particle surfaces and dissolved ions, resulting in a kinetic barrier which makes water crystallization difficult.

The phase composition of water (or solution) changes with temperature following the dynamic equilibrium state principle established by Tsytovich (1945) and experimentally confirmed by Nersesova (1953). This principle states that the amount of unfrozen water for a given soil type (non-saline) is a function of the temperature below 0°C and is virtually independent of the total soil moisture content. It is quantitatively described by the equation (Ivanov, 1962):

$$W_{uw} = W_0 + A'\left[\frac{1}{1 + a'|\Delta t| + b'\Delta t^2} - 1\right], \quad (1)$$

where $\Delta t = t - t_f$; t_f is the initial freezing temperature of water; W_0 is the equilibrium moisture content at t_f; and A′, a′ and b′ are the characteristic soil parameters. For a narrow range of freezing temperatures ($|\Delta t| \leq 10°C$), Eq. (1) can be simplified by assuming $b' = 0$.

The thermodynamic instability of the phase composition of water in frozen soils causes their properties to be highly dynamic at subzero temperatures. The presence of unfrozen water below 0°C provides conditions for water migration during freezing. This results in the formation of cryostructures and cryotextures that, in turn, cause the anisotropy of soil thermal and other properties. All cryostructural types can be grouped into three board classes: massive, layered, and reticulate (Everdingen, 2002).

Model calculations generally consider heat conduction in frozen soils. It is characterized by an effective value of the heat flux transferred by the solid particles and interstitial medium (ice, water and vapour) and through the contacts. It depends on multiple variables which reflect the origin and history of the soil, including moisture content, temperature, dry density, grain size distribution, mineralogical composition, salinity, structure, and texture.

A large number of theoretical models and methods were developed for estimating the thermal conductivity of various particulate materials. However, most of them do not address the structural transformations and their validity is limited to a narrow range of material's density. In permafrost investigations, it is essential that properties of snow, soils and rocks be studied in relation to the history of sediment formation through geologic time. Therefore, a universal theoretical model with changing particle shapes was proposed by the present author to describe the processes of rock formation, snow compaction and glacierization with account for diagenetic and post-diagenetic structural modifications, as well the processes of rock weathering and soil formation. A detailed description of the model was given in earlier publications (Gavril'ev, 1992, Gavriliev, 1996, Gavriliev, 1998). Since then, the model has been amended and improved. We therefore find it necessary to present a brief description of the geometric models and the final predictive equations.

2. Theoretical model accounting for structural transformations of sediments

2.1 Soils and sedimentary rocks

A model for estimating the thermal conductivity of soils and sedimentary rocks should take into account the changes in particle shape over the entire range of porosity from 0 to 1 in order to consider the entire cycle of sediment changes since its deposition. In developing such a model, it should be kept in mind that mineral rock particles undergo some kind of plastic deformation through geologic time, gradually filling the entire space. Particles bind together at the contacts ("the contact spot") and rigid crystal bindings develop between the particles.

Following the real picture of rock weathering and particle shape changes through diagenesis, the author has proposed a model, which presents the solid component in a cubic cell by three intersecting ellipsoids of revolution (Fig. 1) (Gavril'ev, 1992).

In this scheme, depending on the semi-axes ratio of the ellipsoids a/R, the porosity of the system varies from 0 to 1 and the particle attains a variety of shapes, such as cubical, faceted, spherical, worn, and cruciate. This logically represents the real changes in particle shape through the sedimentary history, i.e., the key requirement to the model - adequate representation of the real system – is met. In this scheme, the particles always maintain contacts with each other and the system remains stable and isotropic. The coordinate

number is constant and equal to 6; the relation between the thermal conductivity and porosity is realized by changing the particle shape at various size ratios of the ellipsoids of revolution. At a/R ≥ 1, a contact spot appears automatically in the model, which represents rigid bonding between the particles that provides hard, monolithic rock structure (Gavriliev, 1996).

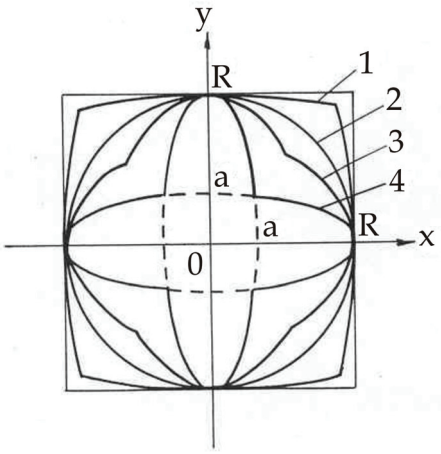

Fig. 1. Particle shapes in the soil thermal conductivity model at different semi-axes ratios of ellipsoids δ = a/R: 1 – faceted (δ > 1); 2 – spherical (δ = 1); 3 – worn (δ < 1); 4 – cruciate (δ < 1)

All calculations are made in terms of the parameter δ = a/R, which is a unique function of the porosity m_2 (dry density γ_s):

$$\lambda = \lambda_{mod} + \varphi_{sc}\,, \tag{2}$$

where λ_{mod} is the resulting thermal conductivity of the model and φ_{sc} is the correction for heat transfer across the contact spot, W/(m•K):

$$\lambda_{mod} = \lambda_{ad}\left[1+\left(\frac{1.3}{1+0.5\vartheta-0.26\vartheta^2}-1\right)\sin\pi m_2\right], \tag{3}$$

where $\vartheta = \lambda_2/\lambda_1; 0 \le \vartheta \le 1$; λ_{ad} is the thermal conductivity of the system where the elementary cell is divided by adiabatic planes; the subscripts "1" and "2" refer to the particle and the fill (air, water and ice), respectively.

The thermal conductivity of the model, λ_{ad}, is given by the following equations:

at $\delta \le 1$

$$\frac{\lambda_{ad}}{\lambda_2} = 1-\frac{\pi\delta}{2}-\delta^2 H+\delta\arcsin\delta/X+\frac{\pi}{\delta K_1}\left[(1-\delta)\left(1-\frac{1}{\delta K_1}\ln\left|\frac{1}{1-\delta K_1}\right|\right)-\right.$$
$$\left.-\left(1-\delta^4\right)\left(\frac{1}{X}+\frac{1}{\delta K_1}\ln\left|1-\frac{\delta K_1}{X}\right|\right)\right]\times\left[1-\frac{4\arcsin\delta/X-\pi\delta}{2\pi(1-\delta)}\right], \tag{4}$$

at $\delta \geq 1$

$$\frac{\lambda_{ad}}{\lambda_2} = 1 - \frac{\pi}{4} - \delta^2 H + \frac{\pi}{2K_1}\left(\delta^2 - \frac{1}{\delta^2}\right) \times \left(\frac{1}{K_1}\ln\left|1 - \frac{\delta K_1}{X}\right| + \frac{\delta}{X}\right) + \\ + \frac{\delta K_1}{X - \delta K_1}\left(\delta \arcsin 1/X - \frac{\pi}{4}\right), \quad (5)$$

where $\delta = a/R$; $X = \sqrt{1+\delta^2}$; $\quad H = \frac{\pi}{2K_1}\left(\frac{1}{K_1}\ln|1-K_1|+1\right)$; $\quad K_1 = 1 - \frac{\lambda_2}{\lambda_1}$.

The correction factor φ_{sc} is given by

$$\varphi_{sc} = \frac{\pi\lambda_1\delta^2}{2}\left[\frac{r_c^2}{2R^2\delta^2} + \frac{\vartheta}{K_1}\left(1 - \sqrt{1 - \frac{r_c^2}{R^2\delta^2}}\right) + \frac{\vartheta}{K_1^2}\ln\frac{1-K_1}{1-K_1\sqrt{1-\frac{r_c^2}{R^2\delta^2}}}\right], \quad (6)$$

where r_c is the radius of the contact spot between the particles.

It is assumed in Eq. (6) that the spot contact between particles is formed of the same material as the particle by its flattening at high pressure or by its squeezing (solution and crystallization) due to selective growth of cement in sandstones (quartz cement grows on quartz particles and feldspar on feldspar particles). In a general case however, the contact spot may consist of a foreign material resulting, for example, from precipitation of salts from solution at the particle contacts. In this case, the correction factor φ_{sc} is given by

$$\varphi_{sc} = \frac{\pi a}{2R^2}\left[\frac{\lambda_3}{K_1^2}\ln\left|\frac{1-K_1\sqrt{1-r_c^2/a}}{(1-K_1)}\right| - \frac{\lambda_2}{K_2^2}\ln\left|\frac{1-K_2\sqrt{1-r_c^2/a^2}}{(1-K_2)}\right| + \\ + \left(\frac{\lambda_2}{K_2} - \frac{\lambda_3}{K_1}\right)\left(1 - \sqrt{1-r_c^2/a^2}\right)\right], \quad (7)$$

where $K_2 = 1 - \lambda_3/\lambda_1$; λ_1, λ_2 and λ_3 are the thermal conductivities of the solid, medium and contact spot (contact cement), respectively.

The relative size of the contact spot is expressed in terms of the system's porosity as:

$$\frac{r_c}{R} = 1.69\sqrt{1 - \sqrt[3]{\frac{\pi}{6(1-m_2)}}}. \quad (8)$$

The soil porosity m_2 or the volume fraction of the mineral particle m_1 is a unique function of the parameter δ and is given by the following equations:

at $\delta \leq 1$

$$m_1 = \frac{\pi\delta^2}{6}\left[1 - \frac{1-\delta^2}{\delta} + \frac{1-\delta}{X}\left(\frac{1+\delta}{\delta} - \frac{1}{X^2} + 3\right)\right], \quad (9)$$

at $\delta \geq 1$

$$m_1 = \frac{\pi\delta^2}{6}\left(1 - \frac{\delta^2 - 1}{\delta X}\right) + \frac{\delta\left(1 + 2\delta^2\right)}{16X^2}\left(\frac{1}{X} + \frac{1}{\sqrt{2 + \delta^2}}\right) \times \left(4\delta \arcsin\frac{1}{\delta X} - \pi\right). \quad (10)$$

The increase in the volume fraction of the solids due to the contact spot is expressed by

$$m_{sc} = \frac{\pi}{4}\left[\frac{r_c^2}{R^2} - 2\left(\delta^2 - \frac{r_c^2}{R^2}\right)\left(1 - \sqrt{1 - \frac{r_c^2}{R^2\delta^2}}\right)\right]. \quad (11)$$

The dry density of the soil is

$$\gamma_d = \left(m_1 + m_{sc}\right)\rho_s\,, \quad (12)$$

where ρ_s is the solids unit weight.

The above equations can be used to calculate the thermal conductivity of soils and sedimentary rocks in the saturated frozen and unfrozen states, as well as in the air-dry state in relation to the porosity m_2 and the thermal conductivity λ_1 of the solid particles (a two-component system). The predictions obtained are presented as nomograms in Fig. 2. It should be noted that in this case, the porosity m_2 refers to the entire volume fraction of the soil or rock which is completely filled either with ice, water, or air. This porosity is related to the volume fraction m_s and dry density γ_s by

$$m_2 = 1 - m_s = 1 - m_1 - m_{sc} = 1 - \gamma_s/\rho_s\,. \quad (13)$$

The model assumes that the material consists of mineral particles of the same composition. However, naturally occurring soils always contain particles of various compositions and they can be treated in modelling as multi-component heterogeneous systems with a statistical particle distribution.

In computations based on the universal model, the average thermal conductivity of soil solid particles may be used, which is approximately estimated in terms of the thermal conductivity and volume fraction of constituent minerals according to the equation (Gavriliev, 1989):

$$\bar{\lambda}_1 = 0.5\left[\sum_{j=1}^{n}\lambda_j m_j + \frac{1}{\sum_{j=1}^{n}\frac{m_j}{\lambda_j}}\right], \quad (14)$$

where λ_j and m_j are the thermal conductivity and volume fraction of the j-th mineral of the soil, respectively. This equation can also be used for calculating the thermal conductivity of rocks characterized by the plane contacts between mineral aggregates.

2.2 Snow

In snowpack, the structural changes of ice crystals occur continuously throughout the winter. The thermodynamic processes in snowpack result in a multi-branch openwork structure of

contacting ice crystals with shapes that continuously change throughout the period of snow existence.

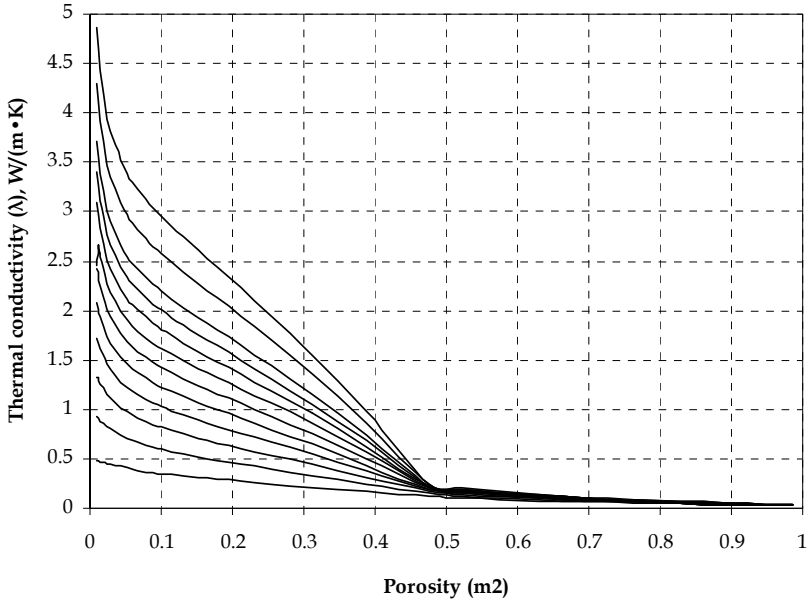

(a)

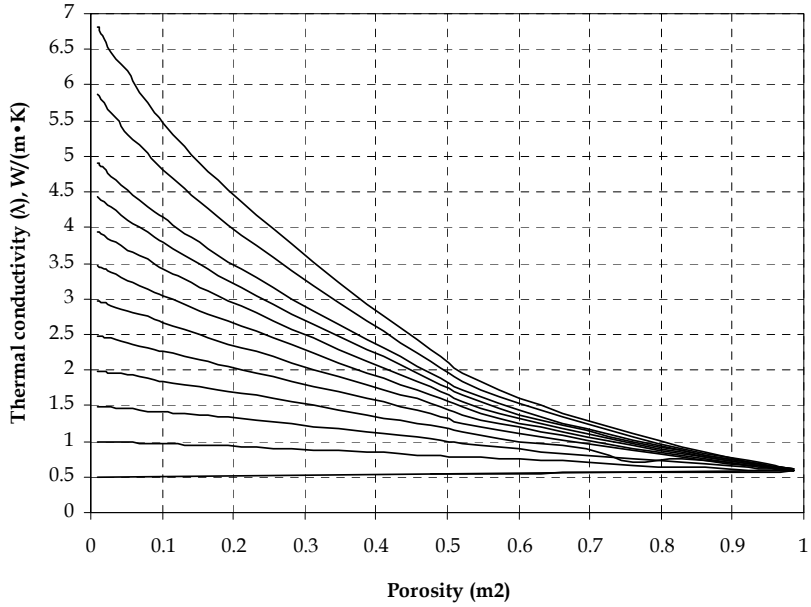

(b)

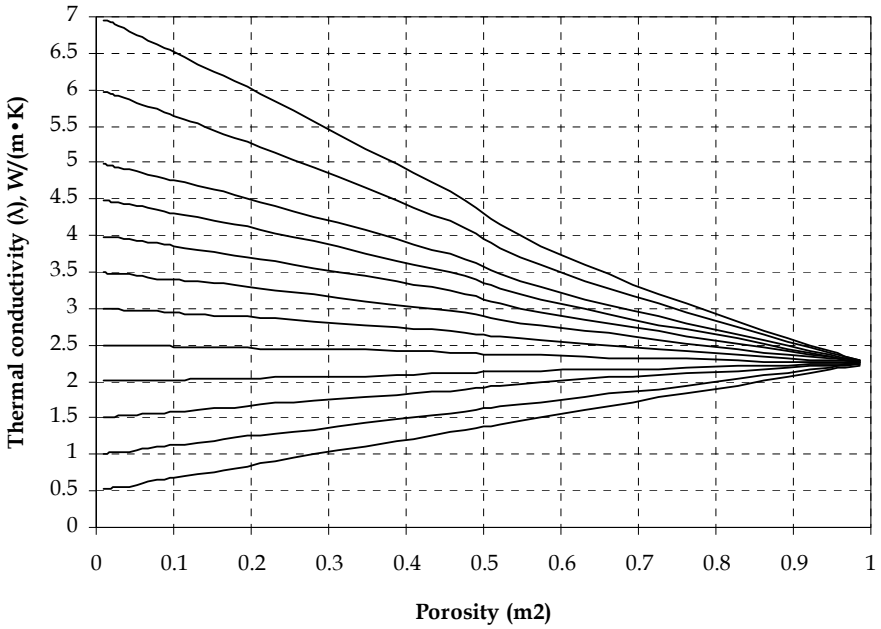

(c)

Fig. 2. Nomograms for calculating the thermal conductivity of soils and rocks in dry (a), saturated unfrozen (b) and frozen (c) states in terms of total porosity m_2 and solids thermal conductivity λ_1 (W/(m•K)): 1 – 0.5; 2 – 1.0; 3 – 1.5; 4 – 2.0; 5 – 2.5; 6 – 3.0; 7 – 3.5; 8 – 4.0; 9 – 4.5; 10 – 5.0; 11 – 6.0; 12 – 7.0

These changes in snow structure through the whole cycle from deposition to glacier formation can be fairly well represented by the same model shown in Fig. 1 (Gavrilyev, 1996a). But the calculations should take into account the heat convection by vapour diffusion due to a temperature gradient in the snow. This can be done by substituting in Eqs. (3) - (6) the effective thermal conductivity of air in snow for its thermal conductivity (λ_a) which is given by

$$\lambda_{ae} = \lambda_a + \frac{LD_s\, e_0}{R_v T^2}\left(\frac{L}{R_v T} - 1\right) \times \exp\left[\frac{L\left(T - T_0\right)}{R_v T_0\, T}\right], \qquad (15)$$

where $e_0 = 6.1 \cdot 10^2$ Pa is the saturation vapour pressure at 0°C (T_0 = 273 K); $R_v = 4.6 \cdot 10^2$ J/(kg•K) is the gas constant of water vapour; T is the absolute temperature, K; L is the latent heat of ice sublimation; D_s is the diffusion coefficient of water vapour in snow; and λ_a is the thermal conductivity of calm air.

The thermal conductivity of air in relation to temperature may be calculated by an equation given by Vargaftik (1963):

$$\lambda_a = \lambda_a^0 \left(\frac{T}{T_0}\right)^{0.82}, \qquad (16)$$

where $\lambda_a^0 = 0.0244$ W/(m•K) is the thermal conductivity of air at temperature T_0.
It is convenient for practical calculations to express the radius of a contact spot directly in terms of the parameter $\delta = a/R$, although this relationship is indirectly reflected in Eq. (8) in terms of porosity. The following correlations have been derived (Gavriliev, 1998):
at $a/R \le 1$

$$\frac{r_c}{R} = 0.25\left(\frac{a}{R}\right)^{2.5}, \tag{17}$$

at $a/R \ge 1$

$$\frac{r_c}{R} = 1.25 - \exp\left[-0.6\left(\frac{a}{R} - 1\right)\right]. \tag{18}$$

Fig. 3 presents a nomogram which can be used to find the thermal conductivity of snow from its temperature and porosity. This nomogram has been developed based on the above theoretical model which takes into account the heat transfer by thermal diffusion of water vapour. In the computations, the diffusion coefficient of water vapour in snow, D_s, is taken to be 0.66 cm²/s, which is the average of the experimental values reported in the literature ranging from 0.40 cm²/s (Sulakvelidze & Okudzhava, 1959) to 0.90 cm²/s (Pavlov, 1962).

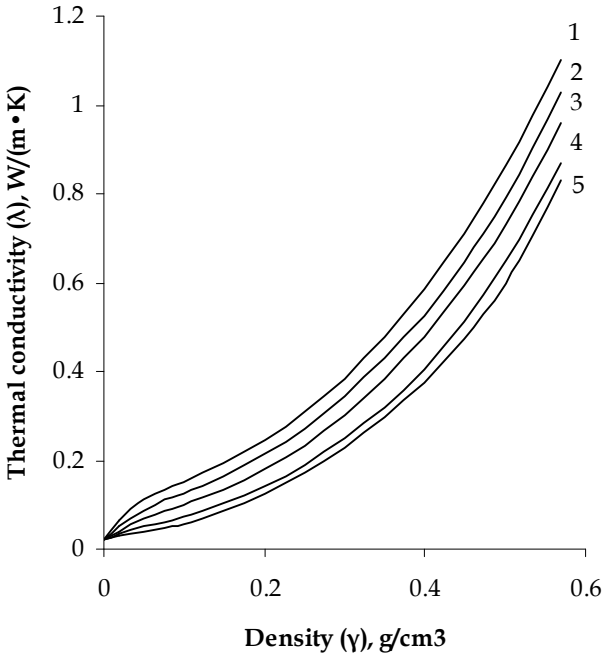

Fig. 3. Nomogram for the calculation of thermal conductivity of snowcover from its density and temperature, °C: (1) -0; (2) -5; (3) -10; (4) -20; (5) -30

3. Effects of coarse inclusions and the layered and reticulate cryostructures on thermal conductivity of frozen soils

For the thermal conductivity of media containing spherical and cubic inclusions with no contacts (or with point contacts), Maxwell (1873) (for a sphere) and Odelevsky (1951) (for a cube) developed a similar equation of the type:

$$\lambda = \lambda_2 \left[1 + \frac{(\lambda_1 - \lambda_2)\, m_1}{\lambda_2 + 0.33\,(1 - m_1)(\lambda_1 - \lambda_2)} \right], \tag{19}$$

where (as before) the subscripts "1" and "2" refer to the inclusions (particles) and the medium, respectively. For the cubical particle shape, Eq. (19) is formally valid across the range of inclusion contents: $0 \le m_1 \le 1$.

The advantage of Eq. (19) is its simplicity. In some cases, Eq. (19) is applicable to permafrost problems, for example, for estimating the thermal conductivity of soils with a cryostructure or of soils containing gravel- or cobble-size inclusions. However, at large differences between the λ_1 and λ_2 values, such as in air-dry soils, the degree of roundness of gravel and cobble inclusions may affect the accuracy of calculations.

For a more general formulation of the problem, an ellipsoidal particle shape may be considered in Eq. (19), since with the change in the ratio of semi-axes the particles transform into other figures, such as a sphere, plate, or cylinder. Eq. (19) may be presented in the following generalized form (Gavriliev, 1986):

$$\lambda = \lambda_2 \left[1 + \frac{(\lambda_1 - \lambda_2)\, m_1}{\lambda_2 + K_f\,(1 - m_1)(\lambda_1 - \lambda_2)} \right], \tag{20}$$

where K_f is the shape factor of particles or inclusions.

In Eq. (20), the inclusion shape factor, K_f, is

$$K_f = abcC(0), \tag{21}$$

where a, b, and c are the semi-axes of the ellipsoids (a > b > c); and C(0) is the integral of the form (Ovchinnikov, 1971)

$$C(0) = \frac{2}{a^3} \left[\frac{\sqrt{1 - p^2 \sin^2 \psi}\, tg\psi - E(\psi, p)}{1 - p^2} \right]. \tag{22}$$

$E(\psi, p)$ is the elliptic integral of the second kind, $\psi = \arcsin\sqrt{1 - c^2/a^2}$ – is the amplitude and $p = \sqrt{\left(1 - b^2/a^2\right)/\left(1 - c^2/a^2\right)}$ – is the modulus of the integral.

The elliptic integral $E(\psi, p)$ is tabulated, and the shape factor of inclusions can be readily found from the ratio of the particle dimensions a, b, and c. For practical purposes, calculations can be limited to the more simple case of ellipsoids of revolution. Then, the integral C(0) is expressed in terms of elementary functions (Carslaw & Jaeger, 1959). Let us consider two examples.

1. The particles have a shape of an oblate ellipsoid of revolution (a = b > c). Then, along the semi-axes we have

$$K_{fc} = \frac{1}{\beta}\left(1 - \frac{c}{a\beta}\arcsin\sqrt{\beta}\right), \tag{23}$$

$$K_{fa} = K_{fb} = \frac{c}{2a\beta}\left(\frac{c}{\sqrt{\beta}}\arcsin\sqrt{\beta} - \frac{c}{a}\right), \tag{24}$$

where $\beta = 1 - c^2/a^2$.

2. The inclusions have a shape of a prolate ellipsoid of revolution (b = c < a)

$$K_{fc} = K_{fb} = \frac{1}{2\beta}\left(1 - \frac{c^2}{2a^2\beta}\ln\frac{1+\sqrt{\beta}}{1-\sqrt{\beta}}\right), \tag{25}$$

$$K_{fa} = \frac{c^2}{a^2\beta}\left(\frac{1}{2\sqrt{\beta}}\ln\frac{1+\sqrt{\beta}}{1-\sqrt{\beta}}\right). \tag{26}$$

Fig. 4 shows graphically the shape factors K_f for oblate and prolate ellipsoids of revolution calculated with Eqs. (23) - (26) in relation to the ratio of the ellipse's semi-minor (c) and semi-major (a) axes at different directions. In the case of a layered cryostructure (c/a = 0), we have $K_f = 1$ (curve 1) for the ice-soil layers oriented across the flow, and $K_f = 0$ (curve 1′) for the orientation along the flow. In the case of cylindrical inclusions (c/a = 0), it follows that perpendicular to the heat flow $K_f = 1/2$ (curve 2′) and parallel to the flow $K_f = 0$ (curve 2).

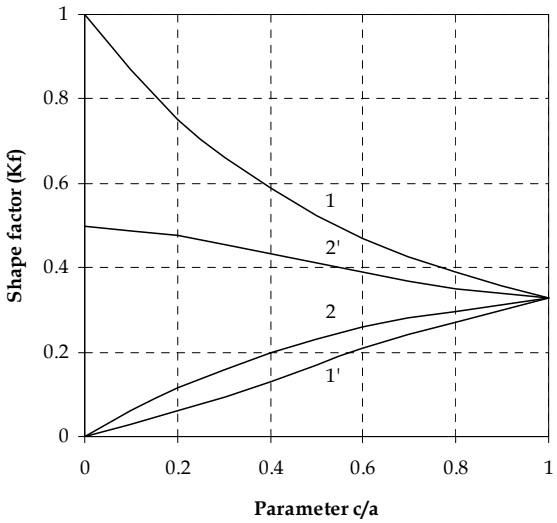

Fig. 4. Shape factor K_f of soil particles in the form of oblate (1 and 1′) and prolate (2 and 2′) ellipsoids of revolution versus parameter c/a for different directions: 1 and 2 – along the axis of revolution; 1′ and 2′ – perpendicular to the axis of revolution

As an example, we will consider frozen soils with cryostructures in more detail below.
Soils with a layered cryostructure exhibit the highest anisotropy of thermophysical properties. In thermal terms, it makes sense to identify the following categories of layered cryostructure: vertical layered, cross layered, and horizontal layered. These cryostructural categories are equivalent to the three main directions of the heat-flow vector relative to the orientation of ice layers: perpendicular, parallel, and intermediate (Fig. 5 a-c).
Soils with a reticulate cryostructure are also anisotropic. The degree of anisotropy depends on the geometry of a reticulate ice network and the direction of the heat-flow vector (Fig. 5 d).

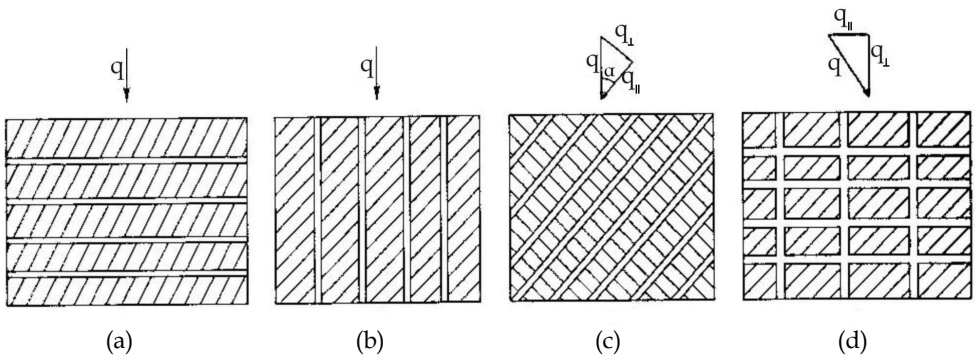

Fig. 5. Schematic representation of frozen soils with layered and reticulate cryostructures at different directions of heat-flow vector. Layered cryostructure for normal (a), parallel (b) and intermediate (c) directions of heat-flow vector relative ice orientation; d – reticulate cryostructure; q – heat-flow vector

The mechanism by which cryostructures develop in sediment is not as yet clearly understood, but the underlying effect is known to be the movement of water to the freezing front. Growing ice lenses dissect the homogeneous (massive) frozen soil into bands or blocks, i.e., the soil elements in the cryostructure are approximately similar in composition and thermal properties. In the reticulate structure, ice is the matrix material and the enclosed soil blocks are commonly rectangular in shape. For estimating the thermal conductivity of soils containing a cryostructure, Ivanov & Gavriliev (1965) considered series and parallel heat flows separately for the layered cryostructure and in combination for the reticulate cryostructure. In the latter case, difficulty arose in practice with how to account for the thickness of ice layers separately along and across the heat flow. A more simple way of taking into account the cryostructure in frozen soils can be found from the theory of generalized conductivity of media containing foreign inclusions. For generality, let us consider the inclusions of ellipsoidal shape, because any type of cryostructure can be obtained by changing the ratio of ellipsoid's semi-axes. For ellipsoids of revolution, for example, the layered cryostructure is obtained by flattening the ellipsoids: $c/a \to 0$ (c and a are the semi-minor and semi-major axes of the ellipsoid, respectively), when they change into plane layers. In the case of prolate ellipsoids of revolution with radius c, at $c/a \to 0$ the soil inclusions in the cryostructure become cylindrical. Any other values of the c/a ratio give reticulate cryostructures with one or other degree of elongation or flattening of the soil inclusions. At $c/a = 1$ the inclusions attain a spherical shape (an analogue of a cubic shape).

Let us consider the cryostructure as an ice matrix with soil inclusions in the form of ellipsoids. We assume in the general case that the soil inclusions are non-uniform in composition. Then, for the effective thermal conductivity of frozen soil, $\lambda_{\perp,\|,+}$, we can use the equation derived earlier by the author (Gavrilyev, 1996b) for very coarse soils with particles of different mineralogical compositions

$$\lambda_{\perp,\|,+} = \lambda_i \left(1 + \frac{1}{B - K_f} \right), \tag{27}$$

where

$$B = 1 \Big/ \sum_{j=1}^{n} \frac{\left(\lambda_j - \lambda_i\right) m_j}{\left(\lambda_j - \lambda_i\right) / K_f + \lambda_i}; \tag{28}$$

K_f is the shape factor of soil inclusions or layers; λ_i is the thermal conductivity of the ice matrix; λ_j and m_j are the thermal conductivity and the volumetric content of the j-th soil inclusion.

The volume fraction of ice, m_i, is

$$m_i = 1 - \sum_{j=1}^{n} m_j \ . \tag{29}$$

It is assumed in Eqs. (27) - (29) that the soil inclusions have a massive structure and are fully saturated (see Section 3 for permafrost soils with a massive cryostructure).

When the ice lenses occur in the soil at angle α to the direction of heat flow, the thermal conductivity of the frozen soil mass is given by

$$\lambda_\alpha = \sqrt{\lambda_\perp^2 \sin^2 \alpha + \lambda_{II}^2 \cos^2 \alpha} \ , \tag{30}$$

where $\lambda_\perp$ and $\lambda_\|$ are the thermal conductivities of the soil with a layered cryostructure, defined by Eq. (27) at corresponding K_f values, for the ice-soil layers perpendicular and parallel to heat flow direction.

The change of rectangular soil inclusions for ellipsoidal ones does not detract from the accuracy of calculations, as it is known from the theoretical predictions of thermal parameters that in the case of inclusions dispersed in a medium, the shape of inclusions has no significant effect on the final calculation results. In case of the uniform composition of frozen soil inclusions, Eq. (27) simplifies to Eq. (20).

Computations of the thermal conductivity of frozen soils with layered and reticulate cryostructures were performed for the ice layers parallel, perpendicular and at 45° angle to the heat flow vector, and for spherical or cubical ($c/a = 1$ and $K_f = 0.33$) soil inclusions in the reticulate cryostructure. The thermal conductivity of the soil containing a cryostructure depends on the size (volume fraction) and orientation of the ice and soil layers relative heat flow direction, as well as the thermal conductivity of these layers.

In the cryostructures, the intermediate layers or inclusions are made of a macroscopically isotropic (massive structure) frozen mass of mineral or organic soils which can vary in

thermal conductivity from 0.5 to 5.0 W/(m•K). It is assumed that the soils comprising the intermediate layers and inclusions are perennially frozen; their thermal properties in relation to natural moisture content have been fairly well studied (Gavriliev, 1989, 1998; Gavriliev & Eliseev, 1970). It is known, for example, that the thermal conductivity of peat in its naturally frozen state is independent of moisture content and is approximately equal to 1.27 W/(m•K). The thermal conductivity of perennially frozen soils in relation to natural moisture content will be discussed in the next section.

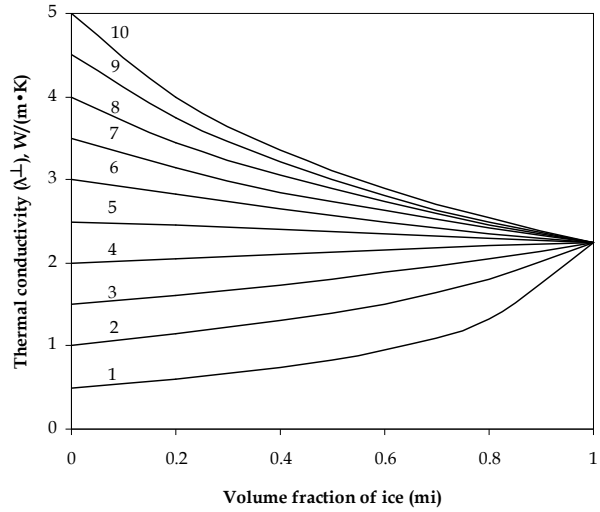

(a)

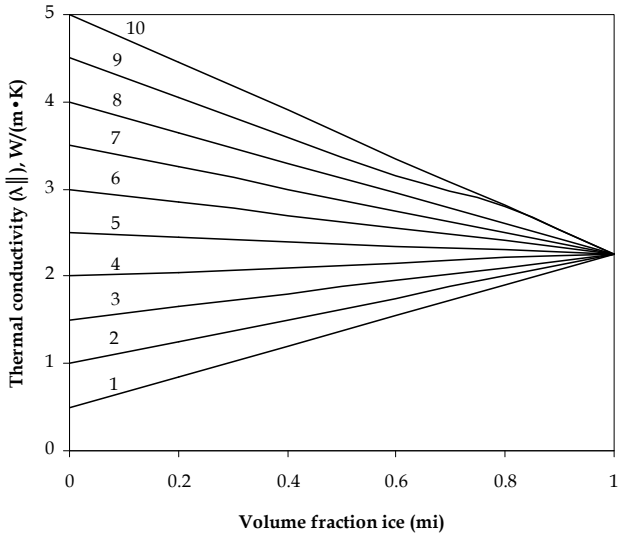

(b)

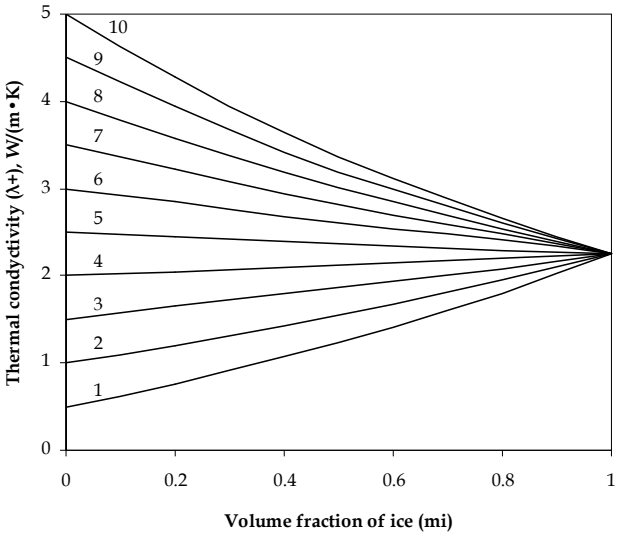

(c)

Fig. 6. Thermal conductivities $\lambda_{\perp}$ (a), $\lambda_{\parallel}$ (b) and λ_{+} (c) of frozen soils with a cryostructure as a function of volume fraction of ice layers (m_i) for various thermal conductivities of intermediate layers or inclusions comprised of frozen organic and mineral soils (λ_{fl}, W/(m•K)). λ_{fl} values: 1-0.5; 2-1.0; 3-1.5; 4-2.0; 5-2.5; 6-3.0; 7-3.5; 8-4.0; 9-4.5; 10-5.0

Based on the calculated thermal conductivity values for the frozen soils with layered and reticulate cryostructures as a function of the volume fraction of ice layers m_i at different thermal conductivities of intermediate layers λ_{fl} (here the subscript "fl" refers to frozen soil), nomograms were developed shown in Fig. 6. For the layered cryostructure, the volume fraction of ice layers m_i is equal to their relative thickness l_i.

At the same values of m_i and λ_{fl}, the thermal conductivity of frozen soils is highest for a layered cryostructure with the soil and ice layers parallel to heat flow and lowest for that with the heat flow direction normal to the ice and soil layers. The soils containing reticulate and layered cryostructures with the ice and soil layers at 45° to heat flow direction have intermediate thermal conductivity values.

4. Permafrost soils with a massive cryostructure

In engineering practice, thermal properties of a given soil type are usually examined in relation to moisture content and dry density. For permafrost soils, there is a unique relationship between these parameters, because naturally occurring soils are near saturation and the air porosity comprises only 2-3% of the total soil volume. The density of frozen soil is then given by Votyakov's equation (1975):

$$\gamma_f = \frac{2.4(1+W)}{2.7W+0.9}, \tag{31}$$

where W is the gravimetric moisture content of the frozen soil expressed as a fraction.

It is sufficient for analysis of the thermal behaviour of permafrost to only consider one of these parameters. Natural moisture content is preferably chosen, since it is easily measured even in the field.

The total moisture content of frozen soils, especially fine-grained soils, varies over a wide range due to moisture migration. For frozen alluvial deposits in Yakutia, for example, the typical values range from 0.07 to 0.30 for sands and from 0.20 to 0.60 for sand-silts and silt-clays (Votyakov, 1975). Correspondingly, the thermal conductivity of soils may exhibit considerable variation.

Fig. 7 shows the experimental results for thermal conductivity, λ, of frozen Yakutian alluvial soils in the wide range of saturation moisture contents W_{sat}. It should be noted that full saturation was assumed in the experiments as a model of the natural state of permafrost soils. As is seen, the dependence of λ on W_{sat} differs between course- and fine-grained soils. With increasing W_{sat}, the thermal conductivity of the frozen sand at the point of full saturation decreases, while that of the silt-clay increases tending to the thermal conductivity of ice. The sand-silts are intermediate between these two soil types.

The observed differences in λ (W_{sat}) can be explained by the differences in the unfrozen water content and in the mineralogical composition of the soils. In the fine soils, the unfrozen water content is quite high (about 0.1) at the measurement temperatures (about -10°C). At low moisture contents, silt-clay can thus be considered as an unfrozen soil. The effect of ice inclusions on overall heat conduction increases with increasing water content, resulting in higher soil thermal conductivity. At high moisture contents, the thermal conductivity of the silt-clay tends to that of ice. In the sands, the unfrozen water content is low and the mineral particles are in direct contact with ice. As the mineral particles have a higher thermal conductivity than ice, the thermal conductivity of the sand decreases with increasing water (ice) content. The same is true for the unfrozen soils. The effect of the unfrozen water film coating the mineral particles is less in the sand-silt compared to the silt-clay. The thermal conductivity of the "mineral particle + unfrozen water" system is likely to have the same values as for ice. The frozen saturated sand-silt has therefore a nearly constant thermal conductivity over the entire range of saturation moisture contents. The mineralogical composition has also an effect, resulting in an increase in the thermal conductivity of solids from finer to coarser soils.

The above features of permafrost thermal conductivity can be estimated based on the analytical theory of thermal conductivity of composite materials. The possible structural models of soil follow from the mechanism of water binding by mineral particles. Soil particles possess excess surface energy which depends on their size and mineral composition. When water enters the ground, it interacts with the mineral particles under the influence of molecular forces and surrounds them in concentric layers until the excess of surface energy is removed. The particles interact through the bound water layer, forming a stable system with dispersed particles. The remaining part of the soil pores is filled with free water. As the soil temperature decreases, primarily near 0°C, the free water begins to freeze. Then more of the bound water freezes with a further decrease in temperature. The strongly bound water remains unfrozen down to about -20°C. When frozen, the system of dispersed particles is cemented by ice, becoming even more stable. Hence, the thermal conductivity of fine-grained permafrost soils at different subzero temperatures can be estimated considering a three-component shell system (mineral particle + unfrozen water + ice) as shown in Fig. 8. Mineral particles in this scheme are assumed to be spherical in shape.

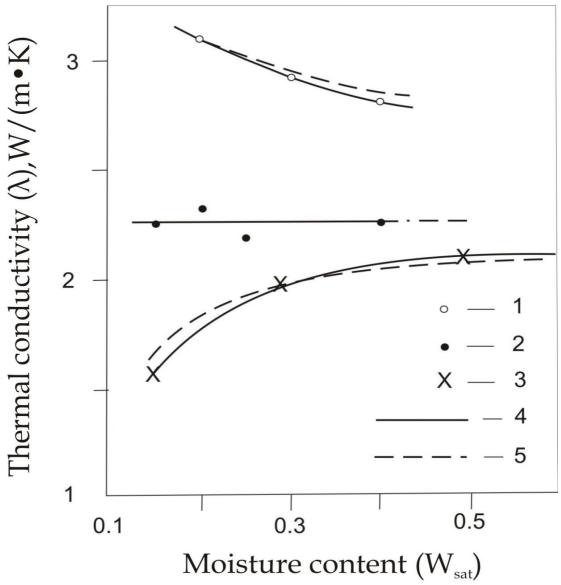

Fig. 7. Thermal conductivity vs. saturation moisture content for alluvial sediments in frozen state: 1 - sand; 2 – sand-silt; 3 – silt-clay; 4 - experimental curves; 5 – predicted curves

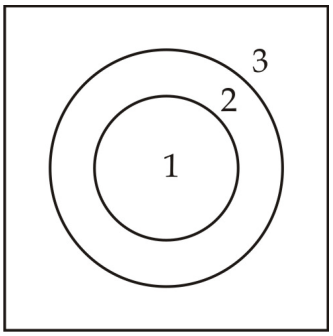

Fig. 8. Three-component shell medium: 1 – soil mineral particle; 2 – unfrozen water; 3 – ice

The effective conductivity λ of such a shell system can be predicted using the Maxwell method based on the solution of Laplace's equation for a medium with a constant temperature gradient at a distance from the spherical particle with a shell. The equation has the form (Belskaya, 1981)

$$\frac{\lambda-\lambda_i}{\lambda-2\lambda_i}=\frac{\sigma\left[\lambda_{uw}-\lambda_i-\dfrac{\varepsilon\left(\lambda_{uw}-\lambda_s\right)\left(2\lambda_{uw}+\lambda_i\right)}{2\lambda_{uw}+\lambda_s}\right]}{2\lambda_i+\lambda_{uw}+\dfrac{2\varepsilon\left(\lambda_{uw}-\lambda_s\right)\left(\lambda_i-\lambda_{uw}\right)}{2\lambda_{uw}+\lambda_s}}, \tag{32}$$

where $\varepsilon = \frac{4\pi R^3_s}{3} / \frac{4\pi R^3_{uw+s}}{3}$ is the volume fraction of the mineral soil solids in the two-component system consisting of mineral solids and unfrozen water; σ is the volume fraction of the mineral solids and unfrozen water in the soil; the subscripts "s", "i" and "uw" refer to the mineral solids, ice and unfrozen water, respectively.

Parameters ε and υ in Eq. (32) can be expressed in terms of the volume fractions of soil solids m_s and unfrozen water m_{uw}

$$\varepsilon = \frac{m_s}{m_s + m_{uw}} \text{ and } \sigma = m_s + m_{uw}$$

Considering the relation of m_s and m_{uw} to the saturation moisture content W_{sat} and unfrozen water content m_{uw}

$$m_s = \frac{\rho_s}{1 + W_{sat}\rho_s} \text{ and } m_{uw} = \frac{\rho_s W_{uw}}{1 + W_{sat}\rho_s},$$

(ρ_s is the solids density), we finally obtain the following expression for the thermal conductivity λ of a saturated frozen soil (Gavriliev, 1989):

$$\lambda = \lambda_i \frac{N + 2M}{N - M}, \tag{33}$$

where

$$N = (1 + W_{sat}\rho_s)\left[2\lambda_i + \lambda_{uw} + \frac{2}{1 + W_{uw}\rho_s} \cdot \frac{(\lambda_{uw} - \lambda_s)(\lambda_i - \lambda_{uw})}{2\lambda_{uw} + \lambda_s}\right], \tag{34}$$

$$M = (1 + W_{uw}\rho_s)(\lambda_{uw} - \lambda_i) - \frac{(\lambda_{uw} - \lambda_s)(2\lambda_{uw} + \lambda_i)}{2\lambda_{uw} + \lambda_s}. \tag{35}$$

In Eqs. (33) - (35), all limiting conditions are satisfied. At $W_{sat} \to \infty$, $\lambda = \lambda_i$. If $W_{sat}=0$ and $W_{uw}=0$, then $\lambda = \lambda_s$. When $W_{uw}=0$, the well-known Maxwell-Odolevsky equation for a two-component medium is obtained, which can be expressed in terms of moisture content as

$$\lambda = \lambda_i \frac{(1 + W_{sat}\rho_s)(2\lambda_i + \lambda_s) + 2(\lambda_s - \lambda_i)}{(1 + W_{sat}\rho_s)(2\lambda_i + \lambda_s) - (\lambda_s - \lambda_i)}. \tag{36}$$

Eq. (36) is also applicable to unfrozen soils, if the thermal conductivity of water λ_w is used instead of λ_i.

The presence of entrapped air reduces the thermal conductivity of frozen soils, and this can be expressed as:

$$\lambda = \frac{2\lambda(1 + W\rho_s)}{2 + \rho_s(3W_{sat} - W)}, \tag{37}$$

where W is the actual moisture content of the soil which should vary in the range

$$W \geq \left(1 - \frac{0.4}{\rho_{moi}}\right) W_{sat} - \frac{0.4}{\rho_s}, \tag{38}$$

where ρ_{moi} is the parameter dependent on the soil condition which has a value of 1 above 0°C and 0.92 below 0°C.

The relation (38) may be particularly useful for estimating the thermal conductivity of the thawed soils where any excess water escapes on thawing (if the thawing layer is not underlain by frozen soil) and only part of the moisture is retained due to surface tension.

For actual computations, the values for thermal conductivity of soil constituents should be specified in Eqs. (34) and (35). For pure ice at t = 0°C λ = 2.25 W/(m•K). The thermal conductivity of unfrozen water can be taken approximately equal to that of free, i.e., λ = 0.58 W/(m•K), since all anomalies in the properties of bound water are related to its strongly adsorbed portion which is insignificant in amount. The thermal conductivity of mineral soil solids depends on the mineral composition of particles and may be approximately estimated by Eq. (14).

The distribution of minerals in soils is influenced by sedimentary conditions which vary widely in nature. The amount of minerals in a soil can be estimated approximately based on the relationship between particle mineralogy and size distribution. The three particle sizes used for soil classification are clay (< 0.002 mm), silt (0.002-0.05 mm), and sand (0.05-2.0 mm). In practice, it is assumed that the content of clay minerals, such as kaolinite, is equal to the amount of clay-sized particles and 50% of silt-sized particles (Kokshenov, 1957). The remainder of the soil consists predominantly of quartz and feldspar, and their relative proportions vary widely depending on the soil origin. If no appropriate data are available, the ratio of quartz to feldspar may be taken as 0.6:0.4 (Kokshenov, 1957).

In computations, the following values for λ_j may be used [W/(m•K)]: 6-7 for quartz, 1.9 for feldspars, and 1.2 for kaolinite.

The distribution of particle sizes in a soil strongly depends on sedimentation conditions. If no granulometric data are available, the values given in Table 1 may be used for approximate estimations.

Soil type	Particle size		
	Clay	Silt	Sand
Sand	0.02	0.10	0.88
Sand-silt	0.06	0.30	0.64
Silt-clay	0.20	0.37	0.43

Table 1. Relative proportions of particles sizes in soils

Comparison of the predicted and experimental data (see Fig. 7) shows that Eqs. (33) - (35) provide satisfactory results. The following values were used in the computations: for λ_s [W/(m•K)]:3.50 for sand, 2.70 for sand-silt, 2.30 for silt-clay; for W_{uw}:0 for sand, 0.03 for sand-silt and 0.10 for silt-clay.

5. Effect of organic matter on soil thermal conductivity

The unconsolidated soil layer on the immediate surface of the earth is enriched with organic remains in the form of humus due to the effects of vegetation, animals (mainly

microorganisms), climate, and human activity. The presence of organic matter has a strong effect on the soil thermal properties.

Humic substances of the soil are specific high-molecular compounds. They play a significant role in creating the soil structure (Tsyganov, 1958). The organic substances exist in the form of very fine particles smaller than 0.2 μ referred to as colloids. Colloids have a very large specific surface area that provides strong bonding of water in soil and the presence of large amounts of unfrozen water at temperatures below freezing. Colloidal particles occur as sols and gels. Sols are smaller particles which can aggregate into gels by coagulation. When bound with water, organic particles form colloidal micelles having a core of an electrically neutral mineral particle surrounded by ionic layers of adsorbed molecules of colloid aggregate matter (hydrates: SiO2, Al2O3, MnO2, etc.) and electrolyte (water). At temperatures below 0°C, the diffuse layer of water freezes, while the bound water remains unfrozen.

At the present stage of research, the problem of organic content effect on the thermal conductivity of soils can only be approached using analytical methods, since there are virtually no experimental data available.

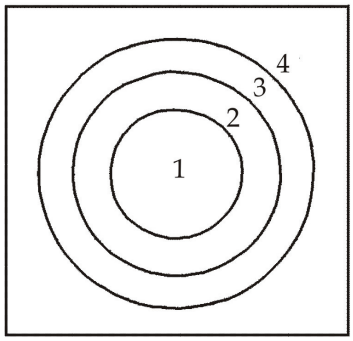

Fig. 9. Schematic representation of the saturated frozen organic soil: 1 – mineral particle; 2 – colloid aggregate; 3 – unfrozen water; 4 - ice

Let us consider the saturated soils. Based on the above consideration, the saturated soil containing organic matter can be represented as a four-component shell system within a cubic cell (Fig. 9) consisting of a mineral particle (1), organic matter (humus) (2), unfrozen water (3), and ice (4). The thermal conductivity of this system (frozen organic soil) calculated with the successive use of Maxwell's method is described by the equation (Gavrilyev, 2001)

$$\lambda_f = \lambda_4 \left[1 + \frac{3Z(1-m_i)}{3\lambda_i + Zm_i} \right], \tag{39}$$

where

$$Z = \lambda_{uw} \frac{2\lambda_{uw} m_{uw} D + \lambda_{org} Q\left[3(1-m_i) - 2m_{uw}\right]}{\lambda_{uw} D\left[3(1-m_i) - m_{uw}\right] + \lambda_{org} m_{uw} Q} - \lambda_i \ , \tag{40}$$

$$D = \lambda_s m_{org} + \lambda_{org}\left(3m_s + m_{org}\right) , \tag{41}$$

$$Q = 2\lambda_{org} m_{org} + \lambda_s \left(3 m_s + m_{org}\right), \tag{42}$$

λ and m are the thermal conductivity and volume fractions of the components, respectively. In the saturated unfrozen organic soil, the ice content m_i is zero, and from Eq. (39) we obtain the following equation for the thermal conductivity λ_t

$$\lambda_t = \lambda_{uw} \frac{2\lambda_{uw} m_{uw} D + \lambda_{org} Q\left(3 - 2 m_{uw}\right)}{\lambda_{uw} D\left(3 - m_{uw}\right) + \lambda_{org} m_{uw} Q} . \tag{43}$$

The volume fractions of the components of the organic soil in the saturated state, m_s, m_{org}, m_{uw} and m_i, can be found using the following equations:

$$m_s = \frac{1}{1 + W_{sat}^0 \rho_s} , \tag{44}$$

$$m_{org} = \frac{n_{org} \rho_s m_s}{\rho_{org}\left(1 - n_{org}\right)}, \tag{45}$$

$$m_{uw} = W_{uw} \gamma_d , \tag{46}$$

$$m_i = \left(W_{sat} - W_{uw}\right)\gamma_d , \tag{47}$$

$$\gamma_d = \rho_s m_s + \rho_{org} m_{org} , \tag{48}$$

$$m_s + m_{org} + m_{uw} + m_i = 1, \tag{49}$$

where $n_{org} = P_{org}/(P_s+P_{org})$ is the relative weight of organic matter; P_s and P_{org} are the weights of the soil mineral particles and organic matter in the dry state; ρ is the unit weight of the components; W_{sat}^0 is the saturation moisture content of the soil containing no organic matter (fraction).

The saturation moisture content of the organic soil W_{sat} is related to that of the soil containing no organics W_{sat}^0 by the relationship:

$$W_{sat} = W_{sat}^0\left(1 - n_{org}\right) - \frac{n_{org}\rho_{uw}}{\rho_{org}} . \tag{50}$$

For the saturated organic soil, the following relationship is valid:

$$\gamma_d = \frac{\rho_s'}{1 + W_{sat}\rho_s'} , \tag{51}$$

where $\rho_s' = \left(\rho_s m_s + \rho_{org} m_{org}\right) \Big/ \left(m_s + m_{org}\right)$ is the unit weight of the organic soil.

In computations of the thermal conductivity of organic soils using Eqs. (39) - (43), the following λ values (W/(m•K)) can be taken for components: λ_{org}=0.26 (Farouki 1986), λ_{uw}=0.58 and λ_i=2.25. The value of λ_s is a function of the soil type of the C horizon and can be estimated from the mineral composition of the particles by Eq. (14).

The λ_j values of minerals are available in reference books (Birch, 1942; Clark, 1966; Kobranova, 1962; Missenard, 1965; Smyslov et al., 1979). The unit weight of organic matter (ρ_{org}) by analogy with peat (Gavriliev & Eliseev, 1970) can be taken as $1.48 \cdot 10^3$ kg/m^3.
Fig. 10 shows the relationship between the thermal conductivity of a silt-clay [λ_s=2.50 W/(m•K)] and the saturation moisture content at different organic contents. It is seen that reduction in the soil thermal conductivity due to the presence of organic matter is strongest at low humus contents ($n_{org} < 0.1$).

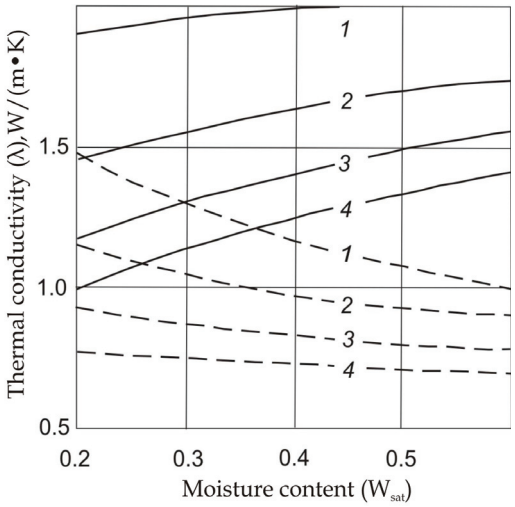

Fig. 10. Thermal conductivity of saturated silt-clay in frozen (solid lines) and thawed (dashed lines) states vs saturation moisture content W_{sat} at different organic contents n_{org} (unit fraction): 1 - 0; 2 – 0.1; 3 – 0.2; 4 – 0.3

We note in conclusion that Eq. (39) can lead to Eq. (33) for permafrost with no second component (m_{org}=0).

6. Summary

Frozen soils are complex multi-component and multi-phase systems consisting of mineral and organic particles, ice, unfrozen water, and gas (vapour). The specific conditions of sedimentation and subsequent diagenesis in permafrost environments result in sediments of permafrost-type with a very complex composition, structure and statistical particle distribution.
A deep understanding of the thermal properties of frozen soils can only be gained through an integral combination of experimental and analytical methods. Experimental methods have limitations in quantitative terms. Having obtained some basic information with experimental techniques, further in-depth study can be made using analytical methods. The development of theoretical approach is needed to understand heat transfer processes and to analyze experimental data on thermal properties of soils and rocks from a common point of view.

Considering the history of sediment formation over a geologic time, a universal model with changing particle shapes is proposed which describes the processes of rock formation from sediments, snow compaction and glacierization with account for diagenetic and post-diagenetic structural modifications, as well the processes of rock weathering and soil formation.

Based on the Maxwell's model with dispersed particles in the main medium, methods of estimating the thermal conductivity are given for:

1. Soils containing coarse inclusions and frozen soils of layered or reticulate cryostructure with account for variation in composition (a two-component system: coarse inclusions + fine fill, layers of frozen soil and ice for a case of layered cryostructure, and soil inclusions in the ice matrix for a case of reticulate cryostructure);
2. Permafrost with a massive cryostructure (a three-component spherical shell system: mineral particle + unfrozen water + ice);
3. Organic soils (a four-component spherical shell system: mineral particle + humus + unfrozen water + ice).

7. References

Belskaya, E., Postnikov, V., Vasiliev, L. & Khusid, B. (1981). Thermal Conductivity of Materials with Shell-Covered Dispersed Fillers (in Russian). *Vestsi AN BSSR Seryia fizika-matematicheskikh navuk,* No.1 (January-March 1981), pp. 91-95, ISSN 0374-4760

Birch, F., Schairer, J. & Spicer, H. (Eds.). (1942). *Handbook of Physical Constants,* Spec. Pap. 36, Geological Society of America, Boulder, Colorado, USA

Carslaw, H. & Jaeger, J. (1959). *Conduction of Heat in Solids* (2nd edition), Oxford University Press, ISBN 0-19-85-3303-9, Oxford, UK

Clark, S. (Ed.). (1966). *Handbook of Physical Constants* (rev. ed.), Geological Society of America, ISBN 0813710979, New York, USA

Everdingen, R. van (Ed.). (1998, revised January, 2002). *Multi-Language Glossary of Permafrost and Related Ground-Ice Terms*, National Snow and Ice Data Center/World Data Center for Glaciology, Boulder, Colorado, Available from http://nsidc.org/fgdc/glossary/

Farouki, O. (1986). *Thermal Properties of Soils,* Trans Tech Publications, ISBN 0-87849-055-8, Clausthal-Zellerfeld, Germany

Gavril'ev, R. I. (1989). Thermal Conductivity of Permafrost Soils in Relation to Natural Moisture Content. *Journal of Engineering Physics and Thermophysics,* Vol.56, No.6, (June, 1989), pp. 701-706, ISSN 1062-0125

Gavril'ev, R. I. (1992). Model for Calculating the Thermal Conductivity of Soils with Their Genesis Taken into Account. *Journal of Engineering Physics and Thermophysics,* Vol.62, No.1, (January, 1992), pp. 68-76, ISSN 1062-0125

Gavriliev, R. & Eliseev, S. (1970). Thermal Properties of Moss and Peat (in Russian), In: *Methods for Determining the Thermal Properties of Soils and Rocks,* N. Ivanov, (Ed.), 139-153, Nauka, Moscow, USSR

Gavriliev, R. (1986). Investigating the Thermal Properties of Soils with Coarse Inclusions (in Russian). *Inzhenernaya Geologiya,* No. 5 (September-October, 1986), pp. 60-71, ISSN 0208-0292

Gavriliev, R. (1996). A Model for Estimating the Thermal Conductivity of Sediments (in Russian), *Proceedings of 1st Conference of Russian Geocryologists,* Book 2, Part 1,

Physics, Chemistry and Mechanics of Frozen Ground, pp. 101-111, Moscow, Russia, June 3-5, 1996

Gavriliev, R. (1998). *Thermal Properties of Soils and Surface Covers in Permafrost Regions* (in Russian), Izdatelstvo SO RAN, ISBN 5-7692-0153-3, Novosibirsk, Russia

Gavriliev, R. (2003). Quantitative Estimation of the Thermal Conductivity of Saturated Frozen Soils. Permafrost. *Proceedings of the Eighth International Conference on Permafrost,* Vol. 1, pp. 283-287, ISBN 90 5809 584 3, Zurich, Switzerland, July 21-25, 2003

Gavriliev, R. (2004). *A Guide on Thermophysical Properties of Environmental Components in the Permafrost Zone* (in Russian), Izdatelstvo SO RAN, ISBN 5-7692-0551-2, Novosibirsk, Russia

Gavriliev, R. I. (2003). On Estimation of the Effect of Cryostructure on the Thermophysical Properties of Frozen Soils (in Russian). *Kriosfera Zemli,* Vol. 7, No.2, (April-June, 2003), pp. 42-47, ISSN 1560-7496

Gavrilyev, R. (1996a). A Mathematical Model for Calculating Thermal Conductivity of Snow Subject to Metamorphism, *Proceedings of 5th International Symposium on Thermal Engineering and Sciences for Cold Regions,* pp. 516-521, Ottawa, Canada, May 19-22, 1996

Gavrilyev, R. (1996b). Calculation of Thermophysical Properties of Large-fragmented Rocks at the Non-uniform Composition of Gruss-crushed Stone and Gravel-pebble Inclusions. *Proceedings of International Symposium on Cold Regions Engineering,* pp. 186-189, Harbin, China, September 11-14, 1996

Gavrilyev, R. (2001). Experimental Study on Thermal Properties of Soils of Central Yakutia, *Proceedings of 7th International Symposium on Thermal Engineering and Sciences for Cold Regions,* pp. 139-143, ISBN 89-952282-5-3, Seoul, Korea, July 12-14, 2001

Ivanov, N. & Gavriliev, R. (1965). *Thermal Properties of Frozen Soils* (in Russian), Nauka, Moscow, USSR

Ivanov, N. (1962). *Heat Exchange in Permafrost* (in Russian), Nauka, Moscow, USSR

Kobranova, V. (1962). *Physical Properties of Rocks* (in Russian), Gostopttekhizdat, Moscow, USSR

Kokshenov, B. (1957). *Determining the Thermal Conductivity of Rocks* (in Russian), Ugletekhizdat, Moscow, USSR

Maxwell, J. C. (1873). *Treatise on Electricity and Magnetism,* Oxford

Missenard, A. (1965). *Conductivite Thermique des Solides, Liquides, Gaz et de Leurs Melanges,* Editions Eyrolles, Paris, France

Nersesova, Z. (1953). Calorimetric Method for Determining the Ice Content of Soils (in Russian), In: *Laboratory Investigations of Frozen Soils,* N.A. Tsytovich, (Ed.), 77-85, Izd-vo AN SSSR, Moscow, USSR

Odelevsky, V.I. (1951). Prediction of Generalized Conductance of Heterogeneous Systems (in Russian). *Zhurnal Tekhnicheskoi Fiziki,* Vol.21, No.6 (June, 1951), pp. 667-685, ISSN 0044-4642

Ovchinnikov, I. (1971). *The Theory of Field* (in Russian), Nedra, Moscow, USSR

Pavlov, A.V. (1962). Thermophysical Properties and Thermal Balance of Snow Cover in the Moscow Area (in Russian), In: *Materials for the Study of Frozen Zones in the Earth Crust,* G.V. Porkhaev, V.K. Shchelokov & S.G. Tsvetkova (Eds.), 3-35, Izd-vo AN SSSR, Moscow, USSR

Sergeev, E., Golodkovskaya, G., Osipov, V. & Trofimov, V. (1971). *Soil and Rock Engineering* (in Russian), Izdatelstvo MGU, Moscow, USSR

Smyslov, A., Moiseenko, U. & Chadovich, T. (1979). *Thermal Regime and Radioactivity of the Earth* (in Russian), Nedra, Leningrad, USSR

Sulakvelidze, G.K. & Okudzhava, A.M. (1959). Snow and Its Properties (in Russian), *Transactions of the Elbrus Alpine Expedition,* Vol.1, No.4 (October-December, 1959), pp. 9-49

Tsyganov, M. (1958). *Soil Science* (in Russian). Selkhozgiz, Moscow, USSR

Tsytovich, N. (1945). On the Theory of the Equilibrium State of Water in Frozen Soils (in Russian). *Izvestia AN SSSR,* Seria Geograficheskaya i Geofizicheskaya, Vol. 9, No. 5-6 (November-December, 1945), pp. 493-502

Vargaftik, N. (Ed.). (1963). *Handbook of Thermophysical Properties of Gases and Fluids* (in Russian), Fizmatgiz, Moscow, USSR

Votyakov, I. (1975). *Physical and Mechanical Properties of Frozen and Thawing Soils in Yakutia* (in Russian), Nauka, Novosibirsk, USSR

12

Heating in Biothermal Systems

Huang, Huang-Wen[1] and Liauh, Chihng-Tsung[2]
[1]*Department of Innovative Information and Technology, Tamkang University*
[2]*Department of Mechanical Engineering, Kun-Shan University*
Taiwan

1. Introduction

Heat therapy is a traditional healing method. The first written reference to hyperthermia occurred in an Egyptian papyrus scroll 5000 years ago (Hall & Cox, 2003). In this chapter, we planned to introduce promising medical treatments which applied thermal energy in living tissues to raise tissue temperatures to therapeutic temperatures. The treatments, based on duration of time, were classified into low-temperature level in the range of 41~45°C (hyperthermia or thermal therapy) and much higher temperatures (thermal ablation treatments) than previous one.

Heating in the biothermal systems involves two primary heat transport modes: thermal conduction and convection. Extreme complicating living vasculatures and organs make heating the target volume and raising temperature to therapeutic temperature at the target volume difficult and, thus, a challenging task.

In this chapter, we will introduce thermal models which were used to describe biothermal systems. One of well-known models, Pennes bio-heat transfer equation (PBHTE) was initially introduced in 1949. Up until now, it still is used widely by research groups around the globe, to deal with temperature or heat that associated with human or living creatures. As well as other models which also described the impact of thermally significant blood vessel (or vascular system) and blood perfusion during treatments will also be introduced in this chapter.

The heating methods that deposited the thermal energy in transport medium (i.e. solid tumor, tissues and liquid so forth) will also be addressed. For example, high-intensity focused ultrasound (HIFU) is one of popular non-invasive method which could deposit heat into deep seated tissue region.

Lastly, we addressed promising future in combining other treating modalities (such as drug treatment) with hyperthermia. It has shown significant results for medical treatments in curing patients with cancers.

2. Heat transport

Thermal transport modes in bio-thermal systems involve three typical modes: conduction, convection and radiation. Limitation and restrictions of therapeutic temperatures on heating (or freezing) subjects are first, to remove tumorous tissues and at the same time without damaging the normal tissues. Table 1 shows significance of thermal transport modes in

typical components of bio-thermal systems, as our subject of discussion refers to cancer treatments using heat. Thermal diffusion plays a dominant transport mode in tissues, and convection is less significant as blood perfuses in solid tissues at capillary level vessels which are small in size and blood within are in slow motion.

	Conduction	Convection	Radiation
Tissues	Significant	Less Significant	Insignificant
Bones	Significant	Insignificant	Insignificant
Blood vessels	Less Significant	Significant	Insignificant
Skins	Insignificant	Significant	Significant

Table 1. Significance of thermal transport modes in typical components of vio-thermal systems

3. Mathematical modelings

To accurately describe physical phenomena in living tissues, we have to rely upon mathematical models (or bio-heat transfer formulation). There are many significant models appeared in history during the development of heating in tissues. Those models help us in analyzing temperature management in treatment planning with accuracy. We introduced them here:

3.1 Pennes bio-heat transfer equation (PBHTE)

In 1948, Pennes (Pennes, 1948) performed a series of experiments which measured temperatures on human forearms of volunteers, and derived a thermal energy conservation equation: the well known bio-heat transfer equation (BHTE) or the traditional bio-heat transfer equation. It is written as

$$\nabla \bullet k \nabla T + q_p + q_m - W c_b (T - T_a) = \rho c_p \frac{\partial T}{\partial t} \tag{1}$$

where T(°>°C) is the local tissue temperature; T_a (°C) is the arterial temperature; c_b (J/kg/°C) is the blood specific heat; c_p (J/kg/°C) is the tissue specific heat; W(kg/m^3/s) is the local tissue blood perfusion rate; k(w/m/°C) is the tissue thermal conductivity; ρ(kg/m^3) is the tissue density; q_p(w/m^3) is the energy deposition rate; and q_m (w/m^3) is the metabolism, which is usually very small compared to the external power deposition term q_p (Roemer et al, 1988). The term $Wc_b(T-T_a)$, which accounts for the effects of blood perfusion, can be the dominant form of energy removal when considering heating process. It assumes that the blood enters the control volume at some arterial temperature T_a, and then comes to equilibrium at the tissue temperature. Thus, the blood leaves the control volume it carries away the energy, and hence acts as an energy sink in hyperthermia treatment.

Although Pennes' equation is an approximation equation and it does not have a physically consistent theoretical basis, it is surprisingly that this simple mathematical formulation predicted temperature fields well in many application situations. The reasons why PBHTE has been widely used in hyperthermia modeling field are two important factors: one is its mathematical simplicity and the other is its ability to predict the temperature field reasonably in applied fields.

Nevertheless, the equation does have some limitations. It does not, nor was it ever intended to, handle several physical effects. The most significant problem is that it does not consider the effect of the directionality of blood flow, and hence does not describe any convective heat transfer mechanism.

3.2 The Chen and Holmes (CH) model

Several investigators have developed alternative formulations to predict temperatures in living tissues. In 1980, Chen and Holmes (Chen and Holmes, 1980) derived the one and it has a very strong physical and physiological basis. The equation can be written as,

$$\nabla\bullet(k+k_p)\nabla T + q_p + q_m - Wc_b(T-T_a) - \rho_b c_b u\bullet\nabla T = \rho c_p \frac{\partial T}{\partial t} \tag{2}$$

Comparing this equation with Pennes' equation, two extra terms have been added. The term $-\rho_b c_b u\bullet\nabla T$ is the convective heat transfer term, which accounts for the thermal interactions between blood vessels and tissues. The term $\nabla\bullet k_p\nabla T$ accounts for the enhanced tissue conductive heat transfer due to blood perfusion term in tissues, where k_p is called the perfusion conductivity, and is a function of blood perfusion rate. The blood perfusion term $-Wc_b(T-T_a)$ shown in CH model, accounts for the effects of the large number of capillary structures whose individual dimensions are small relative to the macroscopic phenomenon under their study. Relatively CH model has a more solid physical basis than Pennes model. However, it requires knowledge of the details of the vascular anatomy and flow pattern to solve it, and that was an extreme complicating task.

3.3 The Weinbaum and Jiji (WJ) model

In 1985, Weinbaum and Jiji (Weinbaum and Jiji, 1985) proposed an alternative mathematical formulation of the bio-heat transfer equation. Their formulation is based on their observations from vascular network of rabbit thighs that blood vessels which are significant for heat transfer in tissues always occur in counter-current pairs. Hence, the major heat transfer mechanism between blood and tissues is the "incomplete counter-current heat exchanger" between thermally significant arteries and veins (with diameters about 50-500μm). Their formulation uses tensor notation and it can be written as

$$\rho c\frac{\partial\theta}{\partial t} - \frac{\partial}{\partial x_i}\left[(k_{ij})_{eff}\frac{\partial\theta}{\partial x_j}\right] = -\frac{\pi^2 n a^2 k_b^2}{4\sigma k} Pe^2 l_j \frac{\partial l_i}{\partial k_j}\frac{\partial\theta}{\partial x_j} + Q_m \tag{3}$$

where θ is the local temperature, ρc is the volume average tissue density and specific heat product, a is the local blood vessel radius, σ is a shape factor for the thermal conduction resistance between adjacent counter-current vessels, n is the number density of blood vessels of size a, k_b is the blood thermal conductivity, Pe is the local Peclet number (=2 ρ_b cnau/k_b), us is average blood flow velocity in the vessels and l_i is the direction cosine of the ith pair of countercurrent vessels. $(k_{ij})_{eff}$ is the effective conductivity tenor element, which is given by,

$$(k_{ij})_{eff} = k(\delta_{ij} + \frac{\pi^2 n a^2 k_b^2}{4\sigma k^2} Pe^2 l_i l_j) \tag{4}$$

where δ_{ij} is the kronecker delta function, and k is the tissue thermal conductivity. Clearly, this equation represents one of the most significant contributions to the bio-heat transfer formulation. But, in practical situations, this equation needs detailed knowledge of the sizes, orientations, and blood flow velocities in the countercurrent vessels to solve it and that presents a formidable task. Furthermore, there are several issues related to the WJ model. First, thoroughly comparison for both predicted temperatures and macroscopic experiments are required. Secondly, the formulation was developed for superficial normal tissues in which the counter-current heat transfer occurs. In tumors, the vascular anatomy is different from the superficial normal tissues, and therefore a new model should be derived for tumors. Some (Wissler, 1987) has questioned the two basic assumptions of WJ model: first, that the arithmetic mean of the arteriole and venule blood temperature can be approximated by the mean tissue temperature; and second, that there is negligible heat transfer between the thermally significant arteriole-venule pairs and surrounding tissue.

3.4 Thermally significant blood vessel model

As CH and WJ models presented, many investigators (Baish et al, 1986; Charny and Levin, 1990) during late 1980, questioned mostly on blood perfusion term or how to estimate blood temperature and local tissue temperatures where blood vessels (counter-current vessels) are involved. As arterial and veinous capillary vessels are small, their thermal contributions to local tissue temperatures are insignificant. However, some larger vessel sizes than the capillaries do have thermally significant impacts on tissue temperatures in either cooling or heating processes. Several investigators (Chato, 1980; Lagendijk, 1982; Huang et al, 1994) examined the effect of large blood vessels on temperature distribution using theoretical studies. Huang et al (Huang et al, 1996) in 1996 presented a more fundamental approach to model temperatures in tissues than do the generally used approximate equations such as the Pennes' BHTE or effective thermal conductivity equations. As such, this type of model can be used to study many important questions at a more basic level. For example, in the particular hyperthermia application studied herein, a simple vessel network model predicts that the role of counter current veins is minimal and that their presence does not significantly affect the tissue temperature profiles: the arteries, however, removed a significant fraction of the power deposited in the tissue. The Huang's model used a simple convective energy balance equation to calculate the blood temperature as a function of position,

$$\dot{M}_i c_b \frac{dT_b}{dx_i} = \dot{Q}_{ap} - h_i A_i (T_b - T_w) \tag{5}$$

Here, $\dot{M}_i$ is the mass flow rate of blood in artery i, c_b is the specific heat of blood, $T_b(x_i)$ is the average blood temperature at position x_i, x_i indicates the direction along the vessel I (either x, y or z depending on the vessel level). $\dot{Q}_{ap}$ is the applied power deposition x_i, h_i is the heat transfer coefficient between the blood and the tissue, A_i is the perimeter of blood vessel i, and $T_w(x_i)$ is the temperature of the tissue at the vessel wall. For the smallest, terminal arterial vessels a decreasing blood flow rate is present giving the energy balance equation,

$$\dot{M}_i c_b \frac{dT_b}{dx_i} = \dot{Q}_{ap} - h_i A_i (T_b - T_w) - \frac{d\dot{M}_i}{dx_i} c_b T_b \tag{6}$$

The blood leaving these terminal arterial vessels at any cross-section is assumed to perfuse the tissue at a constant rate. The detailed description is shown in Huang (Huang et al, 1996). As to venous thermal model, for all of veins except the smallest terminal veins, the above equation (5) holds. For the smallest veins, the T_b replaced by the venous return temperature, $T_{vr}(x_i)$. In the presented study this temperature is taken to be average temperature of four tissue nodes adjacent to the terminal vein in the plane perpendicular to that vein,

$$T_{vr} = \frac{1}{4}\sum_{i=1}^{4} T_{i,adj} \tag{7}$$

For tissue matrix thermal equations, they can be explained most succinctly by considering the Pennes Bio-Heat Transfer Equation as the most general formulation,

$$-k\nabla^2 T + \dot{W}c_b(T - T_a) = \dot{Q}_{ap} \tag{8}$$

Here, k is the thermal conductivity of the tissue matrix, T(x,y,z) is the tissue temperature, $\dot{W}$ is the "perfusion" value and T_a is the arterial blood temperature at some reference location.

3.5 Others

A few studies (Leeuwen et al, 2000; Devashish and Roemer, 2006; Baish, 1994) have modeled the effect of collections of a large number of parallel vessels or of networks of vessels on the resulting temperature distributions. Those were developed in attempt to describe the impact of blood vessels and to properly predict heat transfer processes in bio-thermal systems in a more accurate way.

4. Numerical modelings

As mentioned above the mathematical models for actual thermal problems of interest in hyperthermia or thermal ablation are too complicated to be conveniently solved with exact formulas. The majority of unsolved problems in medical fields is governed by non-linear partial differential equations. In most cases, one thereby reduces the problems to rather simplified models which can be exactly analyzed, for example, analytical solution of the 3D Pennes equation presented by Liu (Liu, 2001; Liu and Deng, 2002) using multidimensional Green function, and 1D transient Pennes equation by Shih et. al. (Shih et al, 2007) using the Laplace transform. But occasionally such an approach does not suffice. Consequently, specialists have recently devoted increasing attention to numerical, as opposed to analytical, techniques. Nowadays one of the major challenges for thermal ablation and hyperthermia simulation is the incorporation of the very detailed information coming from biophysical models into the numerical simulations. Thanks to advanced imaging techniques, accurate tumor static models including detailed description of all vascular matrix objects are currently available. Unfortunately, most of the discretization methods commonly used in computer simulation, mainly based on structured grids, are not capable to represent the detailed geometry of such treatment regions or other complicated entities such as microvascular matrix, horizontal wells, and uniformity, etc. The complexity of multidimensional heat transfer problems in hyperthermia suggests the application of numerical techniques. Several numerical methods have been used in engineering and

science fields; finite difference method, finite element method, finite volume approach, etc. (Morton and Mayers, 2005; Derziger, Peric, 2001; Thomas, 1995; Minkowycz et al, 1988; Anderson et al, 1984).

4.1 Finite difference method

Several mathematical models were discussed above to describe the continuum models of heat transfer in living biological tissue, with blood flow and metabolism. The general form of these equations is given by:

$$\rho c \frac{DT}{Dt} = \rho c \left(\frac{\partial T}{\partial t} + V \bullet \nabla T \right) = \nabla \bullet k \nabla T - w_b c_b (T - T_a) + Q \tag{9}$$

The partial differential equations for thermal ablation or hyperthermia are discretized at the grid point by using the finite difference approximation using Pennes equation.

$$\rho c \frac{\partial T}{\partial t} = k \nabla^2 T - w_b c_b (T - T_a) + Q \tag{10}$$

The Pennes equation is solved with the finite difference formulation when the exact geometry is not particularly important or when the fundamental behavior of a bio-thermal system is analyzed, in particular with heterogeneous and at times anisotropic thermal properties. Define an *Nx* x *Ny* x *Nz* lattice in the (x, y, z) plane that spans our region of interest in 3D with dimension of L*x* x L*y* x L*z* as shown in Figure 2. Let *Nx*, *Ny* and *Nz* be the numbers of equally spaced grid points in the *x*-, *y*-, and *z*-directions, respectively, and $\{x_{ijk} := (i\Delta x, j\Delta y, k\Delta z)\}$ the grid points in the computational domain, where Δx = L*x*/*Nx*, Δy = L*y*/*Ny*, and Δz = L*z*/*Nz*.

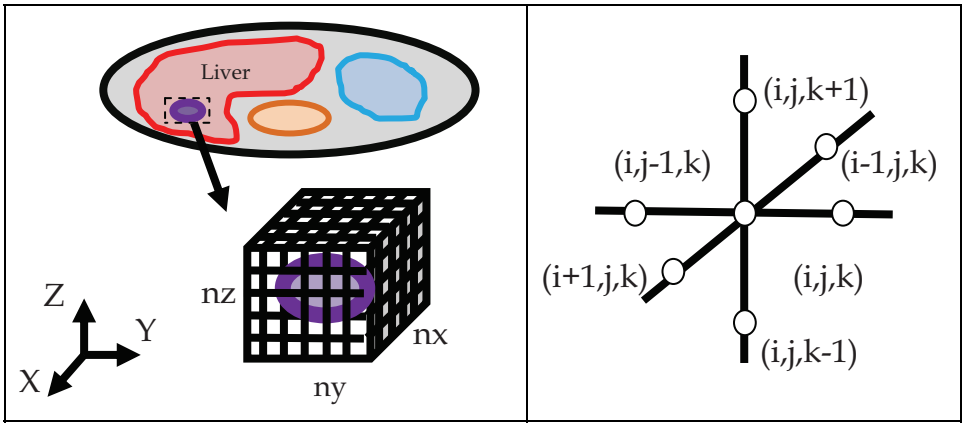

Fig. 1. Schematic representation of the grid system using a finite difference scheme

In a typical numerical treatment, the dependent variables are described by their values at discrete points (a lattice) of the independent variables (e.g. space and/or time), and the partial differential equation is reduced to a large set of difference equations. It would be useful to revise our description of difference equations. Let Γ be the elliptic operator and Π a finite difference approximation of Γ with *p*th order accuracy, i.e.,

$$\Gamma T = k\nabla^2 T - w_b c_b T \tag{11}$$

$$\Pi T \approx \Gamma T + O(h^p)$$

where $h = \max\{\Delta x, \Delta y, \Delta z\}$. Then the semi-discrete equation corresponding to Equation (11) reads $\rho c \frac{\partial T}{\partial t} = \Pi T + Q + w_b c_b T_a$. To integrate in time, one can use the two-level implicit time-stepping scheme:

$$\rho c \frac{T^{n+1} - T^n}{\Delta t} = \Pi\left(\frac{1}{2}T^{n+1} + \frac{1}{2}T^n\right) + Q^n + w_b c_b T_a \tag{12}$$

where Δt is the time step size and T^n is the discrete solution vector at time $t^n = n\Delta t$. This numerical scheme is known as the Crank–Nicolson scheme (Crank and Nicolson, 1947). It yields a truncation error at the nth time-level: $Error = O\left(\Delta t^2 + h^p\right)$. In the matrix form we can represent (2) as:

$$\left(I - \frac{\Delta t}{2\rho c}\Pi\right)T^{n+1} = \left(I + \frac{\Delta t}{2\rho c}\Pi\right)T^n + \frac{\Delta t}{\rho c}(Q^n + w_b c_b T_a) \tag{13}$$

That is at time t^{n+1} the discrete solution is given by:

$$T^{n+1} = \left(I - \frac{\Delta t}{2\rho c}\Pi\right)^{-1}\left[\left(I + \frac{\Delta t}{2\rho c}\Pi\right)T^n + \frac{\Delta t}{\rho c}(Q^n + w_b c_b T_a)\right] \tag{14}$$

Obviously other standard techniques for numerical discretization in time have also been used. For instance the unconditionally stable Alternating Direction Implicit (ADI) finite difference method (Peaceman and Rachford, 1955) was successfully used in the solution of the bio-heat equation in (Qi and Wissler, 1992; Yuan et al, 1995).

4.2 Finite element method

When an analysis is performed in complex geometries, the finite element method (Dennis et al, 2003; Hinton and Owen, 1974) usually handles those geometries better than finite difference. In the finite element method the domain where the solution is sought is divided into a finite number of mesh elements. (for example, a pyramid mesh, as shown in Figure 3). Applying the method of weighted residual to Pennes equation with a weight function, ω, over a single element, Λ_e results in:

$$\oint_{\Lambda_e} \omega\left[\rho c \frac{\partial T}{\partial t} - \nabla \bullet k\nabla T + w_b c_b (T - T_a) - Q\right] d\Lambda_e = 0 \tag{15}$$

A large but finite number of known functions are proposed as the representation of the temperature. The (shape) functions are constructed from simple interpolation functions within each element into which the domain is divided. The value of the function everywhere inside the element is determined by values at the nodes of that element. The temperature can be expressed by,

$$T^{(e)}(x,y,z,t)=\sum_{i=1}^{Nr}N_i(x,y,z)T_i(t) \tag{16}$$

Or in a matrix form, $T^{(e)}(x,y,z,t)=\left[N(x,y,z)\right]\{T(t)\}$

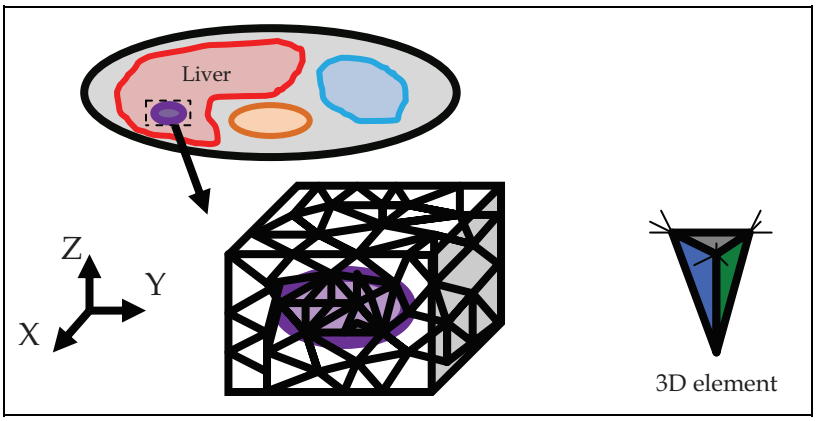

Fig. 2. Schematic representation of the mesh element system using a finite element scheme

In Eq. (16), i , is an element local node number, Nr is the total number of element nodes and N(x,y,z) is the shape function associated with node *i*. Applying integration by parts into Eq. (15) one can obtain

$$\oint_{\Lambda_e}\omega\left[\rho c\frac{\partial T}{\partial t}+w_b c_b(T-T_a)-Q\right]d\Lambda_e+\int_{\Lambda_e}\omega k\nabla T\bullet\nabla N_i d\Lambda_e-\int_{\Gamma_e}\omega(k\nabla T\bullet\hat{n})N_i d\Gamma_e=0 \tag{17}$$

Here, Γ_e is the surface element. Using the Galerkin method, the weight function, ω, is chosen to be the same as the interpolation function for T. Evaluation of each element and then assembling into the global system of linear equations for each node in the domain yields

$$[M]\left\{\dot{T}\right\}+[K]\{T\}+[W]\{T\}=\{R\}+\{P\},$$

$$\text{or } [M]\left\{\dot{T}\right\}+[A]\{T\}=\{B\}$$

where

$$M_{ij}=\int_{\Lambda_e}\omega\rho cN_iN_j d\Lambda_e,\ K_{ij}=\int_{\Lambda_e}\omega k(\nabla N_i\bullet\nabla N_j)d\Lambda_e,\ W_{ij}=\int_{\Lambda_e}\omega W_b c_b N_iN_j d\Lambda_e,$$

$$P_i=\int_{\Gamma_e}\omega k(\nabla\sum_{j=1}^{Nr}T_jN_j\bullet\hat{n})N_i d\Gamma_e,\ R_i=\int_{\Lambda_e}\omega Q_iN_i d\Lambda_e,\ A_{ij}=K_{ij}+W_{ij},\ B_i=R_i+P_i$$

This set of equations cane be solved with any kind on numerical integration in time to obtain the approximate temperature distribution in the domain. For instance one can use the Crank-Nicolson algorithm,

$$\left(\frac{1}{2}[A]+\frac{1}{\Delta t}[M]\right)\{T^{n+1}\}=\left(\frac{1}{2}[A]+\frac{1}{\Delta t}[M]\right)\{T^{n}\}+\frac{1}{2}\left(\{B^{n+1}\}+\{B^{n}\}\right) \tag{18}$$

where the superscript n+1 denotes the current time step and the superscript n, the previous time step.

4.3 Finite volume method

Finite volume methods are based on an integral form instead of a differential equation and the domains of interest are broken into a number of volumes, or grid cells, rather than pointwise approximations at grid points. Some of the important features of the finite volume method are thus similar to those of the finite element method (Oden, 1991). The basic idea of using finite volume method is to eliminate the divergence terms by applying the Gaussian divergence theorem. As a result an integral formulation of the fluxes over the boundary of the control volume is then obtained. Furthermore they allow for arbitrary geometries, using structured or unstructured meshing cells. An additional feature is that the numerical flux is conserved from one discretization cell to its neighbor. This characteristic makes the finite volume method quite attractive when modeling problems for which the flux is of importance, such as in fluid dynamics, heat transfer, acoustics and electromagnetic simulations, etc.

Since finite volume methods are especially designed for equations incorporating divergence terms, they are a good choice for the numerical treatment of the bio-heat-transfer-equation.

The computational domain is discretized into an assembly of grid cells as shown in Figure 4.

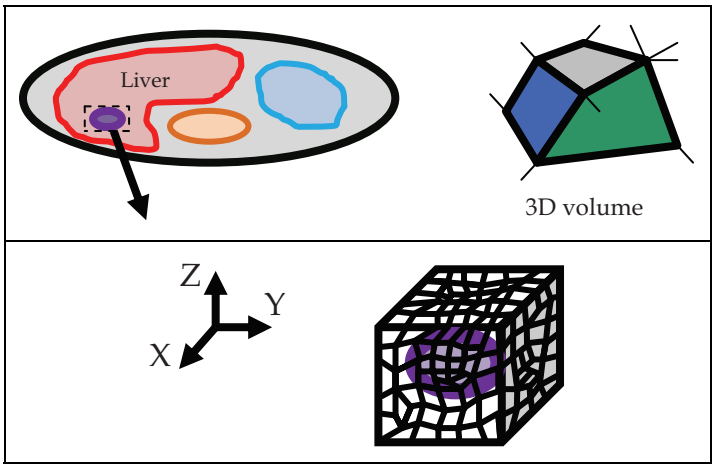

Fig. 3. Schematic representation of the grid cell system using a finite volume scheme

Then the governing equation is applied over each control volume in the mesh. So the volume integrals of Pennes equation can be evaluated over the control volume surrounding node *i* as

$$\oint_{\Omega i}\left[\rho c\frac{\partial T}{\partial t}-\nabla\bullet k\nabla T+w_b c_b(T-T_a)-Q\right]d\Omega=0 \tag{19}$$

By the use of the divergent theorem,

$$\oint_{\Omega i}\left[-\nabla \bullet k\nabla T\right]d\Omega = -\int_{\Gamma_i}\left(k\nabla T \bullet \hat{n}\right)d\Gamma = \int_{\Gamma_i} q_j n_j d\Gamma \tag{20}$$

where the heat flux $q = -k\nabla T$ and

$$\oint_{\Omega i}\left[\rho c\frac{\partial T}{\partial t}\right]d\Omega \cong \rho c\frac{\partial T_i}{\partial t}\bigcap_i,\ \oint_{\Omega i} w_b c_b T d\Omega \cong w_b c_b T_i \bigcap_i,\ \oint_{\Omega i}\left[Q + w_b c_b T_a\right]d\Omega \cong \left(Q_i + w_b c_b T_a\right)\bigcap_i$$

where $\bigcap_i$ is the volume of the control volume, T_i and Q_i represent the numerical calculated temperature and source term at node *i*, respectively. The boundary integral presented in equation (a) is computed over the boundary of the control volume, Ω_i, that surrounds node *i* using an edge-based representation of the mesh, i.e.

$$\int_{\Gamma_i} q_j n_j d\Gamma \cong \sum_{all\ \ edges} G_{ij} q_j + \sum_{all\ \ edges} H_{ij} q_j \tag{21}$$

where G_{ij} denotes the coefficients that must be applied to the edge value of the flux q_j in the x_j direction to obtain the contribution made by the edge to node *i* and H_{ij} represents the boundary edges coefficients that relate to the boundary edge flux q_j when the edge lies on the boundary, where H_{ij}=0 on all edges except on the domain boundaries. The approximation of q_j on edge is evaluated by different schemes based on the temperatures between nodes. For example,

$$q_j = \frac{T_j - T_i}{d_{ij}}$$

where d_{ij} is the distance between the center of the cells *i* and *j*.
The semi-discrete form of the transient bioheat heat transfer equation represents a coupled system of first order differential equations, which can be rewritten in a compact matrix notation as

$$P\frac{\partial T}{\partial t} + RT = S \tag{22}$$

with an initial condition. In equation (22), *P* represents the heat capacity matrix which is a diagonal matrix. *R* is the conductivity matrix including the contributions from the surface integral and perfusion terms. The vector *S* is formed by the independent terms, which arises from the thermal loads and boundary conditions. *T* is the vector of the nodal unknowns. Equation (22) can be further discretized in time to produce a system of algebraic equations. With the objective of validating the finite volume formulation described, one can use the simplest two-level explicit time step and rewrite equation (22) as the following expression

$$P\frac{T^{n+1} - T^n}{\Delta t} + RT^n = S^n \tag{23}$$

where $\Delta t = t_{n+1} - t_n$ is the length of the time interval and the superscripts represent the time levels. Such scheme is just first order accurate in time and the Δt must be chosen according to a stability condition (Lyra, 1994). Other alternatives, such as the generalized trapezoidal

method (Lyra, 1994; Zienkiewicz & Morgan, 1983), multi-stage Runge-Kutta scheme (Lyra, 1994) can be implemented if higher-order time accuracy is required.

4.4 Others

Other classes of methods have also been applied to the partial differential equations, such as boundary element method (Wrobel and Aliabadi, 2002), spectral method (Canuto et al, 2006), multigrid method (Briggs et al, 2000) ect.

5. Heating methods

Heating in bio-thermal systems that have many forms, they can be appeared in different power deposition calculations in PBHTE. They can be classified into three types which are invasive, minimal invasive and non-invasive methods. We introduced most clinical methods here.

5.1 Hyperthermia

Hyperthermia is a heat treatment, and traditionally refers to raise tissue temperatures to therapeutic temperatures in the range of 41~45°C (significantly higher than the usual body-temperature) by external means. In history, the first known, more than 5000 years old, written medical report from the ancient Egypt mentions hyperthermia (Smith, 2002). Also, an ancient tradition in China, "Palm Healing", has used the healing properties of far infrared rays for 3000 years. As our bodies radiate far infrared energy through the skin at 3 to 50 microns, with a peak around 9.4 microns, these natural healers emit energy and heat radiating from their hands to heal. It could be applied in several various treatments: cure of common cold (Tyrrell et al, 1989), help in the rheumatic diseases (Robinson et al, 2002; Brosseau et al, 2003) or application in cosmetics (Narins & Narins, 2003) and for numerous other indicators.

5.2 Thermal ablation

The differentiation between thermal ablation and hyperthermia relates to the treatment temperature and times. Thermal ablation usually refers to heat treatments delivered at temperatures above 55°C for short periods of time (i.e. few seconds to 1 min.). Hyperthermia usually refers to treatments delivered at temperatures around 41-45°C for 30~60 minutes. The goal of thermal ablation is to destroy entire tumors, killing the malignant cells using heat with only minimal damage to surrounding normal tissues. The principle of operation of the thermal ablation techniques is that to produces a concentrated thermal energy (heating or freezing), creating a hyperthermic/hypothermic injury, for example, by a needle-like applicator placed directly into the tumor or using focused ultrasound beams. Thermal ablation comprises several distinct techniques as shown in Figure 1: radiofrequency (RF) ablation, microwave ablation, laser ablation, cryoablation, and high-intensity focused ultrasound ablation. To have a good treatment, it is also crucial to destroy a thin layer of tissue surrounding the tumor because of the uncertainty of tumor margin and the possibility of microscopic disease (Dodd et al, 2000).

When it is not applicable for patients to surgery, one of alternative therapies for malignant tumors is thermal ablation. It is a technique that provides clinicians and patients a repeatable, effective, low cost, and safe treatment to effectively alleviate, and in some cases cure, both primary and metastatic malignancies. However, the common procedures for each thermal ablation technique are not yet clearly defined because the decision to use ablation,

and which ablation technique to use, depends on several factors. In practice, the decision of whether to use thermal ablation depends on the training and preference of the physician in charge and the equipment resources available at his/her medical center. Moreover, physical characteristics of the treatment zone using ablation are also needed to concern, including the zone shape, uniformity, and its location. Up to now clinical results have been indicated that the different techniques of thermal ablation have roughly equivalent effectiveness for treating various tumors.

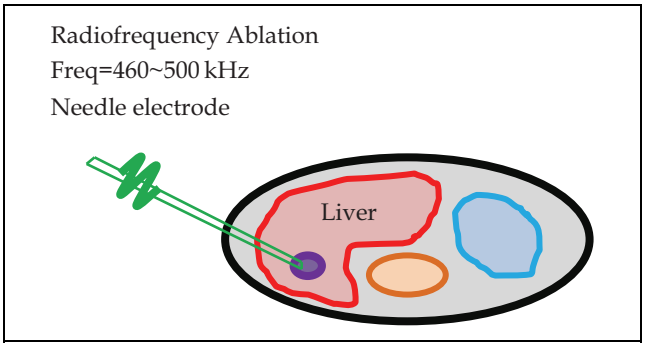

(a)

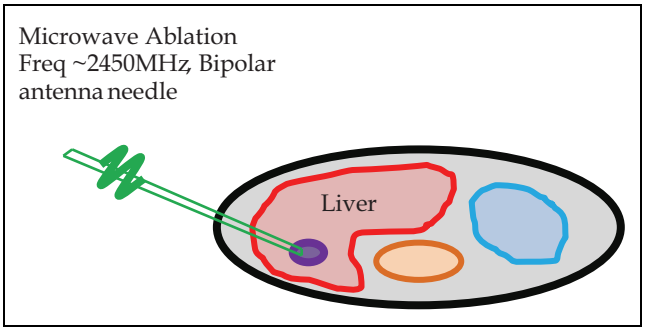

(b)

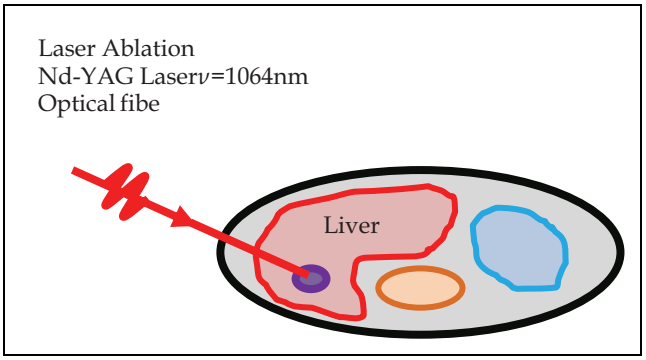

(c)

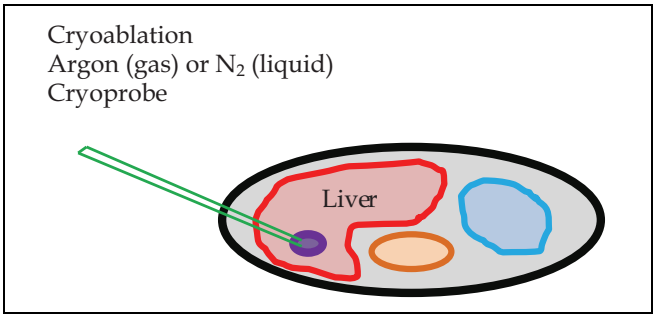

(d)

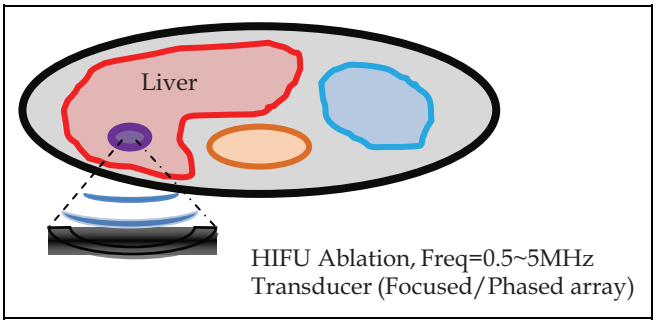

(e)

Fig. 4. Schematics of different thermal ablation techniques. (a) RF ablation (b) Microwave ablation (c) Laser ablation (d) Cryoablation (e) HIFU ablation

Patients referred for thermal ablation are initially evaluated in a clinic setting where the patient's history and pertinent imaging information are reviewed. Meanwhile, the applicability of ablation and the risks and benefits of the procedure are also discussed. Prior to ablation, the evaluation is very similar to a surgical evaluation that any possible risks of bleeding or serious cardiopulmonary issues are considered. Side effects from thermal ablation are also discussed, including postablation syndrome—for example, a short term fever, discomfort, and anorexia.

5.2.1 High-intensity focused ultrasound (HIFU)

HIFU is a non-invasive power deposition method via mechanical oscillation motion of object molecules. One of important features in the heating methods is non-invasiveness and it reduces external surgical operations on body object. Thus this method has become a promising tool for localized tumor therapy. Compared to hyperthermia which lasts long period of treating time, HIFU referred as thermal surgery, could heat the target region elevated temperature up to 50~55°C within a short period of time (i.e. few seconds to 1 min.). Another important feature is that this comparably higher temperature during treatment could cause thermal coagulation and thermal lesion. Therefore, precise location management and monitoring are required during clinic HIFU treatment to prevent irreversible heating process on tissues. Figure 1.e illustrated the method.

5.2.2 Radiofrequency (RF) ablation

Radiofrequency ablation is a "minimally invasive" treatment method mostly for primary and metastatic liver tumors. It is becoming a promising treating method to replace surgical resection. A study (Solbiati et al, 2001) in 2001 of RF ablation in 117 patients has shown 1-, 2-, and 3-year survival rates of 93%, 62%, and 41%, respectively. As compared to traditionally only low or 10-20 % of patients, those will have disease amenable to surgical resection due to limited hepatic reserve, high surgical risk, or unfavorable tumor location.

The mechanics of RF ablation uses the electromagnetic energy which is converted to heat by ionic friction. Tissue damage can occur at temperatures above 43°C with long heating times of several hours (Sapateto and Dewey, 1984). Elevated tissue temperature to 50°C near the probe required 3-min of heating time. Traditional and commercial design of the probe uses 17-gauge needles with active tip exposures of 1, 2 and 3 cm and the remainder of the needle is electrically insulated. Within the probe, water is circulated during the ablation procedure to cool tissue next to the probe and prevent tissue charring. Figure 1.a illustrated the method.

5.2.3 Microwave (MW) ablation

Microwave tumor ablation is also a "minimally invasive" treatment method. In contrast, while RF employs radio-frequency current to generate heat, MW ablation produces an electromagnetic wave that is emitted from a 14.5 gauge (standard) microwave antenna placed directly within the treatment site. The electromagnetic wave produces 60 W of power at a frequency ranging from 900 to 2450 MHz, which generate frictional heat from the agitation of polar water molecules (McTaggart and Dupuy, 2007; Liang and Wang, 2007; Simon et al, 2005). In principle the electromagnetic wave passes through the tissues, it causes polar water molecules to rapidly change their orientation in accordance with the magnetic field. Additionally, the design of MW antenna contributes significantly to the efficiency of MW therapy. Figure 1.b illustrated the method.

5.2.4 Others

Another interesting method to kill tumor cells is cryo-ablation, as shown in Figure 1.d. In contrast with other methods, cryo-ablation use lower temperature to ablate tumors. The procedure can be performed either by a laparoscopic or percutaneous approach under MRI, US or CT guidance. Cryoablation involves a number of freeze-thaw-freeze cycles with argon and helium gas (McTaggart and Dupuy, 2007). Gases are used to remove heat and induce thawing. It is used to treat lesions of the prostate, kidney, liver, lung, bone, and breast (Hayek et al, 2008; Orlacchio et al, 2005). As the tissue freezes, osmolarity increases and causes an imbalance of solutes between the intracellular and extracellular environments. Cellular death initially occurs through cellular dehydration and protein denaturization.

6. Adjuvant to other tumor treatment modalities

Although the effectiveness of hyperthermia alone as a cancer treatment may be not so promising, significant improvements in clinical trials using combined therapies with hyperthermia are observed. Recently, hyperthermia has been applied as an adjunctive therapy with various established cancer treatments such as radiotherapy, chemotherapy, and nano-particle drug treatments, etc. The combination therapies seem to be safe and effective approaches even when other treatments have failed. The rationale of combining

chemotherapy or other therapies with hyperthermia is that the available armamenterium for tumor heating has been substantially improved. The potential to control power distributions in clinic has been significantly improved lately by the development of advanced imaging techniques (particularly, online magnetic resonance tomography), planning systems and other modeling tools.

6.1 Radiotherapy

The efficacy of standard radiotherapy for patients with different tumor sites, for example, cervical, gastrointestinal, and genitourinary tumors, might become poor because the local-control rates after locoregional treatment are disappointingly low. To compensate this defect the combinations of radiotherapy with other therapies have been used. It has been known that hyperthermia probably is the strongest radiosensitizer known, with an enhancement factor of up to 5 (Kampinga and Dikomey, 2001). Although the exact mechanism why heat can cause cells more sensitive to radiation is not known, clinical results reveal that heat primarily interferes with the cells' ability to deal with radiation-induced DNA damage (Kampinga and Dikomey, 2001; Roti, 2004).

Clinical studies have shown that the combination of radiotherapy with hyperthermia increases cytotoxic effects and higher locoregional control rates. In the Netherlands 358 patients with tumors of the bladder, cervix, or rectum were treated with radiotherapy alone (n=176) or radiotherapy plus hyperthermia (n=182) from 1990 to 1996. Results showed the complete-response rates were 39% after radiotherapy and 55% after radiotherapy plus hyperthermia (Van der Zee et al, 2000). Radiotherapy plus hyperthermia was superior to radiotherapy alone and improved tumor response and survival.

Moreover, other clinical results of the combination of radiotherapy with hyperthermia are summarized in some recent studies (Wust et al, 2002; Van der Zee, 2002). The supplementary values of this combined therapy are from 41% to 61% in 3-year local control rate and from 27% to 51% in 3-year overall survival in cervix cancer, from 24% to 69% in 5-year local control rate in lymph nodes of head-and-neck tumors, and from 24% to 42% in 3-year overall survival in esophageal cancer. The differences reported for the other radiosensitizing agents (Horsman et al, 2006), insofar as there are clinical results, are in the range of 10% to 20%. Significant improvements in clinical outcomes by additional treatment with hyperthermia were also shown for cancer of the breast, brain, rectum, bladder, and lung, and for melanoma.

Whether the combination of radiation and heat is given in a simultaneous or sequential schedule, the thermal enhancement will be dependent on the heating time and temperature of both tumors and normal tissues (Horsman and Overgaard, 2002 & 2007).

Besides, hyperthermia has a direct cell-killing effect, specifically in insufficiently perfused parts of the tumor. Several randomized clinical trials have shown that the beneficial effect of hyperthermia, when added to radiotherapy, can be substantial, even while the temperature of 43°C that was thought to be necessary was not achieved in the whole tumor volume.

The improvements in clinical outcomes, despite the inadequacy to heat the whole tumor volume to temperatures of 43°C, can be explained by the more recent findings that hyperthermia has more effects than just that of direct cell kill and radiosensitization. Several additional effects that become apparent at different temperatures between 39° and 45°C have been described: vascular damage resulting in secondary cell death; improvement f perfusion and oxygenation, which results in a better effect of radiation; and stimulation of

the immune system (Dewhirst et al, 2007). All these effects may contribute o the desired eventual effect, which (certainly when combined with RT) is he achievement of local control. Several phase III trials comparing radiotherapy alone or with hyperthermia have shown a beneficial effect of hyperthermia (with existing standard equipment) in terms of local control (eg, recurrent breast cancer and malignant melanoma) and survival (eg, head and neck lymph-node metastases, glioblastoma, cervical carcinoma). Therefore, further development of existing technology and elucidation of molecular mechanisms are justified.

6.2 Chemotherapy

The combination of hyperthermia and chemotherapy has demonstrated several advantages over chemotherapy alone. The architecture of the vasculature in solid tumors is often insufficient due to the rapid growth of tumor tissue compared to normal tissue and/or chaotic, resulting in regions with hypoxia and low pH levels, which is not found in normal tissue. When using a mild hyperthermia (temperatures < 42 C), heat results in vasodilatation which improves the oxygenation of tissue (Iwata et al, 1996). Results reveal that the changes in tumor oxygenation are temperature dependent. This relationship could possibly influence treatment outcome of thermo-chemotherapy when the activity of chemotherapeutic agents is known to be oxygen dependent. This improvement of the blood supply can increase the cell metabolism which allows a greater effect of the chemotherapeutic agent on the tumor cells. Besides, heat also improves the cellular permeability which leads to the increase of the drug uptake by the tumor cells and intracellular spaces, the reaction of chemotherapy with DNA, and the prevention of DNA repair (Herman et al, 1988).

Moreover, the pathologic studies have shown that the enhanced drug cytotoxicity by heating induces both apoptosis and necrosis above a certain threshold temperature (Harmon et al, 1990; Yonezawa et al, 1996). In addition, several studies have also shown that some of the advantages of combining chemotherapy with hyperthermia are not only treating the primary cancers, but also reducing the risk of treatment-induced secondary cancers (Kampinga and Dikomey, 2001; Hurt et al, 2004; Hunt et al, 2007). These factors make cells more sensitive to heat especially in low perfused tissues. Therefore, in addition to direct cytotoxicity, hyperthermia leads in vivo to a selective destruction of tumor cells in hypoxic and, consequently, acidic environment within parts of malignant tumors (Vaupel et al, 1989; Vaupel, 2004).

More recent in vivo studies have demonstrated that the thermal enhancement of cytotoxicity of many chemotherapeutic agents is maximized with heat (Hahn, 1979; Marmor, 1979; Engelhardt, 1987; Dahl, 1988; Bull, 1984; Hildebrandt et al, 2002; Urano et al, 1999). The positive results of thermo-chemotherapy are observed that the rate at which cells are killed by the drug increases with temperatures. Besides, the efficacy of thermo-chemotherapy also depends on the treatment planning. In general, promising results indicate that patients need to take chemotherapeutic agents immediately before hyperthermia. However, some of agents like the antimetabolite gemcitabine, are taken prior to hyperthermia at least 24 h to achieve a synergistic effect in vitro and in vivo (Haveman et al, 1995; Van Bree et al, 1999).

Although the working mechanism of thermo-chemotherapy is not fully understood, with the promising results of clinical trials and the thermal enhancement of drug cytotoxicity from pathologic studies, hyperthermia combined with chemotherapy has demonstrated as one of effective modalities in the present cancer treatment.

6.3 Nano-particle drug therapy

The nanoparticles have been applied to facilitate drug delivery and to overcome some of the problems of drug delivery for cancer treatment. In the past, cancer therapies using anticancer drugs were dissatisfied and had major side effects. Because of their multifunctional character the nanoparticles can deliver larger and more effective doses of chemotherapeutic agents or therapeutic genes into malignant cells, minimize toxic effects on healthy tissues and then alleviate patients suffering from the side-effects of chemotherapy. Nanoparticles can be used to deliver hydrophilic drugs, hydrophobic drugs, proteins, vaccines, biological macromolecules, etc. Several nanoscale delivery devices, such as ceramic nanoparticles, virus, dendrimers (spherical, branched polymers), silica-coated micelles, cross linked liposomes, and carbon nanotubes (Portney and Ozkan, 2006) have been used to improve delivery of anticancer agents to tumor cells (Brigger el al, 2002). Some of the challenges in effectively delivering anticancer drugs have to be solved: how to ensure therapeutic drug molecules reach the targeted tumor, how to release them slowly over a longer period, and how to avoid the human immune system destroying them.

Normally, the structure of a nanoparticle drug carrier has four elements. The first of them is the targeted chemotherapy drug, for example, docetaxel or Taxotere. The second is a matrix made of a biodegradable polymer (polylactic acid), which contains the anticancer drug and breaks down slowly so that the drug is released gradually over several days. The third element is a coating layer of polyethylene glycol, which is used to prevent from attacking by antibodies and macrophage cells of the human immune system. The final element is a targeted tag, in the form of special enzymes attached to the outer coating, which can form electrostatic or covalent bonds with positively charged agents and biomolecules. This tag allows the nanoparticles to bind directly to desired tumor cells but to bypass healthy tissues and eventually to reduce the side effects caused by most chemotherapy drugs.

Several different drug delivery methods (Jain, 2005) have been shown their feasibility to treat human cancers. Lipid-based cationic nanoparticles (Cavalcanti et al, 2005), one of new promising tumor therapies, by loading suitable cytotoxic compounds can cause strong human immune responses and result in the destruction of tumor. Magnetic nanoparticles as the carrier have been used in cancer treatment avoiding side effects of conventional chemotherapy (Alexiou et al, 2006). Recent progress has been made in the application of nanoparticles to cancer treatment, including their use as delivery systems for potent anticancer drugs or genes, as well as agents for more advanced cancer treatment modalities, such as the combination treatments of radiotherapy, chemotherapy, and gene therapy with hyperthermia (Kong et al, 2000).

6.4 Others

Hyperthermia-regulated gene therapy

Major factors determining the effectiveness of gene therapy are the method of gene delivery and the details of the therapeutic gene expression in the targeted tissue. Some researchers have reported that heat can not only enhance the immunogenicity of tumor cells (Kubista et al, 2002), but also regulate the heat-sensitive promoters in the region of interest (Ito et al, 2003; Ito et al, 2006; Ito et al, 2004; Todryk et al, 2003). Heat shock proteins (HSPs) as sensitive promoters are recognized as significant participants in immune reactions (Kubista et al, 2002). Animal studies showed that the hyperthermia-regulated gene therapy using

hsp70 obtained strong prevention of tumor growth, complete regression of tumors, and the induction of systemic antitumor immunity in the cured mice (Ito et al, 2006; Ito et al, 2004; Todryk et al, 2003).

These studies suggest that the combination gene therapy with hyperthermia using hsp70 have great potential in cancer treatment. Nevertheless, results also suggested that inappropriate immune reactivity to hsp70 might lead to pro-inflammatory responses and the development of autoimmune disease. Moreover, endotoxin contamination has been reported to be responsible for the human hsp70 preparation (Gao & Tsan, 2003; Bausinger et al, 2002) and uncontrolled promoter activation by other than heat stressors for the HSP70B promoter system was found (Siddiqui et al, 2008). To have a safe and controllable gene therapy the unintentional activation of heat-responsive promoters should be avoided. Although some effects of heat shock proteins on the immunogenicity of tumor cells have been studied, more work is still needed before the hyperthermia-regulated gene therapy using hsp70 can applied into clinical cancer treatments.

Recently, a combination of gene therapy with magnetic resonance imaging (MRI), high-intensity focused ultrasound (HIFU) and a temperature-sensitive promoter is being evaluated in the cancer field (Moonen, 2007; Silcox et al, 2005; Plathow et al, 2005; Frenkel, 2006; Rome et al, 2005; Walther & Stein, 2009). With the help of advanced imaging techniques one can noninvasively monitor the temperature field induced by a high-intensity focused ultrasound system and simultaneously regulate the gene expression in the treatment region. Results indicated that although the application of MRI-guided HIFU in gene therapy is promising, further technical requirements of the heating and monitoring systems for precise control are still needed.

In recent molecular and biological investigations there have been novel applications such as gene therapy or immunotherapy (vaccination) with temperature acting as an enhancer, to trigger or to switch mechanisms on and off. However, for every particular temperature-dependent interaction exploited for clinical purposes, sophisticated control of temperature, spatially as well as temporally, in deep body regions will further improve the potential.

7. Conclusion

Thermal transport in bio-thermal systems signifies that temperature management in living systems can help us in curing and treatment of ill conditions. In analytic perspective, efforts on mathematical and numerical modelings have showed great progrssing in calculating temperature distributions. Advance in computer technology is one of critical contributing factors. In clinical perspective, many thermal energy related experiments and tests that are adjuvant to other tumor treatment modalities have identified effectiveness in treatments. In this regard, the well knowledge of heat transfer process revealed significant in optimal controling temperature in bio-thermal systems. Thus it shows us another great research and career opportunities in this field.

8. Acknowledgment

Authors would like to express special thanks to Professor Win-li Lin for his valuable suggestions and discussion. The authors would like to thank the National Science Council of Taiwan for partially supporting this research under no. NSC 99-2221-E-168 -026 and NSC 100-2221-E-032 -013.

9. References

Alexiou, C.; Schmid, R. J.; Jurgons, R.; Kremer, M.; Wanner, G.; Bergemann, C.; Huenges, E.; Nawroth, T.; Arnold, W.; Parak, F. G. (2006) Targeting cancer cells: magnetic nanoparticles as drug carriers, Eur Biophys J , 446–450, 35.

Anderson, D.A.; Tannehill, J.C.; Pletcher, R.H. (1984) *Computational Fluid Mechanics and Heat Transfer*, McGraw-Hill, New York.

Baish, J.W. (1994) Formulation of a statistical model of heat transfer in perfused tissue, *ASME J. of Biomechanical Engineering* 116 521-527.

Baish, J.W.; Ayyaswamy, P.S. and Foster, K. R. (1986), Small Scale Temperature Fluctuations in Perfused Tissue during Local Hyperthermia, *ASME Journal of Biomechanical Engineering*, vol. 108, pp. 246-251.

Bausinger, H; Lipsker, D; Ziylan, U; et al. (2002) Endotoxin-free heat shock protein 70 fails to induce APC activation. *Eur J Immunol* 32:3708–13.

Brigger, I. ; Dubernet, C.; Couvreur, P.(2002) Nanoparticles in cancer therapy and diagnosis, Advanced Drug Delivery Reviews, 54, 631-651.

Briggs,William L.; Henson,Van Emden and McCormick, Steve F. (2000) A Multigrid Tutorial (2nd ed.), Philadelphia: *Society for Industrial and Applied Mathematics*, ISBN 0-89871-462-1.

Brosseau, L; Yonge, KA; Robinson, V; Marchand, S; Judd, M; Wells G, et al. (2003) Thermotherapy for treatment of osteoarthritis. *Cochrane Database Syst Rev*, 4: CD004522.

Bull, JMC. (1984)An update on the anticancer effects of a combination of chemotherapy and hyperthermia. *Cancer Res* 44 (Suppl.): 4853–6.

Canuto, C.; Hussaini, M. Y.; Quarteroni, A. and Zang, T.A. (2006) *Spectral Methods. Fundamentals in Single Domains*. Springer-Verlag, Berlin Heidelberg.

Cavalcanti,L. P.; Konovalov, O.; Torriani, I. L.; Haas, H. (2005)Drug loading to lipid-based cationic nanoparticles, *Nucl. Instr. and Meth. in Phys. Res.*, 290–293, 238.Charny, C. K. and Levin, R.L.(1990) Bioheat Transfer in a Branching Countercurrent Network during Hyperthermia, *ASME Journal of Biomechanical Engineering*, vol. 112, pp.80-87.

Chato, J. C. (1980) Heat Transfer to Blood Vessels, *Journal of Biomechanical Engineering*, Tran. ASME 102, pp.110-118.

Chen, M.M. and Holmes, K.R. (1980), Microvascular Contributions in Tissue Heat Transfer, *Annals of the New York Academy of Sciences*, vol. 335, pp.137-150.

Crank, J.; Nicolson, P. (1947) A practical method for numerical evaluation of solution of partial differential equations of the heat-conduction type, *Proc. Camb. Philos. Soc.* 43 50–67.

Dahl, O. (1988) Interaction of hyperthermia and chemotherapy. *Recent Res Cancer Res* 107:157–69.

Deng, Z.S. and Liu, J. (2002) Analytical study on bioheat transfer problems with spatial or transient heating on skin surface or inside biological bodies, *ASME J. Biomech. Eng.* 124 638–649.

Dennis, B.H., et al. (1995) Finite-Element simulation of cooling of realistic 3-D human head and neck. *ASME Trans J. of Biomechanical Eng.*, 125, 6, p. 832-840.

Devashish, S. and Roemer, R.B. (2006) Readdressing the issue of thermally significant blood vessels using a countercurrent vessel network. *ASME J. of Biomechanical Engineering* 128 210-216.

Dewhirst, MW; Vujaskovic, Z; Jones, E; Thrall, D. (2005) Re-setting the biologic ationale for thermal therapy. *Int J Hyperthermia* 21:779 –790.

Dodd, GD 3rd; Soulen, MC; Kane, RA; Livraghi, T; Lees, WR; Yamashita, Y; Gillams, AR; Karahan, OI; Rhim, H., (2000) Minimally invasive treatment of malignant hepatic tumors: at the threshold of a major breakthrough. *Radiographics* 20:9 –27.

Engelhardt, R. (1987) Hyperthermia and drugs. *Recent Res Cancer Res* 104:136–203.

Ferziger, J.H. and Peric, M. (2001), *Computational Methods for Fluid Dynamics*, ISBN 3540420746, 3rd Rev. Ed., Springer-Verlag, Berlin.

Frenkel, V; Li, KC. (2006) Potential role of pulsed-high intensity focused ultrasound in gene therapy. *Future Oncol* 2:111–9.

Gao, B; Tsan, MF. (2003) Endotoxin contamination in recombinant human Hsp70 preparation is responsible for the induction of TNFalpha release by murine macrophages. *J Biol Chem* 278:174–9.

Hahn, GM. (1979) Potential for therapy of drugs and hyperthermia. *Cancer Res* 39:2264–8.

Hall, EJ & Cox, JD, (2003). Physical and biological basis of radiation therapy, in: Cox, JD. & Ang, KK (eds.): *Radiation Oncology*, St. Louis, Mosby, pp 3-62.

Hayek, O. R. El; Alfer, W., Jr.; Reggio, E.; Pompeo, A. C.; Arap, S.; Lucon, A. M.; Srougi, M. (2008) Prostate cryoablation: prospective analysis comparing high- and low-risk prostate cancer outcomes. *Urol. Int.*, 81, 186-190.

Hildebrandt, B; Wust, P; Ahlers, O; et al. (2002) The cellular and molecular basis of hyperthermia. *Crit Rev Hematol Oncol* 43:33–56.

Hinton, E. & Owen, D. R. (1974) *An introduction to finite element computations*, Pineridge Press.

Huang, H. W., Chan, C. and Roemer, R. B. (1994) Analytical Solutions of Pennes Bio-Heat Transfer Equation with a Blood Vessel, *ASME Journal of Biomechanical Engineering*, vol.116, pp.208-212.

Huang, H. W., Chen, Z. P. and R. B. Roemer, (1996) A counter Current Vascular Network Model of Heat Transfer in Tissues, *Trans. ASME, Journal of Biomechanical Engineering* 118, pp. 120-129.

Haveman, J; Rietbroek, RC; Geerdink, A; van Rijn, J; Bakker, PJM.(1995) Effect of hyperthermia on the cytotoxicity of 2′,2′- difluorodeoxycytidine (gemcitabine) in cultured SW1573 cells. *Int J Cancer* 62:627–30.

Herman, TS; Teicher, BA; Jochelson, M; Clark, J; Svensson, G; Coleman, CN. (1988) Rationale for use of local hyperthermia with radiation therapy and selected anticancer drugs in locally advanced human malignancies. *Int J Hyperthermia* 4(2):143–58.

Harmon, BC; Corder, AM; Collins, JR; et al. (1990) Cell death induced in murine mastocytoma by 42–47 _C heating in vitro: Evidence that the form of death changes from apoptosis tonecrosis above a critical heat load. *Int J Radiat Oncol Biol* 58:845–58.

Horsman, MR; Bohm, L; Margison, GP; *et al.* (2006) Tumor radiosensitizers current status of development of various approaches: report of an international Atomic Energy Agency Meeting. *Int J Radiat Oncol Biol hys* 64:551–561.

Horsman, MR; Overgaard, J. (2002) Overcoming tumour radioresistance resulting from hypoxia. In: Steel GG, editor. *Basic clinical radiobiology for radiation oncologists*, 3rd edn. London: Edward Arnold, 169e181.

Horsman, M. R. and Overgaard, J. (2007) Hyperthermia: a Potent Enhancer of Radiotherapy, Clinical Oncology 19: 418e426.

Hurt, CR; Dix, DJ; Sharma, GG; et al. (2004) Genomic instability and enhanced radiosensitivity in Hsp70.1- and Hsp70.3-deficient mice. *Mol Cell Biol* 24:899–911.

Hunt CR, Pandita RK, Laszol A, et al. (2007) Hyperthermia activates a subset of Ataxia-Telangiectasia mutated effectors independent of DNA strand breaks and heat shock protein 70 status. *Cancer Res* 67:3010–7.

Ito, A; Matsuoka, F; Honda, H; Kobayashi, T (2003) Heat shock protein 70 gene therapy combined with hyperthermia using magnetic nanoparticles, *Cancer Gene Ther.* 10(12):918-25.

Ito, A; Honda, H; Kobayashi, T (2006) Cancer immunotherapy based on intracellular hyperthermia using magnetite nanoparticles: a novel concept of "heat-controlled necrosis" with heat shock protein expression, *Cancer Immunol Immunother.* 55(3):320-8. Epub 2005 Aug 25.

Ito, A; Matsuoka, F; Honda, H; Kobayashi, T (2004) Antitumor effects of combined therapy of recombinant heat shock protein 70 and hyperthermia using magnetic nanoparticles in an experimental subcutaneous murine melanoma, *Cancer Immunol Immunother.* 53(1):26-32. Epub 2003 Oct 9.

Iwata, K.; Shakil, A.; Hur, W.J.; Makepeace, C.M.; Griffin, R.J.; Song, C.W., (1996). Tumour pO2 can be increased markedly by mild hyperthermia. Br. J. Cancer Suppl. 27, S217–S221.

Jain, K. K. (2005) Nanotechnology –based Drug Delivery for Cancer, *Technology in Cancer Research & Treatment*, 4, 4,.

Kampinga, HH; Dikomey, E. (2001) Hyperthermia radiosensitization: mode of action and clinical relevance. *Int J Radiat Oncol Biol Phys* 77: 399–408.

Kong, G. *et al*. (2000) Hyperthermia enables tumor-specific nanoparticle delivery: effect of particle size. *Cancer Res.* 60, 4440–4445.

Kubista, B; Trieb, K; Blahovec, H; et al. (2002) Hyperthermia increases the susceptibility of chondro- and osteosarcoma cells to natural killer cell-mediated lysis. *Anticancer Res*, 22:789–792.

Lagendijk, J.J.W.(1982) The Influence of Blood Flow in Large Vessels on the Temperature Distribution in Hyperthermia, *Phys. Med. Biol.*, vol. 27, No. 1, pp. 17-23.

Leeuwen, G.M.J.V.; Kotte, A.N.T.J.; Raaymakers, B.W. and Lagendijk, J.J.W. (2000) Temperature simulations in tissue with a realistic computer generated vessel network, *Phys. Med. Biol.* 45 1035-1049.

Liang, P., Wang, Y. (2007) Microwave ablation of hepatocellular carcinoma, *Oncology*, vol.72 suppl 1, pp.124-131.

Liu, J. (2001) Uncertainty analysis for temperature prediction of biological bodies subject to randomly spatial heating, *J. Biomech.* 34 1637–1642.

Lyra, P.R.M. (1994) *Unstructured grid adaptive algorithms for fluid dynamics and heat conduction*, Ph.D. thesis C/PH/182/94, University of Wales – Swansea.

Marmor, JB. (1979) Interactions of hyperthermia and chemotherapy in animals. *Cancer Res* 39:2269–76.

McTaggart, R. A. and Dupuy, D. E. (2007) Thermal ablation of lung tumors, *Tech. Vasc. Interv. Radiol.* 10, pp. 102-113.

Minkowycz, W.J.; Sparrow,E.M.; Schneider,G.E.; Pletcher,R.H.(1988) *Handbook of Numerical Heat Transfer*, Wiley, New York.

Moonen,Chrit T.W. (2007) Spatio-Temporal Control of Gene Expression and Cancer Treatment Using Magnetic Resonance Imaging–Guided Focused Ultrasound, *Clin Cancer Res 13;* 3482-89

Morton, K.W. and Mayers, D.F. (2005) *Numerical Solution of Partial Differential Equations, An Introduction*. Cambridge University Press.

Narins, DJ; Narins, RS.(2003) Non-surgical radiofrequency face-lift. *J Drugs Dermatol* 2:495-500.

Oden, J.T. (1991), *Finite elements: An Introduction* in: Handbook of Numerical Analysis II (North-Holland,Amsterdam).

Orlacchio, A.Silverman, S. G.; Tuncali, K.; vanSonnenberg, E.; Morrison, P. R.; Shankar, S.; Ramaiya, N.; Richie, J. P.(2005) Renal tumors: MR imaging-guided percutaneous cryotherapy—initial experience in 23 patients. *Radiology*, 236, 716-724.

Peaceman, D.W. and Rachford, H.H.(1955) The numerical solution of parabolic and eliptic differential equations. *J. Soc. Ind. Appl. Math.,* 2 p. 28-41.

Pennes, H. H., (1948) Analysis of Tissue and Arterial Blood Temperature in Resting Forarm, *Journal of Applied Physiology*, Vol. 11, pp. 93-122.

Plathow, C; Lohr, F; Divkovic, G; et al. (2005) Focal gene induction in the liver of rats by a heat-inducible promoter using focused ultrasound hyperthermia: preliminary results. *Invest Radiol* 40:729–35.

Portney, N.G.; Ozkan, M. (2006) Nano-oncology: drug delivery, imaging, and sensing, *Anal Bioanal Chem* 384, 620–630.

Qi, Y. and Wissler, E.H.. (1992) A combined analytical/finite difference technique for analyzing two-dimensional heat transfer in human limbs which contain major arteries and veins. in *ASME Winter Annual Meeting*.

Robinson, V; Brosseau, L; Casimiro, L; Judd, M; Shea, B; Wells G, et al. (2002) Thermotherapy for treating rheumatoid arthritis. *Cochrane Database Syst Rev*, 2: CD002826.

Rome, C; Couillaud, F; Moonen, CT. (2005) Spatial and temporal control of expression of therapeutic genes using heat shock protein promoters. *Methods* 35:188–98.

Roemer, R.B. ; Paliwal, B.R. ; Hetzel, F.W.; Dewhirst, M.W. eds. (1988)Heat transfer in hyperthermia treatments : basic principles and applications, In *Biological, physical and clinical aspects of hyperthermia, New York* : American Institute in Physics, pp.210-242.

Roti, Roti JL.(2004) Introduction: radiosensitization by hyperthermia. *Int J Hypertherm* 20:109e114.

Sapateto, S. A. and Dewey, W. C. (1984) Thermal dose determination in cancer therapy, *Int. J. Radiat. Oncol. Biol. Phys.*, vol. 10, pp. 787-800.

Shih,Tzu-Ching; Yuan, Ping; Lin,Win-Li and Kou,Hong-Sen, (2007)Analytical analysis of the Pennes bioheat transfer equation with sinusoidal heat flux condition on skin surface, *Medical Engineering & Physics* 29, 946–953.

Siddiqui,F.; Avery, P.R.; Li, C.Y.; Zhang, X.; LaRue, S.M.; Dewhirst, M.W.; Ullrich, R.L. (2008) Induction of the human heat shock promoter HSP70B by nutritional stress: implications for cancer gene therapy, *Cancer Invest.* 26 553–561.

Silcox, CE; Smith, RC; King, R; et al. (2005) MRI-guided ultrasonic heating allows spatial control of exogenous luciferase in canine prostate. *Ultrasound Med Biol* 31:965–70.

Simon, C. J.; Dupuy, D. E. and Mayo-Smith, W. W.(2005) Microwaveablation: principles and applications, *Radiographics*, 25 (suppl. 1), S69-S83,.

Smith, E., (2002) Egyptian Surgical Papyrus dated around 3000 B.C. Cited by: van der Zee J: Heating the patient: A promising approach? *Ann Oncol*:13:1173-84.

Solbiati,L.; Livraghi, T.; Goldberg, S. N.; Ierace, T.; Meloni, F.; Dellanoce, M.; Cova, L.; Halpern, E. F. and Gazelle, G. S. (2001) Percutaneous radiofrequency ablation of hepatic metastages from colorectal cancer: Long term results in 117 patients, *Radiology*, vol.221, pp. 159-166.

Thomas, J.W., (1995) *Numerical Partial Differential Equations: Finite Difference Methods*, Springer, New York.

Todryk, SM; Gough, MJ; Pockley, AG (2003) Facets of heat shock protein 70 show immunotherapeutic potential, *Immunology*. 110(1):1-9.

Tyrrell, D; Barrow, I & Authur J. (1989) Local hyperthermia benefits natural and experimental common colds. *BMJ*, 298:1280-3.

Urano, M; Kuroda, M; Nishimura, Y. (1999) For the clinical application of thermochemotherapy given at mild temperatures. *Int J Hyperthermia* 15:79–107.

Van Bree, C; Beumer, C; Rodermond, HM; Haveman, J;Bakker, PJ. (1999) Effectiveness of 2′,2′-difluorodeoxycytidine (gemcitabine) combined with hyperthermia in rat R-1 rhabdomyosarcoma in vitro and in vivo. *Int J Hyperthermia* 15:549–56.

Van der Zee, J.; Gonzalez, D. Gonzalez; Rhoon, G. C van, D P van Dijk, J., Putten, W L J van, (2000) Comparison of radiotherapy alone with radiotherapy plus hyperthermia in locally advanced pelvic tumours: a prospective, randomised, multicentre trial, *THE LANCET,* 355: 1119–25

Van der Zee, J. (2002) Heating the patient: a promising approach? *Ann Oncol* 13:1173–1184.

Vaupel, P; Kallinowski, FK; Okunieff, P. (1989) Blood flow, oxygen and nutrient supply, and metabolic micro-environment of human tumors: a review. *Cancer Res* 49:6449–65.

Vaupel, P. (2004)Tumor microenvironmental physiology and its implications for radiation oncology. *Semin Radiat Oncol* 14:198–206.

Walther, Wolfgang and Stein,Ulrike (2009) Heat-responsive gene expression for gene therapy, *Advanced Drug Delivery Reviews*, Volume 61, Issues 7-8, 41-649

Weinbaum, S. and Jiji, L.M., (1985), A New Simplified Bio-heat Equation for the Effect of Blood Flow on Local Average Tissue Temperature. *ASME Journal of Biomechanical Engineering*, Vol. 107, pp. 131-139.

Wissler, E.H., (1987), Comments on the New Bioheat Equation Proposed by Weinbaum and Jiji, *Trans. ASME, J. of Biomechanical Engineering*, vol. 109, pp. 226-233.

Wrobel, L. C.; Aliabadi, M. H. (2002) *The Boundary Element Method*. New Jersey: Wiley. ISBN 0-470-84139-7.

Wust, P; Hildebrandt, B; Sreenivasa, G, *et al.* (2002) Hyperthermia in combined treatment of cancer. *Lancet Oncol* 3:487– 497.

Yonezawa, M; Otsuka, T; Matsui, N; et al. (1996) Hyperthermia induces apoptosis in malignant fibrous histiocytoma cell *in vitro*. *Int J Cancer* 66:347–51.

Yuan, D.Y.; et al. (1995) Advances in Heat and Mass Transfer in Biotechnology. in *ASME Winter Annual Meeting*.

13

A Generalised RBF Finite Difference Approach to Solve Nonlinear Heat Conduction Problems on Unstructured Datasets

D. Stevens[1], A. LaRocca[1], H. Power[1] and V. LaRocca[2]
[1]*Faculty of Engineering, Division of Energy and Sustainability, University of Nottingham*
[2]*Dipartimento di Ricerche Energetiche ed Ambientali, University of Palermo, Sicily*
[1]*UK*
[2]*Italy*

1. Introduction

Radial Basis Functions have traditionally been used to provide a continuous interpolation of scattered data sets. However, this interpolation also allows for the reconstruction of partial derivatives throughout the solution field, which can then be used to drive the solution of a partial differential equation. Since the interpolation takes place on a scattered dataset with no local connectivity, the solution is essentially meshless. RBF-based methods have been successfully used to solve a wide variety of PDEs in this fashion.
Such full-domain RBF methods are highly flexible and can exhibit spectral convergence rates Madych & Nelson (1990). However, in their traditional implementation the fully-populated matrix systems which are produced lead to computational complexities of at least order-N^2 with datasets of size N. In addition, they suffer from increasingly poor numerical conditioning as the size of the dataset grows, and also with increasingly flat interpolating functions. This is a consequence of ill-conditioning in the determination of RBF weighting coefficients (as demonstrated in Driscoll & Fornberg (2002)), and is described by Robert Schaback Schaback (1995) as the uncertainty relation; better conditioning is associated with worse accuracy, and worse conditioning is associated with improved accuracy. Many techniques have been developed to reduce the effect of the uncertainty relation in the traditional RBF formulation, such as RBF-specific preconditioners Baxter (2002); Beatson et al. (1999); Brown (2005); Ling & Kansa (2005), or adaptive selection of data centres Ling et al. (2006); Ling & Schaback (2004). However, at present the only reliable methods of controlling numerical ill-conditioning and computational cost as problem size increases are domain decomposition Hernandez Rosales & Power (2007); Wong et al. (1999); Zhang (2007); Zhou et al. (2003), or the use of locally supported basis functions Fasshauer (1999); Schaback (1997); Wendland (1995); Wu (1995).
In this work the domain decomposition principle is applied, forming a large number of heavily overlapping systems that cover the solution domain. A small RBF collocation system is formed around each global data centre, with each collocation system used to approximate the governing PDE at its centrepoint, in terms of the solution value at surrounding collocation points. This leads to a sparse global linear system which may be solved using a variety

of standard solvers. In this way, the proposed formulation emulates a finite difference method, with the RBF collocation systems replacing the polynomial interpolation functions used in traditional finite difference methods. However, unlike such polynomial functions RBF collocation is well suited to scattered data, and the method may be applied to both structured and unstructured datasets without modification.

The method is applied here to solve the nonlinear heat conduction equation. In order to reduce the nonlinearity in the governing equation the Kirchhoff integral transformation is applied, and the transformed equation is solved using a Picard iterative process. The application of the Kirchhoff transform necessitates that the thermal property functions be transformed to Kirchhoff space also. If the thermal properties are a known and integrable function of temperature then the transformation may be performed analytically. Otherwise, an integration-interpolation procedure can be performed using 1D radial basis functions, as described in Stevens & Power (2010).

In recent years a number of local RBF collocation techniques have been proposed, and applied a wide variety of problems (for example; Divo & Kassab (2007); Lee et al. (2003); Sarler & Vertnik (2006); Wright & Fornberg (2006)). A more comprehensive review of such methods is given in Stevens et al. (2009). Unlike most local RBF collocation methods that are used in the literature, the technique described here utilises the Hermitian RBF collocation formulation (see section 2 for more details), and allows both the PDE-boundary and PDE-governing operators to be included within in the local collocation systems. This inclusion of the governing PDE within the basis functions is shown in Stevens et al. (2009) to significantly improve the accuracy and stability of solutions obtained for linear transport problems. Additionally, the incorporation of information about the convective velocity field into the basis functions was shown to have a stabilising effect, similar to traditional upwinding methods but without the requirement to alter the stencil configuration based on the local convective field.

The standard approach to the solution of linear and nonlinear heat conduction problems is the use of finite difference and finite volume methods with simple polynomial interpolants Bejan (1993); Holman (2002); Kreith & Bohn (2000). Due to the dominance of diffusion in most cases, central differencing techniques are commonly used to compute the heat fluxes. However, limiter methods (such as the unconditionally stable TVD schemes) may be used for nonlinear heat conduction problems where the effective convection term, which results from the non-zero variation of thermal conductivity with temperature, can be expected to approach the magnitude of the diffusive term (see, for example, Shen & Han (2002)). Full-domain RBF methods have also been examined for use with nonlinear heat conduction problems (see Chantasiriwan (2007)), however such methods are restricted to small dataset sizes, due to the computational cost and numerical conditioning experienced by full-domain RBF techniques on large datasets.

The present work demonstrates how local RBF collocation may be used as an alternative to traditional finite difference and finite volume methods, for nonlinear heat conduction problems. The described method retains freedom from a volumetric mesh, while allowing solution over unstructured datasets. A central stencil configuration is used in each case, and the solution is stabilised via the inclusion of the governing and boundary PDEs within the local collocation systems (“implicit upwinding”), rather than by adjusting the stencil configuration based on the local solution field (“traditional upwinding”). The method is validated using a transient numerical example with a known analytical solution (see section

4), and the ability of the formulation to handle strongly nonlinear problems is demonstrated in the solution of a food freezing problem (see section 5).

2. RBF method formulation

The Hermitian RBF collocation method operates on a domain which is covered by a series of N scattered data points, including a distribution of points over all domain boundaries. The solution is constructed using N distinct basis functions, which are composed of a partial differential operator applied to a radial basis function Ψ_j which is centred on the data point j. The partial differential operator that is applied to each basis function is the PDE boundary operator for points lying on the domain boundary, and the governing PDE for points lying within the domain (see equation 3). A polynomial term is required to complete the underlying vector space. In the present work, the multiquadric radial basis function is used throughout, with $m = 1$.

$$\Psi(r) = \left(r^2 + c^2\right)^{\frac{m}{2}} \quad m \in 2\mathbb{Z}^+ - 1 \tag{1}$$

The multiquadric RBF is a conditionally positive definite function of order m, which requires the addition of a polynomial term of order $m-1$, together with a homogeneous constraint condition, in order to obtain an invertible interpolation matrix. For the $m = 1$ case used in this work, the polynomial is simply a constant term. The 'c' term is known as a 'shape parameter', and describes the relative width of the RBF functions about their centres. The tuning of the shape parameter can have a significant effect upon the accuracy of the solution and the conditioning of the numerical system.
Consider a typical linear boundary value problem

$$\begin{aligned} L[u] &= S(x) \quad on\, \Omega \\ B[u] &= g(x) \quad on\, \partial\Omega \end{aligned} \tag{2}$$

where the operators $L[]$ and $B[]$ are linear partial differential operators on the domain Ω and on the boundary $\partial\Omega$, describing the governing equation and boundary conditions respectively. Data points ξ_j are distributed over the boundary and inside the domain, and the solution is constructed from basis functions centred around the ξ_j. At data points lying on $\partial\Omega$ the boundary operator is applied to the RBF, in order to form the basis function, while the PDE governing operator is applied at those points inside the domain:

$$u(x) = \sum_{j=1}^{NB} \lambda_j B_\xi \Psi\left(\left\|x - \xi_j\right\|\right) + \sum_{j=NB+1}^{N} \lambda_j L_\xi \Psi\left(\left\|x - \xi_j\right\|\right) + \sum_{j=1}^{NP} \lambda_{j+N} P_{m-1}^j(x) \tag{3}$$

The RBF formula (3) is then collocated at each of the data points ξ_j applying the PDE boundary equation, $B[u] = g$, at points on the domain boundary, and the PDE governing equation, $L[u] = f$, at points within the domain. This leads to a symmetric collocation system, as represented by equation (4), which can be solved to obtain the RBF weighting coefficients λ_i.

$$\begin{bmatrix} B_x B_\xi \left[\Psi_{ij}\right] & B_x L_\xi \left[\Psi_{ij}\right] & B_x \left[P_{m-1}^i\right] \\ L_x B_\xi \left[\Psi_{ij}\right] & L_x L_\xi \left[\Psi_{ij}\right] & L_x \left[P_{m-1}^i\right] \\ B_\xi \left[P_{m-1}^j\right]^T & L_\xi \left[P_{m-1}^j\right]^T & 0 \end{bmatrix} \lambda_i = \begin{bmatrix} g_i \\ S_i \\ 0 \end{bmatrix} \tag{4}$$

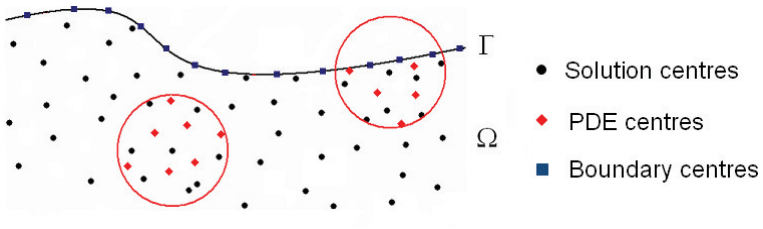

Fig. 1. Local system representation

The basic Hermitian RBF collocation method, as outlined above, is highly accurate and offers excellent convergence rates. However due to the presence of a fully-populated collocation matrix (4) solving even moderately-sized problems becomes computationally expensive. The poor numerical conditioning of this system also places limits upon the size of the dataset that can be solved. To address these issues of computational cost and numerical conditioning, the Hermitian method is applied here in "finite difference mode". In this way a large number of small and highly overlapping collocation systems are formed, leading to a numerical method that is of order-N computational complexity, while maintaining many of the flexibilities present in the global Hermitian RBF collocation method.

The Hermitian RBF method in finite difference mode takes a scattered dataset of internal ("solution") and boundary centres, and forms a local stencil around each non-boundary node (see Figure 1). Additionally, within each stencil a number of PDE centres are distributed. At the boundary centres the boundary operator is enforced within the Hermitian collocation system, at the solution centres the unknown solution value is collocated, and at the PDE centres the PDE governing operator is enforced. In this way a series of small symmetric collocation systems are formed, which can be solved independently to interpolate the solution over the domain in a piecewise fashion.

A series of local RBF collocation systems

$$A^{(k)}\alpha^{(k)} = d^{(k)} \tag{5}$$

are constructed for the interpolation coefficients $\alpha^{(k)}$, where

$$A^{(k)}=\begin{bmatrix} \Psi_{ij} & B_\xi\left[\Psi_{ij}\right] & L_\xi\left[\Psi_{ij}\right] & P_{m-1} \\ B_x\left[\Psi_{ij}\right] & B_xB_\xi\left[\Psi_{ij}\right] & B_xL_\xi\left[\Psi_{ij}\right] & B_x\left[P_{m-1}\right] \\ L_x\left[\Psi_{ij}\right] & L_xB_\xi\left[\Psi_{ij}\right] & L_xL_\xi\left[\Psi_{ij}\right] & L_x\left[P_{m-1}\right] \\ P_{m-1}^T & B_\xi\left[P_{m-1}\right]^T & L_\xi\left[P_{m-1}\right]^T & 0 \end{bmatrix} \quad \text{and} \quad d^{(k)} = \begin{bmatrix} u_i \\ g_i \\ S_i \\ 0 \end{bmatrix} \tag{6}$$

Here the u_i are the unknown values of the solution field u, at the solution centres contained within the local system k. The shape parameter, c, in the multiquadric RBF (1) is kept constant within the local system, but may be allowed to vary from system to system. By defining the shape parameter in terms of the local system support domain size, R, a dimensionless shape parameter may be described (7) which is consistent over varying stencil sizes.

$$c^* = \frac{c}{R} \tag{7}$$

The value of u within the bounds of the local system may be reconstructed as follows

$$u^{(k)}(x) = H(x)^{(k)}\alpha^{(k)} \tag{8}$$

where the "reconstruction vector" $H(x)^{(k)}$ is given by

$$H(x)^{(k)} = \left[\Psi\left(x-\xi_j\right),\ B_\xi\left[\Psi\left(x-\xi_j\right)\right],\ L_\xi\left[\Psi\left(x-\xi_j\right)\right],\ P_{m-1} \right] \tag{9}$$

By inverting the matrix system (6), i.e. $\alpha^{(k)} = \left[A^{(k)}\right]^{-1} d^{(k)}$, it is possible to express the field variable u at any point within the stencil of local system k in terms of the data vector $d^{(k)}$, i.e.

$$u^{(k)} = H(x)^{(k)} \left[A^{(k)}\right]^{-1} d^{(k)} \tag{10}$$

Similarly, the PDE governing operator, L, can be applied to the reconstruction vector $H^{(k)}$ in order to reconstruct its value at any location within the valid domain:

$$\begin{aligned} L\left[u^{(k)}(x)\right] &= L\left[H(x)^{(k)}\right]\alpha^{(k)} \\ &= \left[L_x\left[\Psi\left(x-\xi_j\right)\right],\ L_x B_\xi\left[\Psi\left(x-\xi_j\right)\right],\ L_x L_\xi\left[\Psi\left(x-\xi_j\right)\right],\ L_x\left[P_{m-1}\right]\right]\alpha^{(k)} \end{aligned} \tag{11}$$

As before, by expressing the vector $\alpha^{(k)}$ in terms of the data vector $d^{(k)}$, the value of the PDE governing operator can be given by

$$\begin{aligned} L\left[u^{(k)}(x)\right] &= L\left[H^{(k)}(x)\right]\alpha^{(k)} \\ &= \left(L\left[H^{(k)}(x)\right]\left[A^{(k)}\right]^{-1}\right) d^{(k)} \\ &= W_L^{(k)}(x)\, d^{(k)} \end{aligned} \tag{12}$$

where $W_L^{(k)}$ is a *stencil weights* vector for the differential operator L at local system k. By reconstructing the PDE operator at the system centrepoint, a relation can be obtained linking the values of u_i within the local system

$$\begin{aligned} S(x_{centre}) &= L\left[u^{(k)}(x_{centre})\right] \\ &= W_L^{(k)}(x_{centre})\, d^{(k)} \end{aligned} \tag{13}$$

Applying the above reconstruction to each local system k, a series of N simultaneous equations are produced for $u_i,\ i = 1,\ldots,N$, where N is the global number of solution centres. In the resulting global linear system the corresponding boundary conditions of the problem have already been imposed, at the local interpolation, in those stencils containing boundary points. The resulting linear system is sparse, with the number of non-zero entries in each row equal to the number of solution centres in the corresponding collocation system. Therefore, if the local system size is kept constant, the method may be scaled efficiently to very large datasets. The method of solution for time dependent problems requires the creation of a modified PDE-operator via a finite difference approximation of the time derivative. The procedure is illustrated here using a Θ-weighted Crank-Nicolson approach, but is easily extensible to any number of finite difference time advancement schemes.

For a general initial-boundary value problem

$$\begin{array}{ll} \dfrac{\partial u(x,t)}{\partial t} & = L[u(x,t)] + S_2(x,t) \quad \text{in } \Omega \\ u(x,0) & = f(x) \quad \text{in } \Omega \\ B[u(x,t)] & = g(x,t) \quad \text{on } \Gamma \end{array} \tag{14}$$

a finite difference approximation is made to the time-derivative

$$\frac{u^n - u^{n-1}}{\Delta t} = \Theta L[u^n] + (1-\Theta) L\left[u^{n-1}\right] + S_2(x,t^n) \tag{15}$$

From this approximation, a modified PDE operator is obtained

$$\overline{L}[u^n] = \hat{L}\left[u^{n-1}\right] + S_2(x,t^n) \tag{16}$$

where

$$\begin{aligned} \overline{L} &= 1 - \Theta \Delta t\, L \\ \widehat{L} &= 1 + (1-\Theta)\,\Delta t\, L \end{aligned} \tag{17}$$

The time stepping algorithm implies that the original initial boundary value problem reduces at each time step to the solution of a boundary value problem defined by the non-homogeneous partial differential equation (16), with the non-homogeneous term given in terms of the solution of the problem at the previous time step. As such the solution procedure at each time step is performed in the same way as for the steady problem, using the modified operator, $\overline{L}$, and the corresponding non-homogeneous term, $\hat{L}\left[u^{n-1}\right] + S_2(x,t^n)$.
After solution of the global linear system, and using the current collocation systems and updated data-vectors, a reconstruction of $\hat{L}[u^n]$ at the solution and PDE centres must be made, ready for the next time step. This is done via the creation of further reconstruction arrays

$$\begin{aligned} \hat{L}[u^n(x_i)] &= \hat{L}\left[H^{(k)}(x_i)\right] a^{(k)} \\ &= W_{\hat{L}}^{(k)}(x_i)\, d^{(k)} \end{aligned} \tag{18}$$

for every x_i at which the reconstruction is required, within local system k.
The initial time step is always performed using the $\Theta = 1$ first-order implicit time stepping formulation. Were a value of $\Theta < 1$ to be used, $L\left[u^0\right]$ would be required in order to calculate the non-homogeneous term $\hat{L}\left[u^0\right]$. This quantity is unknown at the initial configuration, and in order to be calculated would require an interpolation of the initial solution field, using a different interpolation system which does not rely on a non-existent previous time step. At subsequent time steps any value of Θ can be chosen without altering the interpolation system.

3. Solution procedure

The nonlinear heat conduction equation is solved, with an arbitrary body source:

$$\rho(T)\, C_p(T) \frac{\partial T}{\partial t} = \frac{\partial}{\partial x_i}\left(k(T) \frac{\partial T}{\partial x_i}\right) + s(x_i,t) \tag{19}$$

where

T is the temperature
ρ is the material density
C_p is the specific heat capacity
k is the thermal conductivity

For convenience, the density and specific heat capacity terms may be combined into the volumetric heat capacity; $c_v(T) = \rho(T) C_p(T)$.
The Kirchhoff integral transformation is applied, in order to reduce the degree of nonlinearity in the governing equation (19). The Kirchhoff transformation is taken as:

$$\psi(T) = \int_{T_0}^{T} k(\chi)\, d\chi \tag{20}$$

By applying the Kirchhoff transformation to the temperature field, equation (19) can be rewritten as:

$$\frac{\partial \psi}{\partial t} = \frac{k(\psi)}{c_v(\psi)} \left(\frac{\partial^2 \psi}{\partial x_i^2} + s(x_i, t) \right) \tag{21}$$

The transformation of the nonlinear diffusion term into Kirchhoff space reduces the equation from a strongly nonlinear to a weakly nonlinear form, by removing the multiplication of first derivatives in the diffusive term:

$$\begin{aligned} \frac{1}{c_v(T)} \frac{\partial}{\partial x_i} \left(k(T) \frac{\partial T}{\partial x_i} \right) &= \frac{1}{c_v(T)} \left[k \frac{\partial^2 T}{\partial x_i^2} + \frac{dk}{dT} \left(\frac{\partial T}{\partial x_i} \right)^2 \right] && \text{Strongly nonlinear} \\ &= \frac{1}{c_v(T)} \frac{\partial^2 \psi}{\partial x_i^2} && \text{Weakly nonlinear} \end{aligned} \tag{22}$$

In order to complete the transformation it is necessary to obtain a closed-form representation of $\psi(T)$ and its inverse function $T(\psi)$, as well as for the two functions $k(\psi)$ and $c_v(\psi)$. If $k(T)$ and $c_v(T)$ are known analytically and are integrable, it is possible to describe these functions exactly. In other cases the functions must be computed numerically . A procedure for this is suggested in Stevens & Power (2010), which can be applied to functions of k and c_v that are sampled in pointwise fashion.
The surface heat flux $q_s(x,t)$ has a corresponding value in Kirchhoff space, which must be used for applied heat-flux boundary conditions:

$$\begin{aligned} q_s(x,\, t) &= -n_i k(T) \frac{\partial T}{\partial x_i} \\ &= -n_i \frac{\partial \psi}{\partial x_i} \end{aligned} \tag{23}$$

In this case the transformation to Kirchhoff space removes the nonlinearity in the boundary condition; a nonlinear heat-flux condition in temperature-space is reduced to a linear Neumann condition in Kirchhoff-space (see equation (23)).
The solution to the nonlinear equation (21) requires a process of nonlinear iterations. The solution procedure performs Picard iterations on the Kirchhoff transform variable and functions thereof, in order to iteratively approach the solution at each timestep. An approximation is taken to the Kirchhoff transform variable ψ, written henceforth as $\hat{\psi}$. From

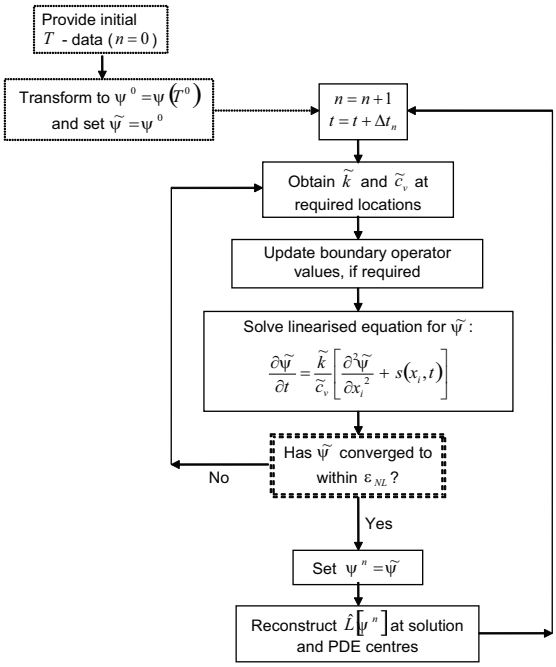

Fig. 2. Schematic description of the nonlinear solution procedure

this, the current guess-values of $\widetilde{k} = k\left(\widetilde{\psi}\right)$ and $\widetilde{c_v} = c_v\left(\widetilde{\psi}\right)$ can be obtained. Within the nonlinear iteration these quantities are considered constant, leading to the linearised equation:

$$\frac{\partial \widetilde{\psi}}{\partial t} = \frac{\widetilde{k}}{\widetilde{c_v}} \left(\frac{\partial^2 \widetilde{\psi}}{\partial x_i \partial x_j} + s\left(x_i, t\right) \right) \tag{24}$$

This equation can be solved directly, using the procedure outlined in section 2. Convergence is examined by comparing the maximum change in $\widetilde{\psi}$ over the nonlinear iteration against a user specified convergence parameter ϵ_{NL}. Once convergence has been reached, the $\hat{L}\left[\widetilde{\psi}^n\right]$ quantity (see equation (16)) can be reconstructed ready for the next time step. This procedure is summarised in Figure 2. The procedure for steady problems is similar, except for the absence of the time-advancement loop and the $\hat{L}\left[\widetilde{\psi}^n\right]$ reconstruction.

4. Validation test case

To validate the implementation of the HRBF-FD method, the unsteady nonlinear heat conduction equation (19) is solved in 3D over a domain, using hypothetical values for the thermal properties and source term. Taking

$$\begin{aligned} k\left(T\right) &= T \\ c_v\left(T\right) &= 1 \\ s\left(x,\, t\right) &= -3 - \left(6 + \lambda r\right) e^{-\lambda t} - 3e^{-2\lambda t} \end{aligned} \tag{25}$$

with α and λ as arbitrary scalar parameters, the governing equation (19) becomes

$$\frac{\partial T}{\partial t} = \frac{\partial}{\partial x_i}\left(T\frac{\partial T}{\partial x_i}\right) - 3 - (6+\lambda r)\, e^{-\lambda t} - 3e^{-2\lambda t} \tag{26}$$

which has an analytical solution given by:

$$T\,(x,\, t) = r\left(1 + \alpha e^{-\lambda t}\right) \tag{27}$$

At the origin, the value of the thermal conductivity becomes zero, and as such the solution becomes singular at this location.

The computational domain is considered to be a cuboid, represented by $x \in [x_{min},\, x_{max}]$, $y \in [y_{min},\, y_{max}]$, $z \in [z_{min},\, z_{max}]$. The analytical solution field (27) is applied at the x_{max}, y_{max} and z_{max} boundaries as a Dirichlet boundary condition. The gradient of the analytical temperature field is imposed at the x_{min}, y_{min} and z_{min} boundaries, i.e.

$$n_i \frac{\partial T}{\partial x_i} = \frac{n_i\, x_i}{r}\left(1 + \alpha e^{-\lambda t}\right) \tag{28}$$

where n_i represents the surface normal at the boundary. At the locations where the Neumann boundaries converge, each of the converging temperature gradient conditions is imposed simultaneously, taking advantage of the double collocation property of the RBF Hermitian method (see LaRocca & Power (2007)). The initial condition is obtained by applying the analytical solution (27) over the interior of the solution domain, at $t = 0$.

Two separate domains are examined. The first domain takes $x_{min} = y_{min} = z_{min} = 0$, and $x_{max} = y_{max} = z_{max} = 2$. As such, the singularity at the origin is included within each of the three Neumann boundaries of the problem. However, the normal temperature gradient at each of these three Neumann surfaces is considered to be zero at the origin, where the singularity lies. This can be considered valid, since the temperature gradient is analytically zero over each of these three surfaces in the limit $r \to 0$. The second domain takes $x_{min} = y_{min} = z_{min} = 1$, and $x_{max} = y_{max} = z_{max} = 3$, leading to a non singular solution throughout the domain, and a non-zero temperature gradient over each of the Neumann boundaries. The two domains described above will be henceforth referred to as the *singular* and the *translated* domains respectively.

The solution domain is discretised using $(11 \times 11 \times 11)$ uniformly distributed solution and boundary centres. Local systems are formed by connecting each of the solution centres to the solution or boundary centre within a single Cartesian index of itself, leading to a stencil of 27 solution or boundary centres. PDE centres are placed at every Cartesian half-index, leading to 8 PDE centres within each local stencil. A dimensionless shape parameter of value $c^* = 5$ is used throughout. The value of the parameters α and λ are both taken to be 0.5. For the transient case, local systems are reformed after every timestep. For the steady case local systems are reformed after every nonlinear iteration. In both cases, the convergence parameter is taken to be $\epsilon_{NL} = 10^{-6}$ in the L_∞ norm. For the transient case a timestep of size $\Delta t = 0.01$ is used, with a variety of time advancement schemes.

Figure 3 shows the variation of the L_2 solution error with time, for the singular case, using three different time advancement schemes. In each case the profile of the error appears similar. The error rises rapidly from the initial condition, reaching its maximum value at around $t = 0.6$. From here the error decreases towards a minimum value at around $t = 5$, before rising again towards a steady value. The second-order $\Theta = 0.5$ time advancement scheme offers the

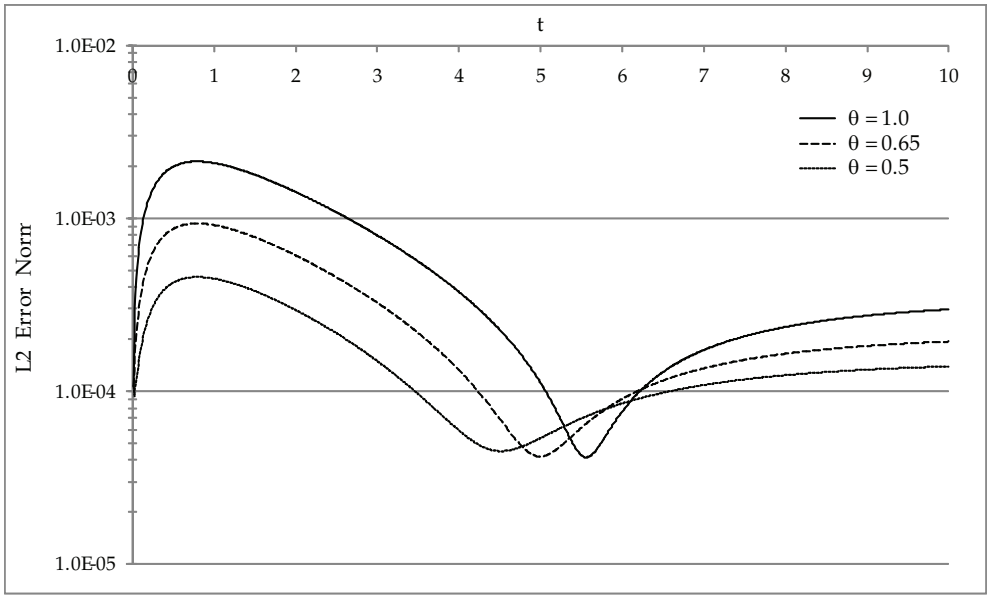

Fig. 3. Variation of L_2 error norm with runtime : Singular case

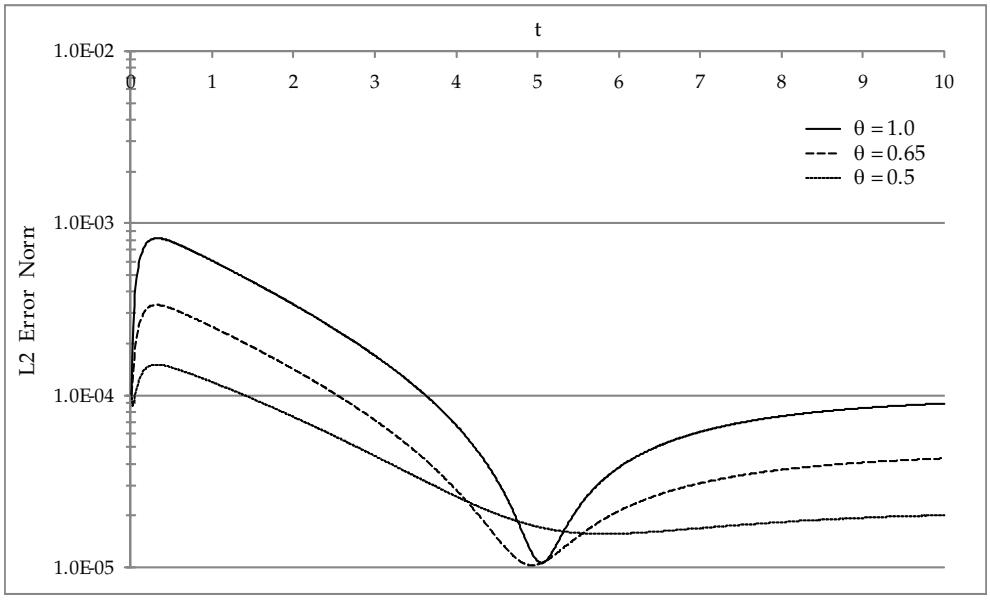

Fig. 4. Variation of L_2 error with runtime : Translated case

best accuracy overall, with the first-order $\Theta = 1$ scheme providing the least accurate solution for most runtimes. The $\Theta = 0.65$ mixed scheme offers accuracy intermediate to the other two schemes.

Figure 4 shows the equivalent error variations for the translated case. Here the accuracy is significantly improved for each of the time advancement schemes, in comparison to the singular case. This is most likely a consequence of the singularity not being present within the solution domain; with the singular case the maximum error is always found at the solution centre closest to the singularity, whereas with the translated case the maximum error location may change as the solution progresses. Once again, the $\Theta = 0.5$ case provides the most accurate solution and the $\Theta = 1$ scheme the least accurate. The error profile appears similar to the singular case, with the main difference being that the peak error is achieved at a much earlier runtime (around $t = 0.2$). In both the singular and translated cases, the solution is replicated to a high degree of accuracy throughout the time advancement procedure.

When the steady solution is obtained directly, using the steady solution procedure, the L_2 error at the solution centres is 1.49×10^{-3} for the singular case, and 3.44×10^{-4} for the translated case. Therefore it appears that approaching the steady solution using any of the transient solution schemes offers a higher degree of accuracy than can be achieved by using the steady solution procedure, when a consistent shape parameter value is used. This is likely a consequence of providing an accurate initial condition to the transient solver. The steady solver begins with an initial guess of $T(x) = 0$.

5. Phase change example

To demonstrate the capability of the method to handle rapid changes in thermal properties, the freezing of mashed potato is considered. The functions for heat capacity and thermal conductivity typically vary rapidly during phase-change, which leads to strong nonlinearity in the PDE governing equation. In this case, a piecewise-linear approximation is taken to the thermal properties in order to facilitate their tuning to experimental results.

The thermal properties for different foodstuffs may vary significantly, however they all share common features (see Figure 5). As their temperature is reduced they go from an unfrozen "liquid" state, through a transitional state, to a fully frozen state at some temperature several degrees below zero. During the transition zone the thermal conductivity changes significantly, and a large spike is observed in the heat capacity, representing the latent heat of fusion. The rapid change in the magnitude of the heat capacity makes the accurate simulation of freezing processes challenging.

Experiments performed at the University of Palermo, Dipartimento di Ricerche Energetiche ed Ambientali, provided data for the freezing of a hemispherical sample of mashed potato. The experiment was then replicated numerically, adjusting the functions for k and c_v using the piecewise linear approximations described above in order to better represent the experimental data. More detail on the experimental setup, the functional parameterisation, and the optimisation procedure are given in Stevens et al. (2011).

To model the freezing process, a 3D hemispherical dataset was created. The dataset is represented in Figure 6, and consists of an unstructured, though fairly regular, distribution of 3380 nodes in total. The base surface of the hemisphere consists of 367 nodes, and at these locations a zero heat-flux boundary condition is applied, representing contact with the insulating material beneath the sample. The upper surface of the hemisphere consists of 1164 nodes, over which a time-varying temperature profile is enforced, as obtained from the (smoothed) experimental results. Additionally, 66 nodes are present along the base edge,

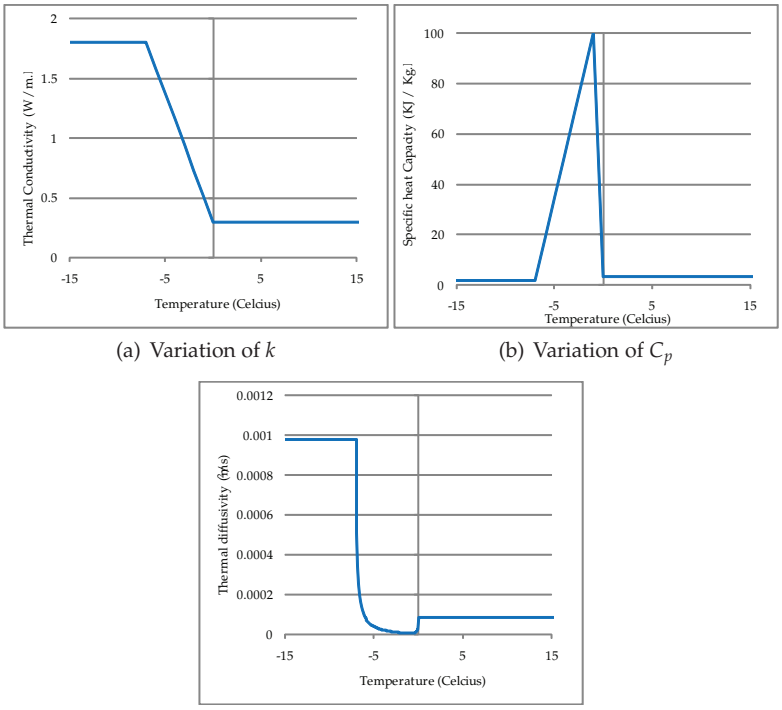

(a) Variation of k

(b) Variation of C_p

(c) Variation of α

Fig. 5. Typical variation of thermal properties with temperature (food freezing case)

where the top surface meets the bottom surface. Over these nodes, both boundary conditions are enforced simultaneously, taking advantage of the double collocation property of the local Hermite collocation method.

The local system size varies slightly, however the modal number of boundary and solution centres present in each local system is 14. Additionally, PDE centres are added to each local system. A tetrahedralisation is performed on each local system, using the boundary and solution centres as nodes, with PDE centres placed at the centre of each resulting tetrahedron. The modal number of PDE centres present in each local system is 24. It is important to note that the tetrahedralisation is performed only to provide suitable staggered locations for the PDE centres, and plays no part in the actual solution procedure, which is entirely meshless. Since the tetrahedralisation is local, it may be performed very cheaply. It is also possible to collocate the PDE centres with the solution and boundary centres, however previous research (see Stevens et al. (2009)) indicates that a staggered placement leads to the most accurate results in the majority of cases.

The simulation is performed using a second-order Crank-Nicholson implicit time advancement scheme, and a timestep of size 50 seconds. The nonlinear convergence parameter is set to $\epsilon_{NL} = 10^{-5}$. The shape parameter is taken as $c^* = 1.0$; significantly lower than in the validation example of section 4. It is typical among RBF methods that cases involving irregular datasets and rapid variations in governing properties will tend to favour

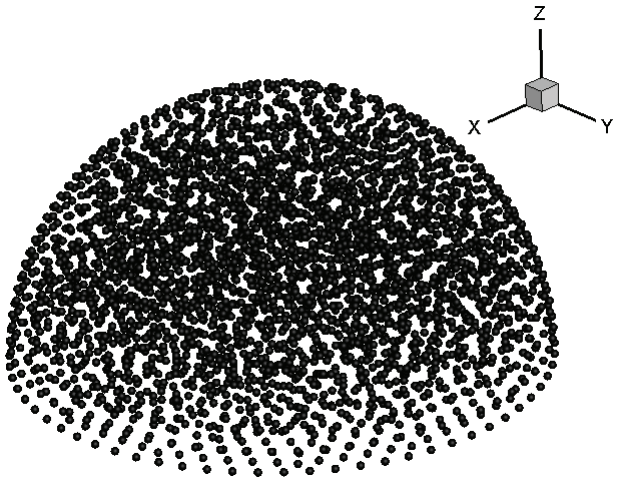

Fig. 6. Computational dataset; boundary and solution centres

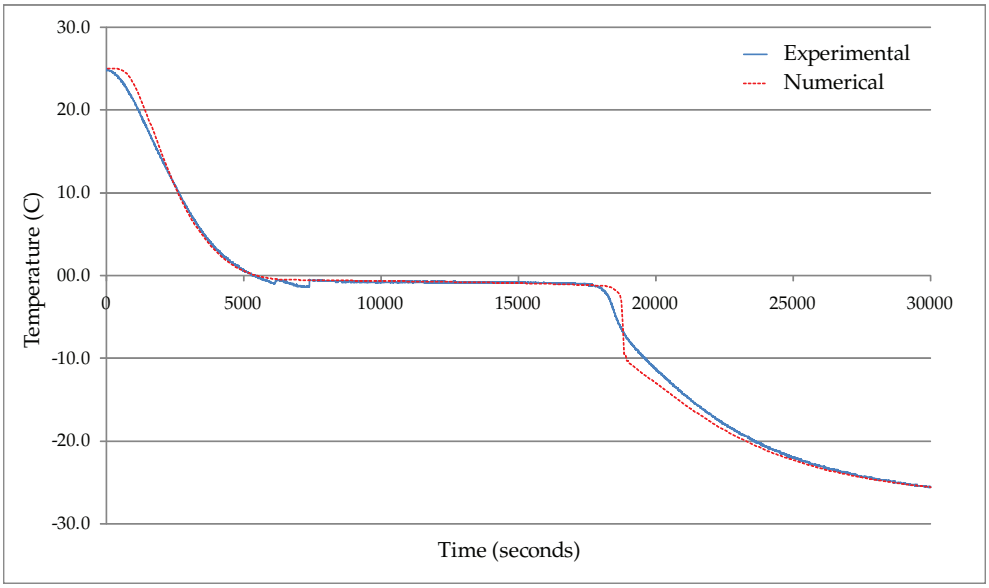

Fig. 7. Comparison of numerical and experimental temperature profiles at the core

lower shape parameters. In this case, a shape parameter of $c^* \geq 2$ can lead to instability in some configurations of the thermal properties shown in Figure 5.

By adjusting eight parameters defining the thermal property functions, it is possible to achieve a good representation of the experimental data. Figure (7) represents the predicted temperature profile at the centre of the base of the hemisphere, compared with the experimental data. The agreement between computational and experimental results is excellent, until around $t = 18000$. At this point, the experimental results show a relatively

gradual drop in temperature between $T_{max} = -1.5^oC$ and $T_s = -4.5^oC$, occurring between $t = 18000$ and $t = 18500$. In contrast, the numerical results predict a near-instantaneous drop in temperature, from T_{max} down to well below T_s, at a slightly later time. This "sudden dropoff" behaviour was replicated across a wide range of thermal parameters, and could represent a limitation in the piecewise-linear approximation to the thermal properties.

The local Hermitian method was able to produce stable results using a wide range of thermal parameters, and convergence at each timestep was typically relatively fast. The size and intensity of the spike in the function for c_p (see Figure 5(b)) is the feature that has most impact upon numerical stability. By increasing the height of the spike sufficiently, it is possible to find configurations where the method is unstable at any shape parameter. This is not unexpected, as an increasingly sharp spike will represent increasingly strong nonlinearities in the governing equation (19), within the phase transition zone. Tests were performed using stencil configurations without PDE centres, i.e. without the "implicit upwinding" feature. However, it was not found to be possible to obtain a stable solution for spikes of intensity close to that which was required to match the experimental results. That inclusion of PDE centres provides a stabilising effect has previously been demonstrated for convection-diffusion problems Stevens et al. (2009), and the stabilising effect appears to be present here also.

6. Discussion

The use of local radial basis function methods in finite difference mode (HRBF-FD) appears to be a viable option for the simulation of nonlinear heat conduction processes, particularly when irregular datasets are required. Traditional polynomial-based finite difference methods are difficult to implement on irregular datasets, and RBF collocation allows a natural generalisation of the principle to irregular data. The inclusion of arbitrary boundary operators within the local collocation systems allows the flexibility to enforce a wide variety of boundary conditions, and the double-collocation property of the Hermitian RBF formulation allows multiple boundary operators to be enforced at a single location where required (such as on converging boundaries).

The inclusion of the governing PDE operator within the local collocation systems is optional, but when present introduces an "implicit upwinding" effect, which stabilises the solution and improves accuracy, at the expense of larger local systems and hence higher computational cost (discussed further in Stevens et al. (2009)). The stabilisation effect is similar to that of stencil-based upwinding, but operates on a centrally defined stencil. Therefore, the HRBF-FD method may be of benefit to problems which may otherwise require upwinding schemes, in particular with unstructured datasets, where the selection of appropriate upwinding stencils may be particularly challenging.

The application of the Kirchhoff transformation greatly simplifies the PDE governing equation and linearises heat-flux boundary conditions, at the cost of requiring thermal property functions to be transformed to Kirchhoff space. Using this Kirchhoff formulation the HRBF-FD method is able to solve a benchmark heat transfer problem to a high degree of accuracy, using both steady and transient solution procedures. Additionally, the method was able to produce stable results for a phase change model involving the freezing of food, in the presence of strongly varying thermal properties. By tuning the thermal properties it was possible to replicate the experimental data to a good degree of accuracy, potentially allowing the calibrated thermal properties to be used in further numerical simulations.

7. References

Baxter, B. (2002). Preconditioned conjugate gradients, radial basis functions, and toeplitz matrices, *Computers and mathematics with applications* 43: 305–318.

Beatson, R., Cherrie, J. & Mouat, C. (1999). Fast fitting of radial basis functions: Methods based on preconditioned gmres iteration, *Advances in Computational Mathematics* 11: 253–270.

Bejan, A. (1993). *Heat Transfer*, John Wiley and Sons.

Brown, D. (2005). On approximate cardinal preconditioning methods for solving pdes with radial basis functions, *Engineering Analysis with Boundary Elements* 29: 343–353.

Chantasiriwan, S. (2007). Multiquadric collocation method for time-dependent heat conduction problems with temperature-dependent thermal properties, *Journal of Heat Transfer* 129: 109–113.

Divo, E. & Kassab, A. (2007). An efficient localised radial basis function meshless method for fluid flow and conjugate heat transfer, *Journal of heat transfer* 129: 124–136.

Driscoll, T. & Fornberg, B. (2002). Interpolation in the limit of increasingly flat radial basis functions, *Computers and mathematics with applications* 43: 413–422.

Fasshauer, G. (1999). Solving differential equations with radial basis functions: multilevel methods and smoothing, *Advances in Computational Mathematics* 11: 139–159.

Hernandez Rosales, A. & Power, H. (2007). Non-overlapping domain decomposition algorithm for the hermite radial basis function meshless collocation approach: applications to convection diffusion problems, *Journal of Algorithms and Technology* 33: 127–159.

Holman, J. (2002). *Heat Transfer*, McGraw-Hill.

Kreith, F. & Bohn, M. (2000). *Principles of Heat Transfer (sixth edition)*, Brookes/Cole.

LaRocca, A. & Power, H. (2007). A double boundary collocation Hermitian approach for the solution of steady state convection diffusion problems, *Comput. Math. Appl.* 55: 1950–1960.

Lee, C., Liu, X. & Fan, S. (2003). Local multiquadric approximation for solving boundary value problems, *Computational Mechanics* 30: 396–409.

Ling, L. & Kansa, E. (2005). A least-squares preconditioner for radial basis functions collocation methods, *Advances in Computational Mathematics* 23: 31–54.

Ling, L., Opfer, R. & Schaback, R. (2006). Results on meshless collocation techniques, *Engineering Analysis with Boundary Elements* 30: 247–253.

Ling, L. & Schaback, R. (2004). On adaptive unsymmetric meshless collocation, *in* S. Atluri & A. Tadeu (eds), *Proceedings of the 2004 international conference on computational and experimental engineering and sciences*, Tech Science Press.

Madych, W. R. & Nelson, S, A. (1990). Multivariate interpolation and conditionally positive definite functions ii, *Mathematics of Computation* 54: 211–230.

Sarler, B. & Vertnik, R. (2006). Meshless explicit local radial basis function collocation methods for diffusion problems, *Comput. Math. Appl.* 51: 1269–1282.

Schaback, R. (1995). Multivariate interpolation and approximation by translates of a basis function, *Approximation Theory VIII*.

Schaback, R. (1997). On the efficiency of interpolation by radial basis functions, *in* A. LeMehaute, C.Rabut & L.L.Schumaker (eds), *Surface fitting and multiresolution methods*, Vanderbilt University Press, pp. 309–318.

Shen, W. & Han, S. (2002). An explicit TVD scheme for hyperbolic heat conduction in complex geometry, *Numerical Heat Transfer, Part B: Fundamentals* 41: 565–590.

Stevens, D., LaRocca, A., Power, H. & LaRocca, V. (2011). Estimation of temperature evolution during the freezing of foodstuffs using a three-dimensional meshless approach, *Journal of Food Engineering* -: (submitted).

Stevens, D. & Power, H. (2010). A scalable meshless formulation based on RBF Hermitian interpolation for 3D nonlinear heat conduction problems, *Computer modelling in engineering and sciences* 55: 111–145.

Stevens, D., Power, H., Lees, M. & Morvan, H. (2009). The use of PDE centres in the local RBF Hermitian method for 3D Convective-Diffusion problems, *J. Comput. Phys.* 228: 4606–4624.

Wendland, H. (1995). Piecewise polynomial, positive definite and compactly supported radial basis functions of minimal degree, *Advances in Computational Mathematics* 4: 389–396.

Wong, A., Hon, Y., Li, T., S.L.Chung & Kansa, E. (1999). Multizone decomposition for simulation of time-dependent problems using the multiquadric scheme, *Computers and Mathematics with Applications* 37: 23–43.

Wright, G. & Fornberg, B. (2006). Scattered node compact finite difference-type formulas generated from radial basis functions, *Journal of Computational Physics* 212: 99–123.

Wu, Z. (1995). Compactly supported positive definite radial basis functions, *Adv. Comput. Math.* 4: 75–97.

Zhang, Y. (2007). Reconstruct multiscale functions using different RBFs in different subdomains, *Applied Mathematics and Computation* 189: 893–901.

Zhou, X., Hon, Y. & Li, J. (2003). Overlapping domain decomposition method by radial basis functions, *Applied Numerical Mathematics* 44: 241–255.

Part 3

Heat Transfer Analysis

14

Heat Transfer Analysis of Reinforced Concrete Beams Reinforced with GFRP Bars

Rami A. Hawileh
American University of Sharjah
United Arab Emirates

1. Introduction

Corrosion of steel reinforcement has been identified as a key factor of deterioration and structural deficiency (Masoudi et al., 2011) in reinforced concrete (RC) structural members. The corrosion state of current RC bridges and high-rise buildings has been a source of concern to designers and engineers. In addition, such structures have been invulnerable to harsh environmental exposures, with little or no maintenance. Furthermore, such structures are experiencing larger amount of loads than their original capacities due to the increase number of users over the years (Bisby, 2003). Several different solutions were proposed to retrofit deteriorated structural members (Masoudi et al., 2011; Hawelih et al., 2011; Al-Tamimi et al., 2011) by replacing cracked concrete, using epoxy injected supplements, and FRP externally bonded systems.

The use of embedded FRP bar reinforcement seems to be a promising solution (Masoudi et al., 2011; Bisby, 2003; Abbasi & Hogg, 2005; Abbasi & Hogg, 2006; Qu et al., 2009; Aiello & Ombres, 2002) to strengthen structural RC members in flexure and shear. Compared to the conventional reinforcing steel bars, the FRP bars seem to have a high strength to weight ratio, moderate modulus of elasticity and resistance to chemical and electrical corrosion. Although FRP materials were shown to have a brittle failure, due to their natural composition, still if designed properly they can show considerable amount of ductility (Rasheed et al, 2010; De Lorenzis & Teng, 2007). One of the draw backs of using FRP embedded bars is their low glass temperature and tendency to change state; from solid to liquid at elevated temperatures. Hence, the performance of FRP reinforced structural members under elevated temperatures draws many doubts and concerns and warrants further investigation. Few experimental tests have been conducted in the previous years on the fire performance of RC beams reinforced with FRP bars due to the high costs of such tests, tremendous amount of preparation, and shortage of specialized facilities (Franssen et al., 2009).

Sadek et al. (Sadek et al., 2006) conducted a full scale experimental program on the fire resistance of RC beams reinforced with steel and Glass Fibre Reinforced Polymer (GFRP) bars. The test matrix composed of different reinforcing rebars used along with different concrete compressive strengths. The testing took place in a special testing facility and the beams were loaded statically at 60% of their ultimate load capacity during the course of the fire test. The tests followed the ASTM E119 (ASTM E119, 2002) standard and fire curve.

Because of forming of flexure and shear cracks, fire was able to penetrate through the cross-section of the tested beams. The beams with low and normal strength concrete achieved a 30 and 45min fire endurance, respectively. On the other hand, the steel reinforced concrete beam achieved 90min fire endurance. The short fire endurance observed was mainly due to the small concrete cover used to protect the flexural reinforcements.

Abbasi and Hogg (Abbasi & Hogg, 2006) conducted two full scale fire tests on RC beams reinforced with GFRP bars as the main reinforcement having a concrete cover of 75mm. The beams were fully loaded up to 40kN and subjected to the ISO 834 (ISO, 1975) fire standard curve. Eurocode 2 (Eurocode, 1992) and ACI-440 (ACI, 2008) procedures were used to design the beams. The beam reinforced with the steel stirrups achieved a 128min fire endurance while the beam reinforced with GFRP stirrups achieved a 94min fire endurance. Both RC beams limited the mid-span deflection to less than L/20; the deflection limit used in the load bearing capacity of BS 476: Part 20. In addition, the RC beams showed that they can pass the building regulations for fire safety by withstanding the fire test more than 90 min.

Hawileh et al. (Hawileh et al., 2009, 2011) developed FE models that predicted the performance of RC beams strengthened with insulated carbon CFRP plates subjected to bottom and top fire loading. The models predicted with reasonable accuracy the experimental results of Williams et al. (Williams et al., 2008). It was concluded the developed models can serve as a valid alternative tool to expensive experimental testing especially in design oriented parametric studies, to capture the response of such beams when subjected to thermal loading.

Different building codes recommend conducting further experimental and analytical research studies to investigate the thermal effect on RC members strengthened or reinforced with FRP sheets, plates or bars. Such studies would lead to a reduction on the tough restrictions and requirements set by the current codes of practice on the use of FRP materials in building and other types of structures. In addition, such studies would draw a better understanding on the behavior of FRP materials under fire actions that would enhance the available documentation and literature that in turn would encourage designers and engineers to use FRP bars more frequently to reinforce RC structural members.

This chapter aims to develop a 3D nonlinear FE model that can accurately predict the temperature distribution at any location with RC beams reinforced with GFRP bars when exposed to the standard fire curve, ISO 834. The model is validated by comparing the predicted average temperature in the GFRP bars with the measured experimental data obtained by Abbasi and Hogg (Abbasi & Hogg, 2006). The developed FE model incorporates the different thermal nonlinear temperature dependant material properties associated with each material including density, specific heat, and thermal conductivity. Transient thermal analysis was carried out using the available FE code, ANSYS (ANSYS, 2007). The results of the developed FE model showed a good matching with the experimental results at all stages of fire loading. Several other observations and conclusion were drawn based on the results of the developed model.

2. Heat transfer equations

Heat transfers via the following three methods: Conduction, Convection, and Radiation. They can occur together or individually depending on the heat source exposure and environment. Conduction transfers heat within the RC beam by movement or vibrations of free electrons

and atoms. On the other hand, convection transfers the heat from the source to the RC beam via cycles of heating and cooling of the surrounding fluids. Radiation is the transfer of heat by electromagnetic waves. The basic one dimensional steady state governing equations for conduction, convection and radiation are presented in Eq. 1-3, respectively.

$$q_k'' = k\,dT/dx \tag{1}$$

$$q_h'' = h\Delta T \tag{2}$$

$$q_r'' = \Phi\varepsilon_t\sigma T_e^4 \tag{3}$$

where,
q_k'' is the heat flux due to conduction
q_h'' is the heat flux due to convection
q_r'' is the heat flux due to radiation
ρ is the density
c is the specific heat
k is the conductivity
h is the convective heat transfer coefficient in (W/m^{2}K), typical vale is 25W/m^{2}K
ΔT is the temperature difference between the solid surface and fluid in (°C or K)
Φ is a configuration or view factor depends on the area (A) of the emitting surface and distance (r) to the receiving surface. ($\Phi = A/\pi r^2$)
ε_t is the emissivity factor, ranged from 0-1.0
σ is the Stefan-Boltzmann constant taken as (5.67×10^{-8} W/m^{2}K^4)
T_e is the absolute temperature of the emitting surface (K)
Furthermore, the three dimensional transient governing heat transfer equation as a function of time is given by Eq. 4. Equation 4 is derived from the Law of Conservation of Energy which states that the total inflow of heat in a unit time across a certain body must be equal to the total outflow per unit time for the same body. It should be noted that Eq. 4 can be solved giving both initial and boundary conditions on a division or all the boundary of the body in question (domain). The initial conditions define the temperature distribution over the domain at the initiation of the heat transfer (i.e. at t = 0). The initial and boundary conditions can be given by Eqs. 5 and 6, respectively:

$$\rho c\frac{\partial T}{\partial t} = k\frac{\partial^2 T}{\partial x^2} + k\frac{\partial^2 T}{\partial y^2} + k\frac{\partial^2 T}{\partial z^2} + S \tag{4}$$

$$T(x,y,z,0) = T_0(x,y,z,0) \tag{5}$$

$$-k\frac{\partial T}{\partial u} = h_c\left(T_S - T_f\right) + h_r\left(T_S - T_f\right) \tag{6}$$

where,
S is the internally generated heat on unit volume per unit time; T is the temperature gradient
t is time; u is the direction of heat; h_c is the heat transfer coefficient of solid surface
T_S is the temperature of solid surface; T_f is the temperature of fluid; h_r is the radiation heat transfer coefficient given by Eq. 7

$$h_r = \sigma \varepsilon_S \left(T_s^2 + T_f^2 \right) \left(T_S + T_f \right) \tag{7}$$

where,

ε_S is the emissivity of the surface in question

σ is the Stefan-Boltzmann constant 5.669 × 10^{-8} W/m^2K^4 (0.1714× 10^{-8} BTU/hr ft^2 R^4)

3. Experimental program

The experimental program of Abbasi and Hogg (Abbasi & Hogg, 2006) is used as a benchmark in this study to validate the accuracy of the developed model. The experimental program (Abbasi & Hogg, 2006) consisted of three RC beams reinforced with GFRP bars. The RC beams were casted using marine siliceous gravel coarse aggregates. Figure 1 shows the cross-section detailing of the tested RC beams. The beams had a height and width of 400 mm and 350 mm, respectively and effective depth of 325 mm. The concrete cover from the beam's soffit to the GFRP flexural reinforcement was 75 mm. The total length of the beam specimens was 4400 mm having an exposed span length of 4250 mm. The beams were reinforced with nine Φ12.7 mm (Area= 1303.6mm^2) GFRP bars, seven were placed in two layers at the tension side and two serving as compression reinforcement. In addition, Φ9 mm stirrups were used as shear reinforcements spaced at 160mm center to center. The concrete compressive strength was 42MPa. The first beam specimen was tested under monotonic loading at ambient temperature conditions to serve as a control beam. The other two beams were tested under sustained static and transient fire loading defined according to ISO 834.

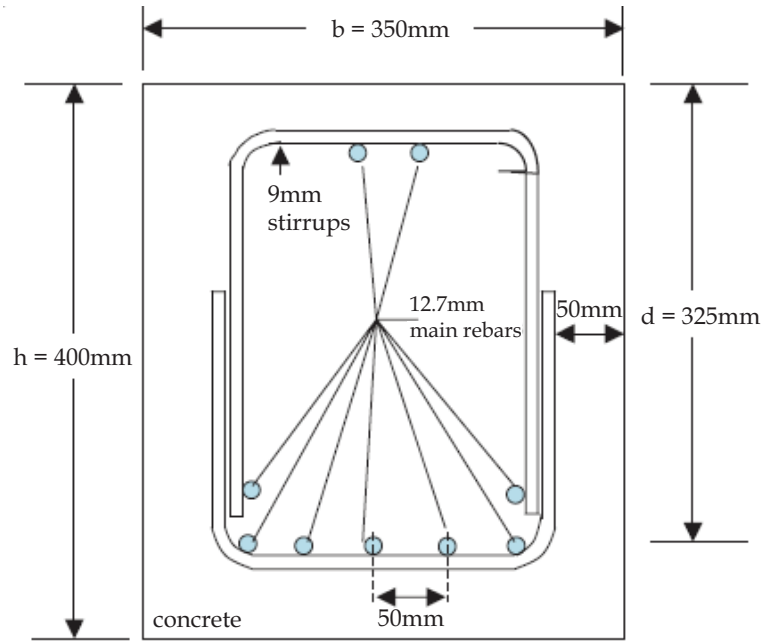

Fig. 1. Details of the tested RC beams (Abbasi & Hogg, 2006)

The fire testing was conducted at the building research establishment (Abbasi & Hogg, 2006). The internal dimensions of the furnace were 4000mm wide, 4000mm long and 2000mm deep. Each side of the furnace contained 10 burners lined in parallel to each other. The top side of the furnace is closed with either the test specimen, or lined with steel cover slabs. On the other hand, the furnace is lined with 1400 grade insulating brick to comply with British Standard and ISO 834 requirements.

4. Finite element model development

The developed FE model has the same geometry, material properties, and loading as the tested GFRP-RC beam by (Abbasi & Hogg, 2006). The FE model was developed and simulated using the commercial FE code, ANSYS 11.0 (ANSYS, 2007). Figure 2 shows a detailed view of the developed FE model. To take advantage of the symmetrical nature of the geometry, material properties and heat transfer actions, only one-quarter of the RC beam was modeled. The development of a one-quarter model will still yields the same accuracy as the full scale model and saves a lot of computational time.

In order to simulate such complex behavior, an analytical procedure must be determined. Firstly, the different material properties and corresponding constitutive laws were collected from the open literature. Then, the development of the geometry and simulation enviroment was conducted using ANSYS (ANSYS, 2007) were different element types, meshing and simulation techniques were incorporated to simulate the concrete and reinforcing GFRP bars elements. Finally, a 3D transient thermal analysis is conducted to simulate the applied ISO 834 fire curve.

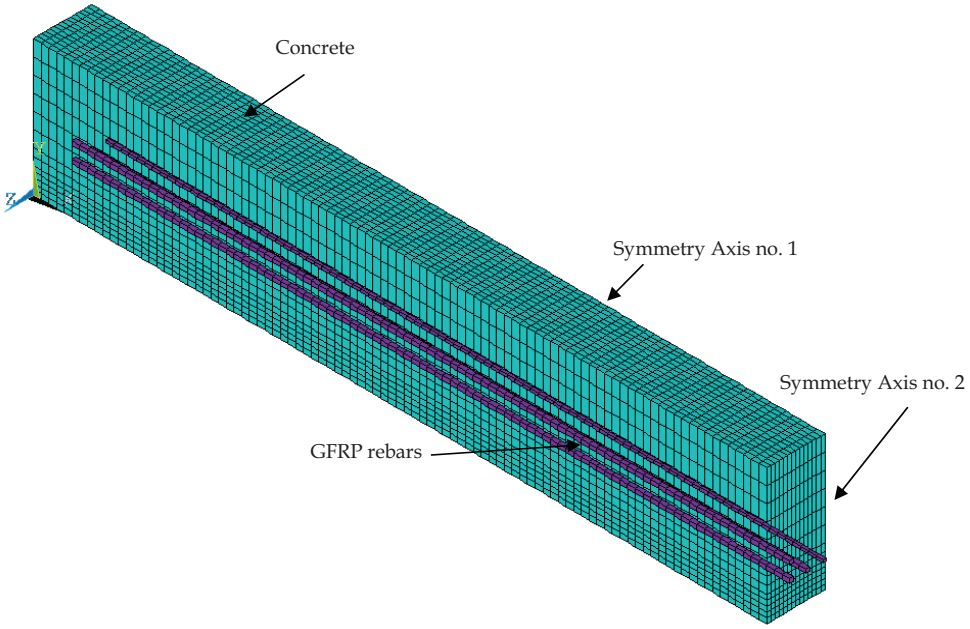

(a) Isoperimetric view

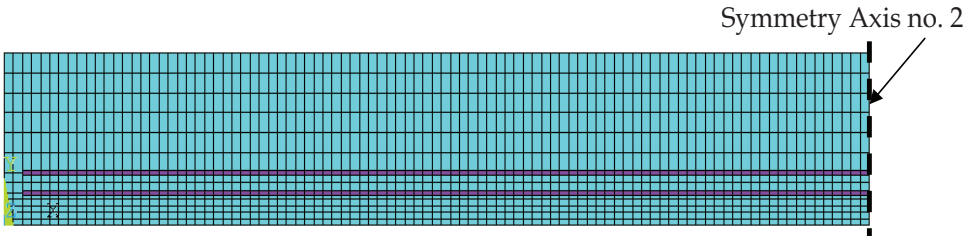

(b) Side view

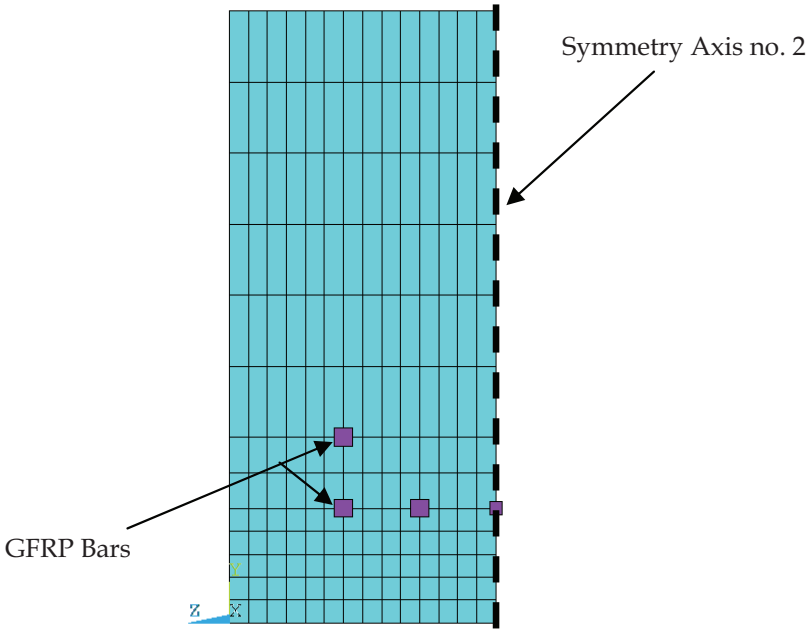

(c) Cross-sectional view

Fig. 2. Developed FE model

Different element types were selected from the ANSYS element type selection library. The thermal elements implemented to model the concrete material and reinforcing GFRP rebars were SOLID70 and LINK33, respectively. SOLID70 has eight nodes with a single degree of freedom at each node, defined as temperature as well as 3-D thermal conduction capability. SOLID70 has 2×2×2 integration scheme for both conductivity and specific heat matrices. On the other hand, GFRP rebars were modeled using LINK33. LINK33 is a thermal uniaxial element with the ability to conduct heat between its two nodes. The element has a single degree of freedom SDF, temperature, at each node. In addition, both elements are applicable to conduct 3-D, steady-state and/or transient thermal analysis (ANSYS, 2007). Figure 3 shows the different element types used in this study.

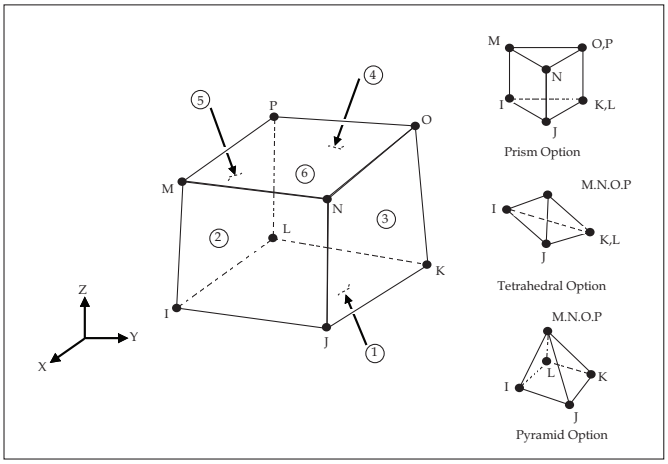

(a) SOLID70

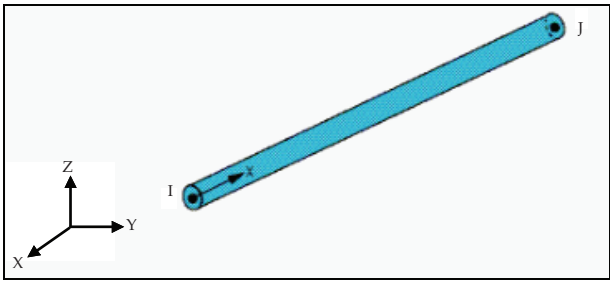

(b) LINK33

Fig. 3. 3-D Thermal elements (ANSYS, 2007)

4.1 Material constitutive models

The thermal material properties are required as inputs to the developed FE model. Table 1 tabulates the thermal properties for the concrete and GFRP bars materials used in this study at room temperatures. Figure 4 shows the thermal concrete material temperature-dependent material properties including the conductivity and normalized density and specific heat.

Material	K_o (W/mm K)	C_o (J/kg K)	ρ (kg/mm^3)
Concrete	2.7×10^{-3}	722.8	2.32×10^{-6}
GFRP	4.0×10^{-5}	1310	1.60×10^{-6}

Table 1. Thermal material properties at ambient room temperature

where,
K_o is the thermal conductivity (W/mm K)
C_o is the heat capacity (J/kg K)
ρ is the density (kg/mm^3)

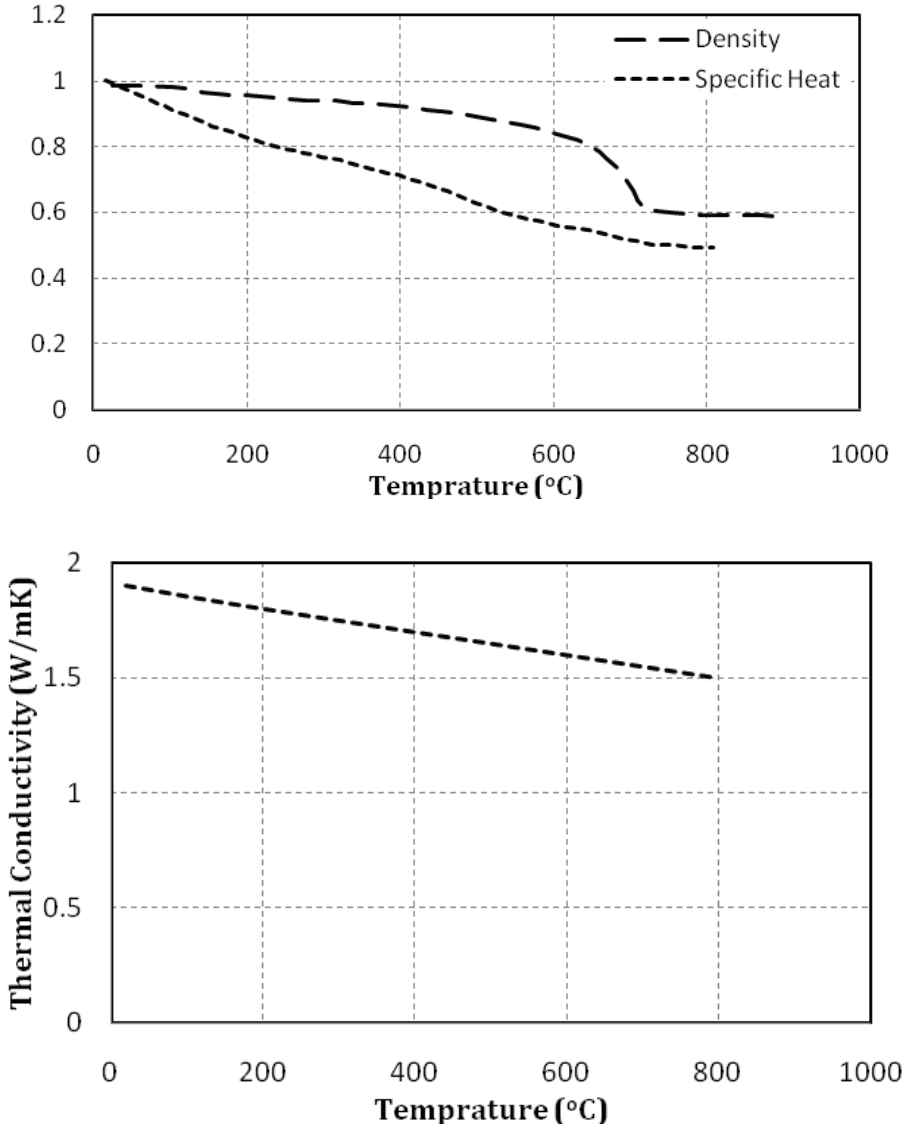

Fig. 4. Thermal temperature-dependent material properties of concrete material

Few limited studies were conducted on the mechanical temperature-dependant properties of GFRP bars (Abbasi & Hogg, 2005). Abbasi and Hogg (Abbasi & Hogg, 2005) recommended empirical equations to predict the mechanical properties (stiffness, tensile strength, etc.) as a function of increasing temperature. To the top of the author's knowledge, there is no available data in the open literature on the thermal material-dependant properties of GFRP bars. Thus, the thermal material properties of the GFRP bars at ambient room temperature are used in this study.

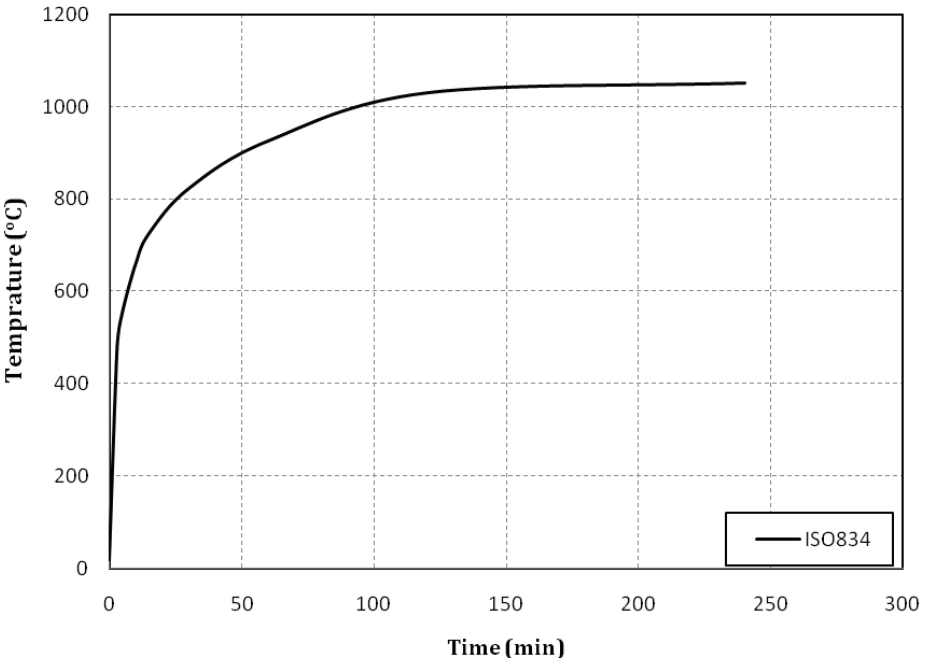

Fig. 5. The applied ISO 834 fire curve

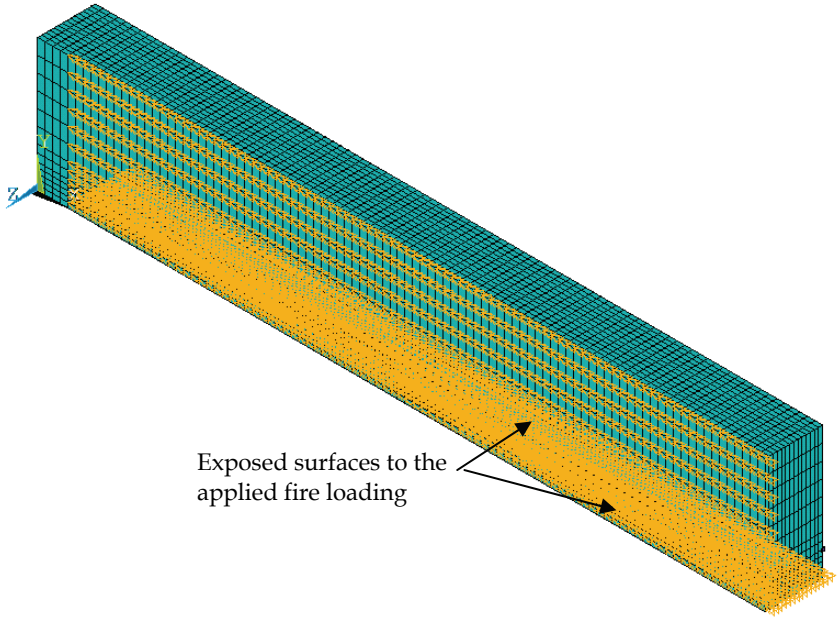

Fig. 6. Location of applied nodal temperatures

4.2 Loading & boundary conditions

The developed FE model was exposed to thermal transient temperature-time curve, ISO834 (ISO, 1975). The applied ISO 834 fire curve is shown in Fig. 5. The ISO 834 curve was applied as nodal temperature loading versus time at the soffit and vertical sides of the RC beam specimen. The locations of the applied nodal transient temperatures are shown in Fig 6. It must be noted that the applied nodal temperatures in the transient analysis domain started at 200mm away from the edge of the RC beam to simulate the furnace boundary conditions.

Since the fire nozzles in the furnace are very close to the tested RC beams, the author applied the average furnace temperature directly to the soffit and sides of the developed FE model (Hawileh et al., 2009, 2011). Thus, heat is transferred mainly by conduction in the developed model. This approach resulted in good matching with the temperature results recorded in the experimental program by Abbasi and Hogg (Abbasi & Hogg, 2006) and will be discussed in the subsequent section.

The average furnace temperature was applied in terms of small time incremental steps. Each time step is composed of several smaller sub-steps that are solved using Newton-Raphson's technique. In this study, automatic time stepping option is turned on to predict and control time step sizes. At the end of each time (temperature) step, convergence is achieved by Newton-Raphson equilibrium iterations when the temperature difference at each node from each iteration to another is less than one degree.

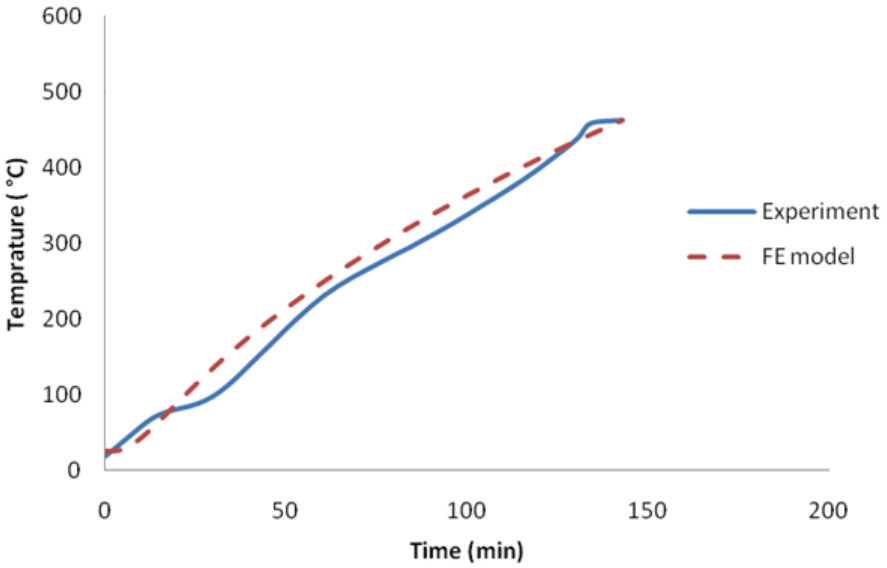

Fig. 7. Comparison between measured and predicted average temperature in the GFRP bars

4.3 Failure criteria

The failure criterion adopted in this study was based upon reaching a critical temperature in the GFRP bars. There has been a lot of debate on defining a critical temperature for FRP

bars. In this study, a critical temperature of 462°C in the GFRP is defined as the failure criteria. Thus, the time to failure (fire endurance) of the RC beam specimen is defined when the temperature in the GFRP bars reached 462°C during fire exposure. The same criteria is used in the experimental program of Abbasi and Hogg (Abbasi & Hogg, 2006).

5. Results and discussions

5.1 Model validation

The predicted FE and experimental results were compared in order to validate the accuracy of the developed model presented in this study. Figure 7 shows a comparison between the predicted and measured average temperature of the GFRP bars during the course of fire loading. The predicted average temperature in the GFRP bars is obtained every 0.5 second time increment. It is clear from Fig. 7 that there is a good correlation between the predicted and measured results throughout the entire thermal fire exposure. It should be noted from Fig. 7 that the predicted average temperature results overestimates the temperature after 25 minutes of fire exposure. This slight deviation could be related to the lack of temperature-dependant material properties of the GFRP bars. The tested RC beam failed approximately after 128min of fire exposure, when the average temperature in the GFRP bars reached 462°C. Similarly, the predicted time to failure is 130 minutes. The percentage difference between the FE model and experimental testing time to failure was 1.5%. Thus, the developed model could serve as a valid numerical tool to predict the temperature distribution of RC beams strengthened with GFRP bars when exposed to transient thermal loading.

5.2 Model behavior

The experimental programs are restricted to limited number of instrumentations (thermocouples and strain gauges) due to their high cost and complex preparation. On the contrary, full fields of temperature distribution at any location (node) within the beam could predicted from the FE simulation of the validated model. Having a viable FE model, further results can be extracted and used. For instance, Fig. 8 shows the temperature evolution across the beam's cross section at different time periods of fire exposure. Figure 8 could be used to determine the nodal temperature at any point (node) within the beam especially at the GFRP bar reinforcement. As expected, the temperature evolution starts at the edges, then propagate within the beam. It seems that the available concrete cover is sufficient to delay the increase of temperature at the GFRP reinforcement level up to 130min. Figure 9 shows the temperature distribution along the RC beam specimen at the end of fire. The FE simulation can thus provide a wide range of results and the developed model could be used as an alternative to the expensive experimental testing.

The experimental program lacked data on the increase of temperature in the individual GFRP bars during the fire exposure. However, the FE model can predict the increase of temperature at any specific location and time. Figures 10 and 11 shows the location of the GFRP bars and temperature evolution in the individual bars at mid-span during fire exposure. It is clear from Fig. 11 that the temperature rise in GFRP Bar 2 is the highest. This is due to the application of the fire curve to the soffit and vertical side of the RC beam specimen. Being located at the corner, Bar 2 thus has the shortest distance to the exposed surfaces. Although Bars 1 and 3 seem to have the same perpendicular distance from the exposed edge, the increase in temperature of Bar 1 seems to be slightly lower than that of

Bar 3. This could be related to the small bar spacing Bar 2 and Bar 4 that would increase of temperature in the closely spaced GFRP bars. Furthermore, upon comparing the increase of temperature in Bars 3 and 4, Bar 3 seems to experience higher temperatures because it is closer to the exposed faces than that of Bar 4. Figure 12 shows the temperature distribution along the GFRP bars after 130min of fire exposure. Figure 12 also shows that the edge GFRP bar (Bar 2) experienced the highest increase of temperature during fire exposure.

6. Summary and conclusions

A nonlinear 3D FE model was developed in this study and validated against the experimental program conducted by Abbasi and Hogg (Abbasi & Hogg, 2006). Good agreement between the measured experimental and predicted FE simulation was obtained for the average temperature in the GFRP bars at all stages of fire exposure. Although the UK Building Regulations (Building Regulations, 2000) for fire safety recommends the minimum periods of the fire resistance for the most structural elements to be of 90 min, the fire tests and FE simulation results showed that concrete beams reinforced with GFRP bars can achieve a fire endurance of about 130 minutes. Thus, using GFRP bars as concrete reinforcement seems to meet the fire design requirements.. Upon the validation of the measured data, the FE modeling could provide full field of results, in terms of 3D temperature distribution. It could be concluded that the developed FE model is a great tool to aid designers and researchers to predict numerically the temperature distribution of RC beams reinforced with GFRP bars. Thus, the validated model could be used as a valid tool in lieu of experimental testing especially in design oriented parametric studies. Furthermore, the developed and verified FE model in this study could be used as a tool for further investigation of the fire performance of RC beams reinforced with GFRP bars under different applied fire curves and boundary conditions.

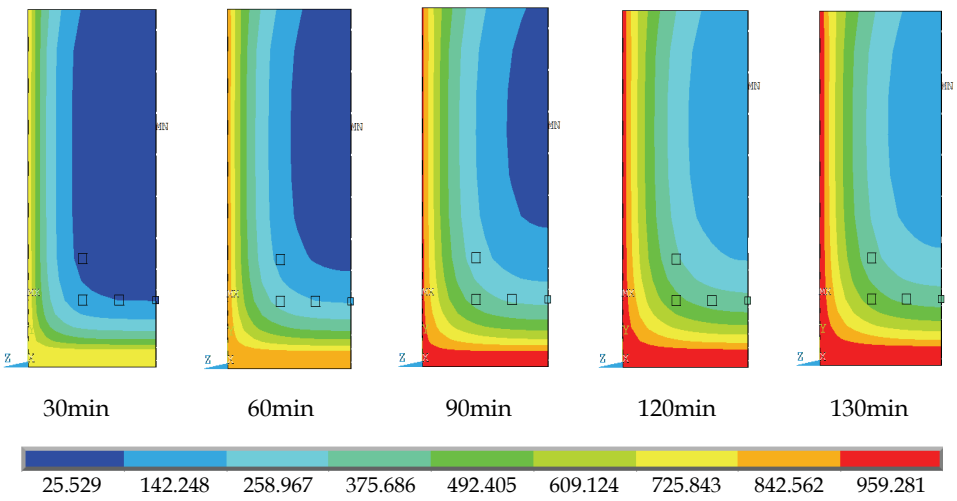

Fig. 8. Temperature evolutions at different time of fire exposures

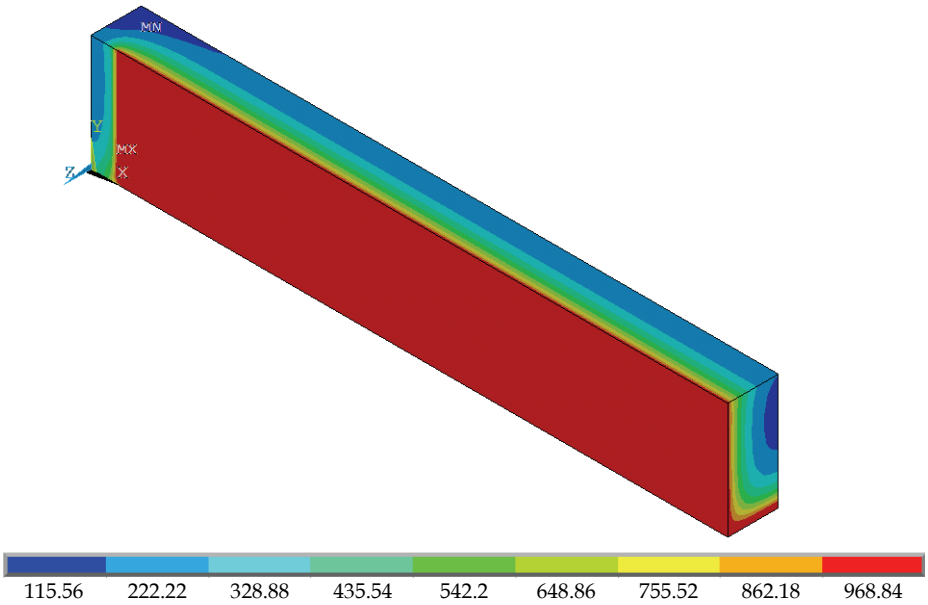

Fig. 9. Temperature distribution at the end of thermal loading

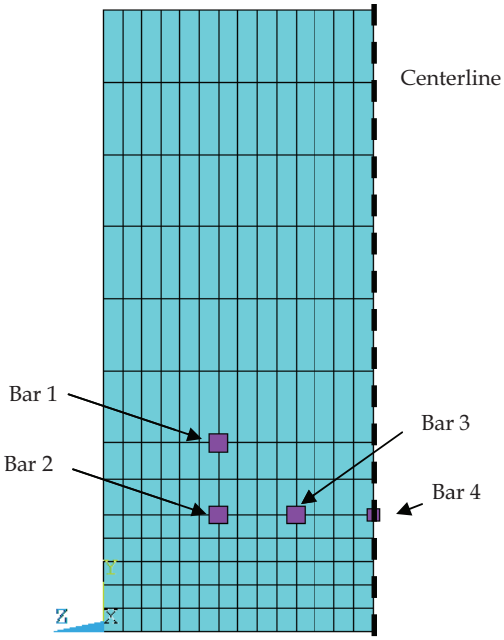

Fig. 10. Location of GFRP bars within Beam's cross-section

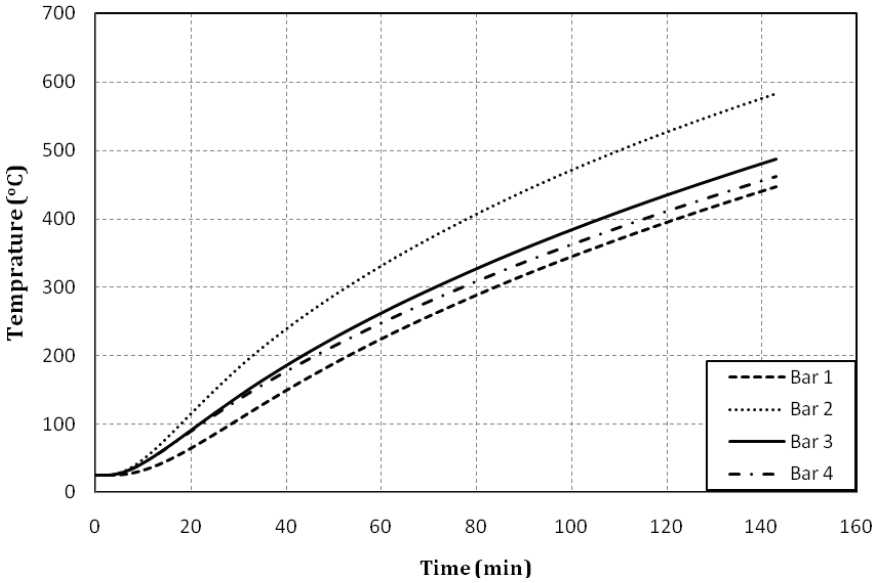

Fig. 11. Predicted temperature evolution in the GFRP bars

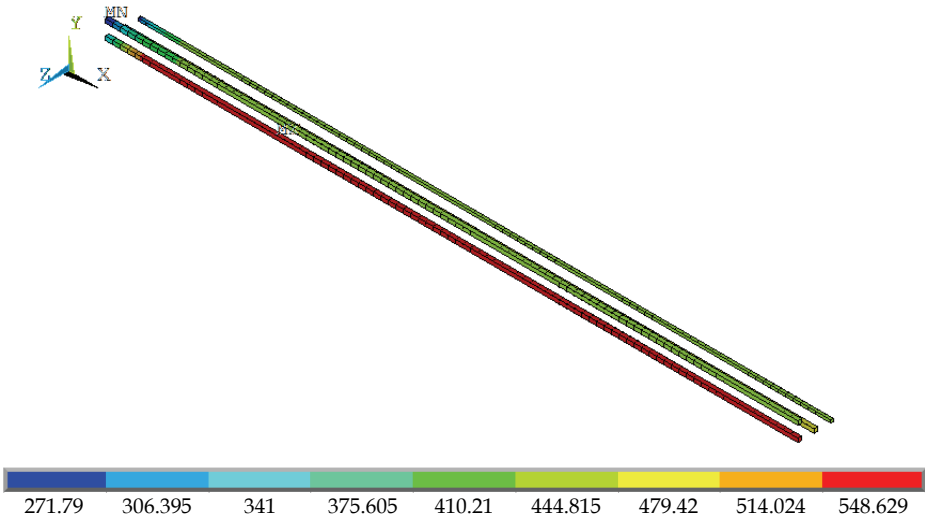

Fig. 12. Temperature distribution along the GFRP bars after 130min of fire exposure

7. Future research

- Experimental studies on the temperature-dependent thermal properties of GFRP bars are warranted.

- Extend the current analysis into a 3D nonlinear thermal-stress analysis that can capture the response of RC beams reinforced with GFRP reinforcement.
- Conduct several parametric studies on the developed model to investigate the temperature distribution under different applied fire exposure curves.
- Investigate the temperature distribution when the beams get exposed to different fire local exposures.

8. References

Abbasi, A. & Hogg, PJ. (2005). Temperature and environmental effects on glass fibre rebar: modulus, strength and interfacial bond strength with concrete. *Composites: part B*, Vol.36, No.5, (2005), pp. 394-404

Abbasi, A. & Hogg, PJ. (2005). Prediction of the Failure Time of Glass Fiber Reinforced Plastic Reinforced Concrete Beams under Fire Conditions. *Journal of Composites for Construction*, Vol.9, No.5, (2005), pp. 450-457

Abbasi, A. & Hogg, PJ. (2006). Fire testing of concrete beams with fibre reinforced plastic rebar. *Composites: part A*, Vol.37, (2006), pp. 1142–1150

ACI Committee, Guide for the design and construction of concrete reinforced with FRP bars. Reported by ACI Committee 440; January 5, 2001.

Aiello, M. & Ombres, L. (2002). Structural Performances of Concrete Beams with Hybrid (Fiber-Reinforced Polymer-Steel) Reinforcements. *Journal of Composites for Construction*, Vol.13, No.5, (2002), pp. 133-140

Al-Tamimi, A., Hawileh, R., Abdalla, J. & Rasheed, H. (2011). Effects of Ratio of CFRP Plate Length to Shear Span and End Anchorage on Flexural Behavior of SCC R/C Beams. *Journal of Composites for Construction. Accepted.*

ANSYS – Release Version 11. A Finite Element Computer Software and User Manual for Nonlinear Structural Analysis, ANSYS 2007; Inc. Canonsburg, PA.

ASTM E119. Standard test methods for fire tests of building construction and materials. West Conshohocken, PA: ASTM international; 2002. 22 pp

Bisby L. Fire behavior of fiber-reinforced polymer reinforced or confined concrete. Ph.D. thesis. Kingston (Canada): Department of Civil Engineering, Queen's University; 2003. 371 pp.

Building Regulations 2000. (2000). Fire Safety, Amendments 2002 to Approved Document B (Fire safety) published by TSO (The Stationary Office).

De Lorenzis L. & Teng JG. (2007). Near-surface mounted FRP reinforcement: an emerging technique for strengthening structures. *J Compos, Part B*, Vol.38, (2007), pp. 119–143.

Eurocode 2, Design of concrete structures, ENV EC2 Part 1.2; 1992.

Franssen, J., Kodur, V. & Zaharia, R. (2009). *Designing Steel Structures for Fire Safety*. Taylor & Francis Group, London, UK.

Hawileh, R. Naser, M. Zaidan, W. & Rasheed, H. (2009). Modeling of insulated CFRP-strengthened reinforced concrete T-beam exposed to fire. *Eng Struct,* Vol.31, No.12, (2009), pp. 3072-79.

Hawileh, R., Tamimi, A., Abdalla, J.A. & Wehbi, M. (2011). Retrofitting Pre-cracked RC Beams Using CFRP and Epoxy Injections. *In Proceeding of the Eight International Conference On Composite Science* and *Technology (ICCST/8).*

Hawileh, R., Naser, M. & Rasheed, H. (2011). Thermal-Stress Finite Element Analysis of CFRP Strengthened Concrete Beam Exposed to Top Surface Fire. *Mechanics of Advanced Materials and Structures*, Vol.18, No.3, (2011). Loading

ISO-834, Fire resistance tests, Elements of building construction. International Standards Organisation, Geneva; 1975.

Kodur, V. &Ahmed, A. (2010). A Numerical Model for Tracing the Response of FRP-Strengthened Reinforced Concrete Beams Exposed to Fire. *Journal of Composites for Construction*, Vol.14, No.6, 2010, pp. 730-742

Masoudi, R., Masoudi, A., Ouezdou, B. & Daoud, A. (2011). Long-term bond performance of GFRP bars in concrete under temperature ranging from 20°C to 80°C. *Construction and Building Materials,* Vol.25, No.2, (2011), pp. 486-493

Rasheed, H.A., Harrison, R.R., Peterman, R.J. & Alkhrdaji, T. (2010). Ductile Strengthening Using Externally Bonded and Near Surface Mounted Composite Systems. *Composite Structures,* Vol.92, No.10, (2009), pp. 2379-2390

Sadek, A., El-Hawary, M. & El-Deeb, A. (2006). Fire Resistance Testing of Concrete Beams Reinforced by GFRP Rebars. *European Journal of Scientific Research,* Vol.15, No.2, (2006), pp. 190-200

Qu, W., Zhang, X., & Huang, H. (2009). Flexural Behavior of Concrete Beams Reinforced with Hybrid (GFRP and Steel) Bars. *Journal of Composites for Construction*, Vol.6, No.2, (2009), pp. 350-359.

Williams, B., Kodur, V.K.R., Green, M.F. & Bisby, L. (2008). Fire Endurance of Fiber-Reinforced Polymer Strengthened Concrete T-Beams. *ACI Struct. J.*, Vol.105, No.1, (2008), pp. 60–67.

15

Modelling of Heat Transfer and Phase Transformations in the Rapid Manufacturing of Titanium Components

António Crespo
Instituto Superior Técnico
Portugal

1. Introduction

Over the last thirty years a new generation of manufacturing processes have been developed whereby fabrication takes place by the sequential addition of material at specific locations on a layer-by-layer basis to produce near-net-shape three-dimensional parts. These processes are generically known as solid freeform fabrication or rapid manufacturing, and their most prominent features are fast delivery times, material wastage reduction and the ability to produce parts directly from a CAD file in a single fabrication step without the need for hard tooling. These characteristics lead to lower costs and faster production cycles than those of hard-tooling based methods, and have made solid freeform fabrication an attractive choice for the production of customised one-of-a-kind parts, prototyping and short-run production. For the manufacture of metallic components these techniques involve the use of a localised energy source, typically a laser beam, to consolidate layers of metallic materials supplied in the form a pre-placed powder bed, blown powder stream or wire feeding. By scanning the interaction zone of the energy source and the material over a substrate and according to a previously defined trajectory, a track of resolidified material is produced and the overlapping of tracks enables the manufacture of near-net-shape components, as shown schematically in Figure 1.

One important feature of rapid manufacturing techniques is that, as a result of layer overlap during part buildup, the deposited material undergoes consecutive thermal cycles with a duration and amplitude which depend on the processing parameters and on the shape and dimensions of the part being manufactured. These thermal cycles induce phase transformations in the material leading to a progressive modification of its microstructure and properties. Since the thermal history varies from point to point in the part, the material will in general present complex distributions of microstructure and properties. To optimise the manufacturing process to obtain parts fulfilling specific requirements, the influence of the processing conditions and build-up strategy on the final microstructure and properties of the material must be assessed. The complexity of the thermal cycles taking place during the manufacture of components and the impossibility of directly monitoring the thermal and microstructural evolution of the material during the fabrication process make empirical or experimental build-up strategy optimisation impractical. However, the optimisation of the process can be carried out efficiently using a computational approach based on a model

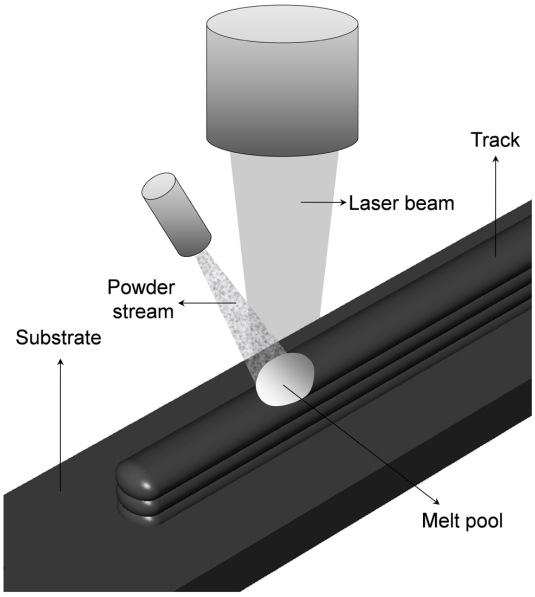

Fig. 1. Rapid manufacturing using a laser beam to consolidate blown powder particles into a final part

that simulates the microstructure formation mechanisms in the material, in particular the phase transformations caused by the heat and mass transfer phenomena that take place during fabrication. Such a model should use as input the processing parameters and the part shape and dimensions to predict the final microstructure and properties distributions in the manufactured part. This type of approach provides a cheap and rapid way of optimising the manufacturing process and obtaining parts fulfilling unique and specific properties requirements. Several researchers such as L. Costa (Costa et al., 2005), S. M. Kelly (Kelly & Kampe, 2004b), Toyserkani et al. (Toyserkani et al., 2004), have successfully used computational approaches to analyse the influence of the processing parameters on several aspects of the process, such as the heat transfer mechanisms, the microstructure formation processes or the evolution of the properties of the material, among others (Crespo et al., 2006; Labudovich et al., 2003; Vasinonta et al., 2001; Wang et al., 2008).

In addition to microstructural transformations, the consecutive thermal cycles imposed on the material are also responsible for the accumulation of internal stresses in parts produced by rapid manufacturing techniques. During the fabrication process, the thermal cycles experienced by the material will give rise to thermal expansion and contraction. Since the deposited material is cyclically subjected to steep temperature variations, the thermal expansion gradients ocurring in the material give rise to the development of internal stresses in the workpiece. These stresses can be high enough to cause yield in some regions or lead to complex residual stresses patterns in the final parts. The study of the development of residual stresses during rapid manufacturing processes has been the subject of several investigations aimed at acquiring a thorough insight into this phenomenon and at establishing processing parameters sets and build-up strategies

conducive to mechanically sound components (Crespo et al., 2008; Deus & Mazumder, 2006; Ghosh & Choi, 2005; Kahlen & Kar, 2001; Labudovich et al., 2003). Although the study of residual stresses formation during manufacture is out of the scope of the present work, the model presented in this chapter has been extended to study these phenomena and a detailed description of the methodology can be found in the work of A. Crespo (Crespo, 2010).
This chapter reports the development of a finite element thermo-kinetic model that couples heat transfer calculations with phase transformation kinetics theory to investigate the influence of the build-up strategy and processing parameters on the distributions of microstructure and properties of titanium parts manufactured by rapid manufacturing processes. The model was validated by comparing its predictions for the phase constitution, Young's modulus and hardness distributions with experimental results measured on parts fabricated by a laser based rapid manufacturing technique, and used to construct processing maps relating the deposition parameters to the microstructure and properties of the parts.

2. Modelling of heat transfer in rapid manufacturing processes

Rapid manufacturing processes are characterised by the continuous addition of material on a layer-by-layer basis to produce a final component. In order to process the different layers into a consolidated part an energy source is typically used to heat up and melt the feedstock material before incorporation into the part (Figure 1). This type of manufacturing subjects the processed material to consecutive thermal cycles which induce a sequence of phase transformations that alter the microstructure and properties of the material, and which, if not properly controlled, may render the final parts useless. Therefore a critical aspect of additive manufacturing is the control of the different heat transfer phenomena that take place during build-up and which determine the properties and quality of the final parts.

2.1 Heat transfer equations

The phase transformations during rapid manufacturing are determined by the thermal history of the material, which is the result of energy absorption by the material, heat conduction within the workpiece being built and heat losses by convection and radiation to the environment. The temperature field evolution within the material can be calculated by solving the three-dimensional heat conduction equation. Thermal conduction in an isotropic solid region Ω is a time dependent 3-D problem described by the following partial differential equation:

$$\rho C_p \frac{dT(\vec{r},t)}{dt} = \nabla \left[k \nabla T(\vec{r},t)\right] + Q, \tag{1}$$

where $T(\vec{r},t)$ is the temperature $(^\circ C)$, ρ the density of the solid (kgm^{-3}), k the thermal conductivity $(W^\circ C^{-1}m^{-1})$, C_p the specific heat $(J^\circ C^{-1}Kg^{-1})$ and Q a generic internal heat generation rate (Wm^{-3}) which can account, for example, for phenomena associated with latent heats of transformation. The thermal properties of materials are usually temperature dependant, that is: $\rho = \rho(T)$, $k = k(T)$ and $C_p = C_p(T)$. To apply the heat conduction equation to time-dependants problems, such as simulating a fabrication process, an initial condition specifying the initial temperature distribution in the part must also be provided:

$$T(\vec{r}, t = 0) = T_0(\vec{r}), \quad \vec{r} \in \Omega. \tag{2}$$

Additionally, the influence of the energy source used to process the material has to be taken into consideration. The best way to model the interaction between the heat source and the material depends on the particular characteristics of the energy source being used such as its power, power density, shape and the way it is absorbed or transferred into the material. Probably the most common way of processing metallic materials for rapid manufacturing purposes is to utilise a laser beam. Assuming, for example, a gaussian distribution of the laser beam power , the energy input into the material can be described by:

$$q_{laser} = \alpha \frac{2.P}{\pi.r_l^2} exp[-\frac{2.r^2}{r_l^2}], \tag{3}$$

where P is the laser beam power, α the absorptivity of the material to the radiation being used, r_l the spot radius of the laser beam and r the distance to its centre, respectively. Energy losses to the environment by convection and radiation are described by:

$$Q_{convection} = h\left[T(\vec{r},t) - T_\infty\right] \tag{4}$$

$$Q_{radiation} = \epsilon\sigma_s\left[T^4(\vec{r},t) - T_\infty^4\right], \tag{5}$$

where h, ϵ, σ_s and T_∞ are the convective heat transfer coefficient, emissivity, Stefan-Boltzmann constant and temperature of the surrounding environment (room temperature), respectively. On the surface of the workpiece, the balance between the heat lost to the environment by convection and radiation and the energy absorbed from the laser radiation can be written as:

$$-k\nabla T\vec{n} = h\left[T(\vec{r},t) - T_\infty\right] + \epsilon\sigma_s\left[T^4(\vec{r},t) - T_\infty^4\right] - q_{laser}, \quad \vec{r} \in \Gamma, \tag{6}$$

where Γ represents the surface (or boundary) of the solid region Ω and $\vec{n}$ is the unitary vector normal to the surface Γ.

2.2 The finite element method

Although the mathematical description of heat transfer during rapid manufacturing processes is easy to formulate, its solution can rarely be analytically determined. In particular, rapid manufacturing processes involve the continuous incorporation of material into the parts being built, which means that the shape of the part is continuously changing and an adequate mathematical description of this type of process must also account for an evolving geometry. The finite element method has been successfully used by previous authors (Costa et al., 2005; Deus & Mazumder, 2006; Kelly & Kampe, 2004b; Toyserkani et al., 2004) to study additive manufacturing processes. The finite element method is a numerical technique for calculating approximate solutions to algebraic, differential and integral equations for which analytical solutions cannot be found. It is frequently applied to physical and engineering problems in areas such as structural mechanics, dynamics, fluid mechanics and heat transfer. This method can efficiently handle complicated geometries and account for non-uniform properties and boundary conditions, and is easily implemented in computer programs to solve complex simulation problems, taking advantage of the large computational power presently available, therefore making this technique a prime choice to study heat transfer during rapid manufacturing processes.

Calculating the solution to a problem using the finite element method is accomplished by using several mathematical tools and can be summarised by the following sequence of steps (Desai & Abel, 1972; Reddy, 2006; Zienkiewicz & Taylor, 2000):

1. the physical domain of the problem being solved is partitioned into a collection of simple geometrical sub-domains called finite elements;
2. in each element, the solution is approximated by a linear combination of adequately chosen interpolation functions and time dependant temperature values at the nodes of the elements: $T(\vec{r},t) \approx \sum_{j=1}^{n} T_j(t)\psi_j(\vec{r})$, with the governing equations of the problem being used to establish algebraic relations between the unknown nodal temperatures $T_j(t)$;
3. the algebraic equations developed for the different elements are assembled by requiring the continuity of $T(\vec{r},t)$ and the balance of certain relevant physical quantities at the interface between neighbouring elements. This produces a system of equations which can be solved to find the coefficients $T_j(t)$ and produce an approximate solution to the problem.

The approximate solution differs from the exact solution due to the approximations made in each of the three steps described above: in the first step errors are introduced because a continuous physical domain is represented by a finite element mesh that does not match it exactly; in the second step errors arise from approximating the exact solution over each element by a finite sum of functions; the solution of the system of assembled equations in the third step usually requires numerical integration, which is another source of error. The overall error in the computed solution can be minimised, for example, by refining the mesh to ensure a more accurate representation of the physical domain (first step), by using a better approximation to the local solution during the development of the algebraic equations in each element (second step) and by defining stricter convergence criteria in the numerical integration (third step). However, error reduction is achieved at the expense of computation time and usually a compromise has to be accepted between the accuracy of the solution and the time to compute it .

In the finite element method the equations governing heat transfer in the elements are expressed in terms of a variational formulation, typically the weak form of the heat conduction equation. Although the weak form of the heat conduction equation will not be derived here, it produces the following set of equations for each element (Reddy, 2006):

$$\sum_{j=1}^{n}\left(M_{ij}^{e}\frac{dT_j^e(\vec{r},t)}{dt}+K_{ij}^{e}T_e^e(\vec{r},t)\right)-Q_i^e-q_i^e=0, \qquad i=1,...,n, \tag{7}$$

where the superscript e is an identification label for each element in the mesh and n is the order of the interpolation functions used to approximate the solution. M_{ij}^e, K_{ij}^e, Q_i^e and q_i^e are defined by:

$$\begin{aligned} M_{ij}^e &= \int_{\Omega^e}\rho C\psi_i\psi_j dV, \quad K_{ij}^e = \int_{\Omega^e} k\nabla\psi_i.\nabla\psi_j dV \\ Q_i^e &= \int_{\Omega^e}\psi_i Q(\vec{r},t)dV, \quad q_i^e = \int_{\Gamma}\psi_i\left[q_{laser}-h\left(T-T_\infty\right)-\epsilon\sigma_s\left(T^4-T_\infty^4\right)\right]dS, \end{aligned} \tag{8}$$

where the dependencies of T on $\vec{r}$ and t have been omitted for simplicity. $Q(\vec{r},t)$ represents the heat flux across the common surfaces of neighbouring elements and the equations of the

different elements are assembled together by requiring the balance of this flux from each element to its neighbours and the continuity of the temperature field $T(\vec{r},t)$. This system of equations is commonly written in matrix form as:

$$\mathbf{M}^e\dot{\mathbf{T}}^e + \hat{\mathbf{K}}^e\mathbf{T} = \mathbf{F}^e, \tag{9}$$

where

$$\begin{aligned}
\mathbf{M}^e &= M_{ij}^e \\
\hat{\mathbf{K}}^e &= K_{ij}^e - I_{ij}\int_{\Gamma_2}\psi_i\left(-h-\epsilon\sigma_s T^3\right)dS \\
\mathbf{F}^e &= Q_i^e + \int_{\Gamma_2}\psi_i\left(q_{laser}+hT_\infty+\epsilon\sigma_s T_\infty^4\right)dS,
\end{aligned} \tag{10}$$

with I_{ij} the identity matrix.
The equations of the single elements are assembled by summing the element equations corresponding to the same nodes:

$$\mathbf{M} = \sum_e \mathbf{M}^e, \quad \hat{\mathbf{K}} = \sum_e \hat{\mathbf{K}}^e, \quad \mathbf{F} = \sum_e \mathbf{F}^e, \tag{11}$$

resulting in the global equation:

$$\mathbf{M}\dot{\mathbf{T}} + \hat{\mathbf{K}}\mathbf{T} = \mathbf{F}. \tag{12}$$

The system of ordinary differential equations expressed by the matrix equation 12 must be completed by providing an initial condition $\mathbf{T}(0) = \mathbf{T}_0$. Therefore we seek to solve the initial value problem defined by:

$$\begin{aligned}
&\mathbf{M}\dot{\mathbf{T}} + \hat{\mathbf{K}}\mathbf{T} = \mathbf{F}, \\
&\mathbf{T}(0) = \mathbf{T}_0.
\end{aligned} \tag{13}$$

This can be converted to a system of algebraic equations by dividing the time domain into steps and using finite differences to approximate the time derivatives. Equation 13 can be solved by considering a weighted average of the time derivatives at two consecutive time steps (t_s and t_{s+1}) and developing an iterative procedure to find the solution at each step (Reddy & Gartling, 1994):

$$\begin{aligned}
\mathbf{T}(t_{s+1}) &= \mathbf{T}(t_s) + \dot{\mathbf{T}}(t_{s+\alpha})(t_{s+1}-t_s), \\
\dot{\mathbf{T}}(t_{s+\alpha}) &= (1-\alpha)\dot{\mathbf{T}}(t_s) + \alpha\dot{\mathbf{T}}(t_{s+1}).
\end{aligned} \tag{14}$$

Different choices of α lead to well known approximation schemes that are commonly found in the literature:

$\alpha = 0,$	forward difference, or Euler, scheme
$\alpha = 1/2,$	Crank-Nicholson scheme
$\alpha = 2/3,$	Galerkin scheme
$\alpha = 1,$	backward difference scheme.

Substitution of Equation 13 in Equation 14 yields the solution to the problem:

$$\begin{aligned}\mathbf{T}(t_{s+1}) = \mathbf{T}(t_s) + (1-\alpha)\mathbf{M}^{-1}\left[\mathbf{T}(t_s)\right]\left\{\mathbf{F}\left[\mathbf{T}(t_s)\right] - \hat{\mathbf{K}}\left[\mathbf{T}(t_s)\right]\mathbf{T}(t_s)\right\}(t_{s-1}-t_s) \\ \alpha\mathbf{M}^{-1}\left[\mathbf{T}(t_{s+1})\right]\left\{\mathbf{F}\left[\mathbf{T}(t_{s+1})\right] - \hat{\mathbf{K}}\left[\mathbf{T}(t_{s+1})\right]\mathbf{T}(t_{s+1})\right\}(t_{s-1}-t_s).\end{aligned} \tag{15}$$

In general Equation 15 leads to an implicit scheme that requires iterative solutions to be found within each time step. The forward difference method is the only one of the above which is an explicit method and is the easiest to implement. It results in a simple iterative solution where $\mathbf{T}(t_{s+1})$ is readily obtained from the solution at the previous step $\mathbf{T}(t_s)$, and is given by:

$$\mathbf{T}(t_{s+1}) = \mathbf{T}(t_s) + \mathbf{M}^{-1}\left[\mathbf{T}(t_s)\right]\left\{\mathbf{F}\left[\mathbf{T}(t_s)\right] - \hat{\mathbf{K}}\left[\mathbf{T}(t_s)\right]\mathbf{T}(t_s)\right\}(t_{s-1}-t_s). \tag{16}$$

Starting from $\mathbf{T}(0) = \mathbf{T}_0$, the solution at subsequent steps can be calculated from Equation 16. Equation 16 is a general expression that relates the temperatures at various points of a geometry by requiring the balance of heat fluxes across the boundaries between neighbouring elements and the continuity of the temperature field, governed by the weak form of the heat conduction equation. The temperature evolution during additive manufacture for a component of arbitrary geometry can be found by implementing Equation 16 as a computer code.

2.3 Representation of the physical domain

A finite element model should ideally describe the geometry of the substrate and the tracks as closely as possible. Frequently the substrate is a parallelepiped which can be easily represented in the form of a finite element mesh. However, it is more difficult to develop a mesh which allows a step wise description of the deposition of tracks with complex 3-D features, such as curved cross sections or curved fronts. To describe the full detail of track overlap during manufacture, the finite element mesh becomes complex and requires many elements for the proper representation of the 3-D features of the tracks, as shown in Figure 2.a.

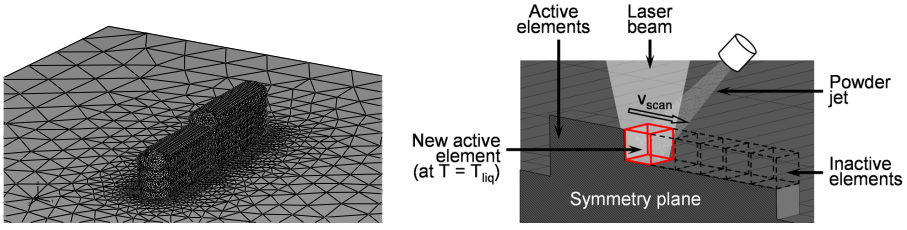

(a) (b)

Fig. 2. (a) Finite element mesh of substrate and tracks. (b) Step-wise approach to simulate the addition of material. New elements are activated at liquidus temperature. Adapted from Crespo and Vilar (Crespo & Vilar, 2010)

One commonly applied strategy to reduce the number of elements is to use a fine mesh only in regions which have complex geometries or where thermal gradients are expected to be high (in the vicinity of interaction zone between the energy source and the material), while using a coarser mesh away from these zones (Figure 2.a). The level of refinement shown in Figure

2.a is necessary if certain aspects of the fabrication process such as the formation of hot-spots or the solidification rate must be predicted, which require the precise shape of the melt pool and of the incorporated material to be taken into account (Bontha et al., 2006; Crespo et al., 2006). When the purpose of the simulation does not demand such a rigorous description of the track shape, simpler meshes may be used by assuming that the shapes of the melt pool and of the tracks can be approximated by simpler geometries. This has the advantage of reducing considerably the number of elements in the mesh, and as a consequence the number of calculations and the computational time necessary to resolve the problem. Several authors have developed finite element models which use simple cubic elements to simulate the addition of material and have demonstrated the validity of this approach (Costa et al., 2005; Deus & Mazumder, 2006), which is also used in the present work. If the deposition if assumed to take place in the mid-plane of the substrate, there is a symmetry plane in respect of which heat flow is symmetrical and one needs only consider half the geometry of the problem, as illustrated in Figure 2.b, further reducing the computational time needed to achieve the solution for the heat transfer problem.

In the model proposed in this chapter, Equation 16 is solved iteratively for each element in the step by step approach described in the previous section. Addition of material is taken into account by activating at each new time step elements with a volume corresponding to the volume of material incorporated into the part during the duration of that step (Figure 2.b), based on a methodology first presented by Costa et al. (Costa et al., 2005). Taking into consideration the results of Neto and Vilar (Neto & Vilar, 2002), who showed that in blown powder laser cladding the powder flying through the laser beam often reaches the liquidus temperature before impinging into the part, the newly active elements are assumed to be at the liquidus temperature.

3. Phase transformations during the rapid manufacturing of titanium components

Titanium alloys are being increasingly used in a wide range of applications due to properties such as high strength to weight ratio, excellent corrosion resistance, high temperature strength and biocompatibility. These properties have made titanium alloys a widespread material in industries such as the aerospace, automotive, biomedical, energy production, chemical, off-shore and marine industries, among others (Boyer et al., 1994; Donachie, 2004).

In the last decade, the Ti-6Al-4V alloy has accounted for more than half the production of titanium alloys worldwide, a market estimated at more than $2,000 million (Leyens & Peters, 2003). This predominance is mainly due to Ti-6Al-4V having the best all-around mechanical characteristics for numerous applications. This alloy is extensively used in the aerospace industry for the production of turbine engines and airframe components, which account for approximately 80% of its total usage. Additionally, Ti-6Al-4V presents excellent biocompatibility and osseointegration properties which have made it a natural choice as a biomaterial for the fabrication of implants and other biomedical devices (Brunette, 2001; Yoshiki, 2007). When compared to other materials usually used for the same purpose, such as stainless steel or CoCr alloys, Ti-6Al-4V allows the production of much stronger, lighter and less stiff implants and with improved biomechanical behaviour.

Ti-6Al-4V is an α/β titanium alloy that contains 6% of the α-phase stabilising element Al, and 4% of the β-phase stabilising element V in its composition. As a result of the combined effect of these two alloying elements, the equilibrium microstructure of Ti-6Al-4V consists of

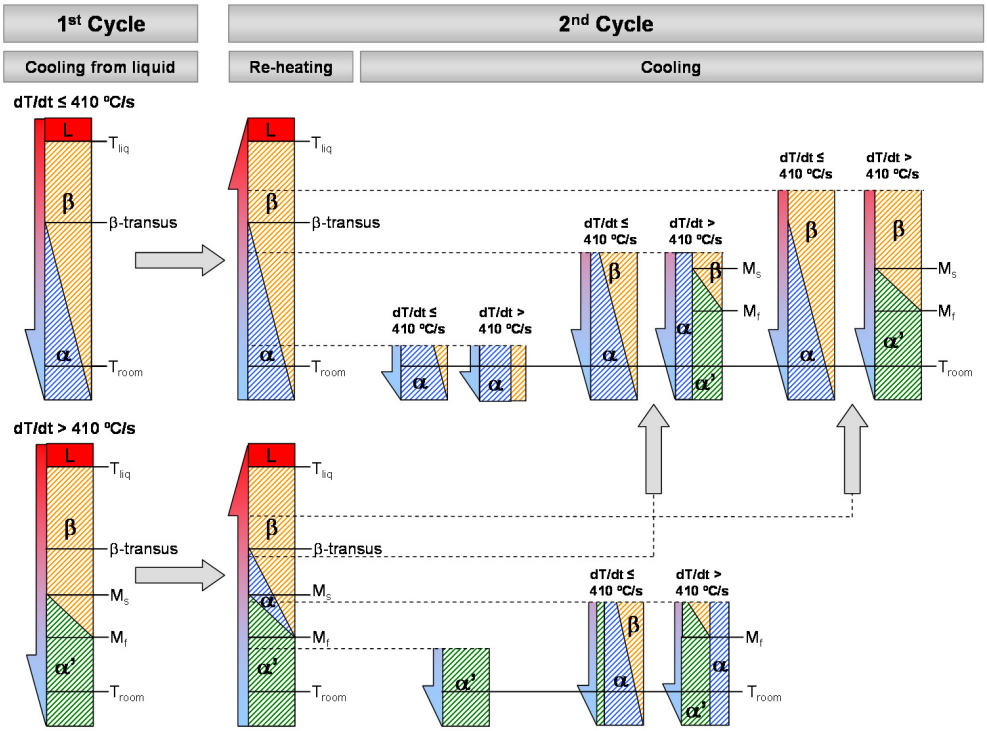

Fig. 3. Phase transformations during rapid manufacturing of Ti-6Al-4V.

a mixture of α and β phases for temperatures between room temperature and 980 °C, which is called the β-transus temperature (Polmear, 1989). The proportion of β phase in equilibrium depends on the temperature, varying from approximately 0.08 at room temperature to 1.00 at the β-transus, and is given by (R. Castro, 1966):

$$f_{\alpha}^{eq}(T) = \begin{cases} 0.925 - 0.925.e^{[0.0085(980-T)]}, & T \leq 980°C/s \\ 0, & T > 980°C/s \end{cases}$$
$$f_{\beta}^{eq}(T) = 1 - f_{\alpha}^{eq}(T), \tag{17}$$

with T in °C. In titanium alloys the β-transus temperature represents the minimum temperature above which β is the only equilibrium phase. The phase transformations that can occur due to the consecutive thermal cycles generated by layer overlap during build-up of parts by rapid manufacturing are represented in the diagram of Figure 3.

3.1 Phase transformations during cooling from the liquid phase

Prior to incorporation into the part the feedstock Ti-6Al-4V is melted, and after solidification its structure consists of β phase. During cooling to room temperature β may undergo two different phase transformations depending on the cooling rate.

3.1.1 Diffusional transformations

For cooling rates lower than 410 °C/s, a $\beta \rightarrow \alpha$ transformation takes place controlled by a diffusional mechanism, starting at the β-transus temperature (980 °C). At room temperature, the final microstructure consists of α and β because the transformation does not reach completion. In isothermal condition the kinetics of this transformation is described by the Johnson-Mehl-Avrami (JMA) equation:

$$f(t) = 1 - exp\left(-jt^n\right), \tag{18}$$

where $f_\alpha(t)$, k and n are the fraction of α formed after time t, the reaction rate constant and the Avrami exponent, respectively. The values for k and n were determined as a function of the temperature by Malinov et al. (Malinov, Markovsky, Sha & Guo, 2001). The Johnson-Mehl-Avrami equation cannot be used to describe the kinetics of anisothermal transformations because the reaction rate constant k depends on the temperature. As a consequence, the direct integration of the Johnson-Mehl-Avrami equation to calculate the transformed proportion during cooling is not possible. Nevertheless, good results have been achieved by generalising the Johnson-Mehl-Avrami equation to anisothermal conditions using the additivity rule (Malinov, Guo, Sha & Wilson, 2001; S. Denis, 1992). In this method, continuous cooling is replaced by a series of small consecutive isothermal steps where the Johnson-Mehl-Avrami equation can be applied. During the first isothermal time step, $[t_0, t_1[$, at temperature T_0, the fraction of α phase formed can be calculated from Equation 18 and is given by:

$$f_\alpha(t_1) = \left\{1 - exp\left[-k_0(t_1 - t_0)^{n_0}\right]\right\}.f_\alpha^{eq}(T_0) \tag{19}$$

where k_0 and n_0 are the reaction rate constant and Avrami exponent at the temperature T_0, respectively. In the next interval, $[t_1, t_2[$, the transformation is assumed to take place at the temperature T_1, but one must take into consideration the fact that a fraction $f_\alpha(t_1)$ of α phase has already formed in the previous step. Substituting the fraction $f_\alpha(t_1)$ in Equation 18, one can calculate the time it would take to form the proportion $f_\alpha(t_1)$ of α phase if the whole transformation had taken place at the temperature T_1:

$$t_1^f = \sqrt[n_1]{-\frac{ln[1 - f_\alpha(t_1)/f_\alpha^{eq}(T_1)]}{k_1}}, \tag{20}$$

where k_1 and n_1 are the reaction rate constant and Avrami exponent at the temperature T_1. The additivity principle requires that t_1^f be the initial time for the new transformation step. Therefore, for the time interval $[t_1, t_2[$, one gets:

$$f_\alpha(t_2) = \left\{1 - exp\left[-k_1(t_1^f + t_2 - t_1)^{n_1}\right]\right\}.f_\alpha^{eq}(T_1). \tag{21}$$

Equation 21 can be generalised for an arbitrary time step $[t_s, t_{s+1}[$ at temperature T_s, leading to a fraction of α formed during that step given by:

$$f_\alpha(t_{s+1}) = \left\{1 - exp\left[-k_s(t_s^f + t_{s+1} - t_s)^{n_s}\right]\right\}.f_\alpha^{eq}(T_s), \tag{22}$$

where t_s^f is given by:

$$t_s^f = \sqrt[n_s]{-\frac{ln[1 - f_\alpha(t_s)/f_\alpha^{eq}(T_s)]}{k_s}}. \tag{23}$$

The application of the additivity rule to the Johnson-Mehl-Avrami equation is illustrated in Figure 4.

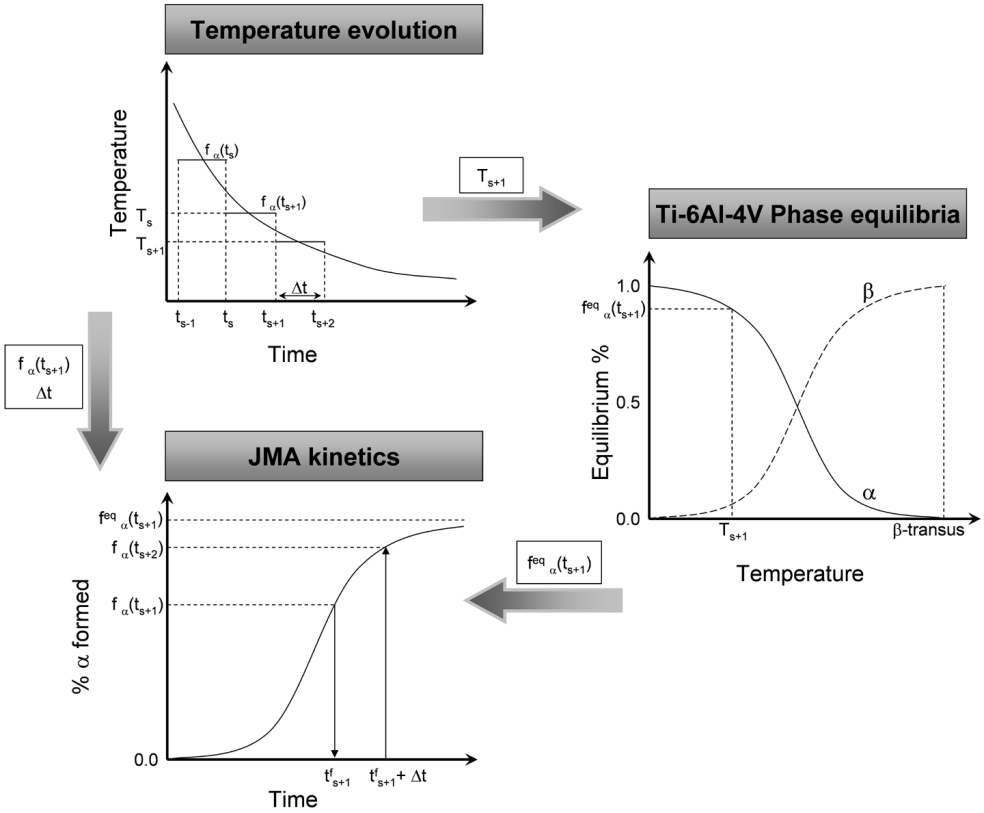

Fig. 4. Generalization of the Johnson-Mehl-Avrami equation for anisothermal transformations.

3.1.2 Martensitic transformations

For cooling rates higher than 410 °C/s the $\beta \rightarrow \alpha$ diffusional transformation is suppressed and β decomposes by a martensitic transformation. The proportion of β transformed into martensite (α') depends essentially on the undercooling below the martensite start temperature (M_s) and is given by (Koistinen & Marburger, 1959):

$$f_{\alpha'}(T) = 1 - exp\left[-\gamma(M_s - T)\right]. \tag{24}$$

The values of γ, M_s and M_f used in the present work (0.015 °C^{-1}, 650 °C and 400 °C respectively) were calculated on the basis of the results of Elmer et al. (Elmer et al., 2004). If the material cools below M_f its microstructure is fully martensitic.

3.2 Phase transformations during re-heating

When new layers are added to the part, the previously deposited material undergoes heating/cooling cycles that may induce microstructural and properties changes. If the microstructure formed in first thermal cycle is composed of $\alpha + \beta$, reheating will lead to diffusion controlled $\alpha \rightarrow \beta$ transformation with a kinetics described by the JMA equation generalised to anisothermal processes (Equation 22). If, on the other hand, the microstructure is martensitic, heating up the material into the tempering range (> 400 °C) will cause the decomposition of α' into a mixture of α and β. This transformation is also diffusion controlled and its kinetics are also described by the JMA equation (Equation 18). The values of k and n in Equation 18 for this reaction were determined by Mur et al. (Mur et al., 1996). If the decomposition is incomplete, tempering results in a three-phase microstructure consisting of $\alpha' + \alpha + \beta$.

3.3 Phase transformations during second cooling

During cooling down to room temperature at cooling rates lower than 410 °C/s β phase decomposes into α by a diffusion controlled mechanism. For cooling rates in excess of 410 °C/s β may undergo a martensitic transformation or be retained at room temperature, depending on the volume fraction of this phase in the alloy. Several authors have observed that β is completely retained upon quenching if its proportion in the alloy is lower than 0.25, because the β phase is enriched in vanadium, a β stabiliser (Fan, 1993; Lee et al., 1991; R. Castro, 1966). If the volume fraction is higher than 0.25 a proportion of β given by (Fan, 1993):

$$f_r = 0.25 - 0.25.f_\beta(T_0), \tag{25}$$

is retained at room temperature, where $f_b(T_0)$ is the volume fraction of β prior to quenching. The remaining β ($f_b(T_0) - f_r$) undergoes a martensitic transformation. As a result, cooling an alloy consisting only of β phase at rates higher than 410 °C/s originates a fully martensitic structure, while materials with smaller volume fractions of this phase retain a variable proportion of β (Figure 3). Thus, the martensite volume fraction is given by:

$$f_{\alpha'}(T) = f_{\alpha'}(T_0) + (f_\beta(T_0) - f_r)\left[1 - exp\left(-\gamma(M_s - T)\right)\right], \tag{26}$$

with $f_{\alpha'}(T_0)$ the volume fraction of α' phase present in the alloy prior to quenching. Similar phase transformations will occur during subsequent thermal cycles and the final microstructure will result from all the consecutive transformations occurring at each point.

3.4 Calculation of mechanical properties

The Young's modulus and hardness were calculated from the phase constitution of the alloy using the rule of mixtures (Costa et al., 2005; Fan, 1993; Lee et al., 1991). The Young's moduli of α, β and α' are 117, 82 and 114 GPa respectively and the Vickers hardnesses are 320, 140 and 350 HV.

4. Results

4.1 Experimental confirmation

The model was first validated by comparing the calculation results with the experimental distributions of microstructure and properties found in Ti-6Al-4V walls produced by laser powder deposition (LPD), a rapid manufacturing technique that uses a focused laser beam to melt a stream of metallic powder and deposit the molten material continuously at precise locations (Laeng et al., 2000; R.Vilar, 1999; 2001).

4.1.1 Simulation results

The model was applied to simulate the phase transformations occurring during the deposition of a 75 layer Ti-6Al-4V wall with 0.32 mm width, 10.00 mm length and 3.50 mm height, represented in Figure 5. The scanning speed was 4 mm/s, the laser beam diameter 0.3 mm, the idle time between the deposition of consecutive layers 6 s and the initial substrate temperature 20 °C. The laser beam power was varied according to the plot of Figure 6.a, reflecting the power adjustments performed by a closed loop online control system utilised during the manufacture of the experimental sample, which acts to keep the size of the melt pool generated by the laser beam at the surface of the workpiece constant. An initial beam power of 130 W was used and progressively decreased with each new deposited layer up to the 20th layer, where a beam power of 50 W was reached and kept constant for the rest of the process. An average absorptivity of 15 % was considered in the calculations, according to the results of Hu *et al.* (Hu & Baker, 1999) regarding the laser deposition of Ti-6Al-4V using a CO_2 laser.

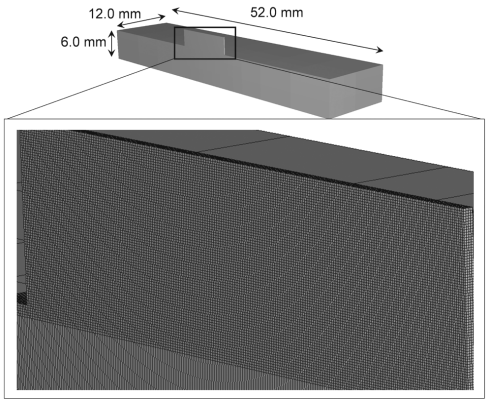

Fig. 5. View of the substrate and the wall with a detail of the wall mesh.

The calculated phase distribution is shown in Figures 6.b and 7. The highest volume fractions of α and β phases (0.03 and 0.07 respectively) occur close to the substrate, and decrease as the distance from the substrate increases, reaching zero in the uppermost layers of the part. Conversely, the volume fraction of martensite is lowest near the substrate (approximately 0.9) and has a maximum at the top of the wall, where the structure is fully martensitic. The cooling rates experienced by the material during the deposition process are always higher than 410 °C/s (Figure 8.a), and, as a consequence, after solidification the material undergoes a martensitic transformation during cooling to room temperature. Figure 8.a

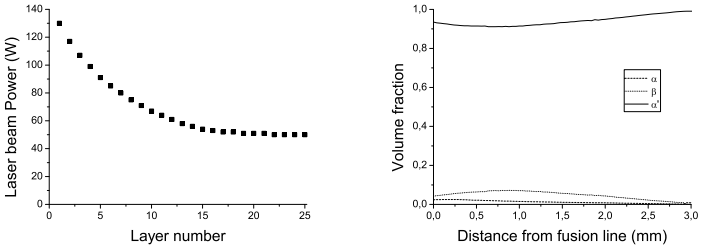

(a) (b)

Fig. 6. (a) Laser beam power used to deposit each layer. (b) Phase constitution as a function of the distance from the fusion line.

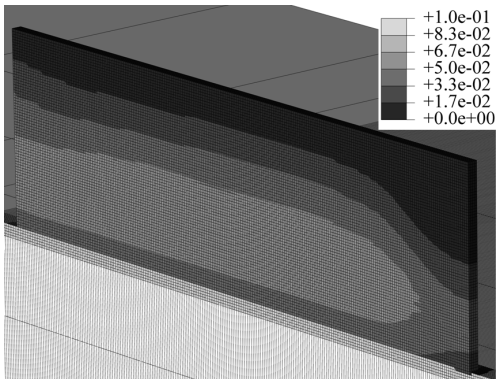

Fig. 7. β phase distribution.

shows that the cooling rate progressively decreases as the number of layers increases and asymptotically approaches a value below the martensite critical cooling rate (410 °C/s). Therefore, the deposition of additional layers would likely lead to the suppression of the martensitic transformation in the top layers of the part.

The thermal cycles originated by layer overlap heat up the previously deposited material to temperatures in the tempering range ($T > 400°C$), causing the progressive decomposition of the martensite into α and β (Figure 8.b).

The idle time between the deposition of consecutive layers used (6 s) is too short to allow the part to cool down to room temperature before the deposition of a new layer. As a result the temperature of the workpiece increases progressively as the deposition advances, eventually stabilising at approximately 270 °C after the deposition of the 15^{th} layer, as depicted in the plot of Figure 9.a.

This facilitates tempering because, as heat accumulates in the part, the material residence time in the tempering temperatures range increases from less than 1 s in the first cycles to approximately 4 s from the 15^{th} cycle onwards (Figure 9.b).

The cumulative effect of the consecutive thermal cycles is sufficient for significant tempering to take place, particularly in the layers deposited at the beginning of the buildup process. For example, the material in the first layer is subjected to 74 thermal cycles subsequent to

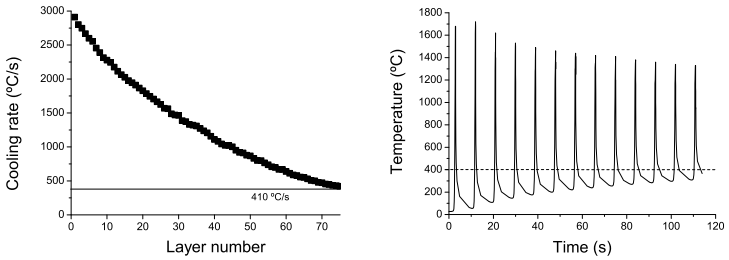

(a) (b)

Fig. 8. (a) Cooling rates experienced by the material deposited in the different layers. (b) Temperature evolution of the material deposited in the first layer for the first 120 s of the fabrication process. Tempering of the martensite takes place at temperatures higher than 400 °C.

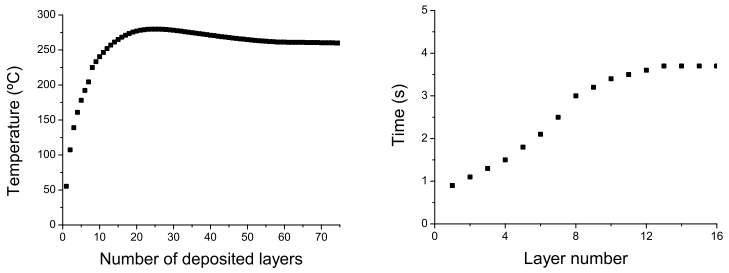

(a) (b)

Fig. 9. (a) Temperature evolution of the interface between the wall and the substrate after the deposition of each layer. (b) Time above 400 °C during the deposition of each layer, measured at the interface between the wall and the substrate.

its deposition, which amounts to approximately 250 s in the tempering range, leading to a decomposition of approximately 10% of the previously formed martensite. The evolution of the phase constitution of the material is presented in Figure 9.a and the Young's modulus and hardness variations along the wall height are presented in Figure 10.b

4.1.2 Experimental results

The distributions of microstructure, Young's modulus and hardness predicted by the model were compared to the values measured on a sample manufactured with similar processing parameters to validate the model. The system used in the experimental tests was developed by C. Meacock and R. Vilar (Meacock, 2009) to manufacture small to medium size parts for biomedical applications and the experimental work described in this section was carried out in collaboration with these authors. The system uses a CO_2 laser with a maximum beam power of 130 W which can be focused to a spot of 0.3 mm in diameter by means of a ZnSe lens with a focal length of 63.5 mm. The system employs a closed loop online control system whereby

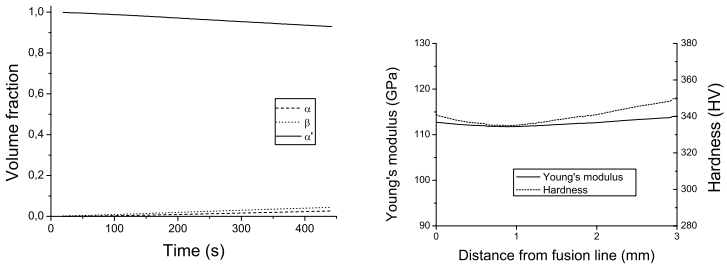

(a) (b)

Fig. 10. (a) Evolution of the phase constitution of the material in the first layer. (b) Distribution of properties along the wall height.

the intensity of the infra-red radiation emitted in the range 1.0-1.7 μm is monitored by a GaAs In doped photodiode. The acquired information is processed by a control function which acts to adjust the laser power in order to maintain constant melt pool dimensions during buildup, allowing for a high stability and dimensional accuracy in the manufacture of the parts. The deposition was conducted using a Ti-6Al-4V powder with a particle size in the range 25-75 μm fed through a capillary at a mass flow rate of 0.14 g/min.

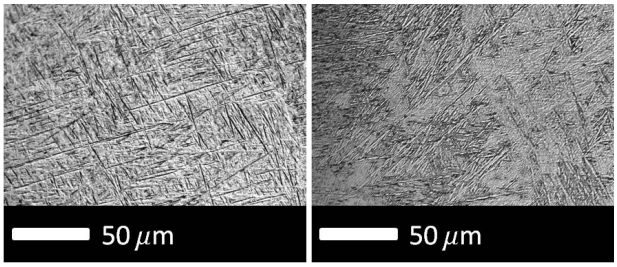

(a) (b)

Fig. 11. (a) Optical micrograph taken approximately 250 μm from the wall apex. (b) Optical micrograph taken approximately 500 μm from the fusion line. Adapted from C. Meacock (Meacock, 2009)

An optical micrograph of the cross section of the manufactured sample reveals an acicular morphology in the upper region of the wall (Figure 11.a). This is observed in the last 15 layers and is consistent with the hexagonal α'-martensite microstructure of Ti-6Al-4V, which typically presents a morphology consisting of long orthogonally oriented plates. Close to the bottom of the wall, the material presents a different microstructure (Figure 11.b), consisting of martensite needles interspersed with regions of $\alpha + \beta$. To quantify the volume fraction of the different phases, X-ray diffraction was conducted on the deposited material. The volume fraction of β phase was calculated from the X-ray diffractograms by the direct comparison method, with the error being the standard deviation of the averaged intensities method (Meacock, 2009). The volume fraction of β phase decreases with increasing distance to the substrate from 0.06 at 0.5 mm to 0.04 at 2.5 mm (Figure 12.a). The β phase results primarily

from the tempering of martensite, which is a slow process when compared to the typical time scales involved in laser processes. However, the deposition of the 75 layers takes approximately 450 s, which is long enough for tempering to occur and a noticeable volume fraction of β phase is observed in the deposited material.

The Young's modulus and hardness of the material were measured by depth sensing indentation testing carried out on the longitudinal section of the wall at 1 mm intervals starting at a distance of 0.5 mm from the fusion line, and the results are presented in Figures 12.b and 12.c, respectively. The Young's modulus is seen to increase slightly with increasing distance from the fusion line, from 110 GPa at 0.5 mm to 114 GPa at 2.5 mm. Likewise, the hardness increases with increasing distance from the fusion line, from 330 HV at a distance of 0.5 mm to 365 HV at 2.5 mm. The values of β volume fraction, Young's modulus and hardness calculated by the model are compared to the experimental values and plotted as a function of the distance from the fusion line in Figure 12.

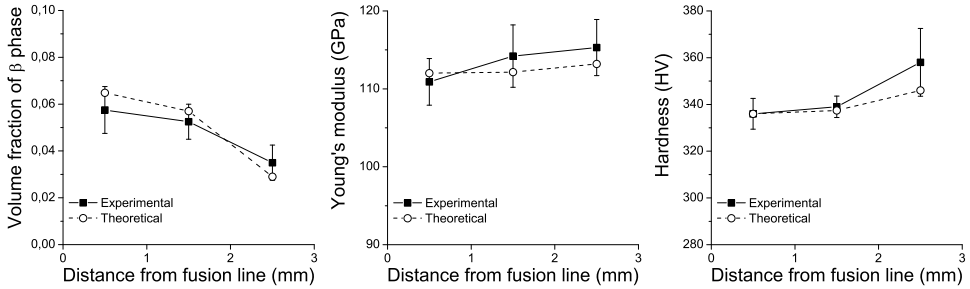

Fig. 12. Comparison between the values obtained using the model and the experimental measurements for: (a) volume fraction of β phase, (b) Young's modulus and (c) Vicker's hardness.

The variation of the volume fraction of β along the height of the wall is small but compares well with the values predicted by the model. The calculated Young's modulus and hardness show an overall good correlation with the experimental values and are within the experimental error limits, although the Young's modulus varies only slightly in the material.

5. Development of processing maps

To optimise the deposition process in order to obtain parts fulfilling specific requirements it is necessary to assess how the choice of processing parameters affects the properties of the deposited material. To this end, the model was used to obtain processing maps relating the scanning speed (v), idle time between the deposition of consecutive layers (Δt) and substrate temperature (T_{sub}) to the microstructure, hardness and Young's modulus distributions in parts produced by laser powder deposition. A summary of these results has been published elsewhere (Crespo & Vilar, 2010) but a more detailed analysis of the heat transfer and metallurgical phenomena is presented in this section. A thin wall geometry was considered with a width of 1 mm, a length of 14 mm and a height of 5 mm, produced by overlapping 10 layers of Ti-6Al-4V on a substrate of the same material with the dimensions 100*25*140 mm (Figure 13). The deposition was assumed to take place along the longitudinal

direction of the substrate and on its mid plane so that a symmetry plane exists and only half of the geometry needs to be considered for calculation purposes. A laser beam with a power P = 1000 W focused to a spot d_{beam} = 1.5 mm in diameter (at e^{-2} of the maximum intensity) was used so that a melt pool of approximately 1 mm in diameter is created in the laser / material interaction zone, matching the track width. An average absorptivity of 15 % was used in the calculations, assuming the utilisation of a CO_2 laser (Hu & Baker, 1999).

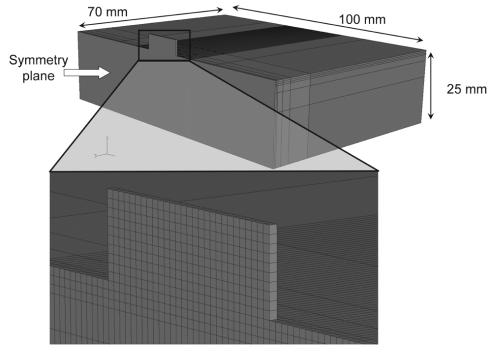

Fig. 13. Finite element mesh.

5.1 Influence of scanning speed and idle time

Figure 14 shows the computed Young's modulus and hardness distributions along the wall height using a scanning speed of 20 mm/s and an idle time of 10 s. The final part presents a fully martensitic microstructure and uniform distributions of Young's modulus and hardness, 114 GPa and 350 HV, respectively (Figure 14). During the fabrication process the material undergoes cooling rates in excess of 10^3 °C/s, which favour the transformation of the β phase formed upon solidification by a martensitic mechanism. Some tempering occurs due to re-heating caused by the overlapping of the following layers, but its extent is small because it takes several minutes for significant martensite decomposition to occur, whereas the residence time of the material within the tempering temperature range (above 400 °C) during the complete build-up process is less than 10 s (around 1 s for each subsequently deposited layer, Figure 15). A 10 s idle time is sufficient for the part to cool down to approximately 20 °C before the deposition of each new layer, therefore the average substrate temperature increases only slightly during build-up of the part (Figure 15). Using lower idle times leads to a progressive increase of the workpiece temperature during the deposition process (Figure 16.a), but the deposited material still presents a martensitic microstructure because the cooling rates are not significantly affected by the temperature increase in the part at the scanning speed used (20 mm/s). For this scanning speed the cooling rates are much higher than the critical cooling rate for the martensitic transformation (410 °C/s) and asymptotically approach a limit value between 1500 °C/s (for Δt = 2 s) and 1900 °C/s (for $\Delta t > 30$ s) as the number of deposited layers increases (Figure 16.b).

Another critical parameter to play a role in the formation of the microstructure of the material is the scanning speed used to perform the manufacture. Low values of this parameter can cause the suppression of the martensitic transformation because they lead to longer interaction times between the heat source (laser radiation) and the material, allowing more time for heat

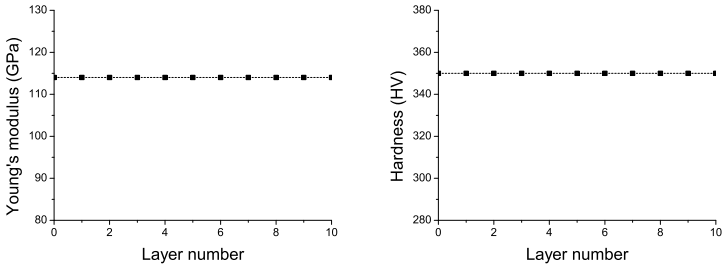

(a) (b)

Fig. 14. (a) Young's modulus (GPA) and (b) Vickers hardness (HV) distributions in a part produced using a scanning speed of 20 mm/s.

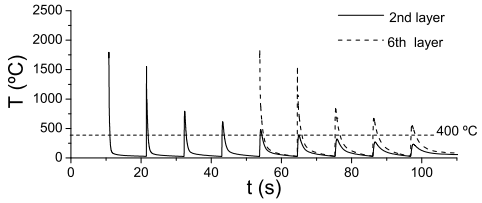

Fig. 15. Temperature variation during build-up for the 2nd and 6th layers of deposited material. The total time above 400 °C, where tempering takes place, is approximately 1s for each of the 5 layers deposited subsequently, which is not sufficient for significant tempering to occur.

to be conducted away from the interaction zone and reducing the temperature gradient in the wall, as shown in Figure 17. As a consequence of heat conduction to the substrate being the main mechanism of heat extraction from the interaction zone, a lower temperature gradient in the build direction slows down the heat flow, causing a reduction of the cooling rate which is approximately given by:

$$\frac{\partial T}{\partial t} = \frac{k}{c_p \rho} \frac{\partial^2 T}{\partial x^2}, \tag{27}$$

where xx' is the build-up (vertical) direction. Figure 18.a shows the variation of the cooling rate experienced during the deposition of the 10^{th} layer of material, with the scanning speed for two different values of the idle time. For low scanning speeds, the material in the last layers cools from above the β-transus at rates lower than 410 °C/s and the martensitic transformation is replaced by the diffusional $\beta \rightarrow \alpha$ transformation, leading to a microstructure composed of 0.92 α + 0.08 β in this region (Figure 18.b). As a result, the final part presents a non-uniform distribution of hardness, 350 HV in the bottom layers and 305 HV

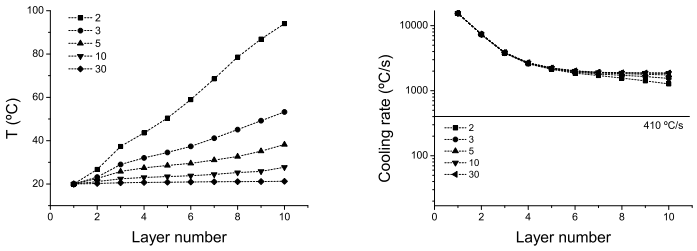

(a) (b)

Fig. 16. (a) Average temperature in the part immediately before the deposition of each layer for different values of idle time, v_{scan} = 20 mm/s and an initial substrate temperature of 20 °, and (b) cooling rates experienced by the material in each of the layers deposited (plotted in logarithmic scale).

in the upper region (Figure 19.b). The Young's modulus is practically uniformly distributed (Figure 19.a), 113 GPa in the lower region (practically only α') and 114 GPa in the upper layers (0.92 α + 0.08 β), because α and α' have similar Young's modulus and the proportion of β in the alloy is very low. From the plot of Figure 18.a it is apparent that scanning speeds equal to 12 mm/s or higher result in cooling rates above 410 °C/s and lead to β transforming by a martensitic mechanism, originating an α' structure. Scanning speeds lower than 12 mm/s lead to lower cooling rates and to parts with two microstructurally distinct regions, a bottom region composed of α', and a top region composed of 0.92 α and 0.08 β, resulting from the diffusion controlled $\beta \rightarrow \alpha$ transformation.

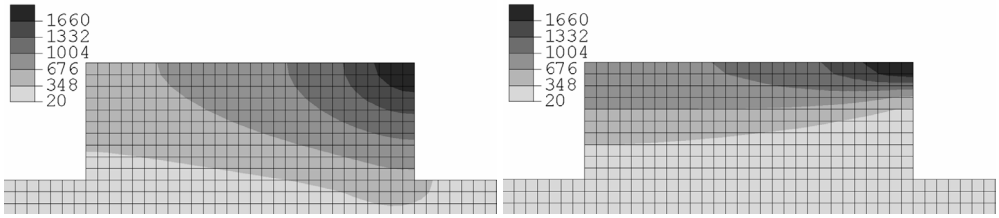

a *b*

Fig. 17. Temperature (°C) distribution at the end of the last deposition step using scanning speeds of (a) 5mm/s and (b) 20 mm/s. 20 mm/s. Adapted from Crespo and Vilar (Crespo & Vilar, 2010)

5.2 Influence of substrate temperature

In addition to the scanning speed and idle time, the substrate temperature has an important influence on the microstructure and properties of the material. Increasing the temperature of the substrate has two principal effects:

1. Firstly, pre-heating the substrate to temperatures close to or above M_f (400 °C) gives rise to different microstructures because the material cannot complete the martensitic

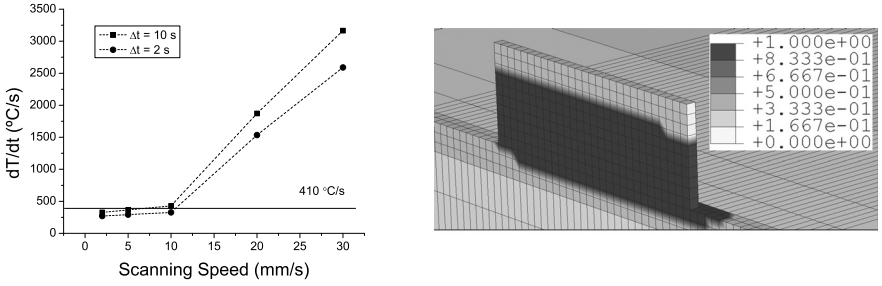

a *b*

Fig. 18. (a) Cooling rate experienced by the material deposited in the last layer as a function of the scanning speed for $\Delta t = 2$ s and $\Delta t = 10$ s; (b) volume fraction of martensite in the microstructure of a part fabricated using a scanning speed of 5 mm/s.

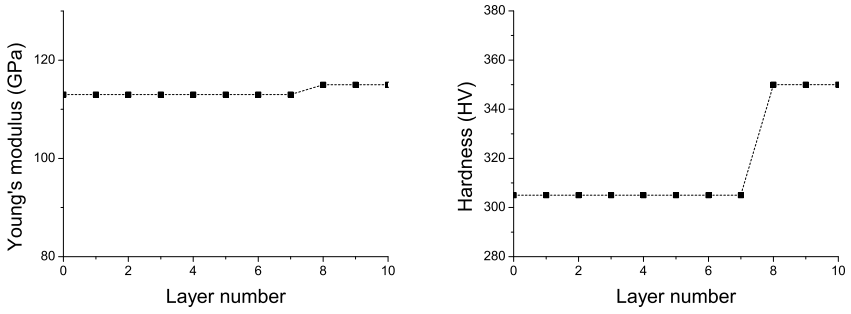

a *b*

Fig. 19. (a) Young's modulus (GPA) and (b) Vickers hardness (HV) distributions in a part fabricated using a scanning speed of 5 mm/s.

transformation before the deposition of the next layer. For example, if the substrate is pre-heated to 500 °C, the $\beta \rightarrow \alpha'$ transformation is stopped at about 75% of its extent, and at this temperature vanadium diffuses into the β phase (less than 20 s are necessary to achieve a concentration of 10 wt.%), stabilising and retaining this phase upon cooling to room temperature and leading to a material with roughly 0.75 of α and 0.25 of β (Fan, 1993; Katzarov et al., 2002; Malinov, Markovsky, Sha & Guo, 2001);

2. Secondly, increasing the temperature of the substrate acts to reduce the temperature gradient throughout the material. This leads to lower cooling rates which facilitate the decomposition of β into α by a diffusional process.

The joint influence of the scanning speed, idle time and substrate temperature on the final microstructure and properties of the parts is best analysed in terms of processing maps that relate this information. One of the most relevant applications of the model is the construction

of such processing maps to allow the prediction of the microstructure of the material and its properties given any set of processing parameters. The maps in Figure 20.a and 20.b (Crespo & Vilar, 2010) show the dependence of the cooling rate on the scanning speed and on the idle time for substrate temperatures of 20 and 500 °C, respectively, and allow finding the processing windows leading to specific microstructures.

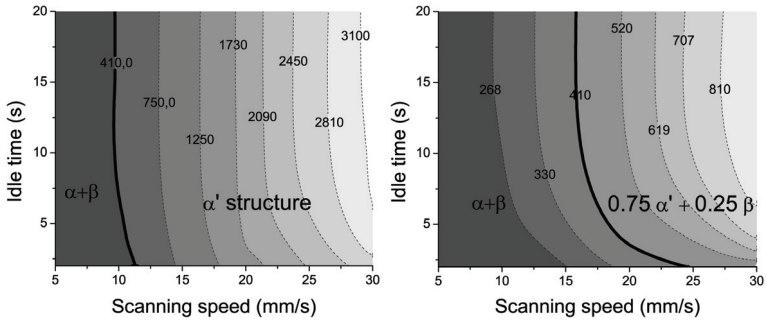

Fig. 20. (a) Contour plot of the cooling rate as a function of v and Δt for $T_{sub} = 20°C$. The cooling rate is mostly dependent on the scanning speed, as evidenced by the constant cooling rate lines being almost vertical. (b) Contour plot showing the dependence of the cooling rate on the scanning speed and the idle time using a substrate pre-heated to 500 °C. Adapted from Crespo and Vilar (Crespo & Vilar, 2010).

For example, when the deposition takes place on a substrate pre-heated at 500 °C, a scanning speed of 20 mm/s results in a martensitic transformation if an idle time of 5 s is used, while for 16 mm/s, idle times longer than 15 s are necessary to achieve the martensite critical cooling rate. More generally, any set of parameters to the right of the bold line ($\partial T/\partial t = 410°C/s$) shown in the plot of Figure 20.b leads to a martensitic transformation in the material. For these sets of parameters, after the deposition of the last layer, the material is at 500 °C and its microstructure consists approximately of 0.75 α' + 0.25 β, with a vestigial proportion of α formed during tempering. During cooling to room temperature, the β phase remains stable and is retained due to the enrichment in vanadium and the final part has a uniform microstructure containing 0.75 α' + 0.25 β (Fan, 1993). This material presents a uniform hardness of 300 HV and a Young's modulus of 106 GPa, which is the minimum that can be obtained for the Ti-6Al-4V alloy. The distributions of Young's modulus and Vickers hardness are shown in Figure 21.a and b, respectively.

These results are in agreement with results published by other authors. In particular the diffusional transformation of β phase in Ti-6Al-4V components produced by laser assisted deposition at low scanning speeds was verified by Kelly et al. (v=0.625 - 2.5 mm/s) (Kelly & Kampe, 2004a) and Qian et al. (v=6.7 - 10.0 mm/s) (Qian et al., 2005), whereas the occurrence of a martensitic transformation at higher speeds was confirmed by Groh (d. Groh, 2006).

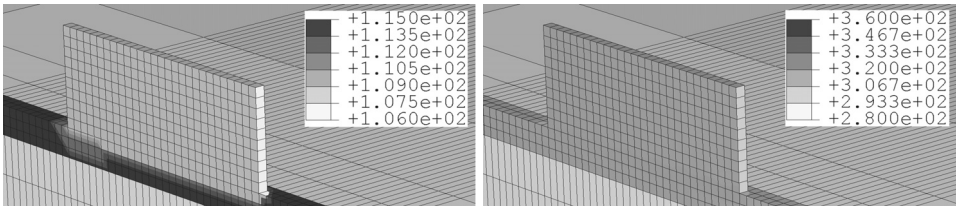

Fig. 21. (a) Young's modulus (GPA) and (b) Vickers hardness (HV) distributions in a part fabricated using a scanning speed of 15 mm/s on a substrate at 500 °C. Adapted from Crespo and Vilar (Crespo & Vilar, 2010).

6. Conclusion

A thermo-kinetic finite element model coupling heat transfer calculations and phase transformation kinetics theory which predicts the microstructure and properties distributions in titanium parts produced by rapid manufacturing was developed. The results of the model were compared to experimental measurements of the phase constitution and properties performed on samples produced by a laser based technique using identical parameters to the ones utilised in the model and showed a good agreement. The model was also applied to the development of processing maps relating the deposition parameters to the microstructure and properties of the parts. From the results achieved it was concluded that:

1. Computational methods are an efficient way to study heat transfer and the associated metallurgical phenomena which occur during manufacture of components;
2. This type of approach provides a cheap and rapid way to construct processing maps for the optimisation of fabrication processes;
3. Pre-heating the substrate allows controlling the final distribution of microstructure and properties in Ti-6Al-4V parts produced by rapid manufacturing;
4. By changing the processing parameters during the build-up process it possible to control the properties in Ti-6Al-4V produced by rapid manufacturing processes

6.1 Future work

The model can be easily modified to describe the microstructural transformations of other Ti alloys. In the case of α/β alloys these modifications simply amount to changing the kinetic parameters used to describe the various transformations simulated in the model and future work will include the application of the model to simulate the microstructural evolution of different titanium alloys. The phase transformations kinetics subroutine is a generic algorithm that describes the phase transformations of Ti-6Al-4V as a function of the heat treatment and is not specific to rapid manufacturing processes. This subroutine can be used to describe other processing techniques and, more generally, any heat treatment of the Ti-6Al-4V alloy. Additionally, more experimental work will be carried out to achieve a thorough validation of the model for different processing conditions.

7. Acknowledgements

The author thankfully acknowledges the valuable help and contributions from Dr. C. Meacock and Prof. R. Vilar.

8. References

Bontha, S., Klingbeil, N. W., Kobryn, P. A. & Fraser, H. L. (2006). Thermal process maps for predicting solidification microstructure in laser fabrication of thin-wall structures, *Journal of Materials Processing Technology* 178: 135–142.

Boyer, R., Welsch, G. & Coolings, E. W. (1994). *Materials Properties Handbook : titanium alloys*, ASM International.

Brunette, D. M. (2001). *Titanium in Medicine*, Springer.

Costa, L., Vilar, R., Reti, T. & Deus, A. M. (2005). Rapid tooling by laser powder deposition: Process using finite element analysis, *Acta Materialia* 14: 3987–3999.

Crespo, A. (2010). *Mathematical Simulation of Laser Powder Deposition Applied to the Production of Prosthesis and Implants of Ti and Ti-6Al-4V*, PhD thesis, Instituto Superior Técnico.

Crespo, A., Deus, A. M. & Vilar, R. (2006). Finite element analysis of laser powder deposition of titanium, *Proceedings of ICALEO 2006-25th International Congress on Applications of Lasers and Electro-Optics*, Scottsdale, Arizona, pp. 1016–1021.

Crespo, A., Deus, A. M. & Vilar, R. (2008). Modeling of phase transformations and internal stresses in laser powder deposition, *Proceedings of GCL-HPL 2008*, Lisbon, Portugal, pp. 713120–713120–10.

Crespo, A. & Vilar, R. (2010). Finite element analysis of the rapid manufacturing of ti-6al-4v parts by laser powder deposition, *Scripta Materialia* 63: 140–143.

d. Groh, H. C. (2006). Development of laser fabricated Ti-6Al-4V, *Technical report*, National Aeronautics and Space Administration John H. Glenn Research Center.

Desai, C. S. & Abel, J. F. (1972). *Introduction to the Finite Element Method*, Van Nostrand Reinhold Company.

Deus, A. M. & Mazumder, J. (2006). Three-dimensional finite element models for the calculation of temperature and residual stress fields in laser cladding, *Proceedings of ICALEO 2006-25th International Congress on Applications of Lasers and Electro-Optics*, Scottsdale, Arizona, pp. 496–505.

Donachie, M. J. (2004). *Titanium, A Technical Guide - 2nd Edition*, ASM International.

Elmer, J. W., Palmer, T. A., Babu, S. S., Zhang, W. & DebRoy, T. (2004). Phase transformations dynamics during welding of Ti-6Al-4V, *Journal of Applied Physics* 95: 8327–8339.

Fan, Z. Y. (1993). On the young moduli of Ti-6Al-4V alloys, *Scripta Metallurgica Et Materialia* 29: 1427–1432.

Ghosh, S. & Choi, J. (2005). Three-dimensional transient finite element analysis for residual stresses in the laser aided direct metal/material deposition process, *Journal of Laser Applications* 17: 144–158.

Hu, C. & Baker, T. N. (1999). A semi-empirical model to predict the melt depth developed in overlapping laser tracks on a Ti-6Al-4V alloy, *Journal of Materials Processing Technology* 94: 116–122.

Kahlen, F. J. & Kar, A. (2001). Residual stresses in laser-deposited metal parts, *Journal of Laser Applications* 13: 60–69.

Katzarov, I., Malinov, S. & Sha, W. (2002). Finite element modeling of the morphology of beta to alpha phase transformation in Ti-6Al-4V alloy, *Metallurgical and Materials Transactions A* 33: 1027–1040.

Kelly, S. & Kampe, S. (2004a). Microstructural evolution in laser-deposited multilayer Ti-6Al-4V builds: Part I. microstructural characterization, *Metallurgical and Materials Transactions A* 35: 1861–1867.

Kelly, S. & Kampe, S. (2004b). Microstructural evolution in laser-deposited multilayer Ti-6Al-4V builds: Part II. thermal modeling, *Metallurgical and Materials Transactions A* 35: 1869–1879.

Koistinen, D. P. & Marburger, R. E. (1959). A general equation prescribing the extent of the austenite-martensite transformation in pure iron-carbon alloys and plain carbon steels, *Acta Metallurgica* 7: 59–60.

Labudovich, M., Hu, D. & Kovacevic, R. (2003). A three dimensional model for direct laser metal powder deposition and rapid prototyping, *Journal of Materials Science* 38: 35–49.

Laeng, J., Stewart, J. G. & Liou, F. W. (2000). Laser metal forming processes for rapid prototyping - a review, *International Journal of Production Research* 38(16): 3973–3996.

Lee, Y. T., Peters, M. & Welsch, G. (1991). Elastic-moduli and tensile and physical-properties of heat-treated and quenched powder metallurgical Ti-6Al-4V-alloy, *Metallurgical and Materials Transactions A* 22: 709–714.

Leyens, C. & Peters, M. (2003). *Titanium and Titanium Alloys*, Wiley-VCH.

Malinov, S., Guo, Z., Sha, W. & Wilson, A. (2001). Differential scanning calorimetry study and computer modeling of beta double right arrow alpha phase transformation in a Ti-6Al-4V alloy, *Metallurgical and Materials Transactions A* 32: 879–887.

Malinov, S., Markovsky, P., Sha, W. & Guo, Z. (2001). Resistivity study and computer modelling of the isothermal transformation kinetics of Ti-6Al-4V and Ti-6Al-2Sn-4Zr-2Mo-0.08Si alloys, *Journal of Alloys and Compounds* 314: 181–192.

Meacock, C. (2009). *Laser Powder Microdeposition of Biomedical Alloys*, PhD thesis, Instituto Superior Tecnico.

Mur, F. X. G., Rodriguez, D. & Planell, J. A. (1996). Influence of tempering temperature and time on the alpha'-Ti-6Al-4V martensite, *Journal of Alloys and Compounds* 234: 287–289.

Neto, O. O. D. & Vilar, R. (2002). Physical-computational model to describe the interaction between a laser beam and a powder jet in laser surface processing, *Journal of Laser Applications* 14: 46–51.

Polmear, I. J. (1989). *Light Alloys*, Edward Arnold.

Qian, L., Mei, J., Liang, J. & Wu, X. (2005). Influence of position and laser power on thermal history and microstructure of direct laser fabricated Ti-6Al-4V samples, *Materials Science and Technology* 21: 597–605.

R. Castro, L. S. (1966). Contribution to metallographic and structural study of titanium alloy ta6v, *Memoires Scientifiques de la Revue De Metallurgie* 63: 1025–1058.

Reddy, J. N. (2006). *An Introduction to the Finite element Method*, McGraw-Hill.

Reddy, J. N. & Gartling, D. K. (1994). *The Finite Element Method in Heat Transfer and Fuid Dynamics*, CRC Press.

R.Vilar (1999). Laser cladding, *Journal of Laser Applications* 11(2): 64–79.

R.Vilar (2001). Laser cladding, *International Journal of Powder Metallurgy* 37(2): 31–48.

S. Denis, D. Farias, A. S. (1992). Mathematical-model coupling phase-transformations and temperature evolutions in steels, *Isij International* 32: 316–325.

Toyserkani, E., Khajepour, A. & Corbin, S. (2004). 3-d finite element modeling of laser cladding by powder injection: effects of laser pulse shaping on the process, *Optics and Lasers in Engineering* 41: 849–867.

Vasinonta, A., Beuth, J. L. & Grifith, M. (2001). A process map for consistent build conditions in the solid freeform fabrication of thin-walled structures, *Journal of Manufacturing Science and Engineering - Transactions of the AIME* 123(4): 615–622.

Wang, L., Felicelli, S., Gooroochurn, Y., Wang, P. & Horstemeyer, M. (2008). Optimization of the lens process for steady molten pool size, *Materials Science and Engineering A* 474: 148–156.

Yoshiki, O. (2007). *Bioscience and Bioengineering of Titanium Materials*, Elsevier.

Zienkiewicz, O. C. & Taylor, R. L. (2000). *The Finite Element Method*, Butterwoth Heinemann.

16

Measurement of Boundary Conditions - Surface Heat Flux and Surface Temperature

Wei Liu
Japan Atomic Energy Agency
Japan

1. Introduction

In order to understand a heat transfer phenomenon, it is sometimes very important to know the change in heat flux and temperature with time or the distribution of the heat flux and temperature on the surface of a heating block. Furthermore, with the development of computational thermal-fluid dynamics, experimental data that are of the CFD level, both spatially and temporally, are needed to validate the simulation results. However, it is difficult to measure the surface heat flux and surface temperature if no sensors are allowed setting on the surface, which may be a disturbance to the phenomenon itself occurring on the surface. This chapter introduces a technique for the measurement of surface temperature and surface heat flux.

2. Technique for the measurement of surface temperature and surface heat flux

The technique for the measurement of surface temperature and surface heat flux involves two steps: (1) measurement of the inner block temperatures using special micro temperature sensors, which are placed at a depth of several micrometers beneath the surface; and (2) solving an inverse heat conduction problem (IHCP) to obtain the surface heat flux and surface temperature, by using the measured inner block temperature data. In other words, the introduction of the IHCP enables us to derive the boundary conditions, which include both surface heat flux and surface temperature, without necessitating the use of a sensor on the surface of interest.

2.1 Inverse heat conduction problem (IHCP)

When compared to a normal heat conduction problem, that enables us to calculate temperature distributions inside a block by solving the heat conduction equation, with the initial and boundary conditions as input, the IHCP is an analysis method that enables us to calculate the boundary conditions by solving the heat conduction equation with Laplace transform technique, with the initial conditions and inner temperature as input. A considerable number of research studies (Burggraf, 1964; Sparrow et al., 1964; Imber, 1974; Shoji, 1978; Monde, 2003a, 2003b; Woodfield, 2006a, 2006b) have adopted analytical approaches for solving the IHCPs. Although limited to fairly simple geometry, explicit analytical solutions to IHCP have been derived and are very fast computational. If a one-(two-) dimensional heating block comprises two unknown boundaries, as shown in Fig. 1,

then it needs two (rows of) inner-temperature readings to close the heat conduction equation and to obtain the heat fluxes and temperatures on the two boundaries. However, if the heating block has only a single unknown boundary, theoretically, then it needs only a single (line of) inner-temperature reading to close the heat conduction equation. Noting that the recent introduction of new concepts such as moving window (for two rows of measuring data to close two unknown boundary conditions) (Woodfield, 2006a) and superposition of successive corrections in approximating the temperature readings (for one row of measuring data to close one unknown boundary condition) (Woodfield, 2006b) has made the use of the IHCP practical.

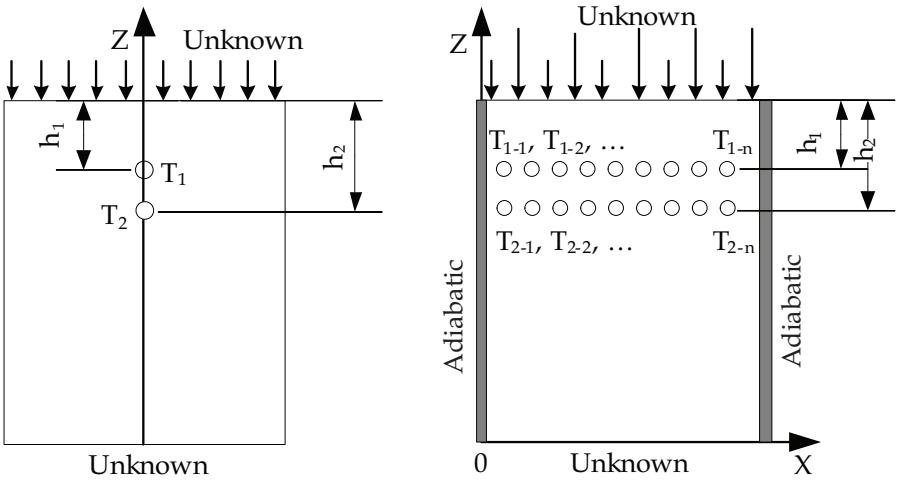

(a) One-dimensional (b) Two-dimensional

Fig. 1. A Heating block with two unknown boundaries

To solve the IHCP accurately, there is a demand for the measured inner temperature data. That is, the data should have sensed the effect of the boundary under study. This necessitates the use of highly sensitive temperature sensors located in close proximity to the surface. This is very important in tracing a fast-changing transient phenomenon. In a high-frequency process such as boiling, the high-frequency effects are strongly damped within the heating block because of the thermal inertia of the heating block. Thus, the temperature sensors must be located as close as possible to the surface of interest. If a sinusoidal heat flux boundary $q_{0(\omega t)}$ is imposed on one surface of a one-dimensional solid with initial temperature T_0 and the other surface is kept adiabatic, as shown in Fig. 2, the exact solution for the temperature within the solid is given by Eq. (1) (Carslaw, 2003), where λ and α are the thermal conductivity and thermal diffusivity, respectively. Equation (1) clearly shows that the effect of the oscillation diminishes quickly with an increase in the depth into the heating block, which is more pronounced for high frequencies. This sets an upper limit to the frequency of the fluctuations that can be detected by a sensor placed within the heating block. In other words, if a temperature sensor is placed at a distance from the surface, it may be impossible to detect the effects from a high-frequency mode. Further, using the readings taken at that point as the input data of the IHCP will result in the inaccurate prediction of

the boundary conditions. As an example, a comparison of the surface heat fluxes between the predictions obtained from the Woodfield's analytical approach and the exact values at different frequencies is shown in Fig. 3 (Woodfield, 2006a). In the calculation, copper is used for the heating block and the exact solution calculated from Eq. (1) with h1 = 2 mm is used as the input data. h_1 = 2 mm represents the depth at which the temperature sensor is placed. As shown in the figure, the agreement between the sine waves of the actual and predicted heat fluxes is remarkably good at low frequencies of 1 and 3 Hz; however, the accuracy decreases as the frequency increases. This means that when the sensor is placed at a depth of 2 mm beneath the surface, it cannot sense the effect of the surface heat flux with a frequency higher than 5 Hz. Therefore, a new technique through which the temperature sensors can be placed very close to the surface of interest is necessary.

$$T - T_0 = \frac{q_0}{\lambda}\sqrt{\frac{a}{\omega}}e^{-h_1\sqrt{\frac{\omega}{2a}}}\sin\left(\omega t - h_1\sqrt{\frac{\omega}{2a}} - \frac{\pi}{4}\right) + \frac{2q_0 a\omega}{\pi\lambda}\int_0^\infty \frac{\cos(uh_1)}{\omega^2 + a^2u^4}e^{-au^2t}du \tag{1}$$

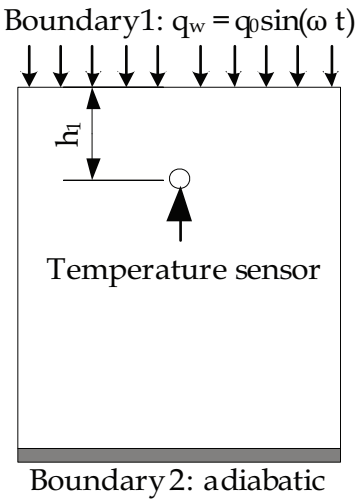

Fig. 2. A One-dimensional block with the sinusoidal heat flux boundary imposed on one surface

2.2 Special micro temperature sensors

As already mentioned, in order to accurately calculate the boundary conditions by using the IHCP, the temperature sensors in the heating block should be positioned as close as possible to the surface of interest. Furthermore, in order to determine the distribution of heat flux and temperature on the boundary in detail, we need to solve the two-dimensional IHCP, which requires the temperature sensors to have a high spatial resolution.

We therefore introduced special micron-sized thermocouples that share a single positive pole (Enomoto & Furuhama, 1984; Buchholz et al., 2004; Liu & Takase, 2009). A schematic illustration of the thermocouples is shown in Fig. 4. In a heating block made of copper, the temperature junctions are located at multiple points from No. 1 to No. N. Each junction has

a constantan wire as its negative pole, but shares a common positive pole made of copper. The temperature sensors are thus of the T-type. The common positive pole can be formed by using a film-formation technique - such as sputtering - after the constantan wires are set into the copper block. The thickness of the sputtering film can be controlled accurately within several micrometers. This means that the temperature junctions can be formed at a depth of several microns beneath the surface of interest.

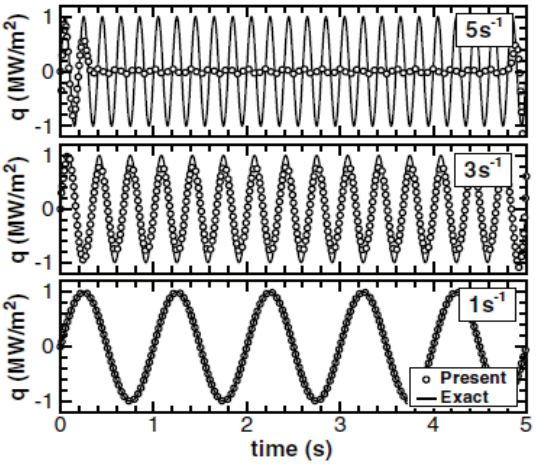

Fig. 3. Effect of inner-temperature measuring position on the accuracy of the IHCP predictions (temperature measured at a depth of 2 mm beneath the surface is used as the input of IHCP, (Woodfield, 2006a))

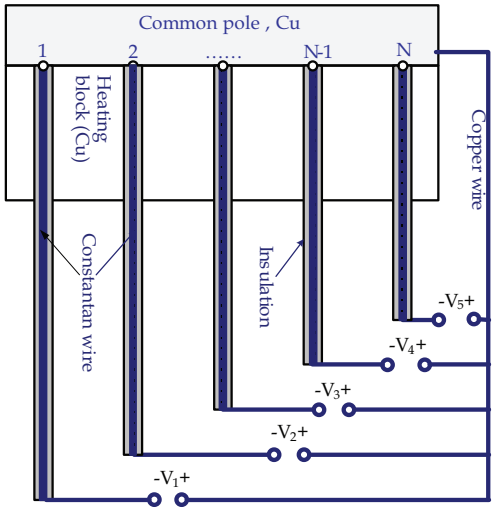

Fig. 4. Schematic illustration of the special micron-sized T-type thermocouples that share a single positive pole

By using teflon-coated (76μm) and polyimide-coated (50μm) constantan wires, we succeeded in developing temperature sensors with a pitch of 0.5 mm and at a depth of 3.1 μm, and temperature sensors with a pitch of 0.16 mm and at a depth of 1.3 μm, respectively, beneath the surface of interests. Figure 5 shows a comparison between the imposed sinusoidal heat flux and the sinusoidal heat flux predicted from the IHCP on the basis of the temperature calculated using Eq. (1) with h_1 = 3.1 μm. As shown in the figure, there is a very good agreement between the imposed and predicted sinusoidal heat fluxes at the frequencies of 20 and 50 Hz. These cases correspond to the bubble frequencies under subcooled and saturated atmospherical pressure pool boiling conditions, respectively. The figure theoretically clarifies that the high-frequency changed boundary conditions can be traced by using the temperature sensor located at a depth of 3.1 □m beneath the surface.
The new sensors are of the wire type and are therefore highly sensitive. With sharing a common positive pole, the number of wiring lines is decreased and it is easier to obtain a high spatial resolution. The response time of the sensors is assumed to be zero. These characteristics, together with the fact that temperature junctions can be easily placed several microns beneath the surface, contribute to the effectiveness of the IHCP technique in tracing the boundary conditions.

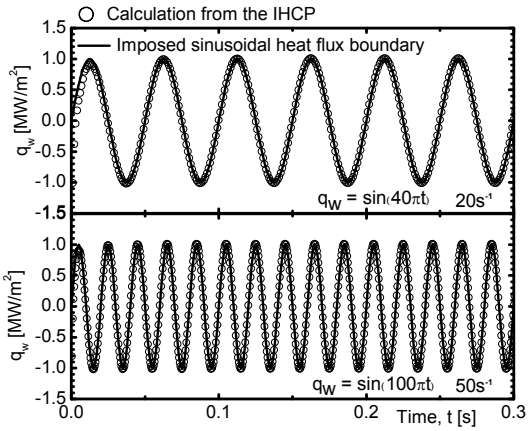

Fig. 5. Effect of inner-temperature measuring position on the accuracy of the IHCP predictions (temperature measured at a depth of 3.1 μm beneath the surface is used as the input of IHCP)

Note that as shown in Fig. 1, the standard IHCP requires the sensors to be placed at two different depths. However, in the case where only one boundary is unknown (with the adiabatic or semi-infinite assumption valid on the other boundary), only one row of sensors is required in order to obtain the boundary conditions about the surface of interest. This is highly desirable since the overall cost incurred when allocating the sensors is reduced. As recommended by Woodfield, if the Fourier number $\frac{at}{H^2} < 0.1$, where H is the thickness of the heating block, then for practical use, the block can be treated as being semi-infinite.
Further, note that the thin copper film, which acts as the common pole of the temperature sensors, is to be coated with a protection film to prevent it from oxidation. Selection of the type of protection film is very important for the realization of durable temperature sensors.

3. Measurement example

The above mentioned measurement technique was successfully used in the measurement of the surface heat flux and surface temperature during a boiling process. The experimental apparatus used is shown in Fig. 6. It includes a boiling vessel and a heating block. The heating block is made of copper and is peripherally insulated. The heating block is composed of two parts, upper and lower. The image of the upper part is shown in Fig. 7, in which 10 special micro temperature sensors are placed radially at a pitch of 0.5 mm and at a depth of 3.1 μm from the boiling surface. The upper and lower parts of the heating block are joined together by using a high-temperature adhesive. A cartridge heater is inserted into the lower heating block.

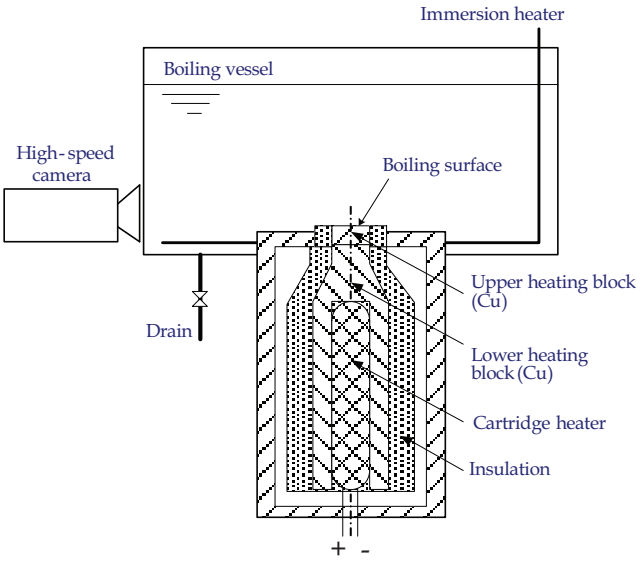

Fig. 6. Experimental apparatus

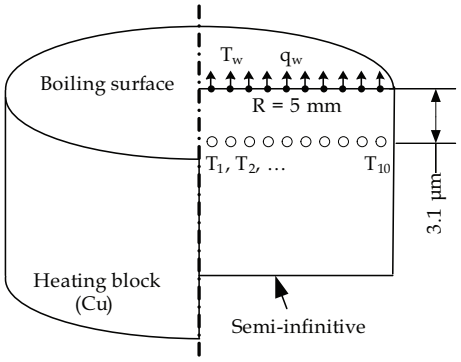

Fig. 7. The upper heating block

The data collected by two micron-sized thermocouples that share a common positive pole are shown in Fig. 8. In the figure, T_4 and T_{10} are the temperatures measured at the same depth but at different radial positions. The figure shows that the thermocouples are effective in measuring the temperatures. The data taken at T_4, which is just below a bubble, were used as the input data for solving a semi-infinite one-dimensional IHCP in order to obtain the surface heat flux and surface temperature, the results of which are shown in Fig. 9. The peak of the heat flux corresponds to the formation of a large, deformed bubble.

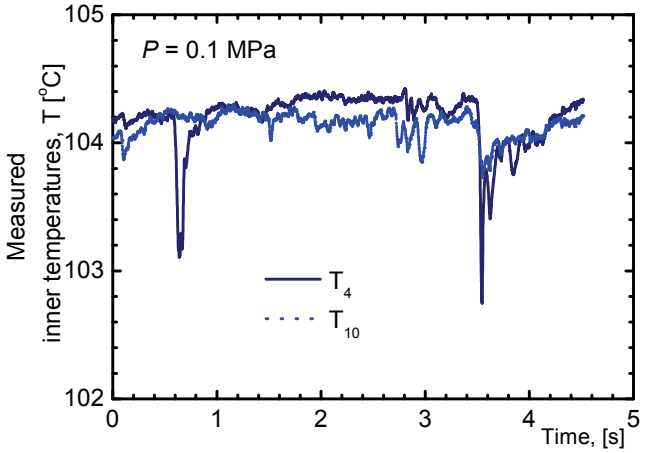

Fig. 8. Temperatures measured during the boiling processes by the micron-sized thermocouples sharing a common positive pole

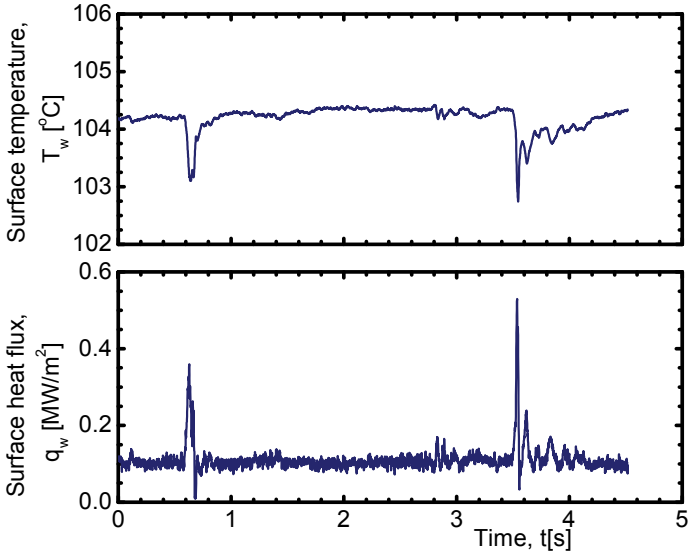

Fig. 9. Measured surface heat flux and surface temperature during the boiling process

4. Conclusions

In this chapter, a technique for the measurement of surface temperature and surface heat flux was introduced. This technique involves two steps: (1) measurement of the inner block temperatures near the surface using special micro temperature sensors; and (2) solving an IHCP to obtain the surface heat flux and surface temperature by using the measured inner block temperature data as input. For the inner block temperature measurement, special T-type temperature sensors with a common positive pole were introduced. By using the film formation technique of sputtering, the temperature junctions can be placed at a depth of several micrometers beneath the surface of interest.

The developed system was used to determine the change in the surface heat flux and surface temperature during a boiling process. The results from the experiments showed that the special T-type micro temperature sensors can effectively trace the temperature change during a boiling process. By using the measured inner temperatures, one-dimensional IHCP was solved to obtain the surface heat flux and surface temperature. The increase in the surface heat flux with the formation of big bubbles was calculated successfully.

5. References

Buchholz M., Luttich T., Auracher H., Marquardt W., (2004). Experimental investigation of local process in pool boiling along the entire boiling curve, *Int. J. Heat Fluid*, Vol. 25, 243 -261

Burggraf, O.R., (1964). An exact solution of the inverse problem in heat conduction theory and applications, *ASME J. Heat Transfer*, Vol. 86, 373-382

Carslaw H.S., Jaeger J.C., Conduction of Heat in Solids, Oxford University Press, 2003.

Enomoto Y. & Furuhama S., (1984). Research on thin film thermocouple for transient surface temperature measurement in internal combustion engine, *Transactions of Japan Society of Mechanical Engineering, series B*, Vol.50, No.453, 1353-1362, (In Japanese).

Imber M., (1974). Temperature extrapolation mechanism for two-dimensional heat flow, *AIAA J.* Vol.12, No.8, 1089-1093

Liu W. & Takase K. (2009). Measurement of surface heat flux and surface temperature in Nucleate Pool Boiling Using Micro-Thermocouples, *Proceedings of the 17th International Conference on Nuclear Engineering,* ICONE17-75880

Monde M., Arima H. & Mitsutake Y., (2003a) Estimation of surface temperature and heat flux using inverse solution for one-dimensional heat conduction, *ASME J. Heat Transfer,* Vol .*125,* 213-223.

Monde M., Arima H., Liu W., Mitsutake Y. & Hammad J.A., (2003b). An analytical solution for two-dimensional inverse heat conduction problems using Laplace transform, *Int. J. Heat Mass Transfer,* Vol. 46, 2135-2148

Shoji M. (1978). Study of inverse problem of heat conduction, *Transactions of Japan Society of Mechanical Engineering, series B,* Vol. 44, No.381, 1633-1643 (in Japanese).

Sparrow E.M., Haji-Sheikh A. & Lundgren T.S., (1964). The inverse problem in transient heat conduction, *ASME J. Appl. Mech.,* Vol. 31, 369-375

Woodfield P.L., Monde M. & Mitsutake Y., (2006a). Implementation of an analytical inverse heat conduction technique to practical problems, *Int. J. Heat Mass Transfer,* Vol. 49, 187-197.

Woodfield P.L., Monde M., Mitsutake Y., (2006b). Improved analytical solution for inverse heat conduction problems on thermally thick and semi-infinite solids, Int. *J. Heat Mass Transfer,* Vol. 49, 2864-2876.

17

Properties and Numerical Modeling-Simulation of Phase Changes Material

Pavel Fiala, Ivo Behunek and Petr Drexler
Brno univerzity of technology, Faculty of electrical engineering and communication, Department of theoretical and experimental electrical engineering, Kolejni 4, Brno Czech Republic

1. Introduction

There exists a domain of models that is principially classified into the linear and non-linear fields of modelling. In the field of non-linear modelling, significant progress has been made since the 1960s thanks to the widespread and regularly available computer technology. This dynamic development influenced a large number of problems including the description of physical behaviour of non-trivial tasks. Non-linear models are solved in the material, spatial, and time domains. However, certain non-linear model domains are not sufficiently developed or regularly used for analysis of the more simple tasks. This group includes task models using non-linear discontinuous characteristics of materials, which can be exemplified by the change of state of a material during heating or cooling. In this section, we would like to use several descriptive examples to expose the problem of thermal tasks solution utilizing applied materials with a phase change (PCM) (Gille, T.; at al. 2007, Volle, F. at al. 2010, Shi, L.P.; at al. 2006). These are mostly coupled tasks (Fiala,P. December 1998). Within the specification of different aspects of the solution process, emphasis will be placed on the final accuracy of the results of numerical analyses, and therefore (rather than focusing on a complete description of the model) the text will accentuate problematic spots within the solution of such tasks.
The PCM characteristics are demonstrated on the task of designing a low-temperature accumulator, an efficient cooler of electronic components, and a separator of impurities in an industrial oil emulsion.

1.1 Energy, transformation, accumulation

Within the last decade, scientific interest in the fields of basic and applied research has been focused more intensively on the problem of increasing the share of renewable sources of energy in total energy consumption per capita (Solar energy 2010). In this context, we have seen major development in the field of energy harvesting (Murat Kenisarin, & Khamid Mahkamov May 2006, John Greenman at al. May 2005, Junrui Liang & Wei-Hsin Liao 2010, Vijay Raghunathan at al. April 2005, Jirku T at al. May 2010), or the acquirement of energy from hitherto unused forms. The reason for such processes in technology naturally consists in the fact that the reserves of classical primary sources of energy and fossil fuels (Behunek, I. 2002, WORLD ENERGY STATISTICS from the IEA 2002) available to current industrial

society are limited. Moreover, such classification applies also to the possibilities of utilizing the energy of water and wind.
A large number of countries have committed themselves to the reduction of greenhouse gas emissions and the related increase of renewable sources of energy (Ministery of industry and trade of Czech Republic, Stat energetic conception 2004, Ministery of industry and trade of Czech Republic 2000) share in total energy consumption. However, the effort to comply with these commitments may be realized in absurd ways such as an uncontrolled surge in the number of constructed solar photovoltaic systems, which is further aggravated by the related problem of their integration into the energy production system of a country, Fig. 1.

Fig. 1. A photovoltaic power plant design, the Czech Republic

One of the applicable alternative source solutions consist in utilizing solar radiation (Solar energy, 2010) within its entire spectrum. Among the advantages of this energy harvesting method there are mainly the low cost of the impinging energy, the unimpeded availability of the source in many regions of the Earth, and the polution-free operation. Conversely, the related disadvantages can be identified in the low density of the impinging radiation power flow in the visible and the near-visible spectrum ($\lambda \in$<440,780> nm), the comparatively low efficiency of transformation into other forms of energy (considering the currently used photovoltaic elements), and the fact that the cost of a produced energy unit is often rather high when compared to other clean sources of electrical energy (such as nuclear power plants) (Kleczek, J. 1981). In consequence of the uneven power flow density of the solar source within the daily or yearly cycle and owing to weather changes, the solar energy application method is affected by the problems of effective utilization, regulation in power systems, and necessity of accumulating the energy acquired from solar radiation.
A feasible technique of energy accumulation seems to consist in direct exploitation of physical effect of material properties as related to metals, liquids and gases (Gille, T. 2007, Shi, L.P. 2006). Accumulators will facilitate power take-off during any time period depending on the needs of the consumer or the power system operator, which provides for the balance in the cost/power take-off relation within the required time interval. Thus, the power distribution network stability will be improved, with substantial reduction of the probability of black-out (Black-out 2003). There occurs the compensation of time disproportion between the potential of the sources and the eletrical energy on the one hand and the consumption in time and place on the other. Solar energy accumulation can be technologically realized through a wide variety of methods; also, research in the field is

being consistently developed (Juodkazis, Saulius; at al. November 2004, Zhen Ren at al. Januar 2010, Liu, Y.-T.; at al. 2008).
Some of the proposed approaches are based on classical solutions. These include the accumulation of energy utilizing the potential energy of mass in a gravitational field (water), the kinetic energy of mass (flywheels), the non-linearities in the state of a mass phase – the compression of gases. Another group of accumulators is based on the solution utilizing the energy of an electromagnetic field. In this case, the most common is the application of electric accumulators or microbiological systems [mikrobiolog akumulator]. Yet another one of the fields to be quoted comprises energy accumulation using the properties of chemical bonds of non-trivial chemical systems (the production of synthetic fuels), electrochemical bonds, and the utilization of photochemical energy (the accumulation of low-potential heat in solar-powered systems).
The process of designing chemical accumulator forms utilizes the physical effects of non-linear behaviour of materials at phase changes. (Behunek,I. April 2004, Behunek I & Fiala P. Jun 2007).

2. Heat accumulation

Principles are known (Baylin, F. 1979) for the utilization of characteristics of chemical-physical effects, and in this context there exist four basic methods of thermal energy accumulation. The first method consists in the utilization of specific thermal capacity of substances (sensible heat), the second one is built on the application of change in the state of substances (latent heat) , the third one lies in the thermochemical reaction, and the fourth one applies the sorption and desorption of gas / water vapour.
Generally, the thermochemical reactions method provides a higher density of accumulated energy than the sensible heat or phase change options (Mar, R.W. & Bramletta, T.T. 1980). An endothermic reaction product contains energy in the form of a chemical bond that is released retroactively during an exothermic reaction. The energy release occurs through the action of a catalyst, which is a suitable characteristic for long-term accumulation. Other advantages of thermochemical accumulation include the possibility of transporting the products over long distances, the possibility of product storage at both low (with a low rate of loss) and very high temperatures (Goldstein, M. 1961), the low cost, and the fact that products of the reaction can be used as the medium in thermodynamic cycles (The Australian National University 2004). Currently, research (Mar, R.W. 1978, Mar, R.W. 1980) is conducted in this field. In order to accumulate energy, we can utilize heat balance at sorption/desorption of moisture in the working substance. The difference with respect to other types of heat accumulation consists in the fact that sorption does not directly depend on the temperature,. but rather on relative humidity of the surrounding air. Therefore, the described method of accumulation may be realized at a constant temperature, which is an aspect utilizable in discharging the accumulator. In the progress of charging, relative humidity of air is decreased to the required level through heating the air to achieve a higher temperature (Close, D.J. & Dunkle, R.V. 1977, Verdonschet, J.K.M. 1981).

2.1 Classical heat accumulation methods

The classical accumulation of heat utilizes the so-called sensible heat of substances (Kleczek, J., 1981) being the simplest one of all the methods, this approach was historically used in the first place. Traditional materials applied for the accumulation of heat are water and gravel.

The weight and specific heat capacity of these materials indicate the accumulable quantity of heat. This quantity is given by the calorimetric equation

$$Q = \int_{T_1}^{T_2} V \rho c \mathrm{d}T \tag{1}$$

where T_1 is the temperature at the beginning and T_2 the temperature at the end of charging.

2.2 Water heat reservoirs

If water is utilized in the process of accumulation, it is usually held in a suitable container during heating (Garg, H.P., at al. 1985). Even though the applicaton of water has proved to be advantageous in many respects, there are also many drawbacks, especially for the preservation of low-potential heat. Water has the highest specific heat capacity of all known substances (Vohlídal J. et al. 1999). It can be applied as an accumulation and working medium (exchangers are not necessary); charging and discharging can be simulated in an exact manner. If water is applied, heat storage or offtake causes temperature fluctuation and the thermal potential is lost (namely the accumulator is charged at a sufficiently high input temperature T, which is averaged in the reservoir to a mean temperature $T_{stř}$ and, during the subsequent heat offtake, the original temperature T can not be reached) (Fisher L.S. 1976, Lavan, Z. & Thomson, J. 1977). With water accumulators, liquid photothermal collectors need to be applied; this means that expensive and rather complicated technologie and installation methods are used as opposed to the hot.-air option) .

2.3 Gravel heat accumulators

For multi-day or seasonal accumulation (Behunek, I. April 2004), heat reservoris utilizing gravel are preferred; here, the air used as the heating medium is heated in hot-air collectors. This system eliminates some of the disadvantages of the previously described method. In regular realizations, Figure 2, heat transfer by conduction is also minimal (the individual gravel pieces touch one another only at the edges); here, however, the characteristics include low heat capacity of the crushed stone (excessive dimensions of the reservoir) as well as a very difficult (even impossible as per (Garg, H.P., et al. 1985) simulation of charging and discharging.

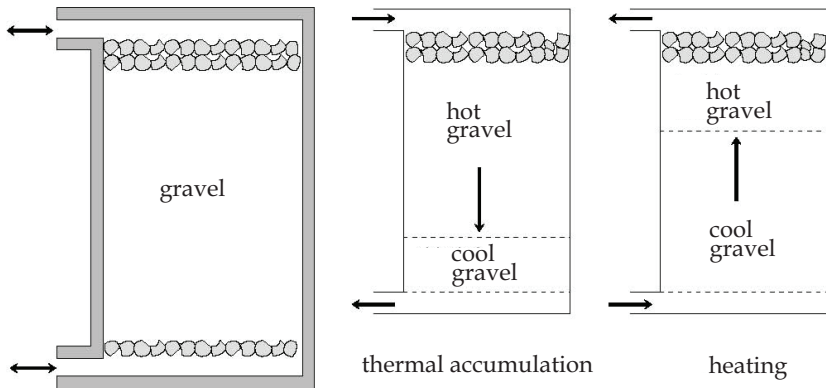

Fig. 2. Schematic description of a heat accumulator using gravel

2.4 Utilizing the change of state in substances for the accumulation of heat

A prospective method of heat accumulation consists in utilizing the change of state of a substance used in a heat reservoir. Such reservoir charges (fillings) are described by the abbreviation PCM (Phase Change Material). According to Ehrenfest (Mechlova, E., Kostal, K. 1999), the changes of state are among the first type of phase changes, where the change of internal energy and substance volume occurs through a jump. If specific melting heat or solidification of the given substance is utilized, the calorimetry equation assumes the form

$$Q = \rho V \Delta h_{\mathrm{m}} + \int_{T_0}^{T_{\mathrm{m}}} V \rho c \mathrm{d}T + \int_{T_{\mathrm{m}}}^{T_{\mathrm{e}}} V \rho c \mathrm{d}T \tag{2}$$

where ρ is the density, V the volume, c the specific heat, Δh_{m} the enthalpy, Q the heat, and T_{m} , T_{e} the temperature according to Figure 3. If heat is supplied to the material, there occurs the transformation from the liquid into the solid state. Phase transition appears when crystal lattice is disrupted, namely when the amplitude of the crystal lattice particles oscillation is comparable with relative distance between the particles. At this moment, the oscillation energy rises above the value of the crystal binding energy, the bond is broken and the crystal transforms into the liquid phase. However, if heat is removed from the substance, there occurs the solidification (crystallization) of material. During crystallization, the orderly motion of molecules gradually assumes the character of thermal oscillations around certain middle positions, namely crystal lattice is formed. In pure crystalline substances, melting and solidification proceed at a constant temperature T_m, which does not vary during the phase transition. In amorphous substances, the phase transition temperature is not constant and the state change occurs within a certain range of temperatures, Figure 4. In simplified terms for a macroscopic description of the numerical model, the phase change of a material is understood as a state in which the material changes its physical characteristics on the basis of variations (external) of its thermodanymic system. This state is often accompanied by a nonlinear effect, Figure 3. The effect involves energy Q supplied to the thermodynamic system of the material, temperature T, latent energy ΔQ necessary to change the externalmacroscopic state of the material, initial state temperature T_0, phase change temperature T_{m} , and temperature T_e limiting the low-temperature mode.

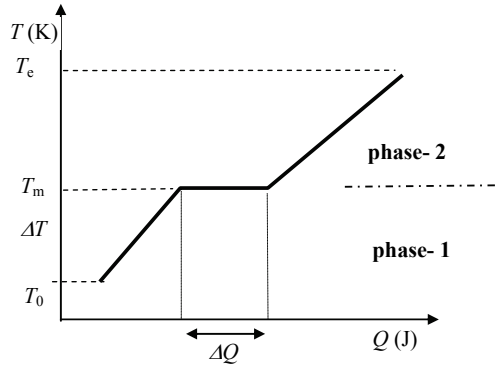

Fig. 3. The PCM macroscopic characteristics

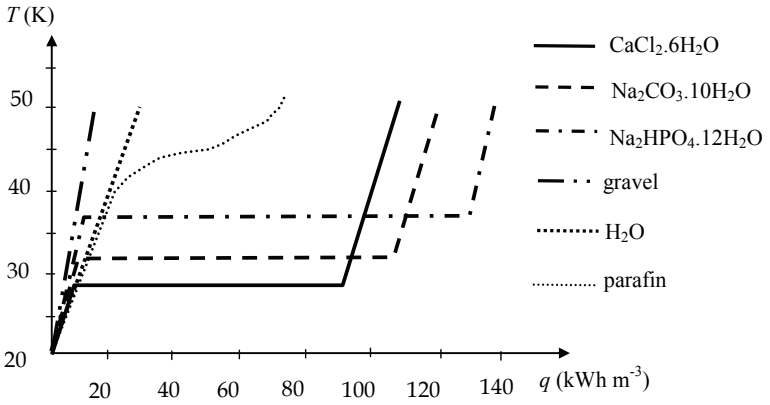

Fig. 4. The course of accumulator charging with PCMs and classical materials

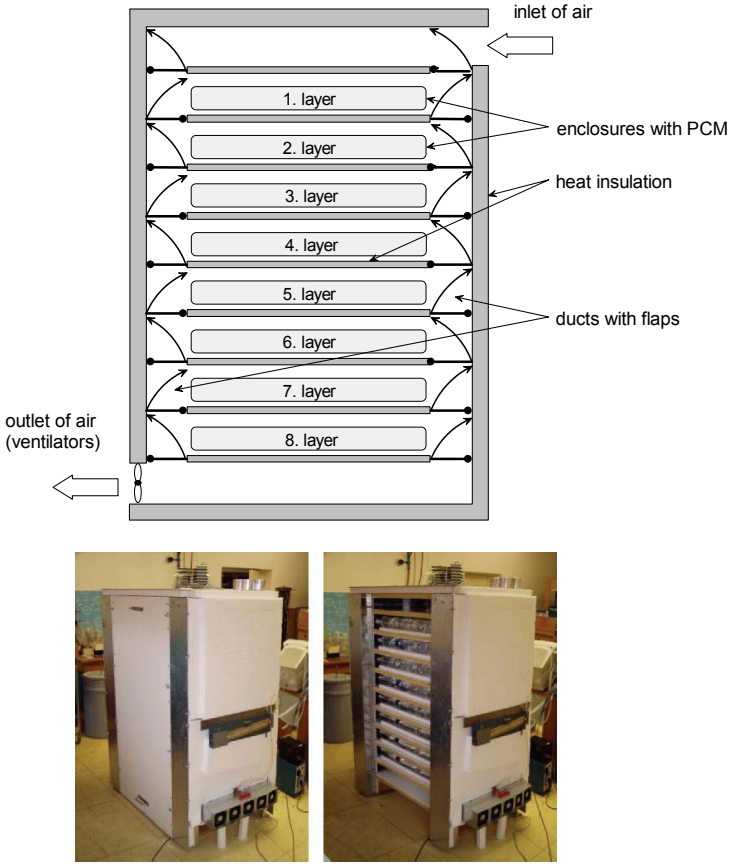

Fig. 5. Experimental model of a heat accumulator

2.5 Requirements placed on the PCM, reservoirs and casings

PCM materials applicable for the accumulation of heat utilizing state change ought to meet the following criteria (Behunek, I. 2002): Physical (a suitable phase diagram in the transition area, a suitable phase transition temperature, small changes of volume during the change of state, high density of the substance, supercooling tolerance, high specific melting heat, good thermal conductivity), chemical (nonflammability, nontoxicity, chemical stability, anticorrosive properties), economical (low asking price, availability, low cost of a suitable accumulator). The structure of PCM reservoirs must conform to standard requirements placed on thermal containers. In general, with respect to the provision of a suitable speed of heat transfer, it is necessary to encase the actual PCM material and insert the resulting containers that hold the PCM into an external envelope; this insertion should be realized in such a way that, through its circulation, the heating medium ensures an optimum transfer of heat energy in both directions (during charging and discharging), Figure 5.

Consequently, there exists substantial similarity to caloric reservoirs containing crushed stone (aggregate) and therefore the rules governing the construction of these reservoirs can be applied.

2.6 Basic classification of PCM materials

If we are to futher consider the properties of PCMs, it is necessary to describe their minimum classicification and properties in phase changes, relation (3).

a. The advantages of *anorganic substances* (GARG, H.P. et al. 1985, VENER, C. 1997) mainly consist in the high value of specific melting heat, good thermal conductivity, nonflammability, and low cost. The negative characteristics include corrosivity of the substances to most metals, decomposition, loss of hygroscopic water, and the possibility of supercooling.

Examples of anorganic PCMs are as follows:
$CaCl_2.6H_2O$, $Na_2SO_4.10H_2O$, $Na_2CO_3.10H_2O$, $MgCl_2.6H_2O$, $CaBr_2.6H_2O$, $Mg(NO_3)_2.6H_2O$, $LiNO_3.3H_2O$, $KF.4H_2O$, $Na_2SO_4.10H_2O$, $Na_2HPO_4.12H_2O$.

$$X(Y)_n \cdot mH_2O \xleftarrow{\text{teplo}} X(Y)_n \cdot pH_2O + (m-p)H_2O \tag{3}$$

b. *Organic substances* (GARG, H.P. et al. 1985, VENER, C. 1997) offer advantages such as a high value of specific melting heat, chemical stability, elimination of supercooling, and no corrosivity. The disadvantages consist in the inferior thermal conductivity, relatively significant variations of volume during the change of state, flammability). Examples of organic PCMs include paraffin, wax, polyethylene glycol, high-density polyethylene, stearic acid ($C_{17}H_{35}COOH$), and palmitic acid ($C_{15}H_{31}COOH$).
c. *Other substances* include compounds, combinations of amorphous and crystalline substances, kombinace amorfních a krystalických látek, clathrates, and other items.

The advantage of low-potential heat accumulation in PCM application consists in the variability. A comparison of PCM and classical materials together with a listing of several PCMs (] LANE, G.A. 1983, FAVIER, A. 1999) is provided in Table 1. The elementary reference quantity is the density of accumulated energy. We assume the initial charging temperature as T_0 20 °C and the final termperature as T_e 50 °C. The course of accumulator loading with various types of filling (charge) is shown in Figure 4; a realization example of a PCM-based accumulator is provided in Figure 5.

Material used for accumulation in heat reservoir	Accumulated energy density q [kWh.m^{-3}]
Water	34,5
Aggregate of stones	23,0
Paraffin	62,4
$CaCl_2$. $6H_2O$	117,4
Na_2CO_3 . $10H_2O$	131,7
Na_2HPO_4 . $12H_2O$	134,7

Table 1. A comparison of accumulated energy density for different substances

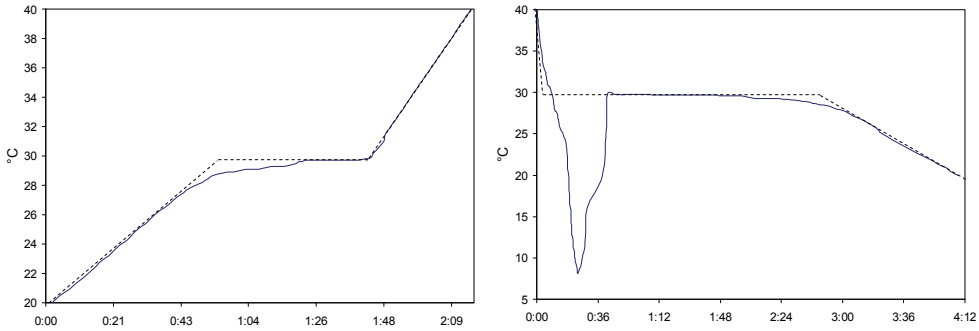

Fig. 6. Phase changes of $CaCl_2.6H_2O$

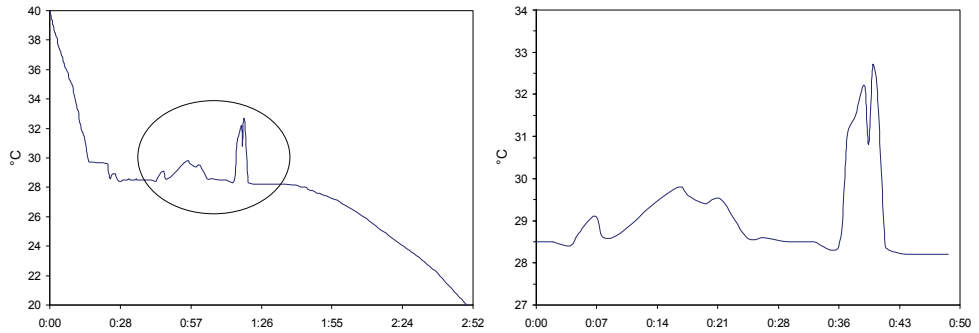

Fig. 7. Phase change of $CaCl_2.6H_2O$ ($CaCl_2.4H_2O$ crystallization)

2.7 Calcium chloride hexahydrate and its modification

In Figure 6, the phase change of $CaCl_2.6H_2O$ during heating and cooling is shown. The dashed lines show the theoretical behaviour under the condition when the melting and freezing were realized at constant temperature T_m – the case of pure crystallic substances. Impurity and the methodology of measuring are the main cause of variations (the probe has to be placed only in small amounts of hexahydrate. During solidification, ing occurred

owing to weak nucleation. Crystallization was initiated thanks to a solid particle of the PCM added to the measured sample. Otherwise, the crystallization would not have occurred. The group of materials for the encasing of hexahydrate may include plastics, mild steel or copper; aluminium or stainless steel are not suitable.
In some cases, temperature fluctuation above T_m may occur during solidification (Figure 7). The explanation was found in the binary diagram.
Figure 4 indicates the binary phase diagram of calcium chloride and water. The hexahydrate contains 50,66 wt% $CaCl_2$, and the tetrahydrate 60,63 wt%. The melting point of the hexahydrate is 29,6 °C, with that of the tetrahydrate being 45,3 °C. The hexahydrate-α tetrahydrate peritectic point is at 49,62 wt% $CaCl_2$-50,38 wt% H_2O, and 29,45 °C. In addition to the stable form, there are two monotropic polymorphs of the tetrahydrate salt, β and γ. The latter two are rarely encountered when dealing with the hexahydrate composition; however, the α tetrahydrate is stable from its liquidus temperature, 32,78 °C, down to the peritectic point, 29,45 °C, thus showing a span of 3,33 °C. When liquid $CaCl_6.6H_2O$ is cooled at the equilibrium, $CaCl_2.4H_2O$ can begin to crystallize at 32,78 °C. When the peritectic is reached at 29,45 °C, the tetrahydrate hydrates further to form hexahydrate, and the material freezes. The maximum amount of tetrahydrate which can be formed is 9,45 wt%, calculated by the lever rule. This process is reversed when solid $CaCl_6.6H_2O$ is heated at the equilibrium. At 29,45 °C the peritectic reaction occurs, forming 9,45% of $CaCl_2.4H_2O$ and the liquid of the peritectic composition. With increasing temperature, the tetrahydrate melts, disappearing completely at 32,78 °C. Under actual freezing and melting conditions, the equilibrium processes described above may occur only partially or not at all. Supercooling of the tetrahydrate may lead to initial crystallization of the hexahydrate at 29,6 °C (or lower if this phase also supercools). It is possible to conduct modification by additives. From a number of potential candidates, $Ba(OH)_2$, $BaCO_3$ and $Sr(OH)_2$ were chosen as they seemed to be feasible. When we used $Ba(OH)_2$ and $Sr(OH)_2$ at 1% part by weight, there was no supercooling. We were able to increase the stability of the equilibrium condition by adding KCl (2 wt%) and NaCl, Figure 8. NaCl is a weak soluble in $CaCl_2.6H_2O$, therefore the part by weight is only about 0,5%. The related disadvantage is that the melting point decreases by ca. 3 °C at 26-27 °C.

2.8 Numerical model of heat accumulators

The effectivity of transferring the heat to active elements in the accumulator consists in the optimum setting of dimensions and shapes in the process of circulation of the medium that transfers energy in the accumulator. Therefore, a necessary precondition of the design consisted in solving the air circulation model under the condition of change in its temperature and thermodynamical variations in the PCM material. The actual model of active elements and its temperature characteristic is not fundamental to this task; the characteristic is known and realizable through commonly appplied methods.
A geometric model of one layer of the accumulator is shown in Figure 10 (Behunek, I. 2004) It consists of 26 PVC pipes in a square configuration (Lienhard, J.H. IV & Lienhard, J.H. V. 2004). Inside of the pipes there are 9,36 litres of modified $CaCl_2.6H_2O$. The air flows through the layer and transfers heat into the pipes. The related numerical solution was realized in two parts. First, we solved the turbulence model and obtained the heat transfer film coefficients. These results constituted the input for the solution of the second part namely the calculation of the thermal model. The time dependence of temperature distribution in the layer is the final result.

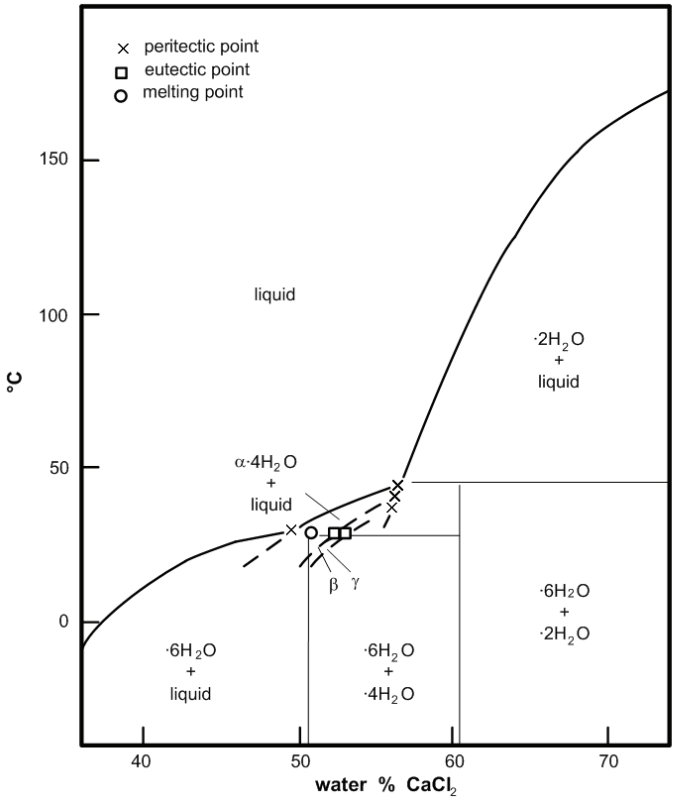

Fig. 8. Binary diagram of $CaCl_2.6H_2O$ [9]

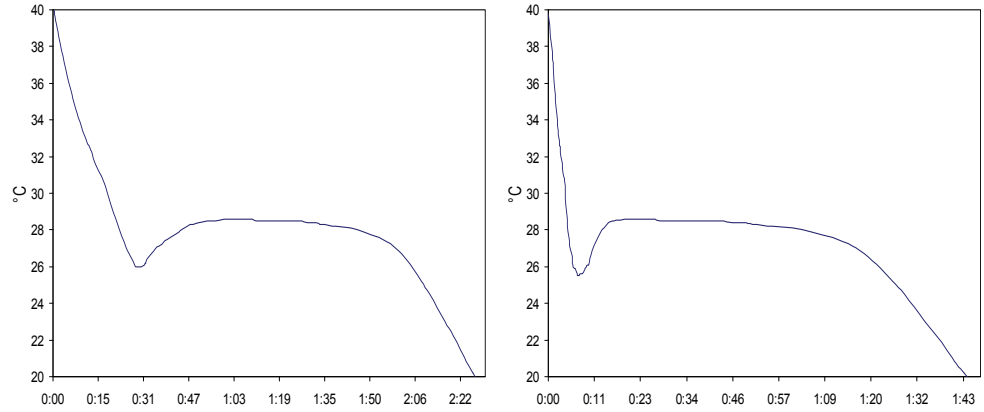

Fig. 9. Modification of $CaCl_2.6H_2O$ at a different rate of heat removal

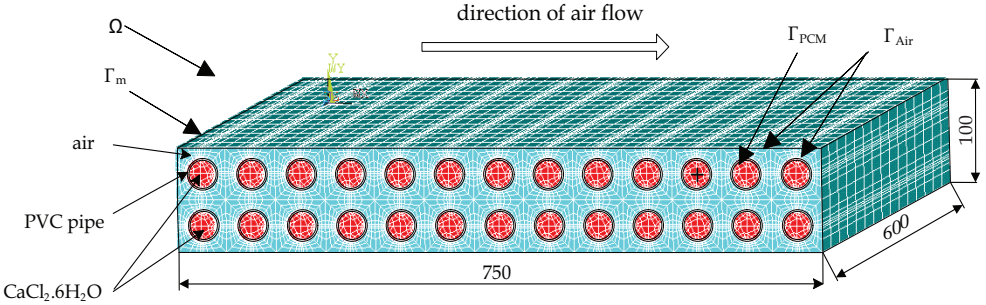

Fig. 10. Geometric model of a layer with the mesh of elements

2.8.1 Mathematical and numerical model

The mathematical model of air velocity distribution uses fluid equations which were derived for the incompressible fluid with the condition

$$div\ \nu = 0 \tag{4}$$

For a steady state of flow there holds the continuity equation

$$div\ \rho\nu = 0 \tag{5}$$

We assume a turbulent flow

$$curl\ \nu = 2w \tag{6}$$

where $\boldsymbol{\omega}$ is the angular velocity of fluid. If we use the Stokes theorem, the Helmholtz theorem for the moving particle and the continuity equation, we can formulate from the equilibrium of forces the Navier-Stokes equation for the fluid element

$$\frac{\partial \boldsymbol{v}}{\partial t} + (grad\boldsymbol{v})\cdot\boldsymbol{v}^T = \boldsymbol{A} - \frac{1}{\rho} grad\ p + \boldsymbol{\upsilon}\cdot\Delta\boldsymbol{v} \tag{7}$$

where $\boldsymbol{A}$ is the external acceleration, $\boldsymbol{\upsilon}$ the vector of kinematic viscosity, and ($grad\ \boldsymbol{v}$) has the dimension of tensor. In equation (7) we substitute pressure losses

$$\begin{aligned} grad\,p = &-\left(K_x\rho v_x|\mathrm{v}| + \frac{f}{D_h}\rho v_x|\mathrm{v}| + C_x\mu v_x\right)\mathrm{u}_x - \left(K_y\rho v_y|\mathrm{v}| + \frac{f}{D_h}\rho v_y|\mathrm{v}| + C_y\mu v_y\right)\mathrm{u}_y \\ &-\left(K_z\rho v_z|\mathrm{v}| + \frac{f}{D_h}\rho v_z|\mathrm{v}| + C_z\mu v_z\right)\mathrm{u}_z \end{aligned} \tag{8}$$

where K are the suppressed pressure losses, f the resistance coefficient, D_h the hydraulic diameter of ribs, C the air permeability of system, μ the dynamic viscosity, and $\boldsymbol{u}_{x,y,z}$ the unit vector of the Cartesian coordinate system. The resistance coefficient is obtained from the Boussinesq theorem

$$f = aRe^{-b} \tag{9}$$

where *Re* is Reynolds number and *a*, *b* are coefficients from [40]. The model of short deformation field is formulated from the condition of steady-state stability, which is expressed

$$\int_{\Omega} \boldsymbol{f}\,\mathrm{d}\Omega + \int \boldsymbol{t}\,\mathrm{d}\Gamma = 0 \tag{10}$$

where $\boldsymbol{f}$ are the specific forces in domain $\boldsymbol{\Omega}$, and $\boldsymbol{t}$ the pressures, tensions and shear stresses on the interface area $\boldsymbol{\Gamma}$. By means of the transformation into local coordinates, we obtain the differential form for the static equilibrium

$$\boldsymbol{f} + div^2 \boldsymbol{T}_{\mathrm{v}} = 0 \tag{11}$$

where div^2 stands for the div operator of tensor quantity and $\boldsymbol{T}_{\mathrm{v}}$ is the tensor of internal tension

$$\boldsymbol{T}_{\mathrm{v}} = \begin{bmatrix} X_{\mathrm{x}} & X_{\mathrm{y}} & X_{\mathrm{z}} \\ Y_{\mathrm{x}} & Y_{\mathrm{y}} & Y_{\mathrm{z}} \\ Z_{\mathrm{x}} & Z_{\mathrm{y}} & Z_{\mathrm{z}} \end{bmatrix} \tag{12}$$

where *X*, *Y*, *Z* are the stress components which act on elements of the area. It is possible to add a form of specific force from (4)-(7) to the condition of static equilibrium. The form of specific force is obtained by means of an external acceleration $\boldsymbol{A}$, on the condition that pressure losses and shear stresses τ are given as

$$\rho\left(\frac{\partial \boldsymbol{v}}{\partial t} + \cdot(grad\boldsymbol{v})\cdot\boldsymbol{v}^{T}\right) - \rho\boldsymbol{A} - \sum_{l=1}^{N_{\mathrm{s}}} \boldsymbol{F}_{\mathrm{l}} + div^2 \boldsymbol{T}_{\mathrm{v}} = \boldsymbol{0} \tag{13}$$

where $\boldsymbol{F}_{\mathrm{l}}$ are the discrete forces and div^2 is the divergence operator of tensor. The model which covers the forces, viscosity, and pressure losses is

$$\rho\left(\frac{\partial \mathrm{v}}{\partial t} + \cdot(grad\,\mathrm{v})\cdot\mathrm{v}^{T}\right) - \rho\mathrm{A} - \sum_{l=1}^{N_{\mathrm{s}}} \mathrm{F}_{\mathrm{l}} + grad\,p - \mu\cdot\Delta\mathrm{v} = 0 \tag{14}$$

We can prepare the discretization of equation (7) by means of the approximation of velocity $\boldsymbol{v}$ and acceleration $\boldsymbol{a}$ (Behunek I, Fiala P. Jun 2007). On the interface there are defined boundary and initial conditions. Initial and boundary conditions can be written; the initial temperature of the air is 50 °C, the initial velocity of the air is 0,4 m.s^{-1}, the outlet pressure is 101,3 kPa + 10 Pa, and the initial temperature of the air inside the accumulator, PVC and $CaCl_2.6H_2O$ is 20 °C. There are the distribution of velocity values indicated in figures 11, 12, and other results for the distribution of turbulent kinetic energy, dissipation, temperature and pressure follow on Figures 13. Calculation of the thermal model (finite element methode (FEM), finite volume methode (FVM), Ansys User's Manual) was realized under the same conditions as the previous turbulence model.

Figure 13 shows the time dependence of temperature in $CaCl_2.6H_2O$ in the pipe marked with a black cross (Figure 11). We can compare the result of the numerical simulation with the measurement. Differences between the simulation and the measurement are caused by the inaccuracy of the model with respect to reality.

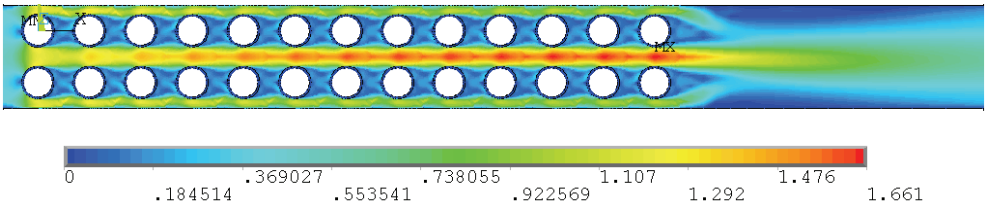

Fig. 11. Velocity distribution of the air

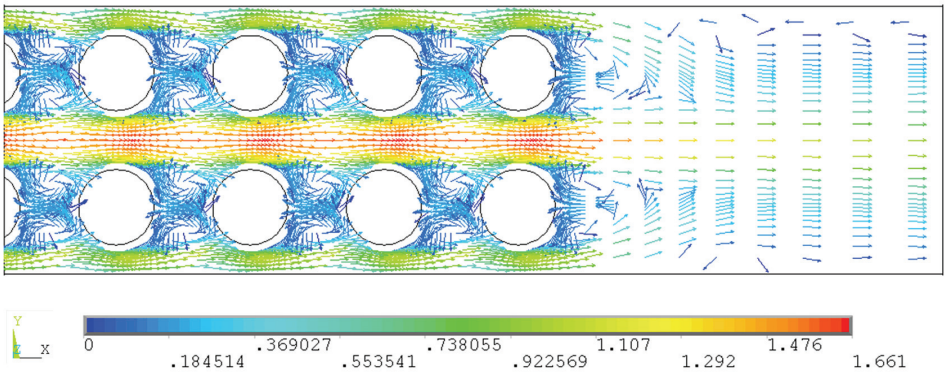

Fig. 12. Velocity distribution of the air (vectors, detail)

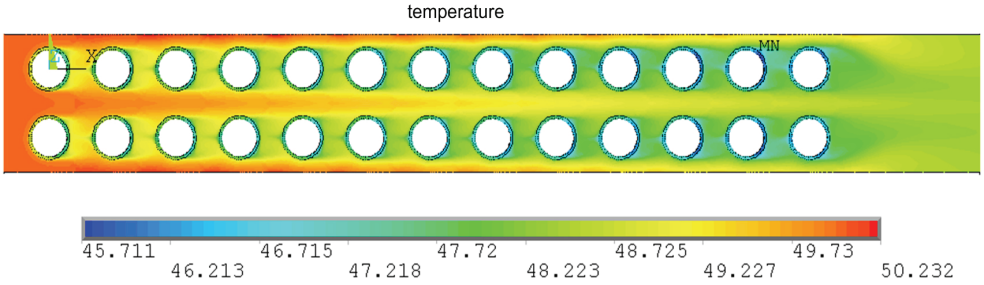

Fig. 13. Distribution of temperature

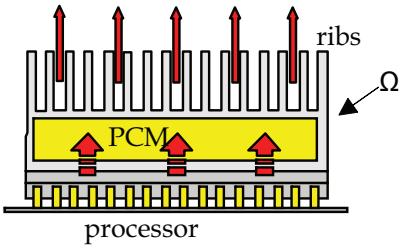

Fig. 14. Example of a processor cooler with a phase change material)

We used tabular values of pure $CaCl_2.6H_2O$; howerer, the pipes contain modified hexahydrate with 1,2% of $BaCO_3$.

3. Cooling system

The PCM may be used for active or passive electronic cooling applications with high power at the package level (see Figure 14).

3.1 Analytical description and solution of heat transfer and phase change

We analyze the problem of heat transfer in a 1D body during the melting and freezing process with an external heat flux or heat convection, which is given by boundary conditions. The solution of this problem is known for the solidification of metals. We tried to apply this theory to the melting of crystalline salts. The 1D body could be a semifinite plane, cylinder or sphere. As the solid and the liquid part of PCM have different temperatures, there occurs heat transfer on the interface. According to Fig. 16, the origin of x is the axis of pipe, centre of sphere, or the origin of plate. Liquid starts to solidify if the surface is cooled by the flowing fluid ($T_w < T_m$). The equation describing the solid state is

$$\frac{\partial T_s}{\partial t} = \frac{a_s}{x^n}\frac{\partial}{\partial x}\left(x^n \frac{\partial T_s}{\partial x}\right) \tag{15}$$

where for the plate $n = 0$, cylinder $n = 1$ and sphere $n = 2$; a_s is the thermal diffusion coefficient in the solid state. For $x = x_0$ we can assume the following boundary conditions: constant temperature

$$T = T_w \tag{16}$$

or constant heat flux

$$\lambda_s \frac{\partial T_s}{\partial x} = -q_w \tag{17}$$

or for convective cooling

$$\lambda_s = \frac{\partial T_s}{\partial x} = -k(T - T_b) \tag{18}$$

where q_w is the specific heat flux and λ_s is the thermal conductivity coefficient. Initial condition ($t = 0$) for (24) is

$$T_s(0) = T_0. \tag{19}$$

For the interface between the solid and the liquid we obtain

$$\rho_s \Delta h_m \frac{\mathrm{d}s}{\mathrm{d}t} = \lambda_s \frac{\partial T_s}{\partial x} + \alpha(T_m - T_0). \tag{20}$$

The analytical solution is exact but we consider several simplifying assumptions. The most important of these is that we can solve the solidification of PCM only in a one-dimensional body.

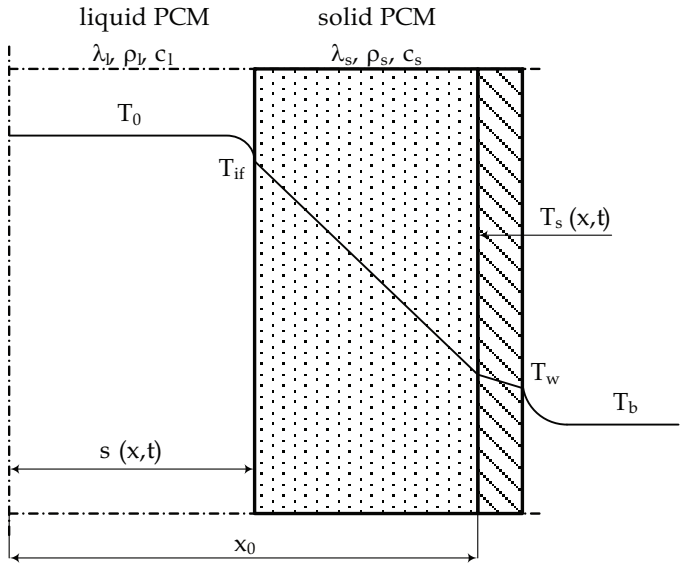

Fig. 15. Heat transfer on the interface between the solid and the liquid parts

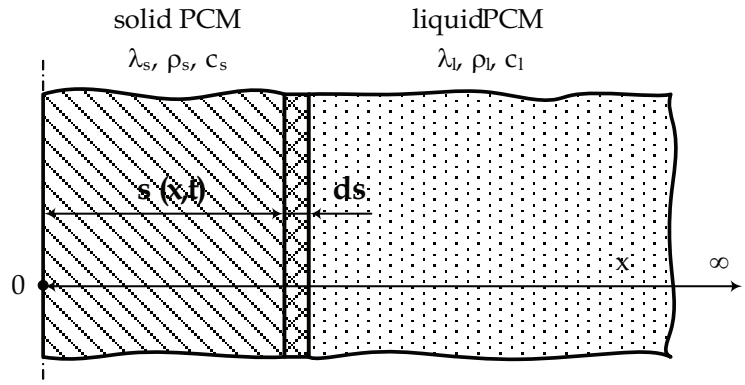

Fig. 16. Solidification of a semi-infinite plate of PCM

We consider a semi-infinite mass of liquid PCM at initial temperature T_0, which was cooled by a sudden drop of surface temperature T_p = 0 °C. This temperature is constant during the whole process of solidification. The simplifying assumptions are as follows: The body is a semi-infinite plane, the heat flux is one-dimensional in the x-axis, the interface between the solid and the liquid is planar, there is an ideal contact on the interface, the temperature of the surface is constant (T_p = 0 °C), the crystallization of PCM is at a constant temperature T_m, the thermophysical properties of the solid and the liquid are different but independent of the temperature, there is no natural convection in the liquid. The initial and boundary conditions involve initial temperature T_0 for $x \geq 0$ at time 0; the temperature equals T_m on the interface between the solid and the liquid ($x = s$)

$$x = s \wedge t > 0 \quad \Rightarrow \quad T_s = T_l = T_m = const \tag{21}$$

The evolved latent heat during the interface motion (the thickness of volume element *ds*, area 1 m², time 1 s) is

$$dQ_{\Delta h_m} = \Delta h_m \rho_l 1 \frac{ds}{dt} \tag{22}$$

Position of the interface is a function of time

$$s = s(t) = 2\varepsilon\sqrt{a_s t}, \tag{23}$$

This dependence is called the parabolic law of solidification, where ε is the root of equation describing the freezing. The boundary and initial condition for the phase change is

$$\lambda_s \left(\frac{\partial T_s}{\partial x} \right)_{x=s} = \lambda_l \left(\frac{\partial T_l}{\partial x} \right)_{x=s} + \Delta h_m \rho_l \frac{ds}{dt} \tag{24}$$

$$x \to \infty \wedge t > 0 \quad \Rightarrow \quad T_l = T_0 = const \tag{25}$$

$$x = 0 \wedge t \geq 0 \quad \Rightarrow \quad T_p = T_s(x = 0) = 0 \text{ °C} \tag{26}$$

If we solve the Fourier relations of heat conduction under the above-given conditions for the solid and the liquid, we get the equations below which allow for the calculation of temperatures in the solid, liquid PCMs as well as the location of interface. The results are shown in Figure 17, (Behunek I & Fiala P. Jun 2007).

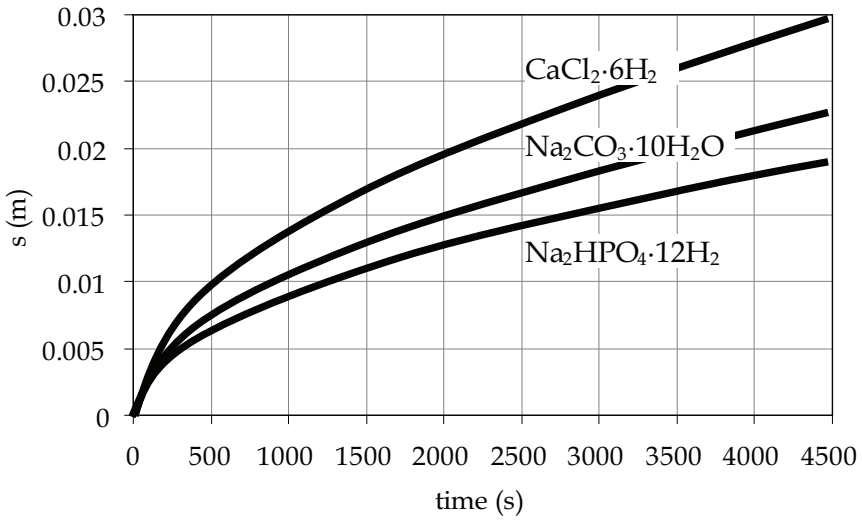

Fig. 17. Position between the solid and the liquid PCM

3.2 Nymerical analysis of heat transfer and phase change

If we compare the results of the analytical solution with the experimental measurement of the materials (Behunek, I. 2002), we can see a good agreement. Outside domain Ω, is the air velocity and pressure are zero. We can write the form for an element of mesh related to the (Behunek I & Fiala P. Jun 2007) Cu-cooler with PCM. For the description of different turbulent models see (Piszachich, W.S. 1985, Wilcox, D.C. 1994). The numerical solution consists of two parts. Firstly, we solve the turbulence model and obtain heat transfer coefficients on the surface of the ribs. These results constitute the input for the second part, in which the thermal model is calculated. We obtain the time dependence of temperature distribution in the PCM. A geometric model of a copper cooler in shown in Figure 19. The $CaCl_2.6H_2O$ is closed inside of the bottom plate (see Figure 14). The size of the plate is 30x30x5 mm, and the ribs are 20 mm in height. The PCM volume is approximately $3{,}8.10^{-6}$ m^3. The plate takes the heat from the processor up and the crystalline salt starts to melt at T_m. The air flows through the ribs and extracts heat from the cooler. In Figure 20, the distribution of air velocity module is indicated. We can see the effective rise of air flow velocity at the bottom of the ribs (detail A in Figures 19, 20). Temperature distribution in the ribs is shown in Figure 20, Figure 21 compares the results of numerical simulation with the measuring in the middle of PCM enclosure (casing). We measured the temperature by means of a probe.

The differences between the simulation and the measurement are due to the inaccuracy of the model with respect to reality. We used tabular values of pure $CaCl_2.6H_2O$ but we modified the hexahydrate with 1,2% of $BaCO_3$ to avoid supercooling and deformation of cooling curves after more cycles of melting and freezing. In order to obtain exact results, we would nevertheless need to obtain exact knowledge of the temperature dependence of thermal conductivity, specific heat and density during phase change (see Figure 22).

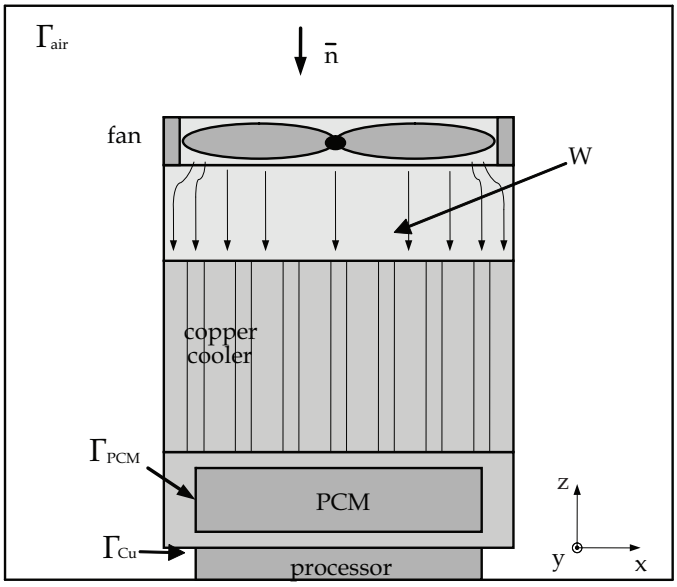

Fig. 18. Geometric model of a Cu-cooler with PCM elements

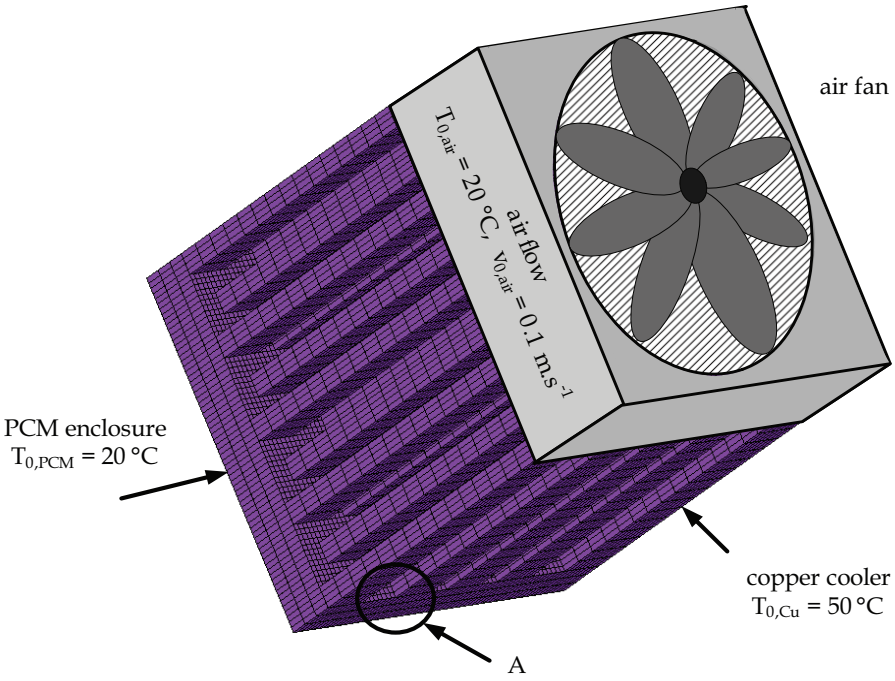

Fig. 19. Geometric model of a Cu-cooler with the mesh of elements

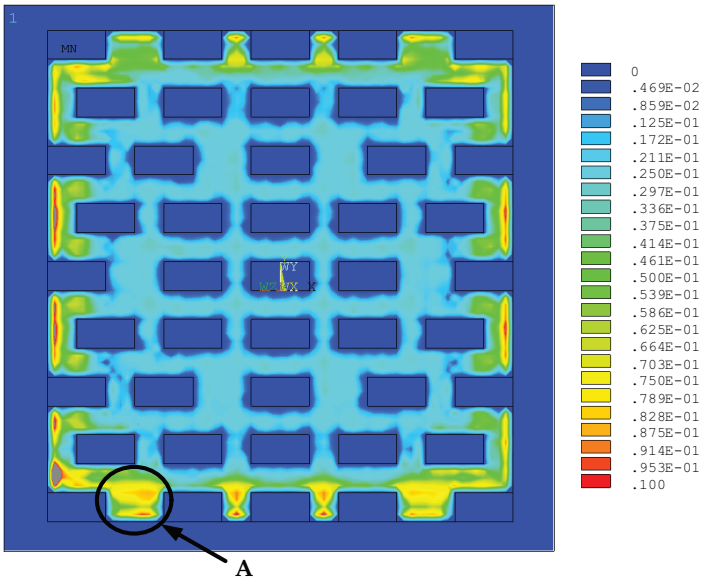

Fig. 20. The distribution of air velocity module

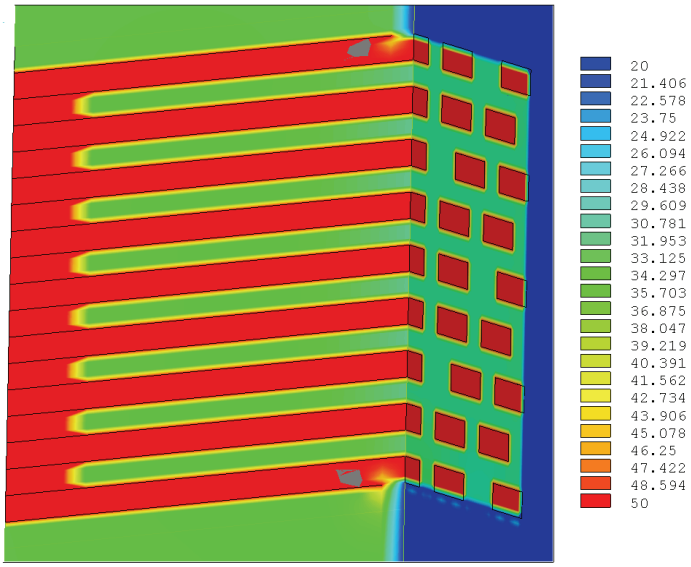

Fig. 21. Temperature distribution in the cooler (the cross section)

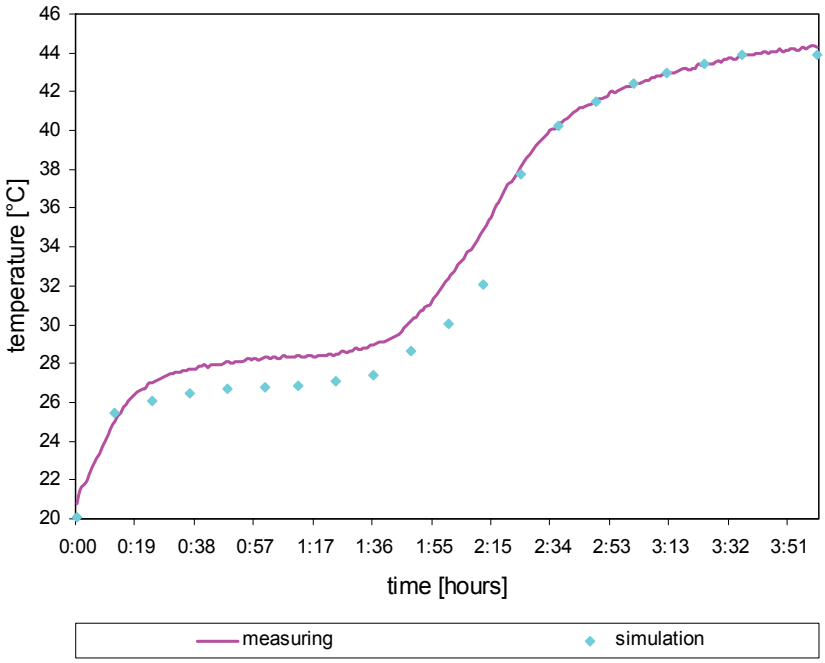

Fig. 22. Comparison between the measurement and the simulation

3.3 Results of the analysis related to accumulators and coolers

The part of the analysis of one layer of a heat accumulator which is derived from the gravel accumulator. We used pure $CaCl_2.6H_2O$ with an additional 1,2% of $BaCO_3$ to increase heat capacity and avoid supercooling. The numerical model was solved by the help of the FEM/FVM in ANSYS software (Ansys User's Manual). If we compare the results of the simulation and the experimental measuring, we will obtain comparatively good congruence. Exact knowledge of the material properties has a crucial effect on the accuracy of the numerical model.

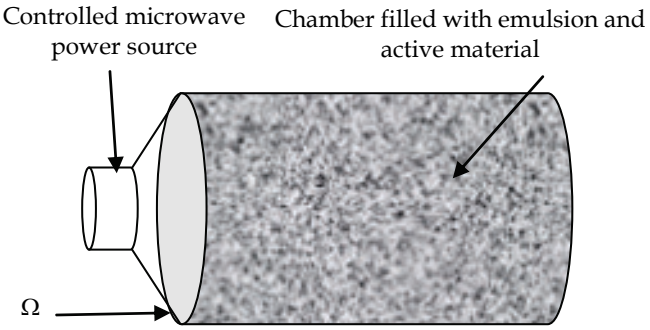

Fig. 23. The basic scheme of the reactor

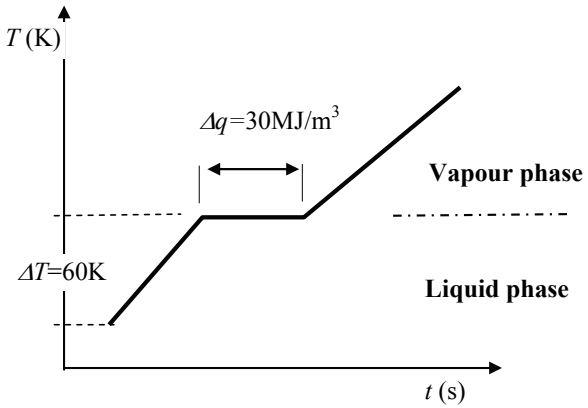

Fig. 24. The phase-change characteristics of water

4. Microwave heating for the separation of the water/oil emulsion

Industrial applications of distribution transformers used in high and mid-performance power distribution systems are supported by maintenance-free systems constructed for the purposes of separation of water bound to the transformer oil. In this case, oil is the insulator whose quality determines the life of the equipment as well as its fault or interference states. The oil is cleaned and filled with adjectives to be reused in functional parts of the transformer, and the related steps are realized in the course of the machine operation. The

described separators may utilize classical properties of H_2O and oil (the mechanical – fluid separation); alternatively, the access of heating or, for example, microwave heating may be applied. In order to use this variant, however, we need to know the process of the material phase change- H_2O to vapour (steam), and the related diversion of the vapour from the separator. Here, the numerical model proved to be superior to all experiments as it enabled us to examine the details of behaviour and states within individual operating modes of the separator. By means of this method, it is possible to model various states of the emulsion as well as fault conditions in the apparatus; thus, we may identify critical sections of the separator design and perform sensitivity analysis of the system. The reactor exploiting active porous substances was designed to enable oil preparation. The reactor is fed with an industrially produced mixture of oil and water; the desired reaction proceeds in the ceramic porous material. To achieve the desired reaction condition, it is necessary to heat the material and, simultaneously, remove the products of the reaction. After the reaction of water, further heating is undesirable with respect to side reactions. Considering the above mentioned requirements, microwave heating was chosen. The microwave heating effect is selective for the reaction of water. The designed reactor operates at the frequency of f = 2.4 GHz, with the magnetron output power of P=800W. This allows selective heating in the active porous material of the chamber. The basic scheme of the reactor is shown in Figure 23.

4.1 Mathematical model

It is possible to carry out an analysis of an MG model as a numerical solution by means of the FEM. The electromagnetic part of the model is based on the solution of full Maxwell's equations

$$\nabla \times \mathrm{E} = -\frac{\partial \mathrm{B}}{\partial t}, \qquad \nabla \times \mathrm{H} = \sigma \mathrm{E} + \frac{\partial \mathrm{D}}{\partial t} + \mathrm{J}_s, \nabla \cdot \mathrm{D} = \rho, \nabla \cdot \mathrm{B} = 0 \quad \text{in region } \Omega. \tag{27}$$

where $\boldsymbol{E}$ and $\boldsymbol{H}$ are the electrical field intensity vector and the magnetic field intensity vector, $\boldsymbol{D}$ a $\boldsymbol{B}$ are the electrical field density vector and the magnetic flux density vector, $\boldsymbol{J}$ is the current density vector of the sources, ρ is the electric charge density, σ is the electric conductivity of the material, and Ω is the definition area of the model. The model is given in manual (Ansys User's Manual). The set of equations (27) is independent of time and gives $\boldsymbol{E}$. For the transient vector $\boldsymbol{E}$ we can write

$$E = \mathrm{Re}\left\{ \underline{E} e^{j\omega t} \right\} . \tag{28}$$

The results were obtained by the solution of the non-linear thermal model with phase change of the medium. The phase change occurs via the phase conversion of water to steam. Figure 28 shows the phase-change time characteristic of water. The thermal model is based on the first thermodynamic law

$$q + \rho \quad c \quad \boldsymbol{v} \cdot divT - div\left(k \quad gradT\right) = \rho c \left(\frac{\partial T}{\partial t} \right), \tag{29}$$

where q is the specific heat, ρ is the specific weight, c is the specific heat capacity, T is the temperature, t is the time, k is the thermal conductivity coefficient, $\boldsymbol{v}$ is the medium flow velocity. If we consider the Snell's principle, the model can be simplified as

$$q - div\left(k \quad gradT\right) = \rho c\left(\frac{\partial T}{\partial t}\right) \tag{30}$$

The solution was obtained by the help of the ANSYS solver. The iteration algorithm (FEM/FVM) was realized using the APDL language as the main program. The simplified description of the algorithm is shown in Figure 25.

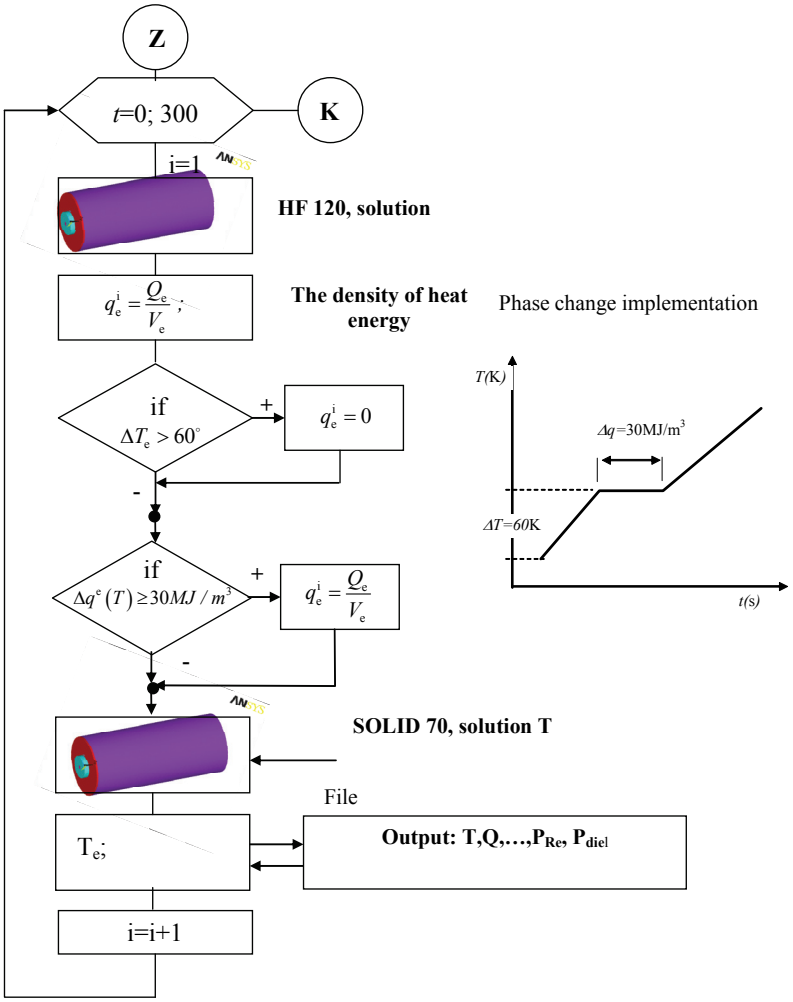

Fig. 25. The simplified iteration algorithm of the model evaluation

4.2 FEM/FVM model

A geometric model using HF119, HF120 and SOLID70 (Ansys User's Manual) in ANSYS software was built – Figure 26. A solution of the coupled field model was performed using the APDL program. The microwave model solution is evaluated according to the specific

heat. The non-linear thermal model including the phase change solves the temperature distribution. The analysis was performed for the time interval $t \in <0,300>$ s and the results were experimentally verified. The simulated results were found to correspond to measured values. A middle electrode was used in the model. The purpose of the middle electrode was to ensure the homogenous distribution of electromagnetic power and, subsequently, to increase the reaction efficiency.

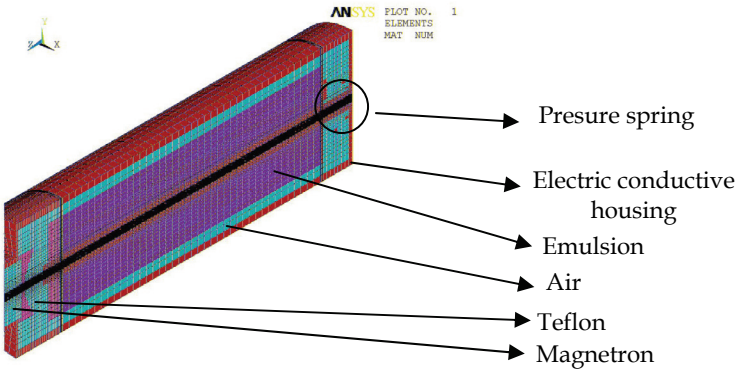

Fig. 26. The geometric model of the HF chamber

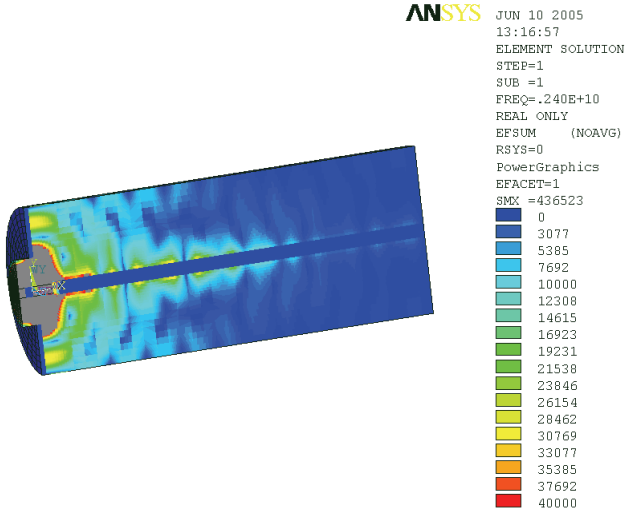

Fig. 27. The distribution of the electric field intensity vector module E

Thesic geometrical model of a separator is shown in Figure. 26; in Figures 26 and 27 we can see the distribution of the electric field vector modules with intensities E as well as the heat generated through the Joule loss in material W_{jh},. Figure 29 shows heating Θ [°C]. In Figure 26, for the given instant of time, the distribution of elements is shown in which phase

change occurred, namely exsiccation and separation of the water from the oil. t=10.8 s, with the magnetron output of P=800W and frequency f=2.4GHz. Figure 31 shows the distribution of temperature rise in the process of exsiccation; here, the indicated aspects include the heat generated through the Joule loss in the material and through dielectric heating for the instant of time t=3.6 s. The distribution of temperature was, for the individual instants, compared with the laboratory measurement.

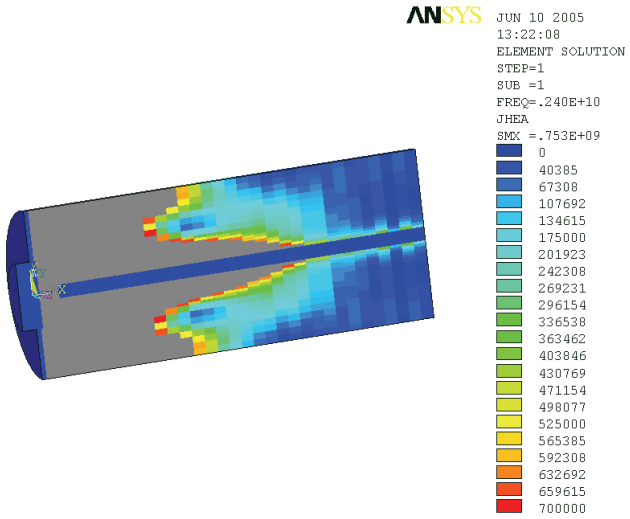

Fig. 28. The distribution module of the Joule heat module W_{jh}

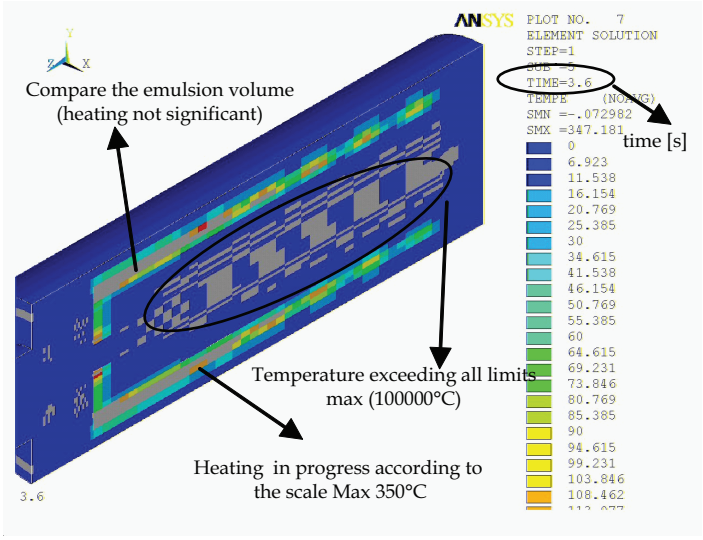

Fig. 29. The distribution of temperature rise Θ

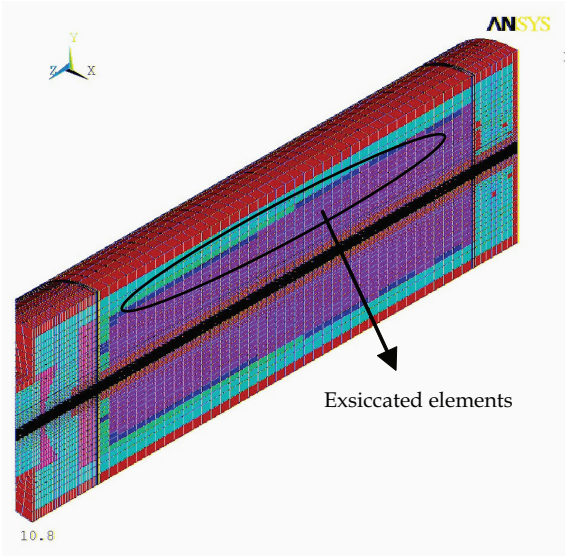

Fig. 30. The emulsion exsiccation process depending on time

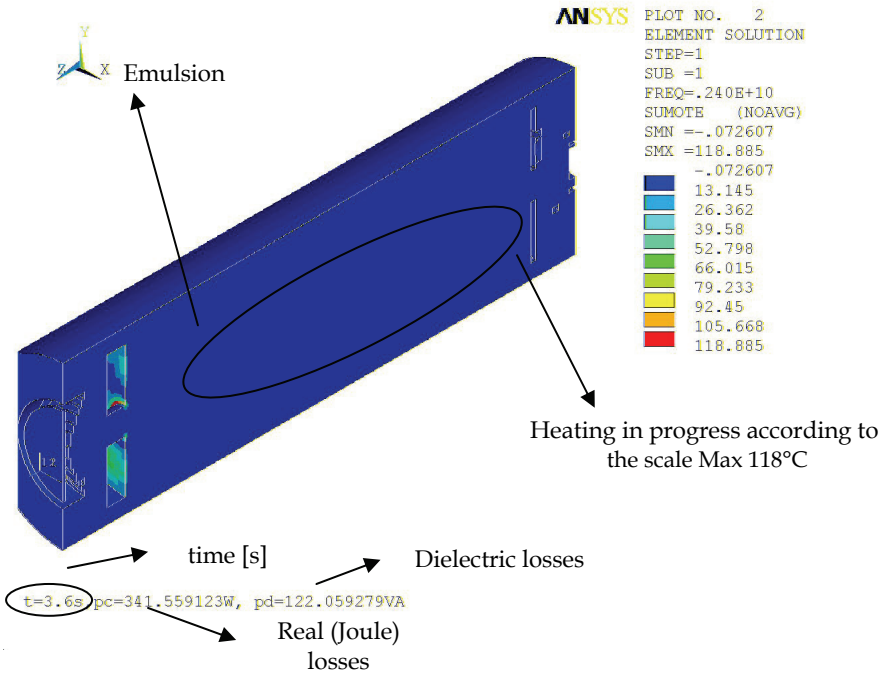

Fig. 31. The emulsion exsiccation process depending on time; emulsion heating generated by the dielectric and Joule losses; the distribution of temperature rise in the PCM model

5. Results of the thermal analysis

We may conclude that, in relation to the desiccated emulsion system, the numerical model enabled us to identify weak points of the design. These drawbacks consist in the fact that, under certain conditions, local spots might occur where uncontrolled temperature rise could result in explosion of the equipment. This status was experimentally verified.
Different variants of the reactor design were analyzed with the aim to evaluate the process and time of desiccation.
Even though modelling realized under the application of PCM produces certain theoretical complications, the actual model is reliable for the assumed boundary and initial conditions if the PCM macroscopic and microscopic properties are respected. This fact was verified experimentally and in laboratory conditions.

6. Acknowledgement

The research described in the paper was financially supported by the FRVS grant, research plan No MSM 0021630516, No MSM 0021630513.

7. References

Ansys User's Manual. Huston (USA): Svanson Analysys System, Inc., 1994-2011.

Baylin, F. (1979). *Low temperature thermal energy storage*. Golden (Colorado, USA): Solar Energy Research Institute Report No. SERI/RR-54-164.

BehuneK, I. (2004). *Operating features of accumulator for solar thermal energy storage*. In Student EEICT 2004, Bratislava: SUT in Bratislava, FEI.

Behunek, I. (2002). *Price analysis of electric heating*. In Czech, Master diploma work, DEEN, FEEC BUT, pages 72.

Behunek,I. (April 2004). *Solar system accumulation energy*. PhD thesis, BUT FEEC Brno, Czech Republic, vol. 10, pp. 41.

Behunek I, Fiala P. (Jun 2007). *Phase change materials for thermal management of IC packages*, Radioengineering Volume: 16 Issue: 2 Pages: 50-55.

Black out. (2003). http://www.cbsnews.com/stories/2003/08/15/national/main568422.shtml

Close, D.J., Dunkle, R.V. (1977). *Use of absorbent beds for energy storage in drying and heating systems*. Solar Energy 19.

Favier, A. (1999). *Almacenamiento de energia*. Dipatimento di Chimica-Fisica ed Elettrochimica, Universita degli Studi di Milano, Milano.

Fiala,P. (December 1998). Modeling of current transformers on a short- circuit. PhD thesis, VUT FEI Brno, vol. 13, ISBN 80-214-1346-8, pp. 41.

Fisher L.S. (1976). The *thermodynamics and some practical aspects of thermally layered heat storage in water*. Turnberry (Scotland): NATO Science Commitee Conference on Thermal Energy.

Garg, H.P., Mullick, S.C., Bhargava, A.K. (1985). *Solar Thermal Energy Storage*. Dordrecht (Holland): D. Reidel Publishing Company.

Gille, T.; Lisoni, J.; Goux, L.; De Meyer, K.; Wouters, D.J. (2007). *Modeling of the mechanical behavior during programming of a non-volatile phase-change memory cell using a coupled electrical-thermal-mechanical finite-element simulator*, Thermal, Mechanical and Multi-Physics Simulation Experiments in Microelectronics and Micro-Systems, 2007. EuroSime 2007. International Conference on Digital, Page(s): 1 - 6

Goldstein, M. (1961). *Some physical chemical aspects of heat storage*. Roma –Italy, UN Conference on New Source of Energy.

Jirku T, Fiala P, Kluge M. (May 2010). *Magnetic resonant harvesters and power management circuit for magnetic resonant harvesters*, Microsystem Technologies –Micro -and Nanosystems-Information Storage and Processing Systems, Volume: 16 Issue: 5 Special Issue: Sp. Iss. SI Pages: 677-690

John Greenman, Chris Melhuish, John Hart. (May 2005). *Energy accumulation and improved performance in microbial fuel cells,* Elsevier, Accepted 10 November 2004, Available online 31 May 2005.

Junrui Liang; Wei-Hsin Liao. (2010). *Impedance analysis for piezoelectric energy harvesting devices under displacement and force excitations,* Information and Automation (ICIA), 2010 IEEE International Conference on Digital Object, Page(s): 42 - 47

Juodkazis, Saulius; Misawa, Hiroaki; Maksimov, Igor. (November 2004). *Thermal accumulation effect in three-dimensional recording by picosecond pulses*, Applied Physics Letters, vol.85, no.22, pp.5239-5241.

Key World Energy Statistics from the IEA. (2002). Paris (France): The International, Energy Agency (IEA).

Leczek, J., (1981) *Solar energy-introduction to helioenergetics*. Prague: Redaction of elektrotechnical literature, In Czech.

Lane, G.A. (1983). *Solar Heat Storage*, Volume I: Background and Scientific Principles. Boca Raton (Florida, USA): CRC Press, Inc.

Lavan, Z., Thomson, J. (1977). *Experimental study of thermally stratified hot water storage tanks*. Solar Energy 19.

Lienhard, J.H. IV, Lienhard, J.H. V. (2004). *A heat transfer textbook*. Cambridge (Massachusetts, USA): Phlogiston Press.

Liu, Y.-T.; Lee, M.H.; Chen, H.T.; Huang, C.-F.; Peng, C.-Y.; Lee, L.-S.; Kao, M.-J. (2008). *Thermal accumulation improvement for fabrication manufacturing of monolithic 3D integrated circuits*, Solid-State and Integrated-Circuit Technology. ICSICT 2008. 9th International Conference on , vol., no., pp.1207-1210.

Mar, R.W. (1978). Material *problems in reversible chemical reaction storage systems for solar energy*. Report No. SAND 78-8693. Sandia Laboratories.

Mar, R.W. (1980). *Materials science issues encountered during the development of thermochemical concept*. In chapter 14 from the book, Solar materials science. London (UK): Academic Press, Inc.

Mar, R.W., BRamletta, T.T. (1980). *Thermochemical storage systems*. New York (USA): Marcel Dekker, Inc.

Ministery of industry and trade of Czech Republic, Stat energetic conception. Prague, 2004.

Ministery of industry and trade of Czech Republic, Energetic policy. Prague, 2000.

Mechlova, E., Kostal, K. (1999). *Physics dictionary for basic university physics lectures*. Prague: Prometheus.

Murat Kenisarin, Khamid Mahkamov. (May 2006). *Solar energy storage using phase change materials*, School of Engineering, University of Durham, Elsevier, Received 27 March 2006; accepted 8 May 2006

Piszachich, W.S. (1985). *Nonlinear Models of Flow, Diffusion and Turbulence*. Leipzig (Germany): Teubner Verlagsgessellschaft.

Shi, L.P.; Chong, T.C.; Wei, X.Q.; Zhao, R.; Wang, W.J.; Yang, H.X.; Lee, H.K.; Li, J.M.; Yeo, N.Y.; Lim, K.G.; Miao, X.S.; Song, W.D. (2006). *Investigation of Nano-Phase Change for*

Phase Change Random Access Memory, Non-Volatile Memory Technology Symposium, 2006. NVMTS 2006. 7th Annual, Digital Object, Page(s): 76 - 80

Solar energy, (2010), www.ausra.com

The Australian National University (2004), Department of Engineering, FEIT, http://solar.anu.edu.au/.

Vener, C. (1997). *Phase change thermal energy storage*. The Department of The Built Environment Brighton, University of Brighton, Brighton.

Verdonschet, J.K.M. (1981). *Thermal storage system based on the heat of adsorption in air-based solar heating system.* The Hague (Holland): C. Den Ouden.

Vijay Raghunathan; Kansal, A.; Hsu, J.; Friedman, J.; Mani Srivastava. (April 2005) *Design considerations for solar energy harvesting wireless embedded systems*, Information Processing in Sensor Networks, 2005. IPSN 2005. Fourth International Symposium on, vol., no., pp. 457- 462.

Vohlídal, Julák, Štulík. (1999). *Chemické a analytické tabulky*. In Czech, Prague: GRADA Publishing.

Volle, F.; Garimella, S.V.; Juds, M.A. (2010). *Thermal Management of a Soft Starter: Transient Thermal Impedance Model and Performance Enhancements Using Phase Change Materials*, Power Electronics, IEEE Transactions on, Volume: 25, Issue: 6, Page(s): 1395 - 1405.

Wilcox, D.C. (1994). *Turbulence modeling for CFD*. La Canada (California, USA): DCW Industries, Inc.

Zhen Ren; Wen-Yan Yin; Yan-Bing Shi; Qing Huo Liu. (Januar 2010). *Thermal Accumulation Effects on the Transient Temperature Responses in LDMOSFETs Under the Impact of a Periodic Electromagnetic Pulse*, Electron Devices, IEEE Transactions on, vol.57, no.1, pp.345-352.

18

Finite Element Methods to Optimize by Factorial Design the Solidification of Cu-5wt%Zn Alloy in a Sand Mold

Moisés Meza Pariona and Viviane Teleginski
State University of Ponta Grossa – UEPG
Brazil

1. Introduction

Throughout the manufacturing industry, casting process simulation has been widely accepted as an important tool in product design and process development to improve yield and casting quality. Casting simulation requires high-quality information concerning thermo-physical and physical properties during solidification. Some properties have been measured for specific alloys, but the number of alloys for which information is available is limited. Furthermore, the information may be incomplete in the sense that not all properties have been measured and sometimes, disparate information from a variety of sources is used to build up the database for one specific alloy. To overcome the lack of data and achieve a better understanding of how changes in composition within a specification range of an alloy may affect solidification properties, it is highly desirable to develop experimental techniques or computer models for calculation of the thermo-physical and physical properties of multi-component alloys for the process of reliable solidification (Guo et al., 2005).

The computer simulation of cooling patterns in castings has done much to broaden our understanding of casting and mold system design. The structural integrity of shaped castings is closely related to the time–temperature history during solidification, and the use of casting simulation could do much to increase this knowledge in the foundry industry. (Ferreira et al., 2005).

The ability of heat to flow across the casting and through the interface from the casting to the mold directly affects the evolution of solidification and plays a notable role in determining the freezing conditions within the casting, mainly in foundry systems of high thermal diffusivity such as chill castings. Gravity or pressure die castings, continuous casting and squeeze castings are some of the processes where the product's soundness is more directly affected by heat transfer at the metal/mold interface (Ferreira et al., 2005).

According to the authors Atwood and Lee (Atwood & Lee, 2003), the mechanical properties of metal products depend upon the phenomena occurring during production. Defects formed during each stage of production can persist or modify the behavior of the metal during subsequent processing steps. Therefore, ensuring that an appropriate microstructure is formed at each stage with minimal defects has always been a focus in the study of metal production. In aluminum alloy shape castings, the final microstructure is directly dependent upon the as-cast microstructure since the only post-casting processing is normally a heat treatment. One microstructural feature that can affect the final properties of aluminum alloy

shape castings is microporosity, formed due to the combined effects of volumetric shrinkage upon solidification. Developing a model to predict the formation of microporosity in solidifying metal castings is one way of helping. Porosity in castings is a defect that results from the interaction of a number of processes: volume change, nucleation and growth of the solid phase, diffusion of dissolved species, and the interaction of interphase surfacial. Although some of these individual processes may be treated analytically, combining the processes into a predictive tool requires the numerical calculation power that has only become available over the last few decades due to the development of digital computers

The use of multivariate experimental design techniques is becoming increasingly widespread in analytical chemistry. Multivariate experimental design techniques, which permit the simultaneous optimization of several control variables, are faster to implement and more cost-effective than traditional univariate (one at a time) approaches (Khajeh, 2009). One of the most popular multivariate design techniques is two level full/fractional factorial, in which every factor is experimentally studied at only two levels. Due to their simplicity and relatively low cost, full factorial design techniques are very useful for preliminary studies or in the initial steps of an optimization, while fractional factorial designs are almost mandatory when the problem involves a large number of factors (Khajeh, 2009). On the other hand, since only two levels are used, the models that may be fit to these designs are somewhat restricted. If a more sophisticated model is needed, as for the location of an optimum set of experimental conditions, then one must resort to augment response surface designs, which employ more than two factor levels. Among these, Box–Behnken is a second-order multivariate design technique based on three-level incomplete factorial designs that received widespread application for evaluation of critical experimental conditions, that is, maximum or minimum of response functions (Khajeh, 2009).

Experimental design is a systematic, rigorous approach to engineering problem solving that applies principles and techniques at the data collection stage so as to ensure the generation of valid, precise, and accurate engineering conclusions (Xiao & Vien, 2004). It is a very economic way of extracting the maximum amount of complex information and saving a significant experimental time and the material used for analyses and personal costs as well (Kincl et al., 2005). Different experimental designs are used for different objectives. For example, randomized block designs can be used to compare data sets, full or fractional factorial design can be used for screening relevant factors (Xiao & Vien, 2004).

The design of mixture experiments configures a special case in response to surface methodologies using mathematical and statistical techniques, with important applications not only in new products design and development, but also in the improvement of the design of existing products. In short, the methodology consists firstly to select the appropriate mixtures from which the response surface might be calculated; having the response surface, a prediction of the property value can be obtained for any design, from the changes in the proportions of its components (Aslan, 2007). The other important issue is for engineering experimenters who wish to find the concentration conditions under which a certain process attains the optimal results. That is, they want to determine the levels of the operational factors at which the response reaches its optimum. The optimum could be either a maximum or a minimum of a function of the design parameters (Aslan, 2007). Factorial design is a useful tool in order to characterize multivariable processes. It gives the possibility to analyze the important influent factors of the process, and to identify any possible interactions among them.

1.1 Mathematical solidification heat transfer model

The mathematical formulation of heat transfer to predict the temperature distribution during solidification is based on the general equation of heat conduction in the unsteady state, which is given in two-dimensional heat flux form for the analysis of the present study (Ferreira et al., 2005; Santos et al., 2005; Shi & Guo, 2004; Dassau et al., 2006).

$$\frac{\partial}{\partial t}(\rho c T) = \frac{\partial}{\partial x}\left(k_x \frac{\partial T}{\partial x}\right) + \frac{\partial}{\partial y}\left(k_y \frac{\partial T}{\partial y}\right) + \dot{Q} \tag{1}$$

where ρ is density [kgm^{-3}]; c is specific heat [J kg^{-1} K^{-1}]; k is thermal conductivity [Wm^{-1}K^{-1}]; $\partial T/\partial t$ is cooling rate [K s^{-1}], T is temperature [K], t is time [s], x and y are space coordinates [m] and $\dot{Q}$represents the term associated to the latent heat release due to the phase change. In this equation, it was assumed that the thermal conductivity, density, and specific heat vary with temperature. In the current system, no external heat source was applied and the only heat generation was due to the latent heat of solidification, L (J/kg) or ΔH (J/kg). $\dot{Q}$ is proportional to the changing rate of the solidified fraction, f_s, as follow (Ferreira et al, 2005; Santos et al, 2005; Shi & Guo, 2004).

$$\dot{Q} = \Delta H \frac{\partial f_s}{\partial t} = \rho L \frac{\partial f_s}{\partial t} = \rho L \frac{\partial f_s}{\partial T}\frac{\partial T}{\partial t} \tag{2}$$

Therefore, Eq. (2) is actually dependent on two factors: temperature and solid fraction. The solid fraction can be a function of a number of solidification variables. But in many systems, especially when undercooling is small, the solid fraction may be assumed as being dependent on temperature only. Different forms have been proposed to the relationship between the solid fraction and the temperature. One of the simple forms is a linear relationship (Shi & Guo, 2004; Pericleous et al., 2006):

$$f_s = \begin{cases} 0 & T > T_l \\ (T_l - T)/(T_l - T_s) & T_s \le T \le T_l \\ 1 & T < T_s \end{cases} \tag{3}$$

where T_l and T_s are, respectively, the liquid and solid temperature (K). Another relation is the widely used Scheil relationship, which assumes uniform solute concentration in the liquid but no diffusion in the solid (Shi & Guo, 2004):

$$f_s = 1 - \left(\frac{T_s - T}{T_s - T_l}\right)^{\frac{-1}{1-k_0}} \tag{4}$$

where k_o the equilibrium partition coefficient of the alloy.

Eq. (1) defines the heat flux (Radovic & Lalovic, 2005), which is released during liquid cooling, solidification and solid cooling in classical models. The heat evolved after solidification was assumed to be equal zero, i.e. for $T < T_s, \dot{Q} = 0$. However, experimental investigations have showed that lattice defects and vacancy are condensed in the already solidified part of the crystal and the enthalpy of the solid increases and thus the latent heat will decrease (Radovic & Lalovic, 2005). Due to this fact, another way to represent the change of the solid fraction during solidification can be written as (Radovic & Lalovic, 2005):

$$f_s = \frac{(T_l - T) + \frac{2}{\pi}(T_s - T_l)\left(1 - cos\left[\frac{\pi(T - T_l)}{2(T_s - T_l)}\right]\right.}{(T_l - T_s)(1 - 2/\pi)} \tag{5}$$

Considering c´, as pseudo specific heat, as $c' = c - L\frac{\partial f_s}{\partial T}$ and combining Eqs. (1) and (2), one obtains (Shi & Guo, 2004 ; Radovic & Lalovic, 2005):

$$\frac{\partial(\rho c'T)}{\partial t} = \nabla(k\nabla T) \tag{6}$$

The boundary condition applied on the outside of the mold is:

$$-k\frac{\partial T}{\partial n} = h(T - T_o) \tag{7}$$

Here h is the heat transfer coefficient for air convection and T_o is the external temperature.

1.2 The factorial design technique

The factorial design technique is a collection of statistical and mathematical methods that are useful for modeling and analyzing engineering problems. In this technique, the main objective is to optimize the response surface that is influenced by various process parameters. Response surface methodology also quantifies the relationship between the controllable input parameters and the obtained response surfaces (Kwak, 2005). The design procedure of response surface methodology is as follows (Gunaraj & Murugan, 1999):

i. Designing of a series of experiments for adequate and reliable measurement of the response of interest.
ii. Developing a mathematical model of the second-order response surface with the best fittings.
iii. Finding the optimal set of experimental parameters that produce a maximum or minimum value of response.
iv. Representing the direct and interactive effects of process parameters through two and three-dimensional plots. If all variables are assumed to be measurable, the response surface can be expressed as follows (Aslan, 2007; Yetilmezsoy et al., 2009; Pierlot et al., 2008; Dyshlovenko et al. 2006):

$$y = f(x_1, x_2, x_3, \ldots x_k) \tag{8}$$

where y is the answer of the system, and x_i the variables of action called variables (or factors).

The goal is to optimize the response variable y. It is assumed that the independent variables are continuous and controllable by experiments with negligible errors. It is required to find a suitable approximation for the true functional relationship between independent variables (or factors) and the response surface. Usually a second-order model is utilized in response surface methodology:

$$y = \beta_0 + \sum_{i=1}^{m}\beta_i x_i + \sum_{i=l}^{m}\beta_{ii}x_i^2 + \sum_{i=l}^{m-1}\sum_{j=2}^{m}\beta_{ij}x_i x_j + \varepsilon \tag{9}$$

where $x_1, x_2, \ldots, x_k$ are the input factors which influence the response y; β_o, β_{ii} $(i=1, 2, \ldots, m)$, β_{ij} $(i=1, 2, \ldots, m;\ j=1,2, \ldots, m)$ are unknown parameters and ε is a random error. The β coefficients, which should be determined in the second-order model, are obtained by the least square method.

The model based on Eq. (9), if m=3 (three variables) this equation is of the following form:

$$y = \beta_0 + \beta_1 x_1 + \beta_2 x_2 + \beta_3 x_3 + \beta_{11} x_1^2 + \beta_{22} x_2^2 + \beta_{33} x_3^2 + \beta_{12} x_1 x_2 + \beta_{13} x_1 x_3 + \beta_{23} x_2 x_3 + \varepsilon \quad (10)$$

where y is the predicted response, β_o model constant; x_1, x_2 and x_3 independent variables; β_1, β_2 and β_3 are linear coefficients; β_{12}, β_{13} and β_{23} are cross product coefficients and β_{11}, β_{22} and β_{33} are the quadratic coefficients (Kwak, 2005).
In general Eq. (9) can be written in matrix form (Aslan, 2007).

$$Y = \boldsymbol{b}X + \varepsilon \quad (11)$$

where $\boldsymbol{Y}$ is defined to be a matrix of measured values, $\boldsymbol{X}$ to be a matrix of independent variables. The matrixes $\boldsymbol{b}$ and ε consist of coefficients and errors, respectively. The solution of Eq. (11) can be obtained by the matrix approach (Kwak, 2005; Gunaraj & Murugan, 1999).

$$b = (X'X)^{-1}X'Y \quad (12)$$

where $\boldsymbol{X'}$ is the transpose of the matrix $\boldsymbol{X}$ and $(\boldsymbol{X'X})^{-1}$ is the inverse of the matrix $\boldsymbol{X'X}$.
The objective of this work was to study the solidification process of the alloy Cu-5 wt %Zn during 1.5 h of cooling. It was optimized through the factorial design in three levels, where the considered parameters were: temperature of the mold, the convection in the external mold and the generation of heat during the phase change. The temperature of the mold was initially fixed in 298, 343 and 423 K, as well as the loss of heat by convection on the external mold was fixed in 5, 70 and 150 W/m^2.K. For the generation of heat, three models of the solid fraction were considered: the linear relationship, Scheil´s equation and the equation proposed by Radovic and Lalovic (Radovic & Lalovic, 2005). As result, the transfer of heat, thermal gradient, flow of heat in the system and the cooling curves in different points of the system were simulated. Also, a mathematical model of optimization was proposed and finally an analysis by the factorial design of the considered parameters was made.

2. Methodology of the numerical simulation

The finite elements method was used in this study (Su, 2001; Shi & Guo, 2004; Janik & Dyja, 2004; Grozdanic, 2002). Software program Ansys version 11 (Handbook Ansys, 2010) was used to simulate the solidification of alloy Cu-5 wt %Zn in green-sand mold. Effects due to fluid motion and contraction are not considered in the present work. The geometry of the cast metal and the greensand mold is illustrated in Figure 1(a), which is represented in three-dimensions. However, in this work the analysis was accomplish in 2-D, which is illustrated in Figure 1(b). Some material properties of Cu-5 wt %Zn alloy were taken from the reference Miettinen (Miettinen, 2001), the other properties were taken from Thermo-calc software (Thermo-calc software, 2010), and in Figure 2 the enthalpy and the phase diagram of alloy Cu-Zn are presented (Thermo-calc software, 2010). Three pseudo specific heat (c´) obtained from the equations (3), (4) and (5) were used and these equations were denoted respectively by models A, B and C, and the sand thermo-physical properties was given by Midea and Shah (Midea and Shah, 2002).
In this study, the Box–Behnken factorial design in three levels (Aslan, 2007; Paterakis et al., 2002; Montgomery, 1999) was chosen to find out the relationship between the response

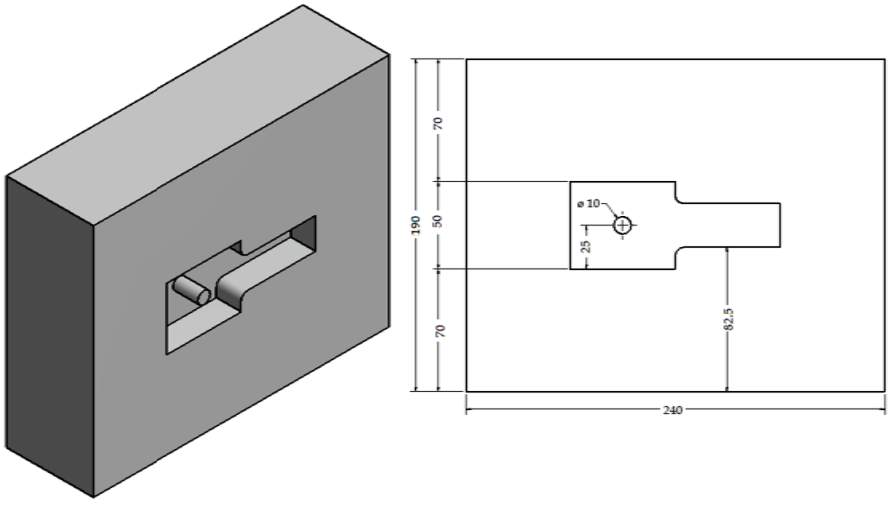

(a) (b)

Fig. 1. The cast part and mold in (a) three dimensional and (b) bi dimensional

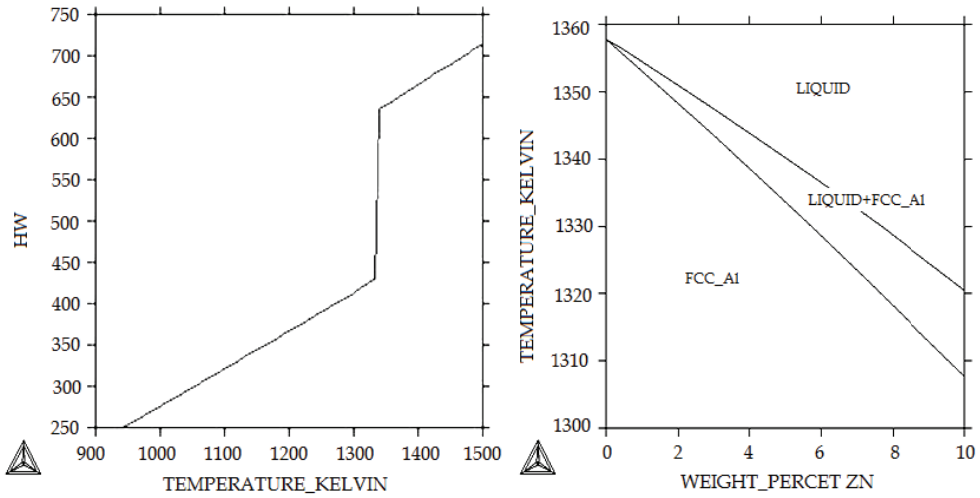

Fig. 2. (a) Enthalpy and phase diagram of Cu-5 wt %Zn alloy and (b) phase diagram of Cu-5wt%Zn alloy (Thermo-calc software, 2010)

functions. Independents variables (factors) and their coded/actual levels considered were the mold temperature (x_1), the convection phenomenon (x_2) and the mathematical model (x_3) of the latent heat release, (Z) represents the result of the temperature after 1.5 h of solidification. The factorial design is shown in Table 1. For this design type a nomenclature was adopted, where for the inferior state of the variable it was denoted by (-1), for the intermediate state by (0) and for the superior state by (+1).

	x_1 Mold Temperature	x_2 Convection phenomenon (h_f)	x_3 Mathematic model	Z - Temperature after 1.5 h of solidification (K)
-1	298 K	5 W/m²K	A	
0	343 K	70 W/m²K	B	
+1	423 K	150 W/m²K	C	
1	-1	-1	-1	806.799
2	-1	-1	0	775.945
3	-1	-1	+1	862.902
4	-1	0	-1	800.301
5	-1	0	0	769.408
6	-1	0	+1	855.752
7	**-1**	**+1**	**-1**	798.197
8	**-1**	**+1**	**0**	767.562
9	**-1**	**+1**	**+1**	854.967
10	0	-1	-1	840.174
11	0	-1	0	809.199
12	0	-1	+1	897.176
13	0	0	-1	833.699
14	0	0	0	802.835
15	0	0	+1	890.279
16	0	+1	-1	832.200
17	0	+1	0	801.430
18	0	+1	+1	890.110
19	+1	-1	-1	899.860
20	+1	-1	0	868.171
21	+1	-1	+1	958.587
22	+1	0	-1	893.996
23	+1	0	0	862.277
24	+1	0	+1	953.026
25	+1	+1	-1	893.136
26	+1	+1	0	861.015
27	+1	+1	+1	952.674

Table 1. Factorial design of the solidification process parameters

The initial and boundary conditions were applied to geometry of Figure 1 according to Table 1. The boundary condition was the convection phenomenon and this phenomenon was applied to the outside walls of the sand mold, as shown in Table 1. The convection transfer coefficient at the mold wall was considered constant in this work, due to lack of experimental data. The effects of the refractory paint and of the gassaging process were not taken into consideration either. The final step consisted in solving the problem of heat transfer of the mold/cast metal system using equation (6), in applied boundary condition and in controlling the convergence condition. Heat transfer is analyzed in 2-D form, as well as the heat flux, the thermal gradient, and in addition, the thermal history for some points in the cast metal and in the mold is discussed.

3. Result and discussion

The result for solidification was discussed for some particular cases, at condition given in lines 7, 8 and 9 from Table 1, which correspond respectively to the lowest temperatures for each mathematical model of latent heat release. Each one of the lines corresponds to the temperature of the mold for the lower state (-) and for convection phenomenon for the higher state (+).

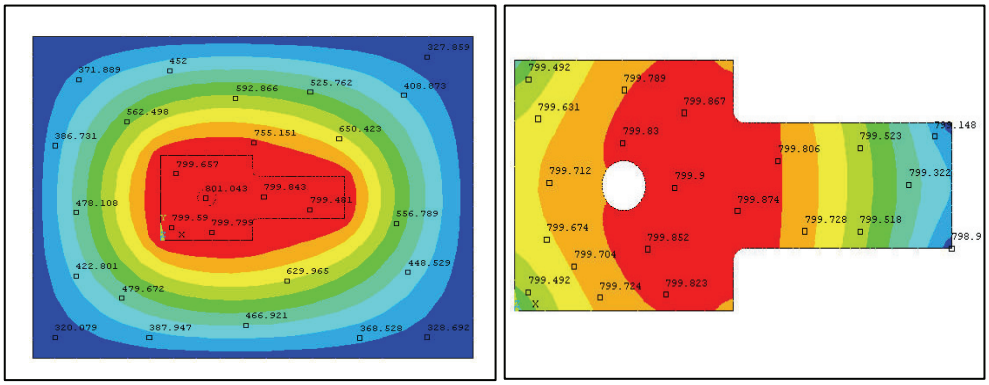

(a) (b)

Fig. 3. Temperature distribution in (a) sand mold system, (b) cast metal (line 9 of Table 1)

The condition mentioned on line 9 of Table 1 was chosen to present heat transfer results, where the temperature field is shown in Figure 3(a) in all the system mold and in the cast metal (Figure 3(b)). This last case can be visualized in more detail in part (b), where an almost uniform temperature is observed. In the geometric structure of the mold there is a core constituted of sand that is represented by a white circle in Figure 3(b), which can be verified also in Figure 1(a). In Figure 4 the results of the thermal gradient and the thermal flux are shown, where the thermal gradient goes from the cold zone to the hot zone. On the other hand, the thermal flux goes from the hot zone to the cold zone. Also the convergence of the solution was studied; this point is discussed in more detail by Houzeaux and Codina (Houzeaux & Codina, 2004).

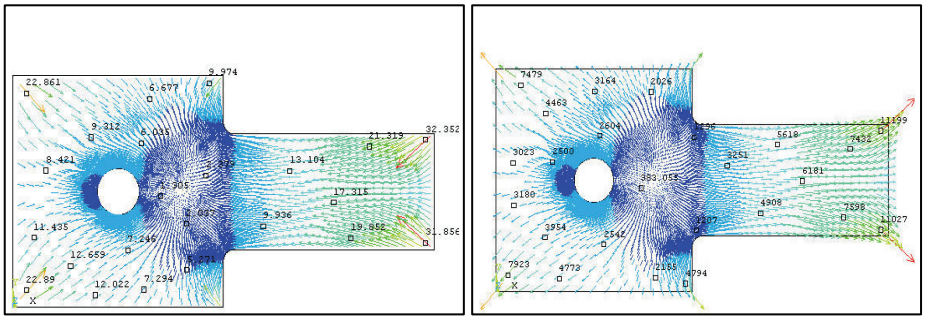

(a) (b)

Fig. 4. (a) Thermal gradient (K/m) in vector form and (b) Heat flux (W/m²) in vector form (line 9 of Table 1)

In order to simulate the cooling curves, two points were considered, as shown in Figure 5: one located in the core (point 2) and the other in the metal (point 1). The three forms of latent heat release were applied into the mathematical model and the resulting thermal profiles were compared.

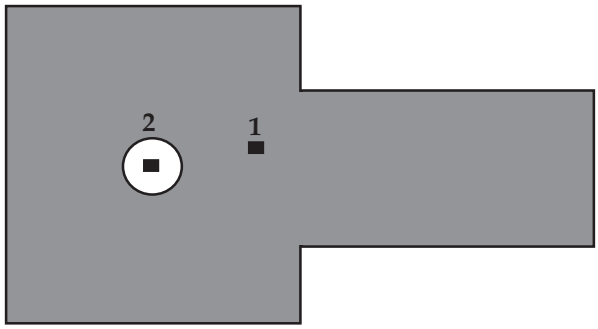

Fig. 5. Reference points for the mold/metal system

The cooling curves were studied for condition of line 7, 8 and 9 from Table 1 as shown in Figure 6. Figure 6 (a) shows a comparison of temperature evolution at point (2) for the three formulations of latent heat release: linear (model A), Scheil (model (B) and Radovic and Lalovic (model C). It can be observed that the highest temperature profile corresponds to model A, followed by model C and last by model B, mainly after the solidification range. Although not presented, a similar behavior has occurred at other positions in the casting. Chen and Tsai (Chen and Tsai, 1990) analyzed theoretically four different modes of latent heat release for two of alloys solidified in sand molds: Al-4,5wt%Cu (wide mushy region, 136K) and a 1wt% Cr steel alloy (narrow mushy region, 33.3K). In their work, they conclude that no significant differences can be observed in the casting temperature for different modes of latent heat release, when the alloy mushy zone is narrow.

The alloy used in the present work, Cu-5wt%Zn, as shown in Figure 2(b), has a narrow mushy zone (less than 10K). Figure 6(a) shows that there is a significant temperature profile difference due to the three different latent heat release modes. In addition, it is important to remark that the latent heat release form has strongly influenced the local solidification time.

Such solidification parameter affects the microstructure characterized by primary and secondary dendritic arm spacings. Correlations between dendritic spacings and local time solidification (t_{SL}) are well known in the literature (Rosa et al., 2008). Investigations correlating ultimate tensile strength (σ_U) and secondary (SDAS) or primary (PDAS) dendrite arm spacings have shown that (σ_U) increases with decreasing (SDAS) or (PDAS) (Quaresma et al., 2000).

Figure 6 (b) shows a comparison of temperature evolution at point (1) for the three formulations of latent heat release. It can be observed again, that the highest temperature profile corresponds to model A, followed by model C and last by model B, and this behavior is repeated for the other points in the mold.

The significant variables indicated by the Pareto chart (which was obtained after multiple linear regression and analysis of variance) were optimized using a Box-Behnken design, which is a response surface methodology, based on a highly fractionalized three-level factorial design.

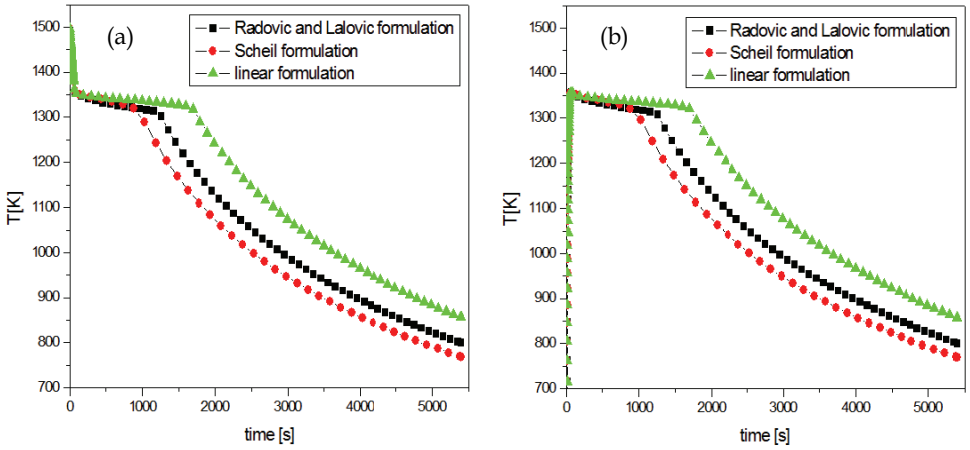

Fig. 6. Thermal profiles for the mold/metal system concerning condition 7, 8 and 9 of Table 1. (a) Inside of the cast – point 1, (b)Inside of the mold – point 2

A three level Box-Behnken desig (Aslan, 2007; Paterakis et al., 2002; Montgomery, 1999; Yetilmezsoy et al., 2009) was used to determine the responses of the three variables x_1, x_2 and x_3, based in Table 1. The result of this analysis is shown in the Pareto's diagram of Figure 7. In this figure the estimated valor of the result Z is presented with the significance level (p) of 95%, showing the variables with and without significant influences. The notation adopted for this analysis was, "L" means linear, "Q" means quadratic. For example, "(1)" is the main effect of the first factor and "2L by 3Q" means the linear interaction of the parameter 2 (convection phenomenon) with the quadratic effect of parameter 3 (latent heat release form).

In Figure 7, two significant influences were found: x_1 (mold temperature) with linear effect and x_3 (mathematical model) with linear and quadratic effects. The other effect of the independent variables and interactions are negligible in this figure. To clarify more this analysis, other type of standard graph was accomplished, and it is shown in Figure 8. This

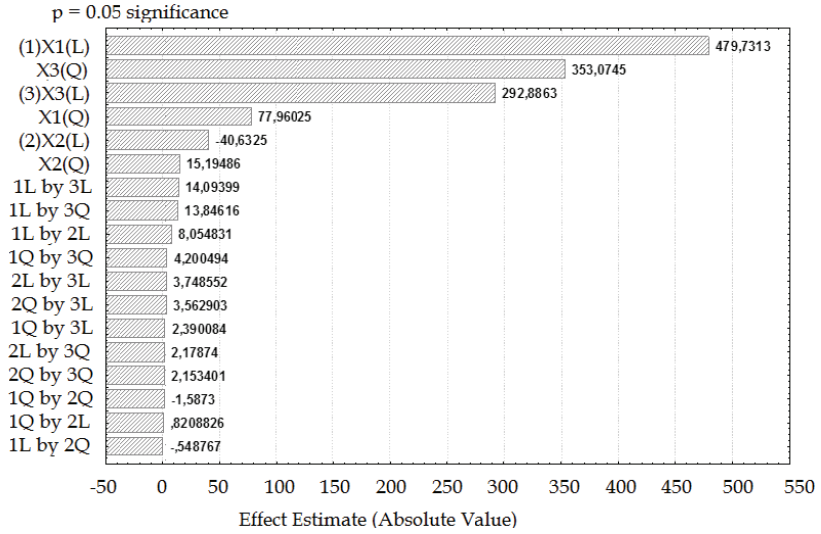

Fig. 7. Pareto chart of standardized effects for the full factorial design

figure of the factorial design was built based on the Student's probability distribution (t) (Montgomery, 1999). In this figure the main effects and their interactions with significant influence can be observed by those dispersed points (around of the straight line). Those points that belong to the concentrated region points are of the negligible influence. It can be observed in Figure 8 that the biggest positive influence is due to the main effect of x_1 (mold initial temperature) with linear behavior, followed by the linear and quadratic effect of parameter 3 (latent heat release form). Parameter x_2 with linear behavior presents a small negative influence on the factorial design and the other effects had a negligible behavior, around zero, as presented in Figure 8. For this analysis a mathematical model was proposed, given Z the following equation:

$$\begin{aligned} Z = {} & 802.7889 + 46.4582x_1 - 3.9348x_2 - 28.3638x_3 - 13.0766x_1^2 - 2.5486x_2^2 \\ & + 59.2232x_3^2 + 0.4273x_1x_2 + 0.7476x_1x_3 + 0.1988x_2x_3 \\ & + 1.27212x_1x_3^2 + 0.2196x_1^2x_3 + 0.6686x_1^2x_3^2 + 0.3273x_2^2x_3 \end{aligned} \tag{13}$$

In this equation the linear and quadratic coefficients are most important and the other coefficients are negligible (they are considered as residue). Precisely the most significant coefficients belong to the variables which strongly influence the result, as it can be observed in Figures 7 and 8. Then according to this consideration, equation (13) reduces to the following equation:

$$\begin{aligned} Z = {} & 802.7889 + 46.4582x_1 - 3.9348x_2 - 28.3638x_3 - 13.0766x_1^2 - 2.5486x_2^2 \\ & + 59.2232x_3^2 + 0.4273x_1x_2 + 0.7476x_1x_3 + 0.1988x_2x_3 \end{aligned} \tag{14}$$

A quadratic equation that correlates the variables and the response was obtained, and the critical points of this equation can be estimated through this mathematical relationship. Then, the derivation of this equation in relation to (x_1), (x_2) and (x_3) results in three new equations, being equations 15, 16 and 17:

$$\frac{dZ}{x_1} = 46.4582 + 26.1532x_1 + 0.4273x_2 + 0.7476x_3 \quad (15)$$

$$\frac{dZ}{x_2} = -3.9348 + 0.4273x_1 + 5.0972x_2 + 0.1988x_3 \quad (16)$$

$$\frac{dZ}{x_3} = 28.3638 + 0.7476x_1 + 0.1988x_2 + 118.4464x_3 \quad (17)$$

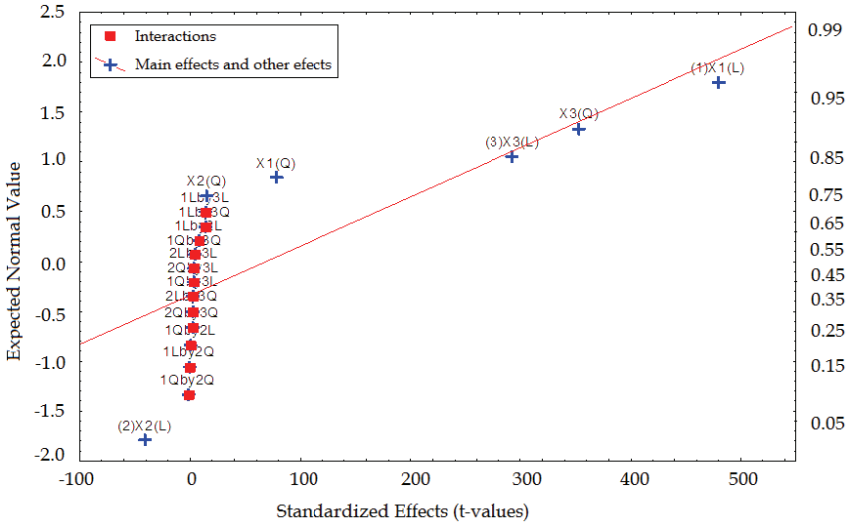

Fig. 8. Curve of standardized effects of the factorial design

The critical point in the surface response are found by solving these equation systems for the condition of $\frac{dZ}{x_1} = 0$, $\frac{dZ}{x_2} = 0$ and $\frac{dZ}{x_3} = 0$. This criterion of solution was based on the recommendations of the authors Martendal et al. (Martendal el al., 2007) and the calculated values for the critical point are: x_1=-1.7850 K, x_2= 0.9306 W/m².K, x_3=-0.2298 mathematical model.

Analyzing this result, we know that the variables x_1, x_2 and x_3 must take values -1 or 0 or +1, according to the criteria adopted in factorial design. Because the calculated values should approach to these values adopted, but it can be observed that some solutions of x_1, x_2 and x_3 are a bit different of these values adopted, this is possible by simplifying considered in equation (13). Then according to these considerations, the approximations must be in such form, where x_1 =-1.7850 ≈-1 (mold temperature, in environment), x_2 = 0.9306 ≈ + 1 (latent heat release, 150 W/m².K) and x_3 =-0.2298 ≈ 0 (mathematic model, Scheil relationship).

The values of x_1 =-1, x_2 = + 1 and x_3 = 0 in Table 1 corresponds to the line 8, that means Z - temperature after 1.5h of solidification that is 767.562 K, justly this value corresponds to the minimum temperature of factorial design. This solution proved the validity of the modeling for the optimization process of the casting by factorial design, despite that this prove of the modeling represents a proof trivial. Also this result is to agree with the result obtained by finite elements, see Figure 6.

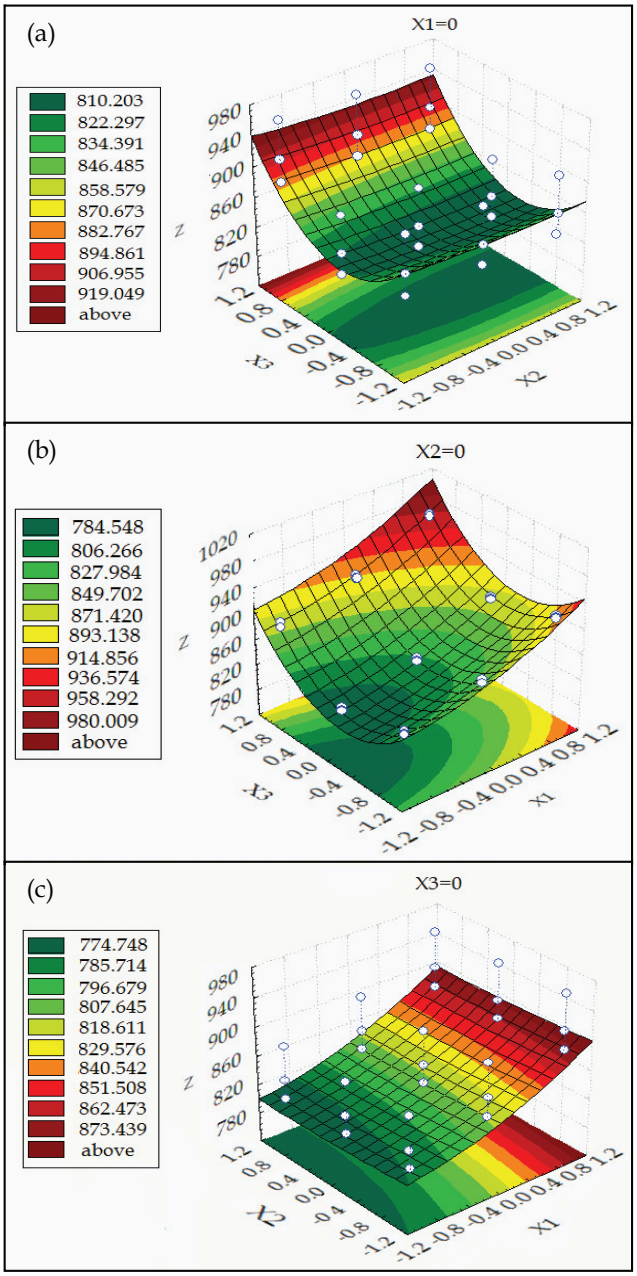

Fig. 9. Response surface plots showing the effect of the (a) x_2 and x_3 factors, x_1 was held at zero level, (b) x_1 e x_3 factors, x_2 was held at zero level and (c) x_1 and x_2 factors, x_3 was held at zero level

While a quantitative analysis of equation (14) was made, will soon be made a qualitative analysis of equation (13) by means of graphic representation of this equation and this discussion will be confronted with factorial design of the solidification process parameters (Table 1) and Figure 8. Figure 9 presents the response surface plots (Aslan, 2007; Paterakis et al., 2002), obtained from equation (13), that describe the influence of the factors on the overall desirability, Figure 9(a) shows the 3D response surface relationship between convection phenomenon (x_2) and latent heat release form (x_3) at zero level of mold temperature (x_1). Note that, for a given value of x_2, as the x_3 increases and the Z decreases until a minimum value for the interval of x_3 between -0.8 and 0.2. After this minimum point, Z changes its behavior and start to increase as the x_3 increases reaching the highest value of 897.176, as can be seen in Table 1. For a given value of x_3, it can be observed that Z profile is almost constant in relation to x_2 increase. Another way to visualize Z variation is to project Z on the x_2 and x_3 plane, in terms of color band. The region limited by the white points on this curve represents the Z confidence interval. For other levels of x_1, the surface graph behavior has the same characteristic as previously mentioned.

Figure 9(b) shows the effect of mold temperature (x_1) and latent heat release form (x_3) at zero level of convection phenomenon (x_2). In this case, x_1 e x_3 generated a complex surface of paraboloid type. According to the surface projection Z on the x_1 and x_3 plane, for a given x_3 value, it can be observed that the variation of Z is linear in relation to x_1 and this fact can be confirmed by the point x_1(L) mentioned at the graph of Figure 8. On the other hand, the same cannot be affirmed in relation to x_3, if the same analysis is done.

For a given value of x_1, the variation of Z is parabolic in relation to x_3 and this fact can be observed by the points x_3(L) and x_3(Q) mentioned at the graph of Figure 8. Note that, for a given value of x_1, as the x_3 increases and the Z increases reaching the highest value of 953.026, as can be seen in Table 1.

Figure 9(c) shows the effect of mold temperature (x_1) and convection phenomenon (x_2) at zero level of latent heat release (x_3). Note that, as the x_1 factor increases, the Z increases. But, for a given value of x_1, it is observed that for every x_2 value, Z is almost constant. As a result, the surface geometry is not a complex one, if we compare to the surface geometry of Figure 9(b).

In this type of analysis, one can realize that the parameters x_1 and x_3 had variations more accentuated than the parameter x_2. This behavior is also verified in Figures 7 and 8. Note that, for a given value of x_1, as the x_2 increases and the Z increases reaching the highest value of 868.171, as can be seen in Table 1.

Three level Box-Behnken design referred to Table 1 showed as results Pareto's diagram of Figure 7 and curve of standardized effect of the factorial design of Figure 8. According to these results was estimated a mathematic model for Z (represents the result of the temperature after 1.5 h of solidification) based in equation (9) and through the process of maximizing and minimizing of this model was found the optimal values of x_1, x_2 and x_3. It was also shown the graphical interpretation of equation (13) so qualitatively and this interpretation this related to factorial design of the solidification process parameters (Table 1). Consequently it was shown that three level Box-Behnken is a very powerful tool to optimize and predict results in quantitative and qualitative way. This tool can be used in research, optimization and prediction of industrial processes, saving manpower, material and time in order to improve cost and quality of the product.

This work has done the numerical simulation by finite element method to the copper alloy solidification in sand mold and also this simulation was accompanied with the process of optimization of solidification parameters. This type of study accompanied with the cellular automata or cellular automaton can help minimize the defects generated during solidification. One microstructural feature that can affect the final properties of copper alloy shape castings is microporosity, formed due to the combined effects of volumetric shrinkage upon solidification. Porosity in castings is a defect that results from the interaction of a number of processes: volume change, nucleation and growth of the solid phase, diffusion of dissolved species, and the interaction of interphase surfaces. Although some of these individual processes may be treated analytically, combining the processes into a predictive tool requires the numerical calculation power that has only become available over the last few decades due to the development of digital computers.

4. Conclusion

In this study, a three-level Box-Behnken factorial design in qualitative form and combining with a response surface methodology was employed for modeling and optimizing three operations parameters of the casting process. According to this study, it was observed when the parameters of the solidification process are in the following state, such as, mold temperature in the environment, convection phenomenon in its fullest expression and the latent heat release to the model Sheil shows a minimum temperature after 1.5 h of solidification. Also this result was verified by finite element method. The factorial design method is a useful tool to determine what factors are crucial in the solidification process and thus, a special care needs to be taken during the project elaboration of the casting. Also this optimization tool can be used in other research areas, optimizing and predicting industrial processes, saving manpower, material and time in order to improve cost and quality of the product.

5. Acknowledgment

The authors acknowledge financial support provided by CNPq (The Brazilian Research Council) and Araucária Foundation (AF).

6. References

Aslan, N. (2007). Modeling and optimization of multi-gravity separator to produce celestite concentrate. *Powder Technology*, Vol. 174, No. 3, (may 2007), pp. 127–133, ISSN 0032-5910.

Atwood, R.C. & Lee, P.D. (2003). Simulation of the three-dimensional morphology of solidification porosity in an aluminum–silicon alloy. *Acta Materialia,* Vol. 51, No. 18, (October 2003), pp. 5447–5466, ISSN 1359-6454.

Chen, J.H. & Tsai, H.L. (1990). Comparison on different modes of latent heat release for modeling casting solidification. *AFS Transactions*, (1990), pp. 539-546. ISSN 0065-8375.

Dassau, E., Grosman, B. & Lewin, D.L. (2006). Modeling and temperature control of rapid thermal processing. *Computers and Chemical Engineering*, Vol. 30, No. 4, (February 2006), pp. 686–697, ISSN 0098-1354.

Dyshlovenko, S., Pierlot, C., Pawlowski, L., Tomaszek, R. & Chagnon, P. (2006). Experimental design of plasma spraying and laser treatment of hydroxyapatite coatings. *Surface & Coatings Technology*, Vol. 201, No. 5, (October 2006), pp. 2054–2060, ISSN 0257-8972.

Ferreira, I. L., Spinelli, J. E., Pires, J. C. & Garcia, A. (2005). The effect of melt temperature profile on the transient metal/mold heat transfer coefficient during solidification. *Materials Science and Engineering*, Vol. A 408, No. 1-2, (November 2005), pp. 317–325, ISSN 0921-5093.

Grozdanic, V. (2002). Numerical simulation of the solidification of a steel rail-wheel casting and the optimum dimension of the riser. *Materiali in Tehnologije*, Vol. 36, No. 3-4, (April 2002), pp. 139-141, ISSN 1580-2949.

Gunaraj, V. & Murugan, N. (1999). Application of response surface methodologies for predicting weld base quality in submerged arc welding of pipes. *Journal of Materials Processing Technology*, Vol. 88, No. 1-3, (April 1999), pp. 266–275, ISSN 0924-0136.

Guo, Z., Saunders, N., Miodownik, A. P. & Schillé, J.-Ph. (2005). Modelling of materials properties and behaviour critical to casting simulation. *Materials Science and Engineering*, Vol. A 413–414, (December 2005), pp. 465–469, ISSN 0921-5093.

Handbook Ansys, Inc, Canonsburg, PA, 2010.

Houzeaux G., Codina R. (2004). A finite element model for the simulation of lost foam casting. *International Journal For Numerical Methods In Fluids*, Vol. 46, No. 2, (July 2004), pp. 203–226, ISSN 1097-0363.

Janik, M. & Dyja, H. (2004). Modelling of three-dimensional temperature field inside the mould during continuous casting of steel. *Journal of Materials Processing Technology*, Vol. 157–158, (December 2004), pp. 177-182, ISSN 0924-0136.

Khajeh, M. (2009). Application of Box–Behnken design in the optimization of a magnetic nanoparticle procedure for zinc determination in analytical samples by inductively coupled plasma optical emission spectrometry. *Journal of Hazardous Materials*, Vol. 172, No. 1, (December 2009), pp. 385–389, ISSN 0304-3894.

Kincl, M., Turk, S. & Vrecer, F. (2005). Application of experimental design methodology in development and optimization of drug release method. *International Journal of Pharmaceutics*, Vol. 291, No. 1-2, (March 2005), pp. 39–49, ISSN 0378-5173.

Kwak, J.S. (2005). Application of Taguchi and response surface methodologies for geometric error in surface grinding process. *International Journal of Machine Tools and Manufacture*, Vol. 45, No. 3, (Mach 2005), pp. 327–334, ISSN 0890-6955.

Martendal, E., Budziak, D. & Carasek, E. (2007). Application of fractional factorial experimental and Box-Behnken designs for optimization of single-drop microextraction of 2,4,6-trichloroanisole and 2,4,6-tribromoanisole from wine samples. *Journal of Chromatography A*, Vol. 1148, No. 2, (May 2007), pp.131–136, ISSN 0021-9673.

Midea, T. & Shah, J.V. (2002). Mold material thermophysical data. *AFS Transaction*, Vol.02-080, (2002), pp. 1-16, ISSN 0065-8375.

Miettinen, J. (2001). Thermodynamic-Kinetic simulation of solidification in binary fcc copper alloys with calculation of thermophysical properties. *Computational Materials Science*, Vol. 22, No. 3-4, (December 2001), pp. 240-260, ISSN 0927-0256.

Montgomery C.D. "Design and Analysis of Experiments", John Wiley & Sons, New York, 1999.

Paterakis, P. G., Korakianiti, E. S., Dallas, P. P & Rekkas, D. M. (2002). Evaluation and simultaneous optimization of some pellets characteristics using a 33 factorial design and the desirability function. *International Journal of Pharmaceutics*, Vol. 248, No. 1-2, (November 2002), pp. 51-60, ISSN 0378-5173.

Pericleous, K., Bojarevics, V., Djambazov, G., Harding, R. A. & Wickins, M. (2006). Experimental and numerical study of the cold crucible melting process. *Applied mathematical modeling*, Vol. 30, No. 11, (November 2006), pp. 1262–1280, ISSN 0307-904.

Pierlot, C., Pawlowski, L., Bigan, M. & Chagnon, P. (2008). Design of experiments in thermal spraying: a review. *Surface & Coatings Technology,* Vol. 202, No. 18, (June 2008), pp. 4483–4490, ISSN 0257-8972.

Quaresma, J. M. V., Santos, C. A. & Garcia, A. (2000). Correlation between unsteady-state solidification conditions, dendrite spacings, and mechanical properties of Al-Cu alloys. *Metallurgical and Materials Transactions*, Vol. A 31, No. 12, (May 2000), pp. 3167- 3177, ISSN 1073-5623.

Radovic, Z. & Lalovic, M. (2005). Numerical simulation of steel ingot solidification process. *Journal of Materials Processing Technology*, Vol. 160, No. 2, (March 2005), pp. 156–159, ISSN 0924-0136.

Rosa, D., Spinelli, J., Ferreira, I. L., Garcia, A. Cellular/dendritic transition and microstructure evolution during transient directional solidification of pb-sb alloys. *Metallurgical and Materials Transactions*, Vol. A 39, (September 2008), pp. 2161-2174. ISSN 1073-5623.

Santos, C. A., Fortaleza, E. L., Ferreira, C. R. F., Spim, J. A. & Garcia A. (2005). A solidification heat transfer model and a neural network based algorithm applied to the continuous casting of steel billets and blooms. *Modelling and Simulaton in Materials. Science and Engineering*, Vol. 13, (September 2005), pp. 1071–1087, ISSN 0965-0393.

Shi, Z. & Guo, Z. X. (2004). Numerical heat transfer modeling for wire casting. *Materials Science and Engineering*, Vol. A 365, No. 1-2, (January 2004), pp. 311–317, ISSN 0921-5093.

Su, X. "Computer aided optimization of an investment bi-metal casting process". Ph.D. Thesis, University of Cincinnati, Department of Mechanical, Industrial and Nuclear Engineering. Cincinnati, 2001.

Thermo-Calc Software, Stockholm, Sweden, 2010.

Xiao, Z. & Vien, A. (2004). Experimental designs for precise parameter estimation for non-linear models. *Minerals Engineering*, Vol. 17, No. 3, (March 2004), pp. 431–436, ISSN 0892-6875.

Yetilmezsoy, K., Demirel, S. & Vanderbei, R. J. (2009). Response surface modeling of Pb(II) removal from aqueous solution by Pistacia vera L.: Box–Behnken experimental design. *Journal of Hazardous Materials*, Vol. 171, No. 1-3, (November 2009), pp. 551–562, ISSN 0304-3894.